Dissertation
submitted to the
Combined Faculties of the Natural Sciences and Mathematics
of the Ruperto-Carola University of Heidelberg, Germany
for the degree of
Doctor of Natural Sciences

put forward by

Stefano Michele Cavaletto

born in Ivrea, Italy

Oral examination: December 11th, 2013

Quantum control of x-ray spectra

Referees: **Hon. Prof. Dr. Christoph H. Keitel**
PD Dr. Sandro M. Wimberger

Zusammenfassung

Die direkte und optische Kontrolle atomarer Röntgenübergänge wird durch die Analyse der Resonanzfluoreszenz- und der Absorptionsspektren theoretisch untersucht. Diese Arbeit ist motiviert durch die rapide, die Anwendung von Quantenkontrollschemata mit Röntgenstrahlen ermöglichende Entwicklung von Hochfrequenzlichtquellen. In einem Zweizustandssystem werden die Rabi-Oszillationen von Innerschalenelektronen untersucht, die von starken Röntgenpulsen erzeugt werden und die gegen den konkurrierenden Auger-Zerfall des Systems aufkommen. Anschließend wird die optische Manipulation hochenergetischer Zustände durch einen optischen Frequenzkamm betrachtet, der deren spontanen Zerfall beeinflusst, indem er zwei benachbarte angeregte Niveaus verbindet. Zuerst wird ein Modell entwickelt, das beschreibt, wie durch die Anwendung von Schmalbandröntgenstrahlen die dynamischen Variablen des Atoms periodisch gestaltet werden können, wodurch im Resonanzfluoreszenzspektrum ein Röntgenfrequenzkamm entsteht. Ein realistischeres Modell zur direkten experimentellen Umsetzung wird daraufhin vorgestellt, um ins Absorptionsspektrum eines ultrakurzen Röntgenpulses einen Kamm einzuprägen. Eine experimentelle Realisierung der hier vorhergesagten Kammstrukturen wird die Überführung der Präzision eines optischen Frequenzkammes in den Röntgenbereich ermöglichen.

Abstract

The direct and optical control of x-ray transitions is studied theoretically by investigating the spectra of resonance fluorescence and absorption. The work is motivated by the rapid advances in x-ray science, enabling the application of quantum-control schemes at short wavelengths. In a two-level system we study Rabi oscillations of atomic inner-shell electrons, induced by intense x-ray pulses and competing with Auger decay, and their signature in the spectrum of resonance fluorescence. Subsequently, optical manipulation of x-ray transitions is examined, by employing an optical frequency comb coupling nearby excited levels to control their spontaneous decay. First, narrow-bandwidth x rays are adopted, giving rise to the periodic shaping of the atomic dynamic variables and the imprinting of a comb onto the x-ray resonance fluorescence spectrum. A more realistic model for an immediate experimental implementation is then provided, by developing a scheme to imprint a comb onto the absorption spectrum of an ultrashort x-ray pulse. An experimental realization of the predicted comb structures is anticipated to transfer the accuracy of optical frequency combs into the x-ray regime.

Within the framework of this thesis, the following articles were published in refereed journals:

- S. M. Cavaletto, C. Buth, Z. Harman, E. P. Kanter, S. H. Southworth, L. Young, and C. H. Keitel,
  Resonance fluorescence in ultrafast and intense x-ray free-electron-laser pulses,
  Phys. Rev. A **86**, 033402 (2012), arXiv:1205.4918.

- B. W. Adams, C. Buth, S. M. Cavaletto, J. Evers, Z. Harman, C. H. Keitel, A. Pálffy, A. Picón, R. Röhlsberger, Y. Rostovtsev, and K. Tamasaku,
  X-ray quantum optics,
  J. Mod. Opt. **60**, 2 (2013).

Within the framework of this thesis, the following articles were submitted for publication in refereed journals:

- S. M. Cavaletto, Z. Harman, C. Buth, and C. H. Keitel,
  X-ray frequency combs from optically controlled resonance fluorescence,
  submitted (2013), arXiv:1302.3141.

- Z. Liu, C. Ott, S. M. Cavaletto, Z. Harman, C. H. Keitel, and T. Pfeifer,
  Generation of high-frequency combs locked to atomic resonances by quantum phase modulation,
  submitted (2013), arXiv:1309.6335.

- S. M. Cavaletto, Z. Harman, C. Ott, C. Buth, T. Pfeifer, and C. H. Keitel,
  Broadband high-resolution x-ray frequency combs,
  submitted (2013).

Contents

Sie begriffen, daß die Vernunft nur das einsieht, was sie selbst nach ihrem Entwurfe hervorbringt, daß sie mit Principien ihrer Urtheile nach beständigen Gesetzen vorangehen und die Natur nöthigen müsse auf ihre Fragen zu antworten, nicht aber sich von ihr allein gleichsam am Leitbande gängeln lassen müsse; denn sonst hängen zufällige, nach keinem vorher entworfenen Plane gemachte Beobachtungen gar nicht in einem nothwendigen Gesetze zusammen, welches doch die Vernunft sucht und bedarf.

Immanuel Kant,
Kritik der reinen Vernunft, Vorrede zur zweiten Auflage

1 Introduction

Optical lasers and frequency combs

A laser, acronym for *light amplification by stimulated emission of radiation*, is an intense source of coherent light [1]. By setting a condition of population inversion in a gain medium, the radiation is amplified by the principle of stimulated emission, first recognized by Einstein in 1916 [2]. The maser, i.e., *microwave amplification by stimulated emission of radiation*, whose idea was conceived by Townes, Gordon, Zeiger, Basov, and Prokhorov, first showed the realization of coherent light in the microwave region and only in 1960, after the work of Townes and Schawlow [3], the first optical laser was realized by Maiman [4]. Owing to the narrow bandwidth and high intensity it provides, the laser played a fundamental role in the development of quantum optics, i.e., the quantum theory of light and of its interaction with matter [5–7], the theory of light coherence [8], and nonlinear optics [9]. Not only are lasers ubiquitous in modern technology, being routinely adopted in everyday-life electronic devices, but they are utilized in several, sometimes completely independent sectors of modern physics. For instance, techniques for laser trapping and cooling of atoms and molecules, whose development could count on the fundamental contributions from Chu, Cohen-Tannoudji, and Philips [10–12], allowed Cornell, Ketterle, and Wieman to successfully demonstrate Bose-Einstein condensation in 1995 [13, 14], more than 70 years after its prediction in 1924 [15–17]. Laser trapped ultracold atoms and ions currently represent an essential tool for quantum information and quantum simulation [18, 19]. Significant advances in our understanding of quantum dynamics in physics and chemistry were stimulated by the availability of ultrashort attosecond-laser pulses, which allow one to observe the electron motion in atoms and molecules [20]. However, one of the fields that most fruitfully took advantage of the innovative possibilities offered by the laser is precision spectroscopy. The high monochromaticity and tunability provided by lasers, along with techniques developed during the 1970s for nonlinear Doppler-free spectroscopy [21], had a significant impact on the precision with which optical frequencies could be measured.

In precision spectroscopy, the direct measurement of a frequency should be preferred to that of a wavelength. Since 1967, in fact, the definition of time (and, therefore, of frequency) is based on "*the radiation corresponding to the transition between the two hyperfine levels of the ground state of the cesium 133 atom*" [22], whose frequency is exactly equal to 9,192,631,770 Hz, in the radio-frequency range. For a long time, this rendered very challenging to extend the possibilities of accurate spectroscopy to frequencies higher than $\sim 100\,\mathrm{GHz}$. A significant progress was achieved only through the introduction and development of optical frequency combs by Hänsch and Hall [23–26].

An optical frequency comb consists in a series of equidistant spectral lines centered at the optical frequency ω_C, as displayed in Fig. 1.1 and thoroughly introduced in Appendix A. The frequency ω_k of each peak in the comb,

$$\omega_k = \omega_\mathrm{C} + k\omega_\mathrm{r} = \omega_\mathrm{o} + k'\omega_\mathrm{r}, \tag{1.1}$$

with k, $k' \in \mathbb{Z}$, is entirely determined by the offset frequency ω_o and the repetition frequency ω_r. The possibility to precisely measure, e.g., with a cesium atomic clock, these two radio frequencies ω_r and ω_o and directly link them to an optical frequency ω_k revolutionized the field of precision

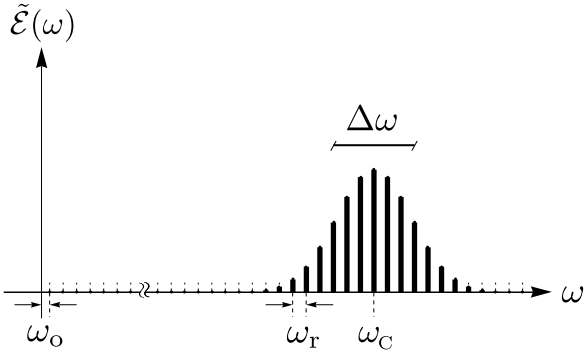

Figure 1.1: The spectrum of an optical frequency comb centered at the optical frequency ω_{C} is represented by the thick lines, with repetition frequency ω_{r} and overall width $\Delta\omega$. By extending the equidistant lines to the origin of the frequency axis, the offset frequency ω_{o} can be determined. Similar pictures are widely adopted in the literature to present the properties of a frequency comb, see, e.g., Refs. [23, 24].

spectroscopy. A comb-like frequency structure was already clearly apparent in mode-locked lasers from the early 1970s [27]: However, it was not until the late 1990s [28, 29] that stabilized mode-locked femtosecond lasers succeeded in providing combs with the required control over ω_{o} and ω_{r}.

Optical frequency combs were initially generated via intracavity phase modulation, i.e., by placing an electro-optic modulator inside a low-loss optical cavity to generate modulation sidebands of the optical carrier frequency [30, 31]. The resulting spectrum is a set of equally distant peaks, with accurately determined spacing frequency, despite being centered at a carrier frequency which is not determined with equal accuracy. Such a comb aimed at bridging wide frequency intervals, i.e., between an optical reference and an unknown optical frequency. It was only subsequently that the spectrum of stabilized mode-locked lasers provided a comb [28, 29, 32–37] to measure an optical transition with unprecedented accuracies, up to 10^{-18} [38, 39]. A significant step forward was in particular the generation of octave-spanning frequency combs, i.e., combs spanning a factor two in frequency: As discussed in Appendix A, this considerably simplified the direct measurement and stabilization of the offset frequency ω_{o}.

In addition to the direct use in metrology and spectroscopy, optical frequency combs play a crucial role in the realization of all-optical atomic clocks [25, 38, 40], by precisely counting optical oscillations, e.g., in trapped-atom and -ion standards [41]. Additional examples of the plethora of applications of optical frequency combs range from the calibration of astronomical spectrographs [42, 43], which are essential for the discovery of earthlike extrasolar planets or for the direct measurement of the cosmic-expansion rate [44], to the control of atomic coherence [45, 46] and molecular dynamics [47]. Furthermore, by virtue of the stabilized offset phase which they exploit, optical frequency combs were widely employed in the quantum control of phase matching in high-order harmonic generation (HHG) [48, 49] and in attosecond-pulse generation [20, 35, 50].

Resonance fluorescence and absorption spectra

Laser spectroscopy of atoms and ions takes advantage of the spectral features of the signal emitted upon interaction with a coherent source of light and which unequivocally characterizes the atomic species under study. The response of a system of atoms or ions which are excited by an external field can be studied by measuring either the resonance fluorescence or the absorption signal which is produced.

The spectrum of resonance fluorescence which is emitted by an ensemble of atoms and ions

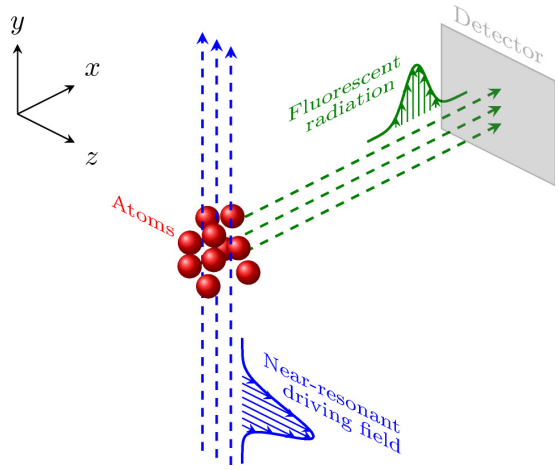

Figure 1.2: An atom ensemble (red) is driven by x rays (blue) tuned to a resonance. The emitted photons (green) are measured perpendicularly to the propagation direction of the x rays.

driven by an intense, near-resonant electric field [51, 52] is one of the cornerstones of quantum optics [53, 54]. The spectrum is measured experimentally by exposing an atomic ensemble to intense light and detecting the scattered photons as shown in Fig. 1.2. During the last decades such studies have received wide attention and have stimulated the development of nonperturbative methods in quantum electrodynamics for the investigation of the coherent interaction between light and matter [55–60].

The resonance fluorescence spectrum of a two-level quantum system driven by a monochromatic electric field has been studied extensively at optical frequencies [55, 56, 61–63]. For a sufficiently strong continuous-wave driving field, a nonlinear three-peak structure appears in the spectrum [64–66], which is explained theoretically by the nonperturbative approach of Mollow [55, 56]. The presence of a strong external field, which resonantly drives an atomic transition, "dresses" the atomic bare energy levels [67], which split as a result of this additional interaction term. This frequently called dynamic (or AC) Stark splitting gives rise to the previously described three-peak structure emerging in the resonance fluorescence spectrum. The same effect can be alternatively understood from a time-dependent perspective, in terms of Rabi flopping of the bare atomic dynamical variables. The external field induces Rabi oscillations of the populations and coherences of the bare atomic levels at a frequency (Rabi frequency) proportional to the strength of the driving field.

A continuous-wave field is one of the few cases for which an exact analytical solution of the equations of motion of the two-level system exists. When the system interacts with a short pulse, a special class of time-dependent functions, including the case of a hyperbolic-secant pulse, were analytically explored for particular values of the physical parameters [68–70] and a rich multipeak structure in the spectrum of resonance fluorescence was predicted [71–77]. This property, which still represents a signature of Rabi oscillations induced by the intense driving field, is also predicted to depend upon the pulse area, but cannot be intuitively explained by means of dressed states [78].

An analogous dependence upon the induced time evolution of an atomic system is exhibited by the absorption spectrum. In usual studies of absorption spectra, a system driven by a strong (pump) field interacts with a weak (probe) continuous-wave field of frequency ω_0: although this field is weak enough not to significantly modify the time evolution of the system, its absorption can strongly depend on its central frequency ω_0. By repeating the experiment for fields of

different central frequency ω_0, one obtains a spectrum containing information complementary to that coming from emission spectra of resonance fluorescence in the absence of the probe field [57, 58, 79, 80].

A different approach characterizes studies of transient absorption in which an ultrashort, broadband pulse is used as a probe field. The transmission and absorption of the different frequency components of the wide-bandwidth probe pulse can be studied as a function of the time delay between the pump and the probe in a time-dependent perspective [81, 82]. Similar pump-probe schemes are of particular interest for many-level systems, in which the pump and the probe pulses are near-resonant to two different atomic transitions. For such cases, a proper choice of the duration of the two pulses and of the delay can induce coherent trapping and other quantum-coherence phenomena, e.g., electromagnetically induced transparency (EIT) [83], stimulated rapid adiabatic passage (STIRAP) [84], and lasing without inversion (LWI) [85], which can be identified experimentally by the observation of the absorption spectrum of a wide-bandwidth probe pulse.

Short-wavelength light sources

The fundamental role played by optical lasers in a manifold of different sectors, from basic research to applied engineering, explains the efforts which, since the invention of the laser, were put into the development of intense, coherent, short-wavelength light sources, in the extreme-ultraviolet (XUV) and x-ray ranges.

Since the time of their discovery by Röntgen in 1895 [86], x rays appeared to be an invaluable tool to investigate the structure of matter, with applications in physics, chemistry, biology, medicine, and engineering. Only in the 1970s, however, it was realized that the synchrotron radiation produced by charged particles circulating in the storage rings used for high-energy physics [87] was a much more intense and versatile source of x-ray radiation than the x-ray tubes which had been utilized until then [88]. An increase in versatility and brilliance (intensity of the emitted light) was achieved by second-generation synchrotron storage rings, explicitly built to produce x rays, and then third-generation synchrotrons, in which the x-ray emission is optimized by inserting straight sections in the ring with, e.g., an undulator [88].

An undulator consists of a set of oppositely directed magnets, producing a magnetic field which forces the electrons passing through them to perform small-amplitude oscillations. X rays emitted at different oscillations add coherently, resulting in a very intense beam [88]. The quality of the emitted x-ray field strongly depends on that of the electron beam passing through the undulator. In fourth-generation x-ray light sources, i.e., free-electron lasers (FELs), this quality is highly improved by preaccelerating the electron beam with a linear accelerator (linac) instead of employing a storage ring. The linac at the Stanford Linear Accelerator Center (SLAC, today called SLAC National Accelerator Laboratory), initially built for high-energy experiments, is now entirely adopted to preaccelerate electrons for the Linac Coherent Light Source (LCLS), the world's first hard x-ray FEL. X-ray free-electron lasers (XFELs) [89–93] provide tunable x-ray pulses of unprecedented brilliance, up to one billion times higher than the intensity available at third-generation synchrotron facilities. The intense and ultrafast pulses now available at XFELs offer new tools for imaging [94–96], along with the opportunity to study nonlinear physics at short wavelengths [97–107].

Despite the name, a free-electron laser is not based on the light amplification of spontaneously emitted radiation in a gain medium. Extending lasing into the x-ray region, in fact, has faced many difficulties [108], mostly due to the lack of high-reflectivity mirrors for x-ray radiation and the very short duration of population inversion due to the fast decay time of x-ray levels. Existing

XFEL facilities are based on the principle of Self-Amplified Spontaneous Emission (SASE) [109–111]. The initially emitted, chaotic radiation interacts with the electron beam, such that this self organizes into bunches of electrons propagating together through the undulator and emitting x rays in phase. This gives rise to very intense femtosecond pulses at hard x-ray frequency which, as a result of the initial chaotic emission, possess only partial temporal coherence and a spiky temporal profile. An analogous situation occurred at the beginning of optical laser science, when the interaction with the chaotic pulses available at that time was investigated [112, 113].

Self-seeding or optical laser-seeding methods are being developed, which are significantly improving the time coherence of the pulses generated at XFELs. In such cases, the emitted light is produced by the amplification of a regular (Gaussian) seeding pulse which exhibits high temporal coherence [114–119]. This results in a considerable improvement in the time coherence of the emitted pulses.

In spite of the enormous advances in XFEL sources, the coherence which they provide is still not sufficient for applications in precision spectroscopy. Owing to the lack of x-ray lasers, the generation of XUV combs via intracavity HHG [120, 121] is presently recognized as the most promising tool to extend precision spectroscopy to the short-wavelength domain [122]. Going up to even higher frequencies, x-ray frequency combs would enable precise measurements of high-energy transitions paralleling the accuracy achieved for optical frequencies, with an improvement of several orders of magnitude. This would allow, to name but a few examples, even more stringent experimental tests of quantum electrodynamics and astrophysical models [123] and search for the variability of the fine-structure constant, to which transitions in highly charged ions are predicted to be more sensitive [124]. One may also envision ultraprecise x-ray atomic clocks [125].

While in conventional HHG an optical pulse in a gas produces a spectrum of odd harmonics of the optical frequency, in intracavity HHG, a train of coherent optical pulses generates a spectrum which in each harmonic line is structured into a fine comb. Based on this scheme, Ref. [122] reported the observation of frequency combs at $\sim$ 40 nm ($\sim$ 30 eV). The required optical peak intensity of $\sim 10^{14}$ W/cm^2 was obtained with a femtosecond enhancement cavity. Yet relativistic effects limit the range in which HHG operates efficiently [126], i.e., where x-ray frequency combs are presently advisable with HHG-based methods. Investigations of alternative schemes are, therefore, timely.

Motivation of the Thesis and key results

The just described advances in nonlinear physics and x-ray science inspired the work presented in this Thesis. In particular, the rapid development of x-ray light sources, which on the one hand opens up novel possibilities, but on the other hand still requires further theoretical and experimental research, stimulated and motivated the investigations which were pursued in this work.

The progress in x-ray science enables the extension of tools and methods from quantum optics to the x-ray regime [127]. Because of the lack of coherent and sufficiently intense light sources at short wavelengths, previous studies of strong-field resonance fluorescence have been relevant for a long time only at optical frequencies, for which a wide range of models and schemes have been investigated [128–134]. Auger decay of inner-shell electronic levels takes place on a femtosecond time scale. In order to actively control these K-shell electrons with an external field, e.g., by repeatedly induce stimulated emission and absorption (Rabi flopping) within their Auger decay time, a very intense and coherent x-ray light source is necessary, which for a long time has not been available. The intense and ultrafast pulses now produced at XFELs, however, offer the

opportunity to induce Rabi flopping on a time scale that can be compared to, and therefore compete with, the ultrafast inner-shell Auger decay. Active control of inner-shell electrons would have a considerable impact on x-ray science, providing the necessary instruments, e.g., for the suppression of x-ray radiation damage via inhibition of Auger decay [135] and the modification of nuclear lifetimes [136, 137]. Recent theoretical and experimental investigations, focusing on resonant-Auger-decay electron spectra [138, 139], were not conclusive. An alternative and more easily accessible point of view could be provided by studies of resonance fluorescence, i.e., by investigating the appearance of Rabi flopping in the x-ray spectrum of photons emitted upon interaction with strong pulses from an XFEL. This motivates the analysis in Chapter 3. For x-ray SASE pulses we show that, although Rabi flopping does not manifest itself clearly because of the large bandwidth of the employed driving x-ray source, tails in the spectrum of resonance fluorescence appear, which represent a good signature of atomic Rabi oscillations induced by the intense x rays driving the system. In the case of laser-like Gaussian pulses, a clear signature of Rabi flopping is predicted, thus rendering the prospects with self-seeded XFELs very promising.

An even more powerful setup is obtained when the just described x-ray-only scheme is augmented by an optical pulse coupling to a nearby excited level. Initial investigations of resonance fluorescence and absorption in three-level systems employed two driving continuous-wave fields [57, 58]. There, it was shown how an optical laser, coupled to a resonant transition, can influence the properties of the other off-resonant transitions. This provides an effective tool to optically manipulate the features of a higher-energy transition, with direct impact upon the related spectra of resonance fluorescence and absorption.

Similar optical-control schemes played a major role in recent studies of EIT at x-ray frequencies [140, 141]: There, a long x-ray pulse propagates through a dense gas of Ne^+ ions which is simultaneously driven by a shorter, intense optical pulse. In the absence of the optical field, the x-ray pulse is strongly absorbed by the dense gas. However, the presence of the optical pulse, owing to the imprinted splitting of the resonant levels, modifies the atomic x-ray absorption spectrum and renders the gas transparent to the x-ray pulse. This results in a pulse-shaping method to optically manipulate the intensity profile of an x-ray field. These results triggered additional studies of laser-induced interference effects in transient absorption and impulsive manipulation of x-ray spectral line shapes [142–147]. In these works, however, only interference effects which ensue from the interaction of an ensemble of ions with a single optical pulse were analyzed.

In Chapters 4, 5, and 6, we aim to extend these single-optical-pulse studies to the case of a driving, periodic train of coherent optical pulses, i.e., an optical frequency comb. This represents a novel example of an x-ray amplitude- and phase-shaping scheme which we study by focusing on those interference effects which emerge in the resonance-fluorescence and absorption spectra. Furthermore, in light of the challenges which currently explored methods for x-ray-comb generation are facing, we study the possibility to exploit this quantum-control scheme to imprint a comb onto the x-ray component of the spectrum. We further investigate how this method may alternatively address those problems which present HHG-based schemes are facing because of the limits set to the efficiency of HHG at high harmonic orders by relativistic effects.

First, we develop a wave-mixing scheme to generate an x-ray frequency comb on the spectrum of resonance fluorescence, by driving a multi-level system with narrow-bandwidth x rays and an optical frequency comb. The width of the peaks in the comb is determined by the bandwidth of the utilized x-ray light source. The scheme is applied to model isolated transitions in He-like ions. Thereby, we predict a comb which is as wide as the driving optical frequency comb and, for Be^{2+}, is centered on the x-ray atomic transition energy at $\sim 120\,\mathrm{eV}$. This is four times higher than the central frequency of XUV frequency combs demonstrated with HHG [122]. The necessary optical-frequency-comb peak intensity is predicted to be $\sim 10^{10}\,\mathrm{W/cm^2}$, by several

orders of magnitude lower than the peak intensities presently required for HHG-based XUV-comb-generation schemes.

Since present x-ray FEL sources do not provide small-bandwidth x rays, we then provide a more robust scheme to imprint a comb onto the absorption spectrum of an ultrashort x-ray pulse, such as those presently generated at XFEL facilities. This second model may be employed, therefore, with currently available x-ray and optical-frequency-comb technology to generate a comb at x-ray photon energies. The scheme allows one to control the width and the number of peaks in the generated x-ray frequency comb, by properly taking advantage of long-lived excited states in a multi-level system. Also in this case, we manage to push the central frequency of the generated comb into the 100-eV range while maintaining the intensity of the driving optical frequency comb at $\sim 10^{10}\,\mathrm{W/cm^2}$.

Structure of the Thesis

The Thesis is organized as follows:

In Chapter 2 we introduce the theoretical background and the notation which is employed throughout the Thesis. We focus on the interaction between light and matter in a time-frequency perspective, stressing those concepts, such as Rabi flopping, which play a major role in the following Chapters.

In Chapter 3 we study, in terms of a two-level model, the coherent interaction of x rays with core electrons by exciting K-shell transitions. In a recent experiment, intense and ultrashort x-ray pulses from the LCLS have been utilized to excite the $1s\,2p^{-1} \rightarrow 1s^{-1}\,2p$ transition at 848 eV in Ne^+ [139]. The electron spectrum of resonant Auger decay was measured to investigate Rabi flopping. However, with only partial coherence of the SASE pulses available at LCLS and the lack of means for single-shot diagnostics, the clear observation of Rabi oscillations and its distinction from noise effects was challenging [139]. In this Chapter, we aim at predicting how the induced Rabi flopping could be detected in the spectrum of resonance fluorescence. This paves the way for further theoretical and experimental studies of active control of inner-shell transitions and their application.

By going from the x-ray-only setup of Chapter 3 to a many-color scheme, in Chapter 4 we study the optical modification of the x-ray resonance fluorescence spectrum in a four-level system driven by small-wavelength x rays and an optical frequency comb. The resulting spectrum is a frequency comb centered at the x-ray atomic transition energy, with as many peaks as the driving optical frequency comb and with intensities comparable to those obtained via HHG-based methods. The comb may be used to bridge an energy difference between an x-ray reference level and an unknown x-ray frequency, similarly to the way optical-frequency comb-generation schemes based on intracavity phase modulation were exploited [30, 31]. We show that our proposed scheme requires lower optical peak intensities than present x-ray comb-generation methods and could be applied, e.g., with highly charged ions as multi-level quantum system, at large x-ray transition energies for which x-ray frequency-comb generation via HHG-based methods would encounter significant obstacles [126].

In contrast to the previous Chapters focusing on resonance fluorescence, Chapter 5 discusses the optically modified absorption spectrum of an ultrashort x-ray pulse which interacts with a low-density gas of particles. In particular, we derive the equations for the calculation of the absorption spectrum of the transmitted x-ray field and investigate the coherent population transfer taking place when an optical pulse couples an x-ray-driven excited level to a nearby metastable state.

These concepts are further implemented in Chapter 6 to investigate how differently the system

studied in Chapter 5 is affected if, instead of a single pulse, an optical frequency comb is employed. Also in this Chapter, similarly to Chapter 4, we aim at developing an x-ray comb-generation scheme which can be utilized at high photon energies, for which HHG-based methods are not advisable. The main difference lies in the assumptions about the x-ray driving field: While in Chapter 5 a narrow-bandwidth x-ray field is assumed to drive an atomic transition in a many-level system, the method developed in Chapter 6 takes advantage of a broadband, ultrashort pulse such as those presently available at FELs. By driving the system with an optical frequency comb, we periodically modify the coherent response of the atomic system, thus imprinting a comb onto the absorption spectrum of the transmitted x-ray field.

Finally, Chapter 7 summarizes the main results of this Thesis and presents possible directions to which this work may lead.

Units

Atomic units (a.u.) are employed throughout the Thesis, unless otherwise stated, for which the electron mass, the reduced Planck constant, the charge of the electron, and the vacuum permittivity are, respectively, $m_e = \hbar = -e = 4\pi\varepsilon_0 = 1\,\text{a.u.}$ The Bohr radius is $a_0 = \frac{4\pi\varepsilon_0\hbar^2}{m_e e^2} = 1\,\text{a.u.}$, and, from the definition of the fine-structure constant $\alpha = \frac{e^2}{4\pi\varepsilon_0\hbar c} \approx \frac{1}{137}$, the speed of light in vacuum is $c = \frac{1}{\alpha}\,\text{a.u.} \approx 137\,\text{a.u.}$ The Hartree, fundamental unit of energy in atomic units, equals $1E_h = \frac{\hbar^2}{a_0^2 m_e} \approx 27.2\,\text{eV}$.

2 Time and spectral properties of the interaction of light with matter

In the present Chapter we introduce the general mathematical model for describing the interaction of a low-density ensemble of particles interacting with an external electric field. As in the following we are always interested in near-resonance conditions between an electromagnetic field and a corresponding atomic transition, we are allowed to model the particles as a set of multi-level systems with a limited number of states. The general framework presented here will be specialized in each Section, where a fixed number of fields and a corresponding number of levels will be studied. The Chapter contains a personal presentation of well known topics and results, a discussion of which is material of standard atomic-physics and quantum-optics textbooks [7, 53, 54, 148–150].

2.1 Theory of the interaction of light with matter

In this Section we introduce the classical theory of the interaction between a single atom, with a nucleus with positive charge Z at position $\boldsymbol{r} = \boldsymbol{0}$, surrounded by Q electrons of positions $\boldsymbol{r}_q$ and velocity $\dot{\boldsymbol{r}}_q$, $q \in \{1, \ldots, Q\}$, and an external electromagnetic field, with classical electric and magnetic fields, $\boldsymbol{E}(\boldsymbol{r}, t)$ and $\boldsymbol{B}(\boldsymbol{r}, t)$, respectively. When both the atom and the electromagnetic field are treated classically, such system is described by the microscopic Maxwell's equations [87]

$$\boldsymbol{\nabla} \cdot \boldsymbol{E}(\boldsymbol{r},\, t) = 4\pi\rho(\boldsymbol{r},\, t), \tag{2.1a}$$

$$\boldsymbol{\nabla} \cdot \boldsymbol{B}(\boldsymbol{r},\, t) = 0, \tag{2.1b}$$

$$\boldsymbol{\nabla} \times \boldsymbol{E}(\boldsymbol{r},\, t) = -\frac{\partial \boldsymbol{B}(\boldsymbol{r},\, t)}{\partial t}, \tag{2.1c}$$

$$\boldsymbol{\nabla} \times \boldsymbol{B}(\boldsymbol{r},\, t) = \frac{1}{c^2}\left(\frac{\partial \boldsymbol{E}(\boldsymbol{r},\, t)}{\partial t} + 4\pi \boldsymbol{J}(\boldsymbol{r},\, t)\right), \tag{2.1d}$$

with the charge and current densities

$$\rho(\boldsymbol{r},\, t) = -\sum_{q=1}^{Q} \delta(\boldsymbol{r} - \boldsymbol{r}_q(t)) + Z\delta(\boldsymbol{r}), \tag{2.2a}$$

$$\boldsymbol{J}(\boldsymbol{r},\, t) = -\sum_{q=1}^{Q} \dot{\boldsymbol{r}}_q(t)\, \delta(\boldsymbol{r} - \boldsymbol{r}_q(t)), \tag{2.2b}$$

together with the Lorentz's force

$$\frac{\partial^2 \boldsymbol{r}_q}{\partial t^2} = -[\boldsymbol{E}(\boldsymbol{r}_q,\, t) + \dot{\boldsymbol{r}}_q \times \boldsymbol{B}(\boldsymbol{r}_q,\, t)]. \tag{2.3}$$

This set of differential equations can be recovered in the Lagrangian formalism [151]. We introduce the generalized coordinates $\boldsymbol{r}_q$, $\boldsymbol{A}(\boldsymbol{r})$, and $U(\boldsymbol{r})$, with associated generalized velocities $\dot{\boldsymbol{r}}_q$,

$\dot{\boldsymbol{A}}(\boldsymbol{r})$, and $\dot{U}(\boldsymbol{r})$. For this purpose, the electromagnetic field is better described by the vector potential $\boldsymbol{A}(\boldsymbol{r},t)$ and the scalar potential $U(\boldsymbol{r},t)$, defined such that [87]

$$\boldsymbol{B}(\boldsymbol{r},t) = \boldsymbol{\nabla}\times\boldsymbol{A}(\boldsymbol{r},t), \tag{2.4a}$$

$$\boldsymbol{E}(\boldsymbol{r},t) = -\boldsymbol{\nabla}U(\boldsymbol{r},t) - \frac{\partial\boldsymbol{A}(\boldsymbol{r},t)}{\partial t}. \tag{2.4b}$$

Lagrange's equations [151]

$$\frac{\mathrm{d}}{\mathrm{d}t}\frac{\partial L}{\partial\dot{\boldsymbol{r}}_q} - \frac{\partial L}{\partial\boldsymbol{r}_q} = 0, \tag{2.5a}$$

$$\frac{\mathrm{d}}{\mathrm{d}t}\frac{\partial\mathscr{L}}{\partial\dot{\zeta}} - \frac{\partial\mathscr{L}}{\partial\zeta} + \boldsymbol{\nabla}\cdot\frac{\partial\mathscr{L}}{\partial(\boldsymbol{\nabla}\zeta)} = 0, \tag{2.5b}$$

where $\zeta\in\{U(\boldsymbol{r}),\, A_i(\boldsymbol{r})\}$, $i\in\{x,\, y,\, z\}$, with the Lagrangian

$$L = \sum_{q=1}^{Q}\frac{|\dot{\boldsymbol{r}}_q|^2}{2} + \int\mathscr{L}\,\mathrm{d}^3r \tag{2.6}$$

and the Lagrangian density

$$\mathscr{L} = \frac{1}{8\pi}[E^2(\boldsymbol{r}) - c^2B^2(\boldsymbol{r})] - \sum_{q=1}^{Q}[\dot{\boldsymbol{r}}_q\cdot\boldsymbol{A}(\boldsymbol{r}) - U(\boldsymbol{r})]\,\delta(\boldsymbol{r}-\boldsymbol{r}_q), \tag{2.7}$$

provide one with the correct Lorentz-Maxwell equations (2.1) and (2.3).

From (2.4), the two potentials $\boldsymbol{A}(\boldsymbol{r},t)$ and $U(\boldsymbol{r},t)$ are not unequivocally determined, as the physical fields $\boldsymbol{E}(\boldsymbol{r},t)$ and $\boldsymbol{B}(\boldsymbol{r},t)$ remain unchanged under the **gauge transformation** $\boldsymbol{A}(\boldsymbol{r},t)\to\boldsymbol{A}(\boldsymbol{r},t)+\boldsymbol{\nabla}f(\boldsymbol{r},t)$, $U(\boldsymbol{r},t)\to U(\boldsymbol{r},t)-\frac{\partial f(\boldsymbol{r},t)}{\partial t}$, for a generic, differentiable function $f(\boldsymbol{r},\,t)$ [87]. The usually chosen gauge is the Coulomb gauge [87], in which

$$\boldsymbol{\nabla}\cdot\boldsymbol{A}(\boldsymbol{r},t) = 0, \tag{2.8a}$$

$$U(\boldsymbol{r},t) = \frac{Z}{r} - \sum_{q'=1}^{Q}\frac{1}{|\boldsymbol{r}-\boldsymbol{r}_{q'}(t)|}, \tag{2.8b}$$

such that the vector potential $\boldsymbol{A}(\boldsymbol{r},t)$ is transverse[1] and the scalar potential $U(\boldsymbol{r},t)$, from direct application of the Maxwell's equations, coincides with the Coulomb potential due to the interaction between particles. In such gauge, the Lagrangian becomes

$$L = \sum_{q=1}^{Q}\frac{|\dot{\boldsymbol{r}}_q|^2}{2} + \sum_{q=1}^{Q}\left[\frac{Z}{r_q} - \sum_{q'=q+1}^{Q}\frac{1}{|\boldsymbol{r}_q(t)-\boldsymbol{r}_{q'}(t)|}\right] + \int\mathscr{L}\,\mathrm{d}^3r, \tag{2.9}$$

with the Lagrangian density

$$\mathscr{L} = \frac{1}{8\pi}[E_\perp^2(\boldsymbol{r}) - c^2B^2(\boldsymbol{r})] - \sum_{q=1}^{Q}\dot{\boldsymbol{r}}_q\cdot\boldsymbol{A}(\boldsymbol{r})\,\delta(\boldsymbol{r}-\boldsymbol{r}_q). \tag{2.10}$$

The electric field is $\boldsymbol{E}(\boldsymbol{r},t) = \boldsymbol{E}_\perp(\boldsymbol{r},t)+\boldsymbol{E}_\parallel(\boldsymbol{r},t)$, with $\boldsymbol{E}_\perp(\boldsymbol{r},t) = -\frac{\partial\boldsymbol{A}(\boldsymbol{r},t)}{\partial t}$ and $\boldsymbol{E}_\parallel = -\boldsymbol{\nabla}U(\boldsymbol{r},t)$.

[1] As follows from Helmholtz's theorem, any vector $\boldsymbol{V}$ is the sum of a transverse (or solenoidal) component $\boldsymbol{V}_\perp$ and a longitudinal (or irrotational) component $\boldsymbol{V}_\parallel$, i.e., $\boldsymbol{V} = \boldsymbol{V}_\perp + \boldsymbol{V}_\parallel$, such that $\boldsymbol{\nabla}\cdot\boldsymbol{V}_\perp = 0$ and $\boldsymbol{\nabla}\times\boldsymbol{V}_\parallel = \boldsymbol{0}$.

After having introduced the conjugate momenta of the generalized coordinates $\boldsymbol{r}_q$ and $\boldsymbol{A}(\boldsymbol{r})$—$U(\boldsymbol{r},t)$ is entirely determined by the position of the particles and is not an independent variable—,

$$\boldsymbol{p}_q = \frac{\partial L}{\partial \dot{\boldsymbol{r}}_q} = \dot{\boldsymbol{r}}_q - \boldsymbol{A}(\boldsymbol{r}_q), \tag{2.11a}$$

$$\boldsymbol{\Pi}(\boldsymbol{r}) = \frac{\partial \mathscr{L}}{\partial \dot{\boldsymbol{A}}} = -\frac{\boldsymbol{E}_\perp(\boldsymbol{r})}{4\pi}, \tag{2.11b}$$

one obtains the minimal-coupling Hamiltonian [7, 148]

$$\begin{aligned} H &= \sum_{q=1}^{Q} \boldsymbol{p}_q \cdot \dot{\boldsymbol{r}}_q + \int \boldsymbol{\Pi}(\boldsymbol{r}) \cdot \dot{\boldsymbol{A}}(\boldsymbol{r}) \, \mathrm{d}^3 r - L \\ &= \sum_{q=1}^{Q} \frac{|\boldsymbol{p}_q + \boldsymbol{A}(\boldsymbol{r}_q)|^2}{2} - \sum_{q=1}^{Q} \left[\frac{Z}{r_q} - \sum_{q'=q+1}^{Q} \frac{1}{|\boldsymbol{r}_q(t) - \boldsymbol{r}_{q'}(t)|} \right] + \frac{1}{8\pi} \int [E_\perp^2(\boldsymbol{r}) + c^2 B^2(\boldsymbol{r})] \, \mathrm{d}^3 r \end{aligned} \tag{2.12}$$

in the Coulomb gauge.

An equivalent description of the electrodynamics can be obtained via a different choice of the Lagrangian [151]. The Lagrange equations are in fact not modified by any transformation [7]

$$L(x, \dot{x}) \to L'(x, \dot{x}) = L(x, \dot{x}) + \frac{\mathrm{d}F(x,t)}{\mathrm{d}t} = L(x, \dot{x}) + \dot{x} \frac{\partial F(x,t)}{\partial x} + \frac{\partial F(x,t)}{\partial t}, \tag{2.13}$$

this implying, though, a different definition of the conjugate momenta

$$p = \frac{\partial L}{\partial \dot{x}} \to p' = \frac{\partial L}{\partial \dot{x}} + \frac{\partial F(x,t)}{\partial x} = p + \frac{\partial F(x,t)}{\partial x}. \tag{2.14}$$

In order to alternatively describe the interaction between light and matter, we introduce, instead of the charge and current densities $\rho(\boldsymbol{r}, t)$ and $\boldsymbol{J}(\boldsymbol{r}, t)$, two new potentials, i.e., the polarization density $\boldsymbol{P}(\boldsymbol{r}, t)$ and magnetization density $\boldsymbol{M}(\boldsymbol{r}, t)$, such that [87]

$$\rho(\boldsymbol{r}, t) = -\boldsymbol{\nabla} \cdot \boldsymbol{P}(\boldsymbol{r}, t), \tag{2.15a}$$

$$\boldsymbol{J}(\boldsymbol{r}, t) = \dot{\boldsymbol{P}}(\boldsymbol{r}, t) + \boldsymbol{\nabla} \times \boldsymbol{M}(\boldsymbol{r}, t). \tag{2.15b}$$

These equalities, together with Eq. (2.2), are satisfied if the polarization and magnetization densities are defined as [7, 148]

$$\boldsymbol{P}(\boldsymbol{r}) = -\sum_{q=1}^{Q} \boldsymbol{r}_q \int_0^1 \delta(\boldsymbol{r} - u\boldsymbol{r}_q) \, \mathrm{d}u, \tag{2.16a}$$

$$\boldsymbol{M}(\boldsymbol{r}) = -\sum_{q=1}^{Q} \boldsymbol{r}_q \times \dot{\boldsymbol{r}}_q \int_0^1 u \, \delta(\boldsymbol{r} - u\boldsymbol{r}_q) \, \mathrm{d}u. \tag{2.16b}$$

These are used to obtain a new Lagrangian L' as in Eq. (2.13) by performing a Power-Zienau-Woolley transformation [152–154], i.e., by adding to L in the Coulomb gauge the total time derivative of the function

$$F = -\int \mathrm{d}^3 r \boldsymbol{P}(\boldsymbol{r}) \cdot \boldsymbol{A}(\boldsymbol{r}). \tag{2.17}$$

The equations of motion do remain unchanged, but the new Lagrangian reads

$$L' = \sum_{q=1}^{Q} \frac{|\dot{\boldsymbol{r}}_q|^2}{2} + \sum_{q=1}^{Q} \left[\frac{Z}{r_q} - \sum_{q'=q+1}^{Q} \frac{1}{|\boldsymbol{r}_q(t) - \boldsymbol{r}_{q'}(t)|} \right] + \int \mathscr{L}' \, \mathrm{d}^3 r, \tag{2.18}$$

with the new Lagrangian density

$$\mathscr{L}' = \frac{1}{8\pi}[E_\perp^2(\boldsymbol{r}) - c^2 B^2(\boldsymbol{r})] + \boldsymbol{M}(\boldsymbol{r}) \cdot \boldsymbol{B}(\boldsymbol{r}) + \boldsymbol{P}(\boldsymbol{r}) \cdot \boldsymbol{E}_\perp(\boldsymbol{r}). \tag{2.19}$$

The new canonical momenta are

$$\begin{aligned} \boldsymbol{p}'_q = \frac{\partial L'}{\partial \dot{\boldsymbol{r}}_q} &= \dot{\boldsymbol{r}}_q - \boldsymbol{B}(\boldsymbol{r}) \times \boldsymbol{r}_q \int_0^1 u \delta(\boldsymbol{r} - u\boldsymbol{r}_q) \, \mathrm{d}u \\ &= \boldsymbol{p}_q + \boldsymbol{A}(\boldsymbol{r}_q) - \boldsymbol{B}(\boldsymbol{r}) \times \boldsymbol{r}_q \int_0^1 u \delta(\boldsymbol{r} - u\boldsymbol{r}_q) \, \mathrm{d}u, \\ \boldsymbol{\Pi}'(\boldsymbol{r}) = \frac{\partial \mathscr{L}'}{\partial \dot{\boldsymbol{A}}} &= -\frac{\partial \mathscr{L}'}{\partial \boldsymbol{E}_\perp} = -\frac{\boldsymbol{E}_\perp(\boldsymbol{r})}{4\pi} - \boldsymbol{P}_\perp(\boldsymbol{r}) = -\frac{\boldsymbol{E}'_\perp(\boldsymbol{r})}{4\pi}, \end{aligned} \tag{2.20}$$

where we have introduced the transformed electric field[2] $\boldsymbol{E}'(\boldsymbol{r}) = \boldsymbol{E}(\boldsymbol{r}) + 4\pi \boldsymbol{P}_\perp(\boldsymbol{r})$. In terms of the new canonical momenta, the Hamiltonian associated with the Lagrangian L' is

$$\begin{aligned} H' &= \sum_q \boldsymbol{p}'_q \cdot \dot{\boldsymbol{r}}_q + \int \boldsymbol{\Pi}'(\boldsymbol{r}) \cdot \dot{\boldsymbol{A}}(\boldsymbol{r}) \, \mathrm{d}^3 r - L' \\ &= \sum_{q=1}^{Q} \frac{1}{2} \left| \boldsymbol{p}'_q + \boldsymbol{B}(\boldsymbol{r}) \times \boldsymbol{r}_q \int_0^1 u \delta(\boldsymbol{r} - u\boldsymbol{r}_q) \, \mathrm{d}u \right|^2 - \sum_{q=1}^{Q} \left[\frac{Z}{r_q} - \sum_{q'=q+1}^{Q} \frac{1}{|\boldsymbol{r}_q(t) - \boldsymbol{r}_{q'}(t)|} \right] \\ &\quad + \frac{1}{8\pi} \int \left[\left| \boldsymbol{E}'_\perp(\boldsymbol{r}) - 4\pi \boldsymbol{P}_\perp(\boldsymbol{r}) \right|^2 + c^2 B^2(\boldsymbol{r}) \right] \mathrm{d}^3 r \\ &\approx \sum_{q=1}^{Q} \frac{|\boldsymbol{p}'_q|^2}{2} - \sum_{q=1}^{Q} \left[\frac{Z}{r_q} - \sum_{q'=q+1}^{Q} \frac{1}{|\boldsymbol{r}_q(t) - \boldsymbol{r}_{q'}(t)|} \right] + \frac{1}{8\pi} \int \left[E'^2_\perp(\boldsymbol{r}) + c^2 B^2(\boldsymbol{r}) \right] \mathrm{d}^3 r \\ &\quad - \boldsymbol{d} \cdot \boldsymbol{E}'_\perp(\boldsymbol{0}) - \boldsymbol{m} \cdot \boldsymbol{B}(\boldsymbol{0}) - \sum_{ij} q_{ij} \frac{\partial E'_{\perp,j}(\boldsymbol{0})}{\partial r_i} + \dots \end{aligned} \tag{2.21}$$

with the electric-dipole (E1) moment $\boldsymbol{d}$, the magnetic-dipole (M1) moment $\boldsymbol{m}$, and the electric-quadrupole (E2) moment q_{ij}, defined as

$$\boldsymbol{d} = -\sum_{q=1}^{Q} \boldsymbol{r}_q, \tag{2.22a}$$

$$\boldsymbol{m} = -\sum_{q=1}^{Q} \frac{1}{2} \boldsymbol{r}_q \times \boldsymbol{p}'_q, \tag{2.22b}$$

$$q_{ij} = -\sum_{q=1}^{Q} \frac{1}{2} \left(r_{q,i} r_{q,j} - \frac{1}{3} \delta_{ij} r_q^2 \right). \tag{2.22c}$$

[2] The transformed electric field which we define here is related to the electric displacement field $\boldsymbol{D}(\boldsymbol{r}) = \frac{\boldsymbol{E}'(\boldsymbol{r})}{4\pi}$. The differentiation is not essential for our purposes, as we are interested in the effect induced by the polarization of the medium only in the far-field region, i.e., at large distance from the particles themselves, where $\boldsymbol{D}(\boldsymbol{r}) = \frac{\boldsymbol{E}(\boldsymbol{r})}{4\pi}$. Indeed, from a formal point of view, this difference would not arise at all if we directly proceeded with a Göppert-Mayer transformation which neglects from the very beginning contributions other than the electric-dipole E1 interaction [7, 148].

Here, we have expanded the electric and magnetic fields on the central coordinate **0** in the **long-wavelength approximation**. The **electric-dipole approximation** neglects the contribution of the magnetic field $\boldsymbol{B}(\boldsymbol{r},t)$ and takes only the first term in the expansion in the electric field $\boldsymbol{E}'_\perp$. It follows that

$$\boldsymbol{p}'_q = \dot{\boldsymbol{r}}_q \tag{2.23}$$

and

$$\begin{aligned} H' = &\sum_{q=1}^{Q} \frac{|\boldsymbol{p}'_q|^2}{2} - \sum_{q=1}^{Q}\left[\frac{Z}{r_q} - \sum_{q'=q+1}^{Q} \frac{1}{|\boldsymbol{r}_q(t) - \boldsymbol{r}_{q'}(t)|}\right] \\ &+ \frac{1}{8\pi}\int \left[E'^2_\perp(\boldsymbol{r}) + c^2 B^2(\boldsymbol{r})\right]\, \mathrm{d}^3 r - \boldsymbol{d}\cdot\boldsymbol{E}'_\perp(\boldsymbol{0}). \end{aligned} \tag{2.24}$$

A quantum theory of light-matter interaction can be obtained by canonical quantization of the Hamiltonian (2.24) [155, 156]. When a quantum system is driven by a strong external field, i.e., the number of photons is large, this interaction can be treated semiclassically, i.e., by describing the atom as a quantum system with a discrete set of energy levels interacting with a classical external field. The electromagnetic response of the system, though, ought to be treated quantum mechanically. As a result, before we introduce the quantum Hamiltonian which we are going to deal with in the next Chapters, we split the total electric field $\boldsymbol{\mathcal{E}}_{\mathrm{tot}}(\boldsymbol{r},\, t)$ into two components, i.e., the strong, external driving field $\boldsymbol{\mathcal{E}}_{\mathrm{ext}}(\boldsymbol{r},\, t)$ and the fluorescence field $\boldsymbol{E}_{\mathrm{em}}(\boldsymbol{r},\, t)$ which is spontaneously emitted by the system of charges,

$$\boldsymbol{\mathcal{E}}_{\mathrm{tot}}(\boldsymbol{r},\, t) = \boldsymbol{\mathcal{E}}_{\mathrm{ext}}(\boldsymbol{r},\, t) + \boldsymbol{E}_{\mathrm{em}}(\boldsymbol{r},\, t). \tag{2.25}$$

A canonical formalism is necessary to describe the dynamical evolution of the spontaneously emitted field only, whereas we assume that the driving field is not affected by the interaction with the atom. Therefore, the vector potential $\boldsymbol{A}(\boldsymbol{r})$ and the conjugate momentum field $\boldsymbol{\Pi}(\boldsymbol{r})$ only refer to the spontaneously emitted electromagnetic field.

The interaction Hamiltonian in the dipole approximation is

$$H = H_0 + H_{\mathrm{AL}} + H_{\mathrm{F}} + H_{\mathrm{AF}}, \tag{2.26}$$

with

$$H_0 = \sum_{q=1}^{Q} \frac{|\boldsymbol{p}_q|^2}{2} - \sum_{q=1}^{Q}\left[\frac{Z}{r_q} - \sum_{q'=q+1}^{Q} \frac{1}{|\boldsymbol{r}_q(t) - \boldsymbol{r}_{q'}(t)|}\right], \tag{2.27a}$$

$$H_{\mathrm{AL}} = -\boldsymbol{d}\cdot\boldsymbol{\mathcal{E}}_{\mathrm{ext}}(\boldsymbol{0}), \tag{2.27b}$$

$$H_{\mathrm{F}} = \frac{1}{8\pi}\int \left[E^2_{\mathrm{em},\perp} + c^2 B^2_{\mathrm{em}}(\boldsymbol{r})\right]\, \mathrm{d}^3 r, \tag{2.27c}$$

$$H_{\mathrm{AF}} = -\boldsymbol{d}\cdot\boldsymbol{E}_{\mathrm{em},\perp}(\boldsymbol{0}), \tag{2.27d}$$

where H_0 describes the electronic structure Hamiltonian of the bare atom, whereas H_{AL} includes the interaction of the atom with the strong external laser field $\boldsymbol{\mathcal{E}}_{\mathrm{ext}}(\boldsymbol{r},\, t)$. The energy of the fluorescence field is given by H_{F}, while H_{AF} accounts for the interaction of such field with the atomic system. The canonical variables are $\boldsymbol{r}_q$ and $\boldsymbol{A}(\boldsymbol{r})$, associated with the canonical momenta $\boldsymbol{p}_q = \dot{\boldsymbol{r}}_q$ and $\boldsymbol{\Pi}(\boldsymbol{r}) = -\frac{\boldsymbol{E}_{\mathrm{em},\perp}(\boldsymbol{r})}{4\pi}$. The quantization of the Hamiltonian H follows the standard

prescription [155, 156] $\boldsymbol{r}_q \to \hat{\boldsymbol{r}}_q$, $\boldsymbol{p}_q \to \hat{\boldsymbol{p}}_q$, $\boldsymbol{A}(\boldsymbol{r}) \to \hat{\boldsymbol{A}}(\boldsymbol{r})$, $\boldsymbol{\Pi}(\boldsymbol{r}) \to \hat{\boldsymbol{\Pi}}(\boldsymbol{r})$, with the commutation relations

$$\begin{aligned} [\hat{\boldsymbol{r}}_q, \hat{\boldsymbol{r}}_{q'}] = [\hat{\boldsymbol{p}}_q, \hat{\boldsymbol{p}}_{q'}] &= 0, \\ [\hat{\boldsymbol{r}}_q, \hat{\boldsymbol{p}}_{q'}] &= \mathrm{i}\delta_{q,q'}, \\ [\hat{\boldsymbol{A}}(\boldsymbol{r}), \hat{\boldsymbol{A}}(\boldsymbol{r}')] = [\hat{\boldsymbol{\Pi}}(\boldsymbol{r}), \hat{\boldsymbol{\Pi}}(\boldsymbol{r}')] &= 0, \\ [\hat{\boldsymbol{A}}(\boldsymbol{r}), \hat{\boldsymbol{\Pi}}(\boldsymbol{r}')] &= \mathrm{i}\delta^3(\boldsymbol{r} - \boldsymbol{r}'). \end{aligned} \tag{2.28}$$

2.2 Atomic spectra

The prediction of atomic spectra in hydrogen and in more general many-electron systems is a problem which dates back to the origin and foundation of quantum mechanics itself and which has played a stimulating role in the development and refinement of quantum theory [149, 150]. A survey of the theory of atomic structure and spectra is not the purpose of this Section. We rather aim at revising those concepts, such as spin orbitals, electron configurations, and angular-momentum coupling, which are essential to understand the properties of a bare many-electron state.

High-precision calculations of atomic spectra require a relativistic quantum-field-theoretical description of the problem, in order to properly take into account relativistic and QED corrections. For our purposes, however, we can limit ourselves to the usual stationary Schrödinger equation,

$$\hat{H}_0|\Psi_i\rangle = \omega_i|\Psi_i\rangle, \tag{2.29}$$

where the electronic structure Hamiltonian for a set of Q electrons, with position and momenta given by $\hat{\boldsymbol{r}}_q$ and $\hat{\boldsymbol{p}}_q$, respectively, $q \in \{1, \ldots, Q\}$, surrounding a nucleus of atomic number Z, is given by

$$\hat{H}_0 = \sum_{q=1}^{Q} \frac{\hat{p}_q^2}{2} - \sum_{q=1}^{Q} \frac{Z}{\hat{r}_q} + \sum_{\substack{q=1 \\ q'>q+1}}^{Q} \frac{1}{|\hat{\boldsymbol{r}}_q - \hat{\boldsymbol{r}}_{q'}|} + \hat{H}_{\mathrm{rel}}. \tag{2.30}$$

Here, $\frac{\hat{p}_q^2}{2}$ is the kinetic energy of the qth electron, $\frac{Z}{\hat{r}_q}$ is its potential energy due to the Coulomb interaction with the nucleus, $\frac{1}{|\hat{\boldsymbol{r}}_q - \hat{\boldsymbol{r}}_{q'}|}$ represents the potential energy due to the Coulomb interaction between the qth and the q'th electron, and $\hat{H}_{\mathrm{rel}}$ accounts for those relativistic corrections to the Schrödinger equation which can be derived from the Dirac Hamiltonian [149]. The eigenstates of the Hamiltonian

$$\hat{H}_0 = \sum_i \omega_i|\Psi_i\rangle\langle\Psi_i| + \int \omega_\lambda|\lambda\rangle\langle\lambda|\,\mathrm{d}\lambda \tag{2.31}$$

are either bound states $|\Psi_i\rangle$, $\langle\Psi_i|\Psi_{i'}\rangle = \delta_{ii'}$, associated with a discrete spectrum of eigenvalues ω_i, or states in the continuum $|\lambda\rangle$, $\langle\lambda|\lambda'\rangle = \delta(\lambda - \lambda')$, with eigenvalues ω_λ. In the next part, we are going to focus on bound states only, in terms of which any atomic operator can be expanded by exploiting the completeness of the basis formed by eigenstates. For instance, the electric-dipole moment operator $\hat{\boldsymbol{d}}$, obtained by quantization of $\boldsymbol{d}$ in Eq. (2.22a), is written as

$$\hat{\boldsymbol{d}} = \sum_{ii'} |\Psi_i\rangle\langle\Psi_i|\hat{\boldsymbol{d}}|\Psi_{i'}\rangle\langle\Psi_{i'}| = \sum_{ii'} \boldsymbol{d}_{ii'}\hat{\sigma}_{ii'}, \tag{2.32}$$

where we have introduced the associated matrix elements $\boldsymbol{d}_{ii'} = \langle\Psi_i|\hat{\boldsymbol{d}}|\Psi_{i'}\rangle = \boldsymbol{d}_{i'i}^*$ and the ladder operators

$$\hat{\sigma}_{ii'} = |\Psi_i\rangle\langle\Psi_{i'}|. \tag{2.33}$$

The electric-dipole moment operator $\hat{\boldsymbol{d}}$ is the sum of a positive- and a negative-frequency component, $\hat{\boldsymbol{d}} = \hat{\boldsymbol{d}}^{+} + \hat{\boldsymbol{d}}^{-}$, with $\hat{\boldsymbol{d}}^{-} = [\hat{\boldsymbol{d}}^{+}]^{\dagger}$ and

$$\hat{\boldsymbol{d}}^{+} = \sum_{\substack{ii' \\ i<i'}} \boldsymbol{d}_{ii'} \hat{\sigma}_{ii'}. \tag{2.34}$$

The presence of the electron-electron interaction prevents one from obtaining an exact analytical solution of Eq. (2.29). The steps taken to extract an approximate numerical solution [149,150] can be nevertheless very informative. The eigenstates $|\Psi_i\rangle$ can be written as a linear combination

$$|\Psi_i\rangle = \sum_b y_{ib} \, |\Phi_b\rangle, \text{ with } y_{ib} = \langle \Phi_b | \Psi_i \rangle, \tag{2.35}$$

of known vectors $|\Phi_b\rangle$, $\langle \Phi_b | \Phi_{b'} \rangle = \delta_{bb'}$, forming a basis of the Hilbert space in which $|\Psi_i\rangle$ lies.

Two criteria should be kept in mind in choosing a proper basis of states $|\Phi_b\rangle$:

1. **Perturbation theory**—Each basis state $|\Phi_b\rangle$ should be as close as possible to one of the states $|\Psi_i\rangle$. This can be achieved, e.g., by choosing a basis formed by the eigenstates of an operator which differs from $\hat{H}_0$ only by a small correction;

2. **Symmetries**—If there exists a set of operators which commute with $\hat{H}_0$, it is convenient to choose a basis of states $|\Phi_b\rangle$ which are also eigenstates of these operators. In this way, the solution of the stationary Schrödinger equation (2.29) corresponds to the diagonalization of an already block-diagonal matrix.

When these criteria are followed, the numerically obtained eigenstates $|\Psi_i\rangle$ often display a major contribution only from one of the basis vectors $|\Phi_b\rangle$ used for the expansion in Eq. (2.35). In other words, for a given index i one can often notice that there exists one index b for which $|y_{ib}|^2 \gg |y_{ib'}|^2$, for $b' \neq b$: a one-to-one correspondence $|\Psi_i\rangle \leftrightarrow |\Phi_b\rangle$ can hence be established and it is customary to label the eigenstate $|\Psi_i\rangle$ via the well defined and known quantum numbers, e.g., electron configuration and angular momenta, of the corresponding basis state $|\Phi_b\rangle$.

In the remaining of this Section, we wish to shortly revise the criteria whereby the basis states $|\Phi_b\rangle$ are chosen and the associated quantum numbers which throughout the Thesis will be employed to label the eigenstates of the bare electronic structure Hamiltonian $\hat{H}_0$. Our discussion follows Refs. [149, 150].

The central-field model

In order to choose a proper set of basis states $|\Phi_b\rangle$, let us write the total Hamiltonian as

$$\hat{H}_0 = \sum_{q=1}^{Q} \left(\frac{\hat{p}_q^2}{2} - \frac{Z}{\hat{r}_q} + V(\hat{r}_q) \right) + \sum_{q=1}^{Q} \left(\sum_{q'=q+1}^{Q} \frac{1}{|\hat{\boldsymbol{r}}_q - \hat{\boldsymbol{r}}_{q'}|} - V(\hat{r}_q) \right) + \hat{H}_{\rm rel}, \tag{2.36}$$

where we have introduced the central potential $V(\hat{r}_q)$, function of the single-electron coordinate $\hat{r}_q$, including the average effect of the other $Q-1$ electrons surrounding it. Under these assumptions, the total Hamiltonian consists of three terms, i.e., (i) the sum of Q terms,

$$H_{\rm cf} = \sum_{q=1}^{Q} H_{{\rm cf},q} = \sum_{q=1}^{Q} \left(\frac{\hat{p}_q^2}{2} - \frac{Z}{\hat{r}_q} + V(\hat{r}_q) \right), \tag{2.37}$$

describing the motion of Q independent electrons in the central field $-\frac{Z}{\hat{r}_q} + V(\hat{r}_q)$, (ii) a first spin-independent correction due to the electron-electron correlation, and (iii) a second correction due to relativistic effects. The eigenvalues and eigenstates of the central-field Hamiltonian $\hat{H}_{\mathrm{cf},q}$ are the starting point for the calculation of the exact solution of Eq. (2.29).

Spin orbitals

The properties of the spectrum of $H_{\mathrm{cf},q}$, i.e., the solution of the eigenvalue problem

$$H_{\mathrm{cf},q}\,\varphi_{n_q l_q m_{l_q} m_{s_q}}(r_q,\,\theta_q,\,\phi_q,\,s_q) = E_{n_q l_q}\,\varphi_{n_q l_q m_{l_q} m_{s_q}}(r_q,\,\theta_q,\,\phi_q,\,s_q), \tag{2.38}$$

have been known for a long time [149, 150]. This Hamiltonian commutes with the qth particle's orbital and spin angular-momentum operators, respectively given by $\hat{\boldsymbol{l}}_q$ and $\hat{\boldsymbol{s}}_q$. In the spherical coordinates r_q, θ_q, and ϕ_q, and for spin $s_q = 1/2$, the eigenstates of $H_{\mathrm{cf},q}$,

$$\varphi_{n_q l_q m_{l_q} m_{s_q}}(r_q,\,\theta_q,\,\phi_q,\,s_q) = \frac{1}{r_q}\,P_{n_q l_q}(r_q)\,Y_{l_q m_{l_q}}(\theta_q,\,\phi_q)\,\chi_{m_{s_q}}(s_q), \tag{2.39}$$

are completely identified by the list of quantum numbers n_q, l_q, m_{l_q}, s_q, and m_{s_q}. Such a set of quantum numbers unequivocally defines a spin orbital, i.e., a one-electron eigenstate of the central-field Hamiltonian $\hat{H}_{\mathrm{cf},q}$. The quantum number l_q is usually identified by a letter, i.e., s, p, d, f, g, ... for $l_q = 0, 1, 2, 3, 4, \ldots$ A spin orbital is also eigenstate of the single-particle orbital- and spin-angular-momentum operators $\hat{l}_q^2$, $\hat{l}_{z_q}$, $\hat{s}_q^2$, and $\hat{s}_{z_q}$, respectively with eigenvalues $l_q(l_q+1)$, m_{l_q}, $s_q(s_q+1) = 3/4$, and m_{s_q}. $\chi_{m_{s_q}}(s_q)$ denotes the spin part of the wavefunction; the radial term $P_{n_q l_q}(r_q)$ depends on the precise shape of the central potential $V(\hat{r}_q)$, whereas the angular part is exclusively associated with the angular momentum of the system, i.e., it is given by the spherical harmonics

$$Y_{l m_l}(\theta,\,\phi) = (-1)^{(m_l+|m_l|)/2}\left[\frac{(2l+1)(l-|m_l|)!}{4\pi(l+|m_l|)!}\right]^{1/2}\mathrm{P}_l^{|m_l|}(\cos(\theta))\,\mathrm{e}^{\mathrm{i}m_l\phi}, \tag{2.40}$$

where we have introduced the Legendre polynomials $\mathrm{P}_l^{m_l}(x)$, associated with the quantum numbers $l = 0, 1, 2, \ldots$ and $m_l = -l, -l+1, \ldots, l-1, l$. The energy eigenvalue $E_{n_q l_q}$ of the Hamiltonian $H_{\mathrm{cf},q}$ depends only on the quantum numbers n_q and l_q, where $n_q \geq l_q + 1$ counts the number of nodes, $n_q - l_q - 1$, of the radial function $P_{n_q l_q}(r_q)$. Spin orbitals which differ only in m_{l_q} or m_{s_q} belong, therefore, to the same degenerate level.

Antisymmetrization

The single-electron spin orbitals (2.39) can be used to calculate the eigenstates $|\Lambda_{\{n_q l_q m_{l_q} m_{s_q}\}}\rangle$ and eigenvalues $E_{\{n_q l_q\}}$ of the many-electron Hamiltonian (2.37), i.e.,

$$H_{\mathrm{cf}}|\Lambda_{\{n_q l_q m_{l_q} m_{s_q}\}}\rangle = E_{\{n_q l_q\}}|\Lambda_{\{n_q l_q m_{l_q} m_{s_q}\}}\rangle. \tag{2.41}$$

Each eigenvalue,

$$E_{\{n_q l_q\}} = \sum_{q=1}^{Q} E_{n_q l_q}, \tag{2.42}$$

depends on the set of Q pairs of quantum numbers $\{n_q,\,l_q\} = \{n_1,\,l_1,\,\ldots,\,n_Q,\,l_Q\}$, whereas each eigenvector $|\Lambda_{\{n_q l_q m_{l_q} m_{s_q}\}}\rangle$ is fixed by the set of Q lists of quantum numbers $\{n_q,\,l_q,\,m_{l_q},\,m_{s_q}\} =$

$\{n_1, l_1, m_{l_1}, m_{s_1}, \ldots, n_Q, l_Q, m_{l_Q}, m_{s_Q}\}$. Any linear combination of the $Q!$ terms

$$\prod_{q=1}^{Q} \varphi_{n_{j_q} l_{j_q} m_{l_{j_q}} m_{s_{j_q}}}(r_q, \theta_q, \phi_q, s_q),$$

associated with each one of the $Q!$ possible permutations $P = j_1, j_2, \ldots, j_Q$ of $1, 2, \ldots, Q$, is an eigenstate of $\hat{H}_{\mathrm{cf}}$ [Eq. (2.37)]. However, there is only one state $|\Lambda_{\{n_q l_q m_{l_q} m_{s_q}\}}\rangle$ with physical meaning, i.e., that linear combination, called Slater determinant, which renders the total wavefunction antisymmetric [156].

Electron configurations

The list of Q pairs of quantum numbers $\{n_q, l_q\} = \{n_1, l_1, \ldots, n_Q, l_Q\}$ is called an electron configuration. The concept of a configuration is not only relevant for the Hamiltonian $\hat{H}_{\mathrm{cf}}$, but also for the total Hamiltonian $\hat{H}_0$. In real atoms, in fact, the presence of electron-electron interaction and of relativistic corrections breaks the degeneracy of the electron configuration, but is usually not so strong to significantly mix states belonging to different configurations—i.e., states whose energy would already be far apart in the absence of these small correction terms.

Coupling

In order to find a good set of basis states $|\Phi_b\rangle$, one should choose vectors which are eigenstates of the operators commuting with the Hamiltonian $\hat{H}_0$ (2.30). The antisymmetrized spin orbitals $|\Lambda_{\{n_q l_q m_{l_q} m_{s_q}\}}\rangle$ clearly do not satisfy this condition and do not represent a good basis for a direct diagonalization of $\hat{H}_0$. An intermediate step is therefore necessary in order to obtain coupled states $|\Phi_b\rangle$, in terms of which the total Hamiltonian is, as previously discussed, block-diagonal.

A coupled basis can be constructed by linear combinations of the spin orbitals $|\Lambda_{\{n_q l_q m_{l_q} m_{s_q}\}}\rangle$ in Eq. (2.41). In the most general case, each one of these coupled states ought to be a linear combination of all the spin orbitals, for any nonequivalent list of quantum numbers $\{n_q, l_q, m_{l_q}, m_{s_q}\}$, i.e.,

$$|\Phi_b\rangle = \sum_{n_1} \sum_{l_1} \sum_{m_{l_1}} \sum_{m_{s_1}} \cdots \sum_{n_Q} \sum_{l_Q} \sum_{m_{l_Q}} \sum_{m_{s_Q}} f_{b,\{n_q l_q m_{l_q} m_{s_q}\}} |\Lambda_{\{n_q l_q m_{l_q} m_{s_q}\}}\rangle. \tag{2.43}$$

However, in particular for low-energy levels, due to the very small degree of configuration mixing, one can usually rely on the *single-configuration approximation*, whereby only those spin orbitals are utilized which are associated with the same electron configuration $\{n_q, l_q\}$, for all the possible values of the remaining parameters $\{m_{l_q}, m_{s_q}\}$,

$$|\Phi_b\rangle = \sum_{m_{l_1}} \sum_{m_{s_1}} \cdots \sum_{m_{l_Q}} \sum_{m_{s_Q}} f_{b,\{n_q l_q m_{l_q} m_{s_q}\}} |\Lambda_{\{n_q l_q m_{l_q} m_{s_q}\}}\rangle, \quad \text{for fixed } n_1, l_1, \ldots, n_Q, l_Q. \tag{2.44}$$

Should this procedure not be sufficient, then a *multi-configuration approximation* is required, i.e., states corresponding to different electron configurations are used to build the coupled eigenstates $|\Phi_b\rangle$. Even when configuration mixing renders a multi-configuration approach necessary, it is often such that a given eigenstate of the total Hamiltonian $|\Psi_i\rangle$ still presents a major contribution coming just from one particular configuration. Therefore, it is customary to denote the basis states $|\Phi_b\rangle$—and then the approximated eigenstates $|\Psi_i\rangle$—via that specific configuration which mostly contributes to the sum (2.43).

Levels and states in LS coupling

When relativistic corrections are neglected in (2.30), the total Hamiltonian $\hat{H}_0$ commutes with the total orbital angular-momentum operator $\hat{\boldsymbol{L}} = \sum_{q=1}^{Q} \hat{\boldsymbol{l}}_q$ and the total spin angular-momentum operator $\hat{\boldsymbol{S}} = \sum_{q=1}^{Q} \hat{\boldsymbol{s}}_q$. For each electron configuration $\{n_q, l_q\}$, one ought to determine that linear combination of spin orbitals which simultaneously diagonalizes $\hat{L}^2$, $\hat{L}_z$, $\hat{S}^2$, and $\hat{S}_z$, with quantum numbers L, M_L, S, and M_S. Each one of the coupled states $|\Phi_b\rangle$, along with the corresponding eigenstate $|\Psi_i\rangle$, can be identified through the dominant electronic configuration $\{n_q, l_q\}$ and the exact angular-momentum quantum numbers L, M_L, S, and M_S.

The previous approximation fails if spin-orbit effects need to be taken into account. In such cases, in fact, the total orbital and spin angular momenta are not constants of motion, due to their mutual interaction: L and S are usually still good quantum numbers, but M_L and M_S are not. Although $\hat{\boldsymbol{L}}$ and $\hat{\boldsymbol{S}}$ are not constants of motion of a Hamiltonian with spin-orbit interactions, the total angular momentum $\hat{\boldsymbol{J}} = \hat{\boldsymbol{L}} + \hat{\boldsymbol{S}}$ commutes with the total Hamiltonian and its eigenstates, associated with the two quantum numbers J and M_J, can be employed to describe the eigenstates of $\hat{H}_0$. The eigenstates of the operators $\hat{J}^2$, $\hat{L}^2$, $\hat{S}^2$, and $\hat{J}_z$ can be related to the eigenstates of $\hat{L}^2$, $\hat{S}^2$, and $\hat{L}_z$, and $\hat{S}_z$ via the Clebsch-Gordan coefficients [155]. As a result, a coupled state $|\Phi_b\rangle$ and the associated eigenstate $|\Psi_i\rangle$ are labeled via the dominant electronic configuration $\{n_q, l_q\}$, the exact total-angular-momentum quantum numbers J and M_J, and the two additional quantum numbers L and S in the LS coupling.

2.3 The quantum field

2.3.1 Canonical quantization of the electromagnetic field

In order to quantize the fluorescent electromagnetic field, we write $\boldsymbol{A}(\boldsymbol{r})$ and $\boldsymbol{\Pi}(\boldsymbol{r})$ in normal modes in the volume V [7, 148, 151], i.e.,

$$\boldsymbol{\Pi}(\boldsymbol{r}) = \sum_{\boldsymbol{k}} \frac{1}{\sqrt{V}}\, \boldsymbol{\pi}_{\boldsymbol{k}}\, \mathrm{e}^{\mathrm{i}\boldsymbol{k}\cdot\boldsymbol{r}}, \qquad \boldsymbol{\pi}_{\boldsymbol{k}} = \int \frac{1}{\sqrt{V}} \boldsymbol{\Pi}(\boldsymbol{r})\, \mathrm{e}^{-\mathrm{i}\boldsymbol{k}\cdot\boldsymbol{r}}\, \mathrm{d}^3 r, \tag{2.45a}$$

$$\boldsymbol{A}(\boldsymbol{r}) = \sum_{\boldsymbol{k}} \frac{1}{\sqrt{V}} \boldsymbol{\mathcal{A}}_{\boldsymbol{k}}\, \mathrm{e}^{\mathrm{i}\boldsymbol{k}\cdot\boldsymbol{r}}, \qquad \boldsymbol{\mathcal{A}}_{\boldsymbol{k}} = \int \frac{1}{\sqrt{V}} \boldsymbol{A}(\boldsymbol{r})\, \mathrm{e}^{-\mathrm{i}\boldsymbol{k}\cdot\boldsymbol{r}}\, \mathrm{d}^3 r, \tag{2.45b}$$

$$\boldsymbol{B}(\boldsymbol{r}) = \sum_{\boldsymbol{k}} \frac{1}{\sqrt{V}} \boldsymbol{\mathcal{B}}_{\boldsymbol{k}}\, \mathrm{e}^{\mathrm{i}\boldsymbol{k}\cdot\boldsymbol{r}}, \qquad \boldsymbol{\mathcal{B}}_{\boldsymbol{k}} = \int \frac{1}{\sqrt{V}} \boldsymbol{B}(\boldsymbol{r})\, \mathrm{e}^{-\mathrm{i}\boldsymbol{k}\cdot\boldsymbol{r}}\, \mathrm{d}^3 r = \mathrm{i}\boldsymbol{k} \times \boldsymbol{\mathcal{A}}_{\boldsymbol{k}}, \tag{2.45c}$$

where $\boldsymbol{\pi}_{\boldsymbol{k}} = \boldsymbol{\pi}^*_{-\boldsymbol{k}}$, $\boldsymbol{\mathcal{A}}_{\boldsymbol{k}} = \boldsymbol{\mathcal{A}}^*_{-\boldsymbol{k}}$, and $\boldsymbol{\mathcal{B}}_{\boldsymbol{k}} = \boldsymbol{\mathcal{B}}^*_{-\boldsymbol{k}}$. Furthermore, since both $\boldsymbol{A}(\boldsymbol{r})$ and $\boldsymbol{\Pi}(\boldsymbol{r})$ are transverse vectors, it follows that

$$\boldsymbol{\nabla} \cdot \boldsymbol{A}(\boldsymbol{r}) = 0 \quad \rightarrow \quad \boldsymbol{k} \cdot \boldsymbol{\mathcal{A}}_{\boldsymbol{k}} = 0, \tag{2.46a}$$

$$\boldsymbol{\nabla} \cdot \boldsymbol{\Pi}(\boldsymbol{r}) = 0 \quad \rightarrow \quad \boldsymbol{k} \cdot \boldsymbol{\pi}_{\boldsymbol{k}} = 0. \tag{2.46b}$$

For each $\boldsymbol{k}$, therefore, one can introduce two orthogonal unit vectors, $\hat{\boldsymbol{e}}^{(1)}_{\boldsymbol{k}}$ and $\hat{\boldsymbol{e}}^{(2)}_{\boldsymbol{k}}$, such that $\hat{\boldsymbol{e}}^{(\lambda)}_{\boldsymbol{k}} \cdot \hat{\boldsymbol{e}}^{(\lambda')}_{\boldsymbol{k}} = \delta_{\lambda\lambda'}$, $\hat{\boldsymbol{e}}^{(\lambda)}_{\boldsymbol{k}} \cdot \boldsymbol{k} = 0$, in terms of which we write

$$\boldsymbol{\pi}_{\boldsymbol{k}} = \sum_{\lambda=1}^{2} \pi_{\boldsymbol{k}\lambda}\, \hat{\boldsymbol{e}}^{(\lambda)}_{\boldsymbol{k}}, \qquad \pi_{\boldsymbol{k}\lambda} = \boldsymbol{\pi}_{\boldsymbol{k}} \cdot \hat{\boldsymbol{e}}^{(\lambda)}_{\boldsymbol{k}}, \tag{2.47a}$$

$$\boldsymbol{\mathcal{A}}_{\boldsymbol{k}} = \sum_{\lambda=1}^{2} \mathcal{A}_{\boldsymbol{k}\lambda}\, \hat{\boldsymbol{e}}^{(\lambda)}_{\boldsymbol{k}}, \qquad \mathcal{A}_{\boldsymbol{k}\lambda} = \boldsymbol{\mathcal{A}}_{\boldsymbol{k}} \cdot \hat{\boldsymbol{e}}^{(\lambda)}_{\boldsymbol{k}}, \tag{2.47b}$$

where $\hat{\boldsymbol{e}}_{\boldsymbol{k}}^{(\lambda)} = \hat{\boldsymbol{e}}_{-\boldsymbol{k}}^{(\lambda)}$ and, therefore, $\pi_{\boldsymbol{k}\lambda} = \pi_{-\boldsymbol{k}\lambda}^*$, $\mathcal{A}_{\boldsymbol{k}\lambda} = \mathcal{A}_{-\boldsymbol{k}\lambda}^*$. After having defined the frequency associated with each mode, $\omega_k = ck$, one can introduce

$$a_{\boldsymbol{k}\lambda} = -\frac{1}{\sqrt{8\pi\omega_k}}\left(4\pi\ \pi_{\boldsymbol{k}\lambda} - \mathrm{i}\omega_k \mathcal{A}_{\boldsymbol{k}\lambda}\right) = \int \alpha_{\boldsymbol{k}\lambda}(\boldsymbol{r})\ \mathrm{d}^3 r, \tag{2.48a}$$

$$a_{-\boldsymbol{k}\lambda}^* = -\frac{1}{\sqrt{8\pi\omega_k}}\left(4\pi\ \pi_{-\boldsymbol{k}\lambda}^* + \mathrm{i}\omega_k \mathcal{A}_{-\boldsymbol{k}\lambda}^*\right) = \int \alpha_{-\boldsymbol{k}\lambda}^*(\boldsymbol{r})\ \mathrm{d}^3 r, \tag{2.48b}$$

with

$$\alpha_{\boldsymbol{k}\lambda} = -\frac{1}{\sqrt{8\pi\omega_k V}}[4\pi\boldsymbol{\Pi}(\boldsymbol{r}) - \mathrm{i}\omega_k \boldsymbol{A}(\boldsymbol{r})] \cdot \hat{\boldsymbol{e}}_{\boldsymbol{k}}^{(\lambda)}\, \mathrm{e}^{-\mathrm{i}\boldsymbol{k}\cdot\boldsymbol{r}}, \tag{2.49}$$

such that

$$\pi_{\boldsymbol{k}\lambda} = -\sqrt{\frac{\omega_k}{8\pi}}(a_{\boldsymbol{k}\lambda} + a_{-\boldsymbol{k}\lambda}^*), \qquad \boldsymbol{\Pi}(\boldsymbol{r}) = -\sum_{\boldsymbol{k}}\sum_{\lambda=1}^{2}\sqrt{\frac{\omega_k}{8\pi V}}(a_{\boldsymbol{k}\lambda}\,\mathrm{e}^{\mathrm{i}\boldsymbol{k}\cdot\boldsymbol{r}} + a_{\boldsymbol{k}\lambda}^*\,\mathrm{e}^{-\mathrm{i}\boldsymbol{k}\cdot\boldsymbol{r}})\,\hat{\boldsymbol{e}}_{\boldsymbol{k}}^{(\lambda)}, \tag{2.50a}$$

$$\mathcal{A}_{\boldsymbol{k}\lambda} = -\mathrm{i}\sqrt{\frac{2\pi}{\omega_k}}(a_{\boldsymbol{k}\lambda} - a_{-\boldsymbol{k}\lambda}^*), \qquad \boldsymbol{A}(\boldsymbol{r}) = -\mathrm{i}\sum_{\boldsymbol{k}}\sum_{\lambda=1}^{2}\sqrt{\frac{2\pi}{\omega_k V}}(a_{\boldsymbol{k}\lambda}\,\mathrm{e}^{\mathrm{i}\boldsymbol{k}\cdot\boldsymbol{r}} - a_{\boldsymbol{k}\lambda}^*\,\mathrm{e}^{-\mathrm{i}\boldsymbol{k}\cdot\boldsymbol{r}})\,\hat{\boldsymbol{e}}_{\boldsymbol{k}}^{(\lambda)}. \tag{2.50b}$$

The calculation of the Poisson brackets [151]

$$\{a_{\boldsymbol{k}\lambda},\, a_{\boldsymbol{k}'\lambda'}^*\} = \int \frac{\partial\alpha_{\boldsymbol{k}\lambda}}{\partial\boldsymbol{A}}\cdot\frac{\partial\alpha_{\boldsymbol{k}'\lambda'}^*}{\partial\boldsymbol{\Pi}} - \frac{\partial\alpha_{\boldsymbol{k}'\lambda'}^*}{\partial\boldsymbol{A}}\cdot\frac{\partial\alpha_{\boldsymbol{k}\lambda}}{\partial\boldsymbol{\Pi}}\ \mathrm{d}^3 r = -\mathrm{i}\,\delta_{\boldsymbol{k}\boldsymbol{k}'}\,\delta_{\lambda\lambda'}, \tag{2.51a}$$

$$\{a_{\boldsymbol{k}\lambda},\, a_{\boldsymbol{k}'\lambda'}\} = \{a_{\boldsymbol{k}\lambda}^*,\, a_{\boldsymbol{k}'\lambda'}^*\} = 0, \tag{2.51b}$$

shows that $a_{\boldsymbol{k}\lambda}$ and $a_{\boldsymbol{k}'\lambda'}^*$ form couples of canonically coupled variables suitable for quantization. In terms of these new variables we write the electric field

$$\boldsymbol{E}_{\mathrm{em},\perp}(\boldsymbol{r}) = \sum_{\boldsymbol{k}}\sum_{\lambda=1}^{2}\sqrt{\frac{2\pi\omega_k}{V}}(a_{\boldsymbol{k}\lambda}\,\mathrm{e}^{\mathrm{i}\boldsymbol{k}\cdot\boldsymbol{r}} + a_{\boldsymbol{k}\lambda}^*\,\mathrm{e}^{-\mathrm{i}\boldsymbol{k}\cdot\boldsymbol{r}})\,\hat{\boldsymbol{e}}_{\boldsymbol{k}}^{(\lambda)}, \tag{2.52}$$

and, after having shown that

$$\begin{aligned}\int E_{\mathrm{em},\perp}^2(\boldsymbol{r})\ \mathrm{d}^3 r\ &= (4\pi)^2\int \Pi^2(\boldsymbol{r})\ \mathrm{d}^3 r = (4\pi)^2\sum_{\boldsymbol{k}}\boldsymbol{\pi}_{\boldsymbol{k}}\cdot\boldsymbol{\pi}_{\boldsymbol{k}}^* \\ &= \sum_{\boldsymbol{k}}\sum_{\lambda=1}^{2} 2\pi\omega_k\,(a_{\boldsymbol{k}\lambda}a_{\boldsymbol{k}\lambda}^* + a_{\boldsymbol{k}\lambda}a_{-\boldsymbol{k}\lambda} + a_{-\boldsymbol{k}\lambda}^*a_{\boldsymbol{k}\lambda}^* + a_{-\boldsymbol{k}\lambda}^*a_{-\boldsymbol{k}\lambda})\end{aligned} \tag{2.53}$$

and similarly that

$$\begin{aligned}\int B_{\mathrm{em}}^2(\boldsymbol{r})\ \mathrm{d}^3 r\ &= \sum_{\boldsymbol{k}}(\mathrm{i}\boldsymbol{k}\times\boldsymbol{\mathcal{A}}_{\boldsymbol{k}})\cdot(-\mathrm{i}\boldsymbol{k}\times\boldsymbol{\mathcal{A}}_{\boldsymbol{k}}^*) = \sum_{\boldsymbol{k}}k^2\boldsymbol{\mathcal{A}}_{\boldsymbol{k}}\cdot\boldsymbol{\mathcal{A}}_{\boldsymbol{k}}^* \\ &= \sum_{\boldsymbol{k}}\sum_{\lambda=1}^{2}\frac{2\pi\omega_k}{c^2}\,(a_{\boldsymbol{k}\lambda}a_{\boldsymbol{k}\lambda}^* - a_{\boldsymbol{k}\lambda}a_{-\boldsymbol{k}\lambda} - a_{-\boldsymbol{k}\lambda}^*a_{\boldsymbol{k}\lambda}^* + a_{-\boldsymbol{k}\lambda}^*a_{-\boldsymbol{k}\lambda}),\end{aligned} \tag{2.54}$$

we conclude that the total energy in the fluorescent electromagnetic field is given by

$$H_{\mathrm{F}} = \frac{1}{8\pi}\int\left[E_{\mathrm{em},\perp}^2 + c^2 B_{\mathrm{em}}^2(\boldsymbol{r})\right]\ \mathrm{d}^3 r = \frac{1}{2}\sum_{\boldsymbol{k}}\sum_{\lambda=1}^{2}\omega_k(a_{\boldsymbol{k}\lambda}a_{\boldsymbol{k}\lambda}^* + a_{\boldsymbol{k}\lambda}^*a_{\boldsymbol{k}\lambda}). \tag{2.55}$$

The quantization of the canonically coupled fields $\boldsymbol{A}(\boldsymbol{r}) \to \hat{\boldsymbol{A}}(\boldsymbol{r})$, $\boldsymbol{\Pi}(\boldsymbol{r}) \to \hat{\boldsymbol{\Pi}}(\boldsymbol{r})$, is equivalent to the quantization of the mode components $a_{\boldsymbol{k}\lambda} \to \hat{a}_{\boldsymbol{k}\lambda}$, $a^*_{\boldsymbol{k}\lambda} \to \hat{a}^\dagger_{\boldsymbol{k}\lambda}$, such that

$$\{a_{\boldsymbol{k}\lambda},\, a^*_{\boldsymbol{k}'\lambda'}\} = -\mathrm{i}\,\delta_{\boldsymbol{k}\boldsymbol{k}'}\,\delta_{\lambda\lambda'} \quad \to \quad [\hat{a}_{\boldsymbol{k}\lambda}, \hat{a}^\dagger_{\boldsymbol{k}'\lambda'}] = \delta_{\boldsymbol{k}\boldsymbol{k}'}\,\delta_{\lambda\lambda'}, \tag{2.56}$$

with creation and annihilation operators $\hat{a}^\dagger_{\boldsymbol{k}\lambda}$ and $\hat{a}_{\boldsymbol{k}\lambda}$ acting on the Fock space $\mathcal{F}_{\boldsymbol{k}\lambda}$ relative to the mode $\boldsymbol{k}\lambda$, with $\mathcal{F}_{\boldsymbol{k}\lambda} = \mathcal{H}_{0_{\boldsymbol{k}\lambda}} \oplus \mathcal{H}_{1_{\boldsymbol{k}\lambda}} \oplus \mathcal{H}_{2_{\boldsymbol{k}\lambda}} \oplus \ldots$ being the direct sum of zero-, one-, two-, ...-particle Hilbert spaces, $\mathcal{F}_{\boldsymbol{k}\lambda} = \mathrm{span}\{|0_{\boldsymbol{k}\lambda}\rangle, |1_{\boldsymbol{k}\lambda}\rangle, |2_{\boldsymbol{k}\lambda}\rangle, \ldots\}$ and

$$\begin{aligned}
\hat{a}^\dagger_{\boldsymbol{k}\lambda}|n_{\boldsymbol{k}\lambda}\rangle &= \sqrt{n_{\boldsymbol{k}\lambda}+1}|n_{\boldsymbol{k}\lambda}+1\rangle,\\
\hat{a}_{\boldsymbol{k}\lambda}|n_{\boldsymbol{k}\lambda}\rangle &= \sqrt{n_{\boldsymbol{k}\lambda}}|n_{\boldsymbol{k}\lambda}-1\rangle,\\
\hat{n}_{\boldsymbol{k}\lambda}|n_{\boldsymbol{k}\lambda}\rangle &= \hat{a}^\dagger_{\boldsymbol{k}\lambda}\hat{a}_{\boldsymbol{k}\lambda}|n_{\boldsymbol{k}\lambda}\rangle = n_{\boldsymbol{k}\lambda}|n_{\boldsymbol{k}\lambda}\rangle.
\end{aligned} \tag{2.57}$$

As a result, the eigenstates of the multi-mode Hamiltonian $\hat{H}_\mathrm{F}$, obtained by quantization of Eq. (2.27c) and (2.55), i.e.,

$$H_\mathrm{F} \quad \to \quad \hat{H}_\mathrm{F} = \frac{1}{2}\sum_{\boldsymbol{k}}\sum_{\lambda=1}^{2}\omega_k(\hat{a}_{\boldsymbol{k}\lambda}\hat{a}^\dagger_{\boldsymbol{k}\lambda} + \hat{a}^\dagger_{\boldsymbol{k}\lambda}\hat{a}_{\boldsymbol{k}\lambda}) = \sum_{\boldsymbol{k}}\sum_{\lambda=1}^{2}\omega_k\left(\hat{a}^\dagger_{\boldsymbol{k}\lambda}\hat{a}_{\boldsymbol{k}\lambda} + \frac{1}{2}\right), \tag{2.58}$$

are the symmetrized product states $|n_{\boldsymbol{k}_1\lambda_1}, n_{\boldsymbol{k}_2\lambda_2}, n_{\boldsymbol{k}_3\lambda_3}, \ldots\rangle = |\{n_{\boldsymbol{k}\lambda}\}\rangle$, i.e.,

$$\hat{H}_\mathrm{F}|\{n_{\boldsymbol{k}\lambda}\}\rangle = \sum_{\boldsymbol{k}}\sum_{\lambda=1}^{2}\omega_k\left(\hat{a}^\dagger_{\boldsymbol{k}\lambda}\hat{a}_{\boldsymbol{k}\lambda} + \frac{1}{2}\right)|\{n_{\boldsymbol{k}\lambda}\}\rangle = \left[\sum_{\boldsymbol{k}}\sum_{\lambda=1}^{2}\left(n_{\boldsymbol{k}\lambda} + \frac{1}{2}\right)\right]|\{n_{\boldsymbol{k}\lambda}\}\rangle. \tag{2.59}$$

We finally observe that, in terms of creation and annihilation operators, the emitted electric field, from quantization of the classical electric field (2.52), is

$$\boldsymbol{E}_{\mathrm{em},\perp}(\boldsymbol{r}) \quad \to \quad \hat{\boldsymbol{E}}_{\mathrm{em},\perp}(\boldsymbol{r}) = \sum_{\boldsymbol{k}}\sum_{\lambda=1}^{2}\sqrt{\frac{2\pi\omega_k}{V}}(\hat{a}_{\boldsymbol{k}\lambda}\,\mathrm{e}^{\mathrm{i}\boldsymbol{k}\cdot\boldsymbol{r}} + \hat{a}^\dagger_{\boldsymbol{k}\lambda}\,\mathrm{e}^{-\mathrm{i}\boldsymbol{k}\cdot\boldsymbol{r}})\,\hat{\boldsymbol{e}}^{(\lambda)}_{\boldsymbol{k}}. \tag{2.60}$$

2.3.2 Electric-field operator in the far-field region

The quantization of the interaction Hamiltonian H_AF (2.27d) results from Eqs. (2.32) and (2.60), such that

$$\begin{aligned}
\hat{H}_\mathrm{AF} = -\hat{\boldsymbol{d}}\cdot\hat{\boldsymbol{E}}_{\mathrm{em},\perp}(\boldsymbol{r}_0) &= -\sum_{ii'}\sum_{\boldsymbol{k}}\sum_{\lambda=1}^{2}\sqrt{\frac{2\pi\omega_k}{V}}(\boldsymbol{d}_{ii'}\hat{\sigma}_{ii'}\hat{a}_{\boldsymbol{k}\lambda}\,\mathrm{e}^{\mathrm{i}\boldsymbol{k}\cdot\boldsymbol{r}_0} + \boldsymbol{d}^*_{ii'}\hat{\sigma}_{i'i}\hat{a}^\dagger_{\boldsymbol{k}\lambda}\,\mathrm{e}^{-\mathrm{i}\boldsymbol{k}\cdot\boldsymbol{r}_0})\cdot\hat{\boldsymbol{e}}^{(\lambda)}_{\boldsymbol{k}}\\
&\approx -\sum_{\substack{ii'\\ i'<i}}\sum_{\boldsymbol{k}}\sum_{\lambda=1}^{2}\sqrt{\frac{2\pi\omega_k}{V}}(\boldsymbol{d}_{ii'}\hat{\sigma}_{ii'}\hat{a}_{\boldsymbol{k}\lambda}\,\mathrm{e}^{\mathrm{i}\boldsymbol{k}\cdot\boldsymbol{r}_0} + \boldsymbol{d}^*_{ii'}\hat{\sigma}_{i'i}\hat{a}^\dagger_{\boldsymbol{k}\lambda}\,\mathrm{e}^{-\mathrm{i}\boldsymbol{k}\cdot\boldsymbol{r}_0})\cdot\hat{\boldsymbol{e}}^{(\lambda)}_{\boldsymbol{k}},
\end{aligned} \tag{2.61}$$

which describes the electric-dipole interaction of an atom at position $\boldsymbol{r}_0$ with the electric field in the rotating-wave approximation [53, 54]. This Hamiltonian, together with $\hat{H}_\mathrm{F}$ (2.58), can be used to derive the Heisenberg equations of motion [156] for the operator $\hat{a}_{\boldsymbol{k}\lambda}$, i.e.,

$$\dot{\hat{a}}_{\boldsymbol{k}\lambda} = \mathrm{i}[\hat{H}_\mathrm{F} + \hat{H}_\mathrm{AF},\, \hat{a}_{\boldsymbol{k}\lambda}] = -\mathrm{i}\omega_k\hat{a}_{\boldsymbol{k}\lambda} + \mathrm{i}\sum_{\substack{ii'\\ i'<i}}\sqrt{\frac{2\pi\omega_k}{V}}(\boldsymbol{d}^*_{ii'}\cdot\hat{\boldsymbol{e}}^{(\lambda)}_{\boldsymbol{k}})\hat{\sigma}_{i'i}\,\mathrm{e}^{-\mathrm{i}\boldsymbol{k}\cdot\boldsymbol{r}_0}, \tag{2.62}$$

which can be formally integrated, leading to

$$\hat{a}_{\boldsymbol{k}\lambda}(t) = \hat{a}_{\boldsymbol{k}\lambda}(t_0)\,\mathrm{e}^{-\mathrm{i}\omega_k(t-t_0)} + \mathrm{i}\sum_{\substack{ii'\\ i'<i}} \sqrt{\frac{2\pi\omega_k}{V}}(\boldsymbol{d}^*_{ii'}\cdot\hat{\boldsymbol{e}}^{(\lambda)}_{\boldsymbol{k}})\,\mathrm{e}^{-\mathrm{i}\boldsymbol{k}\cdot\boldsymbol{r}_0}\int_{t_0}^{t}\hat{\sigma}_{i'i}(t')\,\mathrm{e}^{-\mathrm{i}\omega_k(t-t')}\,\mathrm{d}t'. \tag{2.63}$$

The first term represents the free evolution of the field in the absence of the interaction [53]. Here, we focus on the second contribution, i.e., in the electric-field operator

$$\begin{aligned}\hat{\boldsymbol{E}}_{\mathrm{em},\perp}(\boldsymbol{r},\,t) &= \mathrm{i}\sum_{\boldsymbol{k}}\frac{2\pi\omega_k}{V}\,\mathrm{e}^{\mathrm{i}\boldsymbol{k}\cdot(\boldsymbol{r}-\boldsymbol{r}_0)}\sum_{\substack{ii'\\ i'<i}}\left[\sum_{\lambda=1}^{2}\hat{\boldsymbol{e}}^{(\lambda)}_{\boldsymbol{k}}(\boldsymbol{d}^*_{ii'}\cdot\hat{\boldsymbol{e}}^{(\lambda)}_{\boldsymbol{k}})\right]\int_{t_0}^{t}\hat{\sigma}_{i'i}(t')\,\mathrm{e}^{-\mathrm{i}\omega_k(t-t')}\,\mathrm{d}t' + \mathrm{H.c.}\\ &\approx \mathrm{i}\sum_{\substack{ii'\\ i'<i}}\boldsymbol{d}^*_{ii'}\cdot\int_0^\infty k^2\frac{\omega_k}{4\pi^2}\left[\int\mathrm{e}^{\mathrm{i}\boldsymbol{k}\cdot(\boldsymbol{r}-\boldsymbol{r}_0)}\left(1-\frac{\boldsymbol{k}\boldsymbol{k}}{k^2}\right)\mathrm{d}\Omega_{\boldsymbol{k}}\right]\int_{t_0}^{t}\hat{\sigma}_{i'i}(t')\,\mathrm{e}^{-\mathrm{i}\omega_k(t-t')}\,\mathrm{d}t'\,\mathrm{d}k + \mathrm{H.c.},\end{aligned} \tag{2.64}$$

where H. c. denoted the Hermitian conjugate, we have substituted the sum over $\boldsymbol{k}$ with a three-dimensional integral over $k = |\boldsymbol{k}|$ and over the solid angle $\Omega_{\boldsymbol{k}}$, and have used the relation

$$\sum_{\lambda=1}^{2}\hat{\boldsymbol{e}}^{(\lambda)}_{\boldsymbol{k}}\hat{\boldsymbol{e}}^{(\lambda)}_{\boldsymbol{k}} = 1 - \frac{\boldsymbol{k}\boldsymbol{k}}{k^2}. \tag{2.65}$$

For large values of $|\boldsymbol{r}-\boldsymbol{r}_0|$, in the far-field region, one can approximate the integral over the solid angle with

$$\int\mathrm{e}^{\mathrm{i}\boldsymbol{k}\cdot(\boldsymbol{r}-\boldsymbol{r}_0)}\left(1-\frac{\boldsymbol{k}\boldsymbol{k}}{k^2}\right)\mathrm{d}\Omega_{\boldsymbol{k}} \approx 4\pi\frac{\sin(k|\boldsymbol{r}-\boldsymbol{r}_0|)}{k|\boldsymbol{r}-\boldsymbol{r}_0|}\left(1-\frac{(\boldsymbol{r}-\boldsymbol{r}_0)(\boldsymbol{r}-\boldsymbol{r}_0)}{|\boldsymbol{r}-\boldsymbol{r}_0|^2}\right), \tag{2.66}$$

such that, by adopting the Weißkopf-Wigner approximation, i.e., by substituting k^2 with $(\omega_{ii'}/c)^2$ and extending the integral over k to $-\infty$, we obtain [53]

$$\begin{aligned}\hat{\boldsymbol{E}}_{\mathrm{em},\perp}(\boldsymbol{r},\,t) &= \sum_{\substack{ii'\\ i'<i}}\boldsymbol{d}^*_{ii'}\cdot\left(1-\frac{(\boldsymbol{r}-\boldsymbol{r}_0)(\boldsymbol{r}-\boldsymbol{r}_0)}{|\boldsymbol{r}-\boldsymbol{r}_0|^2}\right)\frac{\omega^2_{ii'}}{c|\boldsymbol{r}-\boldsymbol{r}_0|}\\ &\qquad\times\int_{t_0}^{t}\hat{\sigma}_{i'i}(t')\,\frac{1}{2\pi}\int_{-\infty}^{\infty}\mathrm{e}^{-\mathrm{i}k[c(t-t')-|\boldsymbol{r}-\boldsymbol{r}_0|]} - \mathrm{e}^{-\mathrm{i}k[c(t-t')+|\boldsymbol{r}-\boldsymbol{r}_0|]})\,\mathrm{d}k\,\mathrm{d}t' + \mathrm{H.c.}\\ &= \sum_{\substack{ii'\\ i'<i}}\boldsymbol{d}^*_{ii'}\cdot\left(1-\frac{(\boldsymbol{r}-\boldsymbol{r}_0)(\boldsymbol{r}-\boldsymbol{r}_0)}{|\boldsymbol{r}-\boldsymbol{r}_0|^2}\right)\frac{\omega^2_{ii'}}{c^2|\boldsymbol{r}-\boldsymbol{r}_0|}\left[\hat{\sigma}_{i'i}(t-|\boldsymbol{r}-\boldsymbol{r}_0|/c)+\hat{\sigma}_{i'i}(t+|\boldsymbol{r}-\boldsymbol{r}_0|/c)\right] + \mathrm{H.c.}\end{aligned} \tag{2.67}$$

By taking only the retarded-time term and going back to the definition of the electric-dipole moment operator, we conclude that

$$\hat{\boldsymbol{E}}_{\mathrm{em},\perp}(\boldsymbol{r},\,t) = \sum_{ii'}\frac{\omega^2_{ii'}}{c^2|\boldsymbol{r}-\boldsymbol{r}_0|}\left[\hat{\boldsymbol{d}}_{ii'}(t-|\boldsymbol{r}-\boldsymbol{r}_0|/c)) - \frac{\boldsymbol{r}-\boldsymbol{r}_0}{|\boldsymbol{r}-\boldsymbol{r}_0|}\left(\hat{\boldsymbol{d}}_{ii'}(t-|\boldsymbol{r}-\boldsymbol{r}_0|/c)\cdot\frac{\boldsymbol{r}-\boldsymbol{r}_0}{|\boldsymbol{r}-\boldsymbol{r}_0|}\right)\right]. \tag{2.68}$$

This equation is of fundamental importance, because it tells us that, to know the properties of the electric field, a complete dynamical study of the infinitely many modes $\boldsymbol{k}\lambda$ is unnecessary.

It is namely sufficient to study how the atomic operators $\hat{\sigma}_{ii'}(t)$ evolve in time to automatically also gain knowledge of the properties of the electric field. This suggests to treat the atom as an open quantum system, i.e., to look for equations of motion which involve the sole atomic operators and which include effectively the impact of the interaction Hamiltonian $\hat{H}_{\mathrm{AF}}$ in terms of dissipation of the system.

In conclusion, we can use Eq. (2.68) to write the emitted electric field as the sum of a positive- and a negative-frequency component, i.e.,

$$\hat{\boldsymbol{E}}_{\mathrm{em},\perp}(\boldsymbol{r},\,t) = \hat{\boldsymbol{E}}^{+}_{\mathrm{em},\perp}(\boldsymbol{r},\,t) + \hat{\boldsymbol{E}}^{-}_{\mathrm{em},\perp}(\boldsymbol{r},\,t), \tag{2.69}$$

with $\hat{\boldsymbol{E}}^{-}_{\mathrm{em},\perp}(\boldsymbol{r},\,t) = [\hat{\boldsymbol{E}}^{+}_{\mathrm{em},\perp}(\boldsymbol{r},\,t)]^{\dagger}$ and

$$\hat{\boldsymbol{E}}^{+}_{\mathrm{em},\perp}(\boldsymbol{r},\,t) = \sum_{\substack{ii'\\ i'<i}} \boldsymbol{d}^{*}_{ii'} \cdot \left(1 - \frac{(\boldsymbol{r}-\boldsymbol{r}_0)(\boldsymbol{r}-\boldsymbol{r}_0)}{|\boldsymbol{r}-\boldsymbol{r}_0|^2}\right) \frac{\omega^2_{ii'}}{c^2|\boldsymbol{r}-\boldsymbol{r}_0|}\, \hat{\sigma}_{i'i}(t-|\boldsymbol{r}-\boldsymbol{r}_0|/c). \tag{2.70}$$

2.4 Density matrix formalism and spontaneous decay

A solution of the Heisenberg equations of motion would imply an exact treatment of the infinite number of modes of the electromagnetic field $|\{n_{\boldsymbol{k}\lambda}\}\rangle$. Not only this is not possible, but, owing to Eq. (2.68), would also be of little interest for our purposes.

In the following, we introduce the density matrix of the atomic system. This object is necessary when one deals with an open quantum system. This allows one to describe the dynamics of a small system in interaction with the rest of the universe without having to take the latter into account explicitly. The effect of $\hat{H}_{\mathrm{AF}}$, describing the interaction of the atom with a reservoir of modes of the electromagnetic field, results in the spontaneous decay of the atomic excited states and gives rise to dissipation terms in the equations of motion. Our discussion follows Ref. [157].

2.4.1 Density matrix

A density matrix is the fundamental object to describe an open quantum system [157]. We assume that $\{|i\rangle\}$ is a complete and orthogonal basis spanning the Hilbert space $\mathcal{H}_{\mathrm{S}}$ of the system, whereas the rest of the universe, i.e., the environment, is described by a quantum state in the Hilbert space $\mathcal{H}_{\mathrm{E}}$ spanned by the complete and orthogonal basis $\{|j\rangle\}$. The total state, describing the system and the environment in the tensor-product Hilbert space $\mathcal{H} = \mathcal{H}_{\mathrm{S}} \otimes \mathcal{H}_{\mathrm{E}}$, can be written as a linear combination of tensor-product basis states $\{|i\rangle \otimes |j\rangle\}$, i.e.,

$$|\psi(t)\rangle = \sum_{i,j} a_{ij}(t)\, |i\rangle \otimes |j\rangle. \tag{2.71}$$

Similarly, a general operator acting both on the system and on the environment can be written in this basis as

$$\hat{A} = \sum_{\substack{ii'\\ jj'}} A_{ii',jj'}\, |i\rangle\langle i'| \otimes |j\rangle\langle j'|, \tag{2.72}$$

with expectation value

$$\langle \hat{A} \rangle = \sum_{\substack{ii'\\ jj'}} a^{*}_{ij}(t)\, a_{i'j'}(t)\, A_{ii',jj'}. \tag{2.73}$$

One is usually interested in operators which act directly only on the degrees of freedom of the system, i.e., $\hat{A} = \hat{A}_{\mathrm{S}} \otimes \mathbb{1}_{\mathrm{E}}$, such that $A_{ii',jj'} = A_{\mathrm{S},ii'}\,\delta_{jj'}$. It follows that

$$\langle \hat{A}_{\mathrm{S}} \rangle = \langle \hat{A} \rangle = \sum_{ii'} \Big(\sum_{j} a^{*}_{ij}(t)\, a_{i'j}(t) \Big) A_{\mathrm{S},ii'} = \sum_{ii'} \rho_{\mathrm{S},i'i}\, A_{\mathrm{S},ii'} = \sum_{i} \langle i | \rho_{\mathrm{S}}\, A_{\mathrm{S}} | i \rangle = \mathrm{Tr}_{\mathrm{S}}\{ \hat{\rho}_{\mathrm{S}} \hat{A}_{\mathrm{S}} \}, \tag{2.74}$$

where we have introduced the density matrix of the system

$$\begin{aligned} \rho_{\mathrm{S}}(t) \; &= \sum_{ii'} \rho_{\mathrm{S},ii'}(t) |i\rangle\langle i'| = \sum_{ii'} \Big(\sum_{j} a_{ij}(t)\, a^{*}_{i'j}(t) \Big) |i\rangle\langle i'| \\ &= \sum_{j} \langle j | \psi(t) \rangle \langle \psi(t) | j \rangle = \mathrm{Tr}_{\mathrm{E}}\{ |\psi(t)\rangle\langle\psi(t)| \}, \end{aligned} \tag{2.75}$$

and have used the definition of trace of an operator on the degrees of freedom of the system Tr_{S} and of the environment Tr_{E},

$$\mathrm{Tr}_{\mathrm{S}}\{\hat{A}\} \; = \sum_{i} \langle i | \hat{A} | i \rangle = \sum_{jj'} \Big(\sum_{i} A_{ii,jj'} \Big) |j\rangle\langle j'|, \tag{2.76a}$$

$$\mathrm{Tr}_{\mathrm{E}}\{\hat{A}\} \; = \sum_{j} \langle j | \hat{A} | j \rangle = \sum_{ii'} \Big(\sum_{j} A_{ii',jj} \Big) |i\rangle\langle i'|, \tag{2.76b}$$

$$\mathrm{Tr}\{\hat{A}\} \; = \mathrm{Tr}_{\mathrm{E}}\{\mathrm{Tr}_{\mathrm{S}}\{\hat{A}\}\} = \sum_{ij} \langle i | \otimes \langle j |\, \hat{A}\, |i\rangle \otimes |j\rangle = \sum_{ij} A_{ii,jj}. \tag{2.76c}$$

From the definition of the density matrix $\hat{\rho}_{\mathrm{S}}$ we can see that

$$\rho_{\mathrm{S},ii'} = \sum_{j} a_{ij}\, a^{*}_{i'j} = \rho^{*}_{\mathrm{S},i'i} \quad \Rightarrow \quad \hat{\rho}^{\dagger}_{\mathrm{S}} = \hat{\rho}_{\mathrm{S}}, \tag{2.77}$$

i.e., the density matrix is a Hermitian operator, with diagonal real elements $\rho_{\mathrm{S},ii}$ and complex conjugate off-diagonal elements $\rho_{\mathrm{S},ii'} = \rho^{*}_{\mathrm{S},i'i}$. The diagonal elements of the density matrix, usually called **populations**,

$$\rho_{\mathrm{S},ii} = \mathrm{Tr}_{\mathrm{S}}\{ \hat{\rho}_{\mathrm{S}} |i\rangle\langle i| \} = \sum_{j} |a_{ij}|^2 = \sum_{j} |(\langle i| \otimes \langle j|)\, |\psi(t)\rangle|^2, \tag{2.78}$$

describe the statistical probability to measure the system in the state $|i\rangle$. The off-diagonal terms of the density matrix $\rho_{\mathrm{S},ii'}$, usually called **coherences**, describe the amplitude whereby the system is found in a coherent superposition of states $|i\rangle$ and $|i'\rangle$, i.e.,

$$\rho_{\mathrm{S},ii'} = \mathrm{Tr}_{\mathrm{S}}\{ \hat{\rho}_{\mathrm{S}} |i'\rangle\langle i| \} = \sum_{j} a_{ij}\, a^{*}_{i'j} = \sum_{j} (\langle i| \otimes \langle j|)\, |\psi(t)\rangle\langle\psi(t)| (|i\rangle \otimes |j\rangle|). \tag{2.79}$$

From Eq. (2.74), we can calculate the expectation values of the identity operator $\mathbb{1}_{\mathrm{S}}$ and of the projector operator $|\varphi\rangle\langle\varphi|$, where $|\varphi\rangle$ is a state in $\mathcal{H}_{\mathrm{S}}$, $\langle\varphi|\varphi\rangle = 1$, $|\varphi\rangle = \sum_i c_i |i\rangle$, i.e.,

$$\langle \mathbb{1}_{\mathrm{S}} \rangle \; = \mathrm{Tr}_{\mathrm{S}}\{\hat{\rho}_{\mathrm{S}}\} = \mathrm{Tr}_{\mathrm{S}}\{\mathrm{Tr}_{\mathrm{E}}\{|\psi(t)\rangle\langle\psi(t)|\}\} = \mathrm{Tr}\{|\psi(t)\rangle\langle\psi(t)|\} = \langle\psi(t)|\psi(t)\rangle = 1, \tag{2.80a}$$

$$\langle |\varphi\rangle\langle\varphi| \rangle \; = \mathrm{Tr}_{\mathrm{S}}\{\hat{\rho}_{\mathrm{S}} |\varphi\rangle\langle\varphi|\} = \langle\varphi|\rho_{\mathrm{S}}(t)|\varphi\rangle = \mathrm{Tr}\{|\psi(t)\rangle\langle\psi(t)|\; (|\varphi\rangle\langle\varphi| \otimes \mathbb{1}_{\mathrm{E}})\} = \sum_{j} \Big| \sum_{i} c_i a^{*}_{ij} \Big|^2 \geq 0. \tag{2.80b}$$

This allows one to conclude that the density matrix $\rho_{\mathrm{S}}(t)$ is a positive definite Hermitian matrix with norm equal to 1, for any time t.

When the system and the environment are uncorrelated, i.e., the total Hamiltonian does not include any interaction terms, $\hat{H} = \hat{H}_{\mathrm{S}} \otimes \mathbb{1}_{\mathrm{E}} + \mathbb{1}_{\mathrm{S}} \otimes \hat{H}_{\mathrm{E}}$, then at any time t the total state $|\psi(t)\rangle$ can be factorized into the product $|\psi(t)\rangle = |\psi_{\mathrm{S}}(t)\rangle \otimes |\psi_{\mathrm{E}}(t)\rangle$, and the density matrix

$$\rho_{\mathrm{S}}(t) = \mathrm{Tr}_{\mathrm{E}}\{|\psi_{\mathrm{S}}(t)\rangle\langle\psi_{\mathrm{S}}(t)| \otimes |\psi_{\mathrm{E}}(t)\rangle\langle\psi_{\mathrm{E}}(t)|\} = |\psi_{\mathrm{S}}(t)\rangle\langle\psi_{\mathrm{S}}(t)| \tag{2.81}$$

describes a pure state. From the Schrödinger equation satisfied by $|\psi_{\mathrm{S}}(t)\rangle$, i.e.,

$$\frac{\mathrm{d}|\psi_{\mathrm{S}}(t)\rangle}{\mathrm{d}t} = -\mathrm{i}\hat{H}_{\mathrm{S}}|\psi_{\mathrm{S}}(t)\rangle, \tag{2.82}$$

we obtain the **Liouville-von Neumann equation** [157] describing the dynamics of the density matrix

$$\frac{\partial\hat{\rho}_{\mathrm{S}}(t)}{\partial t} = -\mathrm{i}[\hat{H}_{\mathrm{S}}, \hat{\rho}_{\mathrm{S}}]. \tag{2.83}$$

When the Hamiltonian does contain an interaction term, $\hat{H} = \hat{H}_{\mathrm{S}} \otimes \mathbb{1}_{\mathrm{E}} + \mathbb{1}_{\mathrm{S}} \otimes \hat{H}_{\mathrm{E}} + \hat{H}_{\mathrm{int}}$, the total state $|\psi(t)\rangle$ cannot be written as the previous tensor product. We can introduce the total density matrix $\hat{\rho}_{\mathrm{SE}}(t) = |\psi(t)\rangle\langle\psi(t)|$ evolving under the effect of the total Hamiltonian $\hat{H}$,

$$\frac{\partial\hat{\rho}_{\mathrm{SE}}(t)}{\partial t} = -\mathrm{i}[\hat{H}_{\mathrm{S}} \otimes \mathbb{1}_{\mathrm{E}} + \mathbb{1}_{\mathrm{S}} \otimes \hat{H}_{\mathrm{E}} + \hat{H}_{\mathrm{int}}, \hat{\rho}_{\mathrm{SE}}(t)], \tag{2.84}$$

such that the time evolution of the system density matrix $\hat{\rho}_{\mathrm{S}}(t)$ can be recovered by tracing on the degrees of freedom of the environment, i.e.,

$$\frac{\partial\hat{\rho}_{\mathrm{S}}(t)}{\partial t} = -\mathrm{i}\,\mathrm{Tr}_{\mathrm{E}}\{[\hat{H}_{\mathrm{S}} \otimes \mathbb{1}_{\mathrm{E}} + \mathbb{1}_{\mathrm{S}} \otimes \hat{H}_{\mathrm{E}} + \hat{H}_{\mathrm{int}}, \hat{\rho}_{\mathrm{SE}}(t)]\}. \tag{2.85}$$

This equation of motion, though, is not very informative, as it requires a solution of the Liouville-von Neumann equation for $\rho(t)$ which includes the presence of the environment explicitly. The same problem could be more effectively addressed if one could rely on a dynamical map $\mathcal{V}(t,\, t_0)$ which, given the initial state of the system $\rho_{\mathrm{S}}(t_0)$, is able to predict how this state evolves, $\rho_{\mathrm{S}}(t) = \mathcal{V}(t,\, t_0)\,\rho_{\mathrm{S}}(t_0)$, without having to take into account the presence of the environment explicitly. In other words, we look for a Lindblad form of the Liouville-von Neumann equation,

$$\frac{\partial\hat{\rho}_{\mathrm{S}}(t)}{\partial t} = \mathcal{L}[\hat{\rho}_{\mathrm{S}}(t)], \tag{2.86}$$

with the **Lindblad superoperator** $\mathcal{L}[\hat{\rho}_{\mathrm{S}}(t)]$ acting only on the degrees of freedom of the system. Such a dynamical map must preserve at any time all the defining properties of the density matrix $\hat{\rho}_{\mathrm{S}}(t)$, i.e., hermiticity, positive definiteness, and norm equal to unity.

2.4.2 Spontaneous decay of the excited levels in a quantum system

We adopt a density-matrix formalism to include the effect of the interaction Hamiltonian $\hat{H}_{\mathrm{AF}}$ on the atomic-system dynamics. We introduce the total density matrix $\hat{\rho}_{\mathrm{AF}}(t)$, whose time evolution is given by the Liouville-von Neumann equation

$$\frac{\mathrm{d}\hat{\rho}_{\mathrm{AF}}}{\mathrm{d}t} = -\mathrm{i}[\hat{H}_0 + \hat{H}_{\mathrm{F}} + \hat{H}_{\mathrm{AL}}(t) + \hat{H}_{\mathrm{AF}},\, \hat{\rho}_{\mathrm{AF}}(t)], \tag{2.87}$$

where the total Hamiltonian

$$\hat{H} = \hat{H}_0 + \hat{H}_{\rm F} + \hat{H}_{\rm AL}(t) + \hat{H}_{\rm AF} \tag{2.88}$$

is the quantum counterpart of the classical total Hamiltonian (2.26), where $\hat{H}_0$ is the electronic structure Hamiltonian of the bare atom, $\hat{H}_{\rm F}$ represents the total Hamiltonian of the fluorescence field, $\hat{H}_{\rm AL}(t)$ describes the time-dependent interaction of the atom with the classical laser field $\boldsymbol{\mathcal{E}}_{\rm ext}(\boldsymbol{r},\, t)$, and $\hat{H}_{\rm AF}$ accounts for the interaction of the atomic system with the fluorescence field.

As introduced in the previous Section, one can define an atomic density matrix

$$\hat{\rho}_{\rm A}(t) = {\rm Tr}_{\rm F}\{\hat{\rho}_{\rm AF}(t)\} = \sum_{\{n_{\boldsymbol{k}\lambda}\}} \langle\{n_{\boldsymbol{k}\lambda}\}|\hat{\rho}_{\rm AF}(t)|\{n_{\boldsymbol{k}\lambda}\}\rangle, \tag{2.89}$$

whose evolution in time is obtained by tracing the Liouville-von Neumann equation (2.87) on the electromagnetic-field degrees of freedom, i.e.,

$$\frac{{\rm d}\hat{\rho}_{\rm A}}{{\rm d}t} = -{\rm i}\,{\rm Tr}_{\rm F}\big\{[\hat{H}_0 + \hat{H}_{\rm F} + \hat{H}_{\rm AL}(t) + \hat{H}_{\rm AF},\, \hat{\rho}_{\rm AF}(t)]\big\}. \tag{2.90}$$

The trace on the right-hand side of the previous equation is performed in the **Born-Markov approximation**, by assuming that the environment, formed by the reservoir of modes of the electromagnetic field, loses memory of its past state in a time scale which is much shorter than the time scale characterizing the evolution of the atomic variables [54, 158]. From the electric-dipole interaction Hamiltonian in the rotating-wave approximation, the Born-Markov approximation, and the Weißkopf-Wigner approximation already discussed in the derivation of Eq. (2.68), the following master equation ensues,

$$\frac{{\rm d}\hat{\rho}_{\rm A}}{{\rm d}t} = -{\rm i}[\hat{H}_0 + \hat{H}_{\rm AL}(t),\, \hat{\rho}_{\rm A}(t)] + \mathcal{L}[\hat{\rho}_{\rm A}(t)], \tag{2.91}$$

with the Lindblad superoperator

$$\mathcal{L}[\hat{\rho}_{\rm A}(t)] = \sum_{\substack{ii'\\ i'<i}} -\frac{\Gamma_{ii'}}{2}(\hat{\sigma}_{ii'}\hat{\sigma}_{i'i}\hat{\rho}_{\rm A}(t) - \hat{\sigma}_{i'i}\hat{\rho}_{\rm A}(t)\hat{\sigma}_{ii'}) + \text{ H.c.} \tag{2.92}$$

in which we have utilized the E1 decay rates

$$\Gamma_{ii'} = \frac{4\omega_{ii'}^3|\boldsymbol{d}_{i'i}|^2}{3c^3}. \tag{2.93}$$

It is possible to show that such master equation preserves the norm, the hermiticity, and the positive definiteness of the density matrix at any time [158].

2.5 Selection rules

It is worthwhile to spend a few words on the transition rules, i.e., the conditions that need be fulfilled in order $\boldsymbol{d}_{ii'}$ not to vanish. We observe that $\hat{\boldsymbol{d}}$ is an irreducible tensor operator of rank 1 [155, 159], which can be written as

$$\hat{\boldsymbol{d}} = \hat{d}_{-1}^{(1)}\hat{\boldsymbol{e}}_{\sigma_-} + \hat{d}_0^{(1)}\hat{\boldsymbol{e}}_z + \hat{d}_1^{(1)}\hat{\boldsymbol{e}}_{\sigma_+}, \tag{2.94}$$

where $\hat{d}^{(1)}_m$, $m \in \{0, \pm 1\}$ are the three independent components of the tensor, $\hat{\boldsymbol{e}}_x$, $\hat{\boldsymbol{e}}_y$, and $\hat{\boldsymbol{e}}_z$ are the three unit vectors in the three real independent directions and we have introduced the circular polarization vectors

$$\hat{\boldsymbol{e}}_{\sigma_\pm} = \frac{\mp\hat{\boldsymbol{e}}_x + \mathrm{i}\hat{\boldsymbol{e}}_y}{\sqrt{2}}, \qquad \hat{\boldsymbol{e}}^*_{\sigma_\pm} = -\hat{\boldsymbol{e}}_{\sigma_\mp}, \tag{2.95a}$$

$$\hat{\boldsymbol{e}}_{\sigma_\pm} \cdot \hat{\boldsymbol{e}}^*_{\sigma_\pm} = 1, \qquad \hat{\boldsymbol{e}}_{\sigma_\pm} \cdot \hat{\boldsymbol{e}}^*_{\sigma_\mp} = 0, \tag{2.95b}$$

positive (negative) for polarization $\lambda = \pm 1$.

Spin-degenerate levels. In the case in which spin effects are not important and the eigenstates $|\Psi_i\rangle$ of the bare electronic structure Hamiltonian $\hat{H}_0$ are also eigenstates of the orbital and spin total-angular momentum operators $\hat{L}^2$, $\hat{L}_z$, $\hat{S}^2$, and S_z, with eigenvalues $L_i(L_i+1)$, M_{L_i}, $S_i(S_i+1)$, and M_{S_i}, then these eigenstates can be written as

$$|\Psi_i\rangle = |\tau_i\, L_i\, M_{L_i}\, S_i\, M_{S_i}\rangle, \tag{2.96}$$

where $\tau_i = \{n_{q_i}\, l_{q_i}\}$ collects all the quantum numbers associated with a given electron configuration. The electric-dipole moment operator $\hat{\boldsymbol{d}}$ acts only on the orbital part of the eigenstates $|\Psi_i\rangle$, such that $\boldsymbol{d}_{ii'} = \langle \tau_i\, L_i\, M_{L_i}|\hat{\boldsymbol{d}}|\tau_{i'}\, L_{i'}\, M_{L_{i'}}\rangle\, \delta_{S_i S_{i'}} \delta_{M_{S_i} M_{S_{i'}}}$. The application of the Wigner-Eckart theorem [155, 159] implies that

$$\langle \tau_i\, L_i\, M_{L_i}|\hat{d}^{(1)}_j|\tau_{i'}\, L_{i'}\, M_{L_{i'}}\rangle = \frac{1}{\sqrt{2L_i+1}} \langle \tau_i\, L_i||\mathsf{d}^{(1)}||\tau_{i'}\, L_{i'}\rangle\, \langle L_{i'}\, 1\, M_{L_{i'}}\, m|L_i\, M_{L_{i'}}\rangle, \tag{2.97}$$

where $\langle \tau_i\, L_i||\mathsf{d}^{(1)}||\tau_{i'}\, L_{i'}\rangle$ is the reduced matrix element, independent of the quantum numbers M_{L_i} and $M_{L_{i'}}$, and $\langle L_{i'}\, 1\, M_{L_{i'}}\, m|L_i\, M_{L_{i'}}\rangle$ is the Clebsch-Gordan coefficient. The properties of the Clebsch-Gordan coefficients imply the following selection rules [155], i.e., the matrix element $\langle \tau_i\, L_i\, M_{L_i}|\hat{d}^{(1)}_s|\tau_{i'}\, L_{i'}\, M_{L_{i'}}\rangle$ is nonzero if

$$m = M_{L_i} - M_{L_{i'}}, \tag{2.98}$$

$$|L_i - L_{i'}| \leq 1 \leq L_i + L_{i'}. \tag{2.99}$$

Spin-nondegenerate levels. When spin effects have a determinant influence on the electronic structure of the atom or ion, such that the eigenstates $|\Psi_i\rangle$ of the atomic Hamiltonian need be described as eigenstates of the total-angular-momentum operators $\hat{J}^2$ and $\hat{J}_z$, with eigenvalues $J_i(J_i+1)$ and M_{J_i}, respectively, then in the LS coupling, when L_i and S_i are still good quantum numbers, we can write

$$|\Psi_i\rangle = |\tau_i\, J_i\, M_{J_i}\, L_i\, S_i\rangle. \tag{2.100}$$

The previously described selection rules for L_i and S_i can be used also in this case, i.e., $S_i = S_{i'}$, $|L_i - L_{i'}| \leq 1 \leq L_i + L_{i'}$, but we ought to substitute the old selection rules based on the quantum numbers M_{S_i} and M_{L_i} with new ones for J_i and M_{J_i}. This is achieved by applying the Wigner-Eckart theorem in this new basis [155, 159], thus obtaining

$$\langle \tau_i\, J_i\, M_{J_i}|\hat{d}^{(1)}_j|\tau_{i'}\, J_{i'}\, M_{J_{i'}}\rangle = \frac{1}{\sqrt{2J_i+1}} \langle \tau_i\, J_i||\mathsf{d}^{(1)}||\tau_{i'}\, J_{i'}\rangle\, \langle J_{i'}\, 1\, M_{J_{i'}}\, m|J_i\, M_{J_{i'}}\rangle, \tag{2.101}$$

where $\langle \tau_i\, J_i||\mathsf{d}^{(1)}||\tau_{i'}\, J_{i'}\rangle$ is the new reduced matrix element, independent of the quantum numbers M_{J_i} and $M_{J_{i'}}$, and $\langle J_{i'}\, 1\, M_{J_{i'}}\, m|J_i\, M_{J_{i'}}\rangle$ is the Clebsch-Gordan coefficient. The new selection rules are

$$m = M_{J_i} - M_{J_{i'}}, \tag{2.102}$$

$$|J_i - J_{i'}| \leq 1 \leq J_i + J_{i'}. \tag{2.103}$$

Parity conservation. In the next Chapters we will focus on electron transitions involving single-electron jumps, i.e., a configuration change $\{n_q l_q\} \to \{n'_q l'_q\}$ in which, for all $q \neq \tilde{q}$, where $\tilde{q}$ labels a single given electron, one has $n_q = n'_q$, $l_q = l'_q$. In this case, the properties of a single-electron orbital are sufficient to show that parity conservation implies the additional selection rule [149, 150]

$$l_{\tilde{q}} = l'_{\tilde{q}} \pm 1. \tag{2.104}$$

2.6 Rabi flopping

In the next Chapters we will often refer to Rabi flopping of the atomic population and coherences induced by the interaction of an atom with a strong driving electric field, described by the interaction Hamiltonian

$$\hat{H}_{\rm AL}(t) = -\sum_{ii'} \boldsymbol{d}_{ii'} \cdot \boldsymbol{\mathcal{E}}_{\rm ext}(\mathbf{0},\, t)\hat{\sigma}_{ii'}. \tag{2.105}$$

Rabi oscillations were first studied by Rabi in the context of magnetic resonances [160]. However, the same equations of motion also describe the dynamics of an atomic quantum system driven by an electric field with constant amplitude. We extend this terminology to all the cases in which an external field induces oscillations of the atomic variables, also when this does not take place at a fixed and constant Rabi frequency.

We consider in this Section a two-level system formed by two states $|1\rangle$ and $|2\rangle$, with transition energy ω_{21} and dipole-moment matrix element $\boldsymbol{d}_{12} = d_{12}\,\hat{\boldsymbol{e}}_z$ aligned on the z direction, with decay rate $\Gamma = \Gamma_{21}$ and driven by an external field

$$\boldsymbol{\mathcal{E}}_{\rm ext}(\mathbf{0},\, t) = \frac{\mathcal{E}_0(t)}{2}\left(\mathrm{e}^{\mathrm{i}\omega_{\rm L}t} + \mathrm{e}^{-\mathrm{i}\omega_{\rm L}t}\right)\hat{\boldsymbol{e}}_z, \tag{2.106}$$

with amplitude $\mathcal{E}_0(t)$, central frequency $\omega_{\rm L}$, with detuning $\Delta = \omega_{21} - \omega_{\rm L}$, and polarized in the z direction. In the rotating-wave approximation, the interaction Hamiltonian is

$$\begin{aligned}\hat{H}_{\rm AL} &= -\left(\boldsymbol{d}_{12}\hat{\sigma}_{12} + \boldsymbol{d}_{21}\hat{\sigma}_{21}\right)\cdot\boldsymbol{\mathcal{E}}_{\rm ext}(\mathbf{0},\, t)\\ &\approx -\frac{1}{2}\left[d_{12}\,\mathcal{E}_0(t)\,\mathrm{e}^{\mathrm{i}\omega_{\rm L}t}\,\hat{\sigma}_{12} + d_{21}\,\mathcal{E}_0(t)\,\mathrm{e}^{-\mathrm{i}\omega_{\rm L}t}\,\hat{\sigma}_{21}\right],\end{aligned} \tag{2.107}$$

where one neglects fast oscillating contributions due to the terms $\mathrm{e}^{-\mathrm{i}\omega_{\rm L}t}\,\hat{\sigma}_{12}$ and $\mathrm{e}^{\mathrm{i}\omega_{\rm L}t}\,\hat{\sigma}_{21}$. One can therefore introduce the time-dependent Rabi frequency

$$\Omega(t) = d_{12}\,\mathcal{E}_0(t) \tag{2.108}$$

in terms of which we write the master equation for the atomic density matrix $\hat{\rho}(t)$,

$$\frac{\mathrm{d}\hat{\rho}}{\mathrm{d}t} = -\mathrm{i}\left[\omega_1\hat{\sigma}_{11} + \omega_2\hat{\sigma}_{22} - \frac{\Omega(t)}{2}\,\mathrm{e}^{\mathrm{i}\omega_{\rm L}t}\,\hat{\sigma}_{12} + \frac{\Omega^*(t)}{2}\,\mathrm{e}^{-\mathrm{i}\omega_{\rm L}t}\,\hat{\sigma}_{21},\, \hat{\rho}(t)\right] + \mathcal{L}[\hat{\rho}(t)], \tag{2.109}$$

with the Lindblad superoperator

$$\mathcal{L}[\hat{\rho}(t)] = -\frac{\Gamma}{2}\left[\hat{\sigma}_{21}\hat{\sigma}_{12}\hat{\rho}(t) - 2\hat{\sigma}_{12}\hat{\rho}(t)\hat{\sigma}_{21} + \hat{\rho}(t)\hat{\sigma}_{21}\hat{\sigma}_{12}\right]. \tag{2.110}$$

This gives rise to the following equations of motion for the elements of the density matrix,

$$\dot{\rho}_{11} = \mathrm{i}\left(\frac{\Omega(t)}{2}\,\mathrm{e}^{\mathrm{i}\omega_\mathrm{L}t}\,\rho_{21} - \frac{\Omega^*(t)}{2}\,\mathrm{e}^{-\mathrm{i}\omega_\mathrm{L}t}\,\rho_{12}\right) + \Gamma\,\rho_{22}, \tag{2.111a}$$

$$\dot{\rho}_{22} = -\mathrm{i}\left(\frac{\Omega(t)}{2}\,\mathrm{e}^{\mathrm{i}\omega_\mathrm{L}t}\,\rho_{21} - \frac{\Omega^*(t)}{2}\,\mathrm{e}^{-\mathrm{i}\omega_\mathrm{L}t}\,\rho_{12}\right) - \Gamma\,\rho_{22}, \tag{2.111b}$$

$$\dot{\rho}_{12} = \mathrm{i}\,\omega_{21}\,\rho_{12} + \mathrm{i}\,\frac{\Omega(t)}{2}\,\mathrm{e}^{\mathrm{i}\omega_\mathrm{L}t}\,(\rho_{22} - \rho_{11}) - \frac{\Gamma}{2}\,\rho_{12}, \tag{2.111c}$$

with $\rho_{12} = \rho_{21}^*$. These equations may be written in a Bloch form [161] by exploiting the algebraic properties of the three operators $\hat{\sigma}_- = \hat{\sigma}_{12}$, $\hat{\sigma}_+ = \hat{\sigma}_{21}$, and $\hat{\sigma}_z = \hat{\sigma}_{22} - \hat{\sigma}_{11}$, which form a simple representation of Pauli operators, with standard commutation rules $[\hat{\sigma}_+, \hat{\sigma}_-] = \hat{\sigma}_z$ and $[\hat{\sigma}_z, \hat{\sigma}_\pm] = \pm 2\hat{\sigma}_\pm$. We notice that, owing to the absence of any norm-nonconserving term, $\dot{\rho}_{11} = -\dot{\rho}_{22}$, such that $\rho_{22}(t) = 1 - \rho_{11}(t)$. In terms of the components of the slowly oscillating density matrix $\hat{\varrho}(t)$,

$$\varrho_{ii}(t) = \rho_{ii}(t), \qquad \varrho_{12}(t) = \varrho_{21}^*(t) = \rho_{12}(t)\,\mathrm{e}^{-\mathrm{i}\omega_\mathrm{L}t}, \tag{2.112}$$

these equations can be written as

$$\dot{\varrho}_{11} = \mathrm{i}\left(\frac{\Omega(t)}{2}\,\varrho_{21} - \frac{\Omega^*(t)}{2}\,\varrho_{12}\right) + \Gamma\,\varrho_{22}, \tag{2.113a}$$

$$\dot{\varrho}_{22} = -\mathrm{i}\left(\frac{\Omega(t)}{2}\,\varrho_{21} - \frac{\Omega^*(t)}{2}\,\varrho_{12}\right) - \Gamma\,\varrho_{22}, \tag{2.113b}$$

$$\dot{\varrho}_{12} = \mathrm{i}\,\Delta\,\varrho_{12} + \mathrm{i}\,\frac{\Omega(t)}{2}\,(\varrho_{22} - \varrho_{11}) - \frac{\Gamma}{2}\,\varrho_{12}. \tag{2.113c}$$

In the absence of spontaneous decay and detuning, a solution of the previous equations of motion can be formally obtained by introducing the instantaneous pulse area

$$\vartheta(t) = \int_{-\infty}^{t} \Omega(t')\,\mathrm{d}t', \tag{2.114}$$

with the total area

$$Q = \lim_{t\to\infty} \vartheta(t) = \int_{-\infty}^{\infty} \Omega(t')\,\mathrm{d}t'. \tag{2.115}$$

If $\Omega(t) = 0$ for $t < 0$ and, at $t = 0$, the system is in the initial state $\varrho_{11}(0) = 1$, $\varrho_{12}(0) = \varrho_{21}(0) = 0$, $\varrho_{22}(0) = 0$, the solution of the equations of motion is [70]

$$\varrho_{11}(t) = \frac{1 + \cos[\vartheta(t)]}{2}, \tag{2.116a}$$

$$\varrho_{22}(t) = \frac{1 - \cos[\vartheta(t)]}{2}, \tag{2.116b}$$

$$\varrho_{12}(t) = -\frac{\mathrm{i}}{2}\sin[\vartheta(t)]\,. \tag{2.116c}$$

For pulses of finite area $Q < \infty$, one can predict in the limit of vanishing decay rates and detuning, for an arbitrary shape of the time-dependent Rabi frequency, that the system reaches

the stationary value

$$\varrho_{11,\mathrm{S}} = \frac{1+\cos(Q)}{2}, \tag{2.117a}$$

$$\varrho_{22,\mathrm{S}} = \frac{1-\cos(Q)}{2}, \tag{2.117b}$$

$$\varrho_{12,\mathrm{S}} = -\frac{\mathrm{i}}{2}\sin(Q). \tag{2.117c}$$

For $Q = (2n+1)\pi$, $n \in \mathbb{N}$, the system at the end of the pulse has performed a complete switch in the population, whereas for $Q = 2n\pi$, $n \in \mathbb{N}$, the system at the end of the pulse is in the same state it was at the beginning. We finally notice that the well known solution of the Rabi problem in the case of constant Rabi frequency Ω_R can be recovered by setting $\vartheta(t) = \Omega_\mathrm{R} t$ in Eq. (2.116).

When one includes the presence of the detuning Δ, an exact solution of the set of differential equations (2.113) can be obtained only in two cases. For constant Rabi frequency Ω_R, the solution of the equations of motion

$$\varrho_{11}(t) = 1 + \frac{\Omega_\mathrm{R}}{2\sqrt{\Omega_\mathrm{R}^2+\Delta^2}}\left[1-\cos\left(\sqrt{\Omega_\mathrm{R}^2+\Delta^2}\,t\right)\right], \tag{2.118a}$$

$$\varrho_{22}(t) = -\frac{\Omega_\mathrm{R}}{2\sqrt{\Omega_\mathrm{R}^2+\Delta^2}}\left[1-\cos\left(\sqrt{\Omega_\mathrm{R}^2+\Delta^2}\,t\right)\right], \tag{2.118b}$$

$$\varrho_{12}(t) = -\frac{\mathrm{i}}{2}\sin\left(\sqrt{\Omega_\mathrm{R}^2+\Delta^2}\,t\right), \tag{2.118c}$$

displays oscillations at the effective frequency $\Omega_\mathrm{eff} = \sqrt{\Omega_\mathrm{R}^2+\Delta^2}$ [53]. An analytical solution can be found also in the case of a hyperbolic-secant envelope function, $\Omega(t) = \Omega_\mathrm{max}\,\mathrm{sech}(\gamma t)$, where $\mathrm{sech}(x) = 1/\cosh(x)$ and γ is the bandwidth of the pulse. We will investigate this situation in depth for a three-level system in Chapter 6.

If one takes into account the presence both of detuning and decay rate, an analytical investigation can be performed in the case of constant Rabi frequency. Because of the decay rate Γ, the system, despite being continuously driven by a field of constant Rabi frequency, reaches the stationary solution

$$\varrho_{11,\mathrm{S}} = \frac{4\Delta^2+\Gamma^2+\Omega_\mathrm{R}^2}{4\Delta^2+\Gamma^2+2\Omega_\mathrm{R}^2}, \tag{2.119a}$$

$$\varrho_{22,\mathrm{S}} = \frac{\Omega_\mathrm{R}^2}{4\Delta^2+\Gamma^2+2\Omega_\mathrm{R}^2}, \tag{2.119b}$$

$$\varrho_{12,\mathrm{S}} = -\mathrm{i}\,\frac{\Omega_\mathrm{R}}{\Gamma-2\mathrm{i}\Delta}\,\frac{4\Delta^2+\Gamma^2}{4\Delta^2+\Gamma^2+2\Omega_\mathrm{R}^2}. \tag{2.119c}$$

In the absence of detuning the system, with oscillations at the effective Rabi frequency $\Omega_\mathrm{eff} = \sqrt{\Omega_\mathrm{R}^2+(\Gamma/4)^2}$, reaches this stationary state with a decay rate given by $3\Gamma/4$ [53].

2.7 The spectrum analyzer

An atomic system driven by an external field, whose dynamical evolution follows the equations of motion given by the master equation (2.91), emits photons because of spontaneous decay.

This affects the time evolution of the electric-field operator in Eq. (2.68). The spectral features of the emitted electric field are measured by a spectrometer, i.e., a detector able to distinguish the presence of photons in a frequency interval $[\omega, \omega + \mathrm{d}\omega]$. In this Section, we conclude this introductory Chapter by revising Glauber's theory of the spectrum analyzer [162], which provides us with an operational definition of the spectrum of a classical or quantum electromagnetic field [53].

We model the spectrometer as an ideal two-level system, with ground and excited states, $|g\rangle$ and $|e\rangle$, respectively, with tunable transition energy ω_{eg} and dipole-moment matrix element $\boldsymbol{\mathcal{P}}_{ge} = \boldsymbol{\mathcal{P}}_{eg}^{*} = \mathcal{P}_{ge}\,\hat{\boldsymbol{e}}_{ge}$ with polarization vector $\hat{\boldsymbol{e}}_{ge}$. The fixed polarization of the one-atom detector allows one to model polarization-sensitive measurements.

The total Hamiltonian of a single-atom detector in interaction with an external electric field is given by $\hat{H}$ in Eq. (2.88), where the detector Hamiltonian $\hat{H}_{\mathrm{D}}$, the interaction Hamiltonian $\hat{H}_{\mathrm{DL}}$ between detector and laser field, the quantum-field Hamiltonian $\hat{H}_{\mathrm{F}}$, and the interaction Hamiltonian $\hat{H}_{\mathrm{DF}}$ between detector and quantum field, are given by

$$\hat{H}_{\mathrm{D}} = \frac{\omega_{eg}}{2}\hat{\sigma}_{ee} - \frac{\omega_{eg}}{2}\hat{\sigma}_{gg}, \tag{2.120a}$$

$$\hat{H}_{\mathrm{DL}} = -(\boldsymbol{\mathcal{P}}_{ge}\,\hat{\sigma}_{ge} + \boldsymbol{\mathcal{P}}_{ge}^{*}\,\hat{\sigma}_{eg}) \cdot \boldsymbol{\mathcal{E}}_{\mathrm{ext}}(\boldsymbol{r},\, t) \tag{2.120b}$$

$$\hat{H}_{\mathrm{F}} = \sum_{\boldsymbol{k}\lambda} \hat{a}_{\boldsymbol{k}\lambda}^{\dagger}\hat{a}_{\boldsymbol{k}\lambda} \tag{2.120c}$$

$$\hat{H}_{\mathrm{DF}} = -(\boldsymbol{\mathcal{P}}_{ge}\,\hat{\sigma}_{ge} + \boldsymbol{\mathcal{P}}_{ge}^{*}\,\hat{\sigma}_{eg}) \cdot \hat{\boldsymbol{E}}_{\mathrm{em},\perp}(\boldsymbol{0}). \tag{2.120d}$$

We want to calculate the probability that, by interacting with the external field, the one-atom detector is excited from its initial state $|g\rangle$ to the excited state $|e\rangle$. The system is described in the Schrödinger picture by a total density matrix $\hat{\rho}_{\mathrm{DF}}(t)$, whose time evolution is given by the Liouville-von Neumann equation

$$\frac{\mathrm{d}\hat{\rho}_{\mathrm{DF}}}{\mathrm{d}t} = -\mathrm{i}[\hat{H}_{\mathrm{D}} + \hat{H}_{\mathrm{F}} + \hat{H}_{\mathrm{DL}} + \hat{H}_{\mathrm{DF}},\, \hat{\rho}_{\mathrm{DF}}]. \tag{2.121}$$

In the interaction picture, by including the fast oscillating terms in the definition of the slowly varying density matrix

$$\hat{\varrho}_{\mathrm{DF}}(t) = \mathrm{e}^{\mathrm{i}(\hat{H}_{\mathrm{D}}+\hat{H}_{\mathrm{F}})(t-t_0)}\hat{\rho}_{\mathrm{DF}}(t)\mathrm{e}^{-\mathrm{i}(\hat{H}_{\mathrm{D}}+\hat{H}_{\mathrm{F}})(t-t_0)}, \tag{2.122}$$

the Liouville-von Neumann equation for the transformed density matrix is

$$\frac{\mathrm{d}\hat{\varrho}_{\mathrm{DF}}}{\mathrm{d}t} = -\mathrm{i}[\hat{\mathscr{H}}_{\mathrm{DL}}(t) + \hat{\mathscr{H}}_{\mathrm{DF}}(t),\, \hat{\varrho}_{\mathrm{DF}}(t)], \tag{2.123}$$

with interaction-picture Hamiltonians

$$\hat{\mathscr{H}}_{\mathrm{DL}}(t) = \mathrm{e}^{\mathrm{i}\hat{H}_{\mathrm{D}}(t-t_0)}\hat{H}_{\mathrm{DL}}\mathrm{e}^{-\mathrm{i}\hat{H}_{\mathrm{D}}(t-t_0)}, \tag{2.124a}$$

$$\hat{\mathscr{H}}_{\mathrm{DF}}(t) = \mathrm{e}^{\mathrm{i}(\hat{H}_{\mathrm{D}}+\hat{H}_{\mathrm{F}})(t-t_0)}\hat{H}_{\mathrm{DF}}\mathrm{e}^{-\mathrm{i}(\hat{H}_{\mathrm{D}}+\hat{H}_{\mathrm{F}})(t-t_0)}, \tag{2.124b}$$

which, in terms of the transformed operators

$$\mathrm{e}^{\mathrm{i}\hat{H}_{\mathrm{D}}(t-t_0)}\hat{\sigma}_{ge}\mathrm{e}^{-\mathrm{i}\hat{H}_{\mathrm{D}}(t-t_0)} = \hat{\sigma}_{ge}\,\mathrm{e}^{-\mathrm{i}\omega_{eg}(t-t_0)}, \tag{2.125a}$$

$$\mathrm{e}^{\mathrm{i}\hat{H}_{\mathrm{F}}(t-t_0)}\hat{a}_{\boldsymbol{k}\boldsymbol{\lambda}}\mathrm{e}^{-\mathrm{i}\hat{H}_{\mathrm{F}}(t-t_0)} = \hat{a}_{\boldsymbol{k}\boldsymbol{\lambda}}\,\mathrm{e}^{-\mathrm{i}\omega_k(t-t_0)}, \tag{2.125b}$$

$$\hat{\tilde{\boldsymbol{E}}}_{\mathrm{em},\perp}(\boldsymbol{r},\, t) = \sum_{\boldsymbol{k}}\sum_{\lambda=1}^{2}\sqrt{\frac{2\pi\omega_k}{V}}(\hat{a}_{\boldsymbol{k}\boldsymbol{\lambda}}\,\mathrm{e}^{-\mathrm{i}\omega_k(t-t_0)}\,\mathrm{e}^{-\mathrm{i}\boldsymbol{k}\cdot(\boldsymbol{r}-\boldsymbol{r}_0)} + \hat{a}_{\boldsymbol{k}\boldsymbol{\lambda}}^{\dagger}\,\mathrm{e}^{\mathrm{i}\omega_k(t-t_0)}\,\mathrm{e}^{\mathrm{i}\boldsymbol{k}\cdot(\boldsymbol{r}-\boldsymbol{r}_0)})\,\cdot\,\hat{\boldsymbol{e}}_{\boldsymbol{k}}^{(\lambda)}, \tag{2.125c}$$

can be written as

$$\hat{\mathscr{H}}_{\mathrm{DL}}(t) = -(\boldsymbol{\mathcal{P}}_{ge}\,\hat{\sigma}_{ge}\,\mathrm{e}^{-\mathrm{i}\omega_{eg}(t-t_0)} + \boldsymbol{\mathcal{P}}^*_{ge}\,\hat{\sigma}_{eg}\,\mathrm{e}^{\mathrm{i}\omega_{eg}(t-t_0)})\cdot\boldsymbol{\mathcal{E}}_{\mathrm{ext}}(\boldsymbol{r},\,t), \tag{2.126a}$$

$$\hat{\mathscr{H}}_{\mathrm{DF}}(t) = -(\boldsymbol{\mathcal{P}}_{ge}\,\hat{\sigma}_{ge}\,\mathrm{e}^{-\mathrm{i}\omega_{eg}(t-t_0)} + \boldsymbol{\mathcal{P}}^*_{ge}\,\hat{\sigma}_{eg}\,\mathrm{e}^{\mathrm{i}\omega_{eg}(t-t_0)})\cdot\hat{\tilde{\boldsymbol{E}}}_{\mathrm{em},\perp}(\boldsymbol{r},\,t). \tag{2.126b}$$

The system is assumed to be initially in the state described by the density matrix $\hat{\rho}_{\mathrm{DF}}(t_0) = \hat{\varrho}_{\mathrm{DF}}(t_0) = |g\rangle\langle g| \otimes \hat{\rho}_{\mathrm{F}}$. The interaction-picture Liouville-von Neumann equation can be solved in second order of perturbation theory

$$\begin{aligned}\hat{\varrho}_{\mathrm{DF}}(t) = |g\rangle\langle g| \otimes \hat{\rho}_{\mathrm{F}} - \mathrm{i}\int_{t_0}^{t} [\hat{\mathscr{H}}_{\mathrm{DL}}(t') + \hat{\mathscr{H}}_{\mathrm{DF}}(t'),\, |g\rangle\langle g| \otimes \hat{\rho}_{\mathrm{F}}]\;\mathrm{d}t' \\ - \int_{t_0}^{t}\int_{t_0}^{t'} [\hat{\mathscr{H}}_{\mathrm{DL}}(t') + \hat{\mathscr{H}}_{\mathrm{DF}}(t'),\, [\hat{\mathscr{H}}_{\mathrm{DL}}(t'') + \hat{\mathscr{H}}_{\mathrm{DF}}(t''),\, |g\rangle\langle g| \otimes \hat{\rho}_{\mathrm{F}}]]\;\mathrm{d}t''\;\mathrm{d}t'.\end{aligned} \tag{2.127}$$

The transition probability, i.e., the probability that at time t the one-atom detector is in the excited state $|e\rangle$, is the expectation value of the projector operator $|e\rangle\langle e| \otimes \mathbb{1}_{\mathrm{F}}$, which remains unchanged in the interaction picture. We use the density matrix at second order to compute the transition probability

$$\begin{aligned}&\mathrm{Tr}_{\mathrm{DF}}\left\{\hat{\varrho}_{\mathrm{DF}}(t)|e\rangle\langle e| \otimes \mathbb{1}_{\mathrm{F}}\right\} \\ &= \int_{t_0}^{t}\int_{t_0}^{t'} \mathrm{Tr}_{\mathrm{DF}}\left\{[\hat{\mathscr{H}}_{\mathrm{DL}}(t') + \hat{\mathscr{H}}_{\mathrm{DF}}(t')]\,|g\rangle\langle g| \otimes \hat{\rho}_{\mathrm{F}}\,[\hat{\mathscr{H}}_{\mathrm{DL}}(t'') + \hat{\mathscr{H}}_{\mathrm{DF}}(t'')]\,|e\rangle\langle e| \otimes \mathbb{1}_{\mathrm{F}}\right\}\mathrm{d}t''\;\mathrm{d}t' \\ &\quad + \int_{t_0}^{t}\int_{t_0}^{t'} \mathrm{Tr}_{\mathrm{DF}}\left\{[\hat{\mathscr{H}}_{\mathrm{DL}}(t'') + \hat{\mathscr{H}}_{\mathrm{DF}}(t'')]\,|g\rangle\langle g| \otimes \hat{\rho}_{\mathrm{F}}\,[\hat{\mathscr{H}}_{\mathrm{DL}}(t') + \hat{\mathscr{H}}_{\mathrm{DF}}(t')]\,|e\rangle\langle e| \otimes \mathbb{1}_{\mathrm{F}}\right\}\mathrm{d}t''\;\mathrm{d}t' \\ &= \int_{t_0}^{t}\int_{t_0}^{t} \mathrm{Tr}_{\mathrm{F}}\left\{\langle e|\hat{\mathscr{H}}_{\mathrm{DL}}(t') + \hat{\mathscr{H}}_{\mathrm{DF}}(t')|g\rangle\langle g|\hat{\mathscr{H}}_{\mathrm{DL}}(t'') + \hat{\mathscr{H}}_{\mathrm{DF}}(t'')|e\rangle\hat{\rho}_{\mathrm{F}}\right\}\mathrm{d}t''\;\mathrm{d}t'.\end{aligned} \tag{2.128}$$

This leads to

$$\mathrm{Tr}_{\mathrm{DF}}\left\{\hat{\varrho}_{\mathrm{DF}}(t)|e\rangle\langle e| \otimes \mathbb{1}_{\mathrm{F}}\right\} = |\mathcal{P}_{ge}|^2\int_{t_0}^{t}\int_{t_0}^{t} G(\boldsymbol{r},\,t',\,t'')\,\mathrm{e}^{-\mathrm{i}\omega_{eg}(t''-t')}\;\mathrm{d}t''\;\mathrm{d}t', \tag{2.129}$$

where the two-time expectation value

$$G(\boldsymbol{r},\,t',\,t'') = \left\langle\left\{[\boldsymbol{\mathcal{E}}_{\mathrm{ext}}(\boldsymbol{r},\,t') + \hat{\boldsymbol{E}}_{\mathrm{em},\perp}(\boldsymbol{r},\,t')]\cdot\hat{\boldsymbol{e}}_{ge}\right\}\left\{[\boldsymbol{\mathcal{E}}_{\mathrm{ext}}(\boldsymbol{r},\,t'') + \hat{\boldsymbol{E}}_{\mathrm{em},\perp}(\boldsymbol{r},\,t'')]\cdot\hat{\boldsymbol{e}}^*_{ge}\right\}\right\rangle \tag{2.130}$$

is the autocorrelation function of the field at the fixed position $\boldsymbol{r}$. The two-time Fourier transform of the autocorrelation function represents the probability that a two-level system with energy ω_{ge} is excited by the interaction with the external field. This provides us with an operational definition of the spectrum of an external (classical or quantum) field, which will be used throughout the entire Thesis.

3 Resonance fluorescence in intense x-ray free-electron-laser pulses

In this Chapter, we develop a time-dependent theory of resonance fluorescence in order to investigate, in terms of a two-level model, the coherent interaction of intense x-ray pulses with core electrons by exciting K-shell transitions. In Sec. 3.1 we describe our theoretical approach, by defining the energy spectrum of resonance fluorescence and its main properties and by introducing the two-level model that is used throughout the Chapter. Results are discussed in Sec. 3.2: there, we apply the model to study neon cations driven by x-ray free-electron-laser (XFEL) pulses on the $1s\,2p^{-1} \to 1s^{-1}\,2p$ transition at $\omega_{21} = 848$ eV and examine the spectrum of resonance fluorescence for different driving pulses. In particular, we compare different spectra for the presently available chaotic pulses produced via the self-amplified-spontaneous-emission (SASE) principle and for pulses with a Gaussian temporal profile that seeding techniques are rendering available. Section 3.3 concludes the Chapter. Parts of this Chapter have been published in Ref. [163].

3.1 Theoretical model

3.1.1 Two-level model

The coherent interaction between atoms and ions and x rays tuned to a particular atomic resonance can be described in terms of a two-level model when the transition is isolated from other levels. In our case, we use such a model to study the $1s\,2p_z^{-1} \to 1s^{-1}\,2p_z$ transition in Ne^+ at an energy of 848 eV [139], driven by a near-resonant electric field linearly polarized along the z direction. The two-level model, which is depicted in Fig. 3.1, is justified by the fact that the transition is very well isolated, by more than 70 natural linewidths separated from the next Rydberg excitation $1s \to 3p$ of neutral Ne at 867 eV [139]. For neon, relativistic effects and fine-structure splitting do not play an important role and, therefore, spin-orbit splitting can be neglected. Here and in the remaining of the Section, we aim at specializing the general formalism, introduced in Chapter 2, for the case of a two-level system.

As we did in Eqs. (2.68) and (2.70), we describe the emitted fluorescent light field by a quantum operator $\hat{\boldsymbol{E}}(\boldsymbol{r}, t) = \hat{\boldsymbol{E}}^+(\boldsymbol{r}, t) + \hat{\boldsymbol{E}}^-(\boldsymbol{r}, t)$, where $\hat{\boldsymbol{E}}^+(\boldsymbol{r}, t)$ and $\hat{\boldsymbol{E}}^-(\boldsymbol{r}, t)$ are respectively the positive-frequency and negative-frequency parts of the operator [164]. However, it is sufficient to describe the relatively strong driving field classically [62], via

$$\boldsymbol{\mathcal{E}}(t) = \boldsymbol{\mathcal{E}}_0(t)\cos(\omega_X t + \varphi_X(t) + \varphi_{X,0}), \tag{3.1}$$

where $\boldsymbol{\mathcal{E}}_0(t)$ is the time-dependent electric-field envelope, ω_X the x-ray central frequency, $\varphi_X(t)$ the time-dependent phase of the field and $\varphi_{X,0}$ the carrier-envelope phase (CEP). We assume throughout an electric field linearly polarized along the z direction, $\boldsymbol{\mathcal{E}}_0(t) = \mathcal{E}_0(t)\,\hat{\boldsymbol{e}}_z$, with the unit vector in z direction $\hat{\boldsymbol{e}}_z$. The use of planar undulators at XFEL facilities, in fact, produces linearly polarized x-ray pulses [93]; experimental evidence for a very high degree of linear polarization of Linac-Coherent-Light-Source (LCLS) x rays has been given in Ref. [98, 139]. We further assume a pulse with uniform intensity distribution profile; spatial averaging is therefore not performed.

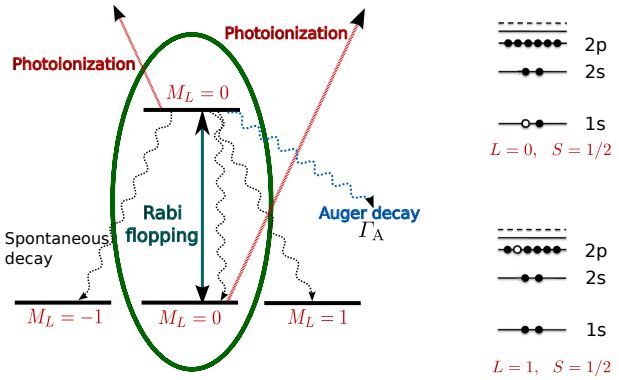

Figure 3.1: Two-level model used to describe the coherent interaction between Ne^+ and the external driving field tuned to the $1s\,2p^{-1} \rightarrow 1s^{-1}\,2p$ transition at 848 eV [139]. The ground state $1s\,2p^{-1}$ is given by $|1\rangle = |L = 1,\, M_L = 0\rangle$ and the core-excited state $1s^{-1}\,2p$ is written as $|2\rangle = |L = 0,\, M_L = 0\rangle$. The external field is linearly polarized along the z direction and induces Rabi flopping between these states. Spontaneous decay, however, also allows the core-excited state to decay to valence-ionized states with $M_L = \pm 1$.

In order to properly model the atomic transition, we have to take into account that, as seen in Fig. 3.1, the $1s\,2p^{-1}$ configuration is a spin doublet state with total orbital angular momentum $L = 1$; consequently, it is triply degenerate in energy. The three eigenstates of the unperturbed atomic Hamiltonian $\hat{H}_0$ with energy ω_1 which diagonalize the z component of the total orbital angular momentum operator $\hat{L}_z$ are $|1_+\rangle$, $|1_0\rangle$ and $|1_-\rangle$, respectively with $M_L = +1,\, 0,\, -1$. Conversely, the $1s^{-1}\,2p$ configuration corresponds to the single eigenstate $|2\rangle$ of the field-free atomic Hamiltonian, with $L = 0$, $M_L = 0$ and energy ω_2. The energy of the atomic transition is $\omega_{21} = \omega_2 - \omega_1$. The relevant raising and lowering atomic operators (2.33) are

$$\hat{\sigma}_{ij} = |i\rangle\langle j|, \quad i, j \in \{1_+,\, 1_0,\, 1_-,\, 2\}. \tag{3.2}$$

The interaction between the ions and the electric field is described in the dipole approximation because the $1s$ orbital of neon is compact, involving dimensions much smaller than the wavelength associated with the transition $1s\,2p^{-1} \rightarrow 1s^{-1}\,2p$, such that nondipole terms are negligible [138]. The Hamiltonian of the system is

$$\hat{H} = \hat{H}_0 + \hat{H}_{\mathrm{int}}, \tag{3.3}$$

where $\hat{H}_0 = \sum_i \omega_i\, \hat{\sigma}_{ii}$ is the unperturbed atomic Hamiltonian [see Eqs. (2.30) and (2.31)] with eigenvalues ω_i, whereas $\hat{H}_{\mathrm{int}}$ [see $\hat{H}_{\mathrm{AL}}$ in Eq. (2.105)] represents the interaction of the ion with the classical, linearly polarized, near-resonant field (3.1) [53],

$$\hat{H}_{\mathrm{int}} = -\hat{\boldsymbol{d}} \cdot \boldsymbol{\mathcal{E}}_0(t) \cos(\omega_{\mathrm{X}} t + \varphi_{\mathrm{X}}(t) + \varphi_{\mathrm{X},0}). \tag{3.4}$$

The operator $\hat{\boldsymbol{d}}$ in (3.4) is the total atomic polarization operator [see Eqs. (2.32) and (2.34)]

$$\hat{\boldsymbol{d}} = \hat{\boldsymbol{d}}^+ + \hat{\boldsymbol{d}}^-, \tag{3.5}$$

with $\hat{\boldsymbol{d}}^- = [\hat{\boldsymbol{d}}^+]^\dagger$ and [149]

$$\begin{aligned} \hat{\boldsymbol{d}}^+ &= \langle 1_+|\hat{\boldsymbol{d}}|2\rangle\, \hat{\sigma}_{1_+2} + \langle 1_0|\hat{\boldsymbol{d}}|2\rangle\, \hat{\sigma}_{1_02} + \langle 1_-|\hat{\boldsymbol{d}}|2\rangle\, \hat{\sigma}_{1_-2} \\ &= \wp(\hat{\boldsymbol{e}}_{\sigma^+}\, \hat{\sigma}_{1_+2} + \hat{\boldsymbol{e}}_z\, \hat{\sigma}_{1_02} + \hat{\boldsymbol{e}}_{\sigma^-}\, \hat{\sigma}_{1_-2}), \end{aligned} \tag{3.6}$$

where $\hat{\boldsymbol{e}}_x$, $\hat{\boldsymbol{e}}_y$, $\hat{\boldsymbol{e}}_z$ are unit vectors in the x, y, z directions and $\hat{\boldsymbol{e}}_{\sigma^\pm} = (\mp\hat{\boldsymbol{e}}_x + \mathrm{i}\hat{\boldsymbol{e}}_y)/\sqrt{2}$ are circular polarization vectors, positive (negative) for polarizations $\lambda = \pm 1$, with $\hat{\boldsymbol{e}}_{\sigma^\pm} = -\hat{\boldsymbol{e}}^*_{\sigma^\mp}$. Due to

spherical symmetry, the dipole matrix element is real, $\wp = \wp^*$, and is the same for all transitions; as the atomic states have a definite parity, $\langle 1_{\pm,0}|\hat{\boldsymbol{d}}|1_{\pm,0}\rangle = \langle 2|\hat{\boldsymbol{d}}|2\rangle = 0$, dipole transitions only couple states with different total angular momentum quantum numbers, $\Delta L = 1$ [149].

Since the external electric field is assumed to be linearly polarized [98, 139], the dipole interaction only couples the states $|2\rangle$ and $|1_0\rangle$ satisfying the condition $\Delta M_L = 0$ [149]: in Eq. (3.4), within the rotating-wave approximation [53] and by using Eq. (3.6), $\hat{H}_{\mathrm{int}}$ reduces to

$$\hat{H}_{\mathrm{int}} = -\frac{\Omega_{\mathrm{R}}(t)}{2}\left(\hat{\sigma}_{1_0 2}\,\mathrm{e}^{\mathrm{i}(\omega_{\mathrm{X}}t+\varphi_{\mathrm{X}}(t))} + \hat{\sigma}_{21_0}\,\mathrm{e}^{-\mathrm{i}(\omega_{\mathrm{X}}t+\varphi_{\mathrm{X}}(t))}\right), \tag{3.7}$$

where we have set the CEP $\varphi_{\mathrm{X},0}$ to 0 and where the instantaneous Rabi frequency

$$\Omega_{\mathrm{R}}(t) = \wp\,\mathcal{E}_0(t) \tag{3.8}$$

has been introduced.

In our model the dynamics of the two x-ray coupled states $|2\rangle$ and $|1_0\rangle$ is independent from the other two states $|1_\pm\rangle$ and one can develop an actual two-level description of the system in which the equations of motion (EOMs) exclusively contain the two aforementioned states $|1_0\rangle = |1\rangle$ and $|2\rangle$ and neglect the other two states entirely.

3.1.2 Density matrix formulation and equations of motion

We investigate in the following the two-level system formed by the states $|1\rangle \equiv |1_0\rangle$ and $|2\rangle$. We introduce the density matrix

$$\rho_{ij}(t) = \langle i|\hat{\rho}(t)|j\rangle = \langle \hat{\sigma}_{ji}(t)\rangle \tag{3.9}$$

($i, j \in \{1, 2\}$), whose evolution is described by the master equation [157]

$$\frac{\mathrm{d}\hat{\rho}}{\mathrm{d}t} = -\mathrm{i}\,[\hat{H}, \hat{\rho}(t)] + \mathcal{L}\hat{\rho}(t) + \mathcal{D}\hat{\rho}(t), \tag{3.10}$$

which is a generalization of Eq. (2.91) in order to include in an effective two-level description of the atomic system the transition, e.g., due to Auger decay, to other states not directly included in the model. The first term $-\mathrm{i}\,[\hat{H}, \hat{\rho}(t)]$ describes the coherent dynamics of the two-level system. In the total Hamiltonian $\hat{H}$ [Eq. (3.3)] the only relevant terms of the unperturbed atomic Hamiltonian $\hat{H}_0$ are $\omega_1\hat{\sigma}_{11}$ and $\omega_2\hat{\sigma}_{22}$. The Lindblad operator $\mathcal{L}\hat{\rho}(t)$ represents the norm-conserving spontaneous decay of the population from the excited state $|2\rangle$ to the ground state $|1\rangle$. The rate at which this process occurs is given by [53]

$$\Gamma_{\mathrm{R},z} = \frac{4\omega_{21}^3}{3c^3}|\wp|^2. \tag{3.11}$$

Atoms and ions with high atomic number are usually characterized by a high fluorescence yield, i.e., the importance of spontaneous decay compared to Auger decay increases with the atomic number of the ion of interest. The last term $\mathcal{D}\hat{\rho}(t)$ denotes the norm-nonconserving term not present in the Lindblad form of the master equation [158]. We introduce this term to describe the decrease of the population of both the upper and lower states [54]. These norm-nonconserving processes include Auger decay, photoionization of the system due to the intense external field and spontaneous decay from the excited level $|2\rangle$ to the two levels $|1_\pm\rangle$ which are not coupled by dipole interaction. We do not include Doppler broadening [165] and collision effects [54] in our

model, because they involve time scales much longer than the decay time of the system and, at room temperature and for a pressure of 1 atmosphere, they can be neglected [1].

Auger decay and photoionization destroy the two-level system by further ionization of Ne^+ to levels which need not be taken into account explicitly. The Auger decay width is Γ_{A}, whereas the rate of photoionization $\Gamma_{\mathrm{P},i}(t)$, $i \in \{1, 2\}$, is [88]

$$\Gamma_{\mathrm{P},i}(t) = \sigma_{\mathrm{X},i}\mathcal{J}_{\mathrm{X}}(t), \tag{3.12}$$

with the photoionization cross section for the level i $\sigma_{\mathrm{X},i} = \sigma_i(\omega_{\mathrm{X}})$, the x-ray flux

$$\mathcal{J}_{\mathrm{X}}(t) = I(t)/\omega_{\mathrm{X}}, \tag{3.13}$$

and the x-ray intensity

$$I(t) = \frac{\mathcal{E}_0^2(t)}{8\pi\alpha}. \tag{3.14}$$

Notice that we evaluate the photoionization cross section and the flux at ω_{X} since the cross sections do not vary much within the bandwidth of the field.

The spontaneous decay of the excited level $|2\rangle$ to the states $|1_\pm\rangle$ also represents a process which does not conserve the norm of our two-level system. The total radiative decay rate is given by

$$\Gamma_{\mathrm{R}} = \Gamma_{\mathrm{R},\sigma^+} + \Gamma_{\mathrm{R},z} + \Gamma_{\mathrm{R},\sigma^-} = 3\Gamma_{\mathrm{R},z}, \tag{3.15}$$

where $\Gamma_{\mathrm{R},z}$ is the spontaneous decay width to the state $|1\rangle$ given in (3.11) and $\Gamma_{\mathrm{R},\sigma^\pm}$ are defined analogously for the other two decay channels; the second equality exploits Eq. (3.6). Since the spontaneous decay of the excited level $|2\rangle$ only depends on the population of the state itself, as we are going to show in the following EOMs, the actual dynamics of states $|1_\pm\rangle$ can be indeed neglected for our purposes.

The total decay processes are included in Eq. (3.10). In order to derive the EOMs for the four relevant components of the density matrix, we move to the rotating frame [166], by introducing the operators

$$\hat{\varsigma}_{ii} = \hat{\sigma}_{ii}, \quad \hat{\varsigma}_{12} = \mathrm{e}^{\mathrm{i}\omega_{\mathrm{X}}t}\,\hat{\sigma}_{12}, \quad \hat{\varsigma}_{21} = \mathrm{e}^{-\mathrm{i}\omega_{\mathrm{X}}t}\,\hat{\sigma}_{21}, \tag{3.16}$$

whose expectation values are denoted by

$$R_{ij}(t) = \langle\hat{\varsigma}_{ji}(t)\rangle, \tag{3.17}$$

which, from (3.9) and (3.16), implies that $R_{ii}(t) = \rho_{ii}(t)$, $R_{12} = \rho_{12}\,\mathrm{e}^{-\mathrm{i}\omega_{\mathrm{X}}t}$ and $R_{21} = \rho_{21}\,\mathrm{e}^{\mathrm{i}\omega_{\mathrm{X}}t}$.

We introduce the vector

$$\vec{R}(t) = (R_{11}(t),\, R_{12}(t),\, R_{21}(t),\, R_{22}(t)\,)^{\mathrm{T}},$$

whose components are given by the elements of the density matrix $R_{ij}(t)$ in the rotating frame. Before the arrival of the light pulse the two-level system is assumed to be in the ground state, i.e., $\vec{R}_0 = (1,\, 0,\, 0,\, 0\,)^{\mathrm{T}}$. This assumption is supported by experimental observations of orbital alignment in ions produced by strong-field ionization [167]. If the fraction of ions in the $M_L = 0$ ground state is lower than 1, the resonance fluorescence spectrum must be multiplied by this factor.

[1] In the case of neon cations driven on the $1s\,2p^{-1} \to 1s^{-1}\,2p$ transition at $\omega_{21} = 848$ eV which we are going to consider in the following, at 300 K and for a pressure of 1 atmosphere, the Doppler broadening is 0.0024 eV, which is much less than the decay width of the system. Using the kinetic theory of gases, the mean time between collisions is approximately 1 ns, longer by many orders of magnitude than the lifetime of a $1s$ hole.

The master equation (3.10) can then be rewritten in matrix form

$$\frac{\mathrm{d}\vec{R}(t)}{\mathrm{d}t} = \mathbf{M}(t)\vec{R}(t), \quad \vec{R}(0) = \vec{R}_0, \tag{3.18}$$

where $\mathbf{M}(t)$ is the following time-dependent matrix

$$\mathbf{M}(t) = \begin{pmatrix} -\gamma_1(t) & -\mathrm{i}\frac{\Omega_\mathrm{R}(t)}{2}\,\mathrm{e}^{-\mathrm{i}\varphi_\mathrm{X}(t)} & \mathrm{i}\frac{\Omega_\mathrm{R}(t)}{2}\,\mathrm{e}^{\mathrm{i}\varphi_\mathrm{X}(t)} & +\Gamma_{\mathrm{R},z} \\ -\mathrm{i}\frac{\Omega_\mathrm{R}(t)}{2}\,\mathrm{e}^{\mathrm{i}\varphi_\mathrm{X}(t)} & \mathrm{i}\Delta - \frac{1}{2}\left(\gamma_1(t)+\gamma_2(t)\right) & 0 & \mathrm{i}\frac{\Omega_\mathrm{R}(t)}{2}\,\mathrm{e}^{\mathrm{i}\varphi_\mathrm{X}(t)} \\ \mathrm{i}\frac{\Omega_\mathrm{R}(t)}{2}\,\mathrm{e}^{-\mathrm{i}\varphi_\mathrm{X}(t)} & 0 & -\mathrm{i}\Delta - \frac{1}{2}\left(\gamma_1(t)+\gamma_2(t)\right) & -\mathrm{i}\frac{\Omega_\mathrm{R}(t)}{2}\,\mathrm{e}^{-\mathrm{i}\varphi_\mathrm{X}(t)} \\ 0 & \mathrm{i}\frac{\Omega_\mathrm{R}(t)}{2}\,\mathrm{e}^{-\mathrm{i}\varphi_\mathrm{X}(t)} & -\mathrm{i}\frac{\Omega_\mathrm{R}(t)}{2}\,\mathrm{e}^{\mathrm{i}\varphi_\mathrm{X}(t)} & -\gamma_2(t) \end{pmatrix}, \tag{3.19}$$

with

$$\gamma_1(t) = \sigma_{\mathrm{X},1}\mathcal{J}_\mathrm{X}(t), \tag{3.20a}$$

$$\gamma_2(t) = \sigma_{\mathrm{X},2}\mathcal{J}_\mathrm{X}(t) + \Gamma_\mathrm{A} + \Gamma_\mathrm{R}, \tag{3.20b}$$

where we have defined the detuning $\Delta = \omega_{21} - \omega_\mathrm{X}$.

The knowledge of the time evolution of the atomic one-time expectation values is used to derive the two-time expectation values necessary for the computation of the spectrum of resonance fluorescence. For this purpose, we introduce the two-time vector

$$\vec{Y}(t_1,t_2) = (Y_{11}(t_1,t_2),\, Y_{12}(t_1,t_2),\, Y_{21}(t_1,t_2),\, Y_{22}(t_1,t_2)\,)^\mathrm{T}, \tag{3.21}$$

whose elements are defined as

$$Y_{ij}(t_1,t_2) = \langle \hat{\varsigma}_{ji}(t_1)\hat{\varsigma}_{12}(t_2)\rangle. \tag{3.22}$$

Applying the quantum regression theorem [166, 168] yields

$$\frac{\partial\vec{Y}(t_1,t_2)}{\partial t_1} = \mathbf{M}(t_1)\vec{Y}(t_1,t_2), \quad t_1 \geq t_2, \tag{3.23}$$

with the initial conditions given by $Y_{ij}(t_2,t_2) = \delta_{i1}R_{2j}(t_2)$. The solution of the first set of differential equations (3.18) provides one with the initial conditions for the second set of differential equations (3.23), whose solution gives

$$\begin{aligned} Y_{12}(t_1,\,t_2) &= \langle \hat{\varsigma}_{21}(t_1)\hat{\varsigma}_{12}(t_2)\rangle \\ &= \langle \hat{\sigma}_{21}(t_1)\hat{\sigma}_{12}(t_2)\rangle\,\mathrm{e}^{-\mathrm{i}\omega_\mathrm{X}(t_1-t_2)}. \end{aligned} \tag{3.24}$$

3.1.3 Spectrum of resonance fluorescence

The study and calculation of the spectral properties of the fluorescent light requires the knowledge of the first-order autocorrelation function of the electric field operator [8, 162]

$$G^{(1)}(t_1,t_2,\boldsymbol{r}) = \langle \hat{\boldsymbol{E}}^-(\boldsymbol{r},\,t_1)\cdot\hat{\boldsymbol{E}}^+(\boldsymbol{r},\,t_2)\rangle, \tag{3.25}$$

which we defined in Eq. (2.130).

In the case of continuous-wave (cw) light, when the first-order autocorrelation function depends explicitly only on the time difference $\tau = t_1 - t_2$, i.e., $G^{(1)}(t_1,t_2,\boldsymbol{r}) = G^{(1)}(\tau,\boldsymbol{r})$, the Wiener-Khintchine theorem [53] states that the power spectrum of resonance fluorescence, $S(\boldsymbol{r},\,\omega)$,

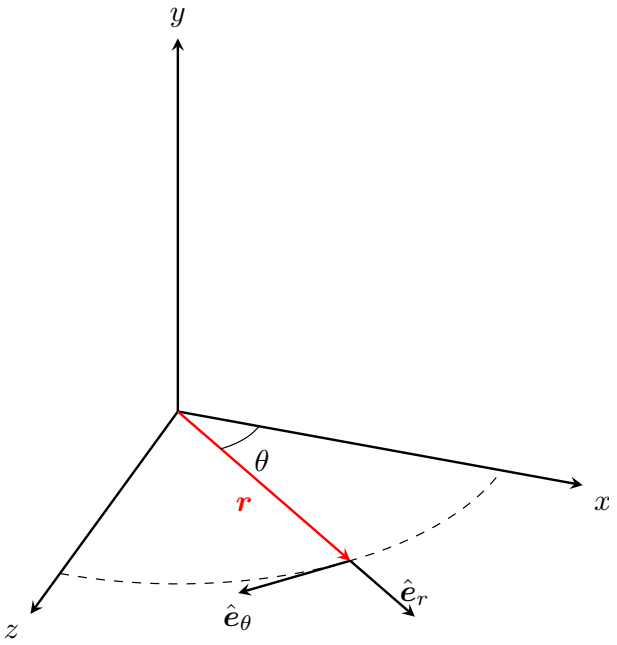

Figure 3.2: Spherical coordinates with respect to the observation point $\boldsymbol{r}$ (red arrow).

associated with the rate of photons emitted at a given frequency is well defined and given by the Fourier transform of $G^{(1)}(\tau, \boldsymbol{r})$ [169]. However, for ultrashort light pulses, $G^{(1)}(t_1, t_2, \boldsymbol{r})$ explicitly depends upon the two distinct instants t_1 and t_2 and the Wiener-Khintchine theorem cannot be analogously used to define a power spectrum. Instead, one needs to study the energy spectrum of resonance fluorescence, $W(\boldsymbol{r}, \omega)$, defined as a quantity proportional to the probability that an ideal photon detector—modeled itself as a two-level system with tunable transition energy ω—is excited by the fluorescent light. In first order of perturbation theory and in the electric dipole approximation, the energy spectrum is defined as [162]

$$W(\boldsymbol{r}, \omega) = \frac{1}{4\pi\alpha} \int_{-\infty}^{+\infty} \int_{-\infty}^{+\infty} G^{(1)}(t_1, t_2, \boldsymbol{r})\, \mathrm{e}^{-\mathrm{i}\omega(t_1 - t_2)}\, \mathrm{d}t_1\, \mathrm{d}t_2. \tag{3.26}$$

Here, $W(\boldsymbol{r}, \omega)\, \mathrm{d}\omega\, \mathrm{d}A$ represents the energy detected on average in the differential energy interval $[\omega, \omega + \mathrm{d}\omega]$ and in a surface element $\mathrm{d}\boldsymbol{A} = r^2\, \mathrm{d}\Omega\, \hat{\boldsymbol{e}}_r$ centered at $\boldsymbol{r} = r\, \hat{\boldsymbol{e}}_r$. Further, α is the fine-structure constant, $\mathrm{d}\Omega$ is the differential solid angle and $\hat{\boldsymbol{e}}_r = \boldsymbol{r}/|\boldsymbol{r}|$ is the unit vector in the direction of observation ($\boldsymbol{0}$ is the position of the atom).

We assume that the driving field propagates along the y axis. As shown in Eqs. (2.68) and (2.70), in the far-field limit and in the electric-dipole approximation—away from the y propagation axis in which also the driving field would be present—the electric-field operator associated with the fluorescent light can be related to the atomic polarization operator $\hat{\boldsymbol{d}}^+(t)$ [Eq. (3.6)] via the relation [53, 57, 62]

$$\hat{\boldsymbol{E}}^+(\boldsymbol{r}, t) = \frac{\omega_{21}^2}{c^2 r} \left(\hat{\boldsymbol{d}}^+(t - r/c) - (\hat{\boldsymbol{d}}^+(t - r/c) \cdot \hat{\boldsymbol{e}}_r)\, \hat{\boldsymbol{e}}_r \right). \tag{3.27}$$

We consider here the resonance fluorescence spectrum emitted by the two-level system displayed in Fig. 3.1 which is measured by rotating the detector around the y axis of Fig. 1.2, i.e. the spectrum at point $\boldsymbol{r} = r\, \hat{\boldsymbol{e}}_r(\theta)$, with $\hat{\boldsymbol{e}}_r(\theta) = \cos\theta\, \hat{\boldsymbol{e}}_x + \sin\theta\, \hat{\boldsymbol{e}}_z$, where θ is the angle between $\hat{\boldsymbol{e}}_r(\theta)$ and the x axis, lying in the $x - z$ plane, as in Fig. 3.2. We further introduce the vector

$\hat{\boldsymbol{e}}_\theta(\theta) = -\sin\theta\,\hat{\boldsymbol{e}}_x + \cos\theta\,\hat{\boldsymbol{e}}_z$, which also lies in the $x-z$ plane and is orthogonal to $\hat{\boldsymbol{e}}_r(\theta)$; in this way, from (3.6) and (3.27), one has that $\hat{\boldsymbol{E}}^+(r\,\hat{\boldsymbol{e}}_r(\theta),\,t) = \hat{E}^+_\theta(r\,\hat{\boldsymbol{e}}_r(\theta),\,t)\,\hat{\boldsymbol{e}}_\theta(\theta) + \hat{E}^+_y(r\,\hat{\boldsymbol{e}}_r(\theta),\,t)\,\hat{\boldsymbol{e}}_y$, with

$$\hat{E}^+_\theta(r\,\hat{\boldsymbol{e}}_r(\theta),\,t) = \frac{\wp\,\omega_{21}^2}{c^2 r}\left[\cos\theta\,\hat{\sigma}_{1_0 2}(t') + \sin\theta\,\frac{\hat{\sigma}_{1_+ 2}(t') - \hat{\sigma}_{1_- 2}(t')}{\sqrt{2}}\right] \tag{3.28}$$

and

$$\hat{E}^+_y(r\,\hat{\boldsymbol{e}}_r,\,t) = \frac{\mathrm{i}}{\sqrt{2}}\,\frac{\wp\,\omega_{21}^2}{c^2 r}\,\left(\hat{\sigma}_{1_+ 2}(t') + \hat{\sigma}_{1_- 2}(t')\right), \tag{3.29}$$

with $t' = t - r/c$. The autocorrelation function (3.25) is

$$G^{(1)}(t_1, t_2, r\,\hat{\boldsymbol{e}}_r(\theta)) = G^{(1)}_\theta(t_1, t_2, r\,\hat{\boldsymbol{e}}_r(\theta)) + G^{(1)}_y(t_1, t_2, r\,\hat{\boldsymbol{e}}_r(\theta)),$$

with

$$\begin{aligned} G^{(1)}_\theta(t_1, t_2, r\,\hat{\boldsymbol{e}}_r(\theta)) = \mathcal{I}(r)\,\Big[&\cos^2\theta\,\langle\hat{\sigma}_{21_0}(t_1')\,\hat{\sigma}_{1_0 2}(t_2')\rangle \\ &+ \frac{\sin^2\theta}{2}\left(\langle\hat{\sigma}_{21_-}(t_1')\,\hat{\sigma}_{1_- 2}(t_2')\rangle + \langle\hat{\sigma}_{21_+}(t_1')\,\hat{\sigma}_{1_+ 2}(t_2')\rangle\right)\Big] \end{aligned} \tag{3.30}$$

and

$$G^{(1)}_y(t_1, t_2, r\,\hat{\boldsymbol{e}}_r(\theta)) = \mathcal{I}(r)\,\frac{1}{2}\left(\langle\hat{\sigma}_{21_-}(t_1')\,\hat{\sigma}_{1_- 2}(t_2')\rangle + \langle\hat{\sigma}_{21_+}(t_1')\,\hat{\sigma}_{1_+ 2}(t_2')\rangle\right), \tag{3.31}$$

where

$$\mathcal{I}(r) = \left(\frac{\omega_{21}^2\,|\wp|}{c^2 r}\right)^2 \tag{3.32}$$

is a factor dependent on the position of observation at which the detector is placed and having the dimension of an intensity [62] and the application of the quantum regression theorem allows one to show that the cross-terms $\langle\hat{\sigma}_{2i}(t_1')\,\hat{\sigma}_{j2}(t_2')\rangle$, with $i,\,j \in \{1_+,\,1_-,\,1_0\}$, $i \neq j$, vanish for any t_1' and t_2'. We notice, therefore, that the photons emitted in transitions to the two undriven states $|1_\pm\rangle$ can be both polarized along the axes $\hat{\boldsymbol{e}}_y$ and $\hat{\boldsymbol{e}}_\theta(\theta)$. Conversely, the photons spontaneously emitted to the state $|1_0\rangle$ are exclusively polarized along the axis $\hat{\boldsymbol{e}}_\theta(\theta)$ and their intensity, varying in space as $\cos^2\theta$, is maximized for $\theta = 0,\,\pi$. For the same angles the intensity of the photons that are emitted in transitions to the two undriven states $|1_\pm\rangle$ and which are linearly polarized along $\hat{\boldsymbol{e}}_\theta(\theta)$ vanishes. For this reason, we choose to study the spectrum of resonance fluorescence for $\theta = 0$, $\hat{\boldsymbol{e}}_r = \hat{\boldsymbol{e}}_x$ and $\hat{\boldsymbol{e}}_\theta = \hat{\boldsymbol{e}}_z$. Polarization-dependent detection of the resonance fluorescence spectrum can take advantage of the properties just presented.

If the detector is placed along the x axis, as shown in Fig. 1.2, then $\hat{\boldsymbol{e}}_r = \hat{\boldsymbol{e}}_x$, $\theta = 0$, and one obtains

$$G^{(1)}(t_1, t_2, r\,\hat{\boldsymbol{e}}_x) = G^{(1)}_z(t_1, t_2, r\,\hat{\boldsymbol{e}}_x) + G^{(1)}_y(t_1, t_2, r\,\hat{\boldsymbol{e}}_x), \tag{3.33}$$

with

$$G^{(1)}_z(t_1, t_2, r\,\hat{\boldsymbol{e}}_x) = \mathcal{I}(r)\,\langle\hat{\sigma}_{21_0}(t_1')\,\hat{\sigma}_{1_0 2}(t_2')\rangle \tag{3.34}$$

and

$$G^{(1)}_y(t_1, t_2, r\,\hat{\boldsymbol{e}}_x) = \mathcal{I}(r)\,\frac{1}{2}\left(\langle\hat{\sigma}_{21_-}(t_1')\,\hat{\sigma}_{1_- 2}(t_2')\rangle + \langle\hat{\sigma}_{21_+}(t_1')\,\hat{\sigma}_{1_+ 2}(t_2')\rangle\right), \tag{3.35}$$

where $\mathcal{I}(r)$ was defined in Eq. (3.32).

With (3.26) and (3.33), the resonance fluorescence energy spectrum is also split into two terms $W(r\,\hat{\boldsymbol{e}}_x,\,\omega) = W_z(r\,\hat{\boldsymbol{e}}_x,\,\omega) + W_y(r\,\hat{\boldsymbol{e}}_x,\,\omega)$. The calculation of $W_y(\omega,\,r\,\hat{\boldsymbol{e}}_x)$ goes beyond the two-level approximation we adopt in this Chapter and requires a complete four-level description of the

system. Here, we describe the appearance of Rabi flopping in the resonance fluorescence spectrum for those photons which are emitted in the transition to the ground state $|1\rangle$. For $\hat{\boldsymbol{e}}_r = \hat{\boldsymbol{e}}_x$ this represents the only contribution in $W_z(r\,\hat{\boldsymbol{e}}_x,\,\omega)$ and its observation can be experimentally realized using a polarization-dependent detection to selectively detect the radiation which is linearly polarized in the z direction, in order to select those fluorescence photons associated with the transition to the state with $M_L = 0$.

Polarization-dependent measurements can be very informative, e.g., they have played an important role for molecules where the valence orbitals can be resolved [170–172]. Reflections from mirrors, gratings, or crystals at angles that achieve high polarization selectivity at the frequency of the atomic transition involved allow one to measure the polarization of the radiation. The use of wavelength-dispersive spectrometers, which involve reflecting x rays from a grating or crystal, can provide one with polarization selectivity. Energy-dispersive spectrometers, such as a cryogenic spectrometer, can be polarization-sensitive if they are pixellated and the x rays are hard enough to Compton scatter in the absorber. In addition, polarization-dependent detection in a parallel and perpendicular setup facilitates background reduction [163].

By introducing the time delay $\tau = t_1 - t_2$ and noticing that $\langle\hat{\sigma}_{21}(t_1)\hat{\sigma}_{12}(t_2)\rangle = \langle\hat{\sigma}_{21}(t_2)\hat{\sigma}_{12}(t_1)\rangle^*$, we conclude that knowledge of $\langle\hat{\sigma}_{21}(t_1)\hat{\sigma}_{12}(t_2)\rangle$ in the region $t_1 \geq t_2$ (and hence $\tau \geq 0$) is sufficient for the calculation of the energy spectrum of resonance fluorescence [166]. We rewrite (3.26) in compact form as

$$W_z(r\,\hat{\boldsymbol{e}}_x,\,\omega) = \frac{3\Gamma_{\mathrm{R},z}\,\omega_{21}}{8\pi\,r^2}\int_{-\infty}^{+\infty}\int_{0}^{+\infty}\mathbf{Re}\left[\mathrm{e}^{-\mathrm{i}\omega\tau}\langle\hat{\sigma}_{21}(t_2+\tau)\hat{\sigma}_{12}(t_2)\rangle\right]\mathrm{d}\tau\;\mathrm{d}t_2, \tag{3.36}$$

where we use Eqs. (3.11), (3.32), and (3.34). As a result, one can use $Y_{12}(t_1,\,t_2)$ from the solution of (3.23) to calculate the energy spectrum of resonance fluorescence.

In the following, we are going to compute $W_z(\Omega,\,\omega) = r^2\,W_z(r\,\hat{\boldsymbol{e}}_x,\,\omega)$ for a detector along the x axis. $W_z(\Omega,\,\omega)\;\mathrm{d}\Omega\,\mathrm{d}\omega$ is the energy emitted into $\mathrm{d}\Omega$ and $\mathrm{d}\omega$; in atomic units $W_z(\Omega,\,\omega)$ has the dimension of 1/steradian. Finally, we notice that the total detected energy emitted into $\mathrm{d}\Omega$ is

$$\mathscr{E} = \int_{-\infty}^{+\infty} W_z(\Omega,\,\omega)\;\mathrm{d}\omega = \frac{3\Gamma_{\mathrm{R},z}\,\omega_{21}}{8}\int_{-\infty}^{+\infty} R_{22}(t)\;\mathrm{d}t, \tag{3.37}$$

exploiting the relation

$$2\pi\,\delta(t_1 - t_2) = \int_{-\infty}^{+\infty}\mathrm{e}^{-\mathrm{i}\omega(t_1-t_2)}\;\mathrm{d}\omega.$$

3.2 Results and discussion

Here we apply our two-level model to study Ne^+ cations driven by x rays on the $1s\,2p^{-1} \rightarrow 1s^{-1}\,2p$ transition at $\omega_{21} = 848$ eV [139], i.e., the detuning is $\Delta = \omega_{21} - \omega_{\mathrm{X}} = 0$. Scattered x rays could be observed if the XFEL beam energy is detuned from resonance. As demonstrated in Ref. [173], for example, Compton scattering, resonant Raman scattering, and Rayleigh scattering can be observed as the resonance is approached from below. At 848 eV, however, resonance fluorescence will dominate the measured spectrum.

The destruction rate of our effective two-level system is dominated by the Auger decay width of Ne $1s^{-1}$ which is $\Gamma_{\mathrm{A}} = 0.27$ eV [174]. The dipole moment $\wp = 0.0524\,a_0$ is computed with the Hartree-Fock-Slater mean-field model [175–179], whereas the photoionization cross sections are computed using the Los Alamos Atomic Physics Codes [180, 181]. From Eq. (3.11) the radiative decay width follows, where $\Gamma_{\mathrm{R},z} = 0.0012$ eV, the total decay rate is $\Gamma_{\mathrm{R}} = 0.0039$ eV [182], in good agreement with Eq. (3.15).

The spectrum $W_z(\Omega, \omega)$ that we will compute represents the emitted photons linearly polarized along the z direction from our two-level model. Off-resonant Rayleigh scattering from $2s$ and $2p$ electrons in Ne is, however, not taken into account. This elastic scattering is predicted to be anisotropically distributed for a linearly polarized electric field: in our case, $\boldsymbol{\mathcal{E}}(t) = \mathcal{E}(t)\,\hat{\boldsymbol{e}}_z$, the intensity of the elastic scattering would be affected by the source-dependent polarization factor $\sin^2\psi$ [88], where ψ is the angle between the z axis and the direction of detection $\hat{\boldsymbol{e}}_r$ at which the detector is placed. This additional contribution is not included in the two-level approximation that we implement in this Chapter. Its only effect is an enlargement of the central peak of the spectrum.

3.2.1 Gaussian x-ray pulses

Self-seeding techniques at LCLS are providing one with pulses with an approximately Gaussian temporal profile [116–118]; it is interesting therefore to predict the evolution of the atomic properties in time and the spectrum of resonance fluorescence for Ne^+ cations for this case. We write the Gaussian pulse as

$$\mathcal{E}_{0,\mathrm{G}}(t) = \mathcal{E}_{\max}\,\mathrm{e}^{-\frac{t^2}{2T^2}}, \quad \varphi_{\mathrm{X}}(t) = 0, \tag{3.38}$$

where $T = \tau_{\mathrm{G}}/(2\sqrt{\ln 2})$ and τ_{G} is the FWHM of $\mathcal{E}^2_{0,\mathrm{G}}(t)$. The FWHM of $|\tilde{\mathcal{E}}_{0,\mathrm{G}}(\omega)|^2$ is $\Delta\omega_{\mathrm{G}} = 4\ln 2/\tau_{\mathrm{G}}$, where

$$\tilde{\mathcal{E}}_{0,\mathrm{G}}(\omega) = \int \mathcal{E}_{0,\mathrm{G}}(t)\,\mathrm{e}^{\mathrm{i}\omega t}\,\mathrm{d}t = T\sqrt{2\pi}\,\mathcal{E}_{\max}\,\mathrm{e}^{-\frac{\omega^2 T^2}{2}}$$

is the Fourier transform of $\mathcal{E}_{0,\mathrm{G}}(t)$ [164]. The peak intensity [Eq. (3.14)] is $I_{\mathrm{G}} = \mathcal{E}^2_{\max}/(8\pi\alpha)$, yielding a maximum Rabi frequency [Eq. (3.8)] $\Omega_{\mathrm{RG,max}} = \wp\mathcal{E}_{\max} = \wp\sqrt{8\pi\alpha\, I_{\mathrm{G}}}$.

Further, we recall the definition (2.115) of the pulse area

$$Q = \int_{-\infty}^{+\infty} \Omega_{\mathrm{R}}(t)\,\mathrm{d}t, \tag{3.39}$$

which in Sec. 2.6 was shown to play an important role in the description of the dynamics of a two-level system in interaction with a regular pulse ($\varphi_{\mathrm{X}}(t) = 0$) and in the properties of the corresponding resonance fluorescence spectrum [71–74]. Let us assume for now that level decay and photoionization are both negligible. Then, for $\Delta = 0$, if n is a natural number and $Q = 2\pi n$, the final population after the interaction with the pulse is in the ground state, whereas for $Q = 2\pi(n + 1/2)$ a complete inversion happens and the total final population occupies the excited state. For a Gaussian regular pulse the area (3.39) is $Q_{\mathrm{G}} = \Omega_{\mathrm{RG,max}}\,\tau_{\mathrm{G}}\sqrt{\pi/(2\ln 2)}$.

We begin by studying the interaction of Ne^+ cations driven by a Gaussian x-ray pulse with peak intensity $I_{\mathrm{G}} = 2.6 \times 10^{17}\,\mathrm{W/cm^2}$ and $\tau_{\mathrm{G}} = 5$ fs: Such x-ray pulses are becoming available from seeding techniques implemented at LCLS [116–118]. In Fig. 3.3 we show the time evolution of the two-level system when Auger decay is included and when it is not included ($\Gamma_{\mathrm{A}} = 0$) in the EOMs (3.18). The time evolution of the total population of the system reveals that Auger decay is the major depopulation mechanism. Photoionization makes, however, also a noticeable contribution at the chosen x-ray intensity; the maximum rates of photoionization are [Eq. (3.12)] $\Gamma_{\mathrm{P1,max}} = 0.03$ eV and $\Gamma_{\mathrm{P2,max}} = 0.04$ eV, which is small compared to the Auger decay width $\Gamma_{\mathrm{A}} = 0.27$ eV. In Ref. [138] this channel was, therefore, neglected entirely. The decay time associated with Auger decay is approximately given by $\Delta\tau = 1/\Gamma_{\mathrm{A}} = 2.4$ fs. As one notices in Fig. 3.3, the total population of the system almost completely vanishes after the pulse of

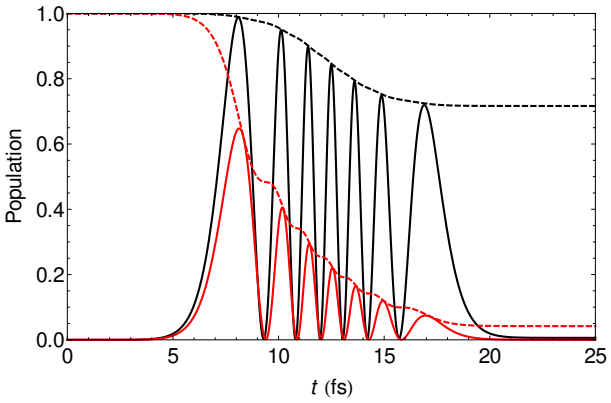

Figure 3.3: Time evolution of the population of a two-level system driven by a Gaussian x-ray pulse (3.38) of peak intensity $I_{\mathrm{G}} = 2.6 \times 10^{17}\,\mathrm{W/cm^2}$ and FWHM duration $\tau_{\mathrm{G}} = 5$ fs, corresponding to a pulse area of $Q_{\mathrm{G}} = 14\pi$. The dashed lines show the total population of the two-level system $\rho_{11}(t) + \rho_{22}(t)$ [Eq. (3.9)] in the absence (black line) and presence (red line) of Auger decay. The solid lines show the corresponding occupation of the excited state $\rho_{22}(t)$.

5 fs. Whether Auger decay is included or not does not interfere with Rabi oscillations which are clearly discernible; the pulse area $Q_{\mathrm{G}} = 7 \times 2\pi$ results in 7 oscillations.

The corresponding energy spectra of resonance fluorescence are shown in Fig. 3.4. The Rabi oscillations induced by the intense external x-ray field appear in both cases with and without Auger decay, with nonvanishing contributions in the region approximately given by $[-\Omega_{\mathrm{RG,max}}\,,\ \Omega_{\mathrm{RG,max}}]$, with the maximum Rabi frequency $\Omega_{\mathrm{R,max,G}} = 3.9$ eV. First, when only spontaneous decay and photoionization are taken into account, a multi-peak structure is predicted, in analogy to what was computed in absence of any decay processes [71]. The presence of many peaks is nontrivially related to the pulse-shape of the electric field, i.e., to its finite duration and width. The seven peaks in the energy spectrum—six lateral peaks and the seventh central one—are related, as was shown in [71], to the pulse area $Q_{\mathrm{G}} = 7 \times 2\pi$. Second, when Auger decay is taken into account, the multipeak structure of the spectrum becomes smoother because of the increase in the decay rate. Furthermore, the intensity of the radiation emitted by the two-level system decreases, since Auger decay destroys it and, consequently, reduces the fraction of atoms which can Rabi flop. The resulting maximum Rabi frequency $\Omega_{\mathrm{R,max,G}} = 3.9$ eV is however much higher than the bandwidth of the pulse, $\Delta\omega_{\mathrm{G}} = 0.36$ eV, the Auger decay width, $\Gamma_{\mathrm{A}} = 0.27$ eV, and the frequency resolution of present spectrometers $\Delta\omega_{\mathrm{res}} = 0.4$ eV [183]. Hence the signature of Rabi flopping, clearly visible in Fig. 3.4, will be detectable.

In Fig. 3.5 and 3.6 we consider different pulses with $\tau_{\mathrm{G}} = 2$ fs and $Q_{\mathrm{G}} = 2\pi(n - 1/2)$ [panels (a)] or $Q_{\mathrm{G}} = 2\pi n$ [panels (b)], for $n \in \{1, 2, 3\}$. One can clearly see a dependence of the population of the two-level system upon the area Q_{G}. When this area is an odd multiple of π [Fig. 3.5a], a major part of the population at the end of the pulse occupies the excited state: One can discern the $n - 1/2$ oscillations due to the interaction with the pulse and the following Auger decay of the system when the pulse is over. As shown in Fig. 3.6a, the long Auger decay which follows the interaction with the pulse results in a high Lorentzian peak in the spectrum of resonance fluorescence at $\omega = \omega_{\mathrm{X}}$ with a width that can be related to the major decay process, i.e., Γ_{A}. This peak results from the fact that the excited system decays freely, radiatively and electronically, without Rabi flopping. In contrast, a considerably different situation appears when the area of the pulse is an even multiple of π [Fig. 3.5b]: after n complete oscillations, the population of the excited state is almost 0 at the end of the pulse. Consequently, the previously

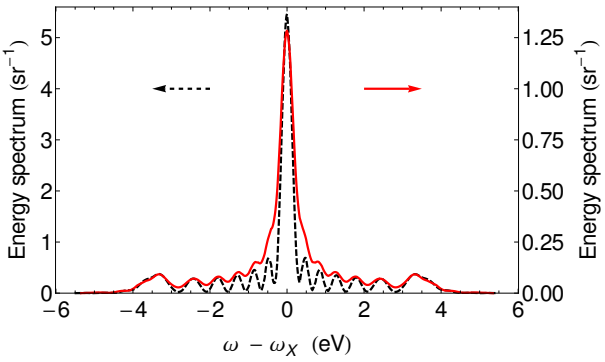

Figure 3.4: Energy spectrum of resonance fluorescence for the Gaussian pulse used in Fig. 3.3 in the absence (black, dashed line) and presence (red, solid line) of Auger decay. As indicated by the arrows, the scale on the left refers to the black, dashed curve, whereas the scale on the right refers to the red, solid curve.

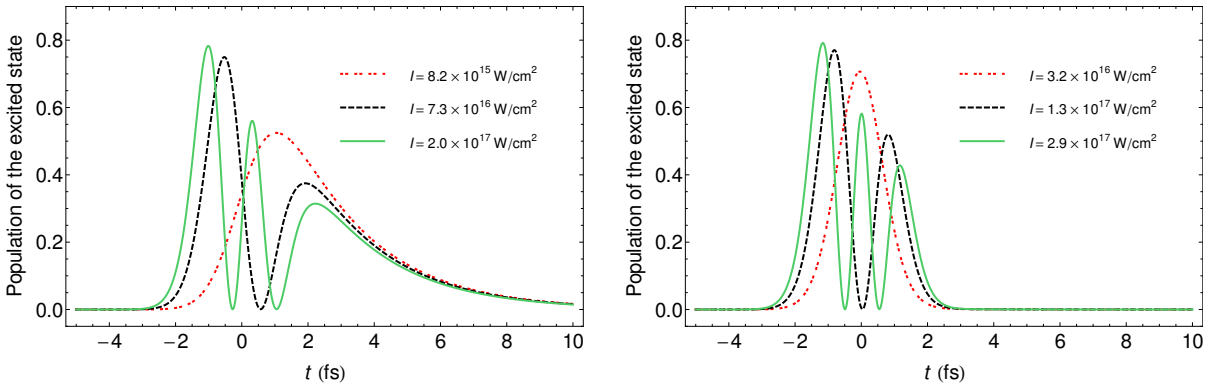

Figure 3.5: Time evolution of the population of the excited state $\rho_{22}(t)$ for a two-level system driven by Gaussian x-ray pulses [Eq. (3.38)] of different peak intensities (shown in the legend) and a FWHM duration $\tau_G = 2$ fs. In panel (a) pulse areas $Q_G = 2\pi(n - 1/2)$, for $n = 1$ (red, dotted line), $n = 2$ (black, dashed line) and $n = 3$ (green, solid line) are used. In panel (b) pulse areas $Q_G = 2\pi n$, for $n = 1$ (red, dotted line), $n = 2$ (black, dashed line) and $n = 3$ (green, solid line) are used.

present post-x-ray-exposure decay does not take place. The total emitted energy is therefore lower because the central peak at ω_{21} is reduced by almost one order of magnitude, as one can clearly see by looking at Fig. 3.6b. In the case of a longer pulse, so that the two-level system has completely Auger decayed before its conclusion, the difference between pulses whose areas are an odd or even multiple of π becomes less important.

The dependence of the resonance fluorescence spectrum upon the duration of the pulse is an additional point that needs to be investigated. In order to observe this dependence, in Fig. 3.7 we study the main features of the spectrum as functions of the normalized pulse area $Q_G/(2\pi)$ and of the pulse FWHM duration τ_G. We recall that for fixed τ_G the area of the Gaussian pulse is directly proportional to the square root of the intensity, $Q_G = 2\pi\wp\tau_G\sqrt{(\alpha/\ln 2)\, I_G}$. In Fig. 3.7a we show the total emitted energy $\mathscr{E}$ [Eq. (3.37)] for three different values of τ_G; for the shortest pulses one can clearly observe an oscillating behaviour of the total emitted energy as a function of $Q_G/(2\pi)$; this behaviour is less pronounced for the longest pulses. It is also worthwhile to notice that for increasing values of Q_G, the intensity can become so high that also for the shortest pulses the system is in any case completely destroyed by photoionization

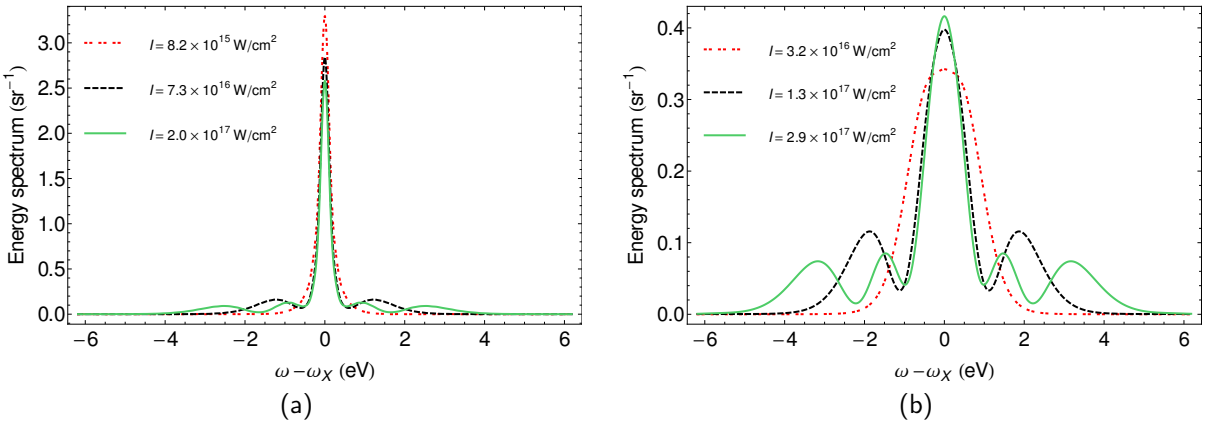

Figure 3.6: Spectrum of resonance fluorescence of a two-level system driven by Gaussian x-ray pulses of different peak intensities (shown in the legend) and a FWHM duration $\tau_G = 2$ fs. Line styles of panels (a) and (b) as in Fig. 3.5.

within the duration of the pulse itself. The increasing importance of photoionization implies a less remarkable difference in the time evolution of systems driven by pulses whose areas are an odd or even multiple of π and, consequently, resonance fluorescence spectra characterized by a lower dependence upon the area of the pulse.

In Fig. 3.7b we display $\pi\Gamma_A W(\omega_X)/2$, where $W(\omega_X)$ is the central maximum value of the spectrum of resonance fluorescence. The constant prefactor $\pi\Gamma_A/2$ allows us to compare the shape of the spectrum of resonance fluorescence with that of a Lorentzian function of Auger decay width Γ_A. If the only process involved was a decay causing a rate width Γ, then the spectrum of resonance fluorescence would be proportional to a Lorentzian function

$$L(\omega) = \frac{\pi\Gamma}{2} L_0 \frac{\Gamma/(2\pi)}{(\omega - \omega_X)^2 + (\Gamma/2)^2}, \tag{3.40}$$

with peak value $L_0 = L(\omega_X)$ and with total emitted energy $\mathscr{E}_L = \int_{-\infty}^{+\infty} L(\omega)\, \mathrm{d}\omega = \pi\Gamma L_0/2$. By computing in Fig. 3.7b the quantity $\pi\Gamma_A W(\omega_X)/2$, we can relate it to the actual total emitted radiation of Fig. 3.7a and understand the relative importance of Auger decay in relation to the other decay processes. By comparing the oscillating features in Fig. 3.7b with those of Fig. 3.7a, one notices that $\pi\Gamma_A W(\omega_X)/2$ approaches $\mathscr{E}$ only for short pulses satisfying $Q = 2\pi(n - 1/2)$. In these cases, as we have already discussed in Fig. 3.5a, the main term is represented by post-x-ray-exposure Auger decay of the system. Nonetheless, because of the nonnegligible role played by Rabi flopping, photoionization and spontaneous decay, one can notice in Fig. 3.7 a clear difference between $\pi\Gamma_A W(\omega_X)/2$ and $\mathscr{E}$.

Figures 3.4 and 3.6 reveal that Rabi flopping produces a clear signature in the spectrum of resonance fluorescence of Gaussian pulses, which self-seeding at LCLS is rendering available [116–118]. However, since shot-to-shot variations in pulse intensity and duration are anticipated, we investigate how the spectrum of resonance fluorescence is influenced by the presence of these fluctuations. For this purpose, we compute the energy spectrum of resonance fluorescence for a wide set of Gaussian pulses [Eq. (3.38)], by independently randomizing their duration and energy. The mean duration is chosen to be $\tau_G = 7$ fs and the mean peak intensity is $I_G = 7 \times 10^{17}$ W/cm^2, giving a mean peak Rabi frequency of approximately 6 eV. We compute the energy spectrum of resonance fluorescence for 500 different realizations of the driving pulses. Thereby, the duration and the intensity are random variables whose probability distribution is Gaussian with a variance

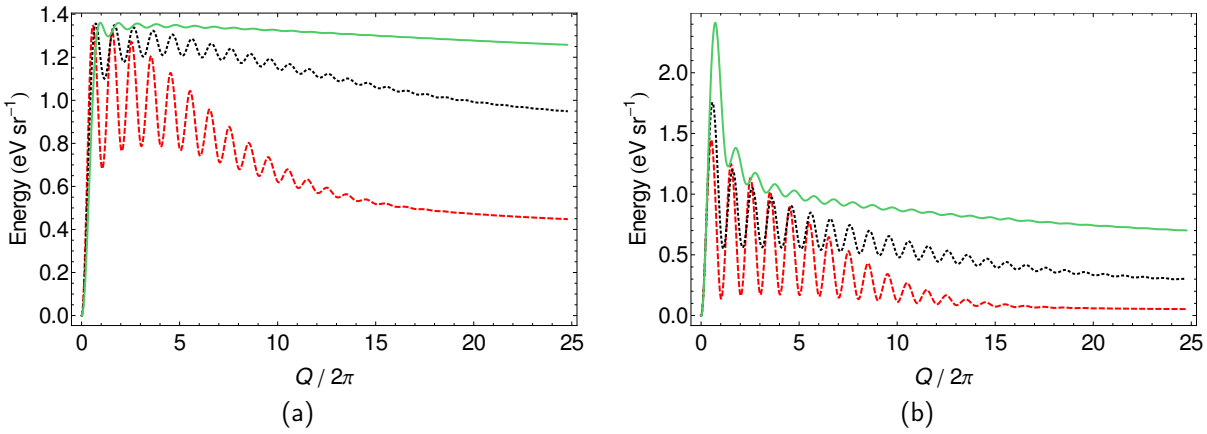

Figure 3.7: (a) Total emitted energy $\mathscr{E} = \int_{-\infty}^{+\infty} S_z(\omega, \Omega)\, \mathrm{d}\omega$ and (b) peak value of the spectrum $W(\omega_\mathrm{X})$ multiplied by $\pi\Gamma_\mathrm{A}/2$ as functions of the normalized pulse area $Q_\mathrm{G}/(2\pi)$ [Eq. (3.39)] for $\tau_\mathrm{G} = 2$ fs (red, dashed line), $\tau_\mathrm{G} = 5$ fs (black, dotted line) and $\tau_\mathrm{G} = 10$ fs (green, solid line).

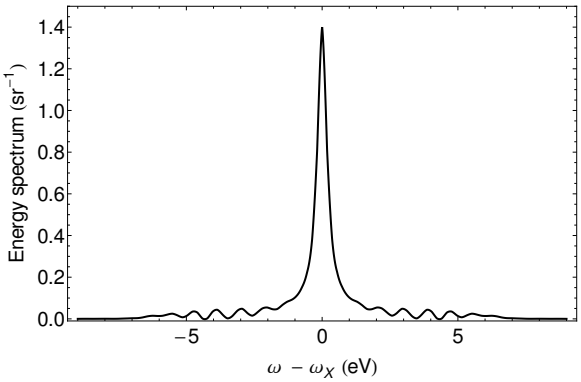

Figure 3.8: Average resonance fluorescence spectrum for 500 different realizations of the Gaussian driving pulses [Eq. (3.38)]. The mean duration of the pulses is $\bar{\tau}_\mathrm{G} = 7$ fs, the mean peak intensity is $\bar{I} = 7 \times 10^{17}\,\mathrm{W/cm^2}$. Here, τ_G and I are Gaussian random variables independently chosen for each realization with a variance equal to the 20% of the respective mean values.

of 20% of the mean value. The resulting average resonance fluorescence spectrum is shown in Fig. 3.8. It reveals that Rabi flopping is discernible even if energy and duration of the pulse vary appreciably from shot to shot.

3.2.2 Self-amplified-spontaneous-emission x-ray pulses

The SASE light is modeled with the Partial Coherence Method (PCM) [184, 185], whose details are discussed in Appendix B. The SASE pulses have a central photon energy which is tuned to the transition energy of Ne^+ of 848 eV, with a bandwidth (FWHM of $|\tilde{\mathcal{E}}(\omega)|^2$) of $\Delta\omega_\mathrm{SASE} = 6$ eV. The envelope function $f(t)$ that we adopt [Eq. (B.8)] has FWHM duration $\tau_\mathrm{env} = 6.5$ fs. Further details are discussed in Appendix B.

In Fig. 3.9a we display the time-dependent Rabi frequency [Eq. (3.8)] $\Omega_\mathrm{R}(t) = \wp\,\mathcal{E}_0(t)$ induced by the amplitude of a SASE pulse and in Fig. 3.9b the phase $\varphi_\mathrm{X}(t)$ of a SASE LCLS pulse obtained with the PCM method. The mean Rabi frequency and phase are also given. In Fig. 3.10a the time evolution of the population of the excited state and the total population of the two-level

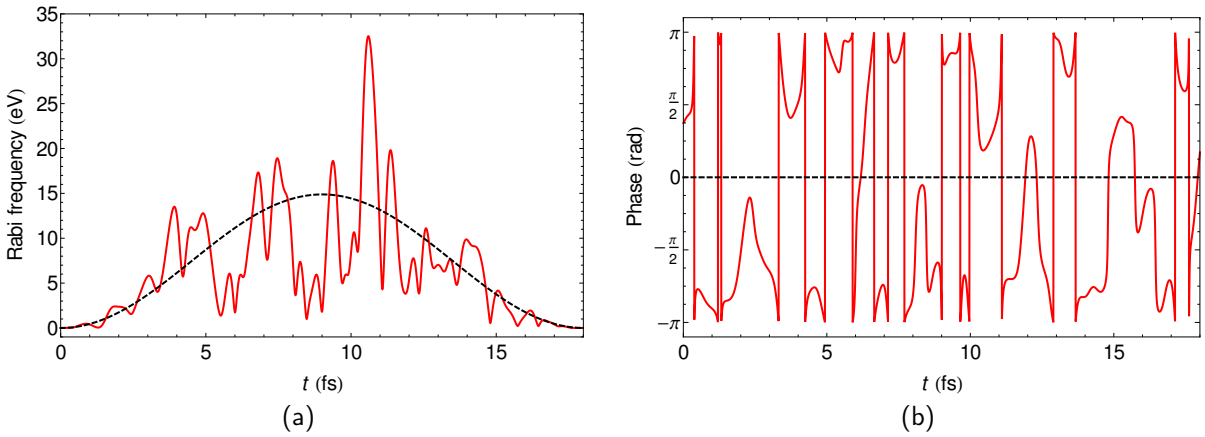

Figure 3.9: (a) The Rabi frequency $\Omega_{\mathrm{R}}(t)$ induced by the amplitude of a SASE pulse and (b) the phase $\varphi_{\mathrm{X}}(t)$ of the SASE pulse (red, solid lines) and their mean value (black, dashed lines). The mean pulse has a duration $\tau_{\mathrm{env}} = 6.5$ fs and a peak intensity $I = 3.8 \times 10^{18}\,\mathrm{W/cm^2}$. Its bandwidth is $\Delta\omega_{\mathrm{SASE}} = 6$ eV.

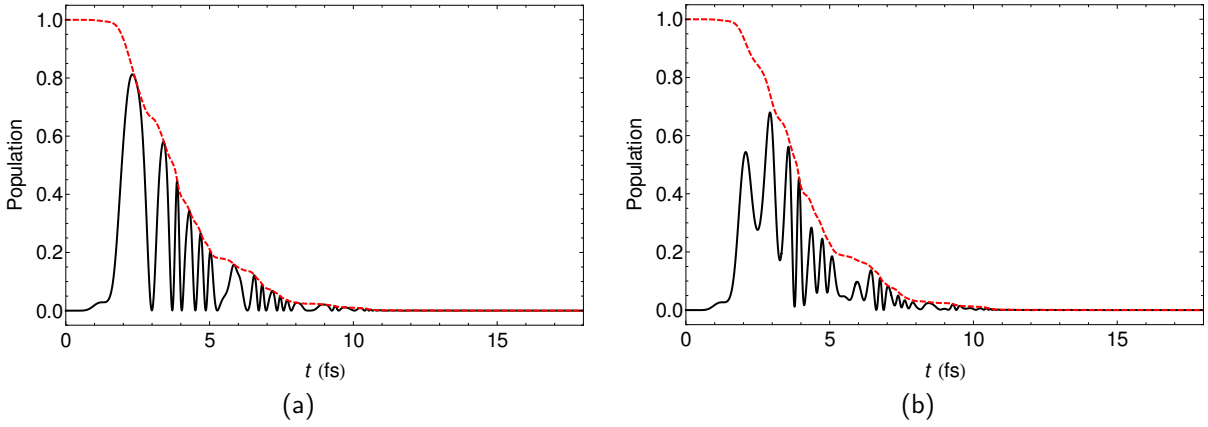

Figure 3.10: Time evolution of a two-level system driven by a SASE pulse with the time-dependent Rabi frequency of Fig. 3.9a. The phase is assumed to be (a) constant, $\varphi_{\mathrm{X}}(t) = 0$, or (b) to be equal to the phase of Fig. 3.9b. The red, dashed line shows the evolution of the total population $\rho_{11}(t) + \rho_{22}(t)$ [Eq. (3.9)]; the black, solid line represents the occupation of the excited state $\rho_{22}(t)$.

system are plotted if the phase of the pulse is supposed constant, $\varphi_{\mathrm{X}}(t) = 0$, and the spiky time-dependent Rabi frequency of Fig. 3.9a is used to integrate the EOMs. In Fig. 3.10b both the Rabi frequency and the phase of Fig. 3.9 are used to integrate the EOMs. If the phase fluctuations are neglected, the decay of the system is slower; in both cases, due to the chaotic SASE pulse shape, the time evolution is very irregular. For the case displayed in Fig. 3.10a, though, one can see the presence of complete oscillations in $\rho_{22}(t)$, reaching its minimum at $\rho_{22}(t) = 0$ and its maximum when $\rho_{11}(t) = 0$: This feature disappears when the phase fluctuations of Fig. 3.9b are taken into account.

In contrast to the case of a Gaussian pulse, one cannot extract from the time evolution of the system any clear relation to the pulse area. Nevertheless, one observes a relation between the Rabi frequency of Fig. 3.9a and the frequency with which the population of the excited state $\rho_{22}(t)$ oscillates in Fig. 3.10. These oscillations, in fact, take place in a time interval which is shorter than the time characterizing the random fluctuations of Fig. 3.9. They are Rabi oscillations

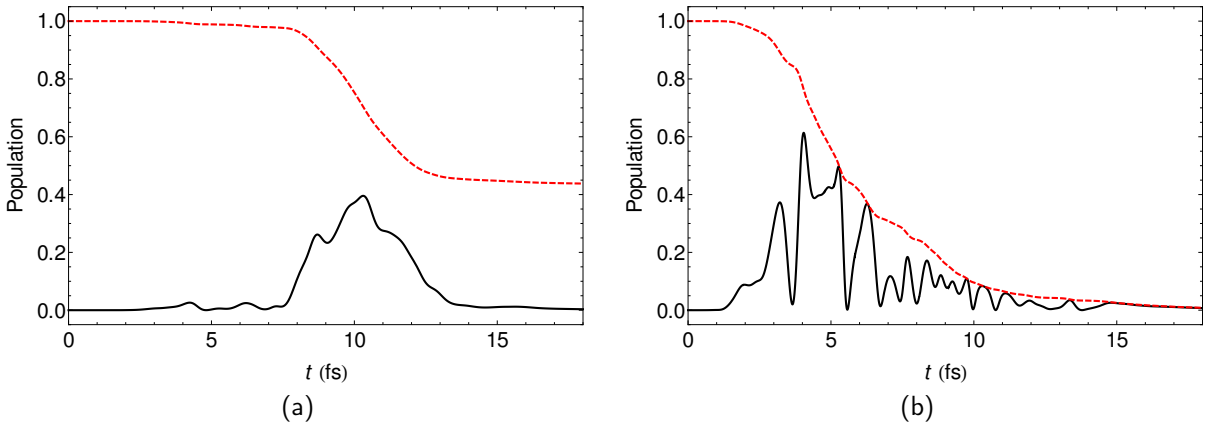

Figure 3.11: Time evolution of a two-level system driven by SASE pulses generated with the PCM described in Appendix B. In both cases the pulses have a mean duration $\tau_{\mathrm{env}} = 6.5$ fs and a bandwidth $\Delta\omega_{\mathrm{SASE}} = 6$ eV. The peak intensity is (a) $I = 3.8 \times 10^{15}\,\mathrm{W/cm^2}$ and (b) $I = 8.8 \times 10^{17}\,\mathrm{W/cm^2}$. The red, dashed line shows the evolution of the total population $\rho_{11}(t) + \rho_{22}(t)$ [Eq. (3.9)]; the black, solid line represents the occupation of the excited state $\rho_{22}(t)$.

induced by the interaction with the intense driving field; as we show in Fig. 3.11, if a pulse of similar bandwidth but of far lower intensity is used to excite the system, the time evolution of the atomic system displays slower oscillations, whose mean frequency increases at increasing intensities. We further notice that, because of photoionization, the increase in the intensity of the driving field reduces the actual decay time of the system: This emerges by comparing the graphs displayed in Fig. 3.11 with that of Fig. 3.10b.

In Fig. 3.12 we display the resonance fluorescence spectrum from SASE x rays. To observe Rabi flopping we need the Rabi oscillations to occur within the coherence time of the pulse; for this reason, the intensity of the external electric field is chosen such that the maximum Rabi frequency is larger than the bandwidth $\Delta\omega_{\mathrm{SASE}}$ of the pulse itself. We look in particular at the emitted spectrum by averaging over 1000 independent SASE pulses. The tails appearing in the spectrum of Fig. 3.12 are nonvanishing contributions at frequencies higher than the bandwidth of the pulse itself. These tails would not appear if the field had equal bandwidth but lower intensity: They represent, therefore, a signature of the Rabi oscillations described in Fig. 3.10. These tails are also in good agreement with the spectrum emitted when a Gaussian transform-limited pulse of identical intensity and time duration—but clearly with much lower bandwidth—is used to excite the system. If the phase of the SASE pulse remained constant and only its amplitude displayed chaotic fluctuations, then the spectrum emitted after one single pulse would be symmetric; furthermore, the average spectrum would present a lower width, due to the absence of phase fluctuations. A clear observation of the tails of Fig. 3.12 and of the enlargement of the resonance fluorescence spectrum at increasing intensities might represent a possible way to detect Rabi flopping also at present SASE facilities.

Analogous conclusions had been drawn for the resonant Auger electron spectrum [138]: The width of the resonant Auger electron line profile was expected to help in estimating the presence of Rabi oscillations in the system. Nonetheless, the very short coherence times at present XFEL facilities limited the actual experimental observability of this effect at LCLS [139].

As last point, we study the dependence of the resonance fluorescence spectrum on the duration of the SASE pulse. In Fig. 3.13 we plot the average spectrum emitted by Ne^+ cations when excited by an ultrashort pulse with peak intensity $I = 1.6 \times 10^{18}\,\mathrm{W/cm^2}$ and bandwidth $\Delta\omega_{\mathrm{SASE}} = 6$ eV.

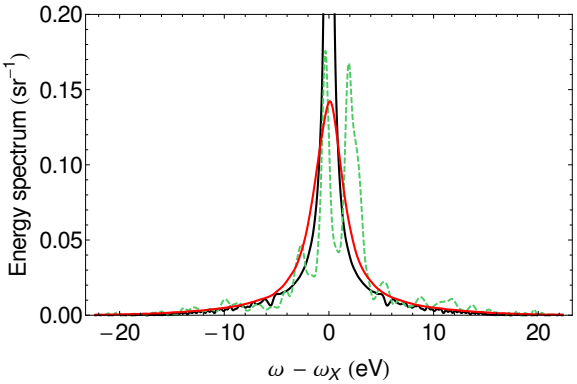

Figure 3.12: Resonance fluorescence spectrum for SASE pulses. The black, dotted line shows the spectrum from a Gaussian pulse with FWHM duration $\tau_{\mathrm{G}} = 6.5$ fs and peak intensity $I_{\mathrm{G}} = 3.8 \times 10^{18}\,\mathrm{W/cm^2}$. The red, solid line is the arithmetic mean over 1000 SASE pulses with average peak intensity I_{G}, FWHM duration τ_{G} and a bandwidth of $\Delta\omega_{\mathrm{SASE}} = 6$ eV. The green, dashed line is for the pulse in Fig. 3.9.

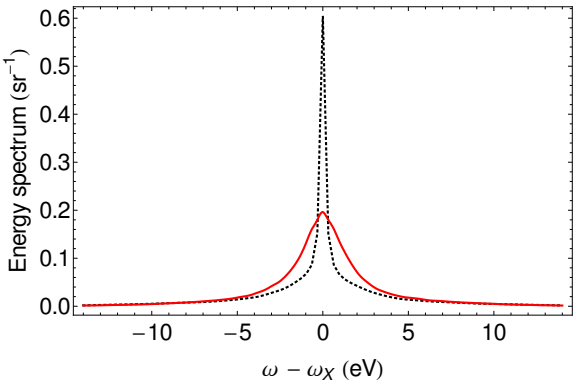

Figure 3.13: Average resonance fluorescence spectrum over SASE pulses. The pulses have an average peak intensity of $I = 1.6 \times 10^{18}\,\mathrm{W/cm^2}$ and bandwidth $\Delta\omega_{\mathrm{SASE}} = 6$ eV. The red, solid line shows the average over SASE pulses with average FWHM duration of $\tau_{\mathrm{env}} = 6.5$ fs; the black, dotted line is associated with pulses of average FWHM duration of $\tau_{\mathrm{env}} = 2$ fs.

The results are obtained by averaging over spectra resulting from SASE pulses respectively with a FWHM duration of $\tau_{\mathrm{env}} = 6.5$ fs and of $\tau_{\mathrm{env}} = 2$ fs. It is worth noticing a remarkable difference between different pulse durations. Naively, after the previous considerations, one would assume that the resonance fluorescence peak has a FWHM associated with the large bandwidth of the pulse $\Delta\omega_{\mathrm{SASE}} = 6$ eV. For the shortest pulses, though, the resonance fluorescence spectrum exhibits a higher central peak whose width is clearly lower than $\Delta\omega_{\mathrm{SASE}}$. The explanation is based on the same arguments that we used to describe the spectra depicted in Fig. 3.6a, in which the post-x-ray-exposure decay results in a high Lorentzian peak of width given by the Auger decay width of the system. Analogously, for the ultrashort SASE pulses with $\tau_{\mathrm{env}} = 2$ fs used in Fig. 3.13, the interaction with the pulse is shorter than the time needed by the system to completely decay; hence, at the end of the pulse, the probability of destruction of the system is about 90%. The Auger decay which follows the interaction with an ultrashort SASE pulse implies, therefore, the high central peak in the resonance fluorescence spectrum shown in Fig. 3.13; for the same reason, its width is lower than the bandwidth of the pulse itself. A similar reduction of the FWHM was also observed in Ref. [139] in the Auger electron spectrum. In that case, by

using the same x-ray pulse to create Ne^+ ions and to drive the $1s\,2p^{-1} \rightarrow 1s^{-1}\,2p$ transition, the system could not completely Auger decay before the end of the pulse. The decay of the excited state with the natural decay time of the system turned out to dominate the observation.

3.3 Conclusions

We develop a two-level model of resonance fluorescence whose time evolution is described by master equations which include the coherent interaction of the system with the classical x-ray field. All processes that destroy the system, namely, Auger decay and photoionization, are fully taken into account. We use our model to describe Ne^+ cations driven by an intense linearly polarized x-ray field tuned to the $1s\,2p^{-1} \rightarrow 1s^{-1}\,2p$ transition at 848 eV; the transition is well isolated, i.e., separated by more than 70 natural linewidths from the lowest lying Rydberg excitation, $1s \rightarrow 3p$ [139]. The intensity available at present x-ray FELs such as LCLS is sufficiently high to induce Rabi flopping at frequencies that compete with the rate of destruction of the system. The two-level approximation allows us to investigate the resonance fluorescence of photons associated with the transition to the state with $M_L = 0$ for two different scenarios. First, we consider SASE radiation from present XFELs; second, we explore resonance fluorescence from coherent Gaussian pulses which are becoming available via the use of self-seeding techniques at fourth-generation x-ray sources [116–119]. The measurement of the spectra predicted in this Chapter need to take advantage of the polarization properties of the emitted light.

In the case of laser-like Gaussian pulses, a clear signature of Rabi flopping is predicted. We show that the observation of Rabi flopping persists even when intensity and duration of the pulse vary appreciably from shot to shot. For SASE pulses, although Rabi flopping does not manifest itself as clearly as in the previous case, we predict the appearance of tails in the spectrum that might represent a good signature of Rabi oscillations in the atomic system. These tails would not appear if the system was excited by a less intense pulse of equally large bandwidth. In the case of the resonant Auger spectrum, however, the presently large bandwidth at LCLS represented a limit for the observation of analogous effects in the resonant Auger electron spectrum [139] and the signature of Rabi flopping did not appear indistinguishably. Also in the case of resonance fluorescence the identification of Rabi flopping in the spectrum might be challenging. The amplitude of the aforementioned tails is predicted to be neither very high nor easily distinguishable. A much clearer signature is, however, identified for ions driven by Gaussian pulses, rendering the prospects with self-seeded LCLS very promising.

4 X-ray frequency combs from resonance fluorescence with narrow-bandwidth x rays

In this Chapter, we develop an x-ray pulse-shaping scheme to imprint a frequency comb onto the x-ray resonance fluorescence spectrum. In Sec. 4.1 we present the theoretical model which we utilize in the remaining of the Chapter. The particles in interaction with three external electric fields are modeled as four-level systems [Sec. 4.1.1]: After having presented the interaction Hamiltonians, we exploit the single-particle equations of motion to prove the existence of a periodic, nontrivial solution. In Sec. 4.1.2 we discuss the space properties of the coherent and incoherent parts of the spectrum due to many-particle effects and prove the existence of a comb in the x-ray spectrum of resonance fluorescence ensuing from the periodic structure of the equations of motion. In Sec. 4.2, the four-level scheme is employed to model He-like Be^{2+} ions in interaction with narrow-bandwidth x rays, an optical laser, and an optical frequency comb. Specifically, we analyze the properties of the imprinted x-ray comb for different parameters of the driving fields. Sec. 4.3 concludes the Chapter. Parts of this Chapter have been presented in Ref. [186].

4.1 Theoretical model

The results presented in this Chapter are triggered by the conclusions which were drawn in Ref. [75]. In particular, when (i) the equations of motion (EOMs) governing the interaction of an atomic system with external driving fields are perfectly periodic such that, (ii) when turn-on effects have ceased, the atomic system reaches a nontrivial periodic solution, then the spectrum of resonance fluorescence contains an incoherent part which consists of equally spaced delta peaks centered at an atomic transition energy. With "*trivial solution*", we refer here to the case in which all the population is stored in the ground state: Although this can be considered an asymptotic "periodic" solution, it is also of very little interest.

In this Chapter we adopt a four-level model in order to implement a resonance fluorescence scheme of x-ray comb generation. Before going into the details, we provide an intuitive explanation of the reasons whereby four levels are needed.

In order to imprint a comb onto the x-ray emission spectrum, the three-level scheme in Fig. 4.1a may be sufficient. There, the transition energy between the ground state $|g\rangle$ and the first excited state $|e_1\rangle$ is in the x-ray regime, whereas the transition energy between the two excited states $|e_2\rangle$ and $|e_1\rangle$ is in the optical range. Population and coherence stored in $|e_2\rangle$ can be transferred to the excited state $|e_1\rangle$ via an optical field driving the corresponding optical transition: The resulting spontaneous decay of $|e_1\rangle$ would imply the emission of optically manipulated x rays. In order to guarantee both an efficient optical driving and a significant x-ray emission, the involved transitions $|g\rangle \leftrightarrow |e_1\rangle$ and $|e_2\rangle \leftrightarrow |e_1\rangle$ ought to be E1 allowed. Parity reasons imply that the remaining transition $|g\rangle \leftrightarrow |e_2\rangle$ is not E1 allowed and cannot be driven efficiently.

The just described three-level system, with optical population transfer from $|e_2\rangle$ to $|e_1\rangle$ and consequent decay to the ground state, converges to a very trivial solution of the EOMs, with all the population stored in the ground state. In contrast to the method which we will employ in Chapter 6, the approach that we develop here does require a nontrivial asymptotic solution of the EOMs, which can be achieved only by repopulating $|e_2\rangle$. Since direct driving from the ground

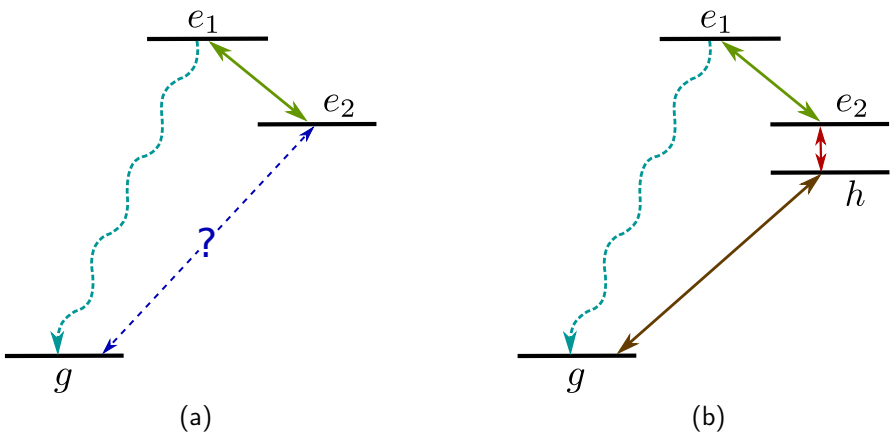

Figure 4.1: (a) Three-level scheme for the generation of an x-ray frequency comb via the manipulation, with an optical frequency comb (green, solid line) driving the $e_2 \leftrightarrow e_1$ transition, of the spontaneous decay (blue, dashed line) from state $|e_1\rangle$ to the ground state $|g\rangle$. (b) Four-level scheme for efficient repopulation of state $|e_2\rangle$ through an intermediate, helper level $|h\rangle$: an x-ray field (brown, solid line) and an optical laser (red, solid line) are used to drive the transitions $g \to h$ and $h \to e_2$, respectively.

state is prevented by the previously described parity reasons, one needs to take advantage of a helper intermediate state $|h\rangle$ [Fig. 4.1b], such that an efficient driving of the E1 allowed transitions $|g\rangle \leftrightarrow |h\rangle$ and $|h\rangle \leftrightarrow |e_2\rangle$ makes it possible to repopulate $|e_2\rangle$.

The remaining of this Section describes in detail the four-level model, whose adoption was intuitively justified here. In particular, we aim at specializing the general description which we provided in Chapter 2 to the case of N particles, at different positions $\boldsymbol{r}_n$, $n \in \{1, \dots, N\}$, modeled as four-level systems interacting with three external fields.

4.1.1 Four-level model

4.1.1.1 Electric-dipole Hamiltonians

We display in Fig. 4.2a the experimental setup that we are going to use in the following. An x-ray field $\boldsymbol{\mathcal{E}}_{\mathrm{X}}(\boldsymbol{r}, t)$, an optical continuous-wave (cw) field $\boldsymbol{\mathcal{E}}_{\mathrm{L}}(\boldsymbol{r}, t)$, and an optical frequency comb $\boldsymbol{\mathcal{E}}_{\mathrm{C}}(\boldsymbol{r}, t)$, irradiate an ensemble of ions. The fields copropagate in the y direction; at time t and position $\boldsymbol{r}$, for $q \in \{\mathrm{X}, \mathrm{L}, \mathrm{C}\}$, they are given by

$$\boldsymbol{\mathcal{E}}_q(\boldsymbol{r}, t) = \mathcal{E}_{q,0}[t - \boldsymbol{r} \cdot (\partial \boldsymbol{k}_q / \partial \omega_q)] \cos\left[\omega_q t + \varphi_q(t) + \varphi_{q,0} - \boldsymbol{k}_q \cdot \boldsymbol{r}\right] \hat{\boldsymbol{e}}_q, \tag{4.1}$$

with amplitude $\mathcal{E}_{q,0}(t)$, carrier frequency ω_q, phase $\varphi_q(t)$, carrier-envelope phase (CEP) $\varphi_{q,0}$, wavevector $\boldsymbol{k}_q = (\omega_q/c)\,\hat{\boldsymbol{e}}_y$, linear polarization vector $\hat{\boldsymbol{e}}_q$, and intensity $I_q = |\mathcal{E}_{q,0}|^2/(8\pi\alpha)$ [164]. Furthermore, $\hat{\boldsymbol{e}}_{\mathrm{X}} = \hat{\boldsymbol{e}}_{\mathrm{L}} = \hat{\boldsymbol{e}}_z$, $\hat{\boldsymbol{e}}_{\mathrm{C}} = \hat{\boldsymbol{e}}_x$, where $\hat{\boldsymbol{e}}_x$, $\hat{\boldsymbol{e}}_y$, and $\hat{\boldsymbol{e}}_z$ are the unit vectors in the x, y, and z direction, and $\partial \boldsymbol{k}_q / \partial \omega_q = \hat{\boldsymbol{e}}_q / c$ are the inverses of the group velocities for each field; further, c is the speed of light in vacuum and $\alpha = 1/c$ is the fine-structure constant. The indeces of refraction n_q for each field are here set equal to 1, thus implying that $k_q = (\omega_q/c)$. This relies on the assumption of a dilute-gas setting, such that the phase velocity of all electric fields, in very good approximation, equals the speed of light, resulting in good phase matching [143, 187, 188]. A direct consequence of this assumption is that $\partial \boldsymbol{k}_q / \partial \omega_q = (1/c)\,\hat{\boldsymbol{e}}_y$.

The bandwidth of $\boldsymbol{\mathcal{E}}_{\mathrm{L}}(\boldsymbol{r}, t)$ is so small that it can be entirely neglected. We also assume that $\boldsymbol{\mathcal{E}}_{\mathrm{X}}(\boldsymbol{r}, t)$ has constant amplitude, $\mathcal{E}_{\mathrm{X},0}(t) = \bar{\mathcal{E}}_{\mathrm{X},0}$, and phase, $\varphi_{\mathrm{X}}(t) = 0$; the effect of the x-ray

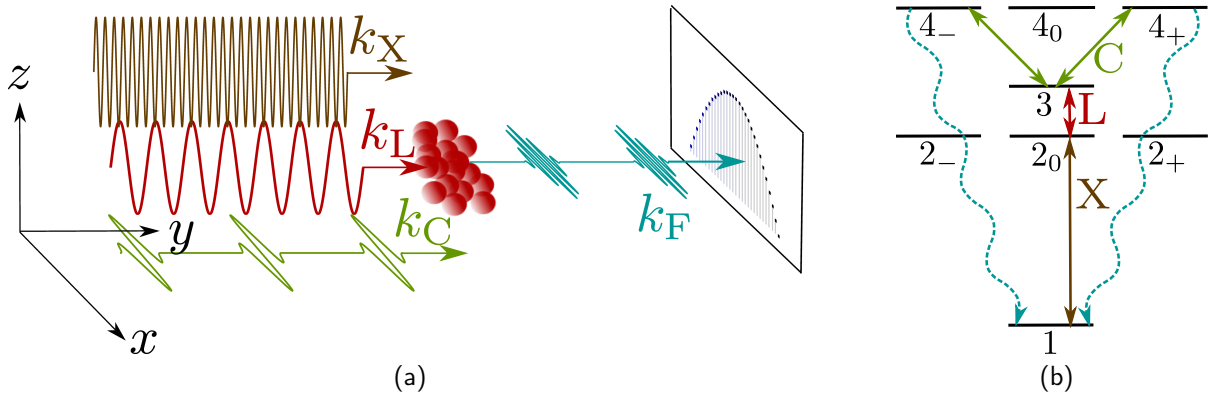

Figure 4.2: (a) An ensemble of ions is driven by narrow-bandwidth x rays ($\boldsymbol{k}_\mathrm{X}$, brown), an auxiliary optical laser ($\boldsymbol{k}_\mathrm{L}$, red), both linearly polarized along the z direction, and an optical frequency comb ($\boldsymbol{k}_\mathrm{C}$, green), linearly polarized along the x direction. All fields propagate in the y direction. The resonance fluorescence spectrum ($\boldsymbol{k}_\mathrm{F}$, blue) exhibits an induced x-ray frequency-comb structure. (b) Four-level scheme of He-like ions interacting with the light fields.

bandwidth is later taken into account by a stochastic approach [189]. For the main part of the Chapter, therefore, we consider two cw fields,

$$\boldsymbol{\mathcal{E}}_\mathrm{X}(\boldsymbol{r},\,t) = \bar{\mathcal{E}}_{\mathrm{X},0}\,\cos\left(\omega_\mathrm{X} t - \boldsymbol{k}_\mathrm{X}\cdot\boldsymbol{r}\right)\hat{\boldsymbol{e}}_z \tag{4.2}$$

and

$$\boldsymbol{\mathcal{E}}_\mathrm{L}(\boldsymbol{r},\,t) = \bar{\mathcal{E}}_{\mathrm{L},0}\cos\left(\omega_\mathrm{L} t - \boldsymbol{k}_\mathrm{L}\cdot\boldsymbol{r}\right)\hat{\boldsymbol{e}}_z, \tag{4.3}$$

both linearly polarized in the $\hat{\boldsymbol{e}}_z$ direction. The optical frequency comb has, in very good approximation, constant phase $\varphi_\mathrm{C}(t) \equiv 0$ and periodic amplitude[1] $\mathcal{E}_{\mathrm{C},0}(t) = \sum_{k=-\infty}^{+\infty} A_k\,\mathrm{e}^{-\mathrm{i}\frac{2\pi k}{T_\mathrm{p}}t}$, with repetition period T_p and Fourier coefficients $A_k = 1/T_\mathrm{p}\int_0^{T_\mathrm{p}}\mathcal{E}_{\mathrm{C},0}(t)\,\mathrm{e}^{\mathrm{i}\frac{2\pi k}{T_\mathrm{p}}t}\,\mathrm{d}t$, i.e.,

$$\mathcal{E}_{\mathrm{C},0}(t) = \mathcal{E}_{\mathrm{C,max}}\sum_{n=-\infty}^{+\infty}\mathcal{G}(t-nT_\mathrm{p}), \tag{4.4a}$$

$$\mathcal{G}(t) = \cos^2\left[\tfrac{\pi}{T_\mathrm{d}}\left(t-\tfrac{T_\mathrm{d}}{2}\right)\right]\mathrm{R}\left[\tfrac{1}{T_\mathrm{d}}\left(t-\tfrac{T_\mathrm{d}}{2}\right)\right], \tag{4.4b}$$

where $\mathcal{E}_{\mathrm{C,max}} = \sqrt{8\pi\alpha I_{\mathrm{C,max}}}$ is its maximum, $I_{\mathrm{C,max}}$ the maximum intensity, and the rectangular function is defined with the help of the Heaviside step function θ as $\mathrm{R}(x) = \theta(x+1/2)-\theta(x-1/2)$. The full width at half maximum (FWHM) of $\mathcal{G}^2(t)$ is $T_\mathrm{FWHM} = 2\,T_\mathrm{d}\arccos\left(\sqrt[4]{1/2}\right)/\pi$ [190], with T_d being the interval in which $\mathcal{G}(t)$ is different from 0, $T_\mathrm{d} \ll T_\mathrm{p}$. The choice of the polarization of the field

$$\boldsymbol{\mathcal{E}}_\mathrm{C}(\boldsymbol{r},\,t) = \mathcal{E}_{\mathrm{C},0}(t-\boldsymbol{r}\cdot\hat{\boldsymbol{e}}_y/c)\,\cos\left(\omega_\mathrm{C} t - \boldsymbol{k}_\mathrm{C}\cdot\boldsymbol{r}\right)\hat{\boldsymbol{e}}_x, \tag{4.5}$$

in the $\hat{\boldsymbol{e}}_x$ direction, will be justified in the following.

The electric fields $\boldsymbol{\mathcal{E}}_\mathrm{X}(\boldsymbol{r},\,t)$, $\boldsymbol{\mathcal{E}}_\mathrm{L}(\boldsymbol{r},\,t)$, and $\boldsymbol{\mathcal{E}}_\mathrm{C}(\boldsymbol{r},\,t)$, drive electric-dipole (E1) transitions in the four-level system of Fig. 4.2b, where level i has energy ω_i and the energy between the levels i and j is given by $\omega_{ij} = \omega_i - \omega_j$, $i,\,j \in S = \{1,\,2_{0,\pm},\,3,\,4_{0,\pm}\}$. The four-level model describes He-like ions, with transition energies in the proper optical and x-ray ranges [191]. Here, the state $|1\rangle$ represents the ground state $1s^2\ {}^1S_0$, with total-angular-momentum quantum number $J = 0$

[1] The function is periodic in a very large time interval $T_\mathrm{g} \ll T_\mathrm{p}$, i.e., $\mathcal{E}_{\mathrm{C},0}(t) = f(t)\sum_{n=-\infty}^{+\infty} A_n\,\mathrm{e}^{-\mathrm{i}\frac{2\pi n}{T_\mathrm{p}}t}$, with $f(t) \approx 1$, $-T_\mathrm{g}/2 < t < T_\mathrm{g}/2$.

and positive parity. The states, $|2_-\rangle$, $|2_0\rangle$, and $|2_+\rangle$, with M_J equal to -1, 0, and 1, describe the level $1s2p\ ^3P_1$, with $J = 1$ and negative parity. Furthermore, $|3\rangle$ represents $1s2s\ ^1S_0$, with $J = 0$ and positive parity, whereas $|4_-\rangle$, $|4_0\rangle$, and $|4_+\rangle$ represent the level $1s2p\ ^1P_1$, with $J = 1$ and negative parity. In He-like ions, level 3 has higher energy than level 2 for a nuclear charge $Z \geq 7$ [191]; otherwise, these two levels are inverted in energy. In Fig. 4.2b and in the remaining part of the discussion of the theoretical model, we assume that $\omega_3 > \omega_2$, i.e., that the three-level system formed by levels 1, 2, and 3, is a Ξ-type system [57, 58]. The generalization of the EOMs to the case of a Λ-type three-level system, as the one formed by levels 1, 2, and 3, when $\omega_3 < \omega_2$, is straightforward.

Other levels, such as $1s2s\ ^3S_1$, $1s2p\ ^3P_0$, and $1s2p\ ^3P_2$, are not included in our description, because they do not couple via E1 interaction to the levels in Fig. 4.2b and the spontaneous-decay times from higher-energy levels to them are by orders of magnitude larger than T_p. The levels 2, 3, and 4, are below the autoionization threshold, since in all configurations one electron occupies the $1s$ orbital [191]. In the following equations, we also neglect ionization of multiply charged ions such as Be^{2+} entirely, since it does not play a relevant role. We have used the ADK formula for tunnel ionization from Ref. [192–194] to compute the multiphoton ionization rate and verified that, for the parameters which will be later adopted in Sec. 4.2, this rate is negligible. The single-photon ionization rate of the excited levels 2, 3, and 4, computed with the Los Alamos National Laboratory Atomic Physics Codes [88, 180] due to the presence of the driving x-ray field, is also shown not to affect our results significantly.

The interaction of the electric fields $\boldsymbol{\mathcal{E}}_q(\boldsymbol{r}, t)$ [Eq. (4.1)] with N ions at positions $\boldsymbol{r}_n$, $n \in \{1, \ldots, N\}$, is described by the Hamiltonian $\hat{H} = \hat{H}_0 + \sum_q \hat{H}_{\mathrm{E1},q}$, where $\hat{H}_0 = \sum_{n=1}^{N} \sum_{i\in S} \omega_i \hat{\sigma}_{ii}^n$ is the atomic electronic structure Hamiltonian [see Eqs. (2.30) and (2.31)] and $\hat{H}_{\mathrm{E1},q} = \sum_{n=1}^{N} \hat{\boldsymbol{d}}_n \cdot \boldsymbol{\mathcal{E}}_q(\boldsymbol{r}_n, t)$ are the E1 interaction Hamiltonians from Eq. (2.105) [53, 159]. Here, $\hat{\boldsymbol{d}}_n$ represents the dipole operator of an ion at position $\boldsymbol{r}_n$ [see Eq. (2.32)],

$$\hat{\boldsymbol{d}}_n = \sum_{i,j\in S} |i\rangle_n\, {}_n\langle i|\hat{\boldsymbol{d}}_n|j\rangle_n\, {}_n\langle j| = \sum_{i,j\in S} \boldsymbol{d}_{ij,n}\, \hat{\sigma}_{ij}^n, \tag{4.6}$$

with matrix elements $\boldsymbol{d}_{ij,n} = {}_n\langle i|\hat{\boldsymbol{d}}_n|j\rangle_n$, $i, j \in S$, $n \in \{1, \ldots, N\}$. Because the dipole moment is a general property of the ion species, i.e., of the atomic number and the charge of the ion, the matrix elements $\boldsymbol{d}_{ij,n} = \boldsymbol{d}_{ij}$ do not explicitly depend on n. Furthermore, since $\hat{\boldsymbol{d}}_n$ is an irreducible tensor operator of rank 1 [159], the just introduced vector components $\boldsymbol{d}_{ij}$, $i, j \in S$, as we did in Eq. (2.94), can be written as

$$\hat{\boldsymbol{d}}_{ij} = d_{ij}^{-1}\hat{\boldsymbol{e}}_{\sigma_-} + d_{ij}^{0}\hat{\boldsymbol{e}}_z + d_{ij}^{1}\hat{\boldsymbol{e}}_{\sigma_+}, \tag{4.7}$$

where we have used the circular-polarization vectors $\hat{\boldsymbol{e}}_{\sigma_\pm}$ from Eq. (2.95) and the matrix elements d_{ij}^k, with $i, j \in S$ and $k \in \{0, \pm 1\}$, which satisfy the selection rules (2.102) and (2.103).

The interaction with the x-ray field (4.2), tuned to the $|1\rangle \leftrightarrow |2_0\rangle$ transition, linearly polarized in the $\hat{\boldsymbol{e}}_z$ direction and with $\boldsymbol{k}_\mathrm{X} = (\omega_\mathrm{X}/c)\,\hat{\boldsymbol{e}}_y$, is described within the rotating-wave approximation (RWA) [53], by the Hamiltonian[2]

$$\hat{H}_{\mathrm{E1,X}} = \frac{\Omega_\mathrm{RX}}{2} \sum_{n=1}^{N} \hat{\sigma}_{12_0}^n\, \mathrm{e}^{\mathrm{i}(\omega_\mathrm{X} t - \boldsymbol{k}_\mathrm{X}\cdot\boldsymbol{r}_n)} + \mathrm{H.c.}, \tag{4.8}$$

where $\Omega_\mathrm{RX} = d_{12_0}^0 \mathcal{E}_{\mathrm{X},0}$ is the x-ray Rabi frequency. We recall that $|1\rangle$ has $J = 0$ and $M_J = 0$, whereas $|2\rangle$ has $J' = 1$ and $M_{J'} = 0$, such that $\boldsymbol{d}_{12_0} = d_{12_0}^0 \hat{\boldsymbol{e}}_z$.

[2] In this Chapter, we assume that all the electric fields have a CEP of $\varphi_{q,0} = \pi$, with $q \in \{\mathrm{X}, \mathrm{L}, \mathrm{C}\}$. This gives rise to a factor -1 which compensates the minus sign in the interaction Hamiltonian $\hat{H}_\mathrm{AL}$ from Eq. 2.105.

Notice that also the transition $|1\rangle \leftrightarrow |4_0\rangle$ can be analogously driven by an x-ray field along the $\hat{\boldsymbol{e}}_z$ direction: The state $|4_0\rangle$ is characterized by quantum numbers $J' = 1$ and $M'_{J'} = 0$, such that $\boldsymbol{d}_{14_0} = d^0_{14_0}\hat{\boldsymbol{e}}_z$. We have found, though, that the detuned E1 driving of the $|1\rangle \leftrightarrow |4_0\rangle$ transition, with $\Delta = \omega_4 - \omega_1 - \omega_\mathrm{X}$, has negligible effects on the evolution of the system and we therefore neglect it [3].

The cw optical field (4.3), tuned to the $|2_0\rangle \leftrightarrow |3\rangle$ transition, linearly polarized in the z direction and with $\boldsymbol{k}_\mathrm{L} = (\omega_\mathrm{L}/c)\,\hat{\boldsymbol{e}}_y$, interacts with the system via the RWA Hamiltonian

$$\hat{H}_\mathrm{E1,L} = \frac{\Omega_\mathrm{RL}}{2}\sum_{n=1}^{N}\hat{\sigma}^n_{2_03}\,\mathrm{e}^{\mathrm{i}(\omega_\mathrm{L}t-\boldsymbol{k}_\mathrm{L}\cdot\boldsymbol{r}_n)} + \mathrm{H.c.}, \tag{4.9}$$

where $\Omega_\mathrm{RL} = d^0_{2_03}\mathcal{E}_{\mathrm{L},0}$ is the Rabi frequency associated with the laser field. Here, $\boldsymbol{d}_{2_03} = d^0_{2_03}\hat{\boldsymbol{e}}_z$ and $d^0_{2_03}$ is the only nonzero component of the vector $\boldsymbol{d}_{2_03}$.

Finally, the interaction with the optical frequency comb (4.5), with $\boldsymbol{k}_\mathrm{C} = (\omega_\mathrm{C}/c)\,\hat{\boldsymbol{e}}_y$, tuned to the $|3\rangle \leftrightarrow |4_\pm\rangle$ transition and linearly polarized on the $\hat{\boldsymbol{e}}_x$ direction, $\hat{\boldsymbol{e}}_x = (\hat{\boldsymbol{e}}^*_{\sigma_-} - \hat{\boldsymbol{e}}^*_{\sigma_+})/\sqrt{2}$, is described by the E1 interaction Hamiltonian

$$\begin{aligned}\hat{H}_\mathrm{E1,C} = &\frac{1}{2}\sum_{n=1}^{N}\boldsymbol{d}_{34_+}\cdot\frac{\hat{\boldsymbol{e}}^*_{\sigma_-}-\hat{\boldsymbol{e}}^*_{\sigma_+}}{\sqrt{2}}\,\mathcal{E}_{\mathrm{C},0}(t-\boldsymbol{r}_n\cdot\hat{\boldsymbol{e}}_y/c)\,\hat{\sigma}^n_{34_+}\,\mathrm{e}^{\mathrm{i}(\omega_\mathrm{C}t-\boldsymbol{k}_\mathrm{C}\cdot\boldsymbol{r}_n)} + \mathrm{H.c.}\\ &+\frac{1}{2}\sum_{n=1}^{N}\boldsymbol{d}_{34_-}\cdot\frac{\hat{\boldsymbol{e}}^*_{\sigma_-}-\hat{\boldsymbol{e}}^*_{\sigma_+}}{\sqrt{2}}\,\mathcal{E}_{\mathrm{C},0}(t-\boldsymbol{r}_n\cdot\hat{\boldsymbol{e}}_y/c)\,\hat{\sigma}^n_{34_-}\,\mathrm{e}^{\mathrm{i}(\omega_\mathrm{C}t-\boldsymbol{k}_\mathrm{C}\cdot\boldsymbol{r}_n)} + \mathrm{H.c.},\end{aligned} \tag{4.10}$$

with $\boldsymbol{d}_{34_\pm} = d^{\mp1}_{34_\pm}\,\hat{\boldsymbol{e}}_{\sigma_\mp}$. Because of the associated Clebsch-Gordan coefficients, one notices that the two quantities $d^{\mp1}_{34_\pm} = \boldsymbol{d}_{34_\pm}\cdot\hat{\boldsymbol{e}}^*_{\sigma_\mp}$ are identical: We set them equal to $\tilde{d}_{34}$ and introduce the time-dependent Rabi frequency $\Omega_\mathrm{RC}(t) = \tilde{d}_{34}\,\mathcal{E}_{\mathrm{C},0}(t)$. It follows that

$$\begin{aligned}\hat{H}_\mathrm{E1,C} = &\sum_{n=1}^{N}\frac{\Omega_\mathrm{RC}(t-\boldsymbol{r}_n\cdot\hat{\boldsymbol{e}}_y/c)}{2}\,\frac{1}{\sqrt{2}}\,\hat{\sigma}^n_{34_+}\,\mathrm{e}^{\mathrm{i}(\omega_\mathrm{C}t-\boldsymbol{k}_\mathrm{C}\cdot\boldsymbol{r}_n)} + \mathrm{H.c.}\\ &+\sum_{n=1}^{N}\frac{\Omega_\mathrm{RC}(t-\boldsymbol{r}_n\cdot\hat{\boldsymbol{e}}_y/c)}{2}\,\frac{-1}{\sqrt{2}}\,\hat{\sigma}^n_{34_-}\,\mathrm{e}^{\mathrm{i}(\omega_\mathrm{C}t-\boldsymbol{k}_\mathrm{C}\cdot\boldsymbol{r}_n)} + \mathrm{H.c.},\end{aligned} \tag{4.11}$$

where the additional factors $\pm1/\sqrt{2}$ account for the amplitude whereby the transitions $|3\rangle \to |4_+\rangle$ and $|3\rangle \to |4_-\rangle$ are driven.

Despite being undriven, the E1-allowed transition $4 \to 1$ undergoes spontaneous decay [see, e.g., Fig. 4.2b]: These photons, decaying from states $|4_\pm\rangle$ with $M_J = \pm1$ to state $|1\rangle$ with $M_J = 0$, differ in energy and polarization from those decaying on the $2 \to 1$ transition. In the following, we show that an x-ray comb emerges in the associated spectrum of resonance fluorescence.

4.1.1.2 Equations of motion and periodicity of the asymptotically reached solution

As displayed by Eq. (2.91), the time evolution of the system obeys the master equation [53] $\mathrm{d}\hat{\rho}/\,\mathrm{d}t = -\mathrm{i}\,[\hat{H},\hat{\rho}] + \mathcal{L}[\hat{\rho}]$, where $\hat{\rho}(t)$ is the density matrix of elements $\rho^n_{ij}(t) = \langle\hat{\sigma}^n_{ji}(t)\rangle =$

[3] In the case of Be^{2+} ions that we consider in the paper, $\Delta = 1.8\,\mathrm{eV}$, whereas $\Gamma_{41} = 5.05\times10^{-4}\,\mathrm{eV}$ is the decay rate of the same transition and we assume an x-ray bandwidth γ_c smaller than the optical-comb repetition frequency $2\pi/T_\mathrm{p} = 4.1\times10^{-6}\,\mathrm{eV}$.

$\mathrm{Tr}\{\hat{\sigma}^n_{ji}(t)\,\hat{\rho}\}$, and $\mathcal{L}[\hat{\rho}]$ describes norm-conserving spontaneous decay,

$$\mathcal{L}[\hat{\rho}] = \sum_{\substack{i,j\in\{1,2_0,3,4_\pm\}\\ \omega_i<\omega_j}} \sum_{n=1}^{N} -\frac{\Gamma_{ji}}{2}(\hat{\sigma}^n_{ji}\hat{\sigma}^n_{ij}\hat{\rho} - \hat{\sigma}^n_{ij}\hat{\rho}\hat{\sigma}^n_{ji}) + \text{H.c.}, \tag{4.12}$$

with spontaneous-decay rates $\Gamma_{ji} = 4\omega^3_{ji}\alpha^3|\boldsymbol{d}_{ij}|^2/3$ [53]; norm-nonconserving terms such as those from autoionization or (multi-) photoionization are not present. Further, for cw x-ray and optical fields, and an optical frequency comb, the EOMs are periodic with the repetition time T_p of the optical frequency-comb pulse train: The master equation admits a periodic solution, $\hat{\rho}^\mathrm{eq}(t) = \hat{\rho}^\mathrm{eq}(t+T_\mathrm{p})$, asymptotically reached after turn-on effects have ceased.

The fields are tuned to the respective transition energies, i.e., $\omega_\mathrm{X} = \omega_{21}$, $\omega_\mathrm{L} = |\omega_{32}|$, and $\omega_\mathrm{C} = \omega_{43}$. The effect of a field on the other transitions to which it is not tuned is negligible. The relevant interactions are highlighted in Fig. 4.2b. The states $|2_\pm\rangle$ and $|4_0\rangle$ are neglected, because they are undriven and the decay from higher-energy levels to them is by orders of magnitude smaller than to the ground state. In the following, therefore, we restrict our attention to the 5 states $|1\rangle$, $|2_0\rangle$, $|3\rangle$, $|4_+\rangle$, and $|4_-\rangle$.

Before writing the EOMs explicitly, we introduce the slowly varying operators [53, 75, 195]

$$\hat{\varsigma}^n_{2_01}(t) = \hat{\sigma}^n_{2_01}(t)\,\mathrm{e}^{-\mathrm{i}(\omega_{21}t-\boldsymbol{k}_\mathrm{X}\cdot\boldsymbol{r}_n)}, \tag{4.13a}$$
$$\hat{\varsigma}^n_{32_0}(t) = \hat{\sigma}^n_{32_0}(t)\,\mathrm{e}^{-\mathrm{i}(\omega_{32}t-\boldsymbol{k}_\mathrm{L}\cdot\boldsymbol{r}_n)}, \tag{4.13b}$$
$$\hat{\varsigma}^n_{31}(t) = \hat{\sigma}^n_{31}(t)\,\mathrm{e}^{-\mathrm{i}[\omega_{31}t-(\boldsymbol{k}_\mathrm{X}+\boldsymbol{k}_\mathrm{L})\cdot\boldsymbol{r}_n]}, \tag{4.13c}$$
$$\hat{\varsigma}^n_{4_\pm3}(t) = \hat{\sigma}^n_{4_\pm3}(t)\,\mathrm{e}^{-\mathrm{i}(\omega_{43}t-\boldsymbol{k}_\mathrm{C}\cdot\boldsymbol{r}_n)}, \tag{4.13d}$$
$$\hat{\varsigma}^n_{4_\pm2_0}(t) = \hat{\sigma}^n_{4_\pm2_0}(t)\,\mathrm{e}^{-\mathrm{i}[\omega_{42}t-(\boldsymbol{k}_\mathrm{L}+\boldsymbol{k}_\mathrm{C})\cdot\boldsymbol{r}_n]}, \tag{4.13e}$$
$$\hat{\varsigma}^n_{4_\pm1}(t) = \hat{\sigma}^n_{4_\pm1}(t)\,\mathrm{e}^{-\mathrm{i}[\omega_{41}t-(\boldsymbol{k}_\mathrm{X}+\boldsymbol{k}_\mathrm{L}+\boldsymbol{k}_\mathrm{C})\cdot\boldsymbol{r}_n]}, \tag{4.13f}$$

and, clearly, $\hat{\varsigma}^n_{ij}(t) = [\hat{\varsigma}^n_{ji}(t)]^\dagger$. Analogously, we define an associated slowly-varying density matrix $\hat{\varrho}(t)$ with matrix elements $\varrho^n_{ij}(t) = \langle\hat{\varsigma}^n_{ji}(t)\rangle$, and introduce the n-dependent Rabi frequency $\Omega^n_\mathrm{RC}(t) = \Omega_\mathrm{RC}(t - \boldsymbol{r}_n\cdot\hat{\boldsymbol{e}}_y/c)$. The interaction Hamiltonians (4.8), (4.9), and (4.11), can be included in the master equation, giving rise to the following EOMs,

$$\frac{\partial\varrho^n_{11}}{\partial t} = -\mathrm{i}\frac{\Omega_\mathrm{RX}}{2}\varrho^n_{2_01} + \mathrm{i}\frac{\Omega_\mathrm{RX}}{2}\varrho^n_{12_0} + \Gamma_{2_01}\varrho^n_{2_02_0} + \Gamma_{4_+1}\varrho^n_{4_+4_+} + \Gamma_{4_-1}\varrho^n_{4_-4_-}, \tag{4.14a}$$

$$\frac{\partial\varrho^n_{12_0}}{\partial t} = -\frac{\Gamma_{2_01}}{2}\varrho^n_{12_0} - \mathrm{i}\frac{\Omega_\mathrm{RX}}{2}(\varrho^n_{2_02_0} - \varrho^n_{11}) + \mathrm{i}\frac{\Omega_\mathrm{RL}}{2}\varrho^n_{13}, \tag{4.14b}$$

$$\frac{\partial\varrho^n_{13}}{\partial t} = -\frac{\Gamma_{32_0}}{2}\varrho^n_{13} - \mathrm{i}\frac{\Omega_\mathrm{RX}}{2}\varrho^n_{2_03} + \mathrm{i}\frac{\Omega_\mathrm{RL}}{2}\varrho^n_{12_0} + \mathrm{i}\frac{\Omega^n_\mathrm{RC}(t)}{2\sqrt{2}}\varrho^n_{14_+} - \mathrm{i}\frac{\Omega^n_\mathrm{RC}(t)}{2\sqrt{2}}\varrho^n_{14_-}, \tag{4.14c}$$

$$\frac{\partial\varrho^n_{14_\pm}}{\partial t} = -\mathrm{i}\frac{\Omega_\mathrm{RX}}{2}\varrho^n_{2_04_\pm} \pm \mathrm{i}\frac{\Omega^n_\mathrm{RC}(t)}{2\sqrt{2}}\varrho^n_{13} - (\Gamma_{4_\pm1} + \Gamma_{4_\pm3})\varrho^n_{14_\pm}, \tag{4.14d}$$

$$\frac{\partial\varrho^n_{2_02_0}}{\partial t} = -\mathrm{i}\frac{\Omega_\mathrm{RX}}{2}\varrho^n_{12_0} + \mathrm{i}\frac{\Omega_\mathrm{RX}}{2}\varrho^n_{2_01} - \mathrm{i}\frac{\Omega_\mathrm{RL}}{2}\varrho^n_{32_0} + \mathrm{i}\frac{\Omega_\mathrm{RL}}{2}\varrho^n_{2_03} - \Gamma_{2_01}\varrho^n_{2_02_0} + \Gamma_{32_0}\varrho^n_{33}, \tag{4.14e}$$

$$\frac{\partial\varrho^n_{2_03}}{\partial t} = -\frac{\Gamma_{2_01}+\Gamma_{32_0}}{2}\varrho^n_{2_03} - \mathrm{i}\frac{\Omega_\mathrm{RX}}{2}\varrho^n_{13} - \mathrm{i}\frac{\Omega_\mathrm{RL}}{2}(\varrho^n_{33} - \varrho^n_{2_02_0}) + \mathrm{i}\frac{\Omega^n_\mathrm{RC}(t)}{2\sqrt{2}}(\varrho^n_{2_04_+} - \varrho^n_{2_04_-}), \tag{4.14f}$$

$$\frac{\partial\varrho^n_{2_04_\pm}}{\partial t} = -\frac{\Gamma_{2_01}+\Gamma_{4_\pm1}+\Gamma_{4_\pm3}}{2}\varrho^n_{2_04_\pm} - \mathrm{i}\frac{\Omega_\mathrm{RX}}{2}\varrho^n_{14_\pm} - \mathrm{i}\frac{\Omega_\mathrm{RL}}{2}\varrho^n_{34_\pm} \pm \mathrm{i}\frac{\Omega^n_\mathrm{RC}(t)}{2\sqrt{2}}\varrho^n_{2_03}, \tag{4.14g}$$

$$\frac{\partial \varrho^n_{33}}{\partial t} = -\mathrm{i}\frac{\Omega_{\mathrm{RL}}}{2}\varrho^n_{2_0 3} + \mathrm{i}\frac{\Omega_{\mathrm{RL}}}{2}\varrho^n_{32_0} - \mathrm{i}\frac{\Omega^n_{\mathrm{RC}}(t)}{2}(\varrho^n_{4_+3} - \varrho^n_{4_-3}) + \mathrm{i}\frac{\Omega^n_{\mathrm{RC}}(t)}{2}(\varrho^n_{34_+} - \varrho^n_{34_-}) - \Gamma_{32_0}\varrho^n_{33} + \Gamma_{4_+3}\varrho^n_{4_+4_+} + \Gamma_{4_-3}\varrho^n_{4_-4_-}, \tag{4.14h}$$

$$\frac{\partial \varrho^n_{34_\pm}}{\partial t} = -\frac{\Gamma_{4_\pm 1} + \Gamma_{4_\pm 3} + \Gamma_{32_0}}{2}\varrho^n_{34_\pm} - \mathrm{i}\frac{\Omega_{\mathrm{RL}}}{2}\varrho^n_{2_0 4_\pm} \mp \mathrm{i}\frac{\Omega^n_{\mathrm{RC}}(t)}{2\sqrt{2}}(\varrho^n_{4_\pm 4_\pm} - \varrho^n_{33}) \pm \mathrm{i}\frac{\Omega^n_{\mathrm{RC}}(t)}{2\sqrt{2}}\varrho^n_{4_\mp 4_\pm}, \tag{4.14i}$$

$$\frac{\partial \varrho^n_{4_\pm 4_\pm}}{\partial t} = \mp\mathrm{i}\frac{\Omega^n_{\mathrm{RC}}(t)}{2\sqrt{2}}\varrho_{34_\pm} \pm \mathrm{i}\frac{\Omega^n_{\mathrm{RC}}(t)}{2\sqrt{2}}\varrho_{4_\pm 3} - (\Gamma_{4_\pm 1} + \Gamma_{4_\pm 3})\varrho^n_{4_\pm 4_\pm}, \tag{4.14j}$$

$$\frac{\partial \varrho^n_{4_\pm 4_\mp}}{\partial t} = \mp\mathrm{i}\frac{\Omega^n_{\mathrm{RC}}(t)}{2\sqrt{2}}\varrho_{34_\mp} \mp \mathrm{i}\frac{\Omega^n_{\mathrm{RC}}(t)}{2\sqrt{2}}\varrho_{4_\pm 3} - (\Gamma_{4_+1} + \Gamma_{4_+3} + \Gamma_{4_-1} + \Gamma_{4_-3})\varrho^n_{4_\pm 4_\mp}. \tag{4.14k}$$

Two main properties ought to be observed:

- the EOMs form a set of linear equations with time-dependent coefficients, where the explicit dependence on time ensues from the n-dependent Rabi frequency $\Omega^n_{\mathrm{RC}}(t)$. This is also the only n-dependent term in the EOMs, with $\Omega^n_{\mathrm{RC}}(t) = \Omega_{\mathrm{RC}}(t - \boldsymbol{r}_n \cdot \hat{\boldsymbol{e}}_y/c)$. The elements of the density matrices associated with different ions can be related, at different times, via the following equality:
$$\varrho^n_{ij}(t) = \varrho^{n'}_{ij}[t + (\boldsymbol{r}_{n'} - \boldsymbol{r}_n)\cdot\hat{\boldsymbol{e}}_y/c]. \tag{4.15}$$
- The EOMs are symmetric under the transformation
$$\{\varrho_{i4_\pm}, \varrho_{4_\pm i}, \varrho_{4_\pm 4_\pm}, \varrho_{4_\pm 4_\mp}\} \to \{-\varrho_{i4_\mp}, -\varrho_{4_\mp i}, \varrho_{4_\mp 4_\mp}, \varrho_{4_\mp 4_\pm}\},$$
for $i \in \{1, 2_0, 3\}$. As a result, the periodic, asymptotically reached solution of the EOMs satisfies the equality $\varrho_{14_+} = -\varrho_{14_-}$.

The EOMs (4.14) form a set of 25 lineal differential equations, with time-dependent coefficients for 25 elements of the 5×5 density matrix $\hat{\varrho}^n$, which can be written in terms of a matrix differential equation. The procedure is the same we already discussed to obtain Eq. (3.18) in the case of a two-level system. We introduce the 25-dimensional vector $\vec{R}(t)$, of elements $R_1 = \varrho_{11}$, $R_2 = \varrho_{12_0}$, …, $R_{25} = \varrho_{4_+4_+}$, which satisfies the matrix differential equation

$$\frac{\mathrm{d}\vec{R}(t)}{\mathrm{d}t} = \mathbf{M}(t)\vec{R}(t), \tag{4.16}$$

where $\mathbf{M}(t)$ is a 25×25 time-dependent, periodic matrix, resulting from Eqs. (4.14). Notice that we have not specified any initial conditions for the vector $\vec{R}(t)$ because the asymptotic, periodic solution $\vec{R}^{\mathrm{eq}}(t)$ which we seek is independent of the initial state occupied by the atomic system.

In order to prove the existence of this periodic solution and, at the same time, display the steps leading to its calculation, we take advantage of the conclusions drawn in Ref. [75]. We introduce the vector $\vec{R}'(t) = \mathbf{A}\vec{R}(t)$, where $\mathbf{A}$ is a time-independent invertible matrix such that, owing to the absence of norm-nonconserving terms in the EOMs, the first component of the vector $R'_1(t) = \mathrm{Tr}\hat{\varrho}^n(t) = \varrho^n_{11}(t) + \varrho^n_{2_0 2_0}(t) + \varrho^n_{33}(t) + \varrho^n_{4_-4_-}(t) + \varrho^n_{4_+4_+}(t) = 1$ is a constant of motion. In terms of the time-dependent, regular matrix $\mathbf{M}'(t) = \mathbf{A}\mathbf{M}(t)\mathbf{A}^{-1}$, the vector $\vec{R}'(t)$, solution of the differential equation

$$\frac{\mathrm{d}\vec{R}'(t)}{\mathrm{d}t} = \mathbf{M}'(t)\vec{R}'(t), \tag{4.17}$$

can be written as [196]

$$\vec{R}'(t) = \mathbf{U}(t, t_0)\vec{R}'(t_0), \tag{4.18}$$

where $\mathbf{U}(t, t_0)$ is a 25×25 matrix, of elements $U_{ij}(t, t_0)$, solution of the system of differential equations

$$\frac{\mathrm{d}\mathbf{U}(t, t_0)}{\mathrm{d}t} = \mathbf{M}'(t)\mathbf{U}(t, t_0), \qquad \mathbf{U}(t_0, t_0) = \mathbb{1}_{25}. \tag{4.19}$$

In order to determine a periodic solution of the EOMs $\vec{R}'^{\mathrm{eq}}(t + T_\mathrm{p}) = \vec{R}'^{\mathrm{eq}}(t)$, with T_p being the period of the EOMs, the following identity need be fulfilled:

$$\vec{R}'^{\mathrm{eq}}(t_0 + T_\mathrm{p}) = \mathbf{U}(t_0 + T_\mathrm{p}, t_0)\vec{R}'^{\mathrm{eq}}(t_0) = \vec{R}'^{\mathrm{eq}}(t_0). \tag{4.20}$$

In other words, one has to determine the eigenstate $\vec{R}'^{\mathrm{eq}}(t_0)$ of $\mathbf{U}(t_0 + T_\mathrm{p}, t_0)$ associated with the eigenvalue $\lambda = 1$. Since $R'_1(t) = 1$ is a constant of motion, it necessarily follows that

$$\mathbf{U}(t, t_0) = \begin{pmatrix} 1 & 0 & \dots & 0 \\ U_{2,1}(t, t_0) & U_{2,2}(t, t_0) & \dots & U_{2,25}(t, t_0) \\ \vdots & \vdots & \ddots & \vdots \\ U_{25,25}(t, t_0) & U_{25,2}(t, t_0) & \dots & U_{25,25}(t, t_0) \end{pmatrix}, \tag{4.21}$$

i.e., that $U_{1j}(t, t_0) = \delta_{1j}$ for $j \in \{1, \dots, 25\}$, and that

$$\begin{aligned} \mathbf{U}(t_0 + T_\mathrm{p}, t_0)\mathbf{P} &= \begin{pmatrix} 1 & 0 & \dots & 0 \\ U_{2,1}(t_0 + T_\mathrm{p}, t_0) & U_{2,2}(t_0 + T_\mathrm{p}, t_0) & \dots & U_{2,25}(t_0 + T_\mathrm{p}, t_0) \\ \vdots & \vdots & \ddots & \vdots \\ U_{25,25}(t_0 + T_\mathrm{p}, t_0) & U_{25,2}(t_0 + T_\mathrm{p}, t_0) & \dots & U_{25,25}(t_0 + T_\mathrm{p}, t_0) \end{pmatrix} \mathbf{P} \\ &= \mathbf{P} \begin{pmatrix} \lambda_1 & 0 & \dots & 0 \\ 0 & \lambda_2 & \dots & 0 \\ \vdots & \vdots & \ddots & \vdots \\ 0 & 0 & \dots & \lambda_{25} \end{pmatrix}, \end{aligned} \tag{4.22}$$

where $\mathbf{P}$ is the invertible matrix, of elements P_{ij}, whose columns are formed by the eigenstates of the matrix $\mathbf{U}(t_0 + T_\mathrm{p}, t_0)$, while λ_i, with $i \in \{1, \dots, 25\}$, are the eigenvalues of the same matrix [196]. This means that, for $i, j \in \{1, \dots, 25\}$,

$$\sum_{k=1}^{25} U_{ik}(t_0 + T_\mathrm{p}, t_0)P_{kj} = \sum_{k=1}^{25} P_{ik}\lambda_k\delta_{kj} = \lambda_j P_{ij} : \tag{4.23}$$

For the particular case in which $i = 1$ and $U_{1k}(t_0 + T_\mathrm{p}, t_0) = \delta_{1k}$, this implies that $P_{1j} = \lambda_j P_{1j}$, for $j \in \{1, \dots, 25\}$. If none of the 25 eigenvalues λ_j is equal to 1, then $P_{1j} = 0$ for all $j \in \{1, \dots, 25\}$, i.e., an entire row of the matrix $\mathbf{P}$ is equal to zero, $\mathbf{P}$ is not invertible, and $\mathbf{U}(t_0 + T_\mathrm{p}, t_0)$ cannot be diagonalized. However, because $\mathbf{U}(t_0 + T_\mathrm{p}, t_0)$ is by construction an invertible, diagonalizable matrix, we can conclude that at least one eigenvalue must be equal to 1. The corresponding eigenstate $\vec{R}'^{\mathrm{eq}}(t_0)$, normalized such that $R'_1(t_0) = 1$, provides those specific initial conditions associated with the sought periodic solution $\vec{R}'^{\mathrm{eq}}(t) = \mathbf{U}(t, t_0)\vec{R}'^{\mathrm{eq}}(t_0)$, i.e., $\vec{R}^{\mathrm{eq}}(t) = \mathbf{A}^{-1}\mathbf{U}(t, t_0)\vec{R}'^{\mathrm{eq}}(t_0)$.

4.1.2 Many-atom spectrum of resonance fluorescence from periodic driving

In this Section we present the properties of the spectrum of resonance fluorescence emitted by an atomic system periodically driven by the external electric fields $\boldsymbol{\mathcal{E}}_{\mathrm{X}}(\boldsymbol{r},\, t)$, $\boldsymbol{\mathcal{E}}_{\mathrm{L}}(\boldsymbol{r},\, t)$, and $\boldsymbol{\mathcal{E}}_{\mathrm{C}}(\boldsymbol{r},\, t)$. As we did in Eqs. (2.68) and (2.70), we introduce the electric-field operator

$$\hat{\boldsymbol{E}}(\boldsymbol{r},\, t) = \hat{\boldsymbol{E}}^{+}(\boldsymbol{r},\, t) + \hat{\boldsymbol{E}}^{-}(\boldsymbol{r},\, t), \tag{4.24}$$

where $\boldsymbol{r} = r\,\hat{\boldsymbol{e}}_r$ is the observation point in a reference frame in which $\mathbf{0}$ corresponds to the position of the ion sample, such that r denotes the distance of the detector from the ions and $\hat{\boldsymbol{e}}_r$ is the unit vector defining the direction of observation. In the electric-dipole approximation, the positive-frequency component of the electric field is related to the electric-dipole moment operator via [53]

$$\hat{\boldsymbol{E}}^{+}(\boldsymbol{r},\, t) = \sum_{\substack{i,\, j\in\{1,\, 2_0,\, 3,\, 4_\pm\}\\ \omega_i<\omega_j}} \Big[\, \frac{\omega_{ji}^2}{c^2\, r}\, [\boldsymbol{d}_{ji} - \hat{\boldsymbol{e}}_r\, (\boldsymbol{d}_{ji}\cdot\hat{\boldsymbol{e}}_r)] \sum_{n=1}^{N} \hat{\sigma}_{ij}^{n}(t - |\boldsymbol{r}-\boldsymbol{r}_n|/c)\Big]. \tag{4.25}$$

This is used for the calculation of the energy spectrum of resonance fluorescence [53, 162]

$$W(\boldsymbol{r},\omega) = \frac{1}{4\pi^2\alpha} \int_{-\infty}^{\infty}\int_{-\infty}^{\infty} \big\langle \hat{\boldsymbol{E}}^{-}(\boldsymbol{r},\, t_1)\cdot\hat{\boldsymbol{E}}^{+}(\boldsymbol{r},\, t_2)\big\rangle\, \mathrm{e}^{-\mathrm{i}\omega(t_1-t_2)}\, \mathrm{d}t_1\, \mathrm{d}t_2, \tag{4.26}$$

where α is the fine structure constant. $W(\boldsymbol{r},\omega)\, \mathrm{d}\omega\, r^2\, \mathrm{d}\Omega$ represents the energy detected in a solid angle $\mathrm{d}\Omega$ centered at the observation point $\boldsymbol{r} = r\,\hat{\boldsymbol{e}}_r$ and in the differential energy interval $[\omega,\, \omega + \mathrm{d}\omega]$.

In the case of periodic driving the energy spectrum diverges and one needs to introduce the power spectrum of resonance fluorescence [162]

$$S(\boldsymbol{r},\omega) = \frac{1}{4\pi^2\alpha} \lim_{T\to\infty} \int_{0}^{T}\int_{0}^{T} \big\langle \hat{\boldsymbol{E}}_{\mathrm{eq}}^{-}(\boldsymbol{r},\, t_1)\cdot\hat{\boldsymbol{E}}_{\mathrm{eq}}^{+}(\boldsymbol{r},\, t_2)\big\rangle\, \mathrm{e}^{-\mathrm{i}\omega(t_1-t_2)}\, \mathrm{d}t_1\, \mathrm{d}t_2, \tag{4.27}$$

such that $S(\boldsymbol{r},\omega)\, \mathrm{d}\omega\, r^2\, \mathrm{d}\Omega$ represents the power detected in a solid angle $\mathrm{d}\Omega$ centered at the observation point and in the differential energy interval $[\omega,\, \omega + \mathrm{d}\omega]$. Here, $\hat{\boldsymbol{E}}_{\mathrm{eq}}^{+}(\boldsymbol{r},\, t)$ is the positive-frequency part of the electric field operator associated with the periodic, asymptotic solution of the EOMs at position $\boldsymbol{r}$ and time t.

4.1.2.1 Many-atom effects in the coherent and incoherent parts of the spectrum of resonance fluorescence

In terms of the polar coordinates r, θ, and ϕ, and of the three unit vectors

$$\hat{\boldsymbol{e}}_r = \sin\theta\, \cos\phi\, \hat{\boldsymbol{e}}_x + \sin\theta\, \sin\phi\, \hat{\boldsymbol{e}}_y + \cos\theta\, \hat{\boldsymbol{e}}_z, \tag{4.28a}$$

$$\hat{\boldsymbol{e}}_\theta = \cos\theta\, \cos\phi\, \hat{\boldsymbol{e}}_x + \cos\theta\, \sin\phi\, \hat{\boldsymbol{e}}_y - \sin\theta\, \hat{\boldsymbol{e}}_z, \tag{4.28b}$$

$$\hat{\boldsymbol{e}}_\phi = -\sin\phi\, \hat{\boldsymbol{e}}_x + \cos\phi\, \hat{\boldsymbol{e}}_y, \tag{4.28c}$$

appearing in Fig. 4.3, the electric-field operator at the observation point $\boldsymbol{r} = r\,\hat{\boldsymbol{e}}_r$ and in the far-field limit is the sum of the following six operators,

$$\hat{\boldsymbol{E}}_{2_0 1}^{+}(\boldsymbol{r},\, t) = -\frac{\omega_{21}^2}{c^2\, r}\, d_{2_0 1}\, \sin\theta\, \hat{\boldsymbol{e}}_\theta \sum_{n=1}^{N} \hat{\varsigma}_{12_0}^{n}(t - |\boldsymbol{r}-\boldsymbol{r}_n|/c)\, \mathrm{e}^{-\mathrm{i}[\omega_{21}(t-|\boldsymbol{r}-\boldsymbol{r}_n|/c) - \boldsymbol{k}_{\mathrm{X}}\cdot\boldsymbol{r}_n]}, \tag{4.29a}$$

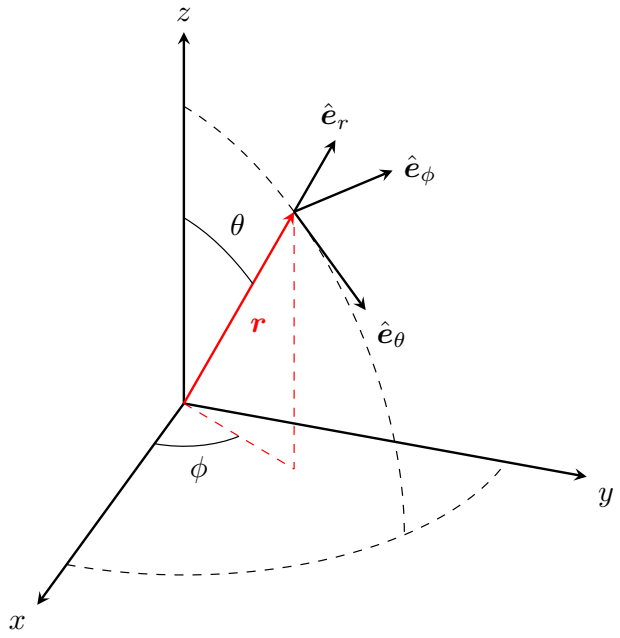

Figure 4.3: Spherical coordinates with respect to the observation point $\boldsymbol{r}$ (the red arrow).

$$\hat{\boldsymbol{E}}^{+}_{32_0}(\boldsymbol{r},\,t) = -\frac{\omega_{32}^2}{c^2\,r}\,d_{32_0}\,\sin\theta\,\hat{\boldsymbol{e}}_\theta \sum_{n=1}^{N} \hat{\varsigma}^n_{2_03}(t-|\boldsymbol{r}-\boldsymbol{r}_n|/c)\,\mathrm{e}^{-\mathrm{i}[\omega_{32}(t-|\boldsymbol{r}-\boldsymbol{r}_n|/c)-\boldsymbol{k}_\mathrm{L}\cdot\boldsymbol{r}_n]}, \tag{4.29b}$$

$$\begin{aligned}\hat{\boldsymbol{E}}^{+}_{4_\pm3}(\boldsymbol{r},\,t) = {}& \frac{\omega_{43}^2}{c^2\,r}\frac{d_{4_\pm3}}{\sqrt{2}}\,[\cos\theta(\mp\cos\phi+\mathrm{i}\sin\phi)\hat{\boldsymbol{e}}_\theta+(\pm\sin\phi+\mathrm{i}\cos\phi)\hat{\boldsymbol{e}}_\phi] \\ & \times\sum_{n=1}^{N}\hat{\varsigma}^n_{34_\pm}(t-|\boldsymbol{r}-\boldsymbol{r}_n|/c)\,\mathrm{e}^{-\mathrm{i}[\omega_{43}(t-|\boldsymbol{r}-\boldsymbol{r}_n|/c)-\boldsymbol{k}_\mathrm{C}\cdot\boldsymbol{r}_n]},\end{aligned} \tag{4.29c}$$

$$\begin{aligned}\hat{\boldsymbol{E}}^{+}_{4_\pm1}(\boldsymbol{r},\,t) = {}& \frac{\omega_{41}^2}{c^2\,r}\frac{d_{4_\pm1}}{\sqrt{2}}\,[\cos\theta(\mp\cos\phi+\mathrm{i}\sin\phi)\hat{\boldsymbol{e}}_\theta+(\pm\sin\phi+\mathrm{i}\cos\phi)\hat{\boldsymbol{e}}_\phi] \\ & \times\sum_{n=1}^{N}\hat{\varsigma}^n_{14_\pm}(t-|\boldsymbol{r}-\boldsymbol{r}_n|/c)\,\mathrm{e}^{-\mathrm{i}[\omega_{41}(t-|\boldsymbol{r}-\boldsymbol{r}_n|/c)-(\boldsymbol{k}_\mathrm{X}+\boldsymbol{k}_\mathrm{L}+\boldsymbol{k}_\mathrm{C})\cdot\boldsymbol{r}_n]},\end{aligned} \tag{4.29d}$$

where the selection rules in Eqs. (2.102) and (2.103) imply that $d^0_{2_01} = \boldsymbol{d}_{2_01}\cdot\hat{\boldsymbol{e}}_z$, $d^0_{32_0} = \boldsymbol{d}_{32_0}\cdot\hat{\boldsymbol{e}}_z$, $d^{\pm1}_{4_\pm3} = \boldsymbol{d}_{4_\pm3}\cdot\hat{\boldsymbol{e}}_{\sigma^*_\pm}$, and $d^{\pm1}_{4_\pm1} = \boldsymbol{d}_{4_\pm1}\cdot\hat{\boldsymbol{e}}_{\sigma^*_\pm}$. Furthermore, the explicit calculation of the Clebsch-Gordan coefficients shows the validity of the following identities, $d^{+1}_{4_+3} = d^{-1}_{4_-3} = \tilde{d}_{43}$, $d^{+1}_{4_+1} = d^{-1}_{4_-1} = \tilde{d}_{41}$.

The calculation of Eq. (4.26) involves terms of the form $\mathrm{e}^{\mathrm{i}\omega_a t}\,\mathrm{e}^{-\mathrm{i}\omega_b t}$, where ω_a and ω_b are elements of the vector $\{\omega_{21},\,\omega_{32},\,\omega_{43},\,\omega_{41}\}$. However, when $\omega_a \neq \omega_b$, the integration of the resulting fast oscillating function vanishes. By further adopting the approximation $|\boldsymbol{r}-\boldsymbol{r}_n| \approx r - \hat{\boldsymbol{e}}_r\cdot\boldsymbol{r}_n$, valid in the far-field limit, we can write the emitted spectrum of resonance fluorescence as the sum of six independent terms, i.e.,

$$W(\boldsymbol{r},\omega) = W_{2_01,12_0}(\boldsymbol{r},\omega) + W_{32_0,2_03}(\boldsymbol{r},\omega) + \sum_{j,\,j'\in\{4_\pm\}}[W_{j3,3j'}(\boldsymbol{r},\omega)+W_{j1,1j'}(\boldsymbol{r},\omega)], \tag{4.30}$$

where we have defined

$$W_{2_01,12_0}(\boldsymbol{r},\omega) = \frac{\omega_{21}^4\,|d_{2_01}|^2}{4\pi^2c^3r^2}\sum_{n=1}^{N}\sum_{n'=1}^{N}\int_{-\infty}^{+\infty}\int_{-\infty}^{+\infty}\left\langle\hat{\varsigma}_{2_01}^{n}(t_1-|\boldsymbol{r}-\boldsymbol{r}_n|/c)\,\hat{\varsigma}_{12_0}^{n'}(t_2-|\boldsymbol{r}-\boldsymbol{r}_{n'}|/c)\right\rangle \times \sin^2\theta\,\mathrm{e}^{-\mathrm{i}(\omega-\omega_{21})(t_1-t_2)}\,\mathrm{e}^{\mathrm{i}[(\omega_{21}/c)\,\hat{\boldsymbol{e}}_r-\boldsymbol{k}_\mathrm{X}]\cdot(\boldsymbol{r}_n-\boldsymbol{r}_{n'})}\,\mathrm{d}t_1\,\mathrm{d}t_2, \tag{4.31a}$$

$$W_{32_0,2_03}(\boldsymbol{r},\omega) = \frac{\omega_{32}^4\,|d_{32_0}|^2}{4\pi^2c^3r^2}\sum_{n=1}^{N}\sum_{n'=1}^{N}\int_{-\infty}^{+\infty}\int_{-\infty}^{+\infty}\left\langle\hat{\varsigma}_{32_0}^{n}(t_1-|\boldsymbol{r}-\boldsymbol{r}_n|/c)\,\hat{\varsigma}_{2_03}^{n'}(t_2-|\boldsymbol{r}-\boldsymbol{r}_{n'}|/c)\right\rangle \times \sin^2\theta\,\mathrm{e}^{-\mathrm{i}(\omega-\omega_{32})(t_1-t_2)}\,\mathrm{e}^{\mathrm{i}[(\omega_{32}/c)\,\hat{\boldsymbol{e}}_r-\boldsymbol{k}_\mathrm{L}]\cdot(\boldsymbol{r}_n-\boldsymbol{r}_{n'})}\,\mathrm{d}t_1\,\mathrm{d}t_2, \tag{4.31b}$$

$$W_{4_\pm3,34_\pm}(\boldsymbol{r},\omega) = \frac{\omega_{43}^4\,|\tilde{d}_{43}|^2}{8\pi^2c^3r^2}\sum_{n=1}^{N}\sum_{n'=1}^{N}\int_{-\infty}^{+\infty}\int_{-\infty}^{+\infty}\left\langle\hat{\varsigma}_{4_\pm3}^{n}(t_1-|\boldsymbol{r}-\boldsymbol{r}_n|/c)\,\hat{\varsigma}_{34_\pm}^{n'}(t_2-|\boldsymbol{r}-\boldsymbol{r}_{n'}|/c)\right\rangle \times (1+\cos^2\theta)\,\mathrm{e}^{-\mathrm{i}(\omega-\omega_{43})(t_1-t_2)}\,\mathrm{e}^{\mathrm{i}[(\omega_{43}/c)\,\hat{\boldsymbol{e}}_r-\boldsymbol{k}_\mathrm{C}]\cdot(\boldsymbol{r}_n-\boldsymbol{r}_{n'})}\,\mathrm{d}t_1\,\mathrm{d}t_2, \tag{4.31c}$$

$$W_{4_\pm3,34_\mp}(\boldsymbol{r},\omega) = \frac{\omega_{43}^4\,|\tilde{d}_{43}|^2}{8\pi^2c^3r^2}\sum_{n=1}^{N}\sum_{n'=1}^{N}\int_{-\infty}^{+\infty}\int_{-\infty}^{+\infty}\left\langle\hat{\varsigma}_{4_\pm3}^{n}(t_1-|\boldsymbol{r}-\boldsymbol{r}_n|/c)\,\hat{\varsigma}_{34_\mp}^{n'}(t_2-|\boldsymbol{r}-\boldsymbol{r}_{n'}|/c)\right\rangle \times (1-\cos^2\theta)\,(\cos 2\phi\pm\mathrm{i}\,\sin 2\phi)\,\mathrm{e}^{-\mathrm{i}(\omega-\omega_{43})(t_1-t_2)}\,\mathrm{e}^{\mathrm{i}[(\omega_{43}/c)\,\hat{\boldsymbol{e}}_r-\boldsymbol{k}_\mathrm{C}]\cdot(\boldsymbol{r}_n-\boldsymbol{r}_{n'})}\,\mathrm{d}t_1\,\mathrm{d}t_2, \tag{4.31d}$$

$$W_{4_\pm1,14_\pm}(\boldsymbol{r},\omega) = \frac{\omega_{41}^4\,|\tilde{d}_{41}|^2}{8\pi^2c^3r^2}\sum_{n=1}^{N}\sum_{n'=1}^{N}\int_{-\infty}^{+\infty}\int_{-\infty}^{+\infty}\left\langle\hat{\varsigma}_{4_\pm1}^{n}(t_1-|\boldsymbol{r}-\boldsymbol{r}_n|/c)\,\hat{\varsigma}_{14_\pm}^{n'}(t_2-|\boldsymbol{r}-\boldsymbol{r}_{n'}|/c)\right\rangle \times (1+\cos^2\theta)\,\mathrm{e}^{-\mathrm{i}(\omega-\omega_{41})(t_1-t_2)}\,\mathrm{e}^{\mathrm{i}[(\omega_{41}/c)\,\hat{\boldsymbol{e}}_r-(\boldsymbol{k}_\mathrm{X}+\boldsymbol{k}_\mathrm{L}+\boldsymbol{k}_\mathrm{C})]\cdot(\boldsymbol{r}_n-\boldsymbol{r}_{n'})}\,\mathrm{d}t_1\,\mathrm{d}t_2, \tag{4.31e}$$

$$W_{4_\pm1,14_\mp}(\boldsymbol{r},\omega) = \frac{\omega_{41}^4\,|\tilde{d}_{41}|^2}{8\pi^2c^3r^2}\sum_{n=1}^{N}\sum_{n'=1}^{N}\int_{-\infty}^{+\infty}\int_{-\infty}^{+\infty}\left\langle\hat{\varsigma}_{4_\pm1}^{n}(t_1-|\boldsymbol{r}-\boldsymbol{r}_n|/c)\,\hat{\varsigma}_{14_\mp}^{n'}(t_2-|\boldsymbol{r}-\boldsymbol{r}_{n'}|/c)\right\rangle \times (1-\cos^2\theta)\,(\cos 2\phi\pm\mathrm{i}\,\sin 2\phi)\,\mathrm{e}^{-\mathrm{i}(\omega-\omega_{41})(t_1-t_2)}\,\mathrm{e}^{\mathrm{i}[(\omega_{41}/c)\,\hat{\boldsymbol{e}}_r-(\boldsymbol{k}_\mathrm{X}+\boldsymbol{k}_\mathrm{L}+\boldsymbol{k}_\mathrm{C})]\cdot(\boldsymbol{r}_n-\boldsymbol{r}_{n'})}\,\mathrm{d}t_1\,\mathrm{d}t_2. \tag{4.31f}$$

In the following, we are going to focus on the spectrum of resonance fluorescence $W_{41,14}(\boldsymbol{r},\omega)$ [53] emitted on the $4\to1$ transition with x-ray energy ω_{41}. The energy at which this part of the spectrum is centered differs from the energy ω_{21} of the x-ray driven transition. Furthermore, the photons emitted by the states $|4_\pm\rangle$ and those emitted by the x-ray driven state $|2_0\rangle$ are characterized by mutually perpendicular polarization directions: These distinct polarizations are a direct consequence of the different directions on which the driving fields are aligned, as displayed in Fig. 4.2. The just described differences in energy and polarization render the x-ray comb emitted on the $|4_\pm\rangle\leftrightarrow|1\rangle$ transition clearly discernible from other spectral component of the resonance fluorescence spectrum, and support our choice to analyze only those four terms $W_{j1,1j'}(\boldsymbol{r},\omega)$, $j,\,j'\in\{4_+,\,4_-\}$, which are centered at the x-ray frequency ω_{41}.

The spectrum of resonance fluorescence is usually divided into a coherent and an incoherent component. This is performed by writing the ladder operators $\hat{\varsigma}_{ij}^{n}(t)$ as the following sum,

$$\hat{\varsigma}_{ij}^{n}(t) = \left\langle\hat{\varsigma}_{ij}^{n}(t)\right\rangle\hat{\mathbb{1}} + \delta\hat{\varsigma}_{ij}^{n}(t), \tag{4.32}$$

with

$$\left\langle\delta\hat{\varsigma}_{ij}^{n}(t)\right\rangle = 0, \tag{4.33a}$$

$$\left\langle\delta\hat{\varsigma}_{ji}^{n}(t)\,\delta\hat{\varsigma}_{i'j'}^{n'}(t')\right\rangle = \left\langle\delta\hat{\varsigma}_{ji}^{n}(t_1)\,\delta\hat{\varsigma}_{i'j'}^{n}(t_2)\right\rangle\,\delta_{nn'}, \tag{4.33b}$$

and, therefore,

$$\langle \hat{\varsigma}^{n}_{j1}(t_1)\, \hat{\varsigma}^{n'}_{1j'}(t_2)\rangle = \langle \hat{\varsigma}^{n}_{j1}(t_1)\rangle\, \langle \hat{\varsigma}^{n'}_{1j'}(t_2)\rangle + \langle \delta\hat{\varsigma}^{n}_{j1}(t_1)\, \delta\hat{\varsigma}^{n}_{1j'}(t_2)\rangle\, \delta_{nn'}. \tag{4.34}$$

This leads to the aforementioned definition of two components in the spectrum of resonance fluorescence [195]. For $j,\, j' \in \{4_+,\, 4_-\}$, for instance, $W_{j1,1j'}(\boldsymbol{r},\omega)$ in Eqs. (4.31) is the sum of a coherent spectrum $W^{\mathrm{coh}}_{j1,1j'}(\boldsymbol{r},\omega)$ and an incoherent part $W^{\mathrm{inc}}_{j1,1j'}(\boldsymbol{r},\omega)$, given by

$$\begin{aligned} W^{\mathrm{coh}}_{j1,1j'}(\boldsymbol{r},\omega) = \frac{\omega_{41}^4\, |\tilde{d}_{41}|^2}{8\pi^2 c^3 r^2} \sum_{n=1}^{N}\sum_{n'=1}^{N} \int_{-\infty}^{+\infty}\int_{-\infty}^{+\infty} \langle \hat{\varsigma}^{n}_{j1}(t_1 - |\boldsymbol{r}-\boldsymbol{r}_n|/c)\rangle\, \langle \hat{\varsigma}^{n'}_{1j'}(t_2 - |\boldsymbol{r}-\boldsymbol{r}_{n'}|/c)\rangle \\ \times s_{jj'}(\theta,\,\phi)\, \mathrm{e}^{-\mathrm{i}(\omega-\omega_{41})(t_1-t_2)}\, \mathrm{e}^{\mathrm{i}[(\omega_{41}/c)\,\hat{\boldsymbol{e}}_r - (\boldsymbol{k}_{\mathrm{X}}+\boldsymbol{k}_{\mathrm{L}}+\boldsymbol{k}_{\mathrm{C}})]\cdot(\boldsymbol{r}_n-\boldsymbol{r}_{n'})}\, \mathrm{d}t_1\, \mathrm{d}t_2, \end{aligned} \tag{4.35}$$

$$\begin{aligned} W^{\mathrm{inc}}_{j1,1j'}(\boldsymbol{r},\omega) = \frac{\omega_{41}^4\, |\tilde{d}_{41}|^2}{8\pi^2 c^3 r^2} \sum_{n=1}^{N} \int_{-\infty}^{+\infty}\int_{-\infty}^{+\infty} \big\langle \delta\hat{\varsigma}^{n}_{j1}(t_1 - |\boldsymbol{r}-\boldsymbol{r}_n|/c)\, \delta\hat{\varsigma}^{n}_{1j'}(t_2 - |\boldsymbol{r}-\boldsymbol{r}_n|/c)\big\rangle \\ \times s_{jj'}(\theta,\,\phi)\, \mathrm{e}^{-\mathrm{i}(\omega-\omega_{41})(t_1-t_2)}\, \mathrm{d}t_1\, \mathrm{d}t_2, \end{aligned} \tag{4.36}$$

where we have introduced the angular factor

$$s_{jj'}(\theta,\,\phi) = \begin{cases} 1+\cos^2\theta & \text{if } j = j', \\ (1-\cos^2\theta)\,(\cos 2\phi \pm \mathrm{i}\,\sin 2\phi) & \text{if } j,\, j' \in \{4_+,\, 4_-\}, \end{cases} \tag{4.37}$$

and have exploited Eq. (4.33b) in order to obtain Eq. (4.36).

The calculation of the spectrum of resonance fluorescence (4.35) can take advantage of the relationship (4.15) between the atomic expectation values $\langle \varsigma^{n}_{ij}(t)\rangle$ and $\langle \varsigma^{n'}_{ij}(t)\rangle$ associated with different ions. We define the expectation value $\langle \varsigma^{\mathrm{eq}}_{ij}(t)\rangle$ for an ion at the fixed position $\boldsymbol{r}_0$, such that the n-ion expectation value is given by $\varrho^{n}_{ij}(t) = \varrho^{\mathrm{eq}}_{ij}[t + (\boldsymbol{r}_0 - \boldsymbol{r}_n)\cdot\hat{\boldsymbol{e}}_y/c]$. By further taking advantage of the relation $|\boldsymbol{r}-\boldsymbol{r}_n| \approx r - \hat{\boldsymbol{e}}_r\cdot\boldsymbol{r}_n$, valid in the far-field limit, we conclude that the coherent component of the spectrum (4.35) is

$$\begin{aligned} W^{\mathrm{coh}}_{j1,1j'}(\boldsymbol{r},\omega) &= \frac{\omega_{41}^4\, |\tilde{d}_{41}|^2}{8\pi^2 c^3 r^2} \int_{-\infty}^{+\infty}\int_{-\infty}^{+\infty} \langle \hat{\varsigma}^{\mathrm{eq}}_{j1}(t_1)\rangle\, \langle \hat{\varsigma}^{\mathrm{eq}}_{1j'}(t_2)\rangle\, \mathrm{e}^{-\mathrm{i}(\omega-\omega_{41})(t_1-t_2)}\, \mathrm{d}t_1\, \mathrm{d}t_2 \\ &\quad \times\, s_{jj'}(\theta,\,\phi) \left| \sum_{n=1}^{N} \mathrm{e}^{\mathrm{i}\{[(\omega-\omega_{41})/c]\,(\hat{\boldsymbol{e}}_r-\hat{\boldsymbol{e}}_y) + (\omega_{41}/c)\,\hat{\boldsymbol{e}}_r - (\boldsymbol{k}_{\mathrm{X}}+\boldsymbol{k}_{\mathrm{L}}+\boldsymbol{k}_{\mathrm{C}})\}\cdot\boldsymbol{r}_n} \right|^2 \\ &= \frac{\omega_{41}^4\, |\tilde{d}_{41}|^2}{8\pi^2 c^3 r^2} \int_{-\infty}^{+\infty}\int_{-\infty}^{+\infty} \langle \hat{\varsigma}^{\mathrm{eq}}_{j1}(t_1)\rangle\, \langle \hat{\varsigma}^{\mathrm{eq}}_{1j'}(t_2)\rangle\, \mathrm{e}^{-\mathrm{i}(\omega-\omega_{41})(t_1-t_2)}\, \mathrm{d}t_1\, \mathrm{d}t_2 \\ &\quad \times\, s_{jj'}(\theta,\,\phi)\, N^2\, |\eta(\hat{\boldsymbol{e}}_r)|^2 . \end{aligned} \tag{4.38}$$

Three factors can be distinguished in Eq (4.38): (i) the Fourier transforms of the single-particle atomic functions $\langle \hat{\varsigma}^{\mathrm{eq}}_{j1}(t)\rangle$ and $\langle \hat{\varsigma}^{\mathrm{eq}}_{1j'}(t)\rangle$, (ii) the space-dependent term characterizing the emission of an oscillating dipole $s_{jj'}(\theta,\,\phi)$, and (iii) another space-dependent factor emerging in the coherent part of the spectrum of resonance fluorescence from many-particle effects and associated with the function

$$\begin{aligned} \eta(\hat{\boldsymbol{e}}_r) &= \frac{1}{N} \sum_{n=1}^{N} \mathrm{e}^{\mathrm{i}\{[(\omega-\omega_{41})/c]\,(\hat{\boldsymbol{e}}_r-\hat{\boldsymbol{e}}_y) + (\omega_{41}/c)\,\hat{\boldsymbol{e}}_r - (\boldsymbol{k}_{\mathrm{X}}+\boldsymbol{k}_{\mathrm{L}}+\boldsymbol{k}_{\mathrm{C}})\}\cdot\boldsymbol{r}_n} \\ &\approx \frac{1}{N} \sum_{n=1}^{N} \mathrm{e}^{\mathrm{i}[(\omega_{41}/c)\,\hat{\boldsymbol{e}}_r - (\boldsymbol{k}_{\mathrm{X}}+\boldsymbol{k}_{\mathrm{L}}+\boldsymbol{k}_{\mathrm{C}})]\cdot\boldsymbol{r}_n}. \end{aligned} \tag{4.39}$$

In Eq. (4.39), in order to go from the first to the second line, we neglected the dependence on ω as we will study this function only for $\omega \approx \omega_{41}$. The factor $\eta(\hat{\boldsymbol{e}}_r)$ in Eq. (4.39) is a very peaked function and determines a preferential emission direction of the coherent part of the spectrum [195]. Notice that the presence of the factor N^2 in Eq. (4.38) is due to the coherent interference of the radiation emitted by different ions in the medium.

The direction $\hat{\boldsymbol{e}}_r$ maximizing the function $\eta(\hat{\boldsymbol{e}}_r)$ strongly depends on the propagation directions of the three driving fields, i.e., on the three wavevectors $\boldsymbol{k}_{\mathrm{X}}$, $\boldsymbol{k}_{\mathrm{L}}$, and $\boldsymbol{k}_{\mathrm{C}}$. As we showed in Fig. 4.2, three collinear fields are employed with wavevectors $\boldsymbol{k}_q = k_q\,\hat{\boldsymbol{e}}_y$ for $q \in \{\mathrm{X},\,\mathrm{L},\,\mathrm{C}\}$. Under these assumptions, the factor $\eta(\hat{\boldsymbol{e}}_r)$ can be calculated by further assuming a constant density of particles in the interaction volume $V = \prod_{i=1}^{3} L_i$ and by approximating the sum in (4.39) with the integral

$$\begin{aligned}\eta(\hat{\boldsymbol{e}}_r) &\approx \prod_{i=1}^{3} \frac{1}{L_i} \int_{-L_i/2}^{L_i/2} \mathrm{d}x_i\, \mathrm{e}^{-\mathrm{i}p_i x_i} = \prod_{i=1}^{3} \mathrm{sinc}(p_i L_i/2) \\ &= \mathrm{sinc}\Big(\frac{\omega_{41} L_1}{2c}\,\sin\theta\,\cos\phi\Big)\,\mathrm{sinc}\Big(\frac{\omega_{41} L_3}{2c}\,\cos\theta\Big)\,\mathrm{sinc}\Big[\frac{\omega_{41} L_2}{2c}\,(\sin\theta\sin\phi - 1) + \frac{L_2 \Delta k}{2}\Big].\end{aligned} \tag{4.40}$$

Here, $\boldsymbol{p} = (\omega_{41}/c)\,\hat{\boldsymbol{e}}_r - (\boldsymbol{k}_{\mathrm{X}} + \boldsymbol{k}_{\mathrm{L}} + \boldsymbol{k}_{\mathrm{C}})$ depends upon θ and ϕ and

$$\Delta k = \frac{\omega_{41}}{c} - |\boldsymbol{k}_{\mathrm{X}} + \boldsymbol{k}_{\mathrm{L}} + \boldsymbol{k}_{\mathrm{C}}|. \tag{4.41}$$

The function $\eta(\hat{\boldsymbol{e}}_r)$ is maximized by $\hat{\boldsymbol{e}}_r = \hat{\boldsymbol{e}}_y$, whereby $\boldsymbol{p} = \Delta k \hat{\boldsymbol{e}}_y$ and $\eta(\hat{\boldsymbol{e}}_y) = \mathrm{sinc}\Big(\frac{L_2 \Delta k}{2}\Big)$. For different detection directions, the function $\eta(\hat{\boldsymbol{e}}_r)$ decreases very fast, unless the interaction volume V is small compared to the wavelength of the x-ray emitted field.

We use the high degree of directionality of the coherent spectrum and look at it in the neighborhood of $\hat{\boldsymbol{e}}_r = \hat{\boldsymbol{e}}_y$, $\theta = \pi/2$, $\phi = \pi/2$. The multiplication factors $s_{jj'}(\theta, \phi)$ [Eq. (4.37)] in Eqs. (4.38) vary much more slowly than the other prefactor $|\eta(\hat{\boldsymbol{e}}_r)|^2$, which falls to 0 in a very small neighborhood of $\hat{\boldsymbol{e}}_y$. One is therefore allowed to evaluate these two functions, $1 + \cos^2\theta = 1$ and $(1 - \cos^2\theta)\,(\cos 2\phi \pm \mathrm{i}\sin 2\phi) = -1$, for $\theta = \phi = \pi/2$. By introducing $\tilde{s}_{jj'} = s_{jj'}(\pi/2,\,\pi/2) = (-1)^{\delta_{jj'}+1}$, it follows that

$$W^{\mathrm{coh}}_{j1,1j'}(r\,\hat{\boldsymbol{e}}_r, \omega) = |\eta(\hat{\boldsymbol{e}}_r)|^2\, W^{\mathrm{coh}}_{j1,1j'}(r\,\hat{\boldsymbol{e}}_y, \omega), \tag{4.42}$$

with

$$W^{\mathrm{coh}}_{j1,1j'}(r\,\hat{\boldsymbol{e}}_y, \omega) = \frac{\omega_{41}^4\,|\tilde{d}_{41}|^2}{8\pi^2 c^3 r^2}\, s_{jj'}\, N^2 \int_{-\infty}^{-\infty}\int_{-\infty}^{-\infty} \langle \hat{\varsigma}^{\mathrm{eq}}_{j1}(t_1)\rangle\,\langle \hat{\varsigma}^{\mathrm{eq}}_{1j'}(t_2)\rangle\, \mathrm{e}^{-\mathrm{i}(\omega-\omega_{41})(t_1-t_2)}\,\mathrm{d}t_1\,\mathrm{d}t_2. \tag{4.43}$$

Finally, by using the fact that, from Eq. (4.11) and from the symmetry of the EOMs (4.14), the periodic solution of the system of differential equations satisfies the equality $\varrho^{\mathrm{eq}}_{14_+}(t) = -\varrho^{\mathrm{eq}}_{14_-}(t)$, i.e., $\langle \hat{\varsigma}^{\mathrm{eq}}_{14_+}(t)\rangle = -\langle \hat{\varsigma}^{\mathrm{eq}}_{14_-}(t)\rangle$, we conclude that the total spectrum emitted on the $|4\rangle \to |1\rangle$ transition $W^{\mathrm{coh}}_{41,14}(r\,\hat{\boldsymbol{e}}_y, \omega) = \sum_{j,\,j' \in \{4_\pm\}} W^{\mathrm{coh}}_{j1,1j'}(r\,\hat{\boldsymbol{e}}_y, \omega)$ is

$$W^{\mathrm{coh}}_{41,14}(r\,\hat{\boldsymbol{e}}_y, \omega) = \frac{\omega_{41}^4\,|\tilde{d}_{41}|^2}{2\pi^2 T_{\mathrm{p}} c^3 r^2}\, N^2 \left| \int_{-\infty}^{-\infty} \langle \hat{\varsigma}^{\mathrm{eq}}_{14_+}(t)\rangle\, \mathrm{e}^{\mathrm{i}(\omega-\omega_{41})t}\,\mathrm{d}t \right|^2. \tag{4.44}$$

We assume a dilute-gas setting, such that the phase velocity of all electric fields, in very good approximation, equals the speed of light, resulting in good phase matching [143, 187, 188]. For

the densities employed here, in fact, the contribution due to $\frac{\Delta k L_2}{2} \approx 10^{-8}$ can be completely neglected and the factor $\eta(\hat{\boldsymbol{e}}_r)$ can be safely approximated by

$$\begin{aligned}\eta(\hat{\boldsymbol{e}}_r) &\approx \prod_{i=1}^{3} \frac{1}{L_i} \int_{-L_i/2}^{L_i/2} \mathrm{d}x_i \, \mathrm{e}^{-\mathrm{i}p_i x_i} = \prod_{i=1}^{3} \operatorname{sinc}(p_i L_i/2) \\ &= \operatorname{sinc}\Big(\frac{\omega_{41} L_1}{2c} \sin\theta \cos\phi\Big) \operatorname{sinc}\Big(\frac{\omega_{41} L_3}{2c} \cos\theta\Big) \operatorname{sinc}\Big[\frac{\omega_{41} L_2}{2c} (\sin\theta \sin\phi - 1)\Big].\end{aligned} \tag{4.45}$$

However, the presence of $\frac{\Delta k L_2}{2}$ may have to be taken into account if a different experimental setting was considered.

Going back to the incoherent part of the spectrum (4.36), we notice that this component is only proportional to N and completely lacks space-directionality contributions ensuing from the coherent superposition of many-particle effects: No terms such as $\eta(\hat{\boldsymbol{e}}_r)$ are present in the incoherent spectrum and the radiation is emitted almost isotropically in space [195], i.e.,

$$W^{\mathrm{inc}}_{j1,1j'}(\boldsymbol{r},\omega) = \frac{\omega_{41}^4 \, |\tilde{d}_{41}|^2}{8\pi^2 T_{\mathrm{p}} c^3 r^2} \, s_{jj'}(\theta,\, \phi) \, N \int_{-\infty}^{+\infty} \int_{-\infty}^{+\infty} \big\langle \delta\hat{\varsigma}_{j1}(t_1) \, \delta\hat{\varsigma}_{1j'}(t_2) \big\rangle \, \mathrm{e}^{-\mathrm{i}(\omega-\omega_{41})(t_1-t_2)} \, \mathrm{d}t_1 \, \mathrm{d}t_2. \tag{4.46}$$

In the forward direction this term is much weaker than the coherent spectrum by a factor N and will hence be neglected in the following.

4.1.2.2 Spot geometry and size

In a typical interaction volume V the two lengths L_1 and L_3 are determined by the spot size of the laser beams, whereas L_2 is given by the length of the ion sample. When $\phi = \pi/2$, the product in Eq. (4.45) exhibits two factors, $\operatorname{sinc}\Big(\frac{\omega_{41} L_3}{2c} \cos\theta\Big)$ and $\operatorname{sinc}\Big[\frac{\omega_{41} L_2}{2c} (\sin\theta - 1)\Big]$, which are compared in Fig. 4.4 as functions of the angle θ. The red, dashed curve represents the function $\operatorname{sinc}^2\Big(\frac{\omega_{41} L_3}{2c} \cos\theta\Big)$ for the small prefactor $\frac{\omega_{41} L_3}{2c}$ associated with a small value of L_3. This curve is almost constantly identical to 1 in the whole region in which the blue, continuous curve, representing the function $\operatorname{sinc}^2\Big[\frac{\omega_{41} L_2}{2c} (\sin\theta \sin\phi - 1)\Big]$ for $L_2 \gg L_3$, differs from 0. In the case of Eq. (4.40), L_2 is larger than both L_1 and L_3 by some orders of magnitude and, in light of the conclusions drawn from Fig. 4.4, it is the dimension that most strictly limits the spot size of the emitted x rays: One is therefore allowed to approximate $|\eta(\hat{\boldsymbol{e}}_r)|^2 \approx \operatorname{sinc}^2\Big[\frac{\omega_{41} L_2}{2c} (\sin\theta \sin\phi - 1)\Big]$.

The beam area is given by the differential area $\mathrm{d}A = r^2 \, \mathrm{d}\theta \, \mathrm{d}\phi$ (the factor $\sin\theta$ is equal to 1 for $\theta = \pi/2$). We assume $\mathrm{d}\theta$ and $\mathrm{d}\phi$ equal to the small angles $\tilde{\theta}$ and $\tilde{\phi}$ responsible for the first zero of the function $|\eta(\hat{\boldsymbol{e}}_r)|^2$, i.e.,

$$\frac{\omega_{41} L_2}{2c} \Big[\sin\Big(\frac{\pi}{2} - \frac{\tilde{\theta}}{2}\Big) \sin\Big(\frac{\pi}{2} - \frac{\tilde{\phi}}{2}\Big) - 1\Big] = -\pi. \tag{4.47}$$

For $\tilde{\phi} = 0$, we find that the previous equality is satisfied by

$$\tilde{\theta} = 2 \arccos\Big(1 - \frac{2\pi c}{\omega_{41} L_2}\Big) \approx 2\sqrt{\frac{4\pi c}{\omega_{41} L_2}}, \tag{4.48}$$

such that the emitted beam has an area of radius

$$r \, \sin\frac{\tilde{\theta}}{2} \approx r \, \sqrt{\frac{4\pi c}{\omega_{41} L_2}} = r \, \sqrt{\frac{2\lambda_{41}}{L_2}} \tag{4.49}$$

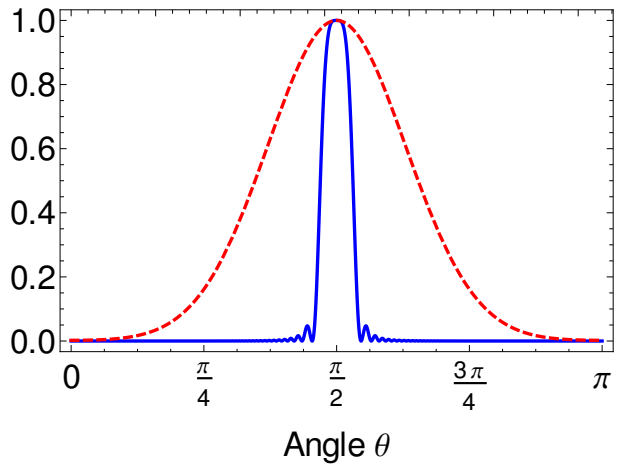

Figure 4.4: The red, dashed curve displays the function $\mathrm{sinc}^2\left(\frac{\omega_{41}L_3}{2c}\cos\theta\right)$ as a function of θ and for the fixed angle $\phi = \pi/2$ with the prefactor $\frac{\omega_{41}L_3}{2c} = 3$. The blue, continuous curve shows the function $\mathrm{sinc}^2\left[\frac{\omega_{41}L_2}{2c}\left(\sin\theta\sin\phi - 1\right)\right]$ as a function of θ and for the fixed angle $\phi = \pi/2$ with the prefactor $\frac{\omega_{41}L_2}{2c} = 300$.

and size

$$\pi\left(r\,\sin\frac{\tilde{\theta}}{2}\right)^2 \approx \frac{4\pi^2 c r^2}{\omega_{41}L_2} = \frac{2\pi r^2\lambda_{41}}{L_2}, \tag{4.50}$$

where $\lambda_{41} = 2\pi c/\omega_{41}$ is the wavelength of the emitted radiation. For $L_2 = 1\,\mathrm{cm}$ and $\lambda_{41} = 10\,\mathrm{nm}$, the mean radius is $\sim 10^{-3}$ times smaller than the distance r at which the detector is placed.

In order to know how much energy per unit frequency is detected at the point $\boldsymbol{r}$ in a differential area $\mathrm{d}A = r^2\,\mathrm{d}\Omega$, we need to perform the integral

$$\begin{aligned} & r^2\int_{\frac{\pi}{2}-\frac{\tilde{\theta}}{2}}^{\frac{\pi}{2}+\frac{\tilde{\theta}}{2}}\int_{\frac{\pi}{2}-\frac{\tilde{\phi}}{2}}^{\frac{\pi}{2}+\frac{\tilde{\phi}}{2}} \sin\theta\, W^{\mathrm{coh}}_{41,14}(r\,\hat{\boldsymbol{e}}_r,\omega)\,\mathrm{d}\phi\,\mathrm{d}\theta \\ & \approx r^2\,W^{\mathrm{coh}}_{41,14}(r\,\hat{\boldsymbol{e}}_y,\omega)\int_{\frac{\pi}{2}-\frac{\tilde{\theta}}{2}}^{\frac{\pi}{2}+\frac{\tilde{\theta}}{2}}\int_{\frac{\pi}{2}-\frac{\tilde{\phi}}{2}}^{\frac{\pi}{2}+\frac{\tilde{\phi}}{2}} \sin\theta\,\mathrm{sinc}^2\left[\frac{\omega_{41}L_2}{2c}\left(\sin\theta\sin\phi - 1\right)\right]\mathrm{d}\phi\,\mathrm{d}\theta \end{aligned} \tag{4.51}$$

This is achieved via a Taylor series of the integrand functions centered at $\theta = \pi/2$, $\phi = \pi/2$, i.e., $\sin\theta = 1 - (\theta - \pi/2)^2/2$, $\sin\phi = 1 - (\phi - \pi/2)^2/2$. Further, since the integrand differs from 0 only in a small region, the integration can be extended to the whole real axis, i.e.,

$$\begin{aligned} & r^2\int_{-\infty}^{\infty}\int_{-\infty}^{\infty}\mathrm{sinc}^2\left[-\frac{\omega_{41}L_2}{4c}\left(\theta'^2+\phi'^2\right)\right]\mathrm{d}\phi'\,\mathrm{d}\theta' = \\ & 2\pi r^2\int_0^{\infty}\rho\,\mathrm{sinc}^2\left(-\frac{\omega_{41}L_2}{4c}\,\rho^2\right)\mathrm{d}\rho = \frac{2\pi^2 c r^2}{\omega_{41}L_2} = \frac{\pi r^2\lambda_{41}}{L_2}. \end{aligned} \tag{4.52}$$

This result is half as large as the differential area in (4.50), because the integrated function is clearly not constant in the differential area itself.

4.1.2.3 Periodic-driving effects in the coherent spectrum of resonance fluorescence

In the previous Sections we have discussed the influence of many-particle effects on the space distribution of the energy spectrum of resonance fluorescence: We have concluded that the

coherent part of the spectrum is almost completely directed in the forward direction, along which it is much stronger than the incoherent part. In the present Section we focus on those properties of the spectrum ensuing from the periodic driving of the system.

In the case of a system periodically driven by the external electric fields, the energy spectrum that we have been dealing with is not well defined. If we go back to Eq. (4.44), in fact, we can observe that the total energy emitted by the system, i.e., the integral of the spectrum over the frequency ω, is equal to

$$\int_{-\infty}^{\infty} \left| \int_{-\infty}^{-\infty} \langle \hat{\varsigma}^{\mathrm{eq}}_{14_+}(t) \rangle \, \mathrm{e}^{-\mathrm{i}(\omega-\omega_{41})t} \, \mathrm{d}t \right|^2 \mathrm{d}\omega = 2\pi \int_{-\infty}^{-\infty} |\langle \hat{\varsigma}^{\mathrm{eq}}_{14_+}(t) \rangle|^2 \, \mathrm{d}t \to \infty.$$

Since the periodic function $|\langle \hat{\varsigma}^{\mathrm{eq}}_{14_+}(t) \rangle|^2$ is strictly positive in the whole time axis, the integral diverges and the energy spectrum is not well defined.

We introduce, therefore, the power spectrum of resonance fluorescence from Eq. (4.27). Calculations analogous to those of the previous Sections show that the coherent part of the power spectrum of resonance fluorescence, in the forward direction and centered at the x-ray transition energy ω_{41}, is equal to

$$\begin{aligned} S^{\mathrm{coh}}_{41,14}(r\,\hat{\boldsymbol{e}}_y, \omega) &= \frac{\omega_{41}^4 \, |\tilde{d}_{41}|^2}{2\pi^2 c^3 r^2} \, N^2 \lim_{T\to\infty} \left| \int_0^T \langle \hat{\varsigma}^{\mathrm{eq}}_{14_+}(t) \rangle \, \mathrm{e}^{\mathrm{i}(\omega-\omega_{41})t} \, \mathrm{d}t \right|^2 \\ &\approx \frac{\omega_{41}^4 \, |\tilde{d}_{41}|^2}{2\pi^2 c^3 r^2} \, N^2 \lim_{M\to\infty} \left| \int_0^{MT_{\mathrm{p}}} \langle \hat{\varsigma}^{\mathrm{eq}}_{14_+}(t) \rangle \, \mathrm{e}^{\mathrm{i}(\omega-\omega_{41})t} \, \mathrm{d}t \right|^2 . \end{aligned} \tag{4.53}$$

By observing that

$$\int_0^{MT_{\mathrm{p}}} \langle \hat{\varsigma}^{\mathrm{eq}}_{14_+}(t) \rangle \, \mathrm{e}^{\mathrm{i}(\omega-\omega_{41})t} \, \mathrm{d}t = \int_0^{T_{\mathrm{p}}} \langle \hat{\varsigma}^{\mathrm{eq}}_{14_+}(t) \rangle \, \mathrm{e}^{\mathrm{i}(\omega-\omega_{41})t} \, \mathrm{d}t \, \frac{1-\mathrm{e}^{\mathrm{i}(\omega-\omega_{41})MT_{\mathrm{p}}}}{1-\mathrm{e}^{\mathrm{i}(\omega-\omega_{41})T_{\mathrm{p}}}}, \tag{4.54}$$

one can conclude that the coherent spectrum is

$$S^{\mathrm{coh}}_{41,14}(r\,\hat{\boldsymbol{e}}_y, \omega) = \frac{\omega_{41}^4 \, |\tilde{d}_{41}|^2}{2\pi^2 c^3 r^2} \, N^2 \left| \int_0^{T_{\mathrm{p}}} \langle \hat{\varsigma}^{\mathrm{eq}}_{14_+}(t) \rangle \, \mathrm{e}^{\mathrm{i}(\omega-\omega_{41})t} \, \mathrm{d}t \right|^2 \lim_{M\to\infty} \frac{1}{MT_{\mathrm{p}}} \frac{1-\cos\left[(\omega-\omega_{41})MT_{\mathrm{p}}\right]}{1-\cos\left[(\omega-\omega_{41})T_{\mathrm{p}}\right]}. \tag{4.55}$$

The limit in Eq. (4.55) can be calculated by defining the function

$$h_M(x) = \frac{1}{2\pi M} \, \frac{1-\cos(Mx)}{1-\cos(x)} = \frac{1}{2\pi M} \, \frac{\sin^2\left(\frac{Mx}{2}\right)}{\sin^2\left(\frac{x}{2}\right)} \tag{4.56}$$

and observing that, since $\cos\left[M(x+2k\pi)\right] = \cos Mx$ for $k \in \mathbb{Z}$, also $h_M(x)$ is periodic with period 2π. We focus, therefore, on the function

$$\tilde{h}_M(x) = \begin{cases} h_M(x) & \text{if } -\pi \le x < \pi, \\ 0 & \text{otherwise}, \end{cases} \tag{4.57}$$

such that

$$h_M(x) = \sum_{k=-\infty}^{+\infty} \tilde{h}_M(x - 2\pi k). \tag{4.58}$$

Since

$$\int_{-\infty}^{\infty} \tilde{h}_M(x) \, \mathrm{d}x = \int_{-\pi}^{\pi} \frac{1}{2\pi M} \, \frac{\sin^2\left(\frac{Mx}{2}\right)}{\sin^2\left(\frac{x}{2}\right)} \, \mathrm{d}x = 1 \tag{4.59}$$

and, for $x \neq 0$,

$$\lim_{M\to\infty} \tilde{h}_M(x) = \lim_{M\to\infty} \frac{1}{2\pi M} \frac{\sin^2\left(\frac{Mx}{2}\right)}{\sin^2\left(\frac{x}{2}\right)} \leq \frac{1}{\sin^2\left(\frac{x}{2}\right)} \lim_{M\to\infty} \frac{1}{2\pi M} = 0, \tag{4.60}$$

one notices that

$$\lim_{M\to\infty} \tilde{h}_M(x) = \delta(x) \qquad \lim_{M\to\infty} h_M(x) = \sum_{k=-\infty}^{+\infty} \delta(x - 2\pi k), \tag{4.61}$$

which leads to

$$\begin{aligned} \lim_{M\to\infty} \frac{1}{MT_\mathrm{p}} \frac{1-\cos\left[(\omega-\omega_{41})MT_\mathrm{p}\right]}{1-\cos\left[(\omega-\omega_{41})T_\mathrm{p}\right]} &= \frac{2\pi}{T_\mathrm{p}} \sum_{m=-\infty}^{+\infty} \delta[(\omega-\omega_{41})T_\mathrm{p} - 2m\pi] \\ &= \frac{2\pi}{T_\mathrm{p}^2} \sum_{m=-\infty}^{+\infty} \delta\left(\omega - \omega_{41} - \frac{2m\pi}{T_\mathrm{p}}\right) \end{aligned} \tag{4.62}$$

and, from Eq. (4.55), to

$$\begin{aligned} S^{\mathrm{coh}}_{41,14}(r\,\hat{\boldsymbol{e}}_y,\omega) &= \frac{\omega_{41}^4\,|\tilde{d}_{41}|^2}{2\pi^2 c^3 r^2} N^2 \left| \int_0^{T_\mathrm{p}} \langle \hat{\varsigma}^{\mathrm{eq}}_{14_+}(t)\rangle\, \mathrm{e}^{\mathrm{i}(\omega-\omega_{41})t}\,\mathrm{d}t \right|^2 \frac{2\pi}{T_\mathrm{p}^2} \sum_{m=-\infty}^{+\infty} \delta\left(\omega - \omega_{41} - \frac{2m\pi}{T_\mathrm{p}}\right) \\ &= \frac{\omega_{41}^4\,|\tilde{d}_{41}|^2}{\pi c^3 r^2} N^2 \sum_{m=-\infty}^{+\infty} \left| \frac{1}{T_\mathrm{p}} \int_0^{T_\mathrm{p}} \langle \hat{\varsigma}^{\mathrm{eq}}_{14_+}(t)\rangle\, \mathrm{e}^{\mathrm{i}\frac{2m\pi}{T_\mathrm{p}}t}\,\mathrm{d}t \right|^2 \delta\left(\omega - \omega_{41} - \frac{2m\pi}{T_\mathrm{p}}\right). \end{aligned} \tag{4.63}$$

By recalling the identity

$$\int_{-\infty}^{\infty} \mathrm{e}^{-\mathrm{i}\varpi t} \sum_{m=-\infty}^{+\infty} \delta\left(\varpi - \frac{2m\pi}{T_\mathrm{p}}\right) \mathrm{d}\varpi = T_\mathrm{p} \sum_{n=-\infty}^{+\infty} \delta\left(t - nT_\mathrm{p}\right), \tag{4.64}$$

one confirms that the total emitted power

$$\int_{-\infty}^{\infty} S^{\mathrm{coh}}_{41,14}(r\,\hat{\boldsymbol{e}}_y,\omega)\,\mathrm{d}\omega = \frac{\omega_{41}^4\,|\tilde{d}_{41}|^2}{\pi T_\mathrm{p} c^3 r^2} N^2 \int_0^{T_\mathrm{p}} \left| \langle \hat{\varsigma}^{\mathrm{eq}}_{14_+}(t)\rangle \right|^2 \mathrm{d}t \tag{4.65}$$

is a well-defined, nondivergent quantity.

To summarize, the spectrum consists of a coherent and an incoherent part [53, 75, 195, 197], whose intensity profiles are highly affected by many-ion effects. The light coherently emitted by many different ions adds constructively in the $\hat{\boldsymbol{e}}_y$ forward direction, along which the driving fields propagate. This implies an enhancement of the spectrum proportional to N^2 along this preferential direction. Conversely, the incoherent part of the spectrum does not undergo this many-particle enhancement: It is proportional to N and is distributed in space with a dipole radiation pattern displaying low space directionality [195, 197]. Hence, in the forward direction, resonance fluorescence is dominated by coherent emission and one can neglect the incoherent part. Owing to the periodicity of the asymptotically reached solution $\hat{\rho}^{\mathrm{eq}}(t)$ [75]—turn-on effects are neglected—the coherent part of the spectrum emitted on the $4 \to 1$ transition in the forward direction consists of an x-ray frequency comb centered at the frequency ω_{41} with the same tooth

spacing as the driving optical frequency comb,

$$S^{\mathrm{coh}}(r\,\hat{\boldsymbol{e}}_y,\omega)=\sum_{m=-\infty}^{+\infty}\mathcal{S}_m\,\delta\Big(\omega-\omega_{41}-\frac{2\pi m}{T_{\mathrm{p}}}\Big), \tag{4.66a}$$

$$\mathcal{S}_m=\frac{\omega_{41}^4\,|\tilde{d}_{41}|^2}{\pi c^3 r^2}\,N^2\,\Big|\frac{1}{T_{\mathrm{p}}}\int_0^{T_{\mathrm{p}}}\varrho^{\mathrm{eq}}_{4_+1}(t)\,\mathrm{e}^{\,\mathrm{i}\frac{2\pi m}{T_{\mathrm{p}}}t}\,\mathrm{d}t\Big|^2. \tag{4.66b}$$

We notice that Eq. (4.66) includes interference in the resonance fluorescence of the two transitions $4_+\to 1$ and $4_-\to 1$ [198, 199]. Because of many-ion effects, the photons emitted in the forward direction are focused in a beam of mean area $\Delta A=2\pi^2cr^2/(\omega_{41}L)$ [195, 197], where L is the mean length of the ion sample: It follows that $P_m=\mathcal{S}_m 2\pi^2cr^2/(\omega_{41}L)$ is the power of the mth peak in the spectrum.

4.2 Results and discussion

In order to bridge an energy difference between two x-ray levels, a sufficiently wide comb is needed. Here, we aim at generating an x-ray comb with the same number of peaks, i.e., overall width, as the driving optical comb, and with emitted power comparable to that of present-day XUV combs generated via HHG [122]. Comparable powers, in fact, guarantee that our predicted comb could be similarly detected and used.

After a description of the general properties of the periodic solution of the EOMs in Sec. 4.2.1, we present in Sec. 4.2.2 an atomic implementation of our model with He-like Be^{2+} ions.

4.2.1 General properties of the solution of the equations motion

In the following, we investigate the properties of the periodic function $\hat{\varrho}^{\mathrm{eq}}(t)$ within a single period, i.e., in the time interval $[0,\,T_{\mathrm{p}}]=[0,\,T_{\mathrm{d}}]\cup[T_{\mathrm{d}},\,T_{\mathrm{p}}]$. Owing to the definition of the periodic amplitude $\mathcal{E}_{\mathrm{C},0}(t)$ in Eq. (4.4), two subintervals can be distinguished, $[0,\,T_{\mathrm{d}}]$ and $[T_{\mathrm{d}},\,T_{\mathrm{p}}]$, respectively associated with the presence and the absence of an optical pulse from the optical frequency comb driving the $3\to 4$ transition. The evolution of the system can be separately analyzed in these two subintervals, although one needs to bear in mind that the features of the resulting density matrix $\hat{\varrho}^{\mathrm{eq}}(t)$ in different subintervals, by virtue of the periodicity of the solution of the EOMs, are mutually related, as we are going to describe in the following.

4.2.1.1 Interaction with one of the pulses from the optical frequency comb

The main parameters determining the time evolution of the density matrix are the peak intensity of the pulses in the optical frequency comb and the intensity of the cw x-ray and optical fields. Here, we discuss their influence on the properties of the periodic function $\hat{\varrho}^{\mathrm{eq}}(t)$ in the time interval $[0,\,T_{\mathrm{d}}]$.

Peak intensity of the pulses in the optical frequency comb.—The power in each peak P_m in the imprinted, x-ray comb [Eq. (4.66b)] is proportional to the modulus squared of the mth Fourier coefficient of $\varrho^{\mathrm{eq}}_{4_+1}(t)$. The properties of a Fourier-series expansion [196] imply that the overall width of the spectrum is inversely proportional to the duration of $\varrho^{\mathrm{eq}}_{4_+1}(t)$. To provide an x-ray comb with as many teeth as in the driving optical one, $\varrho^{\mathrm{eq}}_{4_+1}(t)$ must follow in time the envelope of the driving train of optical pulses from the optical frequency comb. In other words, we seek a solution of the EOMs $\varrho^{\mathrm{eq}}_{4_+1}(t)$ with a pulse-like shape, where $\varrho^{\mathrm{eq}}_{4_+1}(t)$ differs from 0 in

the sole presence of the optical pulses from the optical frequency comb and vanishes exactly in their absence.

We encountered an analogous behaviour while analyzing the time evolution of a two-level system driven by short regular pulses in Secs. 2.6 and 3.2.1. There, we showed that a strong pulse induces Rabi oscillations of the populations and coherences of the two levels at the time-dependent Rabi frequency determined by the strength of the field. After having introduced the pulse area Q, we investigated the specific features emerging when the pulse area $Q = n\pi$ is an integer multiple of π, with $n \in \mathbb{N}$. For n odd, we observed that the pulse causes a complete population inversion, which is followed by (spontaneous or Auger) decay of the excited level. This manifested itself in the spectrum of resonance fluorescence in terms of a strong Lorentzian peak centered at the frequency of the decaying resonance. In contrast, for n even, we showed that, when the interaction with the external field has concluded, the system is led back to the ground state, with strong suppression of the post-pulse-exposure decay of the excited level. A pulse-like shape is displayed by the population and the coherences of the excited level, which vanish in the absence of the external pulse. As a result, the appearance of the previously described Lorentzian peak in the spectrum is considerably hindered and spectral contributions due to the field-induced Rabi oscillations clearly emerge in a wider spectrum of resonance fluorescence.

The just described behaviour, associated with pulses of area $2n\pi$, is here employed on the $3 \to 4$ transition in the four-level system. Short optical pulses of properly set intensity are namely utilized to similarly transfer population and coherence to the excited level 4, thus imprinting a pulse-like shape onto all the elements of the density matrix which are related to the excited states $|4_\pm\rangle$, thus also onto $\varrho^{\mathrm{eq}}_{4_+1}(t)$. As we did in Eq. (2.115), we introduce the pulse area

$$Q_{\mathrm{C}} = \int_0^{T_{\mathrm{p}}} \Omega_{\mathrm{RC}}(t)\ \mathrm{d}t \tag{4.67}$$

associated with one pulse in the optical frequency comb $\boldsymbol{\mathcal{E}}_{\mathrm{C}}(\boldsymbol{r},\, t)$ driving the optical transition $3 \to 4$. The peak intensity $I_{\mathrm{c,max}}$ whereby the pulse area is $Q_{\mathrm{C}} = 2n\pi$ ensures that, after an integer number of Rabi cycles [53], population and coherences of the highest level 4 are led back to 0 [68–71, 73, 163] such that, in the absence of the pulses from the optical frequency comb, the population of the states $|4_\pm\rangle$ and the off-diagonal terms $\varrho^{\mathrm{eq}}_{4_\pm 1}(t)$ vanish exactly. This has a major impact upon the properties of the associated spectrum (4.66): Being associated to the Fourier coefficients [Eq. (4.66b)] of a function which is different from 0 in an interval of duration T_{FWHM}, the spectrum exhibits an overall width of $\sim 2\pi/T_{\mathrm{FWHM}}$.

Conversely, for $Q_{\mathrm{C}} \neq 2n\pi$, the interaction with the pulse would be followed by the spontaneous decay of the highest level. As a result, this long decay would represent the main feature of the off-diagonal element of the density matrix, i.e., $\varrho^{\mathrm{eq}}_{4_+1}(t) \sim \mathrm{e}^{-\Gamma_{41}t}$. This would affect the amplitude of the peaks in Eq. (4.66b) and would result in a spectrum of smaller width, $\Gamma_{41} \ll 2\pi/T_{\mathrm{FWHM}}$, and smaller number of relevant teeth.

Intensity of the cw x-ray and optical fields.—The essential feature displayed by the time evolution of the density matrix $\hat{\varrho}^{\mathrm{eq}}(t)$ in the time interval $[0,\, T_{\mathrm{d}}]$ is the transfer of population and coherences from level 3 to level 4 due to the presence of a pulse from the optical frequency comb. This transfer is only perturbed by the fast spontaneous decay of the excited level 4 to the ground state, resulting in x-ray emission. The direct link between the off-diagonal elements of the density matrix $\varrho^{\mathrm{eq}}_{4_\pm 1}(t)$ and $\varrho^{\mathrm{eq}}_{31}(t)$ is apparent from a close inspection of the EOMs (4.14). The increase in $\varrho^{\mathrm{eq}}_{4_\pm 1}(t)$ is proportional to the decrease in $\varrho^{\mathrm{eq}}_{31}(t)$: In particular, the higher is $\varrho^{\mathrm{eq}}_{31}(0)$ at $t = 0$, when still no coherence has been "moved" to the excited level 4, the larger is the peak value that $\varrho^{\mathrm{eq}}_{4_\pm 1}(t)$ can reach when a complete "coherence transfer" is actually performed. Hence, owing to the just described relation between the peak value of $\varrho^{\mathrm{eq}}_{4_\pm 1}(t)$ and the state of

the system preceding the interaction with the optical-comb pulses, one ought to properly tune the intensities of the cw, x-ray and optical pulses in order to optimize the value of $\varrho_{31}^{\mathrm{eq}}(0)$. This allows one to maximize the peak amplitude of $\varrho_{4_\pm 1}^{\mathrm{eq}}(t)$ and, consequently, the intensity of the lines in the imprinted comb (4.66b).

4.2.1.2 Evolution of the remaining three-level system in the interval in between two pulses from the optical frequency comb

In the time interval $[0,\, T_\mathrm{d}]$, the interaction with one of the pulses in the optical frequency comb leads the system from its initial state $\hat{\varrho}^{\mathrm{eq}}(0)$ to the state $\hat{\varrho}^{\mathrm{eq}}(T_\mathrm{d})$. The implementation of our pulse-shaping scheme, employing $2n\pi$ pulses with $n \in \mathbb{N}$, ensures that the following condition is met, $\varrho_{4_\pm i}^{\mathrm{eq}}(0) = \varrho_{4_\pm i}^{\mathrm{eq}}(T_\mathrm{d})$ for $i \in \{1,\, 2_0,\, 3,\, 4_-,\, 4_+\}$. However, the remaining elements of the density matrix display different values at 0 and at T_d. Since $\hat{\varrho}^{\mathrm{eq}}(t)$ is a periodic solution of the EOMs, with $\hat{\varrho}^{\mathrm{eq}}(0) = \hat{\varrho}^{\mathrm{eq}}(T_\mathrm{p})$, it is apparent that the intensities of the cw x-ray and optical fields, by driving the system also in the time interval in between two optical-comb pulses $[T_\mathrm{d},\, T_\mathrm{p}]$, significantly influence the distinguishing features of the periodic density matrix.

The adoption of a frequency comb consisting of $2n\pi$ pulses guarantees that at time T_d, once the interaction with a pulse from the optical frequency comb has concluded, each one of the elements of the density matrix which are related to level 4, i.e., $\varrho_{4_\pm i}^{\mathrm{eq}}(T_\mathrm{d})$ for $i \in \{1,\, 2_0,\, 3,\, 4_-,\, 4_+\}$, is exactly equal to 0. As a result, in the time interval $[T_\mathrm{d},\, T_\mathrm{p}]$ the system behaves as a three-level system, formed by states $|1\rangle$, $|2_0\rangle$, and $|3\rangle$ and driven by the two cw fields $\boldsymbol{\mathcal{E}}_\mathrm{X}(\boldsymbol{r},t)$ and $\boldsymbol{\mathcal{E}}_\mathrm{L}(\boldsymbol{r},t)$. In the following, we discuss the criteria which these two fields need to meet in order to maximize the value of $\varrho_{31}^{\mathrm{eq}}(0)$. We take advantage of previous results for a three-level system driven by two cw fields [57, 58]. Two situations have to be distinguished:

Rapid spontaneous decay of the three-level system.—Because of the presence of spontaneous decay, the three-level system formed by the states $|1\rangle$, $|2_0\rangle$, and $|3\rangle$, converges to a stationary state within the decay time of the excited levels 2 and 3 [57, 58]. If this decay time is shorter than the repetition period T_p of the optical frequency comb, this stationary state $\hat{\varrho}_\mathrm{S}$ is actually reached in the time interval in between two optical pulses $[T_\mathrm{d},\, T_\mathrm{p}]$. The state $\hat{\varrho}_\mathrm{S}$ is the stationary solution of the EOMs (4.14) for constant Ω_RX and Ω_RL and in the absence of $\Omega_\mathrm{RC}(t)$. Furthermore, $\hat{\varrho}^{\mathrm{eq}}(T_\mathrm{p}) = \hat{\varrho}^{\mathrm{eq}}(0) = \hat{\varrho}_\mathrm{S}$ is completely independent of the state $\hat{\varrho}^{\mathrm{eq}}(T_\mathrm{d})$ into which the interaction with an optical-comb pulse leads the system. As a result, this state does not depend on the properties of the optical frequency comb, but only on Ω_RX and Ω_RL.

In a three-level Λ-type system, i.e., $\omega_{2_0} > \omega_3$, by neglecting the (non-E1) decay rate Γ_{31} from state 3 back to the ground state 1, the stationary state $\hat{\varrho}_\mathrm{S}$ displays matrix elements

$$\begin{aligned} &\varrho_{11,\mathrm{S}} = \frac{\Omega_\mathrm{RL}^2}{\Omega_\mathrm{RX}^2 + \Omega_\mathrm{RL}^2}, \quad \varrho_{2_0 2_0,\mathrm{S}} = 0, \quad \varrho_{33,\mathrm{S}} = \frac{\Omega_\mathrm{RX}^2}{\Omega_\mathrm{RX}^2 + \Omega_\mathrm{RL}^2}, \\ &\varrho_{2_0 1,\mathrm{S}} = 0, \quad \varrho_{31,\mathrm{S}} = -\frac{\Omega_\mathrm{RX}\Omega_\mathrm{RL}}{\Omega_\mathrm{RX}^2 + \Omega_\mathrm{RL}^2}, \quad \varrho_{32_0,\mathrm{S}} = 0, \end{aligned} \tag{4.68}$$

and $\varrho_{31,\mathrm{S}}$ is maximized by setting $\Omega_\mathrm{RX} = \Omega_\mathrm{RL}$. Also for a three-level Ξ-type system, which we do not describe explicitly [58], it is possible to identify a relation between the two Rabi frequencies Ω_RX and Ω_RL which maximizes the stationary value of the off-diagonal term of the density matrix $\varrho_{31,\mathrm{S}}$. This relation sets the criteria for the choice of the optimal intensities I_X and I_L.

Slow spontaneous decay of the three-level system.—When the decay time of the three-level system consisting of the states $|1\rangle$, $|2_0\rangle$, and $|3\rangle$, is much larger than the repetition period T_p of the optical frequency comb, the system does not converge to the stationary solution of the EOMs $\hat{\varrho}_\mathrm{S}$ within a period. The time evolution of the system in the time interval $[T_\mathrm{d},\, T_\mathrm{p}]$ features

Rabi oscillations induced by the presence of the cw fields. The state of the system at T_p, and in particular the value of $\varrho_{31}^\mathrm{eq}(T_\mathrm{p}) = \varrho_{31}^\mathrm{eq}(0)$ which has to be maximized, depends upon the frequency with which the Rabi flopping takes place as well as on the state $\hat{\varrho}^\mathrm{eq}(T_\mathrm{d})$ due to the interaction with an optical-comb pulse.

In a three-level system with negligibly small decay rates, the frequency of the induced oscillations can be determined in a dressed-state picture [57, 58, 67]. As described in Ref. [58], the elements of the density matrix undergo Rabi flopping at frequencies $\Omega_\mathrm{R,eff}$ and $2\Omega_\mathrm{R,eff}$, with

$$\Omega_\mathrm{R,eff} = \frac{1}{2}\sqrt{\Omega_\mathrm{RX}^2 + \Omega_\mathrm{RL}^2}. \tag{4.69}$$

This corresponds to a number of cycles in the time interval $[T_\mathrm{d},\, T_\mathrm{p}]$ equal to $(T_\mathrm{p} - T_\mathrm{d})\,\Omega_\mathrm{R,eff}/(2\pi)$. Being able to predict the number of cycles performed by the system during a period can help in determining the intensities I_X and I_L which maximize the value of $\varrho_{31}^\mathrm{eq}(0)$, as shown in the following atomic implementation of the model.

4.2.2 Atomic implementation

In the following, we apply our four-level approximation to model atomic transitions in He-like Be^{2+} ions in the desired x-ray and optical ranges. The decay rates Γ_{ji} are calculated with `grasp2K` [200–202], $\Gamma_{41} = 1.2 \times 10^{11}\,\mathrm{s}^{-1}$, $\Gamma_{43} = 8.7 \times 10^{6}\,\mathrm{s}^{-1}$, $\Gamma_{23} = 9.7 \times 10^{-2}\,\mathrm{s}^{-1}$, $\Gamma_{21} = 4.1 \times 10^{5}\,\mathrm{s}^{-1}$. These values are also used for the calculation of the dipole moments $\boldsymbol{d}_{ij}$, i.e., for the calculation of the Rabi frequencies given the intensities of the corresponding electric fields. The transition energies $\omega_{21} = 121.9\,\mathrm{eV}$, $\omega_{23} = 0.2699\,\mathrm{eV}$, $\omega_{43} = 2.018\,\mathrm{eV}$, and $\omega_{41} = 123.7\,\mathrm{eV}$, are taken from Ref. [191]. We assume a density of Be^{2+} ions of $10^8\,\mathrm{cm}^{-3}$ which can be reached with an electron-beam ion trap [123, 203]: For such a dilute sample, good phase matching is achieved [143, 187, 188]. Alternative experimental settings, e.g., by gas-discharge or photoionization by an x-ray pre-pulse [139, 204], may allow for higher densities, but one ought to make sure that a stable environment is obtained, such that all pulses in the optical frequency comb encounter a constant density of ions, atoms and free electrons.

The following parameters are used to model the optical frequency comb [Eq. (4.4)], $T_\mathrm{FWHM} = 120\,\mathrm{fs}$, $T_\mathrm{p} = 1\,\mathrm{ns}$, $1/T_\mathrm{p} = 1\,\mathrm{GHz}$ [122, 205–208], i.e., $2\pi/T_\mathrm{p} = 4.1 \times 10^{-6}\,\mathrm{eV}$. From Eq. (A.7), this corresponds to a number of peaks $\Delta k \sim 10^4$. The ion sample has $N = 10^6$ particles over a length of $L = 1\,\mathrm{cm}$ and an area of $1\,\mathrm{mm}^2$. The peak intensity of the train of pulses in the optical frequency comb is about $10^{10}\,\mathrm{W/cm}^2$. This intensity is by orders of magnitude lower than the peak intensities presently required for HHG-based schemes.

The repetition frequency of the optical frequency comb assumed here, 1 GHz, is higher than what experimental techniques render routinely available. However, methods for improving repetition frequencies [209] and peak intensities [122] of the train of pulses from an optical frequency comb are being explored, such that a combination of these schemes may provide combs exhibiting the features of which we take advantage in the following.

The here employed pulse-shaping scheme adopts pulses with area $Q_\mathrm{C} = 2n\pi$, with $n \in \mathbb{N}$. The pulse area defined in Eq. (4.67) is the integral of the single-pulse Rabi frequency $\Omega_\mathrm{RC}(t)$, which is proportional to $Q_\mathrm{C} \propto T_\mathrm{FWHM}\sqrt{I_\mathrm{C,max}}$. For fixed values of Q_C, it follows that $I_\mathrm{C,max} \propto 1/T_\mathrm{FWHM}^2$: An increase in the duration of the pulses by one order of magnitude allows one to decrease by two orders of magnitude the peak intensity of the pulses. In the following calculations, a FWHM duration of $T_\mathrm{FWHM} = 120\,\mathrm{fs}$ is assumed.

4.2.2.1 Four-level system driven by optical 2π pulses

By using an optical frequency comb consisting of 2π pulses, which, for the previously mentioned FWHM duration, corresponds to a peak intensity of $I_{\mathrm{C,max}} = 3.0 \times 10^{10}\,\mathrm{W/cm^2}$, the elements of the density operator $\hat{\varrho}^{\mathrm{eq}}(t)$ which are related to the atomic states $|4_{\pm}\rangle$ vanish in the absence of an optical pulse from the optical frequency comb. The time evolution of $\varrho^{\mathrm{eq}}_{4_+1}(t)$ in the presence of one of the optical-frequency-comb pulses is shown in Fig. 4.5a. The corresponding time evolution of $\varrho^{\mathrm{eq}}_{31}(t)$ is displayed in Fig. 4.5b. It is interesting to observe that, while $\varrho^{\mathrm{eq}}_{4_+1}(t)$ is led back to its (vanishing) initial value at the end of the pulse, the same does not happen for $\varrho^{\mathrm{eq}}_{31}(t)$. Only half cycle is exhibited and, as displayed in Fig. 4.5b, a complete switch in the sign of the matrix element $\varrho^{\mathrm{eq}}_{31}(t)$ takes place. In the interval $[T_{\mathrm{d}},\, T_{\mathrm{p}}]$, therefore, the remaining two fields, $\boldsymbol{\mathcal{E}}_{\mathrm{X}}(\boldsymbol{r},\, t)$ and $\boldsymbol{\mathcal{E}}_{\mathrm{L}}(\boldsymbol{r},\, t)$, need to make up for this switch in the value of $\varrho^{\mathrm{eq}}_{31}(t)$, by guaranteeing that another half oscillation is performed. Fig. 4.5c displays the time evolution of $\varrho^{\mathrm{eq}}_{31}(t)$ in the time interval in between two optical pulses $[T_{\mathrm{d}},\, T_{\mathrm{p}}]$. In Fig. 4.5c, the associated, effective Rabi frequency, corresponding to half cycle in the time interval $(T_{\mathrm{p}} - T_{\mathrm{d}})$, is $\Omega_{\mathrm{R,eff}} = \pi/(T_{\mathrm{p}} - T_{\mathrm{d}})$: This, together with Eq. (4.69), leads to the equality

$$\frac{2\pi}{T_{\mathrm{p}} - T_{\mathrm{d}}} = \sqrt{\Omega^2_{\mathrm{RX}} + \Omega^2_{\mathrm{RL}}}. \tag{4.70}$$

When this condition is met, then the switch induced by the interaction with one optical-frequency-comb pulse is compensated by another half oscillation taking place in $[T_{\mathrm{d}},\, T_{\mathrm{p}}]$. Here, Eq. (4.70) is used to determine the intensities, $I_{\mathrm{X}} = 1.5 \times 10^4\,\mathrm{W/cm^2}$ and $I_{\mathrm{L}} = 1.7 \times 10^8\,\mathrm{W/cm^2}$, which maximize $\varrho^{\mathrm{eq}}_{13}(0)$. Not fulfilling this condition would imply lower values of $\varrho^{\mathrm{eq}}_{13}(0)$ in the asymptotically reached, periodic solution of the EOMs and, therefore, lower peak values of the function $\varrho^{\mathrm{eq}}_{4_\pm 1}(t)$ than the peak value exhibited in Fig. 4.5a.

Having suppressed the post-pulse-exposure decay of $\varrho^{\mathrm{eq}}_{4_+1}(t)$, the resulting spectrum of resonance fluorescence [Eq.(4.66)] is shown in Fig. 4.5d: It is centered at $\omega_{41} = 123.7\,\mathrm{eV}$ and, as the driving optical frequency comb, it contains $\sim 10^4$ peaks of spacing $2\pi/T_{\mathrm{p}} = 4.1 \times 10^{-6}\,\mathrm{eV}$. Fig. 4.5e highlights the comb structure of the spectrum. The optical-comb peak intensity, $I_{\mathrm{C,max}} = 3.0 \times 10^{10}\,\mathrm{W/cm^2}$, is much lower than the peak intensities used for the generation of XUV frequency combs via HHG [205–208]. The power of each peak in the emitted spectrum—about thousands of picowatts—is higher than that measured in Ref. [122].

4.2.2.2 Four-level system driven by optical 4π pulses

The situation is different when an optical frequency comb consisting of 4π pulses is used to drive the system. For the here employed FWHM duration, such pulse area corresponds to a peak intensity of $I_{\mathrm{C,max}} = 1.2 \times 10^{11}\,\mathrm{W/cm^2}$. As one can see in Fig. 4.6a, the off-diagonal element of the density matrix $\varrho^{\mathrm{eq}}_{4_\pm 1}(t)$ performs a complete cycle in the presence of each optical pulse: The mean value of the function is 0 and, because of the properties of a Fourier expansion, one deduces that the spectral component associated with $m = 0$ must vanish. Furthermore, in the time interval $[0,\, T_{\mathrm{d}}]$ a larger number of cycles is exhibited in Fig. 4.6a than in Fig. 4.5a: Larger frequencies than in the previous case are involved and, from Eq. (4.66b), a wider spectrum than in Fig. 4.5d has to be expected. The corresponding evolution of $\varrho^{\mathrm{eq}}_{31}(t)$ in the presence of an optical-frequency-comb pulse is displayed in Fig. 4.6b: Now a complete cycle is performed and $\varrho_{31}(T_{\mathrm{d}})$ almost coincides with $\varrho_{31}(0)$. This simplifies the determination of the intensities I_{X} and I_{L} which maximize $\varrho_{31}(0)$. As shown in Fig. 4.6c, the role played by the Rabi oscillations in $[T_{\mathrm{d}},\, T_{\mathrm{p}}]$ is not determinant. The intensities $I_{\mathrm{X}} = 9.5 \times 10^8\,\mathrm{W/cm^2}$, $I_{\mathrm{L}} = 1.7 \times 10^8\,\mathrm{W/cm^2}$, maximize $\varrho^{\mathrm{eq}}_{31}(0)$, whereby also the peak value of $\varrho^{\mathrm{eq}}_{4_\pm 1}(t)$ is maximized.

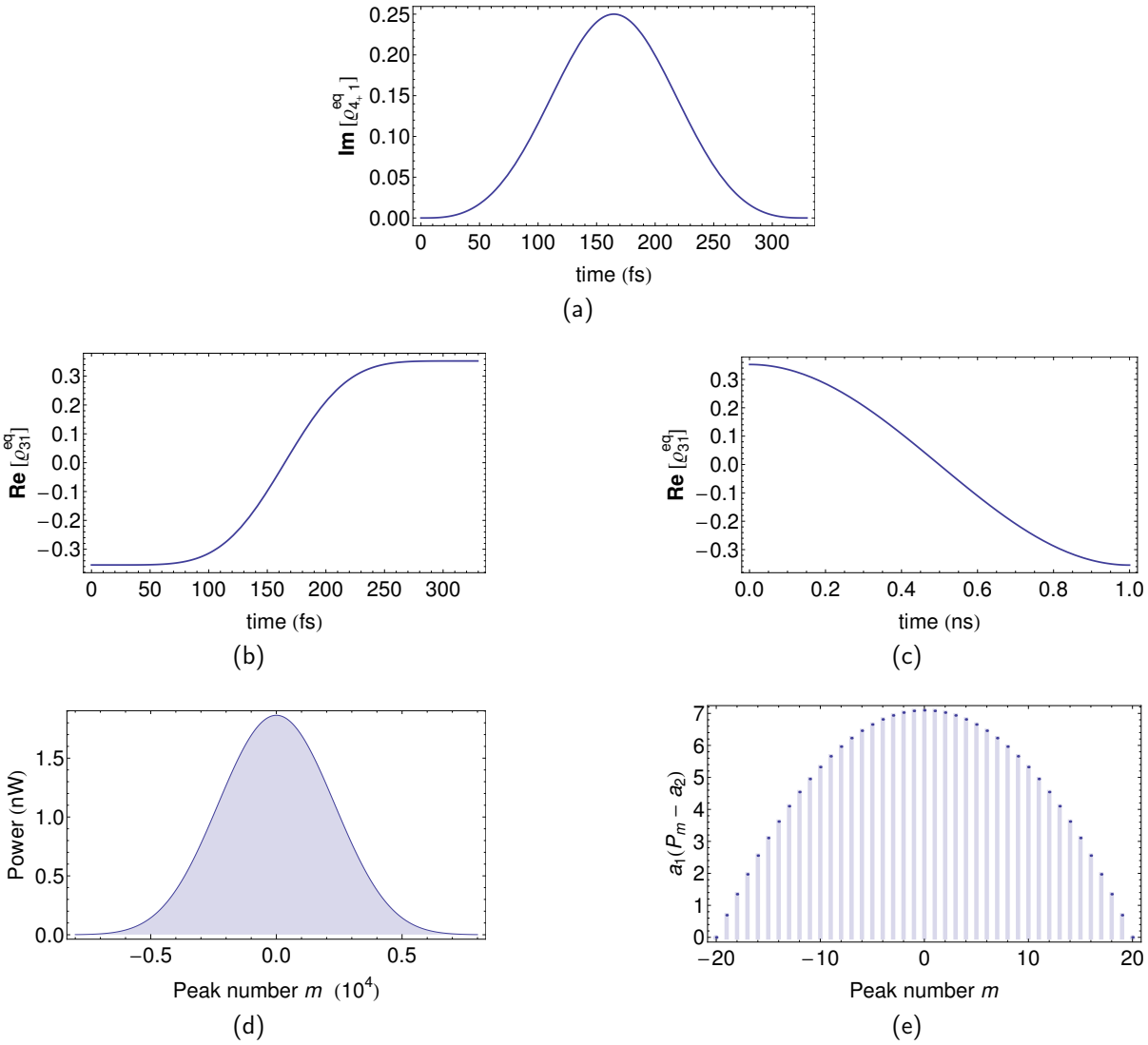

Figure 4.5: Time evolution of the periodic, slowly-varying density matrix $\hat{\varrho}^{\mathrm{eq}}(t)$ and spectrum of resonance fluorescence for Be^{2+} ions. Present-day parameters are used to model the optical frequency comb [Eq. (4.4)], $T_{\mathrm{FWHM}} = 120\,\mathrm{fs}$, $T_{\mathrm{p}} = 1\,\mathrm{ns}$, $1/T_{\mathrm{p}} = 1\,\mathrm{GHz}$ [122, 205–208], i.e., $2\pi/T_{\mathrm{p}} = 4.1 \times 10^{-6}\,\mathrm{eV}$. The ion sample has $N = 10^6$ particles over a length of $L = 1\,\mathrm{cm}$ and an area of $1\,\mathrm{mm}^2$. The driving fields have intensities of $I_{\mathrm{X}} = 1.5 \times 10^4\,\mathrm{W/cm^2}$, $I_{\mathrm{L}} = 1.7 \times 10^8\,\mathrm{W/cm^2}$, and $I_{\mathrm{C,max}} = 3.0 \times 10^{10}\,\mathrm{W/cm^2}$, associated with 2π optical-frequency-comb pulses. The periodic solutions are (a) $\mathbf{Im}[\varrho^{\mathrm{eq}}_{4_+1}(t)]$ for $nT_{\mathrm{p}} < t < nT_{\mathrm{p}} + T_{\mathrm{d}}$, with $T_{\mathrm{d}} = \pi T_{\mathrm{FWHM}}/(2\arccos(\sqrt[4]{1/2}))$, (b) $\mathbf{Re}[\varrho^{\mathrm{eq}}_{31}(t)]$ for $nT_{\mathrm{p}} < t < nT_{\mathrm{p}} + T_{\mathrm{d}}$, and (c) $\mathbf{Re}[\varrho^{\mathrm{eq}}_{31}(t)]$ for $nT_{\mathrm{p}} + T_{\mathrm{d}} < t < (n+1)T_{\mathrm{p}}$. Since all the fields are tuned to the respective transitions, $\mathbf{Re}[\varrho^{\mathrm{eq}}_{4_+1}(t)] = \mathbf{Im}[\varrho^{\mathrm{eq}}_{31}(t)] = 0$. The power P_m of each peak in the spectrum of Eq. (4.66) is displayed (d) for the whole comb, centered at $\omega_{41} = 123.7\,\mathrm{eV}$, and (e) around the maximum. In panel (e), $a_1 = 10^5\,\mathrm{nW}^{-1}$, $a_2 = 1.86\,\mathrm{nW}$.

Also in this case, the choice of a $2n\pi$ area makes sure that $\varrho^{\mathrm{eq}}_{4_+1}(t)$ vanishes in the absence of a pulse from the optical frequency comb. The resulting spectrum of resonance fluorescence [Eq.(4.66)] is shown in Fig. 4.6d: It is centered at $\omega_{41} = 123.7\,\mathrm{eV}$, with a minimum at $m = 0$ and two symmetric maxima. Furthermore, a larger number of peaks is exhibited than in the previous case [Fig. 4.6d]. With $\sim 10^4$ peaks of spacing $2\pi/T_{\mathrm{p}} = 4.1 \times 10^{-6}\,\mathrm{eV}$, the imprinted x-ray spectrum is as wide as the driving optical frequency comb. Fig. 4.6e highlights the comb

structure of the spectrum in the proximity of its maximum, i.e., for $m \sim 3780$. The optical-comb peak intensity, $I_{\mathrm{C,max}} = 1.2 \times 10^{11}\,\mathrm{W/cm^2}$, is still much lower than the peak intensities used for the generation of XUV frequency combs via HHG [205–208]. The power of each peak in the emitted spectrum—about thousands of picowatts—is higher than that measured in Ref. [122].

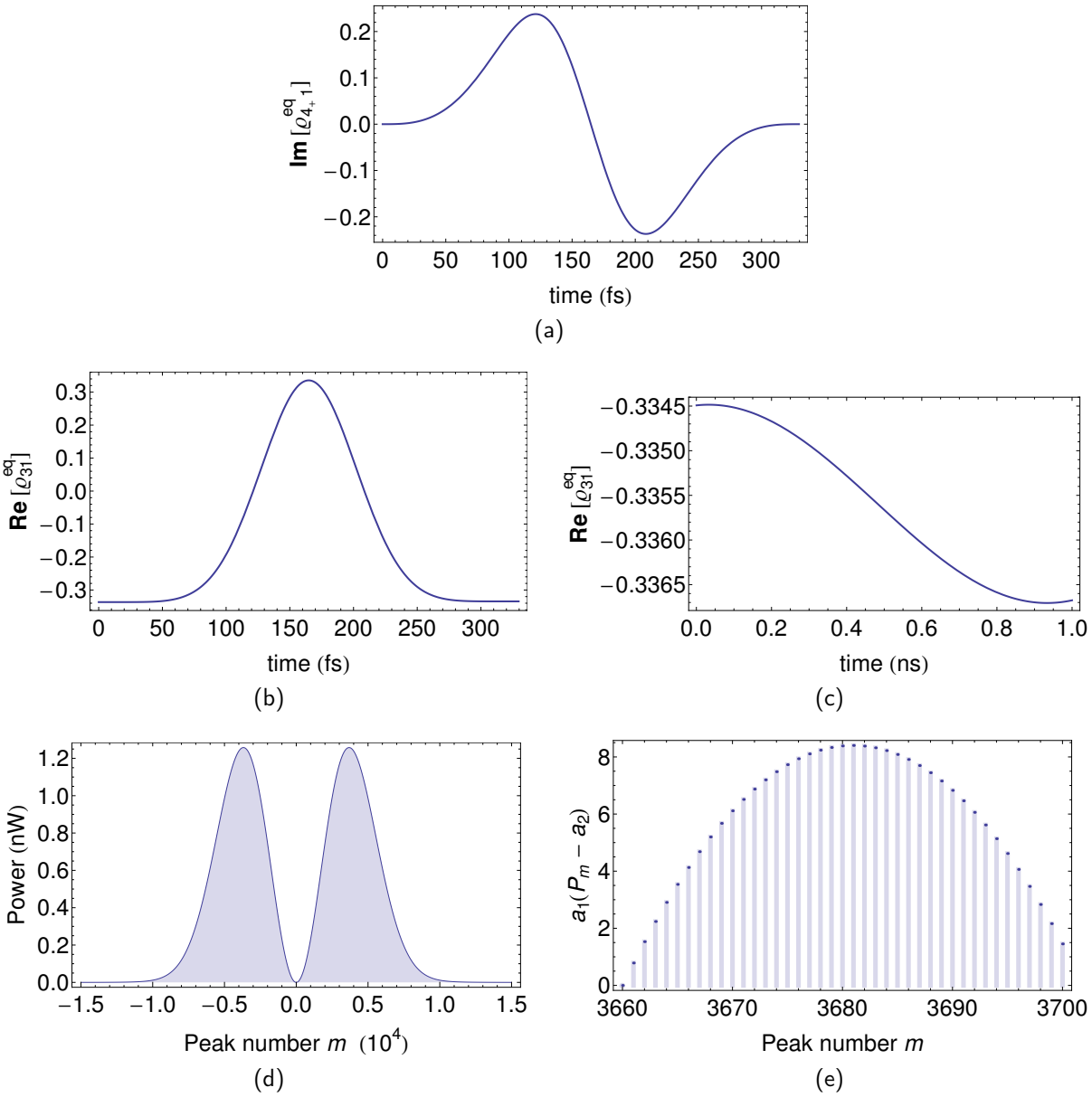

Figure 4.6: Time evolution of the periodic, slowly-varying density matrix $\hat{\varrho}^{\mathrm{eq}}(t)$ and spectrum of resonance fluorescence for Be^{2+} ions. Present-day parameters are used to model the optical frequency comb [Eq. (4.4)], $T_{\mathrm{FWHM}} = 120\,\mathrm{fs}$, $T_{\mathrm{p}} = 1\,\mathrm{ns}$, $1/T_{\mathrm{p}} = 1\,\mathrm{GHz}$ [122, 205–208], i.e., $2\pi/T_{\mathrm{p}} = 4.1 \times 10^{-6}\,\mathrm{eV}$. The ion sample has $N = 10^6$ particles over a length of $L = 1\,\mathrm{cm}$ and an area of $1\,\mathrm{mm}^2$. The driving fields have intensities of $I_{\mathrm{X}} = 9.5 \times 10^8\,\mathrm{W/cm^2}$, $I_{\mathrm{L}} = 1.7 \times 10^8\,\mathrm{W/cm^2}$, and $I_{\mathrm{C,max}} = 1.2 \times 10^{11}\,\mathrm{W/cm^2}$, associated with 4π optical-frequency-comb pulses. We display (a) $\mathbf{Im}[\varrho^{\mathrm{eq}}_{4_+1}(t)]$ for $nT_{\mathrm{p}} < t < nT_{\mathrm{p}} + T_{\mathrm{d}}$, with $T_{\mathrm{d}} = \pi T_{\mathrm{FWHM}}/(2\arccos(\sqrt[4]{1/2}))$, (b) $\mathbf{Re}[\varrho^{\mathrm{eq}}_{31}(t)]$ for $nT_{\mathrm{p}} < t < nT_{\mathrm{p}} + T_{\mathrm{d}}$, and (c) $\mathbf{Re}[\varrho^{\mathrm{eq}}_{31}(t)]$ for $nT_{\mathrm{p}} + T_{\mathrm{d}} < t < (n+1)T_{\mathrm{p}}$. The power P_m of each peak in the spectrum of Eq. (4.66) is displayed (d) for the whole comb, centered at $\omega_{41} = 123.7\,\mathrm{eV}$, and (e) around the maximum. In panel (e), $a_1 = 10^5\,\mathrm{nW}^{-1}$, $a_2 = 1.26\,\mathrm{nW}$.

4.2.3 Bandwidth of the x-ray field

The results presented so far were obtained by assuming cw x rays and neglecting the bandwidth γ_c of the x-ray source. To remove this restriction and incorporate the effect of γ_c, we adopt the stochastic approach from Ref. [189]. The x-ray field $\boldsymbol{\mathcal{E}}_X(t)$ is a stochastic process, varying in the ensemble of all possible realizations: One derives EOMs for the ensemble-averaged density matrix to obtain the ensemble-averaged spectrum. We find that the δ peaks of Eq. (4.66) are broadened and the spectrum is a continuous function with peaks at $\omega_m = 2\pi m/T_p$ of FWHM $\sim 2\gamma_c$. To preserve the comb structure of Eq. (4.66), the x-ray bandwidth must be smaller than the repetition frequency, i.e., $2\gamma_c < 2\pi/T_p = 4.1 \times 10^{-6}\,\mathrm{eV}$: The many-peak structure is otherwise washed out and the spectrum is reduced to a single wide peak. X rays with such a small bandwidth are not available at present. Yet, by increasing the repetition frequency of the optical frequency comb $2\pi/T_p$ [120–122, 209], a wider x-ray-comb tooth spacing results and a larger x-ray bandwidth can be accommodated.

4.3 Conclusions

We present an x-ray pulse-shaping method which we apply to imprint a frequency comb onto cw x rays. The particles, driven by three external fields, are modeled as four-level systems. From many-atom effects, we observe that the coherent part of the power spectrum of resonance fluorescence is the main component of the emitted spectrum, which we calculate from a solution of the single-particle equations of motion. By exploiting an optical frequency comb consisting of pulses with an area which is an integer multiple of 2π, we put forward a manipulation scheme to imprint a pulse-train-like envelope onto the time evolution of the off-diagonal element of the density matrix $\varrho_{4_+1}(t)$, resulting in a spectrum which is a comb of delta peaks centered at the x-ray transition energy ω_{41}. We apply our theory to He-like Be^{2+} at an x-ray energy of 123.7 eV and show that the necessary peak intensity of the driving optical frequency comb is by orders of magnitude lower than the intensities which are required by HHG-based methods.

Following the approach developed in Ref. [75], we develop a scheme which takes advantage of the periodic evolution of the atomic system. This can be achieved if an x-ray source is adopted with a narrow bandwidth, lower than the repetition frequency of the driving optical frequency comb. Although the resolving power required here is not available yet [89–92], new schemes are presently explored aiming at the small x-ray bandwidths of which we take advantage in the atomic implementation of our method [118, 119, 204, 210, 211].

The predicted x-ray comb is valuable as a relative "ruler", e.g., to bridge an energy difference between an x-ray reference level and an unknown x-ray frequency at high energies for which, owing to the inefficiency of HHG at high harmonic orders, x-ray frequency-comb generation via HHG-based methods would encounter significant obstacles [126].

5 Coherent population transfer and absorption spectrum of a broadband x-ray pulse

In the previous Chapters we studied the resonance fluorescence of an ensemble of driven particles in the case in which emitted radiation and driving fields can be separated and distinguished either in space or in frequency. In Chapter 3, in order to calculate the incoherent part of the spectrum of resonance fluorescence due to an ensemble of Ne^+ ions driven by a field propagating along the $\hat{\boldsymbol{e}}_y$ direction, we assumed a detector placed on the perpendicular $\hat{\boldsymbol{e}}_x$ direction. Conversely, in Chapter 4, in order to take advantage of the enhancement of the coherent part of the spectrum of resonance fluorescence in the forward direction due to many-atom effects, we assumed a detector placed on the same propagation direction $\hat{\boldsymbol{e}}_y$ of the three driving fields: In this case, we could exploit the different polarization directions and central frequencies of driving and emitted fields. Furthermore, because of the small-bandwidth x rays employed in Chapter 4 to excite the x-ray $1 \to 2$ transition, we could also rely on the absence of frequency overlap between the spectrum of the x-ray driving field and the spectrum of resonance fluorescence due to the photons emitted on the $4 \to 1$ transition.

In the present and in the next Chapter, a different driving scheme is assumed. In contrast to Chapter 4, where a continuous-wave field was used to drive an x-ray transition, here we assume a wide-bandwidth, ultrashort x-ray pulse tuned to an x-ray transition in a multi-level system. The atomic response of the system is manipulated by coupling the excited state to a nearby, long-lived level by means of an optical field. Since the driving x-ray pulse and the emitted x rays are centered at the same atomic transition energy, the spectral response of the system can be analyzed in two different ways, i.e., (i) off the propagation direction of the driving x-ray pulse, by observing the incoherent part of the spectrum of resonance fluorescence [55, 65, 123, 203], or (ii) in the propagation direction of the driving field, by measuring the absorption spectrum of the transmitted x-ray pulse [81, 82, 147]. This second scheme is the one we are going to employ and investigate in the following.

The present Chapter introduces the theoretical model which we utilize in this and in the next Chapter. In Sec. 5.1 we present the equations of motion describing an ensemble of particles, modeled as a three-level system, interacting with a short x-ray pulse and an optical field. Sec. 5.2 presents a numerical solution of the equations of motion in the case in which the three-level system is driven by an x-ray pulse and a single optical pulse. Results for different optical-pulse shapes and delays are compared. Finally, in Sec. 5.3, we show how the coherent medium response modifies the spectrum of an ultrashort, driving x-ray pulse, by investigating the absorption spectrum of the light which is transmitted through the medium.

5.1 Three-level model and equations of motion

The model that we adopt is depicted in Fig. 5.1. A system of ions, here represented as three-level, Λ-type systems, is driven by two external electric fields, respectively centered at an x-ray and an optical frequency, both linearly polarized in the z direction, propagating in the forward y direction, and nearly tuned to two different transitions in the atomic system.

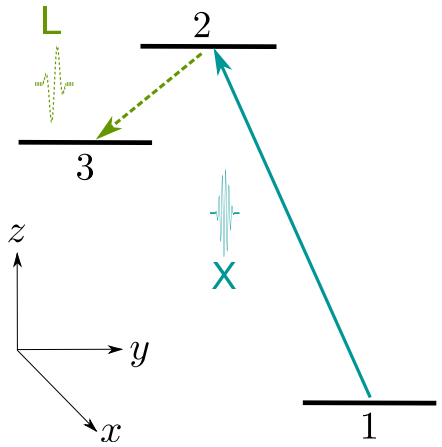

Figure 5.1: An ensemble of ions is driven by an ultrashort, wide-bandwidth x-ray pulse (X, blue), coupling states 1 and 2, and by an additional optical pulse (L, green) coupling the excited state 2 to the metastable state 3. Both fields are linearly polarized along the z direction and propagate in the y direction.

The x-ray field consists of a single pulse,

$$\boldsymbol{\mathcal{E}}_{\mathrm{X}}(\boldsymbol{r},\, t) = \mathcal{E}_{\mathrm{X},0}(t - \boldsymbol{r}\cdot\hat{\boldsymbol{e}}_y/c)\cos\left[\omega_{\mathrm{X}}t + \varphi_{\mathrm{X}}(t - \boldsymbol{r}\cdot\hat{\boldsymbol{e}}_y/c) + \varphi_{\mathrm{X},0} - \boldsymbol{k}_{\mathrm{X}}\cdot\boldsymbol{r}\right]\hat{\boldsymbol{e}}_z, \tag{5.1}$$

with amplitude $\mathcal{E}_{\mathrm{X},0}(t)$, carrier frequency ω_{X}, phase $\varphi_{\mathrm{X}}(t)$, carrier-envelope phase (CEP) $\varphi_{\mathrm{X},0}$, wavevector $\boldsymbol{k}_{\mathrm{X}} = (\omega_{\mathrm{X}}/c)\,\hat{\boldsymbol{e}}_y$, and intensity $I_{\mathrm{X}} = |\mathcal{E}_{\mathrm{X},0}|^2/(8\pi\alpha)$ [164], where $\hat{\boldsymbol{e}}_x$, $\hat{\boldsymbol{e}}_y$, and $\hat{\boldsymbol{e}}_z$ are the unit vectors in the x, y, and z direction, c is the speed of light, and $\alpha = 1/c$ is the fine-structure constant. The optical field is

$$\boldsymbol{\mathcal{E}}_{\mathrm{L}}(\boldsymbol{r},\, t) = \mathcal{E}_{\mathrm{L},0}(t - \boldsymbol{r}\cdot\hat{\boldsymbol{e}}_y/c)\cos\left[\omega_{\mathrm{L}}t + \varphi_{\mathrm{L}}(t - \boldsymbol{r}\cdot\hat{\boldsymbol{e}}_y/c) + \varphi_{\mathrm{L},0} - \boldsymbol{k}_{\mathrm{L}}\cdot\boldsymbol{r}\right]\hat{\boldsymbol{e}}_z, \tag{5.2}$$

where the same notation is used as in Eq. (5.1). The indeces of refraction n_q, with $q \in \{\mathrm{X},\, \mathrm{L}\}$, are here set equal to 1, thus implying that $k_q = (\omega_q/c)$.

The two electric fields $\boldsymbol{\mathcal{E}}_{\mathrm{X}}(\boldsymbol{r},\, t)$ and $\boldsymbol{\mathcal{E}}_{\mathrm{L}}(\boldsymbol{r},\, t)$ drive the electric-dipole (E1) transitions of the three-level Λ-type system of Fig. 5.1, where level i has energy ω_i and the energy between the levels i and j is given by $\omega_{ij} = \omega_i - \omega_j$, $i,\, j \in S = \{1,\, 2,\, 3\}$. The many-level model is used, as in Chapter 4, to describe He-like ions, for which the transition energies are in the proper optical and x-ray ranges [191]. States $|1\rangle$ and $|3\rangle$ represent the ground state $1s^2\ {}^1S_0$ and the metastable state $1s\,2s\ {}^1S_0$, respectively, both with total-angular-momentum quantum numbers $J = 0$, $M_J = 0$, and positive parity. However, the only negative-parity state included in this and in the next Chapter is the state $1s\,2p\ {}^1P_1$, with $J = 1$, $M_J = 0$, here represented by the excited state $|2\rangle$. In He-like ions, level 3 has lower energy than level 2 [191], such that the three states form indeed a three-level, Λ-type system [57, 58].

Other levels, such as $1s\,2s\ {}^3S_1$, $1s\,2p\ {}^3P_0$, $1s\,2p\ {}^3P_1$, and $1s\,2p\ {}^3P_2$, along with the two states $1s\,2p\ {}^1P_1$ with $M_J = \pm 1$, are not included in our description, because they do not couple via E1 interaction to the levels in Fig. 5.1 and the spontaneous-decay times from higher-energy levels to them are by orders of magnitude larger than the time scale on which the evolution of the system takes place. We recall that the levels 2 and 3 are below the autoionization threshold, since in both cases one electron occupies the $1s$ orbital [191]. In the following equations, we are allowed to neglect ionization of multiply charged ions such as Be^{2+} entirely.

In order to describe the interaction of the electric fields $\boldsymbol{\mathcal{E}}_{\mathrm{X}}(\boldsymbol{r},\, t)$ and $\boldsymbol{\mathcal{E}}_{\mathrm{L}}(\boldsymbol{r},\, t)$ with N ions at positions $\boldsymbol{r}_n$, $n \in \{1,\, \ldots,\, N\}$, we take advantage of the general results which we derived

in Chapter 2 for the single-atom case. The interaction is described by the Hamiltonian $\hat{H} = \hat{H}_0 + \sum_{q\in\{\mathrm{X,L}\}} \hat{H}_{\mathrm{E1},q}$, where $\hat{H}_0 = \sum_{n=1}^{N} \sum_{i\in\{1,2,3\}} \omega_i \, \hat{\sigma}_{ii}^n$ is the atomic electronic structure Hamiltonian [see Eqs. (2.30) and (2.31)] and, for $q \in \{\mathrm{X, L}\}$, $\hat{H}_{\mathrm{E1},q} = \sum_{n=1}^{N} \hat{\boldsymbol{d}}_n \cdot \boldsymbol{\mathcal{E}}_q(\boldsymbol{r}_n, t)$ are the E1 interaction Hamiltonians that we introduced in Eq. (2.105) [53, 159]. Here, $\hat{\boldsymbol{d}}_n$, in analogy with Eq. (2.32), represents the dipole operator of an ion at position $\boldsymbol{r}_n$,

$$\hat{\boldsymbol{d}}_n = \sum_{i,j\in\{1,2,3\}} |i\rangle_{n\,n}\langle i|\hat{\boldsymbol{d}}_n|j\rangle_{n\,n}\langle j| = \sum_{i,j\in\{1,2,3\}} \boldsymbol{d}_{ij,n}\, \hat{\sigma}_{ij}^n, \tag{5.3}$$

with matrix elements $\boldsymbol{d}_{ij,n} = {}_n\langle i|\hat{\boldsymbol{d}}_n|j\rangle_n$, $i, j \in \{1, 2, 3\}$, $n \in \{1, \ldots, N\}$. Because the dipole moment is a general property of the ion species, i.e., of atomic number and charge of the ion, the matrix elements $\boldsymbol{d}_{ij,n} = \boldsymbol{d}_{ij}$ do not explicitly depend on n. Furthermore, all the considered states have angular-momentum quantum number $M_J = 0$, whereby $M_{J,i} - M_{J,j} = 0$ for any pairs of states i, j. As a result, the dipole-moment matrix elements $\boldsymbol{d}_{ij} = d_{ij}^0\, \hat{\boldsymbol{e}}_z$ are aligned on the z direction.

We introduce the time- and space-dependent, complex Rabi frequencies

$$\Omega_{\mathrm{RX}}^n(t) = \mathcal{E}_{\mathrm{X},0}(t - \boldsymbol{r}_n \cdot \hat{\boldsymbol{e}}_y/c)\, \mathrm{e}^{\mathrm{i}\,\varphi_{\mathrm{X}}(t - \boldsymbol{r}_n\cdot\hat{\boldsymbol{e}}_y/c)}\, d_{12}^0, \tag{5.4a}$$

$$\Omega_{\mathrm{RL}}^n(t) = \mathcal{E}_{\mathrm{L},0}(t - \boldsymbol{r}_n \cdot \hat{\boldsymbol{e}}_y/c)\, \mathrm{e}^{\mathrm{i}\,\varphi_{\mathrm{L}}(t - \boldsymbol{r}_n\cdot\hat{\boldsymbol{e}}_y/c)}\, d_{32}^0. \tag{5.4b}$$

The x-ray field is nearly tuned to the $1 \to 2$ transition and does not affect the other E1-allowed transition. Within the rotating-wave approximation (RWA) [53], the interaction with the N ions is described by the following Hamiltonian[1],

$$\hat{H}_{\mathrm{E1,X}} = \sum_{n=1}^{N} \frac{\Omega_{\mathrm{RX}}^n}{2}\, \hat{\sigma}_{12}^n\, \mathrm{e}^{\mathrm{i}(\omega_{\mathrm{X}} t - \boldsymbol{k}_{\mathrm{X}}\cdot\boldsymbol{r}_n + \varphi_{\mathrm{X},0})} \;+\; \mathrm{H.c.} \tag{5.5}$$

Similarly, the interaction of the optical field with the ensemble of ions is described by the Hamiltonian

$$\hat{H}_{\mathrm{E1,L}} = \sum_{n=1}^{N} \frac{\Omega_{\mathrm{RL}}^n}{2}\, \hat{\sigma}_{32}^n\, \mathrm{e}^{\mathrm{i}(\omega_{\mathrm{L}} t - \boldsymbol{k}_{\mathrm{L}}\cdot\boldsymbol{r}_n + \varphi_{\mathrm{L},0})} \;+\; \mathrm{H.c.} \tag{5.6}$$

As discussed in Eq. (2.91), the time evolution of the system obeys the master equation [53] $\mathrm{d}\hat{\rho}/\,\mathrm{d}t = -\mathrm{i}\,[\hat{H}, \hat{\rho}] + \mathcal{L}[\hat{\rho}]$, where $\hat{\rho}(t)$ is the density matrix of elements $\rho_{ij}^n(t) = \langle \hat{\sigma}_{ji}^n(t)\rangle = \mathrm{Tr}\{\hat{\sigma}_{ji}^n(t)\, \hat{\rho}\}$, and $\mathcal{L}[\hat{\rho}]$ describes norm-conserving spontaneous decay,

$$\mathcal{L}[\hat{\rho}] = \sum_{\substack{i,\,j\in\{1,\,2,\,3\}\\ \omega_i<\omega_j}} \sum_{n=1}^{N} -\frac{\Gamma_{ji}}{2}(\hat{\sigma}_{ji}^n\hat{\sigma}_{ij}^n\hat{\rho} - \hat{\sigma}_{ij}^n\hat{\rho}\hat{\sigma}_{ji}^n) + \mathrm{H.c.}, \tag{5.7}$$

with spontaneous-decay rates Γ_{ji} [53]; norm-nonconserving terms such as those from autoionization or (multi-) photoionization are not present. The equations of motion (EOMs) satisfied by the elements of the n-ion density matrix $\hat{\rho}^n(t)$ are

$$\frac{\partial\rho_{11}^n}{\partial t} = -\mathrm{i}\frac{\Omega_{\mathrm{RX}}^n}{2}\, \mathrm{e}^{\mathrm{i}(\omega_{\mathrm{X}} t - \boldsymbol{k}_{\mathrm{X}}\cdot\boldsymbol{r}_n + \varphi_{\mathrm{X},0})}\rho_{21}^n + \mathrm{i}\frac{(\Omega_{\mathrm{RX}}^n)^*}{2}\, \mathrm{e}^{-\mathrm{i}(\omega_{\mathrm{X}} t - \boldsymbol{k}_{\mathrm{X}}\cdot\boldsymbol{r}_n + \varphi_{\mathrm{X},0})}\rho_{12}^n + \Gamma_{31}\rho_{33}^n + \Gamma_{21}\rho_{22}^n, \tag{5.8a}$$

[1] In this Chapter, we assume that the minus sign in the interaction Hamiltonian $\hat{H}_{\mathrm{AL}}$ from Eq. 2.105 is included in the CEP $\varphi_{q,0}$, with $q \in \{\mathrm{X, L}\}$.

$$\frac{\partial\rho_{12}^n}{\partial t} = \left(\mathrm{i}\,\omega_{21} - \frac{\Gamma_{21}+\Gamma_{23}}{2}\right)\rho_{12}^n - \mathrm{i}\frac{\Omega_{\mathrm{RX}}^n}{2}\,\mathrm{e}^{\mathrm{i}(\omega_{\mathrm{X}}t-\boldsymbol{k}_{\mathrm{X}}\cdot\boldsymbol{r}_n+\varphi_{\mathrm{X},0})}(\rho_{22}^n-\rho_{11}^n) + \mathrm{i}\frac{\Omega_{\mathrm{RL}}^n}{2}\,\mathrm{e}^{\mathrm{i}(\omega_{\mathrm{L}}t-\boldsymbol{k}_{\mathrm{L}}\cdot\boldsymbol{r}_n+\varphi_{\mathrm{L},0})}\rho_{13}^n, \tag{5.8b}$$

$$\frac{\partial\rho_{13}^n}{\partial t} = \left(\mathrm{i}(\omega_{21}-\omega_{23}) - \frac{\Gamma_{31}}{2}\right)\rho_{13}^n - \mathrm{i}\frac{\Omega_{\mathrm{RX}}^n}{2}\,\mathrm{e}^{\mathrm{i}(\omega_{\mathrm{X}}t-\boldsymbol{k}_{\mathrm{X}}\cdot\boldsymbol{r}_n+\varphi_{\mathrm{X},0})}\rho_{23}^n + \mathrm{i}\frac{(\Omega_{\mathrm{RL}}^n)^*}{2}\,\mathrm{e}^{-\mathrm{i}(\omega_{\mathrm{L}}t-\boldsymbol{k}_{\mathrm{L}}\cdot\boldsymbol{r}_n+\varphi_{\mathrm{L},0})}\rho_{12}^n, \tag{5.8c}$$

$$\begin{aligned}\frac{\partial\rho_{22}^n}{\partial t} = &-\mathrm{i}\frac{(\Omega_{\mathrm{RX}}^n)^*}{2}\,\mathrm{e}^{-\mathrm{i}(\omega_{\mathrm{X}}t-\boldsymbol{k}_{\mathrm{X}}\cdot\boldsymbol{r}_n+\varphi_{\mathrm{X},0})}\rho_{12}^n + \mathrm{i}\frac{\Omega_{\mathrm{RX}}^n}{2}\,\mathrm{e}^{\mathrm{i}(\omega_{\mathrm{X}}t-\boldsymbol{k}_{\mathrm{X}}\cdot\boldsymbol{r}_n+\varphi_{\mathrm{X},0})}\rho_{21}^n \\ &-\mathrm{i}\frac{(\Omega_{\mathrm{RL}}^n)^*}{2}\,\mathrm{e}^{-\mathrm{i}(\omega_{\mathrm{L}}t-\boldsymbol{k}_{\mathrm{L}}\cdot\boldsymbol{r}_n+\varphi_{\mathrm{L},0})}\rho_{32}^n + \mathrm{i}\frac{\Omega_{\mathrm{RL}}^n}{2}\,\mathrm{e}^{\mathrm{i}(\omega_{\mathrm{L}}t-\boldsymbol{k}_{\mathrm{L}}\cdot\boldsymbol{r}_n+\varphi_{\mathrm{L},0})}\rho_{23}^n - (\Gamma_{21}+\Gamma_{23})\rho_{22}^n,\end{aligned} \tag{5.8d}$$

$$\frac{\partial\rho_{23}^n}{\partial t} = \left(-\mathrm{i}\,\omega_{23} - \frac{\Gamma_{21}+\Gamma_{23}+\Gamma_{31}}{2}\right)\rho_{23}^n - \mathrm{i}\frac{(\Omega_{\mathrm{RX}}^n)^*}{2}\,\mathrm{e}^{-\mathrm{i}(\omega_{\mathrm{X}}t-\boldsymbol{k}_{\mathrm{X}}\cdot\boldsymbol{r}_n+\varphi_{\mathrm{X},0})}\rho_{13}^n - \mathrm{i}\frac{(\Omega_{\mathrm{RL}}^n)^*}{2}\,\mathrm{e}^{-\mathrm{i}(\omega_{\mathrm{L}}t-\boldsymbol{k}_{\mathrm{L}}\cdot\boldsymbol{r}_n+\varphi_{\mathrm{L},0})}(\rho_{33}^n-\rho_{22}^n), \tag{5.8e}$$

$$\frac{\partial\rho_{33}^n}{\partial t} = -\mathrm{i}\frac{\Omega_{\mathrm{RL}}^n}{2}\,\mathrm{e}^{\mathrm{i}(\omega_{\mathrm{L}}t-\boldsymbol{k}_{\mathrm{L}}\cdot\boldsymbol{r}_n+\varphi_{\mathrm{L},0})}\rho_{23}^n + \mathrm{i}\frac{(\Omega_{\mathrm{RL}}^n)^*}{2}\,\mathrm{e}^{-\mathrm{i}(\omega_{\mathrm{L}}t-\boldsymbol{k}_{\mathrm{L}}\cdot\boldsymbol{r}_n+\varphi_{\mathrm{L},0})}\rho_{32}^n - \Gamma_{31}\rho_{33}^n + \Gamma_{23}\rho_{22}^n. \tag{5.8f}$$

These equations can be simplified by introducing the slowly varying operators [53, 75, 195]

$$\hat{\tilde{\varsigma}}_{ii}^n(t) = \hat{\sigma}_{ii}^n(t), \tag{5.9a}$$

$$\hat{\tilde{\varsigma}}_{21}^n(t) = \hat{\sigma}_{21}^n(t)\,\mathrm{e}^{-\mathrm{i}(\omega_{\mathrm{X}}t-\boldsymbol{k}_{\mathrm{X}}\cdot\boldsymbol{r}_n+\varphi_{\mathrm{X},0})}, \tag{5.9b}$$

$$\hat{\tilde{\varsigma}}_{23}^n(t) = \hat{\sigma}_{23}^n(t)\,\mathrm{e}^{-\mathrm{i}(\omega_{\mathrm{L}}t-\boldsymbol{k}_{\mathrm{L}}\cdot\boldsymbol{r}_n+\varphi_{\mathrm{L},0})}, \tag{5.9c}$$

$$\hat{\tilde{\varsigma}}_{31}^n(t) = \hat{\sigma}_{31}^n(t)\,\mathrm{e}^{-\mathrm{i}[(\omega_{\mathrm{X}}-\omega_{\mathrm{L}})t-(\boldsymbol{k}_{\mathrm{X}}-\boldsymbol{k}_{\mathrm{L}})\cdot\boldsymbol{r}_n+\varphi_{\mathrm{X},0}-\varphi_{\mathrm{L},0}]}, \tag{5.9d}$$

and, clearly, $\hat{\tilde{\varsigma}}_{ij}^n(t) = [\hat{\tilde{\varsigma}}_{ji}^n(t)]^\dagger$. Analogously, we define a slowly-varying density matrix $\hat{\tilde{\varrho}}(t)$, of matrix elements $\tilde{\varrho}_{ij}^n(t) = \langle\hat{\tilde{\varsigma}}_{ji}^n(t)\rangle$. By further introducing the detuning of the two electric fields

$$\Delta_{\mathrm{X}} = \omega_{21} - \omega_{\mathrm{X}}, \quad \Delta_{\mathrm{L}} = \omega_{23} - \omega_{\mathrm{L}}, \tag{5.10}$$

we can write the EOMs as

$$\frac{\partial\tilde{\varrho}_{11}^n}{\partial t} = -\mathrm{i}\frac{\Omega_{\mathrm{RX}}^n}{2}\tilde{\varrho}_{21}^n + \mathrm{i}\frac{(\Omega_{\mathrm{RX}}^n)^*}{2}\tilde{\varrho}_{12}^n + \Gamma_{31}\tilde{\varrho}_{33}^n + \Gamma_{21}\tilde{\varrho}_{22}^n, \tag{5.11a}$$

$$\frac{\partial\tilde{\varrho}_{12}^n}{\partial t} = \left(\mathrm{i}\Delta_{\mathrm{X}} - \frac{\Gamma_{21}+\Gamma_{23}}{2}\right)\tilde{\varrho}_{12}^n - \mathrm{i}\frac{\Omega_{\mathrm{RX}}^n}{2}(\tilde{\varrho}_{22}^n-\tilde{\varrho}_{11}^n) + \mathrm{i}\frac{\Omega_{\mathrm{RL}}^n}{2}\tilde{\varrho}_{13}^n, \tag{5.11b}$$

$$\frac{\partial\tilde{\varrho}_{13}^n}{\partial t} = \left(\mathrm{i}(\Delta_{\mathrm{X}}-\Delta_{\mathrm{L}}) - \frac{\Gamma_{31}}{2}\right)\tilde{\varrho}_{13}^n - \mathrm{i}\frac{\Omega_{\mathrm{RX}}^n}{2}\tilde{\varrho}_{23}^n + \mathrm{i}\frac{(\Omega_{\mathrm{RL}}^n)^*}{2}\tilde{\varrho}_{12}^n, \tag{5.11c}$$

$$\frac{\partial\tilde{\varrho}_{22}^n}{\partial t} = -\mathrm{i}\frac{(\Omega_{\mathrm{RX}}^n)^*}{2}\tilde{\varrho}_{12}^n + \mathrm{i}\frac{\Omega_{\mathrm{RX}}^n}{2}\tilde{\varrho}_{21}^n - \mathrm{i}\frac{(\Omega_{\mathrm{RL}}^n)^*}{2}\tilde{\varrho}_{32}^n + \mathrm{i}\frac{\Omega_{\mathrm{RL}}^n}{2}\tilde{\varrho}_{23}^n - (\Gamma_{21}+\Gamma_{23})\tilde{\varrho}_{22}^n, \tag{5.11d}$$

$$\frac{\partial\tilde{\varrho}_{23}^n}{\partial t} = \left(-\mathrm{i}\Delta_{\mathrm{L}} - \frac{\Gamma_{21}+\Gamma_{23}+\Gamma_{31}}{2}\right)\tilde{\varrho}_{23}^n - \mathrm{i}\frac{(\Omega_{\mathrm{RX}}^n)^*}{2}\tilde{\varrho}_{13}^n - \mathrm{i}\frac{(\Omega_{\mathrm{RL}}^n)^*}{2}(\tilde{\varrho}_{33}^n-\tilde{\varrho}_{22}^n), \tag{5.11e}$$

$$\frac{\partial\tilde{\varrho}_{33}^n}{\partial t} = -\mathrm{i}\frac{\Omega_{\mathrm{RL}}^n}{2}\tilde{\varrho}_{23}^n + \mathrm{i}\frac{(\Omega_{\mathrm{RL}}^n)^*}{2}\tilde{\varrho}_{32}^n - \Gamma_{31}\tilde{\varrho}_{33}^n + \Gamma_{23}\tilde{\varrho}_{22}^n. \tag{5.11f}$$

Since the only n-dependent coefficients in the previous set of linear differential equations are the two Rabi frequencies $\Omega_{\rm X}^n(t)$ and $\Omega_{\rm RL}^n(t)$ defined in Eq. (5.4), the elements of the density matrices associated with ions at different positions, $\boldsymbol{r}_n$ and $\boldsymbol{r}_{n'}$, are related by the following equality,

$$\tilde{\varrho}_{ij}^{n}(t) = \tilde{\varrho}_{ij}^{n'}[t + (\boldsymbol{r}_{n'} - \boldsymbol{r}_n) \cdot \hat{\boldsymbol{e}}_y/c], \tag{5.12}$$

such that, from Eq. (5.9),

$$\rho_{ij}^{n}(t) = \rho_{ij}^{n'}[t + (\boldsymbol{r}_{n'} - \boldsymbol{r}_n) \cdot \hat{\boldsymbol{e}}_y/c]. \tag{5.13}$$

5.2 Coherent population transfer via optical coupling

In this Section, we solve numerically the EOMs derived in Eq. (5.11) for the three-level scheme of Fig. 5.1 which we apply to describe the dynamics of He-like O^{6+} ions driven by an x-ray pulse tuned to the $1s^2\,{}^1S_0 \to 1s\,2p\,{}^1P_1$ E1 transition at $\omega_{21} = 573.96\,\text{eV}$ in the presence of an optical laser which couples the excited state $1s\,2p\,{}^1P_1$ to the metastable state $1s\,2s\,{}^1S_0$, separated by a transition energy of $\omega_{23} = 5.06\,\text{eV}$. We employ a single-particle description and solve the EOMs in Eq. (5.11) for the density matrix $\hat{\varrho}^{\rm eq}(t)$, associated with a particle at position $\boldsymbol{r}_0 = \boldsymbol{0}$. The system is assumed to be initially in the ground state, i.e., the initial state of the density matrix is $\varrho_{ij}^{\rm eq}(0) = \delta_{i1}\,\delta_{j1}$. The decay rates $\Gamma_{21} = 3.3 \times 10^{12}\,\text{s}^{-1}$ and $\Gamma_{23} = 2.5 \times 10^{7}\,\text{s}^{-1}$ are calculated with `grasp2K` [200–202], whereas the two-photon decay rate $\Gamma_{31} = 2.31 \times 10^{6}\,\text{s}^{-1}$ is taken from Ref. [212]. These values are also used for the calculation of the dipole moments $\boldsymbol{d}_{ij}$ involved in the definition of the Rabi frequencies (5.4). The transition energies ω_{23} and ω_{21} are taken from Ref. [191].

5.2.1 Interaction of the system with an x-ray pulse and an optical laser

Here, we describe numerically how efficiently an optical pulse interacting with the atomic system in Fig. 5.1 can lead to population transfer from the excited level 2 to the metastable state 3.

The x-ray Self-Amplified-Spontaneous-Emission (SASE) pulse [89–92] is generated via the partial-coherence method which we discuss in Appendix B. Here, we assume an x-ray bandwidth $\Delta\omega_{\rm SASE} = 6\,\text{eV}$, an average peak intensity $I_{\rm X,max} = 10^{14}\,\text{W/cm}^2$, average time duration $\tau_{\rm env} = 10\,\text{fs}$ and an average envelope function $\bar{\mathcal{E}}_{\rm X,0}(t) = \bar{\mathcal{E}}_{\rm X,max}\,\cos^2[\pi(t-T_{\rm X0})/T]\,\text{R}[(t-T_{\rm X0})/T]$, where $\bar{\mathcal{E}}_{\rm X,max} = \sqrt{8\pi\alpha\, I_{\rm X,max}}$, α is the fine-structure constant, $T_{\rm X0} = 55\,\text{fs}$ is the time at which the pulse is centered, $T = \pi\tau_{\rm env}/(2\arccos\sqrt[4]{1/2})$ [190], and the rectangular function $R(t)$ is defined with the help of the Heaviside step function $\theta(t)$ as $\text{R}(t) = \theta(t+1/2) - \theta(t-1/2)$. We study the evolution of the population of the two excited levels, $1s\,2p\,{}^1P_1$ and $1s\,2s\,{}^1S_0$, for optical pulses of different shape, central time, and detuning.

In Fig. 5.2, the optical-pulse envelope $\mathcal{E}_{\rm L,0}(t)$ is modeled by a trapezoidal function of peak intensity $I_{\rm L} = 2 \times 10^{13}\,\text{W/cm}^2$ and centered, as the x-ray pulse, at $T_{\rm L0} = 55\,\text{fs}$. The function has a finite rise time of 5 fs and the time interval exhibiting constant amplitude is $\tau_{\rm L} = 100\,\text{fs}$. The x-ray pulse, the optical pulse and the corresponding time evolution of the populations of the two excited states 2 and 3 are shown in Figs. 5.2a and 5.2b, respectively for an optical pulse tuned to the transition at 5.06 eV and for a detuned, 266-nm optical pulse of photon energy 4.65 eV. In the case of a tuned pulse, the populations perform Rabi cycles at constant Rabi frequency $\Omega_{\rm RL}$ [Eq. (5.4)]. Notice that a complete population transfer is not achieved. In the case of a detuned pulse, Rabi oscillations appear, although a less efficient population transfer is featured.

In Fig. 5.3, a smooth-envelope optical pulse is employed. It is centered, as in the previous case, at $T_{\rm L0} = 55\,\text{fs}$ and thus temporally overlaps with the x-ray pulse. We model this optical pulse via

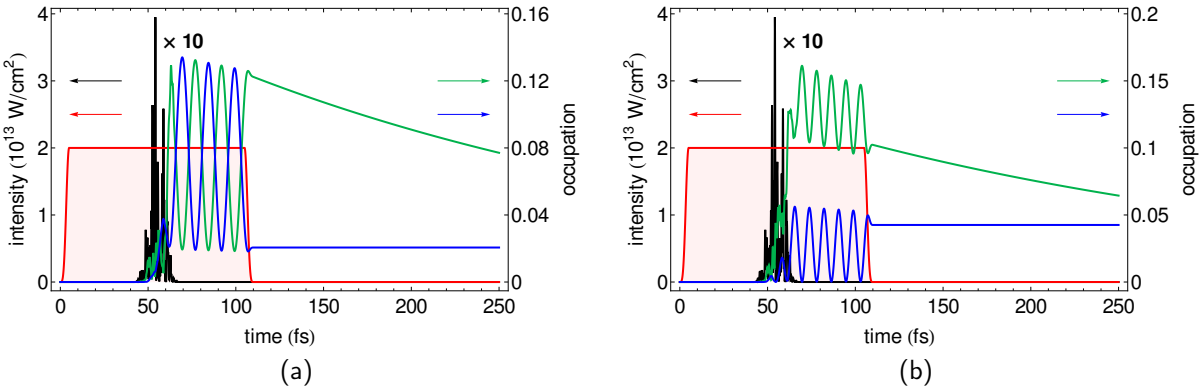

Figure 5.2: Three-level system driven by an x-ray SASE pulse (black), centered at $T_{\mathrm{X0}} = 55\,\mathrm{fs}$, together with a trapezoidal optical pulse (red), centered at $T_{\mathrm{L0}} = 55\,\mathrm{fs}$, overlapping with the x-ray pulse. The population of the excited state $\varrho_{22}^{\mathrm{eq}}(t)$ (green) and of the metastable state $\varrho_{33}^{\mathrm{eq}}(t)$ (blue) are depicted for (a) a tuned optical pulse and (b) a 266-nm pulse, detuned from the corresponding optical transition $2 \to 3$. The value of the intensity of the pulses is exhibited on the left-hand axis. The intensity of the x-ray pulse has still to be multiplied by a factor 10. The value of the populations is exhibited on the right-hand axis.

the envelope function $\mathcal{E}_{\mathrm{L},0}(t) = \mathcal{E}_{\mathrm{L,max}} \cos^2[\pi(t - T_{\mathrm{L0}})/T_{\mathrm{L}}]\, R[(t - T_{\mathrm{L0}})/T_{\mathrm{L}}]$, where the maximum electric-field strength $\mathcal{E}_{\mathrm{L,max}} = \sqrt{8\pi\alpha\, I_{\mathrm{L,max}}}$ and the pulse duration $T_{\mathrm{L}} = \pi\tau_{\mathrm{L}}/(2 \arccos \sqrt[4]{1/2})$ are related to the FWHM of the optical pulse $\tau_{\mathrm{L}} = 40\,\mathrm{fs}$ and to its peak intensity $I_{\mathrm{L,max}} = 2 \times 10^{13}\,\mathrm{W/cm^2}$. The essential features of the corresponding time evolution of the populations of the excited states 2 and 3 were already present in Fig. 5.2. Rabi oscillations of the populations are exhibited in Fig. 5.3a at the time-dependent Rabi frequency $\Omega_{\mathrm{RL}}(t)$ ensued from the time-dependent envelope function $\mathcal{E}_{\mathrm{L},0}(t)$ [Eq. (5.4)]. In the presence of detuning, Fig. 5.3b shows Rabi oscillations featuring less efficient population transfer than in the case of a tuned pulse.

In Fig. 5.3, we present the time evolution of the three-level system when an optical pulse is used which, being centered at $T_{\mathrm{L0}} = 125\,\mathrm{fs}$, does not overlap with the preceding x-ray pulse. The envelope function of the optical pulse is modeled also in this case via the already presented cosine-squared function. When the optical pulse is tuned to the transition $2 \to 3$, several Rabi cycles are exhibited (Fig. 5.4a) and complete population inversions are achieved. Totally different is the case of a detuned pulse (Fig. 5.4b): Rabi oscillations are not induced and only a small amount of population is transferred from the excited state 2 to the metastable state 3 at the optical-field-envelope maximum.

As we have already discussed in Sec. 2.6, the number of Rabi oscillations is related to the pulse area $Q_{\mathrm{L}} = \int_{-\infty}^{\infty} \Omega_{\mathrm{RL}}(t)\, \mathrm{d}t$, where the Rabi frequency $\Omega_{\mathrm{RL}}(t)$ (5.4) associated with the cosine-squared envelope function $\mathcal{E}_{\mathrm{L},0}(t) = \mathcal{E}_{\mathrm{L,max}} \cos^2[\pi(t - T_{\mathrm{L0}})/T_{\mathrm{L}}]\, R[(t - T_{\mathrm{L0}})/T_{\mathrm{L}}]$ leads to

$$Q_{\mathrm{L}} = d_{23}^0 \sqrt{8\pi\alpha\, I_{\mathrm{L,max}}}\, \frac{\pi\tau_{\mathrm{L}}}{2(2 \arccos \sqrt[4]{1/2})}.$$

In the absence of any spontaneous decay or detuning, a system driven by a pulse with area Q_{L} would display a number of cycles $Q_{\mathrm{L}}/2\pi$ in the population oscillations induced by the external field [68–71,73,163]. In particular, for $Q_{\mathrm{L}} = (2n+1)\pi$, with $n \in \mathbb{N}$, a complete population transfer is performed. This is shown in Fig. 5.5, where an optical pulse with cosine-squared envelope and $Q_{\mathrm{L}} = \pi$ is employed. For the FWHM $\tau_{\mathrm{L}} = 40\,\mathrm{fs}$ and the dipole-moment matrix element d_{23} in He-like O^{6+}, this condition corresponds to a peak intensity $I_{\mathrm{L,max}} = 3.7 \times 10^{11}\,\mathrm{W/cm^2}$. The resulting population switch, from the fast decaying level $1s\,2p\,{}^1P_1$ to the metastable state

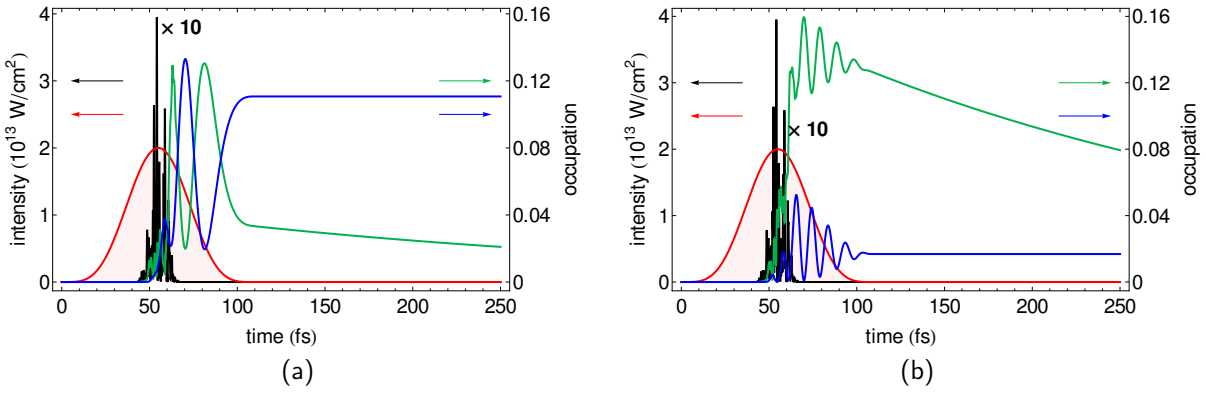

Figure 5.3: (a) and (b) as in Fig. 5.2, for a cosine-squared optical pulse (red) centered at the same $T_{\mathrm{L}0} = 55\,\mathrm{fs}$ as the x-ray pulse.

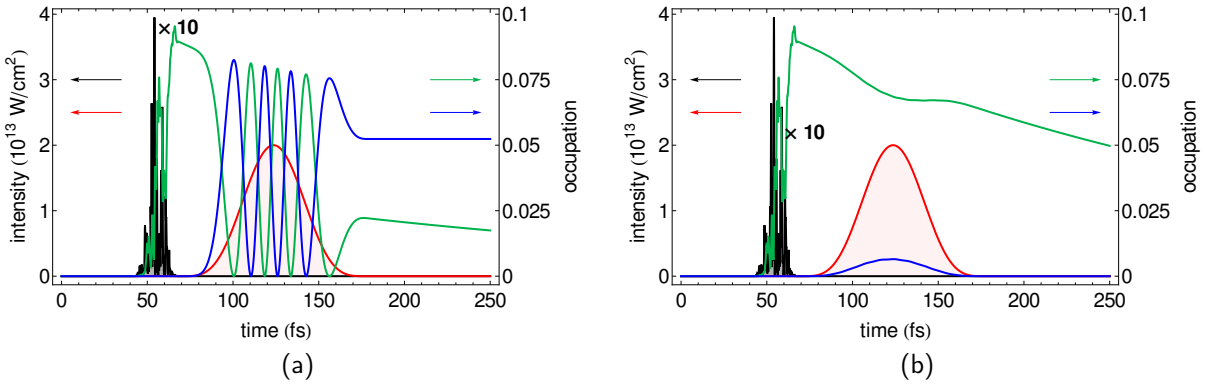

Figure 5.4: (a) and (b) as in Fig. 5.2, for a cosine-squared optical pulse (red) centered at $T_{\mathrm{L}0} = 125\,\mathrm{fs}$, with no temporal overlap with the x-ray pulse (black).

$1s\,2s\,{}^1S_0$, is displayed in Fig. 5.5. In Sec. 6.2 this will be studied analytically for the case of an optical pulse with hyperbolic-secant envelope and employed in the rest of the Chapter to implement a new x-ray pulse-shaping scheme via optical frequency combs.

5.2.2 A system driven by two optical pulses

In the previous part we have discussed how an optical pulse, following the interaction of a multi-level system with an x-ray pulse, can be used to transfer population (and coherence) from the excited state $1s\,2p\,{}^1P_1$ to the long-lived state $1s\,2s\,{}^1S_0$. We have shown that, when the interaction with the optical pulse is concluded, both excited levels are in general occupied (Figs. 5.2, 5.3, and 5.4), unless the parameters of the optical pulse are properly set to satisfy the condition $Q_{\mathrm{L}} = (2n+1)\pi$ (Fig. 5.5). Then, the population still occupying the excited state $1s\,2p\,{}^1P_1$ decays back to the ground state at the decay rate Γ_{21}, whereas the population stored in the metastable state $1s\,2s\,{}^1S_0$, decaying only because of two-photon emission at the much lower decay rate Γ_{31}, is marginally modified (Figs. 5.2, 5.3, and 5.4).

This population, effectively stored in the state $1s\,2s\,{}^1S_0$, can be released by a second optical pulse, as we show in Fig. 5.6. Here, we use two 266-nm pulses, both detuned from the optical

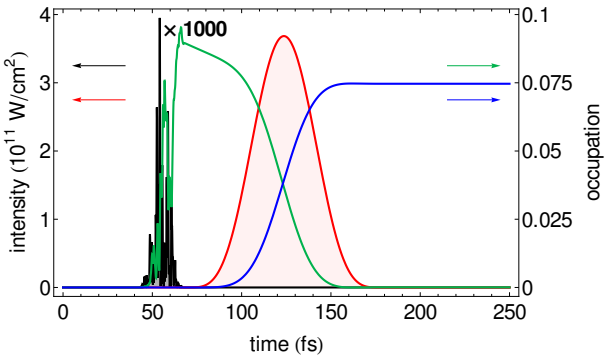

Figure 5.5: Three-level system driven by an x-ray SASE pulse (black), centered at $T_{\mathrm{X0}} = 55\,\mathrm{fs}$, together with a cosine-squared optical pulse (red), centered at $T_{\mathrm{L0}} = 125\,\mathrm{fs}$. The population of the excited state 2 (green) and of the metastable state 3 (blue) are depicted for a tuned optical pulse with pulse area $Q_{\mathrm{L}} = \pi$ and peak intensity $I_{\mathrm{L,max}} = 3.7 \times 10^{11}\,\mathrm{W/cm^2}$. The value of the intensity of the pulses is exhibited on the left-hand axis. The intensity of the x-ray pulse has still to be multiplied by a factor 1000. The value of the populations is exhibited on the right-hand axis.

transition and with trapezoidal envelope functions, $\mathcal{E}_{\mathrm{L},0}(t)$ and $\mathcal{E}_{\mathrm{L2},0}(t)$, as in Fig. 5.2b. Only the first pulse, centered at $T_{\mathrm{L0}} = 55\,\mathrm{fs}$, overlaps with the x-ray pulse. In contrast, the second optical pulse, centered at $T_{\mathrm{L20}} = 1835\,\mathrm{fs}$, is largely delayed, such that it drives the three-level system when the population of the excited state $1s\,2p\,{}^1P_1$ has already completely decayed. This pulse induces new Rabi oscillations which repopulate the excited level $1s\,2p\,{}^1P_1$ and thus lead to new decay of its population. This two-pulse scheme may be implemented with different pulse durations, intensities, and delays. By measuring the emitted signal as a function of the pulse delay, an experimental observation of the spontaneous decay ensuing from the interaction with a second optical pulse would allow, e.g., accurate lifetime measurements of the $1s\,2s\,{}^1S_0$ state.

5.3 Absorption spectrum of a transmitted ultrashort pulse

The ultrashort x-ray pulse (X) in Fig. 5.1 initiates the dynamic evolution of the three-level system, as we also observed in the previous discussion in Sec. 5.2. The coherent response of the medium is associated with the emission of x rays, whose interference with the initial pulse X leads to the reshaping of the pulse spectrum. The modification of the x-ray spectral features of the driving pulse ensuing from the coherent interaction with an ensemble of particles can be investigated by studying the absorption spectrum of the transmitted x-ray field, displaying the energy loss (or gain, depending on the sign of the spectrum) of the frequency components of the broadband pulse [81].

In this Section, we investigate the relationship between the absorption spectrum of the transmitted field and the atomic dipole response. In the particular case of the three-level system displayed in Fig. 5.1, by virtue of the low density of the atomic sample with which the electric fields interact, we can assume that the pulses propagate unperturbed through the medium. The total electric field is given by the sum of the driving fields, $\boldsymbol{\mathcal{E}}_{\mathrm{X}}(\boldsymbol{r}, t)$ and $\boldsymbol{\mathcal{E}}_{\mathrm{L}}(\boldsymbol{r}, t)$, and the emitted field $\boldsymbol{E}_{\mathrm{em}}(\boldsymbol{r}, t)$ resulting from the dipole response of the system,

$$\boldsymbol{\mathcal{E}}(\boldsymbol{r}, t) = \boldsymbol{\mathcal{E}}_{\mathrm{X}}(\boldsymbol{r}, t) + \boldsymbol{\mathcal{E}}_{\mathrm{L}}(\boldsymbol{r}, t) + \boldsymbol{E}_{\mathrm{em}}(\boldsymbol{r}, t). \tag{5.14}$$

The usual approach to the calculation of the absorption spectrum is semiclassical and is based

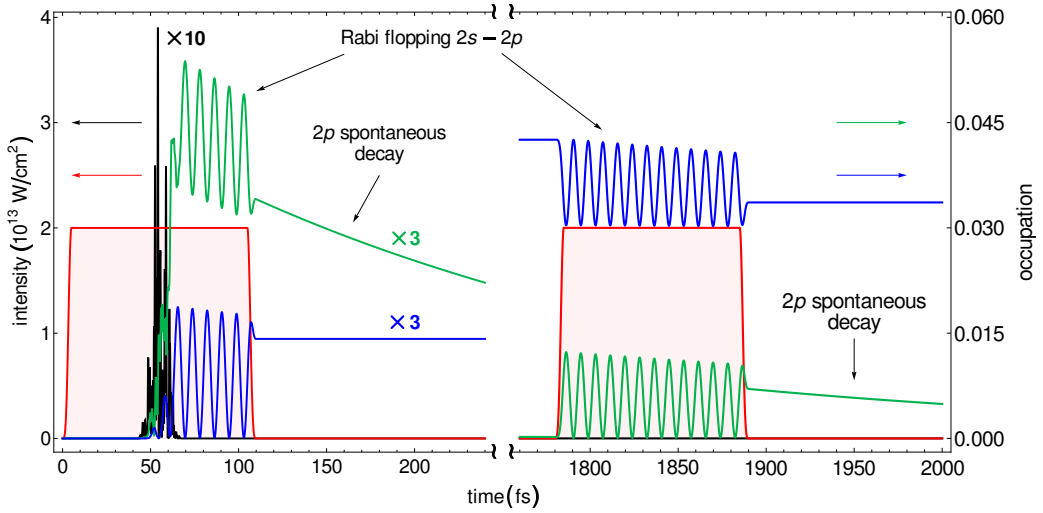

Figure 5.6: Three-level system driven by an x-ray SASE pulse (black), centered at $T_{\mathrm{X0}} = 55\,\mathrm{fs}$, together with two 266-nm, trapezoidal pulses (red). The first pulse is centered at the same time $T_{\mathrm{L0}} = 55\,\mathrm{fs}$ as the x-ray pulse, whereas the second pulse is delayed, $T_{\mathrm{L20}} = 1835\,\mathrm{fs}$, such that the population of the excited state has almost completely decayed before its arrival. The corresponding populations of the excited state $\varrho_{22}^{\mathrm{eq}}(t)$ (green) and of the metastable state $\varrho_{33}^{\mathrm{eq}}(t)$ (blue) display Rabi oscillations between the optically coupled states $1s\,2p\,{}^1P_1$ and $1s\,2s\,{}^1S_0$ and spontaneous decay of the excited state $1s\,2p\,{}^1P_1$. The value of the intensity of the pulses is exhibited on the left-hand axis. The intensity of the x-ray pulse has still to be multiplied by a factor 10. The value of the populations is exhibited on the right-hand axis.

on the solution of Maxwell's equation [53, 144, 146, 164, 213]

$$\left(\nabla^2 - \frac{1}{c^2}\frac{\partial^2}{\partial t^2}\right)\boldsymbol{\mathcal{E}}(\boldsymbol{r},\,t) = \frac{4\pi}{c^2}\frac{\partial^2}{\partial t^2}\boldsymbol{\mathcal{P}}(\boldsymbol{r},\,t), \tag{5.15}$$

with $\boldsymbol{\mathcal{P}}(\boldsymbol{r},\,t)$ being the macroscopic polarization in the medium. The derivation which is presented here leads to the same conclusions by explicitly taking advantage of the concepts and definitions which we introduced in the previous Chapters.

From Eqs. (2.32) and (2.60), the emitted electric field is described by the quantum operator

$$\hat{\boldsymbol{E}}_{\mathrm{em}}(\boldsymbol{r},\,t) = \hat{\boldsymbol{E}}_{\mathrm{em}}^{+}(\boldsymbol{r},\,t) + \hat{\boldsymbol{E}}_{\mathrm{em}}^{-}(\boldsymbol{r},\,t), \tag{5.16}$$

where $\hat{\boldsymbol{E}}_{\mathrm{em}}^{+}(\boldsymbol{r},\,t)$ $[\hat{\boldsymbol{E}}_{\mathrm{em}}^{-}(\boldsymbol{r},\,t)]$ is the positive[negative]-frequency component of the electric field, $\hat{\boldsymbol{E}}_{\mathrm{em}}^{-}(\boldsymbol{r},\,t) = [\hat{\boldsymbol{E}}_{\mathrm{em}}^{+}(\boldsymbol{r},\,t)]^{\dagger}$. The emitted field has two main contributions, i.e., a first term, $\hat{\boldsymbol{E}}_{21}(\boldsymbol{r},\,t) = \hat{\boldsymbol{E}}_{21}^{+}(\boldsymbol{r},\,t) + \hat{\boldsymbol{E}}_{21}^{-}(\boldsymbol{r},\,t)$, describing those x-ray photons emitted on the $2 \to 1$ transition, and a second part, $\hat{\boldsymbol{E}}_{23}(\boldsymbol{r},\,t) = \hat{\boldsymbol{E}}_{23}^{+}(\boldsymbol{r},\,t) + \hat{\boldsymbol{E}}_{23}^{-}(\boldsymbol{r},\,t)$, centered at the optical frequency of the transition $2 \to 3$. Each component of the electric field, in the electric-dipole approximation and in the far-field limit, can be written as the sum of spherical waves emitted by each one of the N ions which, upon interaction with the external fields, behave like oscillating dipoles [Eq. (2.68)]. The positive-frequency parts of the two components of the electric field can be related to the electric-dipole moment operators via the relation [53]

$$\hat{\boldsymbol{E}}_{21}^{+}(\boldsymbol{r},\,t) = \frac{\omega_{21}^2\,d_{21}^0}{c^2}\sum_{n=1}^{N}\frac{\hat{\sigma}_{12}^n(t - |\boldsymbol{r}-\boldsymbol{r}_n|/c)}{|\boldsymbol{r}-\boldsymbol{r}_n|}\left\{\hat{\boldsymbol{e}}_z - \frac{(\boldsymbol{r}-\boldsymbol{r}_n)\,[\hat{\boldsymbol{e}}_z\cdot(\boldsymbol{r}-\boldsymbol{r}_n)]}{|\boldsymbol{r}-\boldsymbol{r}_n|^2}\right\}, \tag{5.17a}$$

$$\hat{\boldsymbol{E}}_{23}^{+}(\boldsymbol{r},\,t) = \frac{\omega_{23}^2\,d_{23}^0}{c^2}\sum_{n=1}^{N}\frac{\hat{\sigma}_{32}^n(t - |\boldsymbol{r}-\boldsymbol{r}_n|/c)}{|\boldsymbol{r}-\boldsymbol{r}_n|}\left\{\hat{\boldsymbol{e}}_z - \frac{(\boldsymbol{r}-\boldsymbol{r}_n)\,[\hat{\boldsymbol{e}}_z\cdot(\boldsymbol{r}-\boldsymbol{r}_n)]}{|\boldsymbol{r}-\boldsymbol{r}_n|^2}\right\}. \tag{5.17b}$$

The semiclassical, x-ray emitted field $\boldsymbol{E}_{\mathrm{X,em}}(\boldsymbol{r},\,t)$ is

$$\boldsymbol{E}^{+}_{\mathrm{X,em}}(\boldsymbol{r},\,t) = \langle \hat{\boldsymbol{E}}^{+}_{21}(\boldsymbol{r},\,t)\rangle = \\ \frac{\omega_{21}^2\, d_{21}^0}{c^2}\sum_{n=1}^{N}\frac{\langle\hat{\varsigma}^n_{12}(t-|\boldsymbol{r}-\boldsymbol{r}_n|/c)\rangle}{|\boldsymbol{r}-\boldsymbol{r}_n|}\,\mathrm{e}^{-\mathrm{i}[\omega_{\mathrm{X}}(t-|\boldsymbol{r}-\boldsymbol{r}_n|/c)-\boldsymbol{k}_{\mathrm{X}}\cdot\boldsymbol{r}_n+\varphi_{\mathrm{X},0}]}\left\{\hat{\boldsymbol{e}}_z-\frac{(\boldsymbol{r}-\boldsymbol{r}_n)\,[\hat{\boldsymbol{e}}_z\cdot(\boldsymbol{r}-\boldsymbol{r}_n)]}{|\boldsymbol{r}-\boldsymbol{r}_n|^2}\right\}. \tag{5.18}$$

Along with the quantum operators, also the (semi)classical electric fields can be divided into a positive- and negative-frequency part, e.g., $\boldsymbol{\mathcal{E}}_{\mathrm{X}}(\boldsymbol{r},\,t) = \boldsymbol{\mathcal{E}}^{+}_{\mathrm{X}}(\boldsymbol{r},\,t) + \boldsymbol{\mathcal{E}}^{-}_{\mathrm{X}}(\boldsymbol{r},\,t)$, with $\boldsymbol{\mathcal{E}}^{-}_{\mathrm{X}}(\boldsymbol{r},\,t) = [\boldsymbol{\mathcal{E}}^{+}_{\mathrm{X}}(\boldsymbol{r},\,t)]^*$ and

$$\boldsymbol{\mathcal{E}}^{+}_{\mathrm{X}}(\boldsymbol{r},\,t) = \frac{1}{2}\,\mathcal{E}_{\mathrm{X},0}(t-\boldsymbol{r}\cdot\hat{\boldsymbol{e}}_y/c)\,\mathrm{e}^{-\mathrm{i}[\omega_{\mathrm{X}}t+\varphi_{\mathrm{X}}(t-\boldsymbol{r}\cdot\hat{\boldsymbol{e}}_y/c)+\varphi_{\mathrm{X},0}-\boldsymbol{k}_{\mathrm{X}}\cdot\boldsymbol{r}]}\,\hat{\boldsymbol{e}}_z. \tag{5.19}$$

An x-ray spectrometer placed in the forward $\hat{\boldsymbol{e}}_y$ direction, at distance r from the ensemble of ions, will measure the total spectrum of the transmitted field. From Eqs. (2.129) and (2.130), this spectrum is given by

$$S(r\,\hat{\boldsymbol{e}}_y,\,\omega) = \int_{-\infty}^{\infty}\int_{-\infty}^{\infty}\left\langle\left(\boldsymbol{\mathcal{E}}^{-}_{\mathrm{X}}(r\,\hat{\boldsymbol{e}}_y,\,t_1)+\hat{\boldsymbol{E}}^{-}_{21}(r\,\hat{\boldsymbol{e}}_y,\,t_1)\right)\cdot\left(\boldsymbol{\mathcal{E}}^{+}_{\mathrm{X}}(r\,\hat{\boldsymbol{e}}_y,\,t_2)+\hat{\boldsymbol{E}}^{+}_{21}(r\,\hat{\boldsymbol{e}}_y,\,t_2)\right)\right\rangle \\ \times\,\mathrm{e}^{-\mathrm{i}\omega(t_1-t_2)}\,\mathrm{d}t_1\,\mathrm{d}t_2. \tag{5.20}$$

The spectrum $S(r\,\hat{\boldsymbol{e}}_y,\,\omega)$ consists of the sum of the following terms:

$$S_1(r\,\hat{\boldsymbol{e}}_y,\,\omega) = \left|\int_{-\infty}^{\infty}\boldsymbol{\mathcal{E}}^{+}_{\mathrm{X}}(r\,\hat{\boldsymbol{e}}_y,\,t)\,\mathrm{e}^{\mathrm{i}\omega t}\,\mathrm{d}t\right|^2, \tag{5.21a}$$

$$S_2(r\,\hat{\boldsymbol{e}}_y,\,\omega) = 2\,\mathbf{Re}\left\{\int_{-\infty}^{\infty}\left(\boldsymbol{\mathcal{E}}^{-}_{\mathrm{X}}(r\,\hat{\boldsymbol{e}}_y,\,t_1)\,\mathrm{e}^{-\mathrm{i}\omega t_1}\right)\mathrm{d}t_1\cdot\int_{-\infty}^{\infty}\left(\boldsymbol{E}^{+}_{\mathrm{X,em}}(r\,\hat{\boldsymbol{e}}_y,\,t_2)\,\mathrm{e}^{\mathrm{i}\omega t_2}\right)\mathrm{d}t_2\right\}, \tag{5.21b}$$

$$S_3(r\,\hat{\boldsymbol{e}}_y,\,\omega) = \int_{-\infty}^{\infty}\int_{-\infty}^{\infty}\langle\hat{\boldsymbol{E}}^{-}_{21}(r\,\hat{\boldsymbol{e}}_y,\,t_1)\cdot\hat{\boldsymbol{E}}^{+}_{21}(r\,\hat{\boldsymbol{e}}_y,\,t_2)\rangle\,\mathrm{e}^{-\mathrm{i}\omega(t_1-t_2)}\,\mathrm{d}t_1\,\mathrm{d}t_2. \tag{5.21c}$$

The first term $S_1(r\,\hat{\boldsymbol{e}}_y,\,\omega)$ represents the spectrum of the initial driving x-ray pulse. The second term $S_2(r\,\hat{\boldsymbol{e}}_y,\,\omega)$ is yielded by the interference between the driving pulse and the emitted x-ray photons, whose properties are optically manipulated by the driving field $\boldsymbol{\mathcal{E}}_{\mathrm{L}}(\boldsymbol{r},\,t)$. Finally, $S_3(r\,\hat{\boldsymbol{e}}_y,\,\omega)$ is the spectrum of resonance fluorescence of the system in the forward direction, which we investigated in the previous Chapters.

The absorption spectrum

$$\sigma(r\,\hat{\boldsymbol{e}}_y,\,\omega) = \frac{S(r\,\hat{\boldsymbol{e}}_y,\,\omega)-S_1(r\,\hat{\boldsymbol{e}}_y,\,\omega)}{S_1(r\,\hat{\boldsymbol{e}}_y,\,\omega)} \approx 2\,\mathbf{Re}\left\{\frac{\int_{-\infty}^{\infty}\hat{\boldsymbol{e}}_z\cdot\boldsymbol{E}^{+}_{\mathrm{X,em}}(r\,\hat{\boldsymbol{e}}_y,\,t)\,\mathrm{e}^{\mathrm{i}\omega(t-r/c)}\,\mathrm{d}t}{\int_{-\infty}^{\infty}\hat{\boldsymbol{e}}_z\cdot\boldsymbol{\mathcal{E}}^{+}_{\mathrm{X}}(r\,\hat{\boldsymbol{e}}_y,\,t)\,\mathrm{e}^{\mathrm{i}\omega(t-r/c)}\,\mathrm{d}t}\right\} \tag{5.22}$$

is defined as the difference between the total spectrum of the transmitted field $S(r\,\hat{\boldsymbol{e}}_y,\,\omega)$ and the initial spectrum of the driving pulse $S_1(r\,\hat{\boldsymbol{e}}_y,\,\omega)$, normalized to $S_1(r\,\hat{\boldsymbol{e}}_y,\,\omega)$. In the previous identity we have used the fact that the emitted electric field is polarized in the z direction, as we are going to show in the following. Since the duration of the driving x-ray pulse $\boldsymbol{\mathcal{E}}_{\mathrm{X}}(r\,\hat{\boldsymbol{e}}_y,\,t)$ is much shorter than the time scale in which the emitted electric field $\boldsymbol{E}^{+}_{\mathrm{X,em}}(r\,\hat{\boldsymbol{e}}_y,\,t)$ evolves, for the calculation of the absorption spectrum we can rely on the approximation

$$\hat{\boldsymbol{e}}_z\cdot\boldsymbol{\mathcal{E}}^{+}_{\mathrm{X}}(r\,\hat{\boldsymbol{e}}_y,\,t) \approx B\,\delta(t-T_0-r/c)\,\mathrm{e}^{-\mathrm{i}(\omega_{\mathrm{X}}T_0+\varphi_{\mathrm{X},0})}, \tag{5.23a}$$

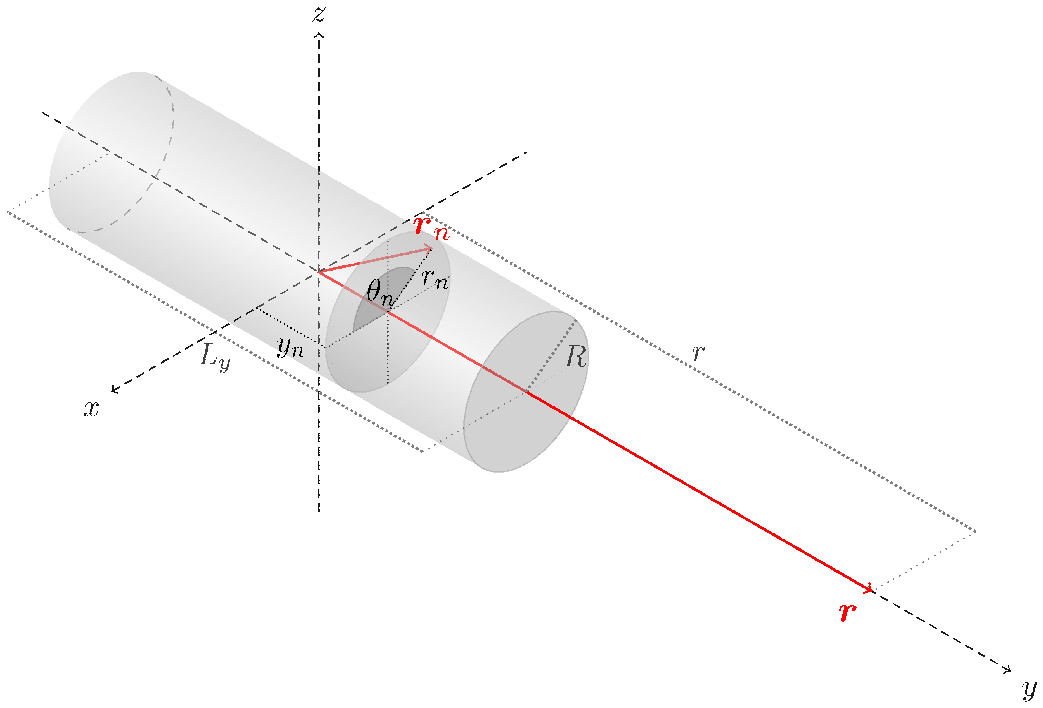

Figure 5.7: Reference frame for the calculation of the total emitted x-ray field at $\boldsymbol{r} = r\,\hat{\boldsymbol{e}}_y$.

$$\begin{aligned}\int_{-\infty}^{\infty} \hat{\boldsymbol{e}}_z \cdot \boldsymbol{\mathcal{E}}^{+}_{\mathrm{X}}(r\,\hat{\boldsymbol{e}}_y,\,t)\,\mathrm{e}^{\mathrm{i}\omega(t-r/c)}\,\mathrm{d}t &= \int_{-\infty}^{\infty} B\,\delta(t-T_0-r/c)\,\mathrm{e}^{-\mathrm{i}(\omega_{\mathrm{X}}T_0+\varphi_{\mathrm{X},0})}\,\mathrm{e}^{\mathrm{i}\omega(t-r/c)}\,\mathrm{d}t \\ &= B\,\mathrm{e}^{\mathrm{i}(\omega-\omega_{\mathrm{X}})T_0}\,\mathrm{e}^{-\mathrm{i}\varphi_{\mathrm{X},0}}.\end{aligned} \tag{5.23b}$$

The total emitted field $\boldsymbol{E}_{\mathrm{X,em}}(r\,\hat{\boldsymbol{e}}_y,\,t)$ ensues from the spherical waves emitted by each one of the N atoms. We assume a cylindrical volume V with constant density N/V, length L_y and radius R. By choosing the reference frame depicted in Fig. 5.7, in which the vector $\boldsymbol{r}_n$ has components $\boldsymbol{r}_n = y_n\,\hat{\boldsymbol{e}}_y + r_n(\cos\theta_n\,\hat{\boldsymbol{e}}_x + \sin\theta_n\,\hat{\boldsymbol{e}}_z)$, with $y_n \in [-L_y/2,\,L_y/2]$, $\theta_n \in [0,\,2\pi]$, and $r_n \in [0,\,R]$, such that $|\boldsymbol{r}-\boldsymbol{r}_n|^2 = (r-y_n)^2+r_n^2$, we can approximate the sum over the N particles with the following integral:

$$\begin{aligned}\boldsymbol{E}^{+}_{\mathrm{X,em}}(r\,\hat{\boldsymbol{e}}_y,\,t) = \frac{N}{V}\,\mathrm{e}^{-\mathrm{i}\varphi_{\mathrm{X},0}}\,\frac{\omega_{21}^2\,d_{21}^0}{c^2}\int_{-L_y/2}^{L_y/2}\mathrm{e}^{\mathrm{i}k_{\mathrm{X}}y_n}\int_0^R r_n\frac{\langle\hat{\varsigma}^n_{12}(t-|\boldsymbol{r}-\boldsymbol{r}_n|/c)\rangle}{|\boldsymbol{r}-\boldsymbol{r}_n|^3}\,\mathrm{e}^{-\mathrm{i}\omega_{\mathrm{X}}(t-|\boldsymbol{r}-\boldsymbol{r}_n|/c)} \\ \times\int_0^{2\pi}\left\{[(r-y_n)^2+r_n^2\,\cos^2\theta_n]\hat{\boldsymbol{e}}_z+[r_n^2\,\sin\theta_n\,\cos\theta_n]\hat{\boldsymbol{e}}_x+[r_n\,(r-y_n)\,\sin\theta_n]\hat{\boldsymbol{e}}_y\right\}\mathrm{d}\theta_n\,\mathrm{d}r_n\,\mathrm{d}y_n.\end{aligned} \tag{5.24}$$

The integral over θ_n vanishes along the y and x directions: The field is therefore polarized in the z direction and is equal to

$$\begin{aligned}\boldsymbol{E}^{+}_{\mathrm{X,em}}(r\,\hat{\boldsymbol{e}}_y,\,t) = \hat{\boldsymbol{e}}_z\,\frac{2\pi N\omega_{21}^2 d_{21}^0}{Vc^2}\,\mathrm{e}^{-\mathrm{i}\varphi_{\mathrm{X},0}} \\ \times\int_{-L_y/2}^{L_y/2}\int_0^R\frac{\langle\hat{\varsigma}^n_{12}(t-|\boldsymbol{r}-\boldsymbol{r}_n|/c)\rangle}{|\boldsymbol{r}-\boldsymbol{r}_n|}\,\mathrm{e}^{-\mathrm{i}\omega_{\mathrm{X}}(t-|\boldsymbol{r}-\boldsymbol{r}_n|/c-y_n/c)}\,r_n\,\mathrm{d}r_n\,\mathrm{d}y_n.\end{aligned} \tag{5.25}$$

We exploit now the fact that, from Eq. (5.12), $\hat{\varsigma}^n_{12}(t) = \hat{\varsigma}^{n'}_{12}[t+(y_{n'}-y_n)/c] = \hat{\varsigma}^{\mathrm{eq}}_{12}[t-y_n/c]$, where the operator $\hat{\varsigma}^{\mathrm{eq}}_{12}(t)$, related to the element of the density matrix $\varrho^{\mathrm{eq}}_{21}(t)$, is associated with

a particle at position $\boldsymbol{r}_0 = \mathbf{0}$. With the change of variables $g = t - |\boldsymbol{r} - \boldsymbol{r}_n|/c + (r - y_n)/c$, one can rewrite the previous integral as

$$\boldsymbol{E}^{+}_{\mathrm{X,em}}(r\,\hat{\boldsymbol{e}}_y,\,t) = \hat{\boldsymbol{e}}_z\,\frac{2\pi N L_y \omega_{21}^2 d_{21}^0}{Vc}\,\mathrm{e}^{-\mathrm{i}\varphi_{\mathrm{X},0}}\int_{t-R^2/(2rc)}^{t}\langle\hat{\varsigma}^{\mathrm{eq}}_{12}(g-r/c)\rangle\,\mathrm{e}^{-\mathrm{i}\omega_{\mathrm{X}}(g-r/c)}\,\mathrm{d}g, \tag{5.26}$$

where we have approximated the lower limit of the integral in g with

$$t - \frac{\sqrt{(r-y_n)^2 + R^2} - (r - y_n)}{c} \approx t - \frac{R^2}{2(r-y_n)c} \approx t - \frac{R^2}{2rc}. \tag{5.27}$$

Going back to the absorption spectrum, by exploiting the properties of the Fourier transform of the integral of a function, we can see that the Fourier transform of the x-ray emitted field provides

$$\begin{aligned}
&\int_{-\infty}^{\infty}\hat{\boldsymbol{e}}_z\cdot\boldsymbol{E}^{+}_{\mathrm{X,em}}(r\,\hat{\boldsymbol{e}}_y,\,t)\,\mathrm{e}^{\mathrm{i}\omega(t-r/c)}\,\mathrm{d}t\\
&= \frac{2\pi N L_y\omega_{21}^2 d_{21}^0}{Vc}\,\mathrm{e}^{-\mathrm{i}\varphi_{\mathrm{X},0}}\int_{-\infty}^{\infty}\left[\int_{t-R^2/(2rc)}^{t}\langle\hat{\varsigma}^{\mathrm{eq}}_{12}(g-r/c)\rangle\,\mathrm{e}^{-\mathrm{i}\omega_{\mathrm{X}}(g-r/c)}\,\mathrm{d}g\right]\mathrm{e}^{\mathrm{i}\omega(t-r/c)}\,\mathrm{d}t\\
&\approx \mathrm{i}\,\frac{2\pi\omega_{21}}{c}\,\mathrm{e}^{-\mathrm{i}\varphi_{\mathrm{X},0}}\int_{-\infty}^{\infty}\frac{N\,L_y}{V}\,d_{21}^0\,\langle\hat{\varsigma}^{\mathrm{eq}}_{12}(t)\rangle\,\mathrm{e}^{\mathrm{i}(\omega-\omega_{\mathrm{X}})t}\,\mathrm{d}t\\
&= \mathrm{i}\,\frac{2\pi\omega_{21}}{c}\,\mathrm{e}^{-\mathrm{i}\varphi_{\mathrm{X},0}}\int_{-\infty}^{\infty}\mathcal{P}(\mathbf{0},\,t)\,\mathrm{e}^{\mathrm{i}(\omega-\omega_{\mathrm{X}})t}\,\mathrm{d}t,
\end{aligned} \tag{5.28}$$

where we have defined the mean polarization in the medium $\boldsymbol{\mathcal{P}}(\mathbf{0},t) = \frac{N\,L_y}{V}d_{21}^0\langle\hat{\varsigma}^{\mathrm{eq}}_{12}(t)\rangle\,\hat{\boldsymbol{e}}_z$, linearly polarized in the z direction, at position $\mathbf{0}$ and time t. The absorption spectrum is, therefore,

$$\begin{aligned}
\sigma(r\,\hat{\boldsymbol{e}}_y,\,\omega) &= 2\,\mathbf{Re}\left\{\frac{\int_{-\infty}^{\infty}\hat{\boldsymbol{e}}_z\cdot\boldsymbol{E}^{+}_{\mathrm{X,em}}(r\,\hat{\boldsymbol{e}}_y,\,t)\,\mathrm{e}^{\mathrm{i}\omega(t-r/c)}\,\mathrm{d}t}{\int_{-\infty}^{\infty}\hat{\boldsymbol{e}}_z\cdot\boldsymbol{\mathcal{E}}^{+}_{\mathrm{X}}(r\,\hat{\boldsymbol{e}}_y,\,t)\,\mathrm{e}^{\mathrm{i}\omega(t-r/c)}\,\mathrm{d}t}\right\}\\
&= \frac{4\pi\omega_{21}}{c}\,\mathbf{Im}\Big\{\frac{1}{B}\int_{-\infty}^{\infty}\mathcal{P}(t)\,\mathrm{e}^{\mathrm{i}(\omega-\omega_{\mathrm{X}})(t-T_0)}\,\mathrm{d}t\Big\},
\end{aligned} \tag{5.29}$$

which, by exploiting the general identity

$$\int_{-\infty}^{\infty}f^{*}(t)\,\mathrm{e}^{\mathrm{i}\varpi t}\,\mathrm{d}t = \Big\{\int_{-\infty}^{\infty}f(t)\,\mathrm{e}^{-\mathrm{i}\varpi t}\,\mathrm{d}t\Big\}^{*},$$

can be shown to be proportional to the imaginary part of the spectral dipole response of the system

$$\begin{aligned}
\sigma(r\,\hat{\boldsymbol{e}}_y,\,\omega) &\propto \omega_{21}\,\mathbf{Im}\Big\{\int_{-\infty}^{\infty}\varrho^{\mathrm{eq}}_{21}(t)\,\mathrm{e}^{\mathrm{i}(\omega-\omega_{\mathrm{X}})(t-T_0)}\,\mathrm{d}t\Big\}\\
&= -\,\omega_{21}\,\mathbf{Im}\Big\{\int_{-\infty}^{\infty}\varrho^{\mathrm{eq}}_{12}(t)\,\mathrm{e}^{-\mathrm{i}(\omega-\omega_{\mathrm{X}})(t-T_0)}\,\mathrm{d}t\Big\}.
\end{aligned} \tag{5.30}$$

In the next Chapter, the optical manipulation of the absorption spectrum 5.30 is investigated in the case in which an optical frequency comb is employed to drive the atomic system.

6 X-ray frequency combs via optically modified absorption

In the previous Chapter an optical pulse was employed to couple an x-ray-excited level to a nearby metastable state and thereby to store populations and coherences in this long-lived state. We also observed that a second optical pulse can be utilized to release these populations and coherences: A periodic release, therefore, would be featured if instead of a single pulse a periodic train of coherent pulses was employed. This leads us to the investigation which we discuss in the present Chapter.

Here, we study the time evolution of a three-level system which, after having been excited by an ultrashort x-ray pulse, is driven by a train of optical pulses. The effect of the coherent response of the atomic system on the absorption spectrum of the transmitted x-ray pulse is further investigated. The theoretical model is introduced in Sec. 6.1. In Sec. 6.2 we study analytically the time evolution of the atomic system and the associated absorption spectrum of the transmitted x-ray field when a single optical pulse follows the x-ray pulse, thus coupling the x-ray-excited state to a nearby level. This single-pulse solution is used recursively in Sec. 6.3 to analyze the time evolution of the three-level system and the associated x-ray absorption spectrum when an optical frequency comb is employed. Sec. 6.4 concludes the Chapter. Parts of this Chapter have been presented in Refs. [214] and [215].

6.1 Theoretical model

In the following, we employ the three-level system depicted in Fig. 6.1. The absorption spectrum of the transmitted x-ray pulse [Eq. (5.30)] ensues from quantum interference between the driving, ultrashort x-ray pulse (X,in in the figure) and the electric field (X,em in the figure) which is emitted as a result of the atomic dipole response, optically manipulated by the field $\boldsymbol{\mathcal{E}}_{\mathrm{C}}(\boldsymbol{r},\, t)$ driving the $2 \rightarrow 3$ transition. At time T_0, before the interaction with this optical field takes place, each particle is in an initial state described by the density matrix $\hat{\rho}^n(T_0)$. This initial state is prepared via the interaction with the ultrashort x-ray pulse $\boldsymbol{\mathcal{E}}_{\mathrm{X}}(\boldsymbol{r},\, t)$ [Eq. (5.1)] and the optical pulse $\boldsymbol{\mathcal{E}}_{\mathrm{L}}(\boldsymbol{r},\, t)$ [Eq. (5.2)] in Fig. 5.1. This preparatory stage, preceding the interaction with $\boldsymbol{\mathcal{E}}_{\mathrm{C}}(\boldsymbol{r},\, t)$, was already analyzed in the previous Chapter and, therefore, is not discussed here. The absorption spectrum of the transmitted x-ray field depends on the initial state $\hat{\rho}^n(T_0)$. In the following, we are going to solve the equations of motion (EOMs) and calculate the associated x-ray absorption spectrum (5.30) for a generic initial state $\hat{\rho}^n(T_0)$: The results will be subsequently analyzed for two specific sets of initial conditions, corresponding to different choices of the driving pulses $\boldsymbol{\mathcal{E}}_{\mathrm{X}}(\boldsymbol{r},\, t)$ and $\boldsymbol{\mathcal{E}}_{\mathrm{L}}(\boldsymbol{r},\, t)$ in the preparatory state which precedes the interaction with $\boldsymbol{\mathcal{E}}_{\mathrm{C}}(\boldsymbol{r},\, t)$.

The driving optical field

$$\boldsymbol{\mathcal{E}}_{\mathrm{C}}(\boldsymbol{r},\, t) = \mathcal{E}_{\mathrm{C},0}(t - \boldsymbol{r}\cdot\hat{\boldsymbol{e}}_y/c)\cos\left[\omega_{\mathrm{C}}t + \varphi_{\mathrm{C}}(t - \boldsymbol{r}\cdot\hat{\boldsymbol{e}}_y/c) + \varphi_{\mathrm{C},0} - \boldsymbol{k}_{\mathrm{C}}\cdot\boldsymbol{r}\right]\hat{\boldsymbol{e}}_z \tag{6.1}$$

is written by exploiting the same notation we already used in Eqs. (5.1) and (5.2). We also introduce the corresponding time- and space-dependent, complex Rabi frequency

$$\Omega^n_{\mathrm{RC}}(t) = \mathcal{E}_{\mathrm{C},0}(t - \boldsymbol{r}_n\cdot\hat{\boldsymbol{e}}_y/c)\,\mathrm{e}^{\mathrm{i}\,\varphi_{\mathrm{C}}(t - \boldsymbol{r}_n\cdot\hat{\boldsymbol{e}}_y/c)}\,d^0_{32}. \tag{6.2}$$

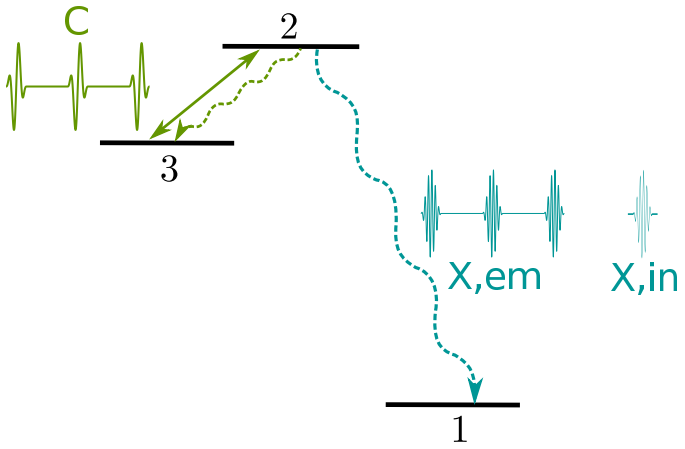

Figure 6.1: An ensemble of ions, after having been excited by an x-ray pulse (X,in blue) as in Fig. 5.1, is driven by an optical field (C, green), linearly polarized along the z direction and propagating in the y direction. The coherent response of the atomic system and the ensuing emission of x rays (X,em, blue) interfering with the driving x-ray pulse (X,in, blue) give rise to the modification of the absorption spectrum of the transmitted x-ray field

The time evolution of a system of N particles, described by the density matrices $\hat{\rho}^n(t)$, with $n \in \{1, \ldots, N\}$, and driven by $\boldsymbol{\mathcal{E}}_{\mathrm{C}}(\boldsymbol{r}, t)$, is given by the solution of the EOMs[1]

$$\frac{\partial \rho_{11}^n}{\partial t} = \Gamma_{31}\rho_{33}^n + \Gamma_{21}\rho_{22}^n, \tag{6.3a}$$

$$\frac{\partial \rho_{12}^n}{\partial t} = \left(\mathrm{i}\,\omega_{21} - \frac{\Gamma_{21}+\Gamma_{23}}{2}\right)\rho_{12}^n + \mathrm{i}\frac{\Omega_{\mathrm{RC}}^n}{2}\,\mathrm{e}^{\mathrm{i}(\omega_{\mathrm{C}}t - \boldsymbol{k}_{\mathrm{C}}\cdot\boldsymbol{r}_n + \varphi_{\mathrm{C},0})}\rho_{13}^n, \tag{6.3b}$$

$$\frac{\partial \rho_{13}^n}{\partial t} = \left(\mathrm{i}(\omega_{21}-\omega_{23}) - \frac{\Gamma_{31}}{2}\right)\rho_{13}^n + \mathrm{i}\frac{(\Omega_{\mathrm{RC}}^n)^*}{2}\,\mathrm{e}^{-\mathrm{i}(\omega_{\mathrm{C}}t - \boldsymbol{k}_{\mathrm{C}}\cdot\boldsymbol{r}_n + \varphi_{\mathrm{C},0})}\rho_{12}^n, \tag{6.3c}$$

$$\frac{\partial \rho_{22}^n}{\partial t} = -\mathrm{i}\frac{(\Omega_{\mathrm{RC}}^n)^*}{2}\,\mathrm{e}^{-\mathrm{i}(\omega_{\mathrm{C}}t - \boldsymbol{k}_{\mathrm{C}}\cdot\boldsymbol{r}_n + \varphi_{\mathrm{C},0})}\rho_{32}^n + \mathrm{i}\frac{\Omega_{\mathrm{RC}}^n}{2}\,\mathrm{e}^{\mathrm{i}(\omega_{\mathrm{C}}t - \boldsymbol{k}_{\mathrm{C}}\cdot\boldsymbol{r}_n + \varphi_{\mathrm{C},0})}\rho_{23}^n - (\Gamma_{21}+\Gamma_{23})\rho_{22}^n, \tag{6.3d}$$

$$\frac{\partial \rho_{23}^n}{\partial t} = \left(-\mathrm{i}\,\omega_{23} - \frac{\Gamma_{21}+\Gamma_{23}+\Gamma_{31}}{2}\right)\rho_{23}^n - \mathrm{i}\frac{(\Omega_{\mathrm{RC}}^n)^*}{2}\,\mathrm{e}^{-\mathrm{i}(\omega_{\mathrm{C}}t - \boldsymbol{k}_{\mathrm{C}}\cdot\boldsymbol{r}_n + \varphi_{\mathrm{C},0})}(\rho_{33}^n - \rho_{22}^n), \tag{6.3e}$$

$$\frac{\partial \rho_{33}^n}{\partial t} = -\mathrm{i}\frac{\Omega_{\mathrm{RC}}^n}{2}\,\mathrm{e}^{\mathrm{i}(\omega_{\mathrm{C}}t - \boldsymbol{k}_{\mathrm{C}}\cdot\boldsymbol{r}_n + \varphi_{\mathrm{C},0})}\rho_{23}^n + \mathrm{i}\frac{(\Omega_{\mathrm{RC}}^n)^*}{2}\,\mathrm{e}^{-\mathrm{i}(\omega_{\mathrm{C}}t - \boldsymbol{k}_{\mathrm{C}}\cdot\boldsymbol{r}_n + \varphi_{\mathrm{C},0})}\rho_{32}^n - \Gamma_{31}\rho_{33}^n + \Gamma_{23}\rho_{22}^n. \tag{6.3f}$$

These equations can be simplified by introducing the new slowly varying operators [53, 75, 195]

$$\hat{\varsigma}_{ii}^n(t) = \hat{\tilde{\varsigma}}_{ii}^n(t) = \hat{\sigma}_{ii}^n(t), \tag{6.4a}$$

$$\hat{\varsigma}_{21}^n(t) = \hat{\tilde{\varsigma}}_{21}^n(t) = \hat{\sigma}_{21}^n(t)\,\mathrm{e}^{-\mathrm{i}(\omega_{\mathrm{X}}t - \boldsymbol{k}_{\mathrm{X}}\cdot\boldsymbol{r}_n + \varphi_{\mathrm{X},0})}, \tag{6.4b}$$

$$\hat{\varsigma}_{23}^n(t) = \hat{\sigma}_{23}^n(t)\,\mathrm{e}^{-\mathrm{i}(\omega_{\mathrm{C}}t - \boldsymbol{k}_{\mathrm{C}}\cdot\boldsymbol{r}_n + \varphi_{\mathrm{C},0})}, \tag{6.4c}$$

$$\hat{\varsigma}_{31}^n(t) = \hat{\sigma}_{31}^n(t)\,\mathrm{e}^{-\mathrm{i}[(\omega_{\mathrm{X}}-\omega_{\mathrm{C}})t - (\boldsymbol{k}_{\mathrm{X}}-\boldsymbol{k}_{\mathrm{C}})\cdot\boldsymbol{r}_n + \varphi_{\mathrm{X},0} - \varphi_{\mathrm{C},0}]}, \tag{6.4d}$$

and the corresponding Hermitian conjugate operators $\hat{\varsigma}_{ij}^n(t) = [\hat{\varsigma}_{ji}^n(t)]^\dagger$, where we have used the x-ray frequency ω_{X}, wavevector $\boldsymbol{k}_{\mathrm{X}}$, and offset phase $\varphi_{\mathrm{X},0}$ from Eq. (5.1). By recalling the

[1] Also in this Chapter, as already done in the previous one, we assume that the minus sign in the interaction Hamiltonian $\hat{H}_{\mathrm{AL}}$ from Eq. 2.105 is included in the carrier-envelope phase $\varphi_{\mathrm{C},0}$.

definition of the operators $\hat{\varsigma}^n_{ij}(t)$, which we introduced in Eq. (5.9), we observe that $\hat{\varsigma}^n_{21}(t)$ and $\hat{\tilde{\varsigma}}^n_{21}(t)$ are identically defined, whereas $\hat{\varsigma}^n_{23}(t)$ and $\hat{\tilde{\varsigma}}^n_{23}(t)$ are in general two different operators, since they are determined by the potentially different carrier frequencies ω_{C} and ω_{L}. In terms of these new operators we also introduce the slowly varying density matrix $\hat{\varrho}(t)$, of matrix elements $\varrho^n_{ij}(t) = \langle \hat{\varsigma}^n_{ji}(t) \rangle$. By using the detunings

$$\Delta_{\mathrm{C}} = \omega_{23} - \omega_{\mathrm{C}} \tag{6.5}$$

and Δ_{X} [Eq. (5.10)], we can deduce from Eqs. (6.3) the EOMs which are satisfied by the matrix elements of $\hat{\varrho}^n(t)$, i.e.,

$$\frac{\partial \varrho^n_{11}}{\partial t} = \Gamma_{31}\varrho^n_{33} + \Gamma_{21}\varrho^n_{22}, \tag{6.6a}$$

$$\frac{\partial \varrho^n_{12}}{\partial t} = \left(\mathrm{i}\Delta_{\mathrm{X}} - \frac{\Gamma_{21}+\Gamma_{23}}{2}\right)\varrho^n_{12} + \mathrm{i}\frac{\Omega^n_{\mathrm{RC}}}{2}\varrho^n_{13}, \tag{6.6b}$$

$$\frac{\partial \varrho^n_{13}}{\partial t} = \left(\mathrm{i}(\Delta_{\mathrm{X}} - \Delta_{\mathrm{C}}) - \frac{\Gamma_{31}}{2}\right)\varrho^n_{13} + \mathrm{i}\frac{(\Omega^n_{\mathrm{RC}})^*}{2}\varrho^n_{12}, \tag{6.6c}$$

$$\frac{\partial \varrho^n_{22}}{\partial t} = -\mathrm{i}\frac{(\Omega^n_{\mathrm{RC}})^*}{2}\varrho^n_{32} + \mathrm{i}\frac{\Omega^n_{\mathrm{RC}}}{2}\varrho^n_{23} - (\Gamma_{21}+\Gamma_{23})\varrho^n_{22}, \tag{6.6d}$$

$$\frac{\partial \varrho^n_{23}}{\partial t} = \left(-\mathrm{i}\Delta_{\mathrm{C}} - \frac{\Gamma_{21}+\Gamma_{23}+\Gamma_{31}}{2}\right)\varrho^n_{23} - \mathrm{i}\frac{(\Omega^n_{\mathrm{RC}})^*}{2}(\varrho^n_{33} - \varrho^n_{22}), \tag{6.6e}$$

$$\frac{\partial \varrho^n_{33}}{\partial t} = -\mathrm{i}\frac{\Omega^n_{\mathrm{RC}}}{2}\varrho^n_{23} + \mathrm{i}\frac{(\Omega^n_{\mathrm{RC}})^*}{2}\varrho^n_{32} - \Gamma_{31}\varrho^n_{33} + \Gamma_{23}\varrho^n_{22}. \tag{6.6f}$$

The definition of $\varsigma^n_{ji}(t)$ and $\hat{\varsigma}^n_{ji}(t)$, together with the properties of the time- and space-dependent Rabi frequency $\Omega^n_{\mathrm{RC}}(t)$, allow one to generalize Eq. (5.13) and use Eqs. (6.6) to prove that

$$\varrho^n_{12}(t) = \varrho^{n'}_{12}[t + (\boldsymbol{r}_{n'} - \boldsymbol{r}_n)\cdot\hat{\boldsymbol{e}}_y/c], \quad \text{for any } t. \tag{6.7}$$

As a result, all the steps which were followed to derive the absorption spectrum in Eq. (5.30) can be similarly repeated also in the presence of the optical field $\boldsymbol{\mathcal{E}}_{\mathrm{C}}(\boldsymbol{r}, t)$.

The EOMs which are satisfied by $\varrho^{\mathrm{eq}}_{12}(t)$ can be obtained from Eq. (6.6) by setting $\boldsymbol{r}_0 = \boldsymbol{0}$. We further introduce the total decay rates Γ_2 and Γ_3 and the detuning Δ, i.e.,

$$\Gamma_2 = \Gamma_{21} + \Gamma_{23}, \quad \Gamma_3 = \Gamma_{31}, \quad \Delta = -\Delta_{\mathrm{C}}, \tag{6.8}$$

and assume that the electric field $\boldsymbol{\mathcal{E}}_{\mathrm{C}}(\boldsymbol{r}, t)$ has constant phase $\varphi_{\mathrm{C}}(t) = 0$, such that the Rabi frequency at the ion position $\boldsymbol{r}_0 = \boldsymbol{0}$ is real, i.e.,

$$\Omega_{\mathrm{RC}}(t) = \mathcal{E}_{\mathrm{C},0}(t)\, d^0_{32} = [\Omega_{\mathrm{RC}}(t)]^*. \tag{6.9}$$

We notice then that the two equations

$$\frac{\partial \varrho^{\mathrm{eq}}_{12}}{\partial t} = \left(\mathrm{i}\Delta_{\mathrm{X}} - \frac{\Gamma_2}{2}\right)\varrho^{\mathrm{eq}}_{12} + \mathrm{i}\frac{\Omega_{\mathrm{RC}}}{2}\varrho^{\mathrm{eq}}_{13}, \tag{6.10a}$$

$$\frac{\partial \varrho^{\mathrm{eq}}_{13}}{\partial t} = \left(\mathrm{i}(\Delta_{\mathrm{X}} + \Delta) - \frac{\Gamma_3}{2}\right)\varrho^{\mathrm{eq}}_{13} + \mathrm{i}\frac{\Omega_{\mathrm{RC}}}{2}\varrho^{\mathrm{eq}}_{12}, \tag{6.10b}$$

form a set of two linear differential equations which are completely independent of the other elements of the density matrix. In order to solve these equations, it is useful to introduce the rescaled variables

$$\bar{\varrho}_{12}(t) = \varrho_{12}^{\mathrm{eq}}\, \mathrm{e}^{\left(-\mathrm{i}\Delta_{\mathrm{X}}+\frac{\Gamma_2}{2}\right)(t-T_0)}, \qquad \bar{\varrho}_{13}(t) = \varrho_{13}^{\mathrm{eq}}\, \mathrm{e}^{\left(-\mathrm{i}(\Delta_{\mathrm{X}}+\Delta)+\frac{\Gamma_3}{2}\right)(t-T_0)}. \tag{6.11}$$

The ensuing set of two linear differential equations

$$\frac{\partial \bar{\varrho}_{12}}{\partial t} = +\mathrm{i}\frac{\Omega_{\mathrm{RC}}}{2}\, \bar{\varrho}_{13}\, \mathrm{e}^{\left(\mathrm{i}\Delta+\frac{\Gamma_2-\Gamma_3}{2}\right)(t-T_0)}, \tag{6.12a}$$

$$\frac{\partial \bar{\varrho}_{13}}{\partial t} = +\mathrm{i}\frac{\Omega_{\mathrm{RC}}}{2}\, \bar{\varrho}_{12}\, \mathrm{e}^{\left(-\mathrm{i}\Delta-\frac{\Gamma_2-\Gamma_3}{2}\right)(t-T_0)}, \tag{6.12b}$$

leads to the second-order differential equations

$$\begin{aligned} \frac{\partial^2 \bar{\varrho}_{12}}{\partial t^2} - \left(\frac{1}{\Omega_{\mathrm{RC}}}\frac{\partial \Omega_{\mathrm{RC}}}{\partial t} + \mathrm{i}\Delta + \frac{\Gamma_2-\Gamma_3}{2}\right)\frac{\partial \bar{\varrho}_{12}}{\partial t} + \frac{\Omega_{\mathrm{RC}}^2}{4}\bar{\varrho}_{12} = 0, \\ \frac{\partial^2 \bar{\varrho}_{13}}{\partial t^2} - \left(\frac{1}{\Omega_{\mathrm{RC}}}\frac{\partial \Omega_{\mathrm{RC}}}{\partial t} - \mathrm{i}\Delta - \frac{\Gamma_2-\Gamma_3}{2}\right)\frac{\partial \bar{\varrho}_{13}}{\partial t} + \frac{\Omega_{\mathrm{RC}}^2}{4}\bar{\varrho}_{13} = 0. \end{aligned} \tag{6.13}$$

In the next Sections, we solve Eq. (6.13) for a single optical pulse and a train of optical pulses: The solution is then employed to calculate the absorption spectrum of the transmitted x-ray field (5.30) and, thereby, to put forward a manipulation scheme for high-photon-energy comb generation.

6.2 Coherent control via a single optical pulse

In this Section, we focus on the interaction of a three-level system with a single hyperbolic-secant pulse driving the $2 \to 3$ transition, as shown in Fig. 6.1. This single-pulse solution will be iteratively used in the next Section to investigate the case of a periodic train of pulses and thereby to imprint a comb onto the x-ray absorption spectrum of the transmitted x-ray field.

6.2.1 Time evolution of the system

The solution of Eq. (6.13) in the single-pulse case can be studied analytically if the Rabi frequency is modeled by a hyperbolic-secant function, i.e., [68–71, 73, 163]

$$\Omega_{\mathrm{RC}}(t) = A\,\mathrm{sech}[\gamma(t-t_0)]. \tag{6.14}$$

Here, γ is the bandwidth of the pulse, associated with a FWHM duration given by $\tau_{\mathrm{FWHM}} = 2\,\mathrm{arccosh}(\sqrt{2})/\gamma$, the constant $A = d_{32}^0\sqrt{8\pi\alpha\, I_{\mathrm{C,max}}}$ is the peak amplitude of the Rabi frequency, associated with the peak intensity of the pulse $I_{\mathrm{C,max}}$, and t_0 is the time at which the pulse is centered. The pulse area defined in Eq. (2.115) is here equal to

$$Q_{\mathrm{C}} = \int_{-\infty}^{+\infty} \Omega_{\mathrm{RC}}(t)\ \mathrm{d}t = \frac{A}{\gamma}\pi = \pi\, d_{32}^0\sqrt{8\pi\alpha\, I_{\mathrm{C,max}}}\,\frac{\tau_{\mathrm{FWHM}}}{2\,\mathrm{arccosh}(\sqrt{2})}. \tag{6.15}$$

Details about the solution of the second-order differential equation (6.13) are provided in Appendix C: There, we show that this solution can be written in terms of the hypergeometric

functions ${}_2F_1(\alpha,\beta;\gamma;z)$. By assuming initial conditions at time T_0 given by $\varrho_{12}^{\mathrm{eq}}(T_0)=\bar{\varrho}_{12}(T_0)=\bar{\varrho}_{12,\mathrm{in}}$, $\varrho_{13}^{\mathrm{eq}}(T_0)=\bar{\varrho}_{13}(T_0)=\bar{\varrho}_{13,\mathrm{in}}$, and by introducing the parameters

$$a=-b=\frac{A}{2\gamma}, \tag{6.16a}$$

$$c=\frac{1}{2}-\mathrm{i}\frac{\Delta}{2\gamma}-\frac{\Gamma_2-\Gamma_3}{4\gamma}, \tag{6.16b}$$

the solution of Eq. (6.13) can be written in terms of the variable

$$z(t)=\frac{\tanh\left[\gamma(t-t_0)\right]+1}{2} \tag{6.17}$$

as

$$\begin{aligned}\bar{\varrho}_{12}(z)=&\,\bar{\varrho}_{12,\mathrm{in}}\,{}_2F_1(a,-a;c;z)\\&+\mathrm{i}\,\bar{\varrho}_{13,\mathrm{in}}\,\frac{a}{1-c}\,\mathrm{e}^{2\gamma\left(\frac{1}{2}-c\right)(t_0-T_0)}\,z^{1-c}\,(1-z)^{c}\,{}_2F_1(1-a,1+a;2-c;z),\end{aligned} \tag{6.18a}$$

$$\begin{aligned}\bar{\varrho}_{13}(z)=&\,\bar{\varrho}_{13,\mathrm{in}}\,{}_2F_1(a,-a;1-c;z)\\&+\mathrm{i}\,\bar{\varrho}_{12,\mathrm{in}}\,\frac{a}{c}\,\mathrm{e}^{2\gamma\left(c-\frac{1}{2}\right)(t_0-T_0)}\,z^{c}\,(1-z)^{1-c}\,{}_2F_1(1-a,1+a;1+c;z),\end{aligned} \tag{6.18b}$$

which, from the definitions in (6.11) and (6.17), lead to

$$\begin{aligned}\varrho_{12}^{\mathrm{eq}}(t)=&\,\mathrm{e}^{\mathrm{i}\Delta_{\mathrm{X}}(t-T_0)}\Big[\bar{\varrho}_{12,\mathrm{in}}\,\mathrm{e}^{-\frac{\Gamma_2}{2}(t-T_0)}\,{}_2F_1\left(a,-a;c;z(t)\right)\\&+\mathrm{i}\,\bar{\varrho}_{13,\mathrm{in}}\,\frac{a}{1-c}\,\mathrm{e}^{-\frac{\Gamma_3}{2}(t_0-T_0)}\,\mathrm{e}^{\mathrm{i}\Delta(t_0-T_0)}\,\mathrm{e}^{-\frac{\Gamma_2}{2}(t-t_0)}\\&\times\,[z(t)]^{1-c}[1-z(t)]^{c}\,{}_2F_1(1-a,1+a;2-c;z(t))\Big],\end{aligned} \tag{6.19a}$$

$$\begin{aligned}\varrho_{13}^{\mathrm{eq}}(t)=&\,\mathrm{e}^{\mathrm{i}\Delta_{\mathrm{X}}(t-T_0)}\Big[\bar{\varrho}_{13,\mathrm{in}}\,\mathrm{e}^{-\frac{\Gamma_3}{2}(t-T_0)}\,\mathrm{e}^{\mathrm{i}\Delta(t-T_0)}\,{}_2F_1\left(a,-a;1-c;z(t)\right)\\&+\mathrm{i}\,\bar{\varrho}_{12,\mathrm{in}}\,\frac{a}{c}\,\mathrm{e}^{-\frac{\Gamma_2}{2}(t_0-T_0)}\,\mathrm{e}^{-\frac{\Gamma_3}{2}(t-t_0)}\,\mathrm{e}^{\mathrm{i}\Delta(t-t_0)}\\&\times\,[z(t)]^{c}[1-z(t)]^{1-c}\,{}_2F_1(1-a,1+a;1+c;z(t))\Big].\end{aligned} \tag{6.19b}$$

Since we assume small decay rates compared to the width of the pulse, the condition $0<\mathbf{Re}(c)<1$ is satisfied. Furthermore, we notice that $a>0$ is a positive constant determined by the intensity of the optical pulse and related to the pulse area via

$$Q_{\mathrm{C}}=2a\pi. \tag{6.20}$$

By exploiting Eq. (C.31), the previous result (6.19) can be alternatively written as

$$\begin{aligned}\varrho_{12}^{\mathrm{eq}}(t)=&\,\mathrm{e}^{\mathrm{i}\Delta_{\mathrm{X}}(t-T_0)}\Big\{\bar{\varrho}_{12,\mathrm{in}}\,\mathrm{e}^{-\frac{\Gamma_2}{2}(t-T_0)}\,{}_2F_1\left(a,-a;c;z(t)\right)\\&+\mathrm{i}\,\bar{\varrho}_{13,\mathrm{in}}\,\frac{a}{2(1-c)}\,\mathrm{e}^{-\frac{\Gamma_3}{2}(t-T_0)}\,\mathrm{e}^{\mathrm{i}\Delta(t-T_0)}\\&\times\,\mathrm{sech}[\gamma(t-t_0)]\,{}_2F_1(1-a,1+a;2-c;z(t))\Big\},\end{aligned} \tag{6.21a}$$

$$\begin{aligned}\varrho_{13}^{\mathrm{eq}}(t)=&\,\mathrm{e}^{\mathrm{i}\Delta_{\mathrm{X}}(t-T_0)}\Big\{\bar{\varrho}_{13,\mathrm{in}}\,\mathrm{e}^{-\frac{\Gamma_3}{2}(t-T_0)}\,\mathrm{e}^{\mathrm{i}\Delta(t-T_0)}\,{}_2F_1\left(a,-a;1-c;z(t)\right)\\&+\mathrm{i}\,\bar{\varrho}_{12,\mathrm{in}}\,\frac{a}{2c}\,\mathrm{e}^{-\frac{\Gamma_2}{2}(t-T_0)}\\&\times\,\mathrm{sech}[\gamma(t-t_0)]\,{}_2F_1(1-a,1+a;1+c;z(t))\Big\}.\end{aligned} \tag{6.21b}$$

Even though this is generally true, the just found formula is of practical interest only when $a = n$, such that the hypergeometric functions are reduced to polynomials in z and the hyperbolic-secant function, approaching 0 at $t \to \infty$, does represent the vanishing behaviour of the complete function.

In order to better visualize the behaviour of the two functions in Eq. (6.19), we consider two different sets of initial conditions, corresponding to different preparatory schemes via the x-ray pulse $\boldsymbol{\mathcal{E}}_{\mathrm{X}}(\boldsymbol{r}, t)$ and the optical pulse $\boldsymbol{\mathcal{E}}_{\mathrm{L}}(\boldsymbol{r}, t)$.

6.2.1.1 X-ray-only preparation

When $\bar{\varrho}_{12,\mathrm{in}} \neq 0$ and $\bar{\varrho}_{13,\mathrm{in}} = 0$, situation simply achieved by exciting the system with an x-ray pulse $\boldsymbol{\mathcal{E}}_{\mathrm{X}}(\boldsymbol{r}, t)$ and no preparatory electric pulse $\boldsymbol{\mathcal{E}}_{\mathrm{L}}(\boldsymbol{r}, t)$, the solution of the EOMs is

$$\bar{\varrho}_{12}(z) = \bar{\varrho}_{12,\mathrm{in}}\, {}_2F_1(a, -a; c; z), \tag{6.22a}$$

$$\bar{\varrho}_{13}(z) = \mathrm{i}\, \bar{\varrho}_{12,\mathrm{in}}\, \frac{a}{c}\, \mathrm{e}^{2\gamma\left(c-\frac{1}{2}\right)(t_0-T_0)}\, z^c (1-z)^{1-c}\, {}_2F_1(1-a, 1+a; 1+c; z), \tag{6.22b}$$

such that

$$\varrho_{12}^{\mathrm{eq}}(t) = \bar{\varrho}_{12,\mathrm{in}}\, \mathrm{e}^{\mathrm{i}\Delta_{\mathrm{X}}(t-T_0)}\, \mathrm{e}^{-\frac{\Gamma_2}{2}(t-T_0)}\, {}_2F_1\left(a, -a; c; z(t)\right), \tag{6.23a}$$

$$\begin{aligned} \varrho_{13}^{\mathrm{eq}}(t) = {} & \mathrm{i}\, \bar{\varrho}_{12,\mathrm{in}}\, \frac{a}{c}\, \mathrm{e}^{\mathrm{i}\Delta_{\mathrm{X}}(t-T_0)}\, \mathrm{e}^{-\frac{\Gamma_2}{2}(t_0-T_0)}\, \mathrm{e}^{-\frac{\Gamma_3}{2}(t-t_0)}\, \mathrm{e}^{\mathrm{i}\Delta(t-t_0)} \\ & \times\, [z(t)]^c\, [1-z(t)]^{1-c}\, {}_2F_1(1-a, 1+a; 1+c; z(t)). \end{aligned} \tag{6.23b}$$

The final state which the system reaches when the interaction with the optical pulse $\boldsymbol{\mathcal{E}}_{\mathrm{C}}(\boldsymbol{r}, t)$ has concluded can be analyzed via the two constants

$$\mu_a = \lim_{t\to\infty}\, {}_2F_1\left(a, -a; c; z(t)\right) = \frac{[\Gamma(c)]^2}{\Gamma(c-a)\,\Gamma(c+a)}, \tag{6.24a}$$

$$\nu_a = \lim_{t\to\infty} [z(t)]^c [1-z(t)]^{1-c}\, {}_2F_1(1-a, 1+a; 1+c; z(t)) = \frac{\Gamma(1+c)\,\Gamma(1-c)}{\Gamma(1-a)\,\Gamma(1+a)} = \frac{c\, \csc(\pi c)}{a\, \csc(\pi a)}, \tag{6.24b}$$

where we have used Eq. (C.15) and the relation [216]

$$\Gamma\left(1+x\right)\, \Gamma\left(1-x\right) = \pi\, x\, \csc\left(\pi x\right). \tag{6.25}$$

These two quantities are important to understand the effect of the optical pulse $\boldsymbol{\mathcal{E}}_{\mathrm{C}}(\boldsymbol{r}, t)$ on the time evolution of the elements of the density matrix $\varrho_{12}^{\mathrm{eq}}(t)$ and $\varrho_{13}^{\mathrm{eq}}(t)$. For example, because of the poles of the Gamma function $\Gamma(z)$ for negative integers $z = -n$ [216–218], we can predict that μ_a and ν_a vanish when the following conditions are met,

$$\left.\begin{aligned} a = \mathbf{Re}(c) + m,\ m \in \mathbb{N} \\ 0 = \mathbf{Im}(c) \end{aligned}\right\} \quad \Rightarrow \quad \mu_a = 0, \tag{6.26a}$$

$$a = 1 + m,\ m \in \mathbb{N} \quad \Rightarrow \quad \nu_a = 0. \tag{6.26b}$$

A vanishing value of μ_a, obtained when the pulse intensity $I_{\mathrm{C,max}}$ is set such that Eq. (6.26a) is satisfied, guarantees that $\varrho_{12}^{\mathrm{eq}}(t)$ vanishes when the interaction with the pulse has concluded. The condition on the real part of c can be in general met, since $a > 0$ and $0 < \mathbf{Re}(c) < 1$. However, the condition on the imaginary part of c can be fulfilled only if the detuning is equal to 0.

On the other hand, a vanishing value of ν_a, implying that $\varrho_{13}^{\mathrm{eq}}(t) = 0$ when the interaction with $\boldsymbol{\mathcal{E}}_{\mathrm{C}}(\boldsymbol{r}, t)$ has concluded, is an essential requirement for the implementation of the recursive procedure we are going to describe and employ in Sec. 6.3. Owing to Eq. (6.20), the value of the pulse intensity for which $\nu_a = 0$, i.e., $a = n$ with $n \in \mathbb{N}_0$, corresponds to a pulse area which is an integer multiple of 2π. The corresponding value of μ_a is

$$\mu_n = {}_2F_1\left(n, -n; c; 1\right) = \frac{[\Gamma(c)]^2}{\Gamma(c+n)\,\Gamma(c-n)} = \frac{(c-n)_n}{(c)_n}, \tag{6.27}$$

where we have used the definition (C.11). For vanishing decay rates, $\mathit{\Gamma}_2 = \mathit{\Gamma}_3 = 0$, when

$$\mu_n = \frac{\left(\frac{1}{2} - \mathrm{i}\frac{\mathit{\Delta}}{2\gamma} - n\right)_n}{\left(\frac{1}{2} - \mathrm{i}\frac{\mathit{\Delta}}{2\gamma}\right)_n} = \prod_{j=0}^{n-1} \frac{\mathrm{i}\frac{\mathit{\Delta}}{2\gamma} + \left(\frac{1}{2} + j\right)}{\mathrm{i}\frac{\mathit{\Delta}}{2\gamma} - \left(\frac{1}{2} + j\right)} \;\Rightarrow\; |\mu_n| = 1, \tag{6.28}$$

the effect of the interaction with the pulse corresponds to a phase shift of $\varrho_{12}^{\mathrm{eq}}(t)$ given by $\arg(\mu_n)$. Furthermore, when also the detuning vanishes, $\mathit{\Delta} = 0$, one can observe that

$$\tilde{\mu}_n = {}_2F_1\left(n, -n; \tfrac{1}{2}; 1\right) = \cos\left(n\pi\right) = (-1)^n \;\Rightarrow\; |\mu_n| = 1,\ \arg\left(\mu_n\right) = n\pi \tag{6.29}$$

and conclude that this phase shift is equal to an integer multiple of π.

Vanishing values of ν_a are obtained also in the large-detuning limit, when $\mathit{\Delta} \gg \gamma$: By recalling the definition of c (6.16), one has namely that

$$\lim_{\mathbf{Im}(c)\to-\infty} \nu_a = \frac{1}{a\csc\left(\pi\, a\right)} \frac{2\,\mathrm{i}\left[\mathbf{Re}(c) + \mathrm{i}\ \mathbf{Im}(c)\right]}{\mathrm{e}^{\mathrm{i}\,\pi\ \mathbf{Re}(c)}\,\mathrm{e}^{-\pi\ \mathbf{Im}(c)}} = 0. \tag{6.30}$$

Also in this case, when the decay rates vanish, $\mathit{\Gamma}_2 = \mathit{\Gamma}_3 = 0$, the corresponding value of μ_a is given by a pure phase shift $\arg(\mu_a)$, as shown by

$$\begin{aligned} \lim_{\frac{\mathit{\Delta}}{\gamma}\to\infty} \mu_a &= \lim_{\frac{\mathit{\Delta}}{\gamma}\to\infty} \frac{\left[\Gamma\left(\frac{1}{2} - \mathrm{i}\frac{\mathit{\Delta}}{2\gamma}\right)\right]^2}{\Gamma\left(\frac{1}{2} - \mathrm{i}\frac{\mathit{\Delta}}{2\gamma} + a\right)\,\Gamma\left(\frac{1}{2} - \mathrm{i}\frac{\mathit{\Delta}}{2\gamma} - a\right)} \\ &= \lim_{\frac{\mathit{\Delta}}{\gamma}\to\infty} \prod_{k=0}^{\infty}\left[1 - \frac{a^2}{\left(\frac{1}{2} - \mathrm{i}\frac{\mathit{\Delta}}{2\gamma} + k\right)^2}\right] \end{aligned} \;\Rightarrow\; \lim_{\frac{\mathit{\Delta}}{\gamma}\to\infty} |\mu_a| = 1, \tag{6.31}$$

where we have used the equality [216]

$$\frac{\Gamma(\alpha)\Gamma(\beta)}{\Gamma(\alpha+\gamma)\Gamma(\beta-\gamma)} = \prod_{k=0}^{\infty}\left(1 + \frac{\gamma}{\alpha+k}\right)\left(1 - \frac{\gamma}{\beta+k}\right). \tag{6.32}$$

In order to visualize the time evolution of the matrix elements $\varrho_{12}^{\mathrm{eq}}(t)$ and $\varrho_{13}^{\mathrm{eq}}(t)$ and thus better understand the results we just presented, in the following we use our three-level model to describe an optical pulse $\boldsymbol{\mathcal{E}}_{\mathrm{C}}(\boldsymbol{r}, t)$ coupling the excited state $1s\,2p\,{}^1P_1$ (level 2) to the metastable state $1s\,2s\,{}^1S_0$ (level 3) in He-like Be^{2+} ions, with optical transition energy $\omega_{23} = 2.02\,\mathrm{eV}$. Level 1 is given by the ground state of the system. The decay rates $\mathit{\Gamma}_{21} = 1.2 \times 10^{11}\,\mathrm{s}^{-1}$ and $\mathit{\Gamma}_{23} = 8.7 \times 10^{6}\,\mathrm{s}^{-1}$ are calculated with `grasp2K` [200–202], whereas the two-photon decay rate $\mathit{\Gamma}_{31} = 1.82 \times 10^{4}\,\mathrm{s}^{-1}$ is taken from Ref. [212]. These values are also used for the calculation of the dipole moments $\boldsymbol{d}_{ij}$, i.e., for the calculation of the Rabi frequency (6.14). The transition energies, $\omega_{23} = 2.02$ eV and $\omega_{21} = 123.7$ eV, are taken from Ref. [191].

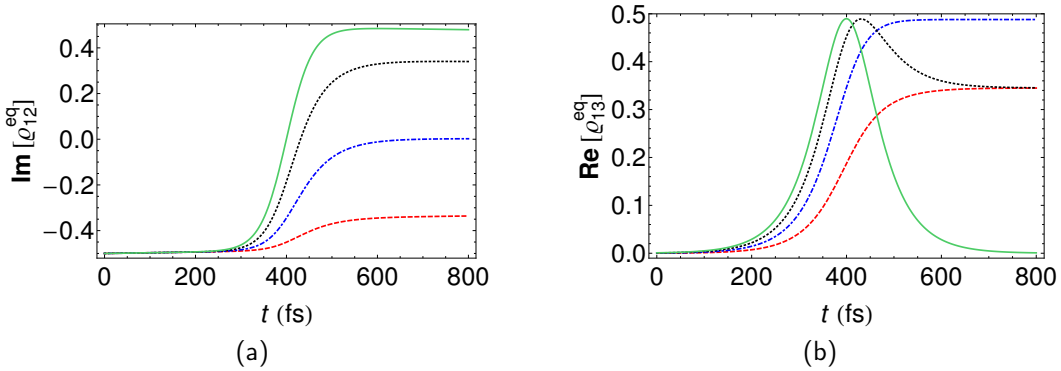

Figure 6.2: Off-diagonal elements of the three-level system of Fig. 6.1, (a) $\varrho_{12}^{\mathrm{eq}}(t)$ and (b) $\varrho_{13}^{\mathrm{eq}}(t)$, prepared at time $T_0 = 0$ in the initial state $\bar{\varrho}_{12,\mathrm{in}} = -\mathrm{i}/2$, $\bar{\varrho}_{13,\mathrm{in}} = 0$, and driven by a single optical pulse, tuned to the $1s\,2s\,{}^1S_0 \to 1s\,2p\,{}^1P_1$ optical transition of Be^{2+} ions at $\omega_{23} = 2.02\,\mathrm{eV}$, centered at $t_0 = 400\,\mathrm{fs}$, with FWHM duration of $\tau_{\mathrm{FWHM}} = 100\,\mathrm{fs}$ and peak intensities $I_{\mathrm{C,max}} = 1.6 \times 10^9\,\mathrm{W/cm^2}$ (red, dashed line), $I_{\mathrm{C,max}} = 6.4 \times 10^9\,\mathrm{W/cm^2}$ (blue, dotdashed line), $I_{\mathrm{C,max}} = 1.4 \times 10^{10}\,\mathrm{W/cm^2}$ (black, dotted line), and $I_{\mathrm{C,max}} = 2.6 \times 10^{10}\,\mathrm{W/cm^2}$ (green, solid line), corresponding to a pulse area $Q_{\mathrm{C}} = \pi/2$ (red, dashed line), $Q_{\mathrm{C}} = \pi$ (blue, dotdashed line), $Q_{\mathrm{C}} = 3\pi/2$ (black, dotted line), and $Q_{\mathrm{C}} = 2\pi$ (green, solid line), respectively.

In Fig. 6.2, we display the evolution of $\varrho_{12}^{\mathrm{eq}}(t)$ and $\varrho_{13}^{\mathrm{eq}}(t)$, initially prepared in $\bar{\varrho}_{12,\mathrm{in}} = -\mathrm{i}/2$, $\bar{\varrho}_{13,\mathrm{in}} = 0$, when a tuned optical pulse drives the $2 \to 3$ transition. Different lines are associated with different values of the pulse area. The green, solid line, corresponding to a pulse area of $Q_{\mathrm{C}} = 2\pi$, confirms the results which we predicted in Eqs. (6.26b) and (6.27), i.e., that for a 2π pulse the coherences between the ground state 1 and the two excited states 2 and 3 perform a finite number of Rabi cycles after which $\varrho_{13}^{\mathrm{eq}}(t)$ is led back to its vanishing initial value. Provided that the decay rates Γ_2 and Γ_3 are much smaller than the bandwidth of the driving pulse, the conclusions which were drawn from Eq. (6.26a) are clearly apparent from the blue, dotdashed line, corresponding to a pulse area of $Q_{\mathrm{C}} = \pi$: The function $\varrho_{12}^{\mathrm{eq}}(t)$ converges to 0 and, correspondingly, the coherence is transferred from the level 2 to the level 3, where it is stored owing to the almost negligible decay rate Γ_3.

In Fig. 6.3 we show how the off-diagonal elements $\varrho_{12}^{\mathrm{eq}}(t)$ and $\varrho_{13}^{\mathrm{eq}}(t)$ evolve in time when the atomic system is driven by a detuned pulse. Intensities corresponding to different values of the induced phase shift $\arg(\mu_a)$ are employed to depict the results. The utilized optical pulses have energy 1.5 eV, with detuning $\Delta = -0.52\,\mathrm{eV} \gg \gamma$, and the decay rates, in spite of their nonvanishing values, are much smaller than the pulse bandwidth γ. Therefore, one can employ the phase-shift description we deduced from Eq. (6.31), valid in the large-detuning limit and for vanishing decay rates, to interpret the displayed evolution in time of the system. The phase-shift mechanism due to the interaction with a detuned pulse is clearly apparent in Fig. 6.3: The amplitudes of both $|\varrho_{12}^{\mathrm{eq}}(t)|$ and $|\varrho_{13}^{\mathrm{eq}}(t)|$ are minimally perturbed by the presence of the optical pulse [Figs. 6.3a and 6.3c]. The phase, however, undergoes a phase shift $\Delta\phi = \arg(\mu_a)$ related to the intensity of the pulse via Eq. (6.24). For large values of the detuning $\Delta \gg \gamma$, this equation can be employed to recover an approximately linear increase of the phase shift $\Delta\phi$ with the pulse peak intensity [214], $\Delta\phi \approx -(1/2)\,\beta \int \mathcal{E}_{\mathrm{C},0}^2(t)\,dt$, where we have introduced the effective dynamic polarizability β [149, 150, 159] of the excited level $1s\,2p$. In Figs. 6.3b and 6.3d, Eq. (6.24) was namely used to determine the peak intensities corresponding to phase shifts equal to integer multiples of $\pi/4$.

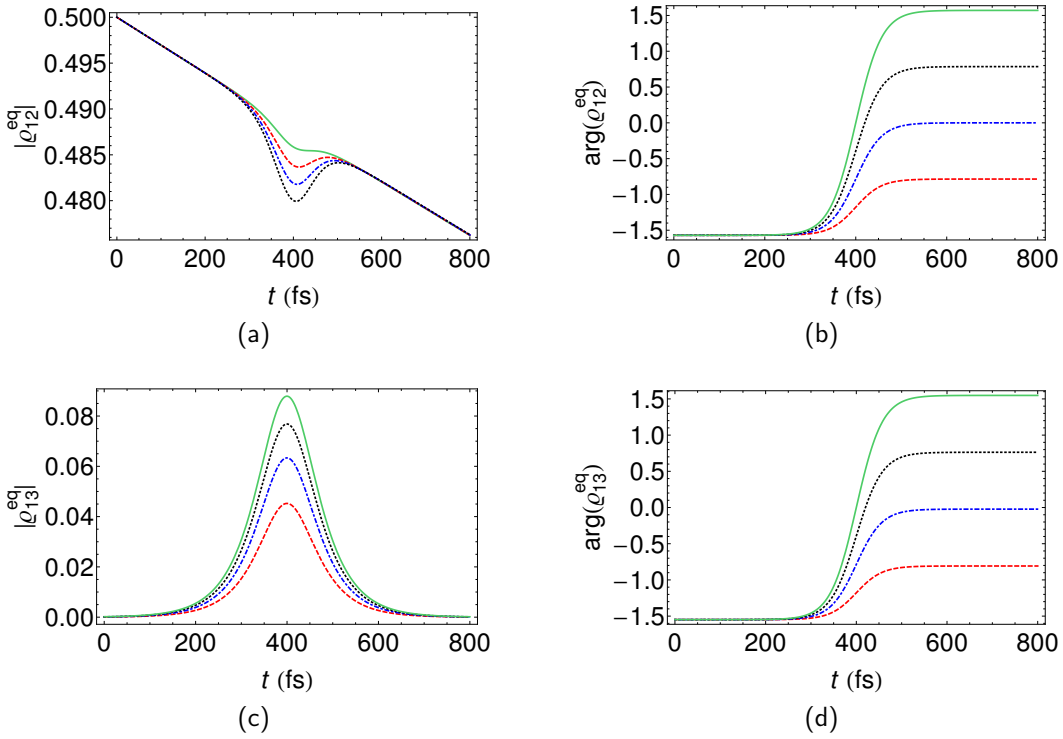

Figure 6.3: Off-diagonal elements of the three-level system of Fig. 6.1, (a) $|\varrho_{12}^{\mathrm{eq}}(t)|$, (b) $\arg[\varrho_{12}^{\mathrm{eq}}(t)]$, (c) $|\varrho_{13}^{\mathrm{eq}}(t)|$, (d) $\arg[\varrho_{13}^{\mathrm{eq}}(t)]$, prepared at time $T_0 = 0$ in the initial state $\bar{\varrho}_{12,\mathrm{in}} = -\mathrm{i}/2$, $\bar{\varrho}_{13,\mathrm{in}} = 0$, and driven by a single optical pulse with energy $\omega_{\mathrm{C}} = 1.5\,\mathrm{eV}$, and detuning $\Delta = -\Delta_{\mathrm{C}} = -0.52\,\mathrm{eV}$ with respect to the $1s\,2s\,{}^1S_0 \to 1s\,2p\,{}^1P_1$ optical transition of Be^{2+} ions at $\omega_{23} = 2.02\,\mathrm{eV}$. The pulse is centered at $t_0 = 400\,\mathrm{fs}$, with FWHM duration of $\tau_{\mathrm{FWHM}} = 100\,\mathrm{fs}$ and peak intensities $I_{\mathrm{C,max}} = 4.5 \times 10^{11}\,\mathrm{W/cm^2}$ (red, dashed line), $I_{\mathrm{C,max}} = 9.1 \times 10^{11}\,\mathrm{W/cm^2}$ (blue, dotdashed line), $I_{\mathrm{C,max}} = 1.4 \times 10^{12}\,\mathrm{W/cm^2}$ (black, dotted line), and $I_{\mathrm{C,max}} = 1.9 \times 10^{12}\,\mathrm{W/cm^2}$ (green, solid line), corresponding to phase shifts $\arg(\mu_a) = \pi/4$ (red, dashed line), $\arg(\mu_a) = \pi/2$ (blue, dotdashed line), $\arg(\mu_a) = 3\pi/4$ (black, dotted line), and $\arg(\mu_a) = \pi$ (green, solid line), respectively.

6.2.1.2 Coherence-storage preparation

In the previous part we have shown that a π-pulse mechanism can be used to store the coherence in the metastable state 3. By employing a similar pulse immediately after that the system has been excited by an x-ray pulse, one leads the system into a state which at time T_0, before the interaction with the optical field $\boldsymbol{\mathcal{E}}_{\mathrm{C}}(\boldsymbol{r}, t)$ takes place, is characterized by $\bar{\varrho}_{12,\mathrm{in}} = 0$ and $\bar{\varrho}_{13,\mathrm{in}} \neq 0$. Here and in the following we assume therefore that such an initial state at time T_0 has been obtained via a preparatory stage of the system, displayed in Fig. 5.1, which consists of an x-ray pulse followed by an optical pulse $\boldsymbol{\mathcal{E}}_{\mathrm{L}}(\boldsymbol{r}, t)$ with area $Q_{\mathrm{L}} = \pi$ and detuning $\Delta = 0$.

If the initial state is given by $\bar{\varrho}_{12,\mathrm{in}} = 0$ and $\bar{\varrho}_{13,\mathrm{in}} \neq 0$, then the solution of the EOMs (6.13) describing the interaction with $\boldsymbol{\mathcal{E}}_{\mathrm{C}}(\boldsymbol{r}, t)$ is given by

$$\bar{\varrho}_{12}(z) = \mathrm{i}\,\bar{\varrho}_{13,\mathrm{in}}\,\frac{a}{1-c}\,\mathrm{e}^{2\gamma\left(\frac{1}{2}-c\right)(t_0-T_0)}\,z^{1-c}\,(1-z)^c\,{}_2F_1(1-a, 1+a; 2-c; z), \tag{6.33a}$$

$$\bar{\varrho}_{13}(z) = \bar{\varrho}_{13,\mathrm{in}}\,{}_2F_1(a, -a; 1-c; z), \tag{6.33b}$$

and

$$\begin{aligned}\varrho_{12}^{\mathrm{eq}}(t) = &\mathrm{i}\,\bar{\varrho}_{13,\mathrm{in}}\,\frac{a}{1-c}\,\mathrm{e}^{\mathrm{i}\Delta_{\mathrm{X}}(t-T_0)}\,\mathrm{e}^{-\frac{\Gamma_3}{2}(t_0-T_0)}\,\mathrm{e}^{\mathrm{i}\Delta(t_0-T_0)}\,\mathrm{e}^{-\frac{\Gamma_2}{2}(t-t_0)}\\ &\times\,[z(t)]^{1-c}\,[1-z(t)]^{c}\,{}_2F_1(1-a,1+a;2-c;z(t)),\end{aligned} \tag{6.34a}$$

$$\varrho_{13}^{\mathrm{eq}}(t) = \bar{\varrho}_{13,\mathrm{in}}\,\mathrm{e}^{\mathrm{i}\Delta_{\mathrm{X}}(t-T_0)}\,\mathrm{e}^{-\frac{\Gamma_3}{2}(t-T_0)}\,\mathrm{e}^{\mathrm{i}\Delta(t-T_0)}\,{}_2F_1\left(a,-a;1-c;z(t)\right). \tag{6.34b}$$

Also in this case it is useful to describe the final state reached by the system after having interacted with the optical pulse $\boldsymbol{\mathcal{E}}_{\mathrm{C}}(\boldsymbol{r},\,t)$ in terms of two constants, i.e.,

$$\begin{aligned}\lambda_a &= \lim_{t\to\infty}[z(t)]^{1-c}\,[1-z(t)]^{c}\,{}_2F_1(1-a,1+a;2-c;z(t)) = \frac{\Gamma(c)\,\Gamma(2-c)}{\Gamma(1-a)\,\Gamma(1+a)}\\ &= \frac{(1-c)\,\csc\left[\pi(1-c)\right]}{a\,\csc\left(\pi a\right)},\end{aligned} \tag{6.35a}$$

$$\xi_a = \lim_{t\to\infty}\,{}_2F_1\left(a,-a;1-c;z(t)\right) = \frac{[\Gamma(1-c)]^2}{\Gamma(1-c-a)\,\Gamma(1-c+a)}, \tag{6.35b}$$

where we have taken advantage of Eq. (C.15). These two quantities contain the necessary information to analyze the effect of $\boldsymbol{\mathcal{E}}_{\mathrm{C}}(\boldsymbol{r},\,t)$ on the time evolution of $\varrho_{12}^{\mathrm{eq}}(t)$ and $\varrho_{13}^{\mathrm{eq}}(t)$. For instance, we can identify those conditions which, if satisfied, render λ_a and ξ_a equal to 0, i.e.,

$$a = 1+m,\; m\in\mathbb{N} \qquad \Rightarrow \qquad \lambda_a = 0, \tag{6.36a}$$

$$\left.\begin{aligned}a &= \mathbf{Re}(1-c)+m,\; m\in\mathbb{N}\\ 0 &= \mathbf{Im}(1-c)\end{aligned}\right\} \qquad \Rightarrow \qquad \xi_a = 0. \tag{6.36b}$$

By properly tuning the pulse intensity $I_{\mathrm{C,max}}$ in order to fulfill the condition in Eq. (6.36b), ξ_a vanishes and, correspondingly, $\varrho_{13}^{\mathrm{eq}}(t)$ converges to 0 when the interaction with the pulse has concluded. The condition on the real part of $1-c$ can be in general met, since $a>0$ and $0<1-\mathbf{Re}(c)<1$. The condition on the imaginary part of $1-c$ requires a vanishing detuning.

In Sec. 6.3 we will take advantage of the condition whereby $\lambda_a=0$, such that $\varrho_{12}^{\mathrm{eq}}(t)$ vanishes when the interaction with $\boldsymbol{\mathcal{E}}_{\mathrm{C}}(\boldsymbol{r},\,t)$ has concluded. Due to Eq. (6.20), the value of the pulse intensity for which $\lambda_a=0$, i.e., $a=n$ with $n\in\mathbb{N}_0$, corresponds to a pulse area which is an integer multiple of 2π. We notice that, under the same conditions, also the previously defined constant ν_a vanishes. The corresponding value of ξ_a is

$$\xi_n = {}_2F_1\left(n,-n;1-c;1\right) = \frac{[\Gamma(1-c)]^2}{\Gamma(1-c+n)\,\Gamma(1-c-n)} = \frac{(1-c-n)_n}{(1-c)_n}, \tag{6.37}$$

where we have used the definition (C.11). For vanishing decay rates, $\Gamma_2=\Gamma_3=0$, when

$$\xi_n = \frac{\left(\frac{1}{2}+\mathrm{i}\frac{\Delta}{2\gamma}-n\right)_n}{\left(\frac{1}{2}+\mathrm{i}\frac{\Delta}{2\gamma}\right)_n} = \prod_{j=0}^{n-1}\frac{\mathrm{i}\frac{\Delta}{2\gamma}-\left(\frac{1}{2}+j\right)}{\mathrm{i}\frac{\Delta}{2\gamma}+\left(\frac{1}{2}+j\right)} \;\Rightarrow\; |\xi_n|=1, \tag{6.38}$$

the effect of the interaction with the pulse corresponds to a phase shift of $\varrho_{13}^{\mathrm{eq}}(t)$ given by $\arg(\xi_n)$. Furthermore, when also the detuning vanishes, $\Delta=0$, this phase shift is equal to an integer multiple of π, i.e.,

$$\tilde{\xi}_n = {}_2F_1\left(n,-n;\tfrac{1}{2};1\right) = \cos\left(n\pi\right) = (-1)^n \;\Rightarrow\; |\xi_n|=1,\; \arg\left(\xi_n\right) = n\pi. \tag{6.39}$$

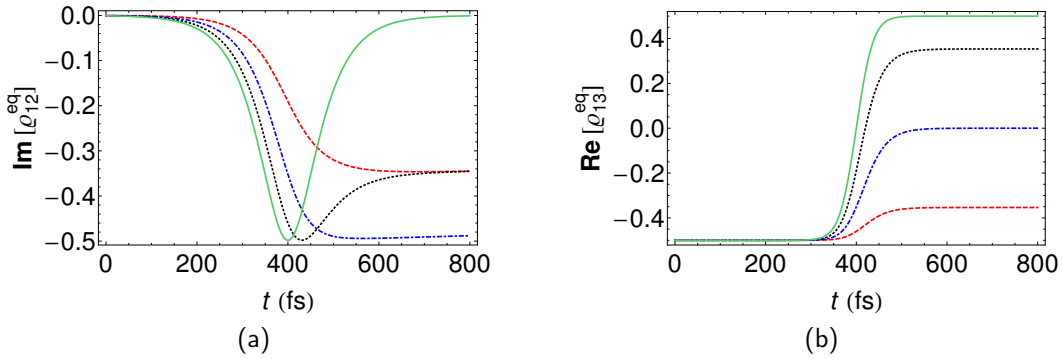

Figure 6.4: (a) and (b) as in Fig. 6.2, with the system prepared at time $T_0 = 0$ in the initial state $\bar{\varrho}_{12,\mathrm{in}} = 0$, $\bar{\varrho}_{13,\mathrm{in}} = -1/2$.

The constant λ_a vanishes also in the large-detuning limit, when, by recalling the definition of c (6.16), one can show that

$$\lim_{\mathbf{Im}(c)\to-\infty} \lambda_a = \frac{1}{a \csc(\pi a)} \frac{2\,\mathrm{i}\,[1 - \mathbf{Re}(c) - \mathrm{i}\,\mathbf{Im}(c)]}{\mathrm{e}^{\mathrm{i}\,\pi\,\mathbf{Re}(c)}\,\mathrm{e}^{-\pi\,\mathbf{Im}(c)}} = 0. \tag{6.40}$$

Also in this case one observes that, for vanishing decay rates $\Gamma_2 = \Gamma_3 = 0$, the corresponding value of ξ_a is given by a pure phase shift $\arg(\xi_a)$,

$$\begin{aligned} \lim_{\frac{\Delta}{\gamma}\to\infty} \xi_a &= \lim_{\frac{\Delta}{\gamma}\to\infty} \frac{\left[\Gamma\left(\frac{1}{2} + \mathrm{i}\frac{\Delta}{2\gamma}\right)\right]^2}{\Gamma\left(\frac{1}{2} + \mathrm{i}\frac{\Delta}{2\gamma} + a\right)\Gamma\left(\frac{1}{2} + \mathrm{i}\frac{\Delta}{2\gamma} - a\right)} \\ &= \lim_{\frac{\Delta}{\gamma}\to\infty} \prod_{k=0}^{\infty}\left[1 - \frac{a^2}{\left(\frac{1}{2} + \mathrm{i}\frac{\Delta}{2\gamma} + k\right)^2}\right] \end{aligned} \quad \Rightarrow \quad \begin{aligned} &\lim_{\frac{\Delta}{\gamma}\to\infty} |\xi_a| = 1, \\ &\lim_{\frac{\Delta}{\gamma}\to\infty} \arg(\xi_a) = -\lim_{\frac{\Delta}{\gamma}\to\infty} \arg(\mu_a), \end{aligned} \tag{6.41}$$

where Eq. (6.31) has been employed.

In the following figures we use the $1s\,2s\,{}^1S_0 \to 1s\,2p\,{}^1P_1$ optical transition of Be^{2+} ions to implement our model and visualize the previously discussed results, with level 1 being given by the ground state of the system. Transition energies and decay rates have already been discussed in Sec. 6.2.1.1.

Fig. 6.4 exhibits the time evolution of $\varrho_{12}^{\mathrm{eq}}(t)$ and $\varrho_{13}^{\mathrm{eq}}(t)$, initially prepared in $\bar{\varrho}_{12,\mathrm{in}} = 0$, $\bar{\varrho}_{13,\mathrm{in}} = -1/2$, when a tuned optical pulse drives the $2 \to 3$ transition. Different lines are associated with different values of the pulse area. The green, solid line, which corresponds to a pulse area $Q_{\mathrm{C}} = 2\pi$, i.e., to $a = 1$, is in full agreement with the predictions from Eqs. (6.36b) and (6.37). The situation is symmetric to the behaviour we predicted and displayed via the green, solid line in Fig. 6.2: For a 2π pulse the system performs a finite number of Rabi oscillations and, when the interaction with the optical pulse $\boldsymbol{\mathcal{E}}_{\mathrm{C}}(\boldsymbol{r}, t)$ has concluded, $\varrho_{12}^{\mathrm{eq}}(t)$ is led back to its initial, vanishing value. The behaviour displayed by the blue, dotdashed line, for a pulse area $Q_{\mathrm{C}} = \pi$ and $a = 1/2$, agrees with Eq. (6.36a): The decay rates are much smaller than the spectral width γ of the pulse and their effect in the equality (6.36a) is almost perfectly negligible such that, after a π pulse, a perfect switch is observed and the coherence, initially stored in the metastable state 3, is transferred from $\varrho_{13}^{\mathrm{eq}}(t)$ to $\varrho_{12}^{\mathrm{eq}}(t)$.

In Fig. 6.5 we show how the off-diagonal elements $\varrho_{12}^{\mathrm{eq}}(t)$ and $\varrho_{13}^{\mathrm{eq}}(t)$ evolve in time when the system is driven by detuned pulses. The results can be explained in the limit of very small decay

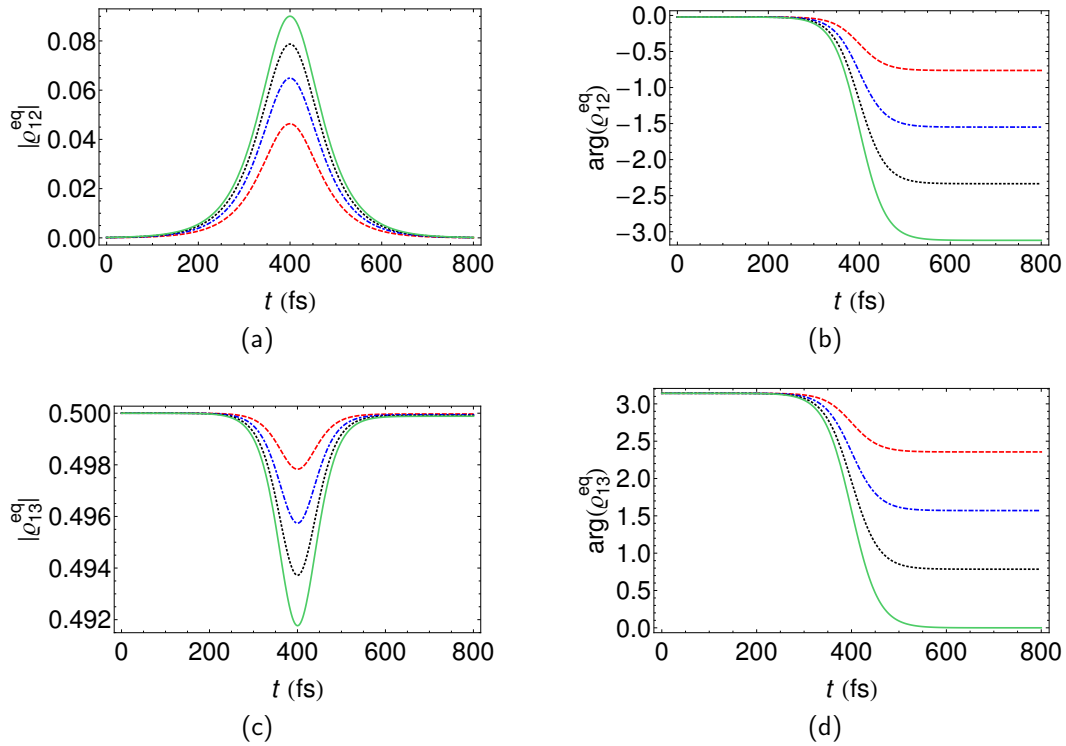

Figure 6.5: Off-diagonal elements of the three-level system of Fig. 6.1, (a) $|\varrho_{12}^{\mathrm{eq}}(t)|$, (b) $\arg[\mathrm{e}^{-\mathrm{i}\Delta t}\,\varrho_{12}^{\mathrm{eq}}(t)]$, (c) $|\varrho_{13}^{\mathrm{eq}}(t)|$, (d) $\arg[\mathrm{e}^{-\mathrm{i}\Delta t}\,\varrho_{13}^{\mathrm{eq}}(t)]$, prepared at time $T_0 = 0$ in the initial state $\bar{\varrho}_{12,\mathrm{in}} = 0$, $\bar{\varrho}_{13,\mathrm{in}} = -1/2$, and driven by a single optical pulse with energy $\omega_{\mathrm{C}} = 1.5\,\mathrm{eV}$, and detuning $\Delta = -\Delta_{\mathrm{C}} = -0.52\,\mathrm{eV}$ with respect to the $1s\,2s\,{}^1S_0 \to 1s\,2p\,{}^1P_1$ optical transition of Be^{2+} ions at $\omega_{23} = 2.02\,\mathrm{eV}$. The pulse is centered at $t_0 = 400\,\mathrm{fs}$, with FWHM duration of $\tau_{\mathrm{FWHM}} = 100\,\mathrm{fs}$ and peak intensities $I_{\mathrm{C,max}} = 4.5 \times 10^{11}\,\mathrm{W/cm^2}$ (red, dashed line), $I_{\mathrm{C,max}} = 9.1 \times 10^{11}\,\mathrm{W/cm^2}$ (blue, dotdashed line), $I_{\mathrm{C,max}} = 1.4 \times 10^{12}\,\mathrm{W/cm^2}$ (black, dotted line), and $I_{\mathrm{C,max}} = 1.9 \times 10^{12}\,\mathrm{W/cm^2}$ (green, solid line), corresponding to a phase kick $\arg(\xi_a) = -\pi/4$ (red, dashed line), $\arg(\xi_a) = -\pi/2$ (blue, dotdashed line), $\arg(\xi_a) = -3\pi/4$ (black, dotted line), and $\arg(\xi_a) = -\pi$ (green, solid line), respectively.

rates and large detuning, i.e., in terms of the phase shift $\arg(\xi_a)$ predicted by Eq. (6.41). We use pulses with the same peak intensities as in Fig. 6.3: In the presence of the optical pulse, the amplitudes of both $|\varrho_{12}^{\mathrm{eq}}(t)|$ and $|\varrho_{13}^{\mathrm{eq}}(t)|$ are minimally affected [Figs. 6.5a and 6.5c], whereas their phases are shifted by $\arg(\xi_a) = -\arg(\mu_a)$ [Figs. 6.5b and 6.5d], where the sign of the phase shift is opposite to the sign of the corresponding kick displayed in Fig. 6.3.

6.2.2 X-ray absorption spectrum

The absorption spectrum associated with the x-ray field which is transmitted by the medium is given by Eq. (5.30) and requires the calculation of the Fourier transform of the function $\varrho_{12}^{\mathrm{eq}}(t)$ in Eq. (6.21) for a three-level system interacting with an optical pulse $\boldsymbol{\mathcal{E}}_{\mathrm{C}}(\boldsymbol{r}, t)$. For simplicity, since $\varrho_{12}^{\mathrm{eq}}(t)$ is the sum of two independent terms, we introduce the two functions

$$f_1(z) = {}_2F_1(a, -a; c; z) - 1, \tag{6.42a}$$

$$f_2(z) = z^{1-c}\,(1-z)^c\,{}_2F_1(1-a, 1+a; 2-c; z), \tag{6.42b}$$

and denote with

$$F_i(\varpi) = \int_{T_0}^{\infty} f_i(z(t))\, \mathrm{e}^{-\mathrm{i}\varpi(t-T_0)}\, \mathrm{d}t = \int_{-\infty}^{\infty} f_i(z(t))\, \mathrm{e}^{-\mathrm{i}\varpi(t-T_0)}\, \mathrm{d}t, \tag{6.43}$$

for $i \in \{1, 2\}$, the corresponding Fourier transforms, where we have extended the lower limit of the integral to $-\infty$ because

$$\lim_{z\to 0} f_i(z) = 0, \tag{6.44}$$

such that each $f_i(t)$ vanishes for $t < T_0$. In terms of the new functions $f_1(t)$ and $f_2(t)$ we can write $\varrho_{12}^{\mathrm{eq}}(t)$ as

$$\varrho_{12}^{\mathrm{eq}}(t) = \mathrm{e}^{\mathrm{i}\Delta_{\mathrm{X}}(t-T_0)}\, \mathrm{e}^{-\frac{\Gamma_2}{2}(t-T_0)} \Big\{ \bar{\varrho}_{12,\mathrm{in}}\, [1 + f_1(t)] + \mathrm{i}\, \bar{\varrho}_{13,\mathrm{in}}\, \frac{a}{1-c}\, \mathrm{e}^{\frac{\Gamma_2-\Gamma_3}{2}(t_0-T_0)}\, \mathrm{e}^{\mathrm{i}\Delta(t_0-T_0)}\, f_2(t) \Big\} \tag{6.45}$$

and, by exploiting the equality [216]

$$\int_0^{\infty} \mathrm{e}^{-\mathrm{i}\varpi t} = \pi\, \delta(\varpi) + \frac{1}{\mathrm{i}\varpi}, \tag{6.46}$$

conclude that

$$\begin{aligned} \int_{T_0}^{\infty} \varrho_{12}^{\mathrm{eq}}(t)\, \mathrm{e}^{-\mathrm{i}(\omega-\omega_{\mathrm{X}})(t-T_0)}\, \mathrm{d}t = \bar{\varrho}_{12,\mathrm{in}} & \left[\frac{1}{\frac{\Gamma_2}{2} + \mathrm{i}\,(\omega-\omega_{21})} + F_1\left(\omega - \omega_{21} - \mathrm{i}\,\tfrac{\Gamma_2}{2}\right) \right] \\ & + \mathrm{i}\, \bar{\varrho}_{13,\mathrm{in}}\, \frac{a}{1-c}\, \mathrm{e}^{\frac{\Gamma_2-\Gamma_3}{2}(t_0-T_0)}\, \mathrm{e}^{\mathrm{i}\,\Delta(t_0-T_0)}\, F_2\left(\omega - \omega_{21} - \mathrm{i}\,\tfrac{\Gamma_2}{2}\right). \end{aligned} \tag{6.47}$$

In this way, we have related the Fourier transform of $\varrho_{12}^{\mathrm{eq}}(t)$ to the two Fourier transforms $F_1(\varpi)$ and $F_2(\varpi)$, whose explicit derivation is performed in Appendix C. These functions are here evaluated at the complex frequency $\varpi = \omega - \omega_{21} - \mathrm{i}\frac{\Gamma_2}{2}$, with negative imaginary part $-\frac{\Gamma_2}{2}$. The final result,

$$\begin{aligned} & \int_{T_0}^{\infty} \varrho_{12}^{\mathrm{eq}}(t)\, \mathrm{e}^{-\mathrm{i}(\omega-\omega_{\mathrm{X}})(t-T_0)}\, \mathrm{d}t \\ & = \bar{\varrho}_{12,\mathrm{in}} \left[\frac{1}{\frac{\Gamma_2}{2} + \mathrm{i}\,(\omega-\omega_{21})} + \mathrm{i}\, \mathrm{e}^{-\mathrm{i}(\omega-\omega_{21})(t_0-T_0)}\, \mathrm{e}^{-\frac{\Gamma_2}{2}(t_0-T_0)}\, \frac{a^2}{2\gamma c}\, \pi\, \mathrm{csch}\Big(\pi\, \tfrac{\omega-\omega_{21}}{2\gamma} - \mathrm{i}\,\pi\, \tfrac{\Gamma_2}{4\gamma}\Big) \right. \\ & \qquad \left. \times\, {}_3F_2\left(1-a, 1+a, 1-\mathrm{i}\,\tfrac{\omega-\omega_{21}}{2\gamma} - \tfrac{\Gamma_2}{4\gamma}; 1+c, 2; 1\right) \right] \\ & \quad + \mathrm{i}\, \bar{\varrho}_{13,\mathrm{in}}\, \frac{a}{2\gamma(1-c)}\, \mathrm{e}^{-\frac{\Gamma_3}{2}(t_0-T_0)}\, \mathrm{e}^{-\mathrm{i}(\omega-\omega_{21}-\Delta)(t_0-T_0)}\, \pi\, \mathrm{sech}\left(\pi\, \tfrac{\omega-\omega_{21}-\Delta}{2\gamma} - \mathrm{i}\pi\, \tfrac{\Gamma_3}{4\gamma}\right) \\ & \qquad \times\, {}_3F_2\left(1-a, 1+a, \tfrac{1}{2} - \mathrm{i}\,\tfrac{\omega-\omega_{21}-\Delta}{2\gamma} - \tfrac{\Gamma_3}{4\gamma}; 2-c, 1; 1\right), \end{aligned} \tag{6.48}$$

is a consequence of Eqs. (C.44) and (C.46).

In the following we discuss the properties of the just computed Fourier transform by separately analyzing the two components of the absorption spectrum (5.30) associated with the two different sets of initial conditions we already identified in the previous Section, i.e., $\bar{\varrho}_{12,\mathrm{in}} \neq 0$, $\bar{\varrho}_{13,\mathrm{in}} = 0$, and $\bar{\varrho}_{12,\mathrm{in}} = 0$, $\bar{\varrho}_{13,\mathrm{in}} \neq 0$. These different sets of initial conditions correspond to different preparatory schemes via the x-ray pulse $\boldsymbol{\mathcal{E}}_{\mathrm{X}}(\boldsymbol{r}, t)$ and the optical pulse $\boldsymbol{\mathcal{E}}_{\mathrm{L}}(\boldsymbol{r}, t)$.

6.2.2.1 X-ray-only preparation

When a single x-ray pulse is used to prepare the system, such that at the initial time T_0 the initial state is characterized by $\varrho_{13,\mathrm{in}}^{\mathrm{eq}} = 0$, the Fourier transform in Eq. (6.48) can be written as

$$\begin{aligned}
&\int_{T_0}^{\infty} \varrho_{12}^{\mathrm{eq}}(t)\, \mathrm{e}^{-\mathrm{i}(\omega-\omega_{\mathrm{X}})(t-T_0)}\, \mathrm{d}t \\
&= \bar{\varrho}_{12,\mathrm{in}} \left[\frac{1}{\frac{\Gamma_2}{2} + \mathrm{i}\,(\omega-\omega_{21})} + \mathrm{i}\, \mathrm{e}^{-\mathrm{i}(\omega-\omega_{21})(t_0-T_0)}\, \mathrm{e}^{-\frac{\Gamma_2}{2}(t_0-T_0)}\, \frac{a^2}{2\gamma c}\, \pi\, \mathrm{csch}\Big(\pi \tfrac{\omega-\omega_{21}}{2\gamma} - \mathrm{i}\,\pi\,\tfrac{\Gamma_2}{4\gamma}\Big) \right. \\
&\qquad \left. \times\ {}_3F_2\left(1-a, 1+a, 1-\mathrm{i}\,\tfrac{\omega-\omega_{21}}{2\gamma} - \tfrac{\Gamma_2}{4\gamma}; 1+c, 2; 1\right)\right].
\end{aligned} \tag{6.49}$$

Two main terms can be identified in the previous function. The first element $\frac{\bar{\varrho}_{12,\mathrm{in}}}{\frac{\Gamma_2}{2}+\mathrm{i}\,(\omega-\omega_{21})}$ in the sum on the left-hand side of Eq. (6.49) is the Fourier transform of a right-handed exponential function, associated with the spontaneous decay of $\varrho_{12}^{\mathrm{eq}}(t)$ which takes place from the initial value $\bar{\varrho}_{12,\mathrm{in}}$ in the absence of the optical pulse $\boldsymbol{\mathcal{E}}_{\mathrm{C}}(\boldsymbol{r}, t)$. The real part of this complex function gives rise to a well-known Lorentzian profile. The second term in the sum on the left-hand side of Eq. (6.49) directly ensues from the presence of the pulse. A deeper insight into the meaning and the properties of Eq. (6.49) can be gained through a Taylor expansion in the coordinate $\varpi = \omega - \omega_{21} - \mathrm{i}\frac{\Gamma_2}{2}$, centered at $\varpi_0 = 0$. Since the following Taylor expansions are valid,

$$\mathrm{csch}\Big(\tfrac{\pi\varpi}{2\gamma}\Big) = \tfrac{2\gamma}{\pi\varpi}[1 + O(\varpi^2)], \tag{6.50a}$$

$$\begin{aligned}
{}_3F_2\left(1-a, 1+a, 1-\mathrm{i}\,\tfrac{\varpi}{2\gamma}; 1+c, 2; 1\right) &= \frac{c}{a^2}\,(1 - {}_2F_1(a, -a : c : 1)) + O(\varpi) \\
&= \frac{c}{a^2}\,(1-\mu_a) + O(\varpi),
\end{aligned} \tag{6.50b}$$

where we have used the definition of μ_a [Eq. (6.24)], we can approximate Eq. (6.49) via

$$\int_{T_0}^{\infty} \varrho_{12}^{\mathrm{eq}}(t)\, \mathrm{e}^{-\mathrm{i}(\omega-\omega_{\mathrm{X}})(t-T_0)}\, \mathrm{d}t \approx \bar{\varrho}_{12,\mathrm{in}}\, \mu_a\, \frac{1}{\frac{\Gamma_2}{2} + \mathrm{i}\,(\omega-\omega_{21})}, \tag{6.51}$$

which is the Fourier transform of a right-handed exponential decay starting at the "effective initial value" $\mu_a\, \bar{\varrho}_{12,\mathrm{in}}$ which the off-diagonal matrix element $\varrho_{12}^{\mathrm{eq}}(t)$ exhibits when the interaction with the optical pulse $\boldsymbol{\mathcal{E}}_{\mathrm{C}}(\boldsymbol{r}, t)$ has concluded. By assuming that $\bar{\varrho}_{12,\mathrm{in}} = -\mathrm{i}\,|\bar{\varrho}_{12,\mathrm{in}}|$, we can write the absorption spectrum in Eq. (5.30) as

$$\sigma(\omega) \propto \omega_{21}\, |\mu_a|\, |\bar{\varrho}_{12,\mathrm{in}}| \left(\cos[\arg(\mu_a)] \frac{\frac{\Gamma_2}{2}}{\frac{\Gamma_2^2}{4} + (\omega-\omega_{21})^2} + \sin[\arg(\mu_a)] \frac{\omega-\omega_{21}}{\frac{\Gamma_2^2}{4} + (\omega-\omega_{21})^2} \right). \tag{6.52}$$

When the system is not optically manipulated by an external field $\boldsymbol{\mathcal{E}}_{\mathrm{C}}(\boldsymbol{r}, t)$, such that $\mu_a = 1$, the absorption spectrum reduces to the well-known Lorentzian profile

$$\sigma(\omega) \propto \omega_{21}\, |\bar{\varrho}_{12,\mathrm{in}}|\, \frac{\frac{\Gamma_2}{2}}{\frac{\Gamma_2^2}{4} + (\omega-\omega_{21})^2}, \tag{6.53}$$

which is yielded by the spontaneous decay of the atomic system following the exposure to the ultrashort x-ray pulse. The function has positive sign, which is associated with absorption of

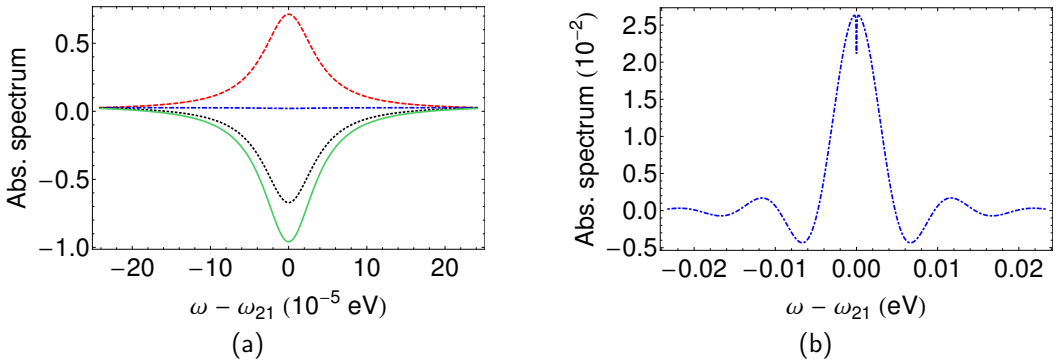

Figure 6.6: Absorption spectrum (6.55) of Be^{2+} ions driven by a single optical pulse tuned to the $1s\,2s\,{}^1S_0 \to 1s\,2p\,{}^1P_1$ optical transition of Be^{2+} ions at $\omega_{23} = 2.02\,\mathrm{eV}$. The spectrum is centered at $\omega_{21} = 123.7\,\mathrm{eV}$. The system is prepared at time $T_0 = 0$ in the initial state $\bar{\varrho}_{12,\mathrm{in}} = -\mathrm{i}/2$, $\bar{\varrho}_{13,\mathrm{in}} = 0$. The pulse is centered at $t_0 = 400\,\mathrm{fs}$, with FWHM duration of $\tau_{\mathrm{FWHM}} = 100\,\mathrm{fs}$ and peak intensities $I_{\mathrm{C,max}} = 4.5 \times 10^{11}\,\mathrm{W/cm^2}$ (red, dashed line), $I_{\mathrm{C,max}} = 9.1 \times 10^{11}\,\mathrm{W/cm^2}$ (blue, dotdashed line), $I_{\mathrm{C,max}} = 1.4 \times 10^{12}\,\mathrm{W/cm^2}$ (black, dotted line), and $I_{\mathrm{C,max}} = 1.9 \times 10^{12}\,\mathrm{W/cm^2}$ (green, solid line), corresponding to a phase kick $\arg(\mu_a) = \pi/4$ (red, dashed line), $\arg(\mu_a) = \pi/2$ (blue, dotdashed line), $\arg(\mu_a) = 3\pi/4$ (black, dotted line), and $\arg(\mu_a) = \pi$ (green, solid line), respectively. In panel (b) a detailed plot of the blue, dotdashed line from panel (a) is provided.

energy as a result of the interaction of the x-ray field with the atomic system. For $|\bar{\varrho}_{12,\mathrm{in}}| = 1/2$, as we are going to assume in the following, the peak value of this single Lorentzian function is

$$\sigma(\omega_{21}) \propto \frac{\omega_{21}}{\Gamma_2}. \tag{6.54}$$

This non-optically-modified spectrum represents the natural scale to compare and represent a general absorption spectrum $\sigma(\omega)$ in the presence of the additional optical field $\boldsymbol{\mathcal{E}}_{\mathrm{C}}(\boldsymbol{r}, t)$. In other words, in the following pictures we will display the normalized absorption spectrum

$$\sigma_{\mathrm{n}}(\omega) = \Gamma_2\ \mathbf{Im}\Big\{\int_{-\infty}^{\infty} \varrho_{12}^{\mathrm{eq}}(t)\,\mathrm{e}^{-\mathrm{i}(\omega-\omega_{\mathrm{X}})(t-T_0)}\,\mathrm{d}t\Big\}. \tag{6.55}$$

Going back to Eq. (6.52), we still observe that the extremal case associated with $\mu_a = \mathrm{i}$ gives rise to the following Fano-like profile

$$\sigma(\omega) \propto \omega_{21}\,|\bar{\varrho}_{12,\mathrm{in}}|\,\frac{\omega-\omega_{21}}{\frac{\Gamma_2^2}{4}+(\omega-\omega_{21})^2}. \tag{6.56}$$

In the following figures we use the $1s\,2s\,{}^1S_0 \to 1s\,2p\,{}^1P_1$ optical transition of Be^{2+} ions to implement our optical-manipulation scheme and visualize the x-ray absorption spectrum (5.30) associated with the Fourier transform in Eq. (6.49). As already discussed in the previous Sections, the optical and x-ray transition energies are respectively given by $\omega_{23} = 2.02\,\mathrm{eV}$ and $\omega_{21} = 123.7\,\mathrm{eV}$. The main decay contribution comes from $\Gamma_2 = 1.2 \times 10^{11}\,\mathrm{s^{-1}} = 5.05 \times 10^{-4}\,\mathrm{eV}$. The optical pulse is centered at $t_0 = 400\,\mathrm{fs}$, with respect to the initial time $T_0 = 0$. Its FWHM duration is $\tau_{\mathrm{FWHM}} = 100\,\mathrm{fs}$ and corresponds to a spectral bandwidth $\gamma = 0.07\,\mathrm{eV}$.

In Fig. 6.6a we display the absorption spectrum (5.30) of the transmitted x-ray field, calculated for an optical pulse $\boldsymbol{\mathcal{E}}_{\mathrm{C}}(\boldsymbol{r}, t)$ tuned to the $2 \to 3$ transition. The same four values of the peak intensity $I_{\mathrm{C,max}}$ are employed as in Fig. 6.2. The Lorentzian profile predicted in Eq. (6.53) can be used to interpret the results displayed in the picture. This is a consequence of the fact that,

for $\Delta = 0$, the intensity-dependent factor $\mu_a = \pm|\mu_a|$ appearing in Eq. (6.52) is a real quantity [see Eq. (6.24a)]. As a result, the employment of different values of the optical peak intensity $I_{\mathrm{C,max}}$, corresponding to different values of the constant μ_a, modifies the peak value and the sign (positive or negative for absorption or gain, respectively) of the Lorentzian profiles depicted in Fig. 6.6a, but does not affect the lineshape.

The blue curve in Figs. 6.2 and 6.6b, however, is not well explained by the Taylor expansion leading to the approximated Fourier transform in Eq. (6.51). In this case, in fact, the corresponding value of the pulse area, $Q_{\mathrm{C}} = \pi$, implies that $\mu_a \approx 0$. The negligible contribution ensuing from the post-pulse-exposure spontaneous decay of the system strongly inhibits the previously described Lorentzian profile and the spectrum is therefore dominated by the Rabi oscillations taking place during the interaction with the external pulse $\boldsymbol{\mathcal{E}}_{\mathrm{C}}(\boldsymbol{r}, t)$. This can be formally shown by considering higher-order terms in the Taylor expansion of Eq. (6.49), i.e.,

$$\begin{aligned}&\int_{T_0}^{\infty} \varrho_{12}^{\mathrm{eq}}(t)\, \mathrm{e}^{-\mathrm{i}(\omega-\omega_{\mathrm{X}})(t-T_0)}\, \mathrm{d}t \\ &= \bar{\varrho}_{12,\mathrm{in}} \left[\mu_a \frac{1}{\frac{\Gamma_2}{2} + \mathrm{i}\,(\omega-\omega_{21})} - \frac{a^2}{c} \frac{\mathrm{e}^{-\mathrm{i}(\omega-\omega_{21})(t_0-T_0)} - 1}{\mathrm{i}(\omega-\omega_{21})}\, {}_2F_1\left(\tfrac{1}{2}, 1 - \mathrm{i}\,\tfrac{\omega-\omega_{21}}{2\gamma}; 2; 1\right)\right],\end{aligned} \tag{6.57}$$

where in the second term in the sum on the right-hand side of Eq. (6.57) we have included that $a = 1/2$ and $\Delta = 0$, we have neglected the contribution from $\Gamma_2/(2\gamma)$, and have employed the following approximation,

$$\begin{aligned}{}_3F_2\left(1-a, 1+a, 1-\mathrm{i}\,\tfrac{\varpi}{2\gamma}; 1+c, 2; 1\right) &\approx {}_3F_2\left(\tfrac{1}{2}, \tfrac{3}{2}, 1-\mathrm{i}\,\tfrac{\omega-\omega_{21}}{2\gamma}; \tfrac{3}{2}, 2; 1\right) \\ &= {}_2F_1\left(\tfrac{1}{2}, 1-\tfrac{\omega-\omega_{21}}{2\gamma}; 2; 1\right).\end{aligned} \tag{6.58}$$

In the Fourier transform (6.57) all the elements can be identified which appear in the x-ray absorption spectrum in Fig. 6.6b: The Lorentzian peak centered at $\omega = \omega_{21}$ is associated with the function $\frac{1}{\frac{\Gamma_2}{2}+\mathrm{i}\,(\omega-\omega_{21})}$ appearing on the right-hand side of Eq. (6.57) and due to the fact that μ_a, despite being very small for $a = 1/2$, does not vanish exactly [see Eq. (6.27)]. The second term in the sum on the right-hand side of Eq. (6.57) determines the overall width of the spectrum, ensuing from the width of the function ${}_2F_1\big(\frac{1}{2}, 1 - \frac{\omega-\omega_{21}}{2\gamma}; 2; 1\big)$, and the oscillating features associated with the function $\frac{\mathrm{e}^{-\mathrm{i}(\omega-\omega_{21})(t_0-T_0)}-1}{\mathrm{i}(\omega-\omega_{21})}$.

The absorption spectrum of the transmitted x-ray field, optically modified via an optical pulse detuned from the corresponding optical transition $2 \to 3$, is analyzed in Fig. 6.7. Here, the same values of detuning and peak intensities are used as in Fig. 6.3. The spectrum can be interpreted via the function (6.52) by taking into account that the factor μ_a, because of the small ratio between the decay rate Γ_2 and the spectral bandwidth of the pulse γ, is a pure phase factor $\mu_a = \mathrm{e}^{\mathrm{i}\arg(\mu_a)}$ [see Eq. (6.31)]. The resulting absorption spectra (5.30) exhibit an optically induced modification of the spectral lineshape: A symmetric Lorentzian lineshape (6.53) is displayed by the green curve ($\mu_a = -1$) and a centrally symmetric Fano-like profile (6.56) can be identified in the blue curve ($\mu_a = \mathrm{i}$). The remaining two lines, associated with complex values μ_a with nonvanishing real and imaginary parts, can be described by the general line profile in Eq. (6.52). Similarly interpretable results were observed via optical coupling of the excited levels of He to the continuum [147].

6.2.2.2 Coherence-storage preparation

When the preparatory stage of the system consists in an x-ray pulse $\boldsymbol{\mathcal{E}}_{\mathrm{X}}(\boldsymbol{r}, t)$ and an optical pulse $\boldsymbol{\mathcal{E}}_{\mathrm{L}}(\boldsymbol{r}, t)$ tuned to the $2 \to 3$ transition and with area equal to π, the system is at the

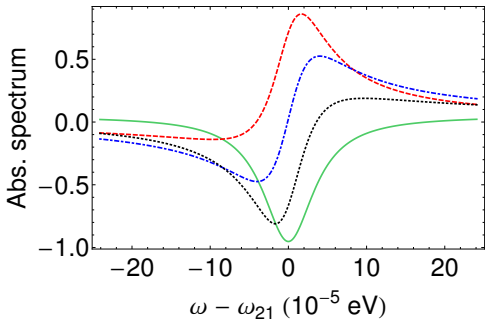

Figure 6.7: Absorption spectrum (6.55) of Be^{2+} ions driven by a single optical pulse of energy $\omega_C = 1.5\,eV$, detuned by $\Delta = -\Delta_C = -0.52\,eV$ from the $1s\,2s\,^1S_0 \rightarrow 1s\,2p\,^1P_1$ optical transition of Be^{2+} ions at $\omega_{23} = 2.02\,eV$. The spectrum is centered at $\omega_{21} = 123.7\,eV$. The system is prepared at time $T_0 = 0$ in the initial state $\bar{\varrho}_{12,in} = -i/2$, $\bar{\varrho}_{13,in} = 0$. The pulse is centered at $t_0 = 400\,fs$, with FWHM duration of $\tau_{FWHM} = 100\,fs$ and peak intensities $I_{C,max} = 4.5 \times 10^{11}\,W/cm^2$ (red, dashed line), $I_{C,max} = 9.1 \times 10^{11}\,W/cm^2$ (blue, dotdashed line), $I_{C,max} = 1.4 \times 10^{12}\,W/cm^2$ (black, dotted line), and $I_{C,max} = 1.9 \times 10^{12}\,W/cm^2$ (green, solid line), corresponding to a phase kick $\arg(\mu_a) = \pi/4$ (red, dashed line), $\arg(\mu_a) = \pi/2$ (blue, dotdashed line), $\arg(\mu_a) = 3\pi/4$ (black, dotted line), and $\arg(\mu_a) = \pi$ (green, solid line), respectively.

initial time T_0 in a state with off-diagonal elements of the density matrix given by $\bar{\varrho}_{12,in} = 0$ and $\bar{\varrho}_{13,in} \neq 0$. Under these conditions, the Fourier transform of $\varrho_{12}^{eq}(t)$ in Eq. (6.48), resulting from optical manipulation of the $2 \rightarrow 3$ transition via the pulse $\boldsymbol{\mathcal{E}}_C(\boldsymbol{r}, t)$, reduces to

$$\begin{aligned}
&\int_{T_0}^{\infty} \varrho_{12}^{eq}(t)\, e^{-i(\omega-\omega_X)(t-T_0)}\, dt \\
&= i\,\bar{\varrho}_{13,in}\, \frac{a}{2\gamma(1-c)}\, e^{-\frac{\Gamma_3}{2}(t_0-T_0)}\, e^{-i(\omega-\omega_{21}-\Delta)(t_0-T_0)}\, \pi\, \mathrm{sech}\left(\pi\tfrac{\omega-\omega_{21}-\Delta}{2\gamma} - i\pi\tfrac{\Gamma_3}{4\gamma}\right) \\
&\quad \times\, {}_3F_2\left(1-a, 1+a, \tfrac{1}{2} - i\,\tfrac{\omega-\omega_{21}-\Delta}{2\gamma} - \tfrac{\Gamma_3}{4\gamma}; 2-c, 1; 1\right).
\end{aligned} \tag{6.59}$$

Three main factors are distinguishable in the function (6.59): an oscillating contribution, given by $e^{-i(\omega-\omega_{21}-\Delta)(t_0-T_0)}$ and associated with the delayed time $t_0 - T_0$ at which the optical pulse $\boldsymbol{\mathcal{E}}_C(\boldsymbol{r}, t)$ drives the system; the hyperbolic-secant component $\mathrm{sech}\left(\pi\frac{\omega-\omega_{21}-\Delta}{2\gamma} - i\pi\frac{\Gamma_3}{4\gamma}\right)$, whose width is determined by the width of the optical pulse γ; and the final term, given by the hypergeometric function $\pi\, {}_3F_2\left(1-a, 1+a, \frac{1}{2} - i\,\frac{\omega-\omega_{21}-\Delta}{2\gamma} - \frac{\Gamma_3}{4\gamma}; 2-c, 1; 1\right)$.

In the following figures we use the $1s\,2s\,^1S_0 \rightarrow 1s\,2p\,^1P_1$ optical transition of Be^{2+} ions to display the modification of the absorption spectrum (5.30), resulting from the coherent response of the atomic system and associated with the Fourier transform in Eq. (6.59). Here, level 1 is given by the ground state of the system. Transition energies and decay rates have already been discussed previously.

Also for this new set of initial conditions the x-ray absorption spectrum, manipulated via an optical pulse $\boldsymbol{\mathcal{E}}_C(\boldsymbol{r}, t)$ tuned to the $2 \rightarrow 3$ transition [Fig. 6.8], displays a clear Lorentzian profile, with linewidth associated with the decay width of the excited level $\Gamma_2 = 5.05 \times 10^{-4}\,eV$. This considerably tiny width can be related neither to the oscillating functions $e^{-i(\omega-\omega_{21}-\Delta)(t_0-T_0)}$, simply because no width can be associated with this pure-phase term, nor to the hyperbolic-secant function $\mathrm{sech}\left(\pi\frac{\omega-\omega_{21}-\Delta}{2\gamma} - i\pi\frac{\Gamma_3}{4\gamma}\right)$, because its spectral width γ is much larger than the linewidth appearing in Fig. 6.8. As a result, the displayed Lorentzian profile must ensue from the third factor in Eq. (6.59), i.e., from the hypergeometric function ${}_3F_2$. This can be shown via

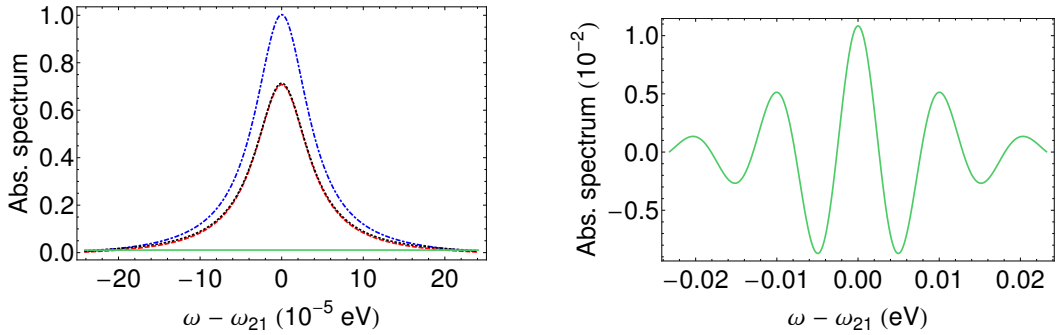

Figure 6.8: Absorption spectrum (6.55) of Be^{2+} ions driven by a single optical pulse, tuned to the $1s\,2s\,{}^1S_0 \to 1s\,2p\,{}^1P_1$ optical transition of Be^{2+} ions at $\omega_{23} = 2.02\,\mathrm{eV}$. The spectrum is centered at $\omega_{21} = 123.7\,\mathrm{eV}$. The system is prepared at time $T_0 = 0$ in the initial state $\bar{\varrho}_{12,\mathrm{in}} = 0$, $\bar{\varrho}_{13,\mathrm{in}} = -1/2$. The pulse is centered at $t_0 = 400\,\mathrm{fs}$, with FWHM duration of $\tau_{\mathrm{FWHM}} = 100\,\mathrm{fs}$ and peak intensities $I_{\mathrm{C,max}} = 4.5 \times 10^{11}\,\mathrm{W/cm^2}$ (red, dashed line), $I_{\mathrm{C,max}} = 9.1 \times 10^{11}\,\mathrm{W/cm^2}$ (blue, dotdashed line), $I_{\mathrm{C,max}} = 1.4 \times 10^{12}\,\mathrm{W/cm^2}$ (black, dotted line), and $I_{\mathrm{C,max}} = 1.9 \times 10^{12}\,\mathrm{W/cm^2}$ (green, solid line), corresponding to a phase kick $\arg(\xi_a) = -\pi/4$ (red, dashed line), $\arg(\xi_a) = -\pi/2$ (blue, dotdashed line), $\arg(\xi_a) = -3\pi/4$ (black, dotted line), and $\arg(\xi_a) = -\pi$ (green, solid line), respectively. In panel (b) a detailed plot of the green, solid line from panel (a) is provided.

the following approximation,

$$\begin{aligned}
&\int_{T_0}^{\infty} \varrho_{12}^{\mathrm{eq}}(t)\, \mathrm{e}^{-\mathrm{i}(\omega-\omega_{\mathrm{X}})(t-T_0)}\, \mathrm{d}t \approx \mathrm{i}\, \frac{\bar{\varrho}_{13,\mathrm{in}}\, a\pi}{2\gamma(1-c)}\, {}_3F_2\left(1-a, 1+a, \tfrac{1}{2} - \mathrm{i}\,\tfrac{\omega-\omega_{21}-\Delta}{2\gamma} - \tfrac{\Gamma_3}{4\gamma}; 2-c, 1; 1\right) \\
&= \mathrm{i}\, \bar{\varrho}_{13,\mathrm{in}} \frac{a}{2\gamma(1-c)}\, \pi\, \frac{\Gamma(2-c)}{\Gamma(1-a)\,\Gamma(1+a)}\, \frac{1}{\Gamma\left(\frac{1}{2} - \mathrm{i}\,\frac{\omega-\omega_{21}-\Delta}{2\gamma} - \frac{\Gamma_3}{4\gamma}\right)} \\
&\quad \times \sum_{n=0}^{\infty} \frac{\Gamma(1-a+n)\,\Gamma(1+a+n)}{[\Gamma(1+n)]^2}\, \frac{\Gamma\left(\frac{1}{2} - \mathrm{i}\,\frac{\omega-\omega_{21}-\Delta}{2\gamma} - \frac{\Gamma_3}{4\gamma} + n\right)}{\Gamma(2-c+n)},
\end{aligned} \tag{6.60}$$

where we have used the definition of the generalized hypergeometric function [see Eqs. (C.40) and (C.11)] and have neglected the two terms $\mathrm{e}^{-\mathrm{i}(\omega-\omega_{21}-\Delta)(t_0-T_0)}$ and $\mathrm{sech}\big(\pi\frac{\omega-\omega_{21}-\Delta}{2\gamma} - \mathrm{i}\pi\frac{\Gamma_3}{4\gamma}\big)$, which are equal to 1 in the small frequency interval determined by the linewidth Γ_2. We have also assumed that $a \neq n$, with $n \in \mathbb{N}$, such that the sum in n does not terminate and the prefactor $[\Gamma(1-a)]^{-1}$ can be taken out of the series. By recalling the definition of the constant λ_a [Eq. (6.35)] and by employing

$$\frac{\Gamma(1-a+n)\,\Gamma(1+a+n)}{[\Gamma(1+n)]^2} \approx 1,$$

to further approximate Eq. (6.60), we can write

$$\begin{aligned}
\int_{T_0}^{\infty} \varrho_{12}^{\mathrm{eq}}(t)\, \mathrm{e}^{-\mathrm{i}(\omega-\omega_{\mathrm{X}})(t-T_0)}\, \mathrm{d}t \approx{}& \mathrm{i}\, \frac{\bar{\varrho}_{13,\mathrm{in}}\, a}{2\gamma(1-c)}\, \frac{\pi\,\lambda_a}{\Gamma\left(\frac{1}{2} - \mathrm{i}\,\frac{\omega-\omega_{21}-\Delta}{2\gamma} - \frac{\Gamma_3}{4\gamma}\right)\Gamma(c)} \\
&\times \sum_{n=0}^{\infty} \frac{\Gamma\left(\frac{1}{2} - \mathrm{i}\,\frac{\omega-\omega_{21}-\Delta}{2\gamma} - \frac{\Gamma_3}{4\gamma} + n\right)}{\Gamma(2-c+n)}.
\end{aligned} \tag{6.61}$$

This result, along with the identity [216]

$$\sum_{n=0}^{\infty} \frac{\Gamma(\alpha+n)}{\Gamma(\beta+n)} = \frac{\Gamma(\alpha)\,\Gamma(-1-\alpha+\beta)}{\Gamma(-1+\beta)\,\Gamma(-\alpha+\beta)},$$

the recurrence relation defining the Gamma function (C.12), and the definition of c (6.16), lead to

$$\begin{aligned}\int_{T_0}^{\infty} \varrho_{12}^{\mathrm{eq}}(t)\,\mathrm{e}^{-\mathrm{i}(\omega-\omega_{\mathrm{X}})(t-T_0)}\,\mathrm{d}t &= \mathrm{i}\,\frac{\bar{\varrho}_{13,\mathrm{in}}\,a}{2\gamma(1-c)}\,\frac{\pi\,\lambda_a}{\Gamma(1-c)\,\Gamma(c)}\,\frac{\Gamma\left(\frac{1}{2}+\mathrm{i}\,\frac{\omega-\omega_{21}-\Delta}{2\gamma}+\frac{\Gamma_3}{4\gamma}-c\right)}{\Gamma\left(\frac{3}{2}+\mathrm{i}\,\frac{\omega-\omega_{21}-\Delta}{2\gamma}+\frac{\Gamma_3}{4\gamma}-c\right)} \\ \approx \mathrm{i}\,\bar{\varrho}_{13,\mathrm{in}}\frac{a}{(1-c)}\,\lambda_a\,\frac{1}{2\gamma}\,\frac{1}{\frac{1}{2}+\mathrm{i}\,\frac{\omega-\omega_{21}-\Delta}{2\gamma}-\frac{\Gamma_3}{4\gamma}-c} &= \mathrm{i}\,\bar{\varrho}_{13,\mathrm{in}}\frac{a}{(1-c)}\,\lambda_a\,\frac{1}{\frac{\Gamma_2}{2}+\mathrm{i}\,(\omega-\omega_{21})}.\end{aligned} \tag{6.62}$$

The obtained approximated Fourier transform is equal to the Fourier transform of a right-handed exponentially decaying function, with decay rate Γ_2 and with the "effective initial value" $\mathrm{i}\,\bar{\varrho}_{13,\mathrm{in}}\frac{a}{(1-c)}\,\lambda_a$ which the off-diagonal matrix element $\varrho_{12}^{\mathrm{eq}}(t)$ exhibits when the interaction with the optical pulse $\boldsymbol{\mathcal{E}}_{\mathrm{C}}(\boldsymbol{r},\,t)$ has concluded [see, e.g., Eqs.(6.34a) and (6.35)]. By assuming that $\bar{\varrho}_{13,\mathrm{in}}$ is real and by observing that, for $\Delta = 0$, also the constants c and λ_a are real, we can take the imaginary part of the approximated Fourier transform (6.62) to recover the Lorentzian spectral profile

$$\sigma(\omega) = -\omega_{21}\,\bar{\varrho}_{13,\mathrm{in}}\,\lambda_a\,\frac{a}{1-c}\,\frac{\frac{\Gamma_2}{2}}{\frac{\Gamma_2^2}{4}+(\omega-\omega_{21})^2}, \tag{6.63}$$

which agrees with the spectra in Fig. 6.8a. The peak value and the sign (positive or negative for absorption or gain, respectively) of the Lorentzian profiles in the picture are associated with the intensity-dependent factor $a\lambda_a$ in Eq. (6.63).

The shape of the blue curve in Fig. 6.8b, calculated for a pulse area $Q_{\mathrm{C}} = 2\pi$ corresponding to $a = 1$ and $\lambda_a = 0$, can be explained by observing that the generalized hypergeometric function ${}_3F_2\big(1-a, 1+a, \frac{1}{2}-\mathrm{i}\,\frac{\omega-\omega_{21}-\Delta}{2\gamma}-\frac{\Gamma_3}{4\gamma}; 2-c, 1; 1\big)$ is equal to 1 for $a = 1$ [see Eq. (C.40)]. The width of the spectrum depicted in the figure is given by the bandwidth of the optical pulse γ, which is also the width of the function $\operatorname{sech}\big(\pi\frac{\omega-\omega_{21}-\Delta}{2\gamma}-\mathrm{i}\pi\frac{\Gamma_3}{4\gamma}\big)$ in Eq. (6.48). The oscillating behaviour featured by the spectrum can be related to the complex exponential function $\mathrm{e}^{-\mathrm{i}(\omega-\omega_{21}-\Delta)(t_0-T_0)}$ in Eq. (6.48).

When the employed optical pulse is significantly detuned from the corresponding optical transition $2 \to 3$ [Fig. 6.9], the spectrum ensues from the Fourier transform of the function $\varrho_{12}^{\mathrm{eq}}(t)$ which we displayed in Fig. 6.5. The features, due to the interaction with the optical pulse, which could be recognized in the time evolution of $\varrho_{12}^{\mathrm{eq}}(t)$, i.e., a small hyperbolic-secant-like modification of the amplitude [Fig. 6.5a] and a phase shift [Fig. 6.5b], have spectral counterparts in the Fourier transform (6.59). These can be immediately identified in the absorption spectrum displayed Fig. 6.9: The central peak of the function is not at $\omega = \omega_{21} + \Delta$, but the central frequency of the spectrum exhibits a "shift" dependent upon the employed intensity and due to the phase shift $\arg(\xi_a)$ in $\varrho_{12}^{\mathrm{eq}}(t)$. The oscillating features of the spectrum, associated with the complex exponential function $\mathrm{e}^{-\mathrm{i}(\omega-\omega_{21}-\Delta)(t_0-T_0)}$ in the Fourier transform (6.48), are now superimposed to an asymmetric function [Fig. 6.9b] due to the product of the remaining factors $\operatorname{sech}\big(\pi\frac{\omega-\omega_{21}-\Delta}{2\gamma}-\mathrm{i}\pi\frac{\Gamma_3}{4\gamma}\big)$ and ${}_3F_2\big(1-a, 1+a, \frac{1}{2}-\mathrm{i}\,\frac{\omega-\omega_{21}-\Delta}{2\gamma}-\frac{\Gamma_3}{4\gamma}; 2-c, 1; 1\big)$.

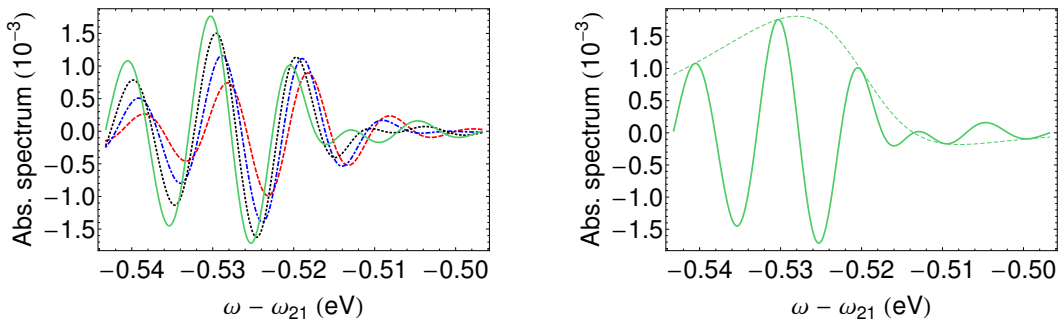

Figure 6.9: Absorption spectrum (6.55) of Be^{2+} ions driven by a single optical pulse, detuned with detuning $\Delta = -\Delta_C = -0.52\,\mathrm{eV}$ from the $1s\,2s\,{}^1S_0 \to 1s\,2p\,{}^1P_1$ optical transition of Be^{2+} ions at $\omega_{23} = 2.02\,\mathrm{eV}$. The spectrum is centered at $\omega_{21} = 123.7\,\mathrm{eV}$. The system is prepared at time $T_0 = 0$ in the initial state $\bar{\varrho}_{12,\mathrm{in}} = 0$, $\bar{\varrho}_{13,\mathrm{in}} = -1/2$. The pulse is centered at $t_0 = 400\,\mathrm{fs}$, with FWHM duration of $\tau_{\mathrm{FWHM}} = 100\,\mathrm{fs}$ and peak intensities $I_{C,\max} = 4.5 \times 10^{11}\,\mathrm{W/cm^2}$ (red, dashed line), $I_{C,\max} = 9.1 \times 10^{11}\,\mathrm{W/cm^2}$ (blue, dotdashed line), $I_{C,\max} = 1.4 \times 10^{12}\,\mathrm{W/cm^2}$ (black, dotted line), and $I_{C,\max} = 1.9 \times 10^{12}\,\mathrm{W/cm^2}$ (green, solid line), corresponding to a phase kick $\arg(\xi_a) = -\pi/4$ (red, dashed line), $\arg(\xi_a) = -\pi/2$ (blue, dotdashed line), $\arg(\xi_a) = -3\pi/4$ (black, dotted line), and $\arg(\xi_a) = -\pi$ (green, solid line), respectively. In panel (b) the green solid line from panel (a) is compared to the green, dashed line, which plots the absorption spectrum Eq. (6.59) when t_0 is set equal to 0.

6.3 Coherent control via an optical frequency comb

In the present Section we employ a periodic train of optical pulses $\boldsymbol{\mathcal{E}}_C(\boldsymbol{r}, t)$, i.e., an optical frequency comb, to drive the $2 \to 3$ transition in the previously described three-level system and thereby imprint a comb onto the absorption spectrum of the wide-bandwidth x-ray pulse $\boldsymbol{\mathcal{E}}_X(\boldsymbol{r}, t)$ exciting the $1 \to 2$ transition. The time evolution of the system upon interaction with the optical frequency comb is calculated via recursive application of the single-pulse solution which we discussed in Sec. 6.2 for given values of the optical-comb peak intensity and detuning.

6.3.1 Time evolution of the system

The optical frequency comb $\boldsymbol{\mathcal{E}}_C(\boldsymbol{r}, t)$ is here modeled via a periodic train of hyperbolic-secant pulses, with repetition period T_p and peak electric-field strength $\mathcal{E}_{C,\max}$. This corresponds to the Rabi frequency (5.4)

$$\Omega_{RC}(t) = \sum_{j=0}^{\infty} \Omega_{RC}^{j}(t) = \sum_{j=0}^{\infty} A\,\mathrm{sech}[\gamma\,(t - t_j)], \tag{6.64}$$

where γ is the single-pulse spectral width, with FWHM duration $\tau_{\mathrm{FWHM}} = 2\,\mathrm{arccosh}(\sqrt{2})/\gamma$, and $A = d_{32}^0\sqrt{8\pi\alpha\,I_{C,\max}}$ is the same constant we already defined in the previous Section, leading to the definition of $a = A/(2\gamma)$. Each pulse is centered at time $t_j = t_0 + jT_p$, $j = 0, 1, 2, \ldots$, with $t_0 > T_0$, and is much shorter than the repetition period, $T_p \gg 1/\gamma$. The Rabi frequency $\Omega_{RC}^{j}(t)$ in Eq. (6.64) is associated with the sole jth pulse.

The solution of the second-order differential equation (6.13) in the presence of the periodic Rabi frequency (6.64) can be obtained by recursively employing the single-pulse solution we described in Sec. 6.2. We define the functions $\bar{\varrho}_{1k}^{j}$, with $k \in \{2, 3\}$ and $j \in \mathbb{N}$, which are solution

of the single-pulse EOMs

$$\frac{\partial \bar{\varrho}_{12}^{j}}{\partial t} = +\mathrm{i}\frac{\Omega_{\mathrm{RC}}^{j}}{2}\,\bar{\varrho}_{13}^{j}\,\mathrm{e}^{\left(\mathrm{i}\Delta+\frac{\Gamma_2-\Gamma_3}{2}\right)\left(t-t_j+\frac{T_\mathrm{p}}{2}\right)}, \tag{6.65a}$$

$$\frac{\partial \bar{\varrho}_{13}^{j}}{\partial t} = +\mathrm{i}\frac{\Omega_{\mathrm{RC}}^{j}}{2}\,\bar{\varrho}_{12}^{j}\,\mathrm{e}^{\left(-\mathrm{i}\Delta-\frac{\Gamma_2-\Gamma_3}{2}\right)\left(t-t_j+\frac{T_\mathrm{p}}{2}\right)}, \tag{6.65b}$$

where Ω_{RC}^{j} is the Rabi frequency associated with the jth pulse, centered at t_j, in the optical frequency comb. With the substitutions $t_0 \to t_j$ and $T_0 \to T_{j0} = t_j - \frac{T_\mathrm{p}}{2}$, the set of differential equations (6.65) coincides with the already discussed EOMs (6.12): The solution (C.32) can therefore be exploited to analogously write the solution of the equations in (6.65). In terms of the j-dependent variables

$$z_j(t) = \frac{\tanh[\gamma(t-t_j)]+1}{2}, \tag{6.66}$$

this solution is namely

$$\begin{aligned}\bar{\varrho}_{12}^{j}(z_j) = {}& \bar{\varrho}_{12,\mathrm{in}}^{j}\,{}_2F_1(a,-a;c;z_j) \\ & + \mathrm{i}\,\bar{\varrho}_{13,\mathrm{in}}^{j}\,\frac{a}{1-c}\,\mathrm{e}^{2\gamma\left(\frac{1}{2}-c\right)\frac{T_\mathrm{p}}{2}}\,z_j^{1-c}\,(1-z_j)^{c}\,{}_2F_1(1-a,1+a;2-c;z_j),\end{aligned} \tag{6.67a}$$

$$\begin{aligned}\bar{\varrho}_{13}^{j}(z_j) = {}& \bar{\varrho}_{13,\mathrm{in}}^{j}\,{}_2F_1(a,-a;1-c;z_j) \\ & + \mathrm{i}\,\bar{\varrho}_{12,\mathrm{in}}^{j}\,\frac{a}{c}\,\mathrm{e}^{2\gamma\left(c-\frac{1}{2}\right)\frac{T_\mathrm{p}}{2}}\,z_j^{c}\,(1-z_j)^{1-c}\,{}_2F_1(1-a,1+a;1+c;z_j).\end{aligned} \tag{6.67b}$$

By employing Eqs. (C.32) and (6.35), we observe that $\bar{\varrho}_{12}^{j}(t)$ and $\bar{\varrho}_{13}^{j}(t)$ undergo time modifications only in the presence of the corresponding jth pulse itself, i.e., only in a short time interval centered at t_j and of amplitude $\sim \frac{1}{\gamma} \ll T_\mathrm{p}$. By employing the Heaviside θ function, this in other words implies that

$$\bar{\varrho}_{1k}^{j}(t)\,\theta\left(-t+t_j-\tfrac{T_\mathrm{p}}{2}\right) = \bar{\varrho}_{1k,\mathrm{in}}^{j}\,\theta\left(-t+t_j-\tfrac{T_\mathrm{p}}{2}\right), \tag{6.68}$$

with the initial conditions at $T_{j0} = t_j - \frac{T_\mathrm{p}}{2}$ given by

$$\bar{\varrho}_{1k,\mathrm{in}}^{j} = \bar{\varrho}_{1k}^{j}\left(t_j-\tfrac{T_\mathrm{p}}{2}\right) \approx \lim_{t\to-\infty}\bar{\varrho}_{1k}^{j}(t), \quad \text{for } k\in\{2,3\}. \tag{6.69}$$

Each pulse is much shorter than the repetition period T_p, such that the total solution $\varrho_{1k}^{\mathrm{eq}}(t)$, with $k \in \{2,3\}$, which results from the interaction with the periodic train of pulses (6.64) can be written as the following sum of jth-pulse functions $\bar{\varrho}_{1k}^{j}$:

$$\begin{aligned}\varrho_{12}^{\mathrm{eq}}(t) = {}& \mathrm{e}^{\left(\mathrm{i}\Delta_\mathrm{X}-\frac{\Gamma_2}{2}\right)\left(t-t_0+\frac{T_\mathrm{p}}{2}\right)}\,\bar{\varrho}_{12}^{0}(t)\,\theta\left(-t+t_0-\tfrac{T_\mathrm{p}}{2}\right) \\ & + \sum_{j=0}^{\infty}\mathrm{e}^{\left(\mathrm{i}\Delta_\mathrm{X}-\frac{\Gamma_2}{2}\right)\left(t-t_j+\frac{T_\mathrm{p}}{2}\right)}\,\bar{\varrho}_{12}^{j}(t)\,\left[-\theta\left(-t+t_j-\tfrac{T_\mathrm{p}}{2}\right)+1-\theta\left(t-t_j-\tfrac{T_\mathrm{p}}{2}\right)\right],\end{aligned} \tag{6.70a}$$

$$\begin{aligned}\varrho_{13}^{\mathrm{eq}}(t) = {}& \mathrm{e}^{\left(\mathrm{i}(\Delta_\mathrm{X}+\Delta)-\frac{\Gamma_3}{2}\right)\left(t-t_0+\frac{T_\mathrm{p}}{2}\right)}\,\bar{\varrho}_{13}^{0}(t)\,\theta\left(-t+t_0-\tfrac{T_\mathrm{p}}{2}\right) \\ & + \sum_{j=0}^{\infty}\mathrm{e}^{\left(\mathrm{i}(\Delta_\mathrm{X}+\Delta)-\frac{\Gamma_3}{2}\right)\left(t-t_j+\frac{T_\mathrm{p}}{2}\right)}\,\bar{\varrho}_{13}^{j}(t)\,\left[-\theta\left(-t+t_j-\tfrac{T_\mathrm{p}}{2}\right)+1-\theta\left(t-t_j-\tfrac{T_\mathrm{p}}{2}\right)\right],\end{aligned} \tag{6.70b}$$

where the Heaviside θ function appearing in the first addends of the sums on the right-hand sides of Eqs. (6.70) is equal to

$$\theta\left(-t+t_0-\tfrac{T_\mathrm{p}}{2}\right)=\begin{cases}1 & \text{if } t<t_0-\frac{T_\mathrm{p}}{2}\\ 0 & \text{otherwise,}\end{cases} \tag{6.71}$$

while the term in the second addends,

$$-\theta\left(-t+t_j-\tfrac{T_\mathrm{p}}{2}\right)+1-\theta\left(t-t_j-\tfrac{T_\mathrm{p}}{2}\right)=\begin{cases}1 & \text{if } t_j-\frac{T_\mathrm{p}}{2}<t<t_j+\frac{T_\mathrm{p}}{2}\\ 0 & \text{otherwise,}\end{cases} \tag{6.72}$$

selects only those times t which lie in the time interval $]t_j - T_\mathrm{p}/2,\, t_j + T_\mathrm{p}/2[$, with $j \in \mathbb{N}$.

The determination of the solution (6.70) requires the calculation of the jth-pulse initial conditions $\bar{\varrho}^{j}_{1k,\mathrm{in}}$, for $k \in \{2, 3\}$. First of all, we notice that, from the definitions (6.69) and (6.70), the value of the functions $\varrho^{\mathrm{eq}}_{1k}(t)$ and $\bar{\varrho}^{j}_{1k}(t)$ at $t_j - T_\mathrm{p}/2$ can be related via the equality

$$\bar{\varrho}^{j}_{1k,\mathrm{in}}=\bar{\varrho}^{j}_{1k}\left(t_j-\tfrac{T_\mathrm{p}}{2}\right)=\varrho^{\mathrm{eq}}_{1k}\left(t_j-\tfrac{T_\mathrm{p}}{2}\right),\quad \text{for } k\in\{2,3\}. \tag{6.73}$$

An analogous relation can be established at $t_j + T_\mathrm{p}/2$ by utilizing Eqs. (6.70), (6.24), and (6.35), i.e.,

$$\begin{aligned}\varrho^{\mathrm{eq}}_{12}\left(t_j+\tfrac{T_\mathrm{p}}{2}\right)\mathrm{e}^{\left(-\mathrm{i}\Delta_\mathrm{X}+\frac{\Gamma_2}{2}\right)T_\mathrm{p}}&=\bar{\varrho}^{j}_{12}\left(t_j+\tfrac{T_\mathrm{p}}{2}\right)\approx\lim_{t\to+\infty}\bar{\varrho}^{j}_{12}(t)\\&=\mu_a\bar{\varrho}^{j}_{12,\mathrm{in}}+\mathrm{i}\,\nu_a\,\frac{a}{1-c}\,\mathrm{e}^{2\gamma\left(\frac{1}{2}-c\right)\frac{T_\mathrm{p}}{2}}\,\bar{\varrho}^{j}_{13,\mathrm{in}},\end{aligned} \tag{6.74a}$$

$$\begin{aligned}\varrho^{\mathrm{eq}}_{13}\left(t_j+\tfrac{T_\mathrm{p}}{2}\right)\mathrm{e}^{\left[-\mathrm{i}(\Delta_\mathrm{X}+\Delta)+\frac{\Gamma_3}{2}\right]T_\mathrm{p}}&=\bar{\varrho}^{j}_{13}\left(t_j+\tfrac{T_\mathrm{p}}{2}\right)\approx\lim_{t\to+\infty}\bar{\varrho}^{j}_{13}(t)\\&=\xi_a\bar{\varrho}^{j}_{13,\mathrm{in}}+\mathrm{i}\,\lambda_a\,\frac{a}{c}\,\mathrm{e}^{2\gamma\left(c-\frac{1}{2}\right)\frac{T_\mathrm{p}}{2}}\,\bar{\varrho}^{j}_{12,\mathrm{in}},\end{aligned} \tag{6.74b}$$

where we have once again exploited the short duration of the independent pulses in the optical frequency comb compared to the repetition period T_p, whereby it also follows that

$$\bar{\varrho}^{j}_{12}(t)\,\theta\left(t-t_j-\tfrac{T_\mathrm{p}}{2}\right)=\left[\mu_a\bar{\varrho}^{j}_{12,\mathrm{in}}+\mathrm{i}\,\nu_a\,\frac{a}{1-c}\,\mathrm{e}^{2\gamma\left(\frac{1}{2}-c\right)\frac{T_\mathrm{p}}{2}}\,\bar{\varrho}^{j}_{13,\mathrm{in}}\right]\theta\left(t-t_j-\tfrac{T_\mathrm{p}}{2}\right), \tag{6.75a}$$

$$\bar{\varrho}^{j}_{13}(t)\,\theta\left(t-t_j-\tfrac{T_\mathrm{p}}{2}\right)=\left[\xi_a\bar{\varrho}^{j}_{13,\mathrm{in}}+\mathrm{i}\,\lambda_a\,\frac{a}{c}\,\mathrm{e}^{2\gamma\left(c-\frac{1}{2}\right)\frac{T_\mathrm{p}}{2}}\,\bar{\varrho}^{j}_{12,\mathrm{in}}\right]\theta\left(t-t_j-\tfrac{T_\mathrm{p}}{2}\right). \tag{6.75b}$$

One can simultaneously take advantage of Eqs. (6.73) and (6.74) to deduce the following recursive relation which connects the jth initial conditions $\bar{\varrho}^{j}_{1k,\mathrm{in}}$ to the $j-1$th initial conditions $\bar{\varrho}^{j-1}_{1k',\mathrm{in}}$:

$$\begin{aligned}\bar{\varrho}^{j}_{12,\mathrm{in}}&=\varrho^{\mathrm{eq}}_{12}\left(t_j-\tfrac{T_\mathrm{p}}{2}\right)=\varrho^{\mathrm{eq}}_{12}\left(t_{j-1}+\tfrac{T_\mathrm{p}}{2}\right)\\&=\mu_a\,\mathrm{e}^{\left(\mathrm{i}\Delta_\mathrm{X}-\frac{\Gamma_2}{2}\right)T_\mathrm{p}}\,\bar{\varrho}^{j-1}_{12,\mathrm{in}}+\mathrm{i}\,\nu_a\,\frac{a}{1-c}\,\mathrm{e}^{\left[\mathrm{i}(2\Delta_\mathrm{X}+\Delta)-\frac{\Gamma_2+\Gamma_3}{2}\right]\frac{T_\mathrm{p}}{2}}\,\bar{\varrho}^{j-1}_{13,\mathrm{in}},\end{aligned} \tag{6.76a}$$

$$\begin{aligned}\bar{\varrho}^{j}_{13,\mathrm{in}}&=\varrho^{\mathrm{eq}}_{13}\left(t_j-\tfrac{T_\mathrm{p}}{2}\right)=\varrho^{\mathrm{eq}}_{13}\left(t_{j-1}+\tfrac{T_\mathrm{p}}{2}\right)\\&=\xi_a\,\mathrm{e}^{\left[\mathrm{i}(\Delta_\mathrm{X}+\Delta)-\frac{\Gamma_3}{2}\right]T_\mathrm{p}}\,\bar{\varrho}^{j-1}_{13,\mathrm{in}}+\mathrm{i}\,\lambda_a\,\frac{a}{c}\,\mathrm{e}^{\left[\mathrm{i}(2\Delta_\mathrm{X}+\Delta)-\frac{\Gamma_2+\Gamma_3}{2}\right]\frac{T_\mathrm{p}}{2}}\,\bar{\varrho}^{j-1}_{12,\mathrm{in}}.\end{aligned} \tag{6.76b}$$

By iteratively using Eq. (6.76), we can relate each set of initial conditions $\varrho^{j}_{1k,\mathrm{in}}$ to the initial conditions $\varrho^{0}_{1k,\mathrm{in}}$ associated with $j=0$. By further employing Eq. (6.68) for $j=0$, i.e., by using the fact that the functions $\bar{\varrho}^{0}_{1k}(t)$ are constant for $t \ll t_0$ such that

$$\bar{\varrho}^{0}_{12,\mathrm{in}} = \bar{\varrho}^{0}_{12}(T_0) = \varrho^{\mathrm{eq}}_{12}(T_0)\,\mathrm{e}^{\left(-\mathrm{i}\Delta_{\mathrm{X}}+\frac{\Gamma_2}{2}\right)\left(T_0-t_0+\frac{T_{\mathrm{p}}}{2}\right)} = \bar{\varrho}_{12,\mathrm{in}}\,\mathrm{e}^{\left(-\mathrm{i}\Delta_{\mathrm{X}}+\frac{\Gamma_2}{2}\right)\left(T_0-t_0+\frac{T_{\mathrm{p}}}{2}\right)}, \tag{6.77a}$$

$$\bar{\varrho}^{0}_{13,\mathrm{in}} = \bar{\varrho}^{0}_{13}(T_0) = \varrho^{\mathrm{eq}}_{13}(T_0)\,\mathrm{e}^{\left[-\mathrm{i}(\Delta_{\mathrm{X}}+\Delta)+\frac{\Gamma_3}{2}\right]\left(T_0-t_0+\frac{T_{\mathrm{p}}}{2}\right)} = \bar{\varrho}_{13,\mathrm{in}}\,\mathrm{e}^{\left[-\mathrm{i}(\Delta_{\mathrm{X}}+\Delta)+\frac{\Gamma_3}{2}\right]\left(T_0-t_0+\frac{T_{\mathrm{p}}}{2}\right)}, \tag{6.77b}$$

we obtain a set of equalities connecting each $\bar{\varrho}^{j}_{1k,\mathrm{in}}$ in Eq. (6.67) to the state of the system $\varrho^{\mathrm{eq}}_{1k,\mathrm{in}}$ at the initial time T_0. The general solution of the EOMs $\varrho^{\mathrm{eq}}_{1k}(t)$ for general initial conditions $\varrho^{\mathrm{eq}}_{1k,\mathrm{in}}$ is thus an immediate consequence of Eqs. (6.70).

A closed-form relation between $\bar{\varrho}^{j}_{1k,\mathrm{in}}$ and $\varrho^{\mathrm{eq}}_{1k,\mathrm{in}}$ cannot be analytically extracted from the recursive relation (6.76) for an arbitrary value of the pulse intensity, such that a numerical solution is required. However, we proceed with an analytical derivation by focusing on those particular cases in which $\nu_a = \lambda_a = 0$. As we already observed in the previous Section while discussing the single-pulse solution of the EOMs, this condition is met when either the parameter $a = A/(2\gamma)$ is an integer number, i.e., $a = n$ with $n \in \mathbb{N}_0$ [see Eqs. (6.27) and (6.37)], or when the detuning is much larger than the spectral width of the optical pulses in the optical frequency comb, i.e., $\Delta \gg \gamma$ [see Eqs. (6.30) and (6.40)]. When the detuning and the intensity of the optical pulses are set such that both ν_a and λ_a vanish, the following closed-form solution can be obtained,

$$\bar{\varrho}^{j}_{12,\mathrm{in}} = \mu_n^j\,\mathrm{e}^{\left(\mathrm{i}\Delta_{\mathrm{X}}-\frac{\Gamma_2}{2}\right)jT_{\mathrm{p}}}\,\bar{\varrho}^{0}_{12,\mathrm{in}}, \tag{6.78a}$$

$$\bar{\varrho}^{j}_{13,\mathrm{in}} = \xi_a^j\,\mathrm{e}^{\left[\mathrm{i}(\Delta_{\mathrm{X}}+\Delta)-\frac{\Gamma_3}{2}\right]jT_{\mathrm{p}}}\,\bar{\varrho}^{0}_{13,\mathrm{in}}, \tag{6.78b}$$

such that, by further exploiting Eq. (6.77), one can conclude that

$$\bar{\varrho}^{j}_{12,\mathrm{in}} = \bar{\varrho}_{12,\mathrm{in}}\,\mathrm{e}^{\left(\mathrm{i}\Delta_{\mathrm{X}}-\frac{\Gamma_2}{2}\right)\left(t_j-\frac{T_{\mathrm{p}}}{2}-T_0\right)}\,\mu_a^j, \tag{6.79a}$$

$$\bar{\varrho}^{j}_{13,\mathrm{in}} = \bar{\varrho}_{13,\mathrm{in}}\,\mathrm{e}^{\left[\mathrm{i}(\Delta_{\mathrm{X}}+\Delta)-\frac{\Gamma_3}{2}\right]\left(t_j-\frac{T_{\mathrm{p}}}{2}-T_0\right)}\,\xi_a^j, \tag{6.79b}$$

and, by using Eq. (6.67), that

$$\begin{aligned}\bar{\varrho}^{j}_{12}(z_j) = {}& \bar{\varrho}_{12,\mathrm{in}}\,\mathrm{e}^{\left(\mathrm{i}\Delta_{\mathrm{X}}-\frac{\Gamma_2}{2}\right)\left(t_j-\frac{T_{\mathrm{p}}}{2}-T_0\right)}\,\mu_a^j\,{}_2F_1(a,-a;c;z_j) \;+\; \mathrm{i}\,\bar{\varrho}_{13,\mathrm{in}}\,\frac{a}{1-c} \\ & \times\,\mathrm{e}^{2\gamma\left(\frac{1}{2}-c\right)\frac{T_{\mathrm{p}}}{2}}\,\mathrm{e}^{\left[\mathrm{i}(\Delta_{\mathrm{X}}+\Delta)-\frac{\Gamma_3}{2}\right]\left(t_j-\frac{T_{\mathrm{p}}}{2}-T_0\right)}\,\xi_a^j\,z_j^{1-c}\,(1-z_j)^c\,{}_2F_1(1-a,1+a;2-c;z_j),\end{aligned} \tag{6.80a}$$

$$\begin{aligned}\bar{\varrho}^{j}_{13}(z_j) = {}& \bar{\varrho}_{13,\mathrm{in}}\,\mathrm{e}^{\left[\mathrm{i}(\Delta_{\mathrm{X}}+\Delta)-\frac{\Gamma_3}{2}\right]\left(t_j-\frac{T_{\mathrm{p}}}{2}-T_0\right)}\,\xi_a^j\,{}_2F_1(a,-a;1-c;z_j) \\ & +\,\mathrm{i}\,\bar{\varrho}_{12,\mathrm{in}}\,\frac{a}{c}\,\mathrm{e}^{2\gamma\left(c-\frac{1}{2}\right)\frac{T_{\mathrm{p}}}{2}}\,\mathrm{e}^{\left(\mathrm{i}\Delta_{\mathrm{X}}-\frac{\Gamma_2}{2}\right)\left(t_j-\frac{T_{\mathrm{p}}}{2}-T_0\right)}\mu_a^j z_j^c\,(1-z_j)^{1-c}\,{}_2F_1(1-a,1+a;1+c;z_j).\end{aligned} \tag{6.80b}$$

By inserting (6.80) into Eq. (6.70), the final solution is obtained. This is shown explicitly only for $\varrho^{\mathrm{eq}}_{12}(t)$, since exactly the same steps are necessary in order to write $\varrho^{\mathrm{eq}}_{13}(t)$ in closed form.

The approximations justified via Eqs. (6.68) and (6.75) can be implemented in Eq. (6.70), thus providing the function

$$\begin{aligned}\varrho_{12}^{\mathrm{eq}}(t) = {}& \mathrm{e}^{\left(\mathrm{i}\Delta_{\mathrm{X}}-\frac{\Gamma_2}{2}\right)\left(t-t_0+\frac{T_{\mathrm{p}}}{2}\right)}\,\bar{\varrho}_{12,\mathrm{in}}^{0}\,\theta\left(-t+t_0-\tfrac{T_{\mathrm{p}}}{2}\right)\\ &+\sum_{j=0}^{\infty}\mathrm{e}^{\left(\mathrm{i}\Delta_{\mathrm{X}}-\frac{\Gamma_2}{2}\right)\left(t-t_j+\frac{T_{\mathrm{p}}}{2}\right)}\left[-\bar{\varrho}_{12,\mathrm{in}}^{j}\,\theta\left(-t+t_j-\tfrac{T_{\mathrm{p}}}{2}\right)+\bar{\varrho}_{12}^{j}(t)\;-\mu_a\,\bar{\varrho}_{12,\mathrm{in}}^{j}\,\theta\left(t-t_j-\tfrac{T_{\mathrm{p}}}{2}\right)\right].\end{aligned} \tag{6.81}$$

The sum in j on the right-hand side of the previous equality can be extended to all integers from $-\infty$ to $+\infty$, provided that a multiplicative factor $\theta(t-t_0+\frac{T_{\mathrm{p}}}{2})$ is included, i.e.,

$$\begin{aligned}\varrho_{12}^{\mathrm{eq}}(t) = {}& \mathrm{e}^{\left(\mathrm{i}\Delta_{\mathrm{X}}-\frac{\Gamma_2}{2}\right)(t-T_0)}\,\bar{\varrho}_{12,\mathrm{in}}\,\theta\left(-t+t_0-\tfrac{T_{\mathrm{p}}}{2}\right)\\ &+\theta\left(t-t_0+\tfrac{T_{\mathrm{p}}}{2}\right)\Bigg\{\sum_{j=-\infty}^{\infty}\mathrm{e}^{\left(\mathrm{i}\Delta_{\mathrm{X}}-\frac{\Gamma_2}{2}\right)\left(t-t_j+\frac{T_{\mathrm{p}}}{2}\right)}\,\bar{\varrho}_{12}^{j}(t)\\ &-\sum_{j=-\infty}^{\infty}\mathrm{e}^{\left(\mathrm{i}\Delta_{\mathrm{X}}-\frac{\Gamma_2}{2}\right)(t-T_0)}\left[\mu_a^{j}\,\theta\left(-t+t_j-\tfrac{T_{\mathrm{p}}}{2}\right)+\mu_a^{j+1}\,\theta\left(t-t_{j+1}+\tfrac{T_{\mathrm{p}}}{2}\right)\right]\,\bar{\varrho}_{12,\mathrm{in}}\Bigg\},\end{aligned} \tag{6.82}$$

where we have utilized Eqs. (6.79) and we have substituted the argument of the second Heaviside function on the third line by taking into account that $t_j = t_{j+1} - T_{\mathrm{p}}$. Rearranging the sum on the third line of the previous equality and thereby exploiting the following identity,

$$\theta\left(-t+t_j-\tfrac{T_{\mathrm{p}}}{2}\right)+\theta\left(t-t_j+\tfrac{T_{\mathrm{p}}}{2}\right)=1, \tag{6.83}$$

leads to

$$\begin{aligned}\varrho_{12}^{\mathrm{eq}}(t) = {}& \mathrm{e}^{\left(\mathrm{i}\Delta_{\mathrm{X}}-\frac{\Gamma_2}{2}\right)(t-T_0)}\,\bar{\varrho}_{12,\mathrm{in}}\,\theta\left(-t+t_0-\tfrac{T_{\mathrm{p}}}{2}\right)\\ &+\sum_{j=-\infty}^{\infty}\left[\mathrm{e}^{\left(\mathrm{i}\Delta_{\mathrm{X}}-\frac{\Gamma_2}{2}\right)\left(t-t_j+\frac{T_{\mathrm{p}}}{2}\right)}\,\bar{\varrho}_{12}^{j}(t)\;-\mathrm{e}^{\left(\mathrm{i}\Delta_{\mathrm{X}}-\frac{\Gamma_2}{2}\right)(t-T_0)}\,\mu_a^{j}\,\bar{\varrho}_{12,\mathrm{in}}\right]\,\theta\left(t-t_0+\tfrac{T_{\mathrm{p}}}{2}\right)\end{aligned} \tag{6.84}$$

and, therefore, to

$$\begin{aligned}\varrho_{12}^{\mathrm{eq}}(t) = {}& \bar{\varrho}_{12,\mathrm{in}}\,\mathrm{e}^{\left(\mathrm{i}\Delta_{\mathrm{X}}-\frac{\Gamma_2}{2}\right)(t-T_0)}\,\theta\left(-t+t_0-\tfrac{T_{\mathrm{p}}}{2}\right)\\ &+\bar{\varrho}_{12,\mathrm{in}}\,\mathrm{e}^{\left(\mathrm{i}\Delta_{\mathrm{X}}-\frac{\Gamma_2}{2}\right)(t-T_0)}\left[\sum_{j=-\infty}^{\infty}\mu_a^{j}\Big({}_2F_1(a,-a;c;z_j(t))-1\Big)\right]\theta\left(t-t_0+\tfrac{T_{\mathrm{p}}}{2}\right)\\ &+\mathrm{i}\,\bar{\varrho}_{13,\mathrm{in}}\,\frac{a}{1-c}\,\mathrm{e}^{\mathrm{i}\Delta_{\mathrm{X}}(t-T_0)}\left[\sum_{j=-\infty}^{\infty}\mathrm{e}^{-\frac{\Gamma_3}{2}(t_j-T_0)}\,\mathrm{e}^{\mathrm{i}\Delta(t_j-T_0)}\,\mathrm{e}^{-\frac{\Gamma_2}{2}(t-t_j)}\right.\\ &\left.\times\;\xi_a^{j}[z_j(t)]^{1-c}\,[1-z_j(t)]^{c}\,{}_2F_1(1-a,1+a;2-c;z_j(t))\right]\theta\left(t-t_0+\tfrac{T_{\mathrm{p}}}{2}\right),\end{aligned} \tag{6.85}$$

where we have employed the single-pulse solution $\bar{\varrho}_{12}^{j}(t)$ from Eq. (6.80). By recalling the definition of c (6.16) and by rearranging the sums in j in the previous identity, we conclude that

$$\varrho_{12}^{\mathrm{eq}}(t) = \bar{\varrho}_{12,\mathrm{in}}\, \mathrm{e}^{\left(\mathrm{i}\Delta_{\mathrm{X}} - \frac{\Gamma_2}{2}\right)(t-T_0)} \left[1 + \sum_{j=0}^{\infty} \mu_a^j \Big({}_2F_1(a,-a;c;z_j(t)) - 1\Big)\right] + \mathrm{i}\,\bar{\varrho}_{13,\mathrm{in}}\, \frac{a}{2(1-c)}\, \mathrm{e}^{\left[\mathrm{i}(\Delta_{\mathrm{X}}+\Delta) - \frac{\Gamma_3}{2}\right](t-T_0)} \sum_{j=0}^{\infty} \xi_a^j\ \mathrm{sech}[\gamma(t-t_j)]\, {}_2F_1(1-a,1+a;2-c;z_j(t)), \tag{6.86a}$$

$$\varrho_{13}^{\mathrm{eq}}(t) = \bar{\varrho}_{13,\mathrm{in}}\, \mathrm{e}^{\left[\mathrm{i}(\Delta_{\mathrm{X}}+\Delta) - \frac{\Gamma_3}{2}\right](t-T_0)} \left[1 + \sum_{j=0}^{\infty} \xi_a^j \Big({}_2F_1(a,-a;1-c;z_j(t)) - 1\Big)\right] + \mathrm{i}\,\bar{\varrho}_{12,\mathrm{in}}\, \frac{a}{2c}\, \mathrm{e}^{\left(\mathrm{i}\Delta_{\mathrm{X}} - \frac{\Gamma_2}{2}\right)(t-T_0)} \sum_{j=0}^{\infty} \mu_a^j\ \mathrm{sech}[\gamma(t-t_j)]\, {}_2F_1(1-a,1+a;1+c;z_j(t)), \tag{6.86b}$$

were analogous steps were followed for the calculation of the off-diagonal matrix element $\varrho_{13}^{\mathrm{eq}}(t)$.

In the following we analyze the solution of the EOMs (6.86) describing the interaction of the three-level system with a train of optical pulses $\boldsymbol{\mathcal{E}}_{\mathrm{C}}(\boldsymbol{r}, t)$ by separately considering the two different sets of initial conditions we already identified while presenting the single-pulse solution in Sec. 6.2. These different sets of initial conditions correspond to different preparatory schemes via the x-ray pulse $\boldsymbol{\mathcal{E}}_{\mathrm{X}}(\boldsymbol{r}, t)$ and the optical pulse $\boldsymbol{\mathcal{E}}_{\mathrm{L}}(\boldsymbol{r}, t)$.

6.3.1.1 X-ray-only preparation

When the initial coherence is created via a single x-ray pulse driving the $1 \to 2$ transition, such that at time T_0 the initial state is characterized by $\varrho_{13,\mathrm{in}}^{\mathrm{eq}} = 0$, then the solution of the EOMs in Eq. (6.86) describing the interaction of the three-level system with the optical frequency comb $\boldsymbol{\mathcal{E}}_{\mathrm{C}}(\boldsymbol{r}, t)$ is given by

$$\varrho_{12}^{\mathrm{eq}}(t) = \bar{\varrho}_{12,\mathrm{in}}\, \mathrm{e}^{\left(\mathrm{i}\Delta_{\mathrm{X}} - \frac{\Gamma_2}{2}\right)(t-T_0)} \left[1 + \sum_{j=0}^{\infty} \mu_a^j \Big({}_2F_1(a,-a;c;z_j(t)) - 1\Big)\right], \tag{6.87a}$$

$$\varrho_{13}^{\mathrm{eq}}(t) = \mathrm{i}\,\bar{\varrho}_{12,\mathrm{in}}\, \frac{a}{2c}\, \mathrm{e}^{\left(\mathrm{i}\Delta_{\mathrm{X}} - \frac{\Gamma_2}{2}\right)(t-T_0)} \sum_{j=0}^{\infty} \mu_a^j\ \mathrm{sech}[\gamma(t-t_j)]\, {}_2F_1(1-a,1+a;1+c;z_j(t)). \tag{6.87b}$$

The amplitudes of both $|\varrho_{12}^{\mathrm{eq}}(t)|$ and $|\varrho_{13}^{\mathrm{eq}}(t)|$ exponentially decrease with time: In particular, for $t > t_0$ and $k \in \{2, 3\}$, we can see that

$$|\varrho_{1k}^{\mathrm{eq}}(t+T_{\mathrm{p}})|^2 = \mathrm{e}^{-\Gamma_2 T_{\mathrm{p}}}\, |\mu_a|^2\, |\varrho_{1k}^{\mathrm{eq}}(t)|^2 = \mathrm{e}^{-\left(\Gamma_2 - 2\frac{\log(|\mu_a|)}{T_{\mathrm{p}}}\right)T_{\mathrm{p}}}\, |\varrho_{1k}^{\mathrm{eq}}(t)|^2 = \mathrm{e}^{-\frac{T_{\mathrm{p}}}{\tau_a}}\, |\varrho_{1k}^{\mathrm{eq}}(t)|^2, \tag{6.88}$$

i.e., the amplitude of $|\varrho_{1k}^{\mathrm{eq}}(t+T_{\mathrm{p}})|^2$ displays an exponential decrease with decay time

$$\tau_a = \frac{1}{\Gamma_2 - 2\frac{\log(|\mu_a|)}{T_{\mathrm{p}}}}. \tag{6.89}$$

The effective decay rate $1/\tau_a$ is the sum of two components, (i) the decay rate of the excited state Γ_2 and (ii) the optically induced decay rate $-2\frac{\log(|\mu_a|)}{T_{\mathrm{p}}}$ associated with the periodic "loss of amplitude" $-2\log(|\mu_a|)$ taking place only in the presence of an optical pulse. The increase

in decay rate related to $-2\frac{\log(|\mu_a|)}{T_\mathrm{p}}$ and ensuing from the interaction with an optical pulse is numerically shown to be negligible if compared to the decay rate Γ_2 of the fast decaying excited level 2. This is also confirmed by the results exhibited in the next figures, where we employ the $1s\,2p\,{}^1P_1 \to 1s\,2s\,{}^1S_0$ $(2 \to 3)$ and the $1s^2\,{}^1S_0 \to 1s\,2p\,{}^1P_1$ $(1 \to 2)$ transitions of He and He-like Be^{2+} to implement our three-level scheme.

The high-frequency, $1 \to 2$ transition in He is in the extended ultraviolet region, with transition energy $\omega_{21} = 21.2\,\mathrm{eV}$ and decay rate $\Gamma_{21} = 1.8 \times 10^9\,\mathrm{s}^{-1}$, corresponding to a decay time of $\sim 6\,\mathrm{ns}$. In order to optically modify the decay of the excited level with an optical frequency comb $\boldsymbol{\mathcal{E}}_\mathrm{C}(\boldsymbol{r}, t)$, the repetition period T_p ought to be lower than its decay time. In the following we employ a quite high repetition frequency of $1/T_\mathrm{p} = 10\,\mathrm{GHz}$. We implement a three-level approximation by considering the impact of the sole $1s\,2s\,{}^1S_0$ level, with transition energy $\omega_{23} = 0.6\,\mathrm{eV}$ and decay rates $\Gamma_{23} = 2.0 \times 10^6\,\mathrm{s}^{-1}$ and $\Gamma_{31} = 51\,\mathrm{s}^{-1}$. In He, however, such a three-level approximation is not completely valid, because the $2 \to 3$ transition is not well isolated and the effect of other nearby levels such as $1s\,3s\,{}^1S_0$, $1s\,3d\,{}^1D_2$, and $1s\,3d\,{}^3D_2$ ought to be taken into account. In contrast to the results presented here, a complete analysis including the effect of other excited levels cannot be addressed via a completely analytical approach and requires a numerical solution of the EOMs (6.13). The following implementation with He, therefore, does not provide quantitatively precise results. However, the solution of the EOMs which we predict with our three-level approximation captures the essential features ensuing from the interaction of the system with an external train of optical pulses. In other words, by numerically taking into account the presence of additional levels, the same qualitative behaviour could be recovered as here, with a slight, quantitative difference in the values of the associated optical-comb parameters such as detuning or peak intensity [214].

In contrast, the here adopted three-level approximation can be safely employed in the case of He-like Be^{2+}, since the corresponding $2 \to 3$ transition is well isolated: Furthermore, the transition energy $\omega_{23} = 2.02\,\mathrm{eV}$ between the excited states $1s\,2s\,{}^1S_0$ and $1s\,2p\,{}^1P_1$ is the only one in the optical range and the contribution from other excited levels is completely negligible. The transition energies are $\omega_{23} = 2.02\,\mathrm{eV}$ and $\omega_{21} = 123.7\,\mathrm{eV}$, as we already discussed in the previous Section. The decay rate of the excited level 2 is equal to $\Gamma_{21} = 1.2 \times 10^{11}\,\mathrm{s}^{-1}$, corresponding to a decay time of $\sim 8\,\mathrm{ps}$. As a result, in the following we assume an optical frequency comb with very high repetition frequency, $1/T_\mathrm{p} = 100\,\mathrm{GHz}$, in order to optically modify the coherent response of the system. The remaining decay rates are $\Gamma_{23} = 8.7 \times 10^6\,\mathrm{s}^{-1}$ and $\Gamma_{31} = 1.8 \times 10^4\,\mathrm{s}^{-1}$. Both for He and He-like Be, the decay rates Γ_{21} and Γ_{23} were calculated with `grasp2K` [200–202], while the two-photon decay rates Γ_{31} were taken from Ref. [212]. Transition energies are taken from Ref. [191].

In Fig. 6.10 we employ a train of 2π, tuned optical pulses to drive the $2 \to 3$ transition in the three-level system. As we already discussed in the single-pulse case of Fig. 6.2, in the presence of an optical pulse an ultrashort transfer of coherence is performed. A periodic coherence transfer ensues, therefore, from the interaction with an optical frequency comb. By fixing the value of the single-pulse area to 2π, we ensure that $\varrho_{13}^\mathrm{eq}(t)$ is led back to its vanishing initial value at conclusion of each pulse [Figs. 6.10c and 6.10d]. The effect of the pulses on the time evolution of the decaying function $\varrho_{12}^\mathrm{eq}(t)$ is described by the constant μ_a, which we defined in Eq. (6.24a). Since the pulses are here tuned to the resonance, $\Delta = 0$, and the decay rates are much smaller than the single-pulse width, $\Gamma_2/\gamma \ll 1$, we can use Eq. (6.29) to show that $\mu_n \approx (-1)^n$. For a pulse area equal to $Q_\mathrm{C} = 2\pi$ and therefore associated with $a = 1$, μ_a is equal to -1. As a result, the optical manipulation of the atomic response, i.e., of $\varrho_{12}^\mathrm{eq}(t)$, gives rise to a periodic phase shift equal to π, which appears in Figs. 6.10a and 6.10b.

For the same two atomic systems we display in Fig. 6.11 the functions $\varrho_{12}^\mathrm{eq}(t)$ and $\varrho_{13}^\mathrm{eq}(t)$ from

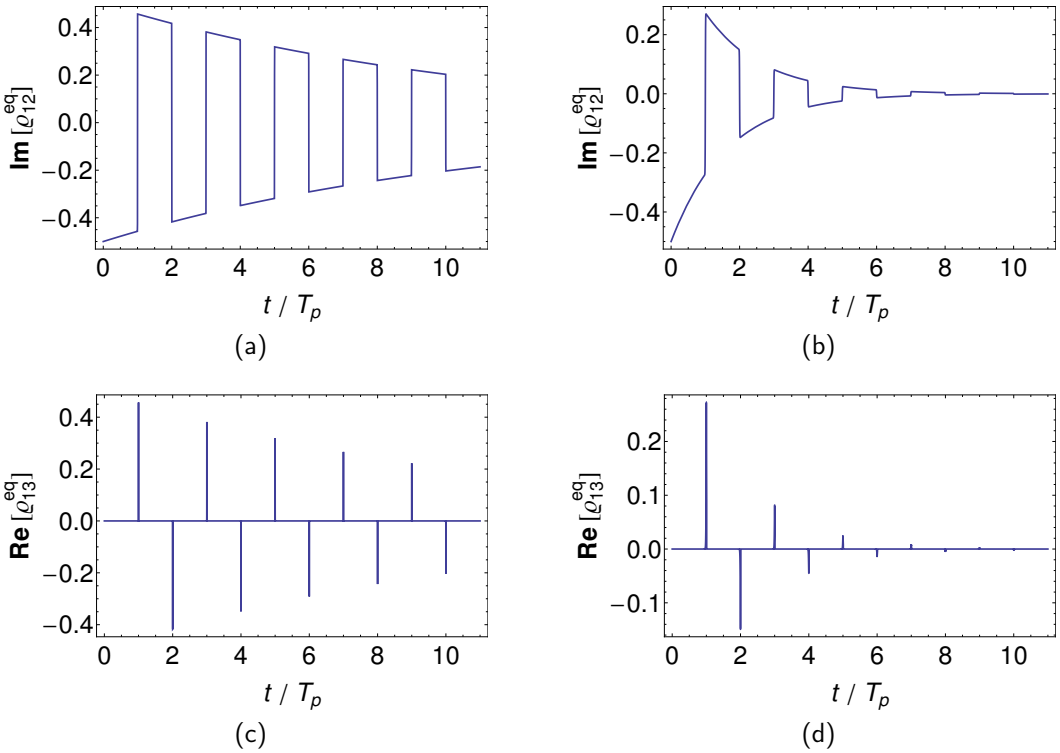

Figure 6.10: Off-diagonal elements $\mathbf{Im}\{\varrho_{12}^{\mathrm{eq}}(t)\}$ [(a) and (b)] and $\mathbf{Re}\{\varrho_{13}^{\mathrm{eq}}(t)\}$ [(c) and (d)] of the three-level system of Fig. 6.1, used to model He and He-like Be^{2+} ions, initially prepared at time $T_0 = 0$ in a state with $\bar{\varrho}_{12,\mathrm{in}} = -\mathrm{i}/2$, $\bar{\varrho}_{13,\mathrm{in}} = 0$, whose $1s\,2s\,{}^1S_0 \to 1s\,2p\,{}^1P_1$ transition is driven by a train of 2π optical pulses, with FWHM duration of $\tau_{\mathrm{FWHM}} = 100\,\mathrm{fs}$, tuned to the optical transition. In the case of He [panels (a) and (c)], the transition energies are $\omega_{23} = 0.6\,\mathrm{eV}$, $\omega_{21} = 21.2\,\mathrm{eV}$, and the decay rate of the excited state is $\Gamma_2 = 1.8 \times 10^9\,\mathrm{s}^{-1}$: We use pulses with repetition period $T_{\mathrm{p}} = 100\,\mathrm{ps}$, i.e., $1/T_{\mathrm{p}} = 10\,\mathrm{GHz}$, and peak intensities $I_{\mathrm{C,max}} = 3.0 \times 10^9\,\mathrm{W/cm^2}$. In the case of He-like Be^{2+} [panels (b) and (d)], the transition energies are $\omega_{23} = 2.02\,\mathrm{eV}$, $\omega_{21} = 123.7\,\mathrm{eV}$, and the decay rate of the excited state is $\Gamma_2 = 1.2 \times 10^{11}\,\mathrm{s}^{-1}$: We use pulses with repetition period $T_{\mathrm{p}} = 10\,\mathrm{ps}$, i.e., $1/T_{\mathrm{p}} = 100\,\mathrm{GHz}$, and peak intensities $I_{\mathrm{C,max}} = 2.6 \times 10^{10}\,\mathrm{W/cm^2}$. In both cases, the peak intensity corresponds to a pulse area $Q_{\mathrm{C}} = 2\pi$. The train of pulses starts at $t_0 = T_0 + T_{\mathrm{p}}$.

Eqs. (6.87) in the large-detuning limit. We assume that the carrier frequency of the optical pulses is $\omega_{\mathrm{C}} = 1.5\,\mathrm{eV}$, resulting in a detuning $\Delta = 0.9\,\mathrm{eV}$ and $\Delta = -0.52\,\mathrm{eV}$, for He and He-like Be^{2+}, respectively. As a consequence of Eq. (6.40), $\varrho_{13}^{\mathrm{eq}}(t)$ is led back to its vanishing initial value at conclusion of each pulse [Figs. 6.11e and 6.11f]. As we already discussed in the single-pulse case, the amplitude of $\varrho_{12}^{\mathrm{eq}}(t)$ is not significantly affected by the presence of the detuned pulses. The same situation is confirmed in the many-pulse case displayed in Figs. 6.11a and 6.11b, which exhibit an essentially unchanged exponential decay of the amplitude of the function. In the large-detuning case, the main effect due to the interaction of the system with the optical frequency comb is namely a periodic shift in the phase of $\varrho_{12}^{\mathrm{eq}}(t)$ [Figs. 6.11c and 6.11d]. The amplitude of each phase shift is fixed by the constant $\arg(\mu_a)$, whose dependence on the optical-comb peak intensity follows from Eq. (6.24).

6.3.1.2 Coherence-storage preparation

When the preparatory stage of the system consists in an x-ray pulse $\boldsymbol{\mathcal{E}}_{\mathrm{X}}(\boldsymbol{r}, t)$ and an optical pulse $\boldsymbol{\mathcal{E}}_{\mathrm{L}}(\boldsymbol{r}, t)$ of area π and tuned to the $2 \to 3$ transition, the state of the system at time T_0

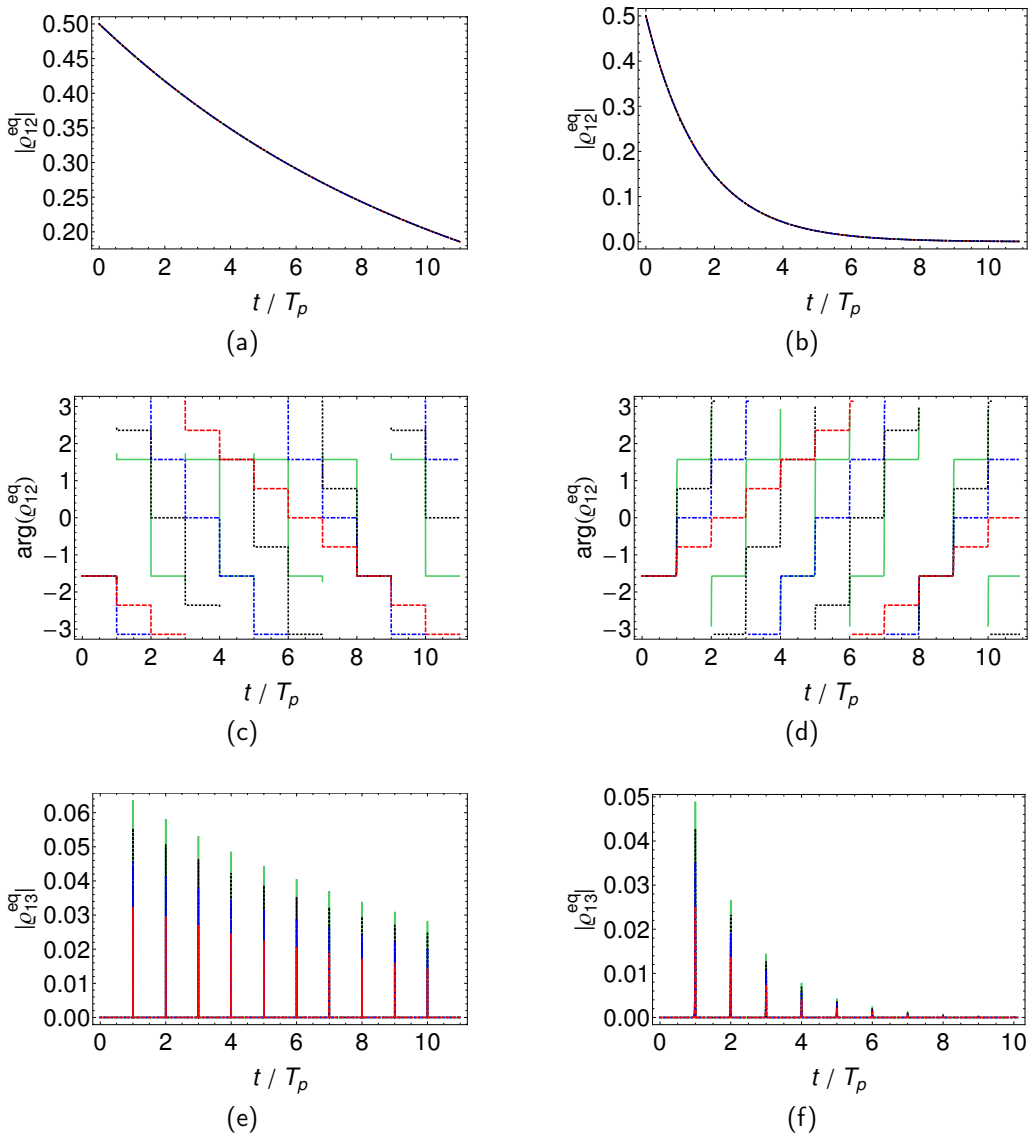

Figure 6.11: Off-diagonal elements $|\varrho_{12}^{\mathrm{eq}}(t)|$ [(a) and (b)], $\arg[\varrho_{12}^{\mathrm{eq}}(t)]$ [(c) and (d)], and $|\varrho_{13}^{\mathrm{eq}}(t)|$ [(e) and (f)], of the three-level system of Fig. 6.1, used to model He and He-like Be^{2+} ions, initially prepared at time $T_0 = 0$ in a state with $\bar{\varrho}_{12,\mathrm{in}} = -\mathrm{i}/2$, $\bar{\varrho}_{13,\mathrm{in}} = 0$, whose $1s\,2s\,{}^1S_0 \to 1s\,2p\,{}^1P_1$ transition is driven by a train of optical pulses with energy $\omega_{\mathrm{C}} = 1.5\,\mathrm{eV}$ and FWHM duration $\tau_{\mathrm{FWHM}} = 100\,\mathrm{fs}$. In the case of He [panels (a), (c), and (e)], the transition energies are $\omega_{23} = 0.6\,\mathrm{eV}$, $\omega_{21} = 21.2\,\mathrm{eV}$, the detuning is $\Delta = -\Delta_{\mathrm{C}} = 0.9\,\mathrm{eV}$, and the decay rate of the excited state is $\Gamma_2 = 1.8 \times 10^9\,\mathrm{s}^{-1}$: We use pulses with repetition period $T_{\mathrm{p}} = 100\,\mathrm{ps}$, i.e., $1/T_{\mathrm{p}} = 10\,\mathrm{GHz}$, and peak intensities $I_{\mathrm{C,max}} = 9.2 \times 10^{10}\,\mathrm{W/cm^2}$ (red, dashed line), $I_{\mathrm{C,max}} = 1.8 \times 10^{11}\,\mathrm{W/cm^2}$ (blue, dotdashed line), $I_{\mathrm{C,max}} = 2.8 \times 10^{11}\,\mathrm{W/cm^2}$ (black, dotted line), and $I_{\mathrm{C,max}} = 3.7 \times 10^{11}\,\mathrm{W/cm^2}$ (green, solid line). In the case of He-like Be^{2+} [panels (b), (d), and (f)], the transition energies are $\omega_{23} = 2.02\,\mathrm{eV}$, $\omega_{21} = 123.7\,\mathrm{eV}$, the detuning is $\Delta = -\Delta_{\mathrm{C}} = -0.52\,\mathrm{eV}$, and the decay rate of the excited state is $\Gamma_2 = 1.2 \times 10^{11}\,\mathrm{s}^{-1}$: We use pulses with repetition period $T_{\mathrm{p}} = 10\,\mathrm{ps}$, i.e., $1/T_{\mathrm{p}} = 100\,\mathrm{GHz}$, and peak intensities $I_{\mathrm{C,max}} = 4.5 \times 10^{11}\,\mathrm{W/cm^2}$ (red, dashed line), $I_{\mathrm{C,max}} = 9.1 \times 10^{11}\,\mathrm{W/cm^2}$ (blue, dotdashed line), $I_{\mathrm{C,max}} = 1.4 \times 10^{12}\,\mathrm{W/cm^2}$ (black, dotted line), and $I_{\mathrm{C,max}} = 1.9 \times 10^{12}\,\mathrm{W/cm^2}$ (green, solid line). In both cases, the peak intensities correspond to a phase kick $\arg(\mu_a) = \pi/4$ (red, dashed line), $\arg(\mu_a) = \pi/2$ (blue, dotdashed line), $\arg(\mu_a) = 3\pi/4$ (black, dotted line), and $\arg(\mu_a) = \pi$ (green, solid line), respectively. The train of pulses starts at $t_0 = T_0 + T_{\mathrm{p}}$.

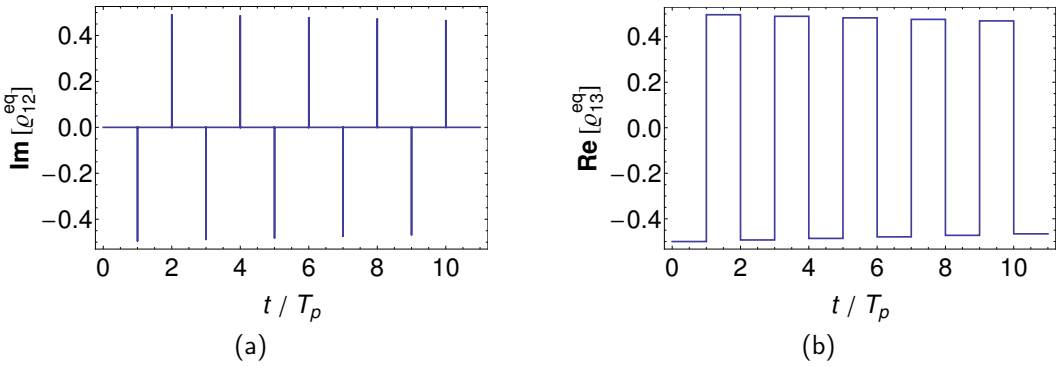

Figure 6.12: Off-diagonal elements (a) $\mathbf{Im}\{\varrho_{12}^{\mathrm{eq}}(t)\}$ and (b) $\mathbf{Re}\{\varrho_{13}^{\mathrm{eq}}(t)\}$ of the three-level system of Fig. 6.1, used to model He-like Be^{2+} ions, initially prepared at time $T_0 = 0$ in a state with $\bar{\varrho}_{12,\mathrm{in}} = 0$, $\bar{\varrho}_{13,\mathrm{in}} = -1/2$, whose $1s\,2s\,{}^1S_0 \to 1s\,2p\,{}^1P_1$ transition is driven by a train of 2π optical pulses tuned to the optical transition with $\tau_{\mathrm{FWHM}} = 100\,\mathrm{fs}$. The transition energy is $\omega_{23} = 2.02\,\mathrm{eV}$: We use pulses with repetition period $T_{\mathrm{p}} = 10\,\mathrm{ns}$, i.e., $1/T_{\mathrm{p}} = 100\,\mathrm{MHz}$, and peak intensities $I_{\mathrm{C,max}} = 2.6 \times 10^{10}\,\mathrm{W/cm^2}$, corresponding to a pulse area $Q_{\mathrm{C}} = 2\pi$. The train of pulses starts at $t_0 = T_0 + T_{\mathrm{p}}$.

is described by the off-diagonal elements of the density matrix $\bar{\varrho}_{12,\mathrm{in}} = 0$ and $\bar{\varrho}_{13,\mathrm{in}} \neq 0$. The corresponding solution of the EOMs upon interaction with an optical frequency comb $\boldsymbol{\mathcal{E}}_{\mathrm{C}}(\boldsymbol{r}, t)$ is

$$\varrho_{12}^{\mathrm{eq}}(t) = \mathrm{i}\,\bar{\varrho}_{13,\mathrm{in}}\,\frac{a}{2(1-c)}\,\mathrm{e}^{\left[\mathrm{i}(\Delta_{\mathrm{X}}+\Delta)-\frac{\Gamma_3}{2}\right](t-T_0)}\,\sum_{j=0}^{\infty}\xi_a^j\,\mathrm{sech}[\gamma(t-t_j)]\,{}_2F_1(1-a,1+a;2-c;z_j(t)), \tag{6.90a}$$

$$\varrho_{13}^{\mathrm{eq}}(t) = \bar{\varrho}_{13,\mathrm{in}}\,\mathrm{e}^{\left[\mathrm{i}(\Delta_{\mathrm{X}}+\Delta)-\frac{\Gamma_3}{2}\right](t-T_0)}\,\left[1+\sum_{j=0}^{\infty}\xi_a^j\Big({}_2F_1(a,-a;1-c;z_j(t))-1\Big)\right]. \tag{6.90b}$$

The amplitudes of $|\varrho_{12}^{\mathrm{eq}}(t)|$ and $|\varrho_{13}^{\mathrm{eq}}(t)|$ exponentially decrease with time: in particular, for $t > t_0$ and $k \in \{2, 3\}$, we can write that

$$|\varrho_{1k}^{\mathrm{eq}}(t+T_{\mathrm{p}})|^2 = \mathrm{e}^{-\Gamma_3 T_{\mathrm{p}}}\,|\xi_a|^2\,|\varrho_{1k}^{\mathrm{eq}}(t)|^2 = \mathrm{e}^{-\left(\Gamma_3 - 2\frac{\log(|\xi_a|)}{T_{\mathrm{p}}}\right)T_{\mathrm{p}}}\,|\varrho_{1k}^{\mathrm{eq}}(t)|^2 = \mathrm{e}^{-\frac{T_{\mathrm{p}}}{\tilde{\tau}_a}}\,|\varrho_{1k}^{\mathrm{eq}}(t)|^2, \tag{6.91}$$

such that a new, effective decay time $\tilde{\tau}_a$ can be defined,

$$\tilde{\tau}_a = \frac{1}{\Gamma_3 - 2\frac{\log(|\xi_a|)}{T_{\mathrm{p}}}}. \tag{6.92}$$

The decay rate $1/\tilde{\tau}_a$ exhibits two contributions, i.e., (i) the decay rate of the metastable state Γ_3 and (ii) an additional term $-2\frac{\log(|\xi_a|)}{T_{\mathrm{p}}}$ associated with the "loss of amplitude" $-2\log(|\xi_a|)$ taking place in the presence of an optical pulse. This second term $-2\frac{\log(|\xi_a|)}{T_{\mathrm{p}}}$ is approximately proportional to the ratio $\tau_{\mathrm{FWHM}}/T_{\mathrm{p}}$ between the duration of the pulses in the comb and its repetition period. The effective decay time $\tilde{\tau}_a$ is related to the decay rate Γ_2 of the rapidly decaying level 2 only indirectly, via this second additional term. In the following figures we use the $1s\,2s\,{}^1S_0 \to 1s\,2p\,{}^1P_1$ optical transition of Be^{2+} ions to display the two functions $\varrho_{12}^{\mathrm{eq}}(t)$ and $\varrho_{13}^{\mathrm{eq}}(t)$ from Eq. (6.90), with level 1 being given by the ground state of the system. Transition energies and decay rates have already been discussed previously.

In Fig. 6.12 we display the evolution in time of $\varrho_{12}^{\mathrm{eq}}(t)$ and $\varrho_{13}^{\mathrm{eq}}(t)$ upon interaction with a train of 2π optical pulses tuned to the $2 \to 3$ transition at $2.02\,\mathrm{eV}$. We use a repetition frequency of

$1/T_\mathrm{p} = 100\,\mathrm{MHz}$, as provided by present-day optical-comb technology; the value of the employed peak intensity, $\sim 10^{10}\,\mathrm{W/cm^2}$, is by orders of magnitude lower than the intensity presently used by XUV-comb-generation methods based on HHG [122, 205–208]. In the long time interval in between two optical pulses the coherence is stored in level 3, whose decay rate Γ_3 is by orders of magnitude smaller than Γ_2. This is apparent from the constant amplitude which the function $|\varrho_{13}^\mathrm{eq}(t)|$ exhibits in the time interval in between two pulses [Fig. 6.12b]. In the presence of the optical pulses, however, the coherence is transferred to the fast decaying excited level 2: The pulse area $Q_\mathrm{C} = 2\pi$ ensures that $\varrho_{12}^\mathrm{eq}(t)$ is led back to its vanishing initial value when the interaction with the pulse has concluded [Fig. 6.12a]. As a result, the "loss of coherence and population" associated with the fast decay of level 2, with decay rate Γ_2, is restricted to the short time intervals $\sim \tau_\mathrm{FWHM}$ in which one of the optical-comb pulses interacts with the ions. The loss of coherence which the system undergoes in the presence of the optical pulses is given by $-2\log(|\xi_a|)$: This loss is clearly apparent in Fig. 6.12b, which shows that the amplitude of $|\varrho_{13}^\mathrm{eq}(t)|$ periodically decreases as a consequence of the interaction with the optical pulses. The effective decay rate $1/\tilde{\tau}_a$ is approximately proportional to the ratio $\tau_\mathrm{FWHM}/T_\mathrm{p}$ between the duration of an optical pulse and the optical-comb repetition period. Since this ratio is much lower than 1, also the effective decay rate $1/\tilde{\tau}_a$ is by orders of magnitude lower than Γ_2. As a result, repetition frequencies such as those employed here, e.g., $1/T_\mathrm{p} = 100\,\mathrm{MHz}$, are sufficient to effectively manipulate the time evolution of the system with the optical frequency comb $\boldsymbol{\mathcal{E}}_\mathrm{C}(t)$. In Sec. 6.3.1.1, where we did not take advantage of the here employed "coherence-storage" mechanism, much higher repetition frequencies had to be utilized to optically manipulate the system withing its effective decay time $\tau_a \approx 1/\Gamma_2$.

The solution of the EOMs displayed in Fig. 6.13 is associated with a train of detuned pulses, with central frequency $\omega_\mathrm{C} = 1.5\,\mathrm{eV}$, i.e., $\Delta = -0.52\,\mathrm{eV}$, and repetition frequency $1/T_\mathrm{p} = 100\,\mathrm{MHz}$. The peak intensities are $\sim 10^{12}$, still some orders of magnitude lower than the intensity obtained in a femtosecond enhancement cavity for the generation of XUV combs with HHG [122, 205–208]. A small transfer of coherence is exhibited by $|\varrho_{13}^\mathrm{eq}(t)|$ and $|\varrho_{12}^\mathrm{eq}(t)|$ in the presence of the optical pulses. Owing to the large detuning of the optical frequency comb, $|\varrho_{12}^\mathrm{eq}(t)|$ is led back to its vanishing initial value when the interaction with each pulse has concluded [Fig. 6.13a]. The loss of coherence taking place when $|\varrho_{12}^\mathrm{eq}(t)|$ is different from zero, despite being small, can be seen in Fig. 6.13c to affect the evolution of the function $|\varrho_{13}^\mathrm{eq}(t)|$, whose amplitude periodically decreases as a result of the interaction with the optical pulses. Furthermore, the optical frequency comb induces periodic shifts in the phases of both $\varrho_{12}^\mathrm{eq}(t)$ and $\varrho_{13}^\mathrm{eq}(t)$ which we display in Figs. 6.13b and 6.13d.

6.3.2 X-ray absorption spectrum

The calculation of the absorption spectrum (5.30) of the transmitted x-ray field requires knowledge of the Fourier transform of the just discussed function $\varrho_{12}^\mathrm{eq}(t)$ (6.86) ensuing from the interaction of the system with the optical frequency comb $\boldsymbol{\mathcal{E}}_\mathrm{C}(\boldsymbol{r}, t)$.

By recalling the definition of the functions $f_1(t)$ and $f_2(t)$ which we introduced in Eq. (6.42) while discussing the interaction of the three-level system with a single pulse, we can reformulate

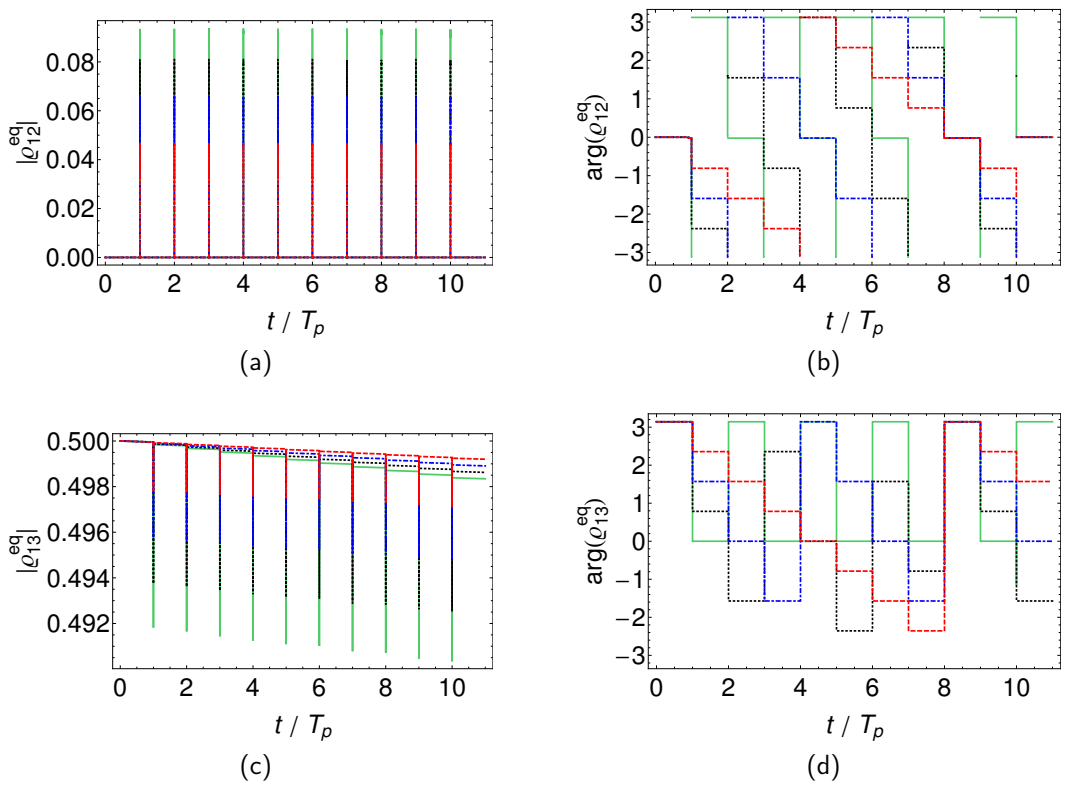

Figure 6.13: Off-diagonal elements of the three-level system of Fig. 6.1, (a) $|\varrho_{12}^{\rm eq}(t)|$, (b) $\arg[{\rm e}^{-{\rm i}\Delta t}\,\varrho_{12}^{\rm eq}(t)]$, (c) $|\varrho_{13}^{\rm eq}(t)|$, (d) $\arg[{\rm e}^{-{\rm i}\Delta t}\,\varrho_{13}^{\rm eq}(t)]$, used to model He-like Be^{2+} ions, initially prepared at time $T_0 = 0$ in the initial state $\bar{\varrho}_{12,\rm in} = 0$, $\bar{\varrho}_{13,\rm in} = -1/2$, and driven by a train of optical pulses with energy $\omega_{\rm C} = 1.5\,{\rm eV}$, and detuning $\Delta = -\Delta_{\rm C} = -0.52\,{\rm eV}$ with respect to the $1s\,2s\,{}^1S_0 \to 1s\,2p\,{}^1P_1$ optical transition of Be^{2+} ions at $\omega_{23} = 2.02\,{\rm eV}$. The pulses have FWHM duration of $\tau_{\rm FWHM} = 100\,{\rm fs}$ and peak intensities $I_{\rm C,max} = 4.5\times10^{11}\,{\rm W/cm^2}$ (red, dashed line), $I_{\rm C,max} = 9.1\times10^{11}\,{\rm W/cm^2}$ (blue, dotdashed line), $I_{\rm C,max} = 1.4\times10^{12}\,{\rm W/cm^2}$ (black, dotted line), and $I_{\rm C,max} = 1.9\times10^{12}\,{\rm W/cm^2}$ (green, solid line), corresponding to a phase kick $\arg(\xi_a) = -\pi/4$ (red, dashed line), $\arg(\xi_a) = -\pi/2$ (blue, dotdashed line), $\arg(\xi_a) = -3\pi/4$ (black, dotted line), and $\arg(\xi_a) = -\pi$ (green, solid line), respectively. The train of pulses starts at $t_0 = T_0 + T_{\rm p}$.

$\varrho_{12}^{\rm eq}(t)$ in terms of these two functions, i.e.,

$$\begin{aligned}\varrho_{12}^{\rm eq}(t) = {}& \bar{\varrho}_{12,\rm in}\,{\rm e}^{\left({\rm i}\Delta_{\rm X}-\frac{\Gamma_2}{2}\right)(t-T_0)}\,\theta\left(-t+t_0-\tfrac{T_{\rm p}}{2}\right)\\ &+\bar{\varrho}_{12,\rm in}\,{\rm e}^{\left({\rm i}\Delta_{\rm X}-\frac{\Gamma_2}{2}\right)(t-T_0)}\sum_{j=-\infty}^{\infty}\mu_a^j f_1(z_j(t))\,\theta\left(t-t_0+\tfrac{T_{\rm p}}{2}\right)\\ &+{\rm i}\,\bar{\varrho}_{13,\rm in}\,\frac{a}{1-c}\,{\rm e}^{\left[{\rm i}\Delta+\frac{\Gamma_2-\Gamma_3}{2}\right](t_0-T_0)}\,{\rm e}^{\left({\rm i}\Delta_{\rm X}-\frac{\Gamma_2}{2}\right)(t-T_0)}\,\theta\left(t-t_0+\tfrac{T_{\rm p}}{2}\right)\\ &\times\sum_{j=-\infty}^{\infty}{\rm e}^{\left[{\rm i}(\Delta T_{\rm p}+\arg\xi_a)+\frac{\Gamma_2-\Gamma_3}{2}T_{\rm p}+\log|\xi_a|\right]j}\,f_2(z_j(t)).\end{aligned}\tag{6.93}$$

The first addend on the right-hand side on the first line of Eq. (6.93) is a right-handed exponentially decaying function, whose Fourier transform can be easily calculated, i.e.,

$$\int_{T_0}^{t_0-\frac{T_{\rm p}}{2}}\bar{\varrho}_{12,\rm in}\,{\rm e}^{\left({\rm i}\Delta_{\rm X}-\frac{\Gamma_2}{2}\right)(t-T_0)}\,{\rm e}^{-{\rm i}(\omega-\omega_{\rm X})(t-T_0)}\,{\rm d}t = \bar{\varrho}_{12,\rm in}\,\frac{1-{\rm e}^{\left[-{\rm i}(\omega-\omega_{21})-\frac{\Gamma_2}{2}\right]\left(t_0-\frac{T_{\rm p}}{2}-T_0\right)}}{\frac{\Gamma_2}{2}+{\rm i}(\omega-\omega_{21})}.\tag{6.94}$$

The second addend on the second line in (6.93) is the product of two functions, the second of which is a sum in j which can be expressed as the convolution of a function with a train of delta peaks,

$$\sum_{j=-\infty}^{\infty} \mu_a^j f_1(z_j(t)) = \int_{-\infty}^{\infty} \mu_a^{\tau/T_\mathrm{p}} f_1(z_0(t-\tau)) \sum_{j=-\infty}^{\infty} \delta(\tau - jT_\mathrm{p})\,\mathrm{d}\tau, \tag{6.95}$$

such that we can take advantage of the properties of the Fourier transform of the convolution and of the product to write

$$\begin{aligned}
&\int_{-\infty}^{\infty} \bar{\varrho}_{12,\mathrm{in}}\, \mathrm{e}^{\left(\mathrm{i}\Delta_\mathrm{X} - \frac{\Gamma_2}{2}\right)(t-T_0)} \sum_{j=-\infty}^{\infty} \mu_a^j f_1(z_j(t))\; \theta\left(t - t_0 + \tfrac{T_\mathrm{p}}{2}\right)\, \mathrm{e}^{-\mathrm{i}(\omega-\omega_\mathrm{X})(t-T_0)}\, \mathrm{d}t \\
&= \bar{\varrho}_{12,\mathrm{in}} \frac{\mathrm{e}^{\left[\mathrm{i}(\omega-\omega_{21}) + \frac{\Gamma_2}{2}\right]T_0}}{2\pi} \int_{-\infty}^{\infty} \int_{-\infty}^{\infty} \mathrm{e}^{\left[-\mathrm{i}(\omega'-\omega_{21}) - \frac{\Gamma_2}{2}\right]t'} \theta\left(t' - t_0 + \tfrac{T_\mathrm{p}}{2}\right)\, \mathrm{d}t' \\
&\quad \times \int_{-\infty}^{\infty} \mu_a^{\tau/T_\mathrm{p}} \sum_{j=-\infty}^{\infty} \delta(\tau - jT_\mathrm{p})\, \mathrm{e}^{-\mathrm{i}(\omega-\omega')\tau}\, \mathrm{d}\tau \quad \int_{-\infty}^{\infty} f_1(z_0(t)) \mathrm{e}^{-\mathrm{i}(\omega-\omega')t}\, \mathrm{d}t \quad \mathrm{d}\omega'.
\end{aligned} \tag{6.96}$$

The right-hand side of the previous equality displays the convolution—the integral in ω'—of two Fourier transforms, the second of which is itself the product of two other Fourier transforms. The integral in t' on the second line in Eq. (6.96) is easily computable, since it involves once again the calculation of the Fourier transform of a right-handed exponentially decaying function,

$$\int_{-\infty}^{\infty} \mathrm{e}^{\left[-\mathrm{i}(\omega'-\omega_{21}) - \frac{\Gamma_2}{2}\right]t'} \theta\left(t' - t_0 + \tfrac{T_\mathrm{p}}{2}\right) \mathrm{d}t' = \frac{\mathrm{e}^{\left[-\mathrm{i}(\omega'-\omega_{21}) - \frac{\Gamma_2}{2}\right]\left(t_0 - \frac{T_\mathrm{p}}{2}\right)}}{\frac{\Gamma_2}{2} + \mathrm{i}(\omega' - \omega_{21})}. \tag{6.97}$$

The first Fourier transform on the third line in Eq. (6.96)—the integral in τ—can be calculated after having expressed $\mu_a^{\tau/T_\mathrm{p}}$ as a complex exponential function, i.e., $\mu_a^{\tau/T_\mathrm{p}} = (|\mu_a|\,\mathrm{e}^{\mathrm{i}\arg\mu_a})^{\tau/T_\mathrm{p}} = \mathrm{e}^{\frac{\log|\mu_a|}{T_\mathrm{p}}\tau}\,\mathrm{e}^{\mathrm{i}\frac{\arg\mu_a}{T_\mathrm{p}}\tau}$, such that one can employ the Fourier transform of the train of delta functions to obtain

$$\begin{aligned}
&\int_{-\infty}^{\infty} \sum_{j=-\infty}^{\infty} \delta(\tau - jT_\mathrm{p})\, \mathrm{e}^{-\mathrm{i}\left(\omega-\omega' - \frac{\arg\mu_a}{T_\mathrm{p}} + \mathrm{i}\frac{\log|\mu_a|}{T_\mathrm{p}}\right)\tau}\, \mathrm{d}\tau \\
&= \frac{2\pi}{T_\mathrm{p}} \sum_{m=-\infty}^{\infty} \delta\left(\omega - \omega' - \tfrac{\arg\mu_a}{T_\mathrm{p}} + \mathrm{i}\tfrac{\log|\mu_a|}{T_\mathrm{p}} - \tfrac{2\pi m}{T_\mathrm{p}}\right).
\end{aligned} \tag{6.98}$$

The second Fourier transform on the third line in Eq. (6.96)—the integral in t—was already calculated in Eq. (C.44) to describe the interaction of the three-level system with a single pulse,

$$\begin{aligned}
&\int_{-\infty}^{\infty} f_1(z_0(t)) \mathrm{e}^{-\mathrm{i}(\omega-\omega')t}\, \mathrm{d}t \\
&= \frac{\mathrm{e}^{-\mathrm{i}(\omega-\omega')t_0}}{2\gamma} \frac{a^2}{c}\, \mathrm{i}\,\pi\, \mathrm{csch}\left(\tfrac{\pi(\omega-\omega')}{2\gamma}\right) {}_3F_2\left(1+a, 1-a, 1-\mathrm{i}\tfrac{(\omega-\omega')}{2\gamma}; 1+c, 2; 1\right).
\end{aligned} \tag{6.99}$$

The presence of the "frequency comb" in Eq. (6.98) renders the calculation of the convolution, i.e., the integral in ω' appearing in Eq. (6.96), immediate.

Similar steps are necessary for the calculation of the Fourier transform of the third term in (6.93) on the third and fourth lines: the sum in j is once again written as the convolution of a

function with a train of delta peaks such that an equation is recovered which requires the use of the already calculated Fourier transform of $f_2(z_0(t))$ [see Eq. (C.46) from the single-pulse case]. These steps are not repeated here.

The just presented calculation allow us to conclude that the Fourier transform of $\varrho_{12}^{\mathrm{eq}}(t)$ from Eq. (6.93) is

$$\begin{aligned}
\int_{T_0}^{\infty} \varrho_{12}^{\mathrm{eq}}(t)\, \mathrm{e}^{-\mathrm{i}(\omega-\omega_{\mathrm{X}})(t-T_0)}\, \mathrm{d}t &= \bar{\varrho}_{12,\mathrm{in}}\, \frac{1-\mathrm{e}^{\left[-\mathrm{i}(\omega-\omega_{21})-\frac{\Gamma_2}{2}\right]\left(t_0-\frac{T_\mathrm{p}}{2}-T_0\right)}}{\frac{\Gamma_2}{2}+\mathrm{i}(\omega-\omega_{21})} \\
&+ \mathrm{i}\,\bar{\varrho}_{12,\mathrm{in}}\, \mathrm{e}^{\left[-\mathrm{i}(\omega-\omega_{21})-\frac{\Gamma_2}{2}\right](t_0-T_0)} \sum_{m=-\infty}^{\infty} \frac{\mathrm{e}^{\left[\mathrm{i}\left(\omega-\omega_{21}-\frac{\arg\mu_a}{T_\mathrm{p}}-\frac{2\pi m}{T_\mathrm{p}}\right)+\frac{\Gamma_2}{2}-\frac{\log|\mu_a|}{T_\mathrm{p}}\right]\frac{T_\mathrm{p}}{2}}}{\frac{\Gamma_2}{2}-\frac{\log|\mu_a|}{T_\mathrm{p}}+\mathrm{i}\left(\omega-\omega_{21}-\frac{\arg\mu_a}{T_\mathrm{p}}-\frac{2\pi m}{T_\mathrm{p}}\right)} \\
&\times \frac{\pi}{2\gamma T_\mathrm{p}}\, \mathrm{csch}\left[\tfrac{\pi}{2\gamma T_\mathrm{p}}(2\pi m+\arg\mu_a-\mathrm{i}\log|\mu_a|)\right] \\
&\times \frac{a^2}{c}\, {}_3F_2\left(1+a,1-a,1-\mathrm{i}\tfrac{1}{2\gamma T_\mathrm{p}}(2\pi m+\arg\mu_a-\mathrm{i}\log|\mu_a|);1+c,2;1\right) \\
&+ \mathrm{i}\,\bar{\varrho}_{13,\mathrm{in}}\, \frac{a}{1-c}\, \mathrm{e}^{\left[-\mathrm{i}(\omega-\omega_{21}-\Delta)-\frac{\Gamma_3}{2}\right](t_0-T_0)} \sum_{m=-\infty}^{\infty} \frac{\mathrm{e}^{\left[\mathrm{i}\left(\omega-\omega_{21}-\Delta-\frac{\arg\xi_a}{T_\mathrm{p}}-\frac{2\pi m}{T_\mathrm{p}}\right)+\frac{\Gamma_3}{2}-\frac{\log|\xi_a|}{T_\mathrm{p}}\right]\frac{T_\mathrm{p}}{2}}}{\frac{\Gamma_3}{2}-\frac{\log|\xi_a|}{T_\mathrm{p}}+\mathrm{i}\left(\omega-\omega_{21}-\Delta-\frac{\arg\xi_a}{T_\mathrm{p}}-\frac{2\pi m}{T_\mathrm{p}}\right)} \\
&\times \frac{\pi}{2\gamma T_\mathrm{p}}\, \mathrm{sech}\left(\tfrac{\pi}{2\gamma T_\mathrm{p}}(2m\pi+\arg\xi_a-\mathrm{i}\log|\xi_a|)\right) \\
&\times {}_3F_2\left(1-a,1+a,\tfrac{1}{2}-\mathrm{i}\tfrac{1}{2\gamma T_\mathrm{p}}(2\pi m+\arg\xi_a-\mathrm{i}\log|\xi_a|);2-c,1;1\right).
\end{aligned} \tag{6.100}$$

This result exhibits two sets of combs, which we analyze separately in the following by distinctly considering the two different sets of initial conditions we already identified in the previous Sections. These sets of initial conditions correspond to different preparatory schemes via the x-ray pulse $\boldsymbol{\mathcal{E}}_{\mathrm{X}}(\boldsymbol{r},\, t)$ and the optical pulse $\boldsymbol{\mathcal{E}}_{\mathrm{L}}(\boldsymbol{r},\, t)$.

6.3.2.1 X-ray-only preparation

When a single x-ray pulse $\boldsymbol{\mathcal{E}}_{\mathrm{X}}(\boldsymbol{r},\, t)$ is used to prepare the system, such that at time T_0 the initial state is characterized by $\varrho_{13,\mathrm{in}}^{\mathrm{eq}} = 0$, then the Fourier transform in Eq. (6.100)

$$\begin{aligned}
\int_{T_0}^{\infty} \varrho_{12}^{\mathrm{eq}}(t)\, \mathrm{e}^{-\mathrm{i}(\omega-\omega_{\mathrm{X}})(t-T_0)}\, \mathrm{d}t &= \bar{\varrho}_{12,\mathrm{in}}\, \frac{1-\mathrm{e}^{\left[-\mathrm{i}(\omega-\omega_{21})-\frac{\Gamma_2}{2}\right]\left(t_0-\frac{T_\mathrm{p}}{2}-T_0\right)}}{\frac{\Gamma_2}{2}+\mathrm{i}(\omega-\omega_{21})} \\
&+ \mathrm{i}\,\bar{\varrho}_{12,\mathrm{in}}\, \mathrm{e}^{\left[-\mathrm{i}(\omega-\omega_{21})-\frac{\Gamma_2}{2}\right](t_0-T_0)} \sum_{m=-\infty}^{\infty} \frac{\mathrm{e}^{\left[\mathrm{i}\left(\omega-\omega_{21}-\frac{\arg\mu_a}{T_\mathrm{p}}-\frac{2\pi m}{T_\mathrm{p}}\right)+\frac{\Gamma_2}{2}-\frac{\log|\mu_a|}{T_\mathrm{p}}\right]\frac{T_\mathrm{p}}{2}}}{\frac{\Gamma_2}{2}-\frac{\log|\mu_a|}{T_\mathrm{p}}+\mathrm{i}\left(\omega-\omega_{21}-\frac{\arg\mu_a}{T_\mathrm{p}}-\frac{2\pi m}{T_\mathrm{p}}\right)} \\
&\times \frac{\pi}{2\gamma T_\mathrm{p}}\, \mathrm{csch}\left[\tfrac{\pi}{2\gamma T_\mathrm{p}}(2\pi m+\arg\mu_a-\mathrm{i}\log|\mu_a|)\right] \\
&\times \frac{a^2}{c}\, {}_3F_2\left(1+a,1-a,1-\mathrm{i}\tfrac{1}{2\gamma T_\mathrm{p}}(2\pi m+\arg\mu_a-\mathrm{i}\log|\mu_a|);1+c,2;1\right)
\end{aligned} \tag{6.101}$$

exhibits (i) a central peak, centered at the atomic transition energy ω_{21} and ensuing from the spontaneous decay of the excited state 2 at rate Γ_2 during the time interval $[T_0, t_0 - T_\mathrm{p}/2]$ preceding the interaction with the periodic train of pulses, and (ii) a set of equidistant peaks,

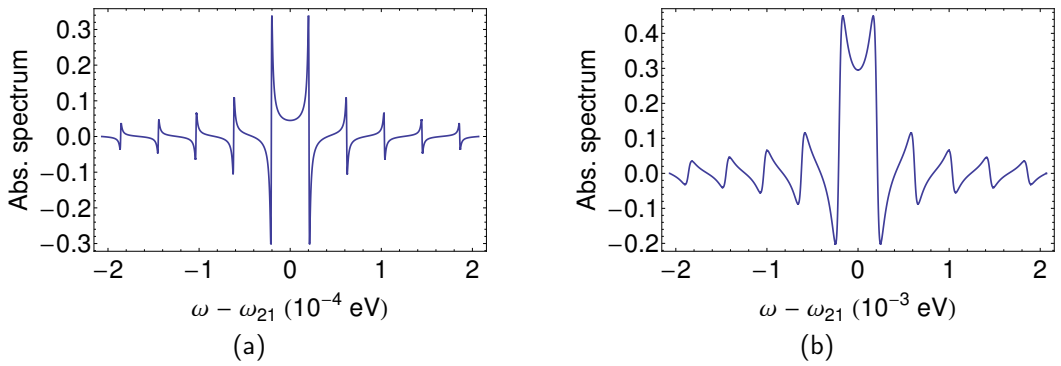

Figure 6.14: Absorption spectrum (6.55) for the three-level system of Fig. 6.1, used to model He and He-like Be^{2+} ions, initially prepared at time $T_0 = 0$ in a state with $\bar{\varrho}_{12,\mathrm{in}} = -\mathrm{i}/2$, $\bar{\varrho}_{13,\mathrm{in}} = 0$, whose $1s\,2s\,{}^1S_0 \to 1s\,2p\,{}^1P_1$ transition is driven by a train of 2π optical pulses, with FWHM duration $\tau_{\mathrm{FWHM}} = 100\,\mathrm{fs}$, tuned to the optical transition. In the case of He [panel (a)], the transition energies are $\omega_{23} = 0.6\,\mathrm{eV}$, $\omega_{21} = 21.2\,\mathrm{eV}$, and the decay rate of the excited state is $\Gamma_2 = 1.8 \times 10^9\,\mathrm{s}^{-1} = 7.45 \times 10^{-6}\,\mathrm{eV}$: We use pulses with repetition period $T_\mathrm{p} = 100\,\mathrm{ps}$, i.e., $1/T_\mathrm{p} = 10\,\mathrm{GHz}$, $2\pi/T_\mathrm{p} = 4.14 \times 10^{-5}\,\mathrm{eV}$, and peak intensities $I_{\mathrm{C,max}} = 3.0 \times 10^9\,\mathrm{W/cm^2}$. In the case of He-like Be^{2+} [panel (b)], the transition energies are $\omega_{23} = 2.02\,\mathrm{eV}$, $\omega_{21} = 123.7\,\mathrm{eV}$, and the decay rate of the excited state is $\Gamma_2 = 1.2 \times 10^{11}\,\mathrm{s}^{-1} = 5.05 \times 10^{-4}\,\mathrm{eV}$: We use pulses with repetition period $T_\mathrm{p} = 10\,\mathrm{ps}$, i.e., frequency $1/T_\mathrm{p} = 100\,\mathrm{GHz}$, $2\pi/T_\mathrm{p} = 4.14 \times 10^{-4}\,\mathrm{eV}$,and peak intensities $I_{\mathrm{C,max}} = 2.6 \times 10^{10}\,\mathrm{W/cm^2}$. In both cases, the peak intensity corresponds to a pulse area $Q_\mathrm{C} = 2\pi$. The train of pulses starts at $t_0 = T_0 + T_\mathrm{p}$.

where each peak is given by the Fourier transform of a right-handed exponentially decaying function. Each peak has a width which is given by the a-dependent effective decay width $\frac{1}{\tau_a} = \frac{\Gamma_2}{2} - \frac{\log|\mu_a|}{T_\mathrm{p}}$ which we defined in Eq. (6.89). The peaks are equally separated by the repetition frequency of the optical frequency comb. The mth peak is centered at frequency $\omega_m = \omega_{21} + \frac{\arg\mu_a}{T_\mathrm{p}} + \frac{2\pi m}{T_\mathrm{p}}$, with $m \in \mathbb{Z}$.

As a result of the Fourier transform (6.101), a comb centered at the high-frequency transition energy ω_{21} and with the same separation frequency as the optical frequency comb is imprinted onto the x-ray absorption spectrum (5.29) of the transmitted, ultrashort x-ray pulse $\boldsymbol{\mathcal{E}}_\mathrm{X}(\boldsymbol{r}, t)$ which is employed to prepare the atomic system in its initial state. The prefactor determining the amplitude of the mth peak can be approximated via Eq. (6.50b),

$$\frac{\pi}{2\gamma T_\mathrm{p}}\ \mathrm{csch}\Big[\tfrac{\pi}{2\gamma T_\mathrm{p}}(2\pi m + \arg\mu_a - \mathrm{i}\log|\mu_a|)\Big] \approx \frac{1}{2\pi m + \arg\mu_a - \mathrm{i}\log|\mu_a|},$$

i.e., the amplitude of the mth peak in the comb decreases as $1/m$. In the next pictures we employ the $1s\,2p\,{}^1P_1 \to 1s\,2s\,{}^1S_0$ $(2 \to 3)$ and the $1s^2\,{}^1S_0 \to 1s\,2p\,{}^1P_1$ $(1 \to 2)$ transitions of He and He-like Be^{2+} to implement our three-level scheme and display the modifications of the absorption spectrum which emerge when an optical frequency comb $\boldsymbol{\mathcal{E}}_\mathrm{C}(\boldsymbol{r}, t)$ is used to optically manipulate the atomic response of the system. Transition energies and decay rates were introduced in Sec. 6.3.1.1.

In Fig. 6.14 we plot the 10 central peaks in the absorption spectrum for He and He-like Be^{2+} ions driven by a train of 2π pulses tuned to the $2 \to 3$ transition. The spectra are centered at the transition energy ω_{21}, respectively given by $\omega_{21} = 21.2\,\mathrm{eV}$ for He and $\omega_{21} = 123.7\,\mathrm{eV}$ for He-like Be^{2+} ions [191]. The corresponding time evolution was exhibited in Fig. 6.10. Each Fano-like peak has a width $1/\tau_a$ which is determined by the decay rate Γ_2 of the fast decaying level 2. The pictures show that the peak separation spacing, given by $2\pi/T_\mathrm{p}$, is comparable to the width of

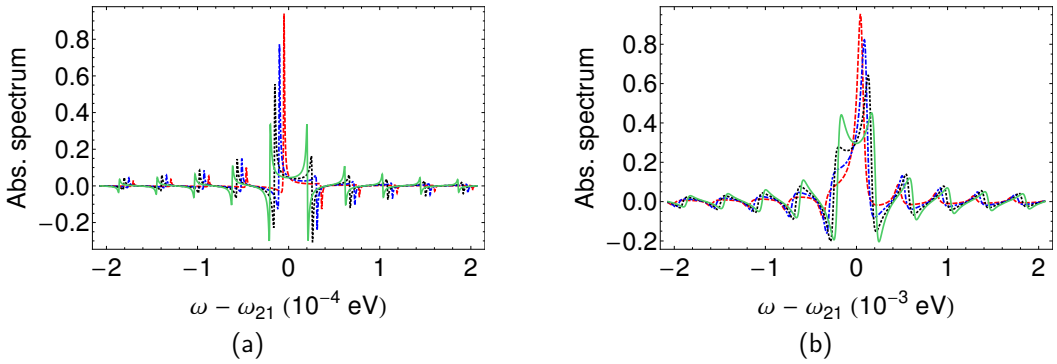

Figure 6.15: Absorption spectrum (6.55) for the three-level system of Fig. 6.1, used to model He and He-like Be^{2+} ions, initially prepared at time $T_0 = 0$ in a state with $\bar{\varrho}_{12,\mathrm{in}} = -\mathrm{i}/2$, $\bar{\varrho}_{13,\mathrm{in}} = 0$, whose $1s\,2s\,{}^1S_0 \to 1s\,2p\,{}^1P_1$ transition is driven by a train of optical pulses with energy $\omega_\mathrm{C} = 1.5\,\mathrm{eV}$ and FWHM duration $\tau_\mathrm{FWHM} = 100\,\mathrm{fs}$. In the case of He [panel (a)], the transition energies are $\omega_{23} = 0.6\,\mathrm{eV}$, $\omega_{21} = 21.2\,\mathrm{eV}$, and the decay rate of the excited state is $\Gamma_2 = 1.8\times10^9\,\mathrm{s}^{-1} = 7.45\times10^{-6}\,\mathrm{eV}$: We use pulses with repetition period $T_\mathrm{p} = 100\,\mathrm{ps}$, i.e., $1/T_\mathrm{p} = 10\,\mathrm{GHz}$, $2\pi/T_\mathrm{p} = 4.14\times10^{-5}\,\mathrm{eV}$, and peak intensities $I_{\mathrm{C,max}} = 9.2\times10^{10}\,\mathrm{W/cm^2}$ (red, dashed line), $I_{\mathrm{C,max}} = 1.8\times10^{11}\,\mathrm{W/cm^2}$ (blue, dotdashed line), $I_{\mathrm{C,max}} = 2.8\times10^{11}\,\mathrm{W/cm^2}$ (black, dotted line), and $I_{\mathrm{C,max}} = 3.7\times10^{11}\,\mathrm{W/cm^2}$ (green, solid line). In the case of He-like Be^{2+} [panel (b)], the transition energies are $\omega_{23} = 2.02\,\mathrm{eV}$, $\omega_{21} = 123.7\,\mathrm{eV}$, and the decay rate of the excited state is $\Gamma_2 = 1.2\times10^{11}\,\mathrm{s}^{-1} = 5.05\times10^{-4}\,\mathrm{eV}$: We use pulses with repetition period $T_\mathrm{p} = 10\,\mathrm{ps}$, i.e., frequency $1/T_\mathrm{p} = 100\,\mathrm{GHz}$, $2\pi/T_\mathrm{p} = 4.14\times10^{-4}\,\mathrm{eV}$,and peak intensities $I_{\mathrm{C,max}} = 4.5\times10^{11}\,\mathrm{W/cm^2}$ (red, dashed line), $I_{\mathrm{C,max}} = 9.1\times10^{11}\,\mathrm{W/cm^2}$ (blue, dotdashed line), $I_{\mathrm{C,max}} = 1.4\times10^{12}\,\mathrm{W/cm^2}$ (black, dotted line), and $I_{\mathrm{C,max}} = 1.9\times10^{12}\,\mathrm{W/cm^2}$ (green, solid line). In both cases, the peak intensities correspond to a phase kick $\arg(\mu_a) = \pi/4$ (red, dashed line), $\arg(\mu_a) = \pi/2$ (blue, dotdashed line), $\arg(\mu_a) = 3\pi/4$ (black, dotted line), and $\arg(\mu_a) = \pi$ (green, solid line), respectively. The train of pulses starts at $t_0 = T_0 + T_\mathrm{p}$.

the peaks in the comb. In He (Fig. 6.14a) the decay time of the excited level 2 is $\sim 6\,\mathrm{ns}$ and a repetition period of $T_\mathrm{p} = 100\,\mathrm{ps}$ is required. This corresponds to a peak separation spacing, $2\pi/T_\mathrm{p} = 4.14\times10^{-5}\,\mathrm{eV}$, which is comparable to the decay rate $\Gamma_2 = 7.45\times10^{-6}\,\mathrm{eV}$. Similar considerations are valid for He-like Be^{2+} (Fig. 6.14b), where, in light of the even smaller decay time $\sim 8\,\mathrm{ps}$ of the excited level 2, an even smaller repetition period, $T_\mathrm{p} = 10\,\mathrm{ps}$, is necessary to effectively imprint a comb onto the absorption spectrum of the transmitted x-ray field. The peak separation spacing $2\pi/T_\mathrm{p} = 4.14\times10^{-4}\,\mathrm{eV}$, which is associated with the fixed value of the repetition period, is comparable to the decay rate $\Gamma_2 = 5.05\times10^{-4}\,\mathrm{eV}$. In both pictures it is apparent that the strength of the peaks decreases, as predicted, with the peak number m. Finally, we notice that, for the case of a tuned pulse with 2π area in the limit of decay rates much lower than the spectral width of the pulses, Eq. (6.29) predicts that $\mu_a \approx -1$, where the constant μ_a determines the frequencies $\omega_m = \omega_{21} + \frac{\arg\mu_a}{T_\mathrm{p}} + \frac{2\pi m}{T_\mathrm{p}}$ at which the peaks in the comb are centered. For $\mu_a = -1$, we can conclude that $\omega_m = \omega_{21} + \frac{\pi(2m+1)}{T_\mathrm{p}}$, as confirmed by Fig. 6.14.

In Fig. 6.15 we plot the 10 central peaks in the absorption spectrum for He (Fig. 6.15a) and He-like Be^{2+} ions (Fig. 6.15b) driven by a train of pulses $\boldsymbol{\mathcal{E}}_\mathrm{C}(\boldsymbol{r}, t)$ with central energy $\omega_\mathrm{C} = 1.5\,\mathrm{eV}$. The employed optical frequency comb is detuned from the corresponding optical transition ω_{23}. The peaks exhibit a Fano-like shape with peak amplitudes undergoing a fast decrease $(1/m)$ at increasing values of the peak number m. The width of the peaks is determined by the effective decay rate $1/\tau_a \approx \Gamma_2$, while the separation spacing is given by the repetition frequency of the optical frequency comb. Different peak intensities $I_{\mathrm{C,max}}$ of the driving field are associated with different values of the frequencies ω_m at which the peaks in the imprinted comb are centered.

These central frequencies $\omega_m = \omega_{21} + \frac{\arg\mu_a}{T_\mathrm{p}} + \frac{2\pi m}{T_\mathrm{p}}$ are shown in Fig. 6.15 to uniformly translate at increasing values of the peak intensity because of the correspondingly rising value of the intensity-dependent parameter $\arg(\mu_a)$. Notice that, in the large-detuning case, Eq. (6.31) predicts that $|\mu_a| \approx 1$, such that $\mu_a \approx \mathrm{e}^{\mathrm{i}\arg(\mu_a)}$. This phase term $\arg(\mu_a)$ represents the shift which $\varrho_{12}^{\mathrm{eq}}(t)$ periodically undergoes upon interaction with the train of optical pulses in the optical frequency comb.

6.3.2.2 Coherence-storage preparation

When the preparation of the three-level system described in Fig. 5.1 consists in an x-ray pulse $\boldsymbol{\mathcal{E}}_\mathrm{X}(\boldsymbol{r}, t)$ followed by a 2π optical pulse tuned to the $2 \to 3$ transition, such that the system at time T_0 is in an initial state characterized by $\varrho_{12,\mathrm{in}}^{\mathrm{eq}} = 0$, then the Fourier transform in Eq. (6.100) reduces to

$$\begin{aligned}
&\int_{T_0}^{\infty} \varrho_{12}^{\mathrm{eq}}(t)\, \mathrm{e}^{-\mathrm{i}(\omega-\omega_\mathrm{X})(t-T_0)}\, \mathrm{d}t \\
&= \mathrm{i}\,\bar{\varrho}_{13,\mathrm{in}}\, \frac{a}{1-c}\, \mathrm{e}^{\left[-\mathrm{i}(\omega-\omega_{21}-\Delta)-\frac{\Gamma_3}{2}\right](t_0-T_0)} \sum_{m=-\infty}^{\infty} \frac{\mathrm{e}^{\left[\mathrm{i}\left(\omega-\omega_{21}-\Delta-\frac{\arg\xi_a}{T_\mathrm{p}}-\frac{2\pi m}{T_\mathrm{p}}\right)+\frac{\Gamma_3}{2}-\frac{\log|\xi_a|}{T_\mathrm{p}}\right]\frac{T_\mathrm{p}}{2}}}{\frac{\Gamma_3}{2}-\frac{\log|\xi_a|}{T_\mathrm{p}}+\mathrm{i}\left(\omega-\omega_{21}-\Delta-\frac{\arg\xi_a}{T_\mathrm{p}}-\frac{2\pi m}{T_\mathrm{p}}\right)} \\
&\quad\times \frac{\pi}{2\gamma T_\mathrm{p}}\, \mathrm{sech}\left(\tfrac{\pi}{2\gamma T_\mathrm{p}}(2m\pi + \arg\xi_a - \mathrm{i}\log|\xi_a|)\right) \\
&\quad\times {}_3F_2\left(1-a, 1+a, \tfrac{1}{2} - \mathrm{i}\tfrac{1}{2\gamma T_\mathrm{p}}(2\pi m + \arg\xi_a - \mathrm{i}\log|\xi_a|); 2-c, 1; 1\right).
\end{aligned} \tag{6.102}$$

This function exhibits a new set of equidistant peaks, whose spacing $2\pi/T_\mathrm{p}$ is the same as in the optical frequency comb and whose spectral widths are given by the effective decay rate $1/\tilde{\tau}_a = \frac{\Gamma_3}{2} - \frac{\log|\xi_a|}{T_\mathrm{p}}$ [Eq. (6.92)], which is by orders of magnitude lower than the effective decay rate $1/\tau_a$ [Eq. (6.89)] from the previously analyzed case. As a result of the coherence-transfer and -storage mechanism which we described in the time domain in Sec. 6.3.1.2, a set of very fine peaks is imprinted onto the absorption spectrum of the transmitted x-ray field. Furthermore, by shaping the envelope of the off-diagonal matrix element $\varrho_{12}^{\mathrm{eq}}(t)$ into a pulse-train-like function, consisting of "pulses" with the same duration as the optical pulses in the optical frequency comb, a wide absorption spectrum is obtained, whose overall spectral width is proportional to the bandwidth γ of the optical-comb pulses. In particular, if we compare Eqs. (6.59) and (6.102), we notice that the many-pulse Fourier transform in this Section is obtained by "sampling" with fine, equidistant peaks of the form

$$\frac{1}{\frac{\Gamma_3}{2}-\frac{\log|\xi_a|}{T_\mathrm{p}}+\mathrm{i}\left(\omega-\omega_{21}-\Delta-\frac{\arg\xi_a}{T_\mathrm{p}}-\frac{2\pi m}{T_\mathrm{p}}\right)}$$

the single-pulse Fourier transform we analyzed in Sec. 6.2.2.2. Finally, we notice that the peaks in the Fourier transform (6.102) are centered at the frequencies $\omega_m = \omega_{21} + \Delta + \frac{\arg\xi_a}{T_\mathrm{p}} + \frac{2\pi m}{T_\mathrm{p}}$, which are directly determined by the detuning Δ and, indirectly, by the peak intensity, pulse duration, and repetition period of the optical frequency comb via the term $\frac{\arg\xi_a}{T_\mathrm{p}}$.

In the next pictures we employ the $1s\,2p\,{}^1P_1 \to 1s\,2s\,{}^1S_0$ $(2 \to 3)$ and the $1s^2\,{}^1S_0 \to 1s\,2p\,{}^1P_1$ $(1 \to 2)$ transitions of He-like Be^{2+} to implement our three-level scheme and display the absorption spectrum (5.30) associated with the Fourier transform in Eq. (6.102). Transition energies and decay rates were introduced in Sec. 6.3.1.2.

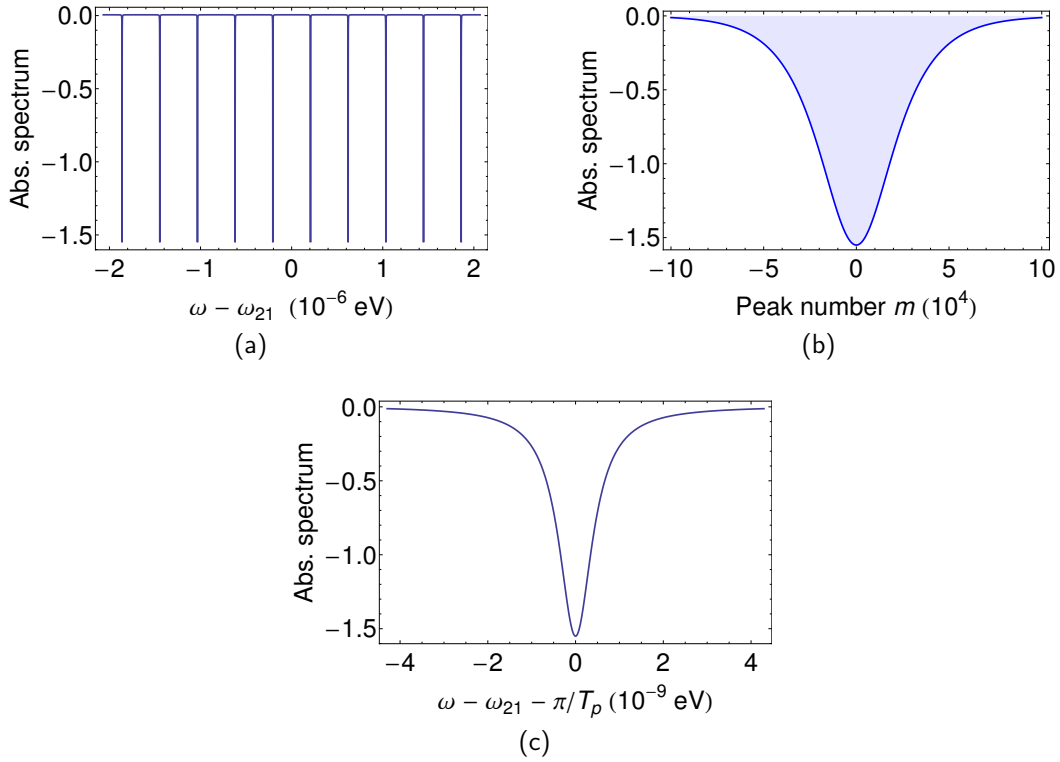

Figure 6.16: Absorption spectrum (6.55) from the three-level system of Fig. 6.1, used to model He-like Be^{2+} ions, initially prepared at time $T_0 = 0$ in a state with $\bar{\varrho}_{12,\mathrm{in}} = 0$, $\bar{\varrho}_{13,\mathrm{in}} = -1/2$, whose $1s\,2s\,{}^1S_0 \to 1s\,2p\,{}^1P_1$ transition is driven by a train of 2π optical pulses, with FWHM duration of $\tau_{\mathrm{FWHM}} = 100\,\mathrm{fs}$, tuned to the optical transition. The spectrum is centered at $\omega_{21} = 123.7\,\mathrm{eV}$. The optical transition energy is $\omega_{23} = 2.02\,\mathrm{eV}$: We use pulses with repetition period $T_\mathrm{p} = 10\,\mathrm{ns}$, i.e., $1/T_\mathrm{p} = 100\,\mathrm{MHz} = 4.14\times10^{-7}\,\mathrm{eV}$, and peak intensities $I_{\mathrm{C,max}} = 2.6\times10^{10}\,\mathrm{W/cm^2}$, corresponding to a pulse area $Q_\mathrm{C} = 2\pi$. The train of pulses starts at $t_0 = T_0+T_\mathrm{p}$. The train of pulses starts at $t_0 = T_0 + T_\mathrm{p}$. In panel (a) the 10 central peaks of the absorption spectrum are displayed, whereas panel (b) shows the peak values of the absorption spectrum, calculated by evaluating the Fourier transform of $\varrho_{12}^{\mathrm{eq}}(t)$ at the central frequencies $\omega_m = \omega_{21} + \frac{\arg\mu_a}{T_\mathrm{p}} + \frac{2\pi m}{T_\mathrm{p}}$ for a peak intensity $I_{\mathrm{C,max}} = 2.6\times10^{10}\,\mathrm{W/cm^2}$.

In Fig. 6.16 we show results for the case of an optical frequency comb $\boldsymbol{\mathcal{E}}_\mathrm{C}(\boldsymbol{r}, t)$ consisting of 2π pulses tuned to the $2 \to 3$ transition. Fine Lorentzian peaks separated by the optical-comb repetition frequency $2\pi/T_\mathrm{p}$ are shown in Fig. 6.16a. From Eq. (6.20), a pulse area $Q_\mathrm{C} = 2\pi$ is associated with $a = 1$, whereby the generalized hypergeometric function ${}_3F_2$ in Eq. (6.102) is also equal to 1. As a result, the amplitude of the mth peak in the Fourier transform of $\varrho_{12}^{\mathrm{eq}}(t)$ is proportional to $\mathrm{sech}\left(\frac{\pi}{2\gamma T_\mathrm{p}}(2m\pi + \arg\xi_a - \mathrm{i}\log|\xi_a|)\right)$ and a wide comb in the absorption spectrum, with an overall width given by the optical-comb spectral width γ, is exhibited in Fig. 6.16b. The number of peaks in this x-ray comb is proportional to $\approx T_\mathrm{p}/\tau_{\mathrm{FWHM}} = 10^5$. Each peak has a very small width, given by $1/\tilde{\tau}_a \ll \Gamma_2$, as clearly appearing in the single Lorentzian peak shown in Fig. 6.16c. For vanishing detuning Δ and in the limit of decay rates Γ_2 and Γ_3 much lower than the single-pulse bandwidth γ, Eq. (6.39) can be employed to predict that $\xi_a \approx (-1)^a$: For $a = 1$, the mth peak in the comb is centered at the frequency $\omega_m = \omega_{21} + \Delta + \frac{\pi(2m+1)}{T_\mathrm{p}}$, as Fig. 6.16a confirms.

In Fig. 6.17 we analyze the large-detuning limit by comparing results from 1.5-eV frequency

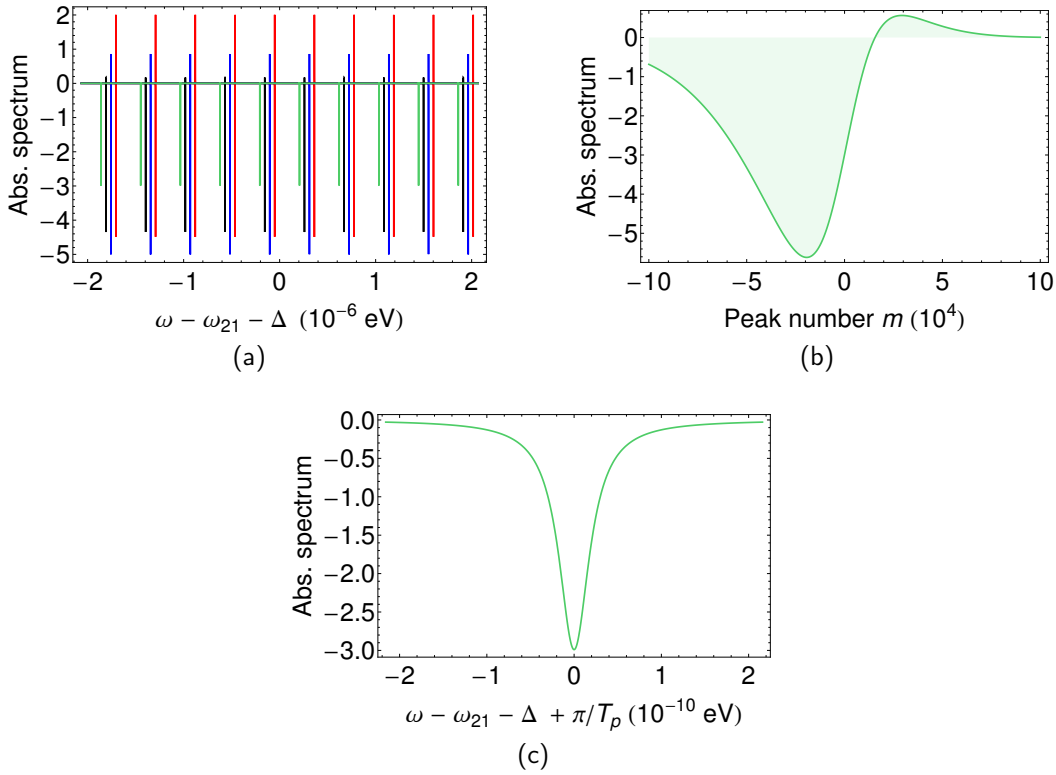

Figure 6.17: Absorption spectrum (6.55) from the three-level system of Fig. 6.1, used to model He-like Be^{2+} ions, initially prepared at time $T_0 = 0$ in the initial state $\bar{\varrho}_{12,\mathrm{in}} = 0$, $\bar{\varrho}_{13,\mathrm{in}} = -1/2$, and driven by a train of optical pulses with energy $\omega_C = 1.5\,\mathrm{eV}$, and detuning $\Delta = -\Delta_C = -0.52\,\mathrm{eV}$ with respect to the $1s\,2s\,{}^1S_0 \to 1s\,2p\,{}^1P_1$ optical transition of Be^{2+} ions at $\omega_{23} = 2.02\,\mathrm{eV}$. The spectrum is centered at $\omega_{21} = 123.7\,\mathrm{eV}$. The pulses have FWHM duration of $\tau_{\mathrm{FWHM}} = 100\,\mathrm{fs}$ and peak intensities $I_{C,\max} = 4.5\times10^{11}\,\mathrm{W/cm^2}$ (red, dashed line), $I_{C,\max} = 9.1\times10^{11}\,\mathrm{W/cm^2}$ (blue, dotdashed line), $I_{C,\max} = 1.4\times10^{12}\,\mathrm{W/cm^2}$ (black, dotted line), and $I_{C,\max} = 1.9\times10^{12}\,\mathrm{W/cm^2}$ (green, solid line), corresponding to a phase kick $\arg(\xi_a) = -\pi/4$ (red, dashed line), $\arg(\xi_a) = -\pi/2$ (blue, dotdashed line), $\arg(\xi_a) = -3\pi/4$ (black, dotted line), and $\arg(\xi_a) = -\pi$ (green, solid line), respectively. The train of pulses starts at $t_0 = T_0 + T_p$. In panel (a) the 10 central peaks of the absorption spectrum are displayed, whereas panel (b) shows the peak values of the absorption spectrum, calculated by evaluating the Fourier transform of $\varrho_{12}^{\mathrm{eq}}(t)$ at the central frequencies $\omega_m = \omega_{21} + \Delta + \frac{\arg\xi_a}{T_p} + \frac{2\pi m}{T_p}$ for a peak intensity $I_{C,\max} = 1.9\times10^{12}\,\mathrm{W/cm^2}$.

combs of different peak intensities. As shown in Eq. (6.41), for large values of Δ the parameter ξ_a describing the effect of a single pulse on the off-diagonal matrix element $\varrho_{12}^{\mathrm{eq}}(t)$ has $|\xi_a| \approx 1$. In Fig. 6.5 we showed that this results in periodic phase shifts of $\varrho_{12}^{\mathrm{eq}}(t)$ whose amplitudes are given by the intensity-dependent value of $\arg(\xi_a)$. These periodic phase shifts influence the central frequency $\omega_{21} + \Delta + \frac{\arg\xi_a}{T_p}$ of the x-ray comb which is imprinted onto the absorption spectrum of the transmitted x-ray field. This is exhibited by Fig. 6.17a, in which combs of different lineshapes and central frequencies are displayed for different values of the driving peak intensity. The overall spectral width of the comb is also proportional to the optical-comb bandwidth γ, as Fig. 6.17b shows. The asymmetric shape featured in the picture is a consequence of the properties, for general values of a and Δ, of the generalized hypergeometric function ${}_3F_2$. The single Lorentzian peak displayed in Fig. 6.17c, exhibiting a fine linewidth given by $1/\tilde{\tau}_a$, is shown for the value of the peak intensity which is associated with $\arg(\xi_a) = -\pi$.

6.4 Conclusions

By coupling an x-ray level to a nearby metastable state via an optical frequency comb, we develop a quantum control scheme to manipulate the coherent response of the atomic system. By controlling the periodic release of population and coherence stored in a metastable state, one can imprint a comb structure onto the absorption spectrum of a broadband, femtosecond x-ray pulse, such as those presently available at XFEL facilities [89–92]. The model can be applied when one of the following two conditions is fulfilled, i.e., either the pulses in the optical frequency comb have a pulse area equal to 2π, or the optical frequency comb is off-resonance. The single-pulse solution, presented in Sec. 6.2, is recursively employed in Sec. 6.3, in order to find a solution of the equations of motion in the case of periodic driving. Two sets of initial conditions are investigated, corresponding to different preparation schemes with an x-ray pulse and an optical pulse, as discussed in the previous Chapter. The three-level scheme models isolated transitions in He-like Be^{2+}: The imprinted comb is therefore centered at the corresponding x-ray transition energy of 123.7 eV; the values of the necessary peak intensity of the driving optical frequency comb, ranging from 10^{10} W/cm^2 to 10^{12} W/cm^2, are by orders of magnitude lower than the peak intensity used for high-frequency-comb generation via other schemes.

In the case in which the driving frequency comb immediately follows the x-ray pulse, as discussed in Secs. 6.3.1.1 and 6.3.2.1, the fast decay of the x-ray-excited state undergoes periodic phase shifts, which imprint a comb onto the absorption spectrum. Each peak in the comb has a width given by the decay rate of the excited state Γ_2. The overall spectral width of the comb is however limited, as the mth peak has an amplitude which decays like $1/m$.

However, if an optical pulse preceding the arrival of the frequency comb is used to store the coherence in the metastable state, as described in Secs. 6.3.1.2 and 6.3.2.2, then the envelope of the off-diagonal matrix element $\varrho_{12}^{\mathrm{eq}}(t)$ is shaped into a pulse-train-like function and an x-ray absorption spectrum is obtained, which is a comb with an overall width given by the optical-comb bandwidth γ.

The exact frequency of the peaks in the predicted x-ray comb is as precisely known as the x-ray line at which the comb is centered. Such comb may be valuable for spectroscopy, e.g., to determine an x-ray line with the same precision with which the reference line is known at which the comb is centered. The scheme is of interest both as a phase and amplitude, x-ray manipulation scheme, as for its potential applications in precision spectroscopy.

7 Summary and outlook

New opportunities and new challenges are opened up by the rapid growth of x-ray science. On the one hand, novel theoretical and experimental investigations can be envisaged thanks to the constantly improving quality of the light which the evolution of x-ray sources, such as the x-ray free-electron laser (XFEL), is rendering available; but on the other hand, in order to maintain such an improvement rate, new, sometimes alternative solutions may have to be considered.

In Chapter 1, we introduce the properties of presently available optical and x-ray light sources, with a particular focus on the advances in free-electron lasers (FELs) and extreme-ultraviolet (XUV) frequency combs.

In Chapter 2, we summarize the theory of the interaction of matter with light. In particular, we show how the properties of the light emitted by a set of atoms or ions interacting with an external field can be related to the time evolution of the driven atomic system, described in the density-matrix formalism through a Liouville-von Neumann master equation. We introduce the concept of Rabi flopping, of fundamental importance in the whole Thesis, and conclude the Chapter with a description of the spectral features of the emitted field, in terms of an idealized spectrum analyzer.

In Chapter 3, we study theoretically the resonance fluorescence spectrum of an ensemble of ions driven by intense, ultrashort x rays, inducing Rabi oscillations of atomic populations and coherences within the decay time of the system. A two-level model is used to describe Ne^+ cations driven by an intense linearly polarized x-ray field tuned to the $1s\,2p^{-1} \rightarrow 1s^{-1}\,2p$ transition at 848 eV. The choice of the system was motivated by previous experimental investigations of the resonant-Auger-decay electron spectra employing the same atomic system. We study the signature of x-ray-induced Rabi oscillations in the resonance fluorescence spectrum. We consider laser-like Gaussian pulses, now available via seeding methods, for which a clear signature of Rabi flopping is predicted. In the case of pulses generated by self-amplified spontaneous emission, Rabi flopping is less clearly visible, although tails in the spectrum appear, due to the high intensity of the driving pulses, which might represent a good signature of x-ray-induced Rabi oscillations.

The work presented in the Chapter motivates further experimental investigation of resonance fluorescence at XFEL facilities. In the case of Ar^+ cations, for instance, the spectrum of resonance fluorescence, because of the higher fluorescence yield compared to that of neon, is more intense than the one shown in Chapter 3. The model which we adopt could be similarly used to study cations such as argon, for which the measurement of the spectrum of resonance fluorescence would present obvious advantages compared to the measurement of the electron spectrum.

Furthermore, for nonstationary light, e.g. when the electric field has a pulse-shaped envelope, the study of the time-dependent power spectrum [74, 166, 219–221], i.e., the time-dependent rate of detected photons, would allow one to investigate how the spectral properties of the fluorescent light evolve during the pulse. Even though, because of the ultrashort nature of XFEL pulses—with duration of the order of 10 to 100 fs—and because of the lack of sufficiently fast detectors, such a power spectrum cannot be measured at present, the study of the time-dependent power spectrum might provide better understanding and further knowledge of the interaction between matter and x rays.

We would like to point out that the topic of Chapter 3 led to an experimental proposal to LCLS, to experimentally validate our theoretical predictions.

While Chapter 3 aims at investigating the direct manipulation of inner-shell levels with intense pulses from an XFEL, the remaining part of the Thesis focuses on the optical manipulation of x-ray transitions in a many-level system. We use an x-ray field to directly drive the transition between the ground state and an x-ray level. The population and coherence of the x-ray-excited state is optically manipulated via one or more optical fields coupling to other nearby levels. In particular, by employing an optical frequency comb, we put forward quantum-control schemes to imprint a frequency comb onto the x-ray spectrum. These schemes may represent an alternative to currently explored comb-generation methods based on high-order harmonic generation (HHG) in order to further increase the comb frequency while keeping the driving intensities on an accessible level. Stringent experimental tests of quantum electrodynamics and astrophysical models [123], and studies of the variability of the fine-structure constant with highly charged ions [124] would significantly benefit of the possibilities opened up by the availability of an x-ray frequency comb. Ultraprecise x-ray clocks may also be envisaged [125].

In Chapter 4, we develop a scheme to imprint a comb onto the resonance fluorescence spectrum emitted by four-level ions driven by narrow-bandwidth x rays. By optimizing the intensities of the driving fields, and in particular by utilizing an optical frequency comb consisting of pulses with an area which is an integer multiple of 2π, we predict a comb in the resonance fluorescence spectrum, which is centered on an atomic x-ray transition and which is as wide as the optical frequency comb employed to excite the system.

The four-level scheme is exemplified by He-like Be^{2+} ions: The x-ray transition energy at which the imprinted comb is centered, equal to 123.7 eV, is four times higher than the central frequency of XUV combs which were demonstrated via HHG-based methods [122]. The presented scheme requires optical-comb peak intensities of $\sim 10^{10}\,\mathrm{W/cm^2}$, by orders of magnitude lower than the intensities necessary for methods based on HHG. The wide comb we predict may be used as a relative "ruler" [30, 31], e.g., to bridge an energy difference between an x-ray reference level and an unknown x-ray frequency at high energies, for which the inefficiency of HHG due to relativistic effects at high harmonic orders would render its adoption not advisable [126].

The scheme takes advantage of narrow-bandwidth x-ray sources: Although we believe that the advances in x-ray science will soon provide the experimental conditions necessary to demonstrate the viability of this scheme, we also recognize that the assumption of a very narrow x-ray bandwidth does not allow an implementation of our scheme with currently available x-ray technology. The following two Chapters aim at overcoming this limitation by employing ultrashort x-ray pulses such as those presently available at FEL facilities.

In Chapter 5, we introduce a three-level model which is adopted to investigate coherent transfer of population and coherence in highly charged ions. The short x-ray pulse populates an excited state which a subsequent optical field couples to a nearby metastable state. The optical field allows one to transfer population and coherence from the x-ray-excited state to the metastable state and vice versa. A two-optical-pulse scheme is discussed, whereby the population "stored" in the long-lived, metastable state by the first optical pulse is subsequently released by the second one. An experimental demonstration of such a two-pulse scheme would represent an important step forward in the development of methods for the optical manipulation of x-ray excited levels. Furthermore, by modifying the time delay between the two pulses, accurate lifetime measurements of metastable states in highly charged ions may be performed. We wish to point out that these investigations are object of an experimental proposal at LCLS.

The same three-level model is employed in Chapter 6 to implement a scheme of x-ray-comb generation. In contrast to the case we present in Chapter 4, the system is initially excited by an ultrashort, broadband x-ray pulse, such as those currently available at FEL facilities [222]: An experimental implementation would therefore be possible with present x-ray technology.

An optical frequency comb coupling the x-ray-excited level to a metastable state is utilized to imprint a comb onto the absorption spectrum of the transmitted x-ray pulse. The dynamical evolution of the three-level system interacting with an optical frequency comb and the properties of the ensuing absorption spectrum depend on the initial state in which the atomic system is prepared. Two sets of initial conditions are investigated:

In Secs. 6.3.1.1 and 6.3.2.1, the sole ultrashort x-ray pulse is utilized to prepare the system in its initial state. The following interaction with the optical frequency comb induces periodic phase shifts of the exponentially decaying atomic variables. A sufficient number of phase shifts has to be induced during the lifetime of the excited level, i.e., the repetition frequency of the optical frequency comb need be higher than the decay rate of the excited state. The model is exemplified by He and He-like Be^{2+} ions with high-frequency transition energies respectively in the extended ultraviolet and in the x-ray ranges. The periodic modification of the dipole response of the atomic system gives rise to an x-ray absorption spectrum exhibiting a comb with the same frequency spacing as the optical frequency comb used to drive the system. The width of each peak in the imprinted comb is given by the decay rate of the fast decaying, x-ray-excited level. The amplitude of the peaks decays like $\sim 1/m$, where m labels the peak number counted from the x-ray transition energy at which the comb is centered.

In Secs. 6.3.1.2 and 6.3.2.2, the three-level system is prepared in its initial state by the combined presence of the short x-ray pulse and of an immediately following optical pulse coupling the x-ray-excited level to the nearby metastable state. Since the latter is characterized by an extremely long decay time, population and coherences are thereby "stored" in this long-lived state. While in Chapter 5 a single pulse is subsequently employed with the sole scope of releasing the coherence from the metastable state, here, the following interaction with the optical frequency comb induces a periodic sequence of coherence *release and storage*. This is achieved via either optical pulses with a 2π area, or pulses which are very detuned from the corresponding atomic optical transition. The x-ray emission, associated with the decay of the x-ray-excited level taking place in the sole presence of the short pulses from the optical frequency comb, gives rise to a comb in the absorption spectrum of the transmitted x-ray field. The comb is centered at the atomic transition energy between the ground state and the x-ray-excited state. Since the long decay time of the metastable state is properly exploited, the three-level system decays at an effective rate which is by orders of magnitude smaller than the decay rate of the x-ray-excited state. As a result, an optical frequency comb with routinely available repetition frequency is sufficient to demonstrate the scheme. The low effective decay rate which we achieve by storing the coherence in the metastable state also determines very sharp peaks in the imprinted comb, whose widths are given by this low effective decay rate. Furthermore, by shaping the atomic variables into a "train of pulses", a wide comb is imprinted onto the x-ray absorption spectrum, with a number of peaks which is comparable to that in the driving optical frequency comb. The model is exemplified by He-like Be^{2+} ions with an x-ray transition energy of 123.7 eV. A comb centered at this energy is predicted upon interaction with an optical frequency comb with peak intensity of $\sim 10^{10}\,\mathrm{W/cm^2}$.

The comb which we predict in the absorption spectrum is referenced to an atomic transition [30, 31], i.e., it provides a series of precisely separated peaks whose positions are as accurately known as the x-ray atomic level at which they are centered. The scheme requires currently available x-ray and optical-frequency-comb technology and its experimental demonstration is presently under design [223].

In this Thesis, we employed ensembles of ions with low density such that good phase matching is achieved. Phase-matching effects would have to be taken into account explicitly if one studied ensembles of particles with higher densities than those assumed here. This can be achieved via a self-consistent solution of the Maxwell-Liouville equations of motion through the medium,

i.e., by solving the Liouville-von Neumann equation by taking into account consistently how the atomic response at a given point in space modifies the electric-field strength. Not only would this generalize the approach that we developed in this work, but it may also provide better understanding of our study and would help the actual experimental implementation of the theoretical models.

The quantum-control schemes which we present in Chapters 4 and 6 are applied to He-like Be^{2+} ions, which gives rise to combs centered at a transition energy of 123.7 eV. The schemes, however, have general validity and can be used to model different atomic systems. Qualitatively similar results can be obtained from other He-like ions, such as Ne^{8+}; in this case, for a transition energy of 922.0 eV [191], we predict a comb in the kiloelectronvolt range, although for the transition energy at 6.679 eV intense optical frequency combs are not available yet.

Our models can be readily applied to different atomic transitions, e.g., $1s^2 \to 1s\,np$ with $n \geq 3$, in more highly charged He-like ions at higher photon energies, e.g., $\sim 500\,\mathrm{eV}$. The model would not have to be modified, since the level structure remains unchanged. However, one would have to properly choose the atomic number Z of the ion in order to ensure that the corresponding $1s\,np \to 1s\,ns$ transition has energy in the optical range, such that it can be effectively driven via currently available optical frequency combs. However, ionic species with too high atomic numbers should be avoided, since the decay rate of the excited state $1s\,np$ to the ground state increases with Z as $\sim Z^4$ [159]. If the decay from the excited state is too fast, it can become in fact challenging to efficiently transfer population and coherence with an optical laser to a nearby metastable state.

Towards an experimental implementation of our schemes, it would be important to rely on a more complete description of the atomic structure, in which the role of all atomic levels is taken into account numerically. This would be particularly significant if one planned to employ, e.g., a pulse of attosecond pulses, whose spectral width is from 100 to 1,000 times larger than the width of the pulses employed throughout this Thesis. A broadband pulse, in fact, puts into question the three- or four-level approximation of which we took advantage here, as several transitions may have energies lying within the energy width of the driving pulses. A numerical approach including the presence of practically all atomic levels would also be advisable if one decided to consider, as previously described, higher-photon-energy transitions such as $1s^2 \to 1s\,np$ in heavier ions. In this case, the intermediate excited levels with $n' < n$ may be accessed, e.g., via spontaneous decay and their role may not be negligible.

The same many-level schemes which we utilized throughout the Thesis may be employed to describe a frequency comb in the gamma range taking advantage of nuclear transitions [127, 224–226]. In this case, one would have to determine proper isotopes in which an excited state can be optically coupled to a nearby level. The application of the concepts from this Thesis in nuclei, however, may not be immediate. In particular, dipole matrix elements, i.e., oscillator strengths, in nuclear transitions are extremely small. On the one hand, this renders the natural widths of the excited levels tiny, such that only an exiguous amount of the energy in a broadband driving pulse effectively contributes to the excitation of the level. On the other hand, small oscillator strengths correspond to small Rabi frequencies. As a result, the model may be applied with nuclear transitions, but very high intensities of the driving x-ray and optical fields may be required. Therefore, one would have to find a proper nuclear isotope in which our scheme can be applied at presently accessible peak intensities.

A Time-frequency description of a frequency comb

In this Appendix we revise the main features characterizing frequency combs in the time and frequency domain.

Fig. A.1a displays three pulses from a train of coherent pulses in an optical frequency comb. The electric field can be written in very good approximation as

$$\mathcal{E}_{\mathrm{C}}(t) = \frac{1}{2}\,\mathbf{Re}\{\mathcal{E}_{\mathrm{C},0}(t)\,\mathrm{e}^{-\mathrm{i}\omega_{\mathrm{C}}t}\} = \frac{1}{2}\sum_{k=-\infty}^{+\infty}\mathbf{Re}\{A_k\,\mathrm{e}^{-\mathrm{i}(\omega_{\mathrm{C}}+k\omega_{\mathrm{r}})t}\}, \tag{A.1}$$

where ω_{C} is the optical carrier frequency and $\mathcal{E}_{\mathrm{C},0}(t)$ is a (real) periodic envelope function, of period T_{p} and repetition frequency $\omega_{\mathrm{r}} = 2\pi/T_{\mathrm{p}}$, which can be written as a Fourier series of Fourier coefficients

$$A_k = \frac{1}{T_{\mathrm{p}}}\int_{-\frac{T_{\mathrm{p}}}{2}}^{\frac{T_{\mathrm{p}}}{2}}\mathcal{E}_{\mathrm{C},0}(t)\,\mathrm{e}^{\mathrm{i}k\omega_{\mathrm{r}}t}\,\mathrm{d}t. \tag{A.2}$$

In frequency space the spectrum of the field is given by

$$\tilde{\mathcal{E}}_{\mathrm{C}}(\omega) = \int_{-\infty}^{\infty}\mathcal{E}_{\mathrm{C}}(t)\,\mathrm{e}^{\mathrm{i}\omega t}\,\mathrm{d}t = \frac{1}{2}\sum_{k=-\infty}^{+\infty}A_k\,\delta(\omega-\omega_{\mathrm{C}}-k\omega_{\mathrm{r}}) + \frac{1}{2}\sum_{k=-\infty}^{+\infty}A_k^*\,\delta(\omega+\omega_{\mathrm{C}}+k\omega_{\mathrm{r}}), \tag{A.3}$$

i.e., the spectrum is a comb of delta peaks, equally separated by the repetition frequency ω_{r}, as shown in Fig. A.1b.

To render this more explicit, let us suppose that the optical frequency comb is the result of a periodic train of Gaussian pulses, i.e., the periodic envelope function is

$$\mathcal{E}_{\mathrm{C},0}(t) = \mathcal{E}_{\mathrm{C,max}}\sum_{n=-\infty}^{\infty}\mathcal{G}(t-nT_{\mathrm{p}}), \tag{A.4}$$

with

$$\mathcal{G}(t) = \mathrm{e}^{-\frac{t^2}{2T^2}}, \tag{A.5a}$$

$$\tilde{\mathcal{G}}(\omega) = \int_{-\infty}^{\infty}\mathcal{G}(t)\,\mathrm{e}^{\mathrm{i}\omega t}\,\mathrm{d}t = T\sqrt{2\pi}\,\mathrm{e}^{-\frac{\omega^2T^2}{2}}. \tag{A.5b}$$

We define $\tau = 2\sqrt{\ln(2)}T$ and $\Delta\omega = 2\sqrt{\ln(2)}/T$ as the FWHM of $|\mathcal{G}(t)|^2$ and $|\tilde{\mathcal{G}}(\omega)|^2$, respectively. By supposing that each single pulse is much shorter than the repetition period T_{p}, one has

$$A_k = \frac{1}{T_{\mathrm{p}}}\int_{-\frac{T_{\mathrm{p}}}{2}}^{\frac{T_{\mathrm{p}}}{2}}\mathcal{E}_{\mathrm{C},0}(t)\,\mathrm{e}^{\mathrm{i}k\omega_{\mathrm{r}}t}\,\mathrm{d}t = \frac{1}{T_{\mathrm{p}}}\int_{-\infty}^{\infty}\mathcal{G}(t)\,\mathrm{e}^{\mathrm{i}k\omega_{\mathrm{r}}t}\,\mathrm{d}t = \frac{\tilde{\mathcal{G}}(k\omega_{\mathrm{r}})}{T_{\mathrm{p}}}. \tag{A.6}$$

We can see that A_k is given by the single-pulse Fourier transform $\tilde{\mathcal{G}}(\omega)$, sampled with spacing ω_{r}. The overall width of the comb is given by the width of the single-pulse spectrum, $\Delta\omega = 4\ln(2)/\tau$,

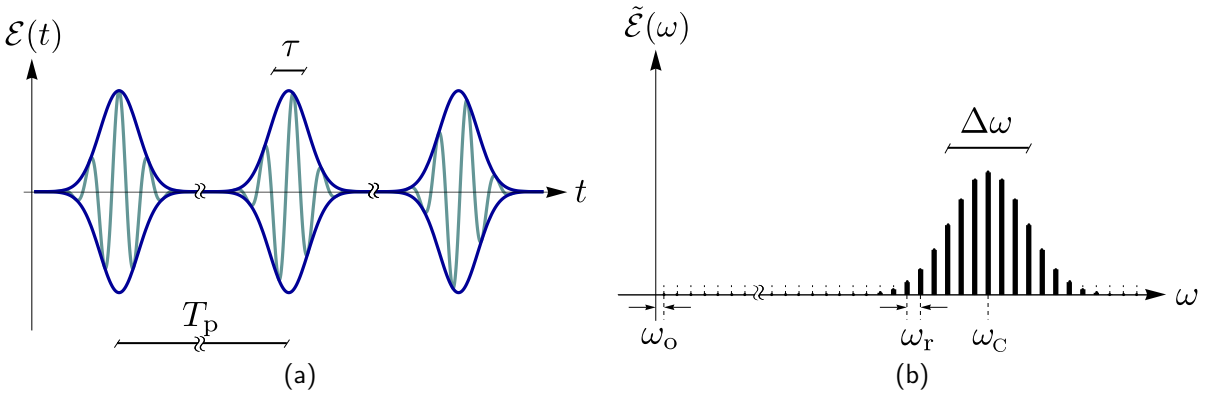

Figure A.1: The electric field of an optical frequency comb in the (a) time and (b) frequency domain. In panel A.1a the light blue line represents the total electric field $\mathcal{E}_\mathrm{C}(t)$, whereas the dark blue line is the envelope $\mathcal{E}_{\mathrm{C},0}(t)$, with repetition period T_p and FWHM τ. In panel A.1b, the spectrum of the frequency comb is displayed by the thick lines, with repetition frequency ω_r and overall width $\Delta\omega$. By extending the equidistant lines to the origin of the frequency axis, the offset frequency ω_o can be determined. Similar pictures are widely used in the literature to present the properties of a frequency comb, see, e.g., Refs. [23, 24].

which is inversely proportional to the single-pulse FWHM τ. The effective number of peaks in the comb is given by

$$\Delta k \sim \frac{\Delta\omega}{\omega_\mathrm{r}} \sim \frac{T_\mathrm{p}}{\tau}. \tag{A.7}$$

The position of a peak

$$\omega_\mathrm{C} + k\omega_\mathrm{r} = \omega_\mathrm{o} + k'\omega_\mathrm{r}, \tag{A.8}$$

with k, $k' \in \mathbb{Z}$, is entirely determined by two radio frequencies, namely, the offset frequency ω_o and the repetition frequency ω_r. Here, the offset frequency is defined as that frequency ω_o, with $0 < \omega_\mathrm{o} < \omega_\mathrm{r}$, such that $\omega_\mathrm{C} = \omega_\mathrm{o} + K\omega_\mathrm{r}$, with $K \in \mathbb{N}$ and $k' = k + K$. Eq. (A.8) represents the key element for the direct radio-frequency–optical-frequency link allowed by optical frequency combs. By measuring with a cesium clock the two frequencies ω_o and ω_r, the determination of k' immediately permits one to know the position of the corresponding frequency peak with the precision of the clock. In an octave-spanning comb, i.e., a comb whose largest frequency modes are about twice as large as its smallest ones, the measurement of the offset frequency is straightforward [35]: one can, namely, optically measure the beat note between the frequency-doubled k'th mode, i.e., $2(\omega_\mathrm{o} + k'\omega_\mathrm{r})$, and the actual $2k'$th mode $\omega_\mathrm{o} + 2k'\omega_\mathrm{r}$, which directly provides the offset frequency

$$2(\omega_\mathrm{o} + k'\omega_\mathrm{r}) - (\omega_\mathrm{o} + 2k'\omega_\mathrm{r}) = \omega_\mathrm{o}. \tag{A.9}$$

B Partial coherence method

We use the Partial Coherence Method (PCM) introduced in Ref. [184] to generate random realizations of the temporal shape of self-amplified-spontaneous-emission (SASE) x-ray free-electron-laser (XFEL) pulses, whose knowledge is an important prerequisite for meaningful investigations of nonlinear x ray-matter interaction [138]. Those parameters which can be measured at present XFELs, such as the average spectral intensity and the pulse duration, are taken into account as input parameters [185]. The PCM is used to generate non-transform-limited pulses, with a coherence time lower than the average FWHM duration of the pulse and with significant fluctuations in the pulse shape from shot to shot.

The pulses are generated starting from their frequency representation $\tilde{\mathcal{E}}(\omega)$, whose amplitude is given by the average spectral intensity of the pulse. If the phase of $\tilde{\mathcal{E}}(\omega)$ was constant, then by Fourier transform one would obtain a transform-limited pulse. In order to generate a SASE pulse, we let the spectral phase vary in $[-\pi, \pi[$.

The PCM models the classical electric field $\mathcal{E}(t)$ [Eq. (3.1)]. We introduce the complex electric field [164] $\mathcal{E}^{\pm}(t) = \frac{1}{2}\mathcal{E}_0(t)\,\mathrm{e}^{\mp\mathrm{i}(\varphi_\mathrm{X}(t)+\omega_\mathrm{X}t)}$ and the complex field envelope $\tilde{\mathcal{E}}(t) = \frac{1}{2}\mathcal{E}_0(t)\,\mathrm{e}^{-\mathrm{i}\varphi_\mathrm{X}(t)}$, such that $\mathcal{E}(t) = \tilde{\mathcal{E}}(t)\,\mathrm{e}^{-\mathrm{i}\omega_\mathrm{X}t} + \tilde{\mathcal{E}}^*(t)\,\mathrm{e}^{\mathrm{i}\omega_\mathrm{X}t}$. It follows that [164]

$$|\mathcal{E}(t)|^2 = 2|\mathcal{E}^{\pm}(t)|^2 = 2|\tilde{\mathcal{E}}(t)|^2 = \frac{|\mathcal{E}_0(t)|^2}{2}. \tag{B.1}$$

We define the Fourier transform of $\tilde{\mathcal{E}}(t)$ as

$$\tilde{\mathcal{E}}(\omega) = \int_{-\infty}^{+\infty} \tilde{\mathcal{E}}(t)\mathrm{e}^{\mathrm{i}\omega t}\,\mathrm{d}t = |\tilde{\mathcal{E}}(\omega)|\,\mathrm{e}^{-\mathrm{i}\phi(\omega)} \tag{B.2}$$

and from Parseval's theorem it follows that

$$\int_{-\infty}^{+\infty} |\tilde{\mathcal{E}}(t)|^2\,\mathrm{d}t = \frac{1}{2\pi}\int_{-\infty}^{+\infty} |\tilde{\mathcal{E}}(\omega)|^2\,\mathrm{d}\omega. \tag{B.3}$$

Analogously one can define $\mathcal{E}(\omega)$ and $\mathcal{E}^+(\omega)$ as the Fourier transforms of $\mathcal{E}(t)$ and $\mathcal{E}^+(t)$, respectively. One notices that $\mathcal{E}^+(\omega) = \tilde{\mathcal{E}}\,(\omega - \omega_\mathrm{X})$ and therefore $\mathcal{E}(\omega) = \tilde{\mathcal{E}}\,(\omega - \omega_\mathrm{X}) + \tilde{\mathcal{E}}\,(\omega + \omega_\mathrm{X})$, such that, from Parseval's theorem (B.3), one finds in agreement with (B.1) that

$$\int_{-\infty}^{+\infty} |\mathcal{E}(t)|^2\,\mathrm{d}t = \frac{1}{2\pi}\int_{-\infty}^{+\infty} 2\,|\tilde{\mathcal{E}}(\omega)|^2\,\mathrm{d}\omega. \tag{B.4}$$

The average spectral intensity of a SASE pulse is modeled here—close to measured spectral intensities—as a Gaussian function, such that

$$|\tilde{\mathcal{E}}(\omega)|^2 = |\tilde{\mathcal{E}}_{\mathrm{sp,max}}|^2\mathrm{e}^{-\frac{\omega^2}{\Omega^2}}, \tag{B.5}$$

whose FWHM is $\Delta\omega_\mathrm{SASE} = 2\Omega\sqrt{\ln 2}$. The FWHM duration of the squared modulus of the inverse Fourier transform of $|\tilde{\mathcal{E}}(\omega)|$ [164], which is here also a Gaussian function, is $\tau_\mathrm{SASE} = 4\ln 2/\Delta\omega_\mathrm{SASE}$. It follows that

$$|\mathcal{E}(\omega)|^2 = |\tilde{\mathcal{E}}_{\mathrm{sp,max}}|^2\Big(\mathrm{e}^{-\frac{(\omega-\omega_\mathrm{X})^2}{\Omega^2}} + \mathrm{e}^{-\frac{(\omega+\omega_\mathrm{X})^2}{\Omega^2}}\Big). \tag{B.6}$$

The average spectral intensity, however, does not provide any information about the spectral phase of the pulse. In analogy to the phase retrieval in x-ray crystallography [88], the knowledge of the spectral amplitude is not sufficient to completely determine the temporal shape of the pulse via inverse Fourier transform. In the PCM approximate phase retrieval is achieved by assuming initially a random frequency-dependent spectral phase varying in $[-\pi, \pi[$.

We define a discrete spectral component of the electric field $\tilde{\mathcal{E}}(\omega_i) = |\tilde{\mathcal{E}}(\omega_i)|\,\mathrm{e}^{-\mathrm{i}\phi_i}$, with a sampling interval $|\omega_{i+1} - \omega_i| \ll \Delta\omega_{\mathrm{SASE}}$. ϕ_i are random numbers in $[-\pi, \pi[$. The discrete inverse Fourier transform of $\tilde{\mathcal{E}}(\omega_i)$ provides the time-dependent discrete field $\mathcal{R}(t_j)$.

The complex function $\mathcal{R}(t)$, obtained by interpolating $\mathcal{R}(t_j)$, spans an infinitely long interval in time because of the fluctuating ϕ_i. To generate SASE pulses of finite duration, we multiply $\mathcal{R}(t)$ by a temporal filter function $f(t)$. This function is nonzero only in a finite domain and the FWHM duration of $|f(t)|^2$ is τ_{env}. The finite duration of FEL pulses is determined by the electron bunch duration [227] and is usually measured. All together, we approximate the complex electric field by

$$\tilde{\mathcal{E}}(t) = \frac{1}{2}\mathcal{E}_0(t)\,\mathrm{e}^{-\mathrm{i}\varphi_{\mathrm{X}}(t)} = \mathcal{R}(t)f(t). \tag{B.7}$$

Along the way, we notice that the inverse Fourier transform of $\mathcal{R}(t)f(t)$ is given by the convolution of the respective inverse Fourier transforms $\tilde{\mathcal{E}}(\omega)$ and $\tilde{f}(\omega)$. $\tilde{\mathcal{E}}(\omega)$ has a random fluctuating phase $\phi(\omega)$, whereas $|\tilde{f}(\omega)|^2$ has a spectral FWHM $\Delta\omega_{\mathrm{env}}$ related to the inverse of τ_{env}. Hence, the spectral amplitude of a single pulse generated with the PCM also displays a spiky structure, where the average FWHM frequency of each spike is about $\Delta\omega_{\mathrm{env}}$ [227]. In addition, since the average value of $\phi(\omega)$ is 0, the average spectral amplitude results from the convolution of $|\tilde{\mathcal{E}}(\omega)|$ and $\tilde{f}(\omega)$ and, because $\tau_{\mathrm{env}} \gg \tau_{\mathrm{SASE}}$, the width of $\tilde{f}(\omega)$ is much narrower than the width of $|\tilde{\mathcal{E}}(\omega)|$. Consequently, the convolution

$$\int_{-\infty}^{+\infty} |\tilde{\mathcal{E}}(\omega - \omega')|\tilde{f}(\omega')\,\mathrm{d}\omega' \approx |\tilde{\mathcal{E}}(\omega)|,$$

i.e., the multiplication by the envelope function $f(t)$ does not affect significantly the average spectral intensity of $\tilde{\mathcal{E}}(t)$.

To generate SASE pulses [Fig. 3.9] we use the envelope function

$$f(t) = \begin{cases} f_0 \cos^2(\pi t/T) & ; \quad \text{if } |t| \le T/2 \\ 0 & ; \quad \text{if } |t| > T/2 \end{cases} \tag{B.8}$$

with $T = \pi\tau_{\mathrm{env}}/(2\arccos\sqrt[4]{1/2})$ [190]. The Fourier transform of $f(t)$ is

$$\tilde{f}(\omega) = \frac{T}{2}\, f_0 \frac{\mathrm{sinc}\left(\frac{\omega T}{2}\right)}{1 - \left(\frac{\omega T}{2\pi}\right)^2}. \tag{B.9}$$

Then, $\Delta\omega_{\mathrm{env}} \approx 2.41/\tau_{\mathrm{env}}$ is the FWHM of $|\tilde{f}(\omega)|^2$. One notices that, for $\tau_{\mathrm{env}} = 6.5$ fs and $\Delta\omega_{\mathrm{SASE}} = 6$ eV, one has $\Delta\omega_{\mathrm{env}} = 0.24$ eV $\ll \Delta\omega_{\mathrm{SASE}} = 6$ eV.

Alternative approaches have also been developed and adopted, e.g., in [113, 228]. In these cases, the electric field is written as a Fourier series in time domain

$$\mathcal{E}(t) = \sum_{k=-\infty}^{\infty} a_k\, \cos(\omega_k t) + b_k\, \sin(\omega_k t), \tag{B.10}$$

where the real coefficients a_k and b_k are independent zero-mean Gaussian random variables. Basically, this represents only a different description of $\tilde{\mathcal{E}}(\omega)$ compared with the PCM.

C Mathematical details about hypergeometric functions

C.1 The hypergeometric differential equation

In the present Section we focus on the mathematical details of the solution of the set of two second-order differential equations

$$\begin{aligned}\frac{\partial^2\bar{\varrho}_{12}}{\partial t^2}-\left(\frac{1}{\Omega_\mathrm{R}}\frac{\partial\Omega_\mathrm{R}}{\partial t}+\mathrm{i}\Delta+\frac{\Gamma_2-\Gamma_3}{2}\right)\frac{\partial\bar{\varrho}_{12}}{\partial t}+\frac{\Omega_\mathrm{R}^2}{4}\bar{\varrho}_{12}=0,\\ \frac{\partial^2\bar{\varrho}_{13}}{\partial t^2}-\left(\frac{1}{\Omega_\mathrm{R}}\frac{\partial\Omega_\mathrm{R}}{\partial t}-\mathrm{i}\Delta-\frac{\Gamma_2-\Gamma_3}{2}\right)\frac{\partial\bar{\varrho}_{13}}{\partial t}+\frac{\Omega_\mathrm{R}^2}{4}\bar{\varrho}_{13}=0,\end{aligned} \tag{C.1}$$

when

$$\Omega_\mathrm{R}(t)=A\,\mathrm{sech}[\gamma(t-t_0)]. \tag{C.2}$$

First of all, we introduce the variable

$$z(t)=\frac{\tanh\left[\gamma(t-t_0)\right]+1}{2} \tag{C.3}$$

and observe that, from Eqs. (C.2) and (C.3), the following identities can be derived,

$$\frac{1}{\Omega_\mathrm{R}}\frac{\partial\Omega_\mathrm{R}}{\partial t}=-\gamma\tanh\left[\gamma(t-t_0)\right]=-\gamma(2z-1), \tag{C.4a}$$

$$\Omega_\mathrm{R}^2=A^2\{1-\tanh^2\left[\gamma(t-t_0)\right]\}=4A^2z(1-z), \tag{C.4b}$$

$$\frac{\partial z}{\partial t}=\frac{\gamma}{2}\,\mathrm{sech}^2[\gamma(t-t_0)]=\frac{\gamma}{2A^2}\Omega_\mathrm{R}^2, \tag{C.4c}$$

$$\frac{\partial^2 z}{\partial t^2}=\frac{\gamma}{A^2}\Omega_\mathrm{R}\frac{\partial\Omega_\mathrm{R}}{\partial t}=-\frac{\gamma^2}{A^2}\Omega_\mathrm{R}^2(2z-1), \tag{C.4d}$$

such that

$$\frac{\partial\bar{\varrho}_{12}}{\partial t}=\frac{\partial z}{\partial t}\frac{\partial\bar{\varrho}_{12}}{\partial z}=\frac{\gamma}{2A^2}\Omega_\mathrm{R}^2\frac{\partial\bar{\varrho}_{12}}{\partial z}, \tag{C.5a}$$

$$\frac{\partial^2\bar{\varrho}_{12}}{\partial t^2}=\frac{\partial^2 z}{\partial t^2}\frac{\partial\bar{\varrho}_{12}}{\partial z}+\left(\frac{\partial z}{\partial t}\right)^2\frac{\partial^2\bar{\varrho}_{12}}{\partial z^2}=-\frac{\gamma^2}{A^2}\Omega_\mathrm{R}^2(2z-1)\frac{\partial\bar{\varrho}_{12}}{\partial z}+\frac{\gamma^2}{4A^4}\Omega_\mathrm{R}^4\frac{\partial^2\bar{\varrho}_{12}}{\partial z^2}. \tag{C.5b}$$

These equalities can be used to write the differential equations (C.1) in terms of the new variable z [Eq. (C.3)], i.e.,

$$z(1-z)\frac{\partial^2\bar{\varrho}_{12}}{\partial z^2}+\left(\frac{1}{2}-\mathrm{i}\frac{\Delta}{2\gamma}-\frac{\Gamma_2-\Gamma_3}{4\gamma}-z\right)\frac{\partial\bar{\varrho}_{12}}{\partial z}+\frac{A^2}{4\gamma^2}\bar{\varrho}_{12}=0, \tag{C.6a}$$

$$z(1-z)\frac{\partial^2\bar{\varrho}_{13}}{\partial z^2}+\left(\frac{1}{2}+\mathrm{i}\frac{\Delta}{2\gamma}+\frac{\Gamma_2-\Gamma_3}{4\gamma}-z\right)\frac{\partial\bar{\varrho}_{13}}{\partial z}+\frac{A^2}{4\gamma^2}\bar{\varrho}_{13}=0. \tag{C.6b}$$

By introducing

$$a = -b = \frac{A}{2\gamma}, \tag{C.7a}$$

$$c = \frac{1}{2} - \mathrm{i}\frac{\Delta}{2\gamma} - \frac{\Gamma_2 - \Gamma_3}{4\gamma}, \tag{C.7b}$$

the previous equations (C.6) can be written in the standard form of a hypergeometric differential equation [216–218]

$$z(1-z)\frac{\partial^2 \bar{\varrho}_{12}}{\partial z^2} + [c - (a+b+1)z]\frac{\partial \bar{\varrho}_{12}}{\partial z} - ab\bar{\varrho}_{12} = 0, \tag{C.8a}$$

$$z(1-z)\frac{\partial^2 \bar{\varrho}_{13}}{\partial z^2} + [1 - c - (a+b+1)z]\frac{\partial \bar{\varrho}_{13}}{\partial z} - ab\bar{\varrho}_{13} = 0, \tag{C.8b}$$

whose general solution is [68–71, 73, 163, 216–218]

$$\bar{\varrho}_{12}(z) = B_1\, {}_2F_1(a, b; c; z) + B_2\, z^{1-c}\, {}_2F_1(a+1-c, b+1-c; 2-c; z), \tag{C.9a}$$

$$\bar{\varrho}_{13}(z) = B_3\, {}_2F_1(a, b; 1-c; z) + B_4\, z^{c}\, {}_2F_1(a+c, b+c; 1+c; z), \tag{C.9b}$$

where ${}_2F_1(a, b; c; z)$ is the Gaussian hypergeometric function [216–218]

$${}_2F_1(a, b; c; z) = \sum_{n=0}^{\infty} \frac{(a)_n (b)_n}{(c)_n} \frac{z^n}{n!}, \tag{C.10}$$

and

$$(q)_n = \begin{cases} 1 & \text{if } n = 0, \\ q(q+1)\cdots(q+n-1) = \frac{\Gamma(q+n)}{\Gamma(q)} & \text{if } n > 0. \end{cases} \tag{C.11}$$

We have also introduced the Gamma function $\Gamma(z)$ [216–218], defined in the complex plane except for negative integers $z = -n$, with $n = 0, 1, 2, \ldots$, as the function satisfying the identity

$$\Gamma(z) = \frac{\Gamma(z+1)}{z}. \tag{C.12}$$

Negative integers are poles of the function, with residue $(-1)^n/(n!)$. For complex numbers with positive real part, i.e., $\mathbf{Re}(z) > 0$, the Gamma function can be defined from the absolutely convergent series

$$\Gamma(z) = \int_0^{\infty} t^{z-1}\, \mathrm{e}^{-t}\, \mathrm{d}t. \tag{C.13}$$

From the definition (C.10) of the hypergeometric function ${}_2F_1(a, b; c; z)$ we can see that, if either a or b is a nonpositive integer, the series terminates. In other words, if $a = -m$, where $m = 0, 1, 2, \ldots$, then $(a)_n = (-m)_n = 0$ for all $n > m$ and the series in (C.10) reduces to the finite sum

$${}_2F_1(a, b; c; z) = \sum_{n=0}^{m} \frac{(-m)_n (b)_n}{(c)_n} \frac{z^n}{n!}.$$

For $c = -l$, with $l = 0, 1, 2, \ldots$, the series is indeterminate if neither a nor b is a negative integer $-m$, with $m < l$. For all other cases the convergence of the series is guaranteed for all z such that $|z| < 1$. For $|z| = 1$, the series (C.10) (i) converges absolutely if $\mathbf{Re}(a + b - c) < 0$, (ii) converges

conditionally when $z \neq 1$ and $0 \leq \mathbf{Re}(a+b-c) < 1$, and (iii) diverges when $1 \leq \mathbf{Re}(a+b-c)$. We also notice that (i) for $z = 0$ we have

$$ {}_2F_1(\alpha, \beta; \gamma; 0) = 1, \tag{C.14}$$

whereas (ii) for $z \to 1$ we find

$$ {}_2F_1(\alpha, \beta; \gamma; 1) = \frac{\Gamma(\gamma)\,\Gamma(\gamma-\alpha-\beta)}{\Gamma(\gamma-\alpha)\,\Gamma(\gamma-\beta)} \;\text{ if } \mathbf{Re}(\gamma) > \mathbf{Re}(\alpha+\beta). \tag{C.15}$$

The hypergeometric function ${}_2F_1(a, b; c; z)$ satisfies the following identities [216–218]:

$$ {}_2F_1(b, a; c; z) = {}_2F_1(a, b; c; z), \tag{C.16a}$$

$$ {}_2F_1(c-a, c-b; c; z) = (1-z)^{a+b-c}\, {}_2F_1(a, b; c; z), \tag{C.16b}$$

$$ \frac{\partial\, {}_2F_1(a, b; c; z)}{\partial z} = \frac{ab}{c}\, {}_2F_1(1+a, 1+b; 1+c; z), \tag{C.16c}$$

$$ abz\, {}_2F_1(a+1, b+1; \gamma+2; z) = \gamma(\gamma+1)\, {}_2F_1(a, b; \gamma; z) - \gamma(\gamma+1)\, {}_2F_1(a, b; \gamma+1; z), \tag{C.16d}$$

$$ \begin{aligned} (1-z)\, {}_2F_1(a+1, b+1; \gamma+1; z) &= \frac{\gamma}{b}\, {}_2F_1(a, b; \gamma; z) + \frac{b-\gamma}{b}\, {}_2F_1(a+1, b; \gamma+1; z) \\ &= \frac{\gamma}{a}\, {}_2F_1(a, b; \gamma; z) + \frac{a-\gamma}{a}\, {}_2F_1(a, b+1; \gamma+1; z), \end{aligned} \tag{C.16e}$$

$$ \begin{aligned} \gamma\, {}_2F_1(a, b; \gamma; z) &= (\gamma-b)\, {}_2F_1(a, b; \gamma+1; z) + b\, {}_2F_1(a, b+1; \gamma+1; z) \\ &= (\gamma-a)\, {}_2F_1(a, b; \gamma+1; z) + a\, {}_2F_1(a+1, b; \gamma+1; z). \end{aligned} \tag{C.16f}$$

whereby, by using Eqs. (6.12), (C.4b) (C.5a), (C.7), and (C.16c), we can rewrite $\bar{\varrho}_{13}$ as

$$ \begin{aligned} \bar{\varrho}_{13} = & -\frac{2\mathrm{i}}{\Omega_R}\, \mathrm{e}^{2\gamma\left(c-\frac{1}{2}\right)(t-T_0)}\, \frac{\gamma}{2A^2}\, \Omega_{\mathrm{R}}^2\, \frac{\partial \bar{\varrho}_{12}}{\partial z} \\ = & -\frac{\mathrm{i}}{a}\, (1-z)^{\frac{1}{2}}\, z^{\frac{1}{2}}\, \mathrm{e}^{2\gamma\left(c-\frac{1}{2}\right)(t-T_0)} \left[B_1\, \frac{ab}{c}\, {}_2F_1(1+a, 1+b; 1+c; z) \right. \\ & + B_2\, (1-c)\, z^{-c}\, {}_2F_1(a+1-c, b+1-c; 2-c; z) \\ & \left. + B_2\, \frac{(a+1-c)(b+1-c)}{2-c}\, z^{1-c}\, {}_2F_1(a+2-c, b+2-c; 3-c; z) \right]. \end{aligned} \tag{C.17}$$

We also observe that

$$ t(z) = t_0 + \frac{1}{2\gamma} \log \frac{z}{1-z} \quad \Rightarrow \quad \mathrm{e}^{2\gamma\left(c-\frac{1}{2}\right)(t-T_0)} = \left(\frac{z}{1-z} \right)^{c-\frac{1}{2}}\, \mathrm{e}^{2\gamma\left(c-\frac{1}{2}\right)(t_0-T_0)} \tag{C.18}$$

such that, by exploiting Eq. (C.18) in Eq. (C.17), one has

$$ \begin{aligned} \bar{\varrho}_{13} = & -\mathrm{i}\, \mathrm{e}^{2\gamma\left(c-\frac{1}{2}\right)(t_0-T_0)}\, (1-z)^{1-c} \left[B_1\, \frac{b}{c}\, z^c\, {}_2F_1(1+a, 1+b; 1+c; z) \right. \\ & + B_2 \left(\frac{1-c}{a}\, {}_2F_1(a+1-c, b+1-c; 2-c; z) \right. \\ & \left. \left. + \frac{(a+1-c)(b+1-c)}{a(2-c)}\, z\, {}_2F_1(a+2-c, b+2-c; 3-c; z) \right) \right]. \end{aligned} \tag{C.19}$$

The first addend on the first line in the sum on the right-hand side of Eq. (C.19) can be alternatively written by using the relation

$$(1-z)^{1+a'+b'-c'}\,{}_2F_1(1+a',1+b';1+c';z) = {}_2F_1(c'-a',c'-b';1+c';z), \tag{C.20}$$

where we have used the substitution $c = 1+c'$, $a = 1+a'$, and $b = 1+b'$ in Eq. (C.16b). To rewrite the other two terms in the second and third lines of Eq. (C.19), one has to employ the identities in Eq. (C.16). By substituting $c = 2-c'$, $a = 1-a'$, and $b = 1-b'$ in Eq. (C.16b) and then $\gamma = 1-c'$, $a = -a'$, $b = -b'$ in Eqs. (C.16e) and (C.16f), one finds

$$\begin{aligned}
&\frac{1-c'}{a'}\,(1-z)^{1+a'+b'-c'}\,{}_2F_1(a'+1-c',b'+1-c';2-c';z)\\
&=\frac{1-c'}{a'}\,(1-z)\,{}_2F_1(1-a',1-b';2-c';z)\\
&=\frac{1-c'}{a'}\left[-\frac{1-c'}{b'}\,{}_2F_1(-a',-b';1-c';z)+\frac{1-c'+b'}{b'}\,{}_2F_1(1-a',-b';2-c';z)\right]\\
&=\frac{1-c'}{a'}\Big[-\frac{1-c'}{a'b'}\,(1-c'+a'+b')\,{}_2F_1(-a',-b';1-c';z)\\
&\quad+\frac{(1-c'+b')(1-c'+a')}{a'b'}\,{}_2F_1(-a',-b';2-c';z)\Big].
\end{aligned} \tag{C.21}$$

Similarly, we use $c = 3-c'$, $a = 1-a'$, and $b = 1-b'$ in Eq. (C.16b) and then $\gamma = 1-c'$, $a = -a'$, $b = -b'$ in Eqs. (C.16d) to show that

$$\begin{aligned}
&\frac{(a'+1-c')(b'+1-c')}{a'(2-c')}\,z\,(1-z)^{1+a'+b'-c'}\,{}_2F_1(a'+2-c',b'+2-c';3-c';z)\\
&=\frac{(a'+1-c')(b'+1-c')}{a'(2-c')}\,z\,{}_2F_1(1-a',1-b';3-c';z)\\
&=\frac{(1-c')}{a'}\,\frac{(a'+1-c')(b'+1-c')}{a'b'}\,\left[{}_2F_1(-a',-b';1-c';z)-{}_2F_1(-a',-b';2-c';z)\right].
\end{aligned} \tag{C.22}$$

We further notice that, for $a = -b$, from (C.16a) it follows that

$${}_2F_1(-a,-b;c;z) = {}_2F_1(a,b;c;z) \quad \text{when } a=-b. \tag{C.23}$$

The sum of the last two terms in the second and third lines on the right-hand side of Eq. (C.19) is proportional to the sum of Eqs. (C.21) and (C.22). By using $a = -b$ and, therefore, Eq. (C.23), we observe that the coefficient multiplying ${}_2F_1(a,b;1-c;z)$ is related to the following sum,

$$\begin{aligned}
&\frac{(1-c)}{a}\,\left[-\frac{1-c}{ab}(1-c+a+b)+\frac{(a+1-c)(b+1-c)}{ab}\right]\\
&=\frac{(1-c)}{a}\,\left[\frac{(1-c)^2-[(1-c+a)(1-c-a)]}{a^2}\right]=\frac{(1-c)}{a},
\end{aligned} \tag{C.24}$$

whereas the coefficient multiplying ${}_2F_1(a,b;2-c;z)$ is 0, such that

$$\begin{aligned}
&(1-z)^{1-c}\left[\frac{1-c}{a}\,{}_2F_1(a+1-c,b+1-c;2-c;z)\right.\\
&\quad\left.+\frac{(a+1-c)(b+1-c)}{a(2-c)}\,z\,{}_2F_1(a+2-c,b+2-c;3-c;z)\right]\\
&=\frac{1-c}{a}\,{}_2F_1(a,b;1-c;z).
\end{aligned} \tag{C.25}$$

In conclusion,

$$\bar{\varrho}_{13} = -\mathrm{i}\,\mathrm{e}^{2\gamma\left(c-\frac{1}{2}\right)(t_0-T_0)}\left[B_1\,\frac{b}{c}\,z^c\,{}_2F_1(a+c,b+c;1+c;z)+B_2\,\frac{1-c}{a}\,{}_2F_1(a,b;1-c;z)\right], \tag{C.26}$$

whereby a general relationship among the coefficients B_is is obtained:

$$\begin{aligned} B_3 &= -\mathrm{i}\,\mathrm{e}^{2\gamma\left(c-\frac{1}{2}\right)(t_0-T_0)}\,B_2\,\frac{1-c}{a},\\ B_4 &= -\mathrm{i}\,\mathrm{e}^{2\gamma\left(c-\frac{1}{2}\right)(t_0-T_0)}\,B_1\,\frac{b}{c}. \end{aligned} \tag{C.27}$$

Owing to Eq. (C.14) and to the fact that $c \neq 1$, $c \neq 0$, one finds from Eq. (C.9) that

$$B_1 = \bar{\varrho}_{12}(z=0) = \bar{\varrho}_{12,\mathrm{in}}, \tag{C.28a}$$

$$B_3 = \bar{\varrho}_{13}(z=0) = \bar{\varrho}_{13,\mathrm{in}}, \tag{C.28b}$$

$$B_2 = \mathrm{i}\frac{a}{1-c}\,\mathrm{e}^{2\gamma\left(\frac{1}{2}-c\right)(t_0-T_0)}\,\bar{\varrho}_{13,\mathrm{in}}, \tag{C.28c}$$

$$B_4 = \mathrm{i}\frac{a}{c}\,\mathrm{e}^{2\gamma\left(c-\frac{1}{2}\right)(t_0-T_0)}\,\bar{\varrho}_{12,\mathrm{in}}. \tag{C.28d}$$

By further using Eq. (C.20) to obtain

$$z^c\,{}_2F_1(a+c,-a+c;1+c;z) = z^c(1-z)^{1-c}\,{}_2F_1(1-a,1+a;1+c;z), \tag{C.29a}$$

$$z^{1-c}\,{}_2F_1(a+1-c,-a+1-c;2-c;z) = z^{1-c}(1-z)^c\,{}_2F_1(1-a,1+a;2-c;z), \tag{C.29b}$$

one can employ the just found relations to go from Eq. (C.9) to

$$\begin{aligned} \bar{\varrho}_{12}(z) = {}& \bar{\varrho}_{12,\mathrm{in}}\,{}_2F_1(a,-a;c;z)\\ &+\mathrm{i}\,\bar{\varrho}_{13,\mathrm{in}}\,\frac{a}{1-c}\,\mathrm{e}^{2\gamma\left(\frac{1}{2}-c\right)(t_0-T_0)}\,z^{1-c}\,(1-z)^c\,{}_2F_1(1-a,1+a;2-c;z), \end{aligned} \tag{C.30a}$$

$$\begin{aligned} \bar{\varrho}_{13}(z) = {}& \bar{\varrho}_{13,\mathrm{in}}\,{}_2F_1(a,-a;1-c;z)\\ &+\mathrm{i}\,\bar{\varrho}_{12,\mathrm{in}}\,\frac{a}{c}\,\mathrm{e}^{2\gamma\left(c-\frac{1}{2}\right)(t_0-T_0)}\,z^{c}\,(1-z)^{1-c}\,{}_2F_1(1-a,1+a;1+c;z). \end{aligned} \tag{C.30b}$$

Notice that the hypergeometric functions in (C.30), because of the divergence of ${}_2F_1\,(\alpha,\beta;\gamma;z)$ for $z=1$ if $\mathbf{Re}(\alpha+\beta-\gamma)>0$, do diverge at $z=1$, unless $a \in \mathbb{N}_0$. The function $\bar{\varrho}_{12}(t)$ $[\bar{\varrho}_{13}(t)]$ remains, nonetheless, finite because of the presence of the factor $(1-z)^c$ $[(1-z)^{1-c}]$. When $a \in \mathbb{N}_0$, however, the hypergeometric function is a finite polynomial in z and the factor $(1-z)^c$ $[(1-z)^{1-c}]$ is responsible not only for making $\bar{\varrho}_{12}(t)$ $[\bar{\varrho}_{13}(t)]$ finite, but to make it actually vanish. In this case, i.e., for those parameters a and c which render the hypergeometric function ${}_2F_1\,(\alpha,\beta;\gamma;z)$ a finite polynomial, it is useful to exploit the following identities:

$$\begin{aligned} z^{1-c}(1-z)^c &= \left\{\frac{1+\tanh\left[\gamma(t-t_0)\right]}{1-\tanh\left[\gamma(t-t_0)\right]}\right\}^{\frac{1}{2}-c}\sqrt{\frac{1-\tanh^2\left[\gamma(t-t_0)\right]}{4}}\\ &= \frac{1}{2}\,\mathrm{sech}[\gamma(t-t_0)]\,\mathrm{e}^{2\gamma\left(\frac{1}{2}-c\right)(t-t_0)}, \end{aligned} \tag{C.31a}$$

$$z^c(1-z)^{1-c} = \left\{\frac{1+\tanh\left[\gamma(t-t_0)\right]}{1-\tanh\left[\gamma(t-t_0)\right]}\right\}^{c-\frac{1}{2}} \sqrt{\frac{1-\tanh^2\left[\gamma(t-t_0)\right]}{4}} = \frac{1}{2}\,\mathrm{sech}[\gamma(t-t_0)]\,\mathrm{e}^{2\gamma(c-\frac{1}{2})(t-t_0)}, \tag{C.31b}$$

in order to write

$$\bar{\varrho}_{12}(z) = \bar{\varrho}_{12,\mathrm{in}}\,{}_2F_1(a,-a;c;z) + \mathrm{i}\,\bar{\varrho}_{13,\mathrm{in}}\,\frac{a}{2(1-c)}\,\mathrm{sech}[\gamma(t-t_0)]\,\mathrm{e}^{2\gamma(\frac{1}{2}-c)(t-T_0)}\,{}_2F_1(1-a,1+a;2-c;z), \tag{C.32a}$$

$$\bar{\varrho}_{13}(z) = \bar{\varrho}_{13,\mathrm{in}}\,{}_2F_1(a,-a;1-c;z) + \mathrm{i}\,\bar{\varrho}_{12,\mathrm{in}}\,\frac{a}{2c}\,\mathrm{sech}[\gamma(t-t_0)]\,\mathrm{e}^{2\gamma(c-\frac{1}{2})(t-T_0)}\,{}_2F_1(1-a,1+a;1+c;z). \tag{C.32b}$$

C.2 Particular solution

By assuming that $a=\frac{n}{2}$, and $c=\frac{1}{2}$, the solution (C.30) reads

$$\bar{\varrho}_{12}(t) = \mathrm{e}^{\mathrm{i}\Delta_{\mathrm{X}}(t-T_0)}\left[\bar{\varrho}_{12,\mathrm{in}}\,{}_2F_1\left(\tfrac{n}{2},-\tfrac{n}{2};\tfrac{1}{2};z(t)\right) + \mathrm{i}\,\bar{\varrho}_{13,\mathrm{in}}\,n\,\sqrt{z(t)\,(1-z(t))}\,{}_2F_1\left(1-\tfrac{n}{2},1+\tfrac{n}{2};\tfrac{3}{2};z(t)\right)\right], \tag{C.33a}$$

$$\bar{\varrho}_{13}(t) = \mathrm{e}^{\mathrm{i}\Delta_{\mathrm{X}}(t-T_0)}\left[\bar{\varrho}_{13,\mathrm{in}}\,{}_2F_1\left(\tfrac{n}{2},-\tfrac{n}{2};\tfrac{1}{2};z(t)\right) + \mathrm{i}\,n\,\bar{\varrho}_{12,\mathrm{in}}\,\sqrt{z(t)\,(1-z(t))}\,{}_2F_1(1-\tfrac{n}{2},1+\tfrac{n}{2};\tfrac{3}{2};z(t))\right]. \tag{C.33b}$$

We use the relations

$${}_2F_1\left(1-\tfrac{n}{2},1+\tfrac{n}{2};\tfrac{3}{2};z\right) = \frac{\sin(n\arcsin\sqrt{z})}{n\sqrt{z(1-z)}}, \tag{C.34a}$$

$${}_2F_1\left(\tfrac{n}{2},-\tfrac{n}{2};\tfrac{1}{2};z\right) = \cos(n\arcsin\sqrt{z}), \tag{C.34b}$$

$$\arcsin\sqrt{z} = \arccos\sqrt{1-z} = \frac{\arccos\left(1-2z\right)}{2} = \frac{\arccos\left\{-\tanh\left[\gamma(t-t_0)\right]\right\}}{2}, \tag{C.34c}$$

to find

$$\bar{\varrho}_{12}(t) = \mathrm{e}^{\mathrm{i}\Delta_{\mathrm{X}}(t-T_0)}\left[\bar{\varrho}_{12,\mathrm{in}}\cos\left(\tfrac{n}{2}\,\arccos\left\{-\tanh\left[\gamma(t-t_0)\right]\right\}\right) + \mathrm{i}\,\bar{\varrho}_{13,\mathrm{in}}\,\sin\left(\tfrac{n}{2}\,\arccos\left\{-\tanh\left[\gamma(t-t_0)\right]\right\}\right)\right], \tag{C.35a}$$

$$\bar{\varrho}_{13}(t) = \mathrm{e}^{\mathrm{i}\Delta_{\mathrm{X}}(t-T_0)}\left[\bar{\varrho}_{13,\mathrm{in}}\cos\left(\tfrac{n}{2}\,\arccos\left\{-\tanh\left[\gamma(t-t_0)\right]\right\}\right) + \mathrm{i}\,\bar{\varrho}_{12,\mathrm{in}}\,\sin\left(\tfrac{n}{2}\,\arccos\left\{-\tanh\left[\gamma(t-t_0)\right]\right\}\right)\right], \tag{C.35b}$$

i.e., the general solution can be written in terms of Chebyshev polynomials.

C.3 Fourier transforms for the calculation of the absorption spectrum

In the present Section we provide the details for the calculation of the Fourier transforms of the two functions

$$f_1(z) = {}_2F_1(a,-a;c;z) - 1, \tag{C.36a}$$

$$f_2(z) = z^{1-c}\,(1-z)^c\,{}_2F_1(1-a, 1+a; 2-c; z). \tag{C.36b}$$

We notice that the two functions $f_i(z(t))$ depend on time via $z(t)$ [Eq. (C.3)]. By observing that

$$z(t) = \frac{\tanh\left(\gamma(t-t_0)+1\right)}{2} \quad \Rightarrow \quad t(z) = t_0 + \frac{1}{2\gamma}\log\frac{z}{1-z} \qquad \frac{\partial t}{\partial z} = \frac{1}{2\gamma}\,\frac{1}{z(1-z)}, \tag{C.37}$$

we write

$$F_i(\varpi) = \int_{-\infty}^{\infty} f_i(z(t))\,\mathrm{e}^{-\mathrm{i}\varpi(t-T_0)}\,\mathrm{d}t = \frac{\mathrm{e}^{-\mathrm{i}\varpi(t_0-T_0)}}{2\gamma}\int_0^1 f_i(z)\,\frac{z^{-\mathrm{i}\frac{\varpi}{2\gamma}-1}}{(1-z)^{-\mathrm{i}\frac{\varpi}{2\gamma}+1}}\,\mathrm{d}z. \tag{C.38}$$

Furthermore [216],

$$\int_0^1 {}_2F_1(\alpha,\beta;\gamma;z)\,\frac{z^{\rho-1}}{(1-z)^{1-\sigma}}\,\mathrm{d}z = \frac{\Gamma(\rho)\,\Gamma(\sigma)}{\Gamma(\rho+\sigma)}\,{}_3F_2\left(\alpha,\beta,\rho;\gamma,\rho+\sigma;1\right) \tag{C.39}$$

for $\mathbf{Re}(\rho) > 0$, $\mathbf{Re}(\sigma) > 0$, and $\mathbf{Re}(\gamma+\sigma-\alpha-\beta) > 0$, where ${}_3F_2\left(a_1,a_2,a_3;b_1,b_2;z\right)$ is the generalized hypergeometric function [216–218]

$${}_3F_2(a_1,a_2,a_3;b_1,b_2;z) = \sum_{n=0}^{\infty}\frac{(a_1)_n(a_2)_n(a_3)_n}{(b_1)_n(b_2)_n}\,\frac{z^n}{n!}. \tag{C.40}$$

${}_3F_2(a_1,a_2,a_3;b_1,b_2;z)$ has convergence properties similar to those described for ${}_2F_1(a,b;c;z)$, namely, if at least one of the as is a nonpositive integer, $a_i = -m$, $m = 0, 1, 2, \ldots$, then the series terminates. If one of the bs is a nonpositive integer, $b_i = -l$, $l = 0, 1, 2, \ldots$, the series is indeterminate if none of the as is a negative integer $-m$, with $m < l$. For all other cases the convergence of the series is guaranteed for all z such that $|z| < 1$. For $|z| = 1$, the series (i) converges if $\mathbf{Re}(a_1+a_2+a_3-b_1-b_2) < 0$, (ii) converges conditionally for $z \neq 1$ and $0 \leq \mathbf{Re}(a_1+a_2+a_3-b_1-b_2) < 1$, and (iii) diverges if $1 \leq \mathbf{Re}(a_1+a_2+a_3-b_1-b_2)$. The condition $\mathbf{Re}(\gamma+\sigma-\alpha-\beta) > 0$, therefore, guarantees the convergence of ${}_3F_2\left(\alpha,\beta,\rho;\gamma,\rho+\sigma;1\right)$.

In order to calculate $F_1(\varpi)$, we observe from Eq. (C.16c) that

$$\frac{\partial f_1(z)}{\partial z} = -\frac{a^2}{c}\,{}_2F_1(1+a,1-a;1+c,z)$$

and that

$$\frac{\partial}{\partial z}\frac{z^{\phi}}{(1-z)^{\phi}} = \phi\frac{z^{\phi-1}}{(1-z)^{1+\phi}}.$$

For $-1 < \mathbf{Re}\phi < 1$, by using an integration by parts, we can write

$$\int_0^1 f_1(z)\frac{z^{\phi-1}}{(1-z)^{1+\phi}}\,\mathrm{d}z = \int_0^1 \frac{a^2}{c}\,{}_2F_1(1+a,1-a;1+c,z)\frac{z^{\phi}}{\phi\,(1-z)^{\phi}}\,\mathrm{d}z, \tag{C.41}$$

which, since the conditions for the application of Eq. (C.39) are fulfilled, brings to the result

$$\int_0^1 f_1(z)\,\frac{z^{\phi-1}}{(1-z)^{1+\phi}}\,\mathrm{d}z = \frac{a^2}{c}\,\frac{\Gamma(1+\phi)\,\Gamma(1-\phi)}{\phi\,\Gamma(2)}\,{}_3F_2\left(1+a,1-a,1+\phi;1+c,2;1\right). \tag{C.42}$$

By applying this result with $\phi = -\mathrm{i}\frac{\varpi}{2\gamma}$ and observing that [216]

$$\Gamma\left(1+\mathrm{i}x\right)\,\Gamma\left(1-\mathrm{i}x\right) = \pi\,x\,\mathrm{csch}(\pi x), \tag{C.43}$$

we obtain that

$$F_1(\varpi) = \frac{\mathrm{e}^{-\mathrm{i}\varpi(t_0-T_0)}}{2\gamma}\,\frac{a^2}{c}\,\mathrm{i}\,\pi\,\operatorname{csch}\!\left(\tfrac{\pi\varpi}{2\gamma}\right)\,{}_3F_2\left(1+a,1-a,1-\mathrm{i}\tfrac{\varpi}{2\gamma};1+c,2;1\right). \tag{C.44}$$

The hypergeometric function ${}_3F_2\left(1+a,1-a,1-\mathrm{i}\frac{\varpi}{2\gamma};1+c,2;1\right)$ is finite, since the condition of convergence at $z=1$, namely, $\mathbf{Re}\left(-\mathrm{i}\frac{\varpi}{2\gamma}-c\right)>0$, is satisfied. The hyperbolic cosecant function, however, diverges at $\varpi=0$. This divergence is here avoided because of the imaginary part of ϖ, guaranteeing that, for any ω, the condition $\varpi=0$ is never met. If Γ_2 was equal to 0, then the function $f_1(t)$, after the excitation due to the pulse, would reach a stationary value, which would produce a Dirac delta contribution in its Fourier transform, related to the just discussed divergence of the hyperbolic cosecant in $F_1(\varpi)$.

The calculation of $F_2(\varpi)$ is a direct consequence of Eq. (C.39). Using the fact that [216]

$$\Gamma\left(\tfrac{1}{2}+\mathrm{i}x\right)\,\Gamma\left(\tfrac{1}{2}-\mathrm{i}\,x\right)=\pi\,\operatorname{sech}(\pi\,x), \tag{C.45}$$

we find

$$\begin{aligned}
F_2(\varpi) &= \frac{\mathrm{e}^{-\mathrm{i}\varpi(t_0-T_0)}}{2\gamma}\int_0^1 {}_2F_1(1-a,1+a;2-c;z(t))\,\frac{z^{-\mathrm{i}\frac{\varpi}{2\gamma}+1-c-1}}{(1-z)^{1-\mathrm{i}\frac{\varpi}{2\gamma}-c}}\,\mathrm{d}z\\
&= \frac{\mathrm{e}^{-\mathrm{i}\varpi(t_0-T_0)}}{2\gamma}\,\Gamma\left(-\mathrm{i}\tfrac{\varpi}{2\gamma}+1-c\right)\,\Gamma\left(\mathrm{i}\tfrac{\varpi}{2\gamma}+c\right)\,{}_3F_2\left(1-a,1+a,-\mathrm{i}\,\tfrac{\varpi}{2\gamma}+1-c;2-c,1;1\right)\\
&= \frac{\mathrm{e}^{-\mathrm{i}\varpi(t_0-T_0)}}{2\gamma}\,\pi\,\operatorname{sech}\left(\tfrac{\pi\varpi}{2\gamma}+\mathrm{i}\,\pi\,\left(\tfrac{1}{2}-c\right)\right)\,{}_3F_2\left(1-a,1+a,-\mathrm{i}\tfrac{\varpi}{2\gamma}+1-c;2-c,1;1\right).
\end{aligned} \tag{C.46}$$

The integral in z in the previous equation can be solved with Eq. (C.39) because ϖ has a negative complex part $-\mathrm{i}\frac{\Gamma_2}{2}$ which is due to the exponential decay in (6.19). As a result, the series which defines the generalized hypergeometric function ${}_3F_2\left(1-a,1+a,-\mathrm{i}\frac{\varpi}{2\gamma}+1-c;2-c,1;1\right)$ converges, since $\mathbf{Re}(1-a+1+a-\mathrm{i}\frac{\varpi}{2\gamma}+1-c-(2-c+1))=\mathbf{Re}(-\mathrm{i}\frac{\varpi}{2\gamma})=\mathbf{Im}(\frac{\varpi}{2\gamma})<0$.

If such an exponential decay was not present, then the Fourier transform (C.46) would generally diverge, unless $a=1+m$, $m=0,\,1,\,2,\ldots$. From Eq.(6.36b), these are the only values for which $\lim_{t\to\infty}\varrho_{12}(t)=0$, i.e., for which, even without the exponential decay included in the imaginary part of ϖ, the function would have finite support and the Fourier transform would be well defined. In all other cases, if the exponential decay of $\varrho_{12}(t)$ is not present, then the nonzero limit that $\varrho_{12}(t)$ reaches at $t\to\infty$ implies the presence of a Dirac-delta contribution in the Fourier transform, i.e., the divergence of Eq. (C.46).

Bibliography

[1] P. W. Milonni and J. H. Eberly, *Laser Physics* (Wiley, New York, 2010).

[2] A. Einstein, "Zur Quantentheorie der Strahlung," Z. Phys. **18**, 121 (1917).

[3] A. L. Schawlow and C. H. Townes, "Infrared and optical masers," Phys. Rev. **112**, 1940–1949 (1958).

[4] T. H. Maiman, "Stimulated optical radiation in ruby," Nature **187**, 493–494 (1960).

[5] P. A. M. Dirac, "The quantum theory of the emission and absorption of radiation," Proceedings of the Royal Society of London. Series A, Containing Papers of a Mathematical and Physical Character **114**, pp. 243–265 (1927).

[6] E. Fermi, "Quantum theory of radiation," Rev. Mod. Phys. **4**, 87–132 (1932).

[7] R. Loudon, *The Quantum Theory of Light* (Oxford University Press, Oxford, 2000).

[8] R. J. Glauber, "The quantum theory of optical coherence," Phys. Rev. **130**, 2529–2539 (1963).

[9] M. Schubert and B. Wilhelmi, *Nonlinear optics and quantum electronics* (Wiley, 1986).

[10] S. Chu, "Nobel lecture: The manipulation of neutral particles," Rev. Mod. Phys. **70**, 685–706 (1998).

[11] C. N. Cohen-Tannoudji, "Nobel lecture: Manipulating atoms with photons," Rev. Mod. Phys. **70**, 707–719 (1998).

[12] W. D. Phillips, "Nobel lecture: Laser cooling and trapping of neutral atoms," Rev. Mod. Phys. **70**, 721–741 (1998).

[13] M. H. Anderson, J. R. Ensher, M. R. Matthews, C. E. Wieman, and E. A. Cornell, "Observation of bose-einstein condensation in a dilute atomic vapor," Science **269**, 198–201 (1995).

[14] K. B. Davis, M. O. Mewes, M. R. Andrews, N. J. van Druten, D. S. Durfee, D. M. Kurn, and W. Ketterle, "Bose-einstein condensation in a gas of sodium atoms," Phys. Rev. Lett. **75**, 3969–3973 (1995).

[15] S. N. Bose, "Plancks Gesetz und Lichtquantenhypothese," Z. Phys. **26**, 178 (1924).

[16] A. Einstein, "Quantentheorie des einatomigen idealen Gases," Sitzungsberichte der Preuß. Akad. d. Wiss., phys.-math. Klasse **1**, 261 (1924).

[17] A. Einstein, "Quantentheorie des einatomigen idealen Gases. 2. Abhandlung," Sitzungsberichte der Preuß. Akad. d. Wiss., phys.-math. Klasse **1**, 3 (1925).

[18] R. Feynman, "Simulating physics with computers," Int. J. Theor. Phys. **21**, 437 (1982).

[19] J. I. Cirac and P. Zoller, "New frontiers in quantum information with atoms and ions," Physics Today **57**, 38–44 (2004).

[20] F. Krausz and M. Ivanov, "Attosecond physics," Rev. Mod. Phys. **81**, 163–234 (2009).

[21] N. Bloembergen, "Nonlinear optics and spectroscopy," Science **216**, 1057–1064 (1982).

[22] "`http://physics.nist.gov/cuu/Units/current.html`," .

[23] T. Udem, R. Holzwarth, and T. W. Hänsch, "Optical frequency metrology," Nature **416**, 233–237 (2002).

[24] S. T. Cundiff and J. Ye, "*Colloquium* : Femtosecond optical frequency combs," Rev. Mod. Phys. **75**, 325–342 (2003).

[25] J. L. Hall, "Nobel lecture: Defining and measuring optical frequencies," Rev. Mod. Phys. **78**, 1279–1295 (2006).

[26] T. W. Hänsch, "Nobel lecture: Passion for precision," Rev. Mod. Phys. **78**, 1297–1309 (2006).

[27] J. N. Eckstein, A. I. Ferguson, and T. W. Hänsch, "High-resolution two-photon spectroscopy with picosecond light pulses," Phys. Rev. Lett. **40**, 847–850 (1978).

[28] T. Udem, J. Reichert, R. Holzwarth, and T. W. Hänsch, "Accurate measurement of large optical frequency differences with a mode-locked laser," Opt. Lett. **24**, 881–883 (1999).

[29] J. Reichert, R. Holzwarth, T. Udem, and T. W. Hänsch, "Measuring the frequency of light with mode-locked lasers," Opt. Commun. **172**, 59 – 68 (1999).

[30] M. Kourogi, K. Nakagawa, and M. Ohtsu, "Wide-span optical frequency comb generator for accurate optical frequency difference measurement," Quantum Electronics, IEEE Journal of **29**, 2693–2701 (1993).

[31] J. Ye, L.-S. Ma, T. Daly, and J. L. Hall, "Highly selective terahertz optical frequency comb generator," Opt. Lett. **22**, 301–303 (1997).

[32] T. Udem, J. Reichert, R. Holzwarth, and T. W. Hänsch, "Absolute optical frequency measurement of the cesium D_1 line with a mode-locked laser," Phys. Rev. Lett. **82**, 3568–3571 (1999).

[33] J. Reichert, M. Niering, R. Holzwarth, M. Weitz, T. Udem, and T. W. Hänsch, "Phase coherent vacuum-ultraviolet to radio frequency comparison with a mode-locked laser," Phys. Rev. Lett. **84**, 3232–3235 (2000).

[34] S. A. Diddams, D. J. Jones, J. Ye, S. T. Cundiff, J. L. Hall, J. K. Ranka, R. S. Windeler, R. Holzwarth, T. Udem, and T. W. Hänsch, "Direct link between microwave and optical frequencies with a 300 THz femtosecond laser comb," Phys. Rev. Lett. **84**, 5102–5105 (2000).

[35] D. J. Jones, S. A. Diddams, J. K. Ranka, A. Stentz, R. S. Windeler, J. L. Hall, and S. T. Cundiff, "Carrier-envelope phase control of femtosecond mode-locked lasers and direct optical frequency synthesis," Science **288**, 635–639 (2000).

[36] M. Niering, R. Holzwarth, J. Reichert, P. Pokasov, T. Udem, M. Weitz, T. W. Hänsch, P. Lemonde, G. Santarelli, M. Abgrall, P. Laurent, C. Salomon, and A. Clairon, "Measurement of the hydrogen $1S$- $2S$ transition frequency by phase coherent comparison with a microwave cesium fountain clock," Phys. Rev. Lett. **84**, 5496–5499 (2000).

[37] R. Holzwarth, T. Udem, T. W. Hänsch, J. C. Knight, W. J. Wadsworth, and P. S. J. Russell, "Optical frequency synthesizer for precision spectroscopy," Phys. Rev. Lett. **85**, 2264–2267 (2000).

[38] L.-S. Ma, Z. Bi, A. Bartels, L. Robertsson, M. Zucco, R. S. Windeler, G. Wilpers, C. Oates, L. Hollberg, and S. A. Diddams, "Optical frequency synthesis and comparison with uncertainty at the 10^{-19} level," Science **303**, 1843–1845 (2004).

[39] C. Orzel, "Searching for new physics through atomic, molecular and optical precision measurements," Physica Scripta **86**, 068101 (2012).

[40] S. A. Diddams, T. Udem, J. C. Bergquist, E. A. Curtis, R. E. Drullinger, L. Hollberg, W. M. Itano, W. D. Lee, C. W. Oates, K. R. Vogel, and D. J. Wineland, "An optical clock based on a single trapped $^{199}Hg^{+}$ ion," Science **293**, 825–828 (2001).

[41] J. Ye, H. J. Kimble, and H. Katori, "Quantum state engineering and precision metrology using state-insensitive light traps," Science **320**, 1734–1738 (2008).

[42] C.-H. Li, A. J. Benedick, P. Fendel, A. G. Glenday, F. X. Kartner, D. F. Phillips, D. Sasselov, A. Szentgyorgyi, and R. L. Walsworth, "A laser frequency comb that enables radial velocity measurements with a precision of 1[thinsp]cm[thinsp]s-1," Nature **452**, 610–612 (2008).

[43] T. Steinmetz, T. Wilken, C. Araujo-Hauck, R. Holzwarth, T. W. Hänsch, L. Pasquini, A. Manescau, S. D'Odorico, M. T. Murphy, T. Kentischer, W. Schmidt, and T. Udem, "Laser frequency combs for astronomical observations," Science **321**, 1335–1337 (2008).

[44] M. T. Murphy, T. Udem, R. Holzwarth, A. Sizmann, L. Pasquini, C. Araujo-Hauck, H. Dekker, S. D'Odorico, M. Fischer, T. W. Hänsch, and A. Manescau, "High-precision wavelength calibration of astronomical spectrographs with laser frequency combs," Monthly Notices of the Royal Astronomical Society **380**, 839–847 (2007).

[45] M. C. Stowe, F. C. Cruz, A. Marian, and J. Ye, "High resolution atomic coherent control via spectral phase manipulation of an optical frequency comb," Phys. Rev. Lett. **96**, 153001 (2006).

[46] M. C. Stowe, A. Pe'er, and J. Ye, "Control of four-level quantum coherence via discrete spectral shaping of an optical frequency comb," Phys. Rev. Lett. **100**, 203001 (2008).

[47] A. Pe'er, E. A. Shapiro, M. C. Stowe, M. Shapiro, and J. Ye, "Precise control of molecular dynamics with a femtosecond frequency comb," Phys. Rev. Lett. **98**, 113004 (2007).

[48] M. Lewenstein, P. Balcou, M. Y. Ivanov, A. L'Huillier, and P. B. Corkum, "Theory of high-harmonic generation by low-frequency laser fields," Phys. Rev. A **49**, 2117–2132 (1994).

[49] P. Del'Haye, A. Schliesser, O. Arcizet, T. Wilken, R. Holzwarth, and T. J. Kippenberg, "Optical frequency comb generation from a monolithic microresonator," Nature **450**, 1214–1217 (2007).

[50] A. Baltuška, T. Udem, M. Uiberacker, M. Hentschel, E. Goulielmakis, C. Gohle, R. Holzwarth, V. S. Yakovlev, A. Scrinzi, T. W. Hänsch, and F. Krausz, "Attosecond control of electronic processes by intense light fields," Nature **421**, 611–615 (2003).

[51] P. L. Knight and P. W. Milonni, "The Rabi frequency in optical spectra," Physics Reports **66**, 21 – 107 (1980).

[52] R. Loudon, "Non-classical effects in the statistical properties of light," Rep. Prog. Phys. **43**, 913 (1980).

[53] M. O. Scully and S. Zubairy, *Quantum Optics* (Cambridge University Press, Cambridge, 1997).

[54] P. Meystre and M. Sargent III, *Elements of Quantum Optics* (Springer, Berlin Heidelberg, New York, 2007).

[55] B. R. Mollow, "Power spectrum of light scattered by two-level systems," Phys. Rev. **188**, 1969–1975 (1969).

[56] B. R. Mollow, "Pure-state analysis of resonant light scattering: Radiative damping, saturation, and multiphoton effects," Phys. Rev. A **12**, 1919–1943 (1975).

[57] L. M. Narducci, M. O. Scully, G.-L. Oppo, P. Ru, and J. R. Tredicce, "Spontaneous emission and absorption properties of a driven three-level system," Phys. Rev. A **42**, 1630–1649 (1990).

[58] A. S. Manka, H. M. Doss, L. M. Narducci, P. Ru, and G.-L. Oppo, "Spontaneous emission and absorption properties of a driven three-level system. II. The Λ and cascade models," Phys. Rev. A **43**, 3748–3763 (1991).

[59] G. S. Agarwal, S. L. Haan, and J. Cooper, "Radiative decay of autoionizing states in laser fields. I. General theory," Phys. Rev. A **29**, 2552–2564 (1984).

[60] G. S. Agarwal, S. L. Haan, and J. Cooper, "Radiative decay of autoionizing states in laser fields. II. Photoemission spectra," Phys. Rev. A **29**, 2565–2577 (1984).

[61] H. J. Carmichael and D. F. Walls, "A quantum-mechanical master equation treatment of the dynamical Stark effect," J. Phys. B **9**, 1199 (1976).

[62] H. J. Kimble and L. Mandel, "Theory of resonance fluorescence," Phys. Rev. A **13**, 2123–2144 (1976).

[63] H. J. Kimble and L. Mandel, "Resonance fluorescence with excitation of finite bandwidth," Phys. Rev. A **15**, 689–699 (1977).

[64] F. Schuda, C. R. Stroud Jr, and M. Hercher, "Observation of the resonant Stark effect at optical frequencies," J. Phys. B **7**, L198 (1974).

[65] F. Y. Wu, R. E. Grove, and S. Ezekiel, "Investigation of the spectrum of resonance fluorescence induced by a monochromatic field," Phys. Rev. Lett. **35**, 1426–1429 (1975).

[66] R. E. Grove, F. Y. Wu, and S. Ezekiel, "Measurement of the spectrum of resonance fluorescence from a two-level atom in an intense monochromatic field," Phys. Rev. A **15**, 227–233 (1977).

[67] C. Cohen-Tannoudji and S. Reynaud, "Dressed-atom description of resonance fluorescence and absorption spectra of a multi-level atom in an intense laser beam," J. Phys. B **10**, 345 (1977).

[68] N. Rosen and C. Zener, "Double Stern-Gerlach experiment and related collision phenomena," Phys. Rev. **40**, 502–507 (1932).

[69] R. T. Robiscoe, "Extension of the Rosen-Zener solution to the two-level problem," Phys. Rev. A **17**, 247–260 (1978).

[70] A. Bambini and P. R. Berman, "Analytic solutions to the two-state problem for a class of coupling potentials," Phys. Rev. A **23**, 2496–2501 (1981).

[71] K. Rzążewski and M. Florjańczyk, "The resonance fluorescence of a two-level system driven by a smooth pulse," J. Phys. B **17**, L509 (1984).

[72] M. Florjaczyk, K. Rzążewski, and J. Zakrzewski, "Resonance scattering of a short laser pulse on a two-level system: Time-dependent approach," Phys. Rev. A **31**, 1558–1562 (1985).

[73] M. Lewenstein, J. Zakrzewski, and K. Rzążewski, "Theory of fluorescence spectra induced by short laser pulses," J. Opt. Soc. Am. B **3**, 22–35 (1986).

[74] T.-S. Ho and H. Rabitz, "Time-dependent resonant-fluorescence spectrum of two-level atoms in strong short-pulsed fields: A nonperturbative treatment," Phys. Rev. A **37**, 1576–1587 (1988).

[75] M. A. Newbold and G. J. Salamo, "Power spectrum of light scattered by a two-level atom in the presence of a pulse-train driving field," Phys. Rev. A **22**, 2098–2107 (1980).

[76] M. Wilkens and K. Rzążewski, "Resonance fluorescence of an arbitrarily driven two-level atom," Phys. Rev. A **40**, 3164–3178 (1989).

[77] Z. Ficek, J. Seke, A. V. Soldatov, and G. Adam, "Fluorescence spectrum of a two-level atom driven by a multiple modulated field," Phys. Rev. A **64**, 013813 (2001).

[78] E. J. Robinson, "Temporal 'diffraction' and eigenvalue interpretation of the resonance fluorescence spectrum of two-level systems driven by short pulses," J. Phys. B **19**, L657 (1986).

[79] B. R. Mollow, "Absorption and emission line-shape functions for driven atoms," Phys. Rev. A **5**, 1522–1527 (1972).

[80] B. R. Mollow, "Stimulated emission and absorption near resonance for driven systems," Phys. Rev. A **5**, 2217–2222 (1972).

[81] W. T. Pollard and R. A. Mathies, "Analysis of femtosecond dynamic absorption spectra of nonstationary states," Annual Review of Physical Chemistry **43**, 497–523 (1992). PMID: 1463575.

[82] E. Goulielmakis, Z.-H. Loh, A. Wirth, R. Santra, N. Rohringer, V. S. Yakovlev, S. Zherebtsov, T. Pfeifer, A. M. Azzeer, M. F. Kling, S. R. Leone, and F. Krausz, "Real-time observation of valence electron motion," Nature **466**, 739–743 (2010).

[83] M. Fleischhauer, A. Imamoglu, and J. P. Marangos, "Electromagnetically induced transparency: Optics in coherent media," Rev. Mod. Phys. **77**, 633–673 (2005).

[84] K. Bergmann, H. Theuer, and B. W. Shore, "Coherent population transfer among quantum states of atoms and molecules," Rev. Mod. Phys. **70**, 1003–1025 (1998).

[85] O. Kocharovskaya, "Amplification and lasing without inversion," Physics Reports **219**, 175 – 190 (1992).

[86] W. C. Röntgen, "Über eine neue Art von Strahlung," Aus den Sitzungberichten der Würzburger physik.-medic. Gesellschaft **1**, 137 (1985).

[87] J. Jackson, *Classical Electrodynamics* (Wiley, New York, 1998).

[88] J. Als-Nielsen and D. McMorrow, *Elements of modern x-ray physics* (John Wiley & Sons, New York, 2001).

[89] P. Emma, R. Akre, J. Arthur, R. Bionta, C. Bostedt, J. Bozek, A. Brachmann, P. Bucksbaum, R. Coffee, F.-J. Decker, Y. Ding, D. Dowell, S. Edstrom, A. Fisher, J. Frisch, S. Gilevich, J. Hastings, G. Hays, P. Hering, Z. Huang, R. Iverson, H. Loos, M. Messerschmidt, A. Miahnahri, S. Moeller, H.-D. Nuhn, G. Pile, D. Ratner, J. Rzepiela, D. Schultz, T. Smith, P. Stefan, H. Tompkins, J. Turner, J. Welch, W. White, J. Wu, G. Yocky, and J. Galayda, "First lasing and operation of an angstrom-wavelength free-electron laser," Nature Photonics **4**, 641 – 647 (2010).

[90] W. Ackermann, G. Asova, V. Ayvazyan, A. Azima, N. Baboi, J. Bähr, V. Balandin, B. Beutner, A. Brandt, A. Bolzmann, R. Brinkmann, O. I. Brovko, M. Castellano, P. Castro, L. Catani, E. Chiadroni, S. Choroba, A. Cianchi, J. T. Costello, D. Cubaynes, J. Dardis, W. Decking, H. Delsim-Hashemi, A. Delserieys, G. Di Pirro, M. Dohlus, S. Düsterer, A. Eckhardt, H. T. Edwards, B. Faatz, J. Feldhaus, K. Flöttmann, J. Frisch, L. Fröhlich, T. Garvey, U. Gensch, C. Gerth, M. Görler, N. Golubeva, H.-J. Grabosch, M. Grecki, O. Grimm, K. Hacker, U. Hahn, J. H. Han, K. Honkavaara, T. Hott, M. Hüning, Y. Ivanisenko, E. Jaeschke, W. Jalmuzna, T. Jezynski, R. Kammering, V. Katalev, K. Kavanagh, E. T. Kennedy, S. Khodyachykh, K. Klose, V. Kocharyan, M. Körfer, M. Kollewe, W. Koprek, S. Korepanov, D. Kostin, M. Krassilnikov, G. Kube, M. Kuhlmann, C. L. S. Lewis, L. Lilje, T. Limberg, D. Lipka, F. Löhl, H. Luna, M. Luong, M. Martins, M. Meyer, P. Michelato, V. Miltchev, W. D. Möller, L. Monaco, W. F. O. Müller, O. Napieralski, O. Napoly, P. Nicolosi, D. Nölle, T. Nuñez, A. Oppelt, C. Pagani, R. Paparella, N. Pchalek, J. Pedregosa-Gutierrez, B. Petersen, B. Petrosyan, G. Petrosyan, L. Petrosyan, J. Pflüger, E. Plönjes, L. Poletto, K. Pozniak, E. Prat, D. Proch, P. Pucyk, P. Radcliffe, H. Redlin, K. Rehlich, M. Richter, M. Roehrs, J. Roensch, R. Romaniuk, M. Ross, J. Rossbach, V. Rybnikov, M. Sachwitz, E. L. Saldin, W. Sandner, H. Schlarb, B. Schmidt, M. Schmitz, P. Schmüser, J. R. Schneider, E. A. Schneidmiller, S. Schnepp, S. Schreiber, M. Seidel, D. Sertore, A. V. Shabunov, C. Simon, S. Simrock, E. Sombrowski, A. A. Sorokin, P. Spanknebel, R. Spesyvtsev, L. Staykov, B. Steffen, F. Stephan, F. Stulle, H. Thom, K. Tiedtke, M. Tischer, S. Toleikis, R. Treusch, D. Trines, I. Tsakov, E. Vogel, T. Weiland, H. Weise, M. Wellhöfer, M. Wendt, I. Will, A. Winter, K. Wittenburg, W. Wurth, P. Yeates, M. V. Yurkov, I. Zagorodnov, and K. Zapfe, "Operation of a free-electron laser from the extreme ultraviolet to the water window," Nature Photonics **1**, 336–342 (2007).

[91] D. Pile, "X-rays: First light from SACLA," Nature Photonics **5**, 456–457 (2011).

[92] M. Altarelli, R. Brinkmann, M. Chergui, W. Decking, B. Dobson, S. Düsterer, G. Grübel, W. Graeff, H. Graafsma, J. Hajdu, J. Marangos, J. Pflüger, H. Redlin, D. Riley, I. Robinson, J. Rossbach, A. Schwarz, K. Tiedtke, T. Tschentscher, I. Vartaniants, H. Wabnitz, H. Weise, R. Wichmann, K. Witte, A. Wolf, M. Wulff, and M. Yurkov, "The European X-Ray Free-Electron Laser, Technical Design Report," Tech. rep., DESY, Hamburg, Germany (2006).

[93] J. N. Galayda, J. Arthur, D. F. Ratner, and W. E. White, "X-ray free-electron lasers—present and future capabilities [Invited]," J. Opt. Soc. Am. B **27**, B106–B118 (2010).

[94] R. Neutze, R. Wouts, D. van der Spoel, E. Weckert, and J. Hajdu, "Potential for biomolecular imaging with femtosecond x-ray pulses," Nature **406**, 752–757 (2000).

[95] H. N. Chapman, P. Fromme, A. Barty, T. A. White, R. A. Kirian, A. Aquila, M. S. Hunter, J. Schulz, D. P. DePonte, U. Weierstall, R. B. Doak, F. R. N. C. Maia, A. V. Martin, I. Schlichting, L. Lomb, N. Coppola, R. L. Shoeman, S. W. Epp, R. Hartmann, D. Rolles, A. Rudenko, L. Foucar, N. Kimmel, G. Weidenspointner, P. Holl, M. Liang, M. Barthelmess, C. Caleman, S. Boutet, M. J. Bogan, J. Krzywinski, C. Bostedt, S. Bajt, L. Gumprecht, B. Rudek, B. Erk, C. Schmidt, A. Homke, C. Reich, D. Pietschner, L. Struder, G. Hauser, H. Gorke, J. Ullrich, S. Herrmann, G. Schaller, F. Schopper, H. Soltau, K.-U. Kuhnel, M. Messerschmidt, J. D. Bozek, S. P. Hau-Riege, M. Frank, C. Y. Hampton, R. G. Sierra, D. Starodub, G. J. Williams, J. Hajdu, N. Timneanu, M. M. Seibert, J. Andreasson, A. Rocker, O. Jonsson, M. Svenda, S. Stern, K. Nass, R. Andritschke, C.-D. Schroter, F. Krasniqi, M. Bott, K. E. Schmidt, X. Wang, I. Grotjohann, J. M. Holton, T. R. M. Barends, R. Neutze, S. Marchesini, R. Fromme, S. Schorb, D. Rupp, M. Adolph, T. Gorkhover, I. Andersson, H. Hirsemann, G. Potdevin, H. Graafsma, B. Nilsson, and J. C. H. Spence, "Femtosecond x-ray protein nanocrystallography," Nature **470**, 73–77 (2011).

[96] M. M. Seibert, T. Ekeberg, F. R. N. C. Maia, M. Svenda, J. Andreasson, O. Jonsson, D. Odic, B. Iwan, A. Rocker, D. Westphal, M. Hantke, D. P. DePonte, A. Barty, J. Schulz, L. Gumprecht, N. Coppola, A. Aquila, M. Liang, T. A. White, A. Martin, C. Caleman, S. Stern, C. Abergel, V. Seltzer, J.-M. Claverie, C. Bostedt, J. D. Bozek, S. Boutet, A. A. Miahnahri, M. Messerschmidt, J. Krzywinski, G. Williams, K. O. Hodgson, M. J. Bogan, C. Y. Hampton, R. G. Sierra, D. Starodub, I. Andersson, S. Bajt, M. Barthelmess, J. C. H. Spence, P. Fromme, U. Weierstall, R. Kirian, M. Hunter, R. B. Doak, S. Marchesini, S. P. Hau-Riege, M. Frank, R. L. Shoeman, L. Lomb, S. W. Epp, R. Hartmann, D. Rolles, A. Rudenko, C. Schmidt, L. Foucar, N. Kimmel, P. Holl, B. Rudek, B. Erk, A. Homke, C. Reich, D. Pietschner, G. Weidenspointner, L. Struder, G. Hauser, H. Gorke, J. Ullrich, I. Schlichting, S. Herrmann, G. Schaller, F. Schopper, H. Soltau, K.-U. Kuhnel, R. Andritschke, C.-D. Schroter, F. Krasniqi, M. Bott, S. Schorb, D. Rupp, M. Adolph, T. Gorkhover, H. Hirsemann, G. Potdevin, H. Graafsma, B. Nilsson, H. N. Chapman, and J. Hajdu, "Single mimivirus particles intercepted and imaged with an x-ray laser," Nature **470**, 78–81 (2011).

[97] S. M. Vinko, O. Ciricosta, B. I. Cho, K. Engelhorn, H.-K. Chung, C. R. D. Brown, T. Burian, J. Chalupsky, R. W. Falcone, C. Graves, V. Hajkova, A. Higginbotham, L. Juha, J. Krzywinski, H. J. Lee, M. Messerschmidt, C. D. Murphy, Y. Ping, A. Scherz, W. Schlotter, S. Toleikis, J. J. Turner, L. Vysin, T. Wang, B. Wu, U. Zastrau, D. Zhu, R. W. Lee,

P. A. Heimann, B. Nagler, and J. S. Wark, "Creation and diagnosis of a solid-density plasma with an x-ray free-electron laser," Nature **482**, 59–62 (2012).

[98] L. Young, E. P. Kanter, B. Krässig, Y. Li, A. M. March, S. T. Pratt, R. Santra, S. H. Southworth, N. Rohringer, L. F. DiMauro, G. Doumy, C. A. Roedig, N. Berrah, L. Fang, M. Hoener, P. H. Bucksbaum, J. P. Cryan, S. Ghimire, J. M. Glownia, D. A. Reis, J. D. Bozek, C. Bostedt, and M. Messerschmidt, "Femtosecond electronic response of atoms to ultra-intense x-rays," Nature **466**, 56 (2010).

[99] G. Doumy, C. Roedig, S.-K. Son, C. I. Blaga, A. D. DiChiara, R. Santra, N. Berrah, C. Bostedt, J. D. Bozek, P. H. Bucksbaum, J. P. Cryan, L. Fang, S. Ghimire, J. M. Glownia, M. Hoener, E. P. Kanter, B. Krässig, M. Kuebel, M. Messerschmidt, G. G. Paulus, D. A. Reis, N. Rohringer, L. Young, P. Agostini, and L. F. DiMauro, "Nonlinear atomic response to intense ultrashort x rays," Phys. Rev. Lett. **106**, 083002 (2011).

[100] M. Hoener, L. Fang, O. Kornilov, O. Gessner, S. T. Pratt, M. Gühr, E. P. Kanter, C. Blaga, C. Bostedt, J. D. Bozek, P. H. Bucksbaum, C. Buth, M. Chen, R. Coffee, J. Cryan, L. DiMauro, M. Glownia, E. Hosler, E. Kukk, S. R. Leone, B. McFarland, M. Messerschmidt, B. Murphy, V. Petrovic, D. Rolles, and N. Berrah, "Ultraintense x-ray induced ionization, dissociation, and frustrated absorption in molecular nitrogen," Phys. Rev. Lett. **104**, 253002 (2010).

[101] C. Buth, J.-C. Liu, M. H. Chen, J. P. Cryan, L. Fang, J. M. Glownia, M. Hoener, R. N. Coffee, and N. Berrah, "Ultrafast absorption of intense x rays by nitrogen molecules," J. Chem. Phys. **136**, 214310 (2012).

[102] J. P. Cryan, J. M. Glownia, J. Andreasson, A. Belkacem, N. Berrah, C. I. Blaga, C. Bostedt, J. Bozek, C. Buth, L. F. DiMauro, L. Fang, O. Gessner, M. Guehr, J. Hajdu, M. P. Hertlein, M. Hoener, O. Kornilov, J. P. Marangos, A. M. March, B. K. McFarland, H. Merdji, V. S. Petrović, C. Raman, D. Ray, D. Reis, F. Tarantelli, M. Trigo, J. L. White, W. White, L. Young, P. H. Bucksbaum, and R. N. Coffee, "Auger electron angular distribution of double core-hole states in the molecular reference frame," Phys. Rev. Lett. **105**, 083004 (2010).

[103] L. Fang, M. Hoener, O. Gessner, F. Tarantelli, S. T. Pratt, O. Kornilov, C. Buth, M. Gühr, E. P. Kanter, C. Bostedt, J. D. Bozek, P. H. Bucksbaum, M. Chen, R. Coffee, J. Cryan, M. Glownia, E. Kukk, S. R. Leone, and N. Berrah, "Double core-hole production in $\mathbf{N}_2$: Beating the Auger clock," Phys. Rev. Lett. **105**, 083005 (2010).

[104] S. W. Epp, J. R. Crespo López-Urrutia, G. Brenner, V. Mäckel, P. H. Mokler, R. Treusch, M. Kuhlmann, M. V. Yurkov, J. Feldhaus, J. R. Schneider, M. Wellhöfer, M. Martins, W. Wurth, and J. Ullrich, "Soft x-ray laser spectroscopy on trapped highly charged ions at FLASH," Phys. Rev. Lett. **98**, 183001 (2007).

[105] S. W. Epp, J. R. Crespo López-Urrutia, M. C. Simon, T. Baumann, G. Brenner, R. Ginzel, N. Guerassimova, V. Mäckel, P. H. Mokler, B. L. Schmitt, H. Tawara, and J. Ullrich, "X-ray laser spectroscopy of highly charged ions at FLASH," J. Phys. B **43**, 194008 (2010).

[106] O. Postavaru, Z. Harman, and C. H. Keitel, "High-precision metrology of highly charged ions via relativistic resonance fluorescence," Phys. Rev. Lett. **106**, 033001 (2011).

[107] M. C. Simon, J. R. Crespo López-Urrutia, C. Beilmann, M. Schwarz, Z. Harman, S. W. Epp, B. L. Schmitt, T. M. Baumann, E. Behar, S. Bernitt, R. Follath, R. Ginzel, C. H. Keitel, R. Klawitter, K. Kubiček, V. Mäckel, P. H. Mokler, G. Reichardt, O. Schwarzkopf, and J. Ullrich, "Resonant and near-threshold photoionization cross sections of Fe^{14+}," Phys. Rev. Lett. **105**, 183001 (2010).

[108] S. Suckewer and P. Jaeglé, "X-ray laser: past, present, and future," Laser Physics Letters **6**, 411–436 (2009).

[109] A. M. Kondratenko and E. L. Saldin, Dokl. Akad. Nauk SSSR **249**, 843 (1979).

[110] A. M. Kondratenko and E. L. Saldin, Sov. Phys. Dokl. **24**, 986 (1979).

[111] R. Bonifacio, C. Pellegrini, and L. Narducci, "Collective instabilities and high-gain regime in a free electron laser," Opt. Commun. **50**, 373 – 378 (1984).

[112] A. T. Georges, P. Lambropoulos, and P. Zoller, "Saturation and stark splitting of resonant transitions in strong chaotic fields of arbitrary bandwidth," Phys. Rev. Lett. **42**, 1609–1613 (1979).

[113] G. Vannucci and M. C. Teich, "Computer simulation of superposed coherent and chaotic radiation," Appl. Opt. **19**, 548–553 (1980).

[114] J. Feldhaus, E. L. Saldin, J. R. Schneider, E. A. Schneidmiller, and M. V. Yurkov, "Possible application of X-ray optical elements for reducing the spectral bandwidth of an X-ray SASE FEL," Opt. Commun. **140**, 341 – 352 (1997).

[115] E. L. Saldin, E. A. Schneidmiller, Y. V. Shvyd'ko, and M. V. Yurkov, "X-ray FEL with a meV bandwidth," Nucl. Instrum. Methods Phys. Res., Sect. A **475**, 357 – 362 (2001).

[116] G. Geloni, V. Kocharyan, and E. Saldin, "Scheme for generation of highly monochromatic X-rays from a baseline XFEL undulator," arXiv:1003.2548v1 (2010).

[117] G. Geloni, V. Kocharyan, and E. Saldin, "Cost-effective way to enhance the capabilities of the LCLS baseline," arXiv:1008.3036v1 (2010).

[118] J. Amann, W. Berg, V. Blank, F.-J. Decker, Y. Ding, P. Emma, Y. Feng, J. Frisch, D. Fritz, J. Hastings, Z. Huang, J. Krzywinski, R. Lindberg, H. Loos, A. Lutman, H.-D. Nuhn, D. Ratner, J. Rzepiela, D. Shu, Y. Shvyd'ko, S. Spampinati, S. Stoupin, S. Terentyev, E. Trakhtenberg, D. Walz, J. Welch, J. Wu, A. Zholents, and D. Zhu, "Demonstration of self-seeding in a hard-x-ray free-electron laser," Nature Photonics **6**, 693–698 (2012).

[119] E. Allaria, R. Appio, L. Badano, W. A. Barletta, S. Bassanese, S. G. Biedron, A. Borga, E. Busetto, D. Castronovo, P. Cinquegrana, S. Cleva, D. Cocco, M. Cornacchia, P. Craievich, I. Cudin, G. D'Auria, M. Dal Forno, M. B. Danailov, R. De Monte, G. De Ninno, P. Delgiusto, A. Demidovich, S. Di Mitri, B. Diviacco, A. Fabris, R. Fabris, W. Fawley, M. Ferianis, E. Ferrari, S. Ferry, L. Froehlich, P. Furlan, G. Gaio, F. Gelmetti, L. Giannessi, M. Giannini, R. Gobessi, R. Ivanov, E. Karantzoulis, M. Lonza, A. Lutman, B. Mahieu, M. Milloch, S. V. Milton, M. Musardo, I. Nikolov, S. Noe, F. Parmigiani, G. Penco, M. Petronio, L. Pivetta, M. Predonzani, F. Rossi, L. Rumiz, A. Salom, C. Scafuri, C. Serpico, P. Sigalotti, S. Spampinati, C. Spezzani, M. Svandrlik, C. Svetina, S. Tazzari, M. Trovo, R. Umer, A. Vascotto, M. Veronese, R. Visintini, M. Zaccaria, D. Zangrando,

and M. Zangrando, "Highly coherent and stable pulses from the fermi seeded free-electron laser in the extreme ultraviolet," Nat. Photon. **6**, 699–704 (2012).

[120] R. J. Jones, K. D. Moll, M. J. Thorpe, and J. Ye, "Phase-coherent frequency combs in the vacuum ultraviolet via high-harmonic generation inside a femtosecond enhancement cavity," Phys. Rev. Lett. **94**, 193201 (2005).

[121] C. Gohle, T. Udem, M. Herrmann, J. Rauschenberger, R. Holzwarth, H. A. Schuessler, F. Krausz, and T. W. Hänsch, "A frequency comb in the extreme ultraviolet," Nature **436**, 234–237 (2005).

[122] A. Cingöz, D. C. Yost, T. K. Allison, A. Ruehl, M. E. Fermann, I. Hartl, and J. Ye, "Direct frequency comb spectroscopy in the extreme ultraviolet," Nature **482**, 68–71 (2012).

[123] S. Bernitt, G. V. Brown, J. K. Rudolph, R. Steinbrügge, A. Graf, M. Leutenegger, S. W. Epp, S. Eberle, K. Kubiček, V. Mäckel, M. C. Simon, E. Träbert, E. W. Magee, C. Beilmann, N. Hell, S. Schippers, A. Müller, S. M. Kahn, A. Surzhykov, Z. Harman, C. H. Keitel, J. Clementson, F. S. Porter, W. Schlotter, J. J. Turner, J. Ullrich, P. Beiersdorfer, and J. R. Crespo López-Urrutia, "An unexpectedly low oscillator strength as the origin of the Fe XVII emission problem," Nature **492**, 225–228 (2012).

[124] J. C. Berengut, V. A. Dzuba, V. V. Flambaum, and A. Ong, "Electron-hole transitions in multiply charged ions for precision laser spectroscopy and searching for variations in α," Phys. Rev. Lett. **106**, 210802 (2011).

[125] W. G. Rellergert, D. DeMille, R. R. Greco, M. P. Hehlen, J. R. Torgerson, and E. R. Hudson, "Constraining the evolution of the fundamental constants with a solid-state optical frequency reference based on the ^{229}Th nucleus," Phys. Rev. Lett. **104**, 200802 (2010).

[126] M. C. Kohler, T. Pfeifer, K. Z. Hatsagortsyan, and C. H. Keitel, "Chapter 4 - Frontiers of atomic high-harmonic generation," in "Advances in Atomic, Molecular, and Optical Physics," , vol. 61, P. Berman, E. Arimondo, and C. Lin, eds. (Academic Press, New York, 2012), pp. 159 – 208.

[127] B. W. Adams, C. Buth, S. M. Cavaletto, J. Evers, Z. Harman, C. H. Keitel, A. Pálffy, A. Picón, R. Röhlsberger, Y. Rostovtsev, and K. Tamasaku, "X-ray quantum optics," Journal of Modern Optics **60**, 2–21 (2013).

[128] S.-Y. Zhu and M. O. Scully, "Spectral line elimination and spontaneous emission cancellation via quantum interference," Phys. Rev. Lett. **76**, 388–391 (1996).

[129] P. Zhou and S. Swain, "Ultranarrow spectral lines via quantum interference," Phys. Rev. Lett. **77**, 3995–3998 (1996).

[130] E. Paspalakis and P. L. Knight, "Phase control of spontaneous emission," Phys. Rev. Lett. **81**, 293–296 (1998).

[131] C. H. Keitel, "Narrowing spontaneous emission without intensity reduction," Phys. Rev. Lett. **83**, 1307–1310 (1999).

[132] M. Macovei and C. H. Keitel, "Laser control of collective spontaneous emission," Phys. Rev. Lett. **91**, 123601 (2003).

[133] Z. Ficek and S. Swain, *Quantum Interference and Coherence* (Springer, New York, 2005).

[134] M. Kiffner, M. Macovei, J. Evers, and C. H. Keitel, "Vacuum-induced processes in multilevel atoms," in "Prog. Opt.", , vol. 55, E. Wolf, ed. (Elsevier, 2010), chap. 3, p. 85.

[135] S. P. Hau-Riege, R. A. London, and A. Szoke, "Dynamics of biological molecules irradiated by short x-ray pulses," Phys. Rev. E **69**, 051906 (2004).

[136] W. R. Phillips, I. Ahmad, D. W. Banes, B. G. Glagola, W. Henning, W. Kutschera, K. E. Rehm, J. P. Schiffer, and T. F. Wang, "Charge-state dependence of nuclear lifetimes," Phys. Rev. Lett. **62**, 1025–1028 (1989).

[137] Y. A. Litvinov, F. Bosch, H. Geissel, J. Kurcewicz, Z. Patyk, N. Winckler, L. Batist, K. Beckert, D. Boutin, C. Brandau, L. Chen, C. Dimopoulou, B. Fabian, T. Faestermann, A. Fragner, L. Grigorenko, E. Haettner, S. Hess, P. Kienle, R. Knöbel, C. Kozhuharov, S. A. Litvinov, L. Maier, M. Mazzocco, F. Montes, G. Münzenberg, A. Musumarra, C. Nociforo, F. Nolden, M. Pfützner, W. R. Plaß, A. Prochazka, R. Reda, R. Reuschl, C. Scheidenberger, M. Steck, T. Stöhlker, S. Torilov, M. Trassinelli, B. Sun, H. Weick, and M. Winkler, "Measurement of the β^+ and orbital electron-capture decay rates in fully ionized, hydrogenlike, and heliumlike ^{140}Pr ions," Phys. Rev. Lett. **99**, 262501 (2007).

[138] N. Rohringer and R. Santra, "Resonant Auger effect at high x-ray intensity," Phys. Rev. A **77**, 053404 (2008).

[139] E. P. Kanter, B. Krässig, Y. Li, A. M. March, P. Ho, N. Rohringer, R. Santra, S. H. Southworth, L. F. DiMauro, G. Doumy, C. A. Roedig, N. Berrah, L. Fang, M. Hoener, P. H. Bucksbaum, S. Ghimire, D. A. Reis, J. D. Bozek, C. Bostedt, M. Messerschmidt, and L. Young, "Unveiling and driving hidden resonances with high-fluence, high-intensity x-ray pulses," Phys. Rev. Lett. **107**, 233001 (2011).

[140] C. Buth, R. Santra, and L. Young, "Electromagnetically induced transparency for x rays," Phys. Rev. Lett. **98**, 253001 (2007).

[141] T. E. Glover, M. P. Hertlein, S. H. Southworth, T. K. Allison, J. van Tilborg, E. P. Kanter, B. Krassig, H. R. Varma, B. Rude, R. Santra, A. Belkacem, and L. Young, "Controlling x-rays with light," Nature Physics **6**, 69–74 (2010).

[142] C. Buth and R. Santra, "Theory of x-ray absorption by laser-dressed atoms," Phys. Rev. A **75**, 033412 (2007).

[143] C. Buth and R. Santra, "X-ray refractive index of laser-dressed atoms," Phys. Rev. A **78**, 043409 (2008).

[144] M. B. Gaarde, C. Buth, J. L. Tate, and K. J. Schafer, "Transient absorption and reshaping of ultrafast XUV light by laser-dressed helium," Phys. Rev. A **83**, 013419 (2011).

[145] J. C. Baggesen, E. Lindroth, and L. B. Madsen, "Theory of attosecond absorption spectroscopy in krypton," Phys. Rev. A **85**, 013415 (2012).

[146] M. Wu, S. Chen, K. J. Schafer, and M. B. Gaarde, "Ultrafast time-dependent absorption in a macroscopic three-level helium gas," Phys. Rev. A **87**, 013828 (2013).

[147] C. Ott, A. Kaldun, P. Raith, K. Meyer, M. Laux, J. Evers, C. H. Keitel, C. H. Greene, and T. Pfeifer, "Lorentz meets Fano in spectral line shapes: A universal phase and its laser control," Science **340**, 716–720 (2013).

[148] C. Cohen-Tannoudji, J. Dupont-Roc, and G. Grynberg, *Photons and atoms: introduction to quantum electrodynamics* (Wiley, 1997).

[149] C. J. Foot, *Atomic Physics* (Oxford University Press, 2005).

[150] R. Cowan, *The Theory of Atomic Structure and Spectra* (University of California Press, Berkeley Los Angeles, London, 1981).

[151] H. Goldstein, *Classical Mechanics* (Pearson Education, London, 2002).

[152] E. A. Power and S. Zienau, "Coulomb gauge in non-relativistic quantum electrodynamics and the shape of spectral lines," Phil. Trans. R. Soc. Lond. A **251**, 427–54 (1959).

[153] R. G. Woolley, "Molecular quantum electrodynamics," Phil. Trans. R. Soc. Lond. A **321**, 557–72 (1971).

[154] E. A. Power and T. Thirunamachandran, "On the nature of the Hamiltonian for the interaction of radiation with atoms and molecules: $(e/mc)\boldsymbol{p}\cdot\boldsymbol{A}$, $-\boldsymbol{\mu}\cdot\boldsymbol{E}$, and all that," American Journal of Physics **46**, 370–378 (1978).

[155] A. Messiah, *Quantum Mechanics* (Dover Publications, Mineola, 1999).

[156] J. J. Sakurai, *Modern Quantum Mechanics* (Pearson Education, London, 2006).

[157] K. Blum, *Density Matrix Theory and Applications* (Plenum Press, New York, 1981).

[158] W. Louisell, *Quantum Statistical Properties of Radiation* (Wiley, New York, 1997).

[159] W. R. Johnson, *Atomic Structure Theory: Lectures on Atomic Physics* (Springer, Berlin Heidelberg, New York, 2007).

[160] I. I. Rabi, "Space quantization in a gyrating magnetic field," Phys. Rev. **51**, 652–654 (1937).

[161] F. Bloch and A. Siegert, "Magnetic resonance for nonrotating fields," Phys. Rev. **57**, 522–527 (1940).

[162] R. J. Glauber, "Les Houches 1964 Lecture Notes," in "Quantum Optics and Electronics," , C. DeWitt, A. Blandin, and C. Cohen-Tannoudji, eds. (Gordon and Breach, New York, 1965), Les Houches.

[163] S. M. Cavaletto, C. Buth, Z. Harman, E. P. Kanter, S. H. Southworth, L. Young, and C. H. Keitel, "Resonance fluorescence in ultrafast and intense x-ray free-electron-laser pulses," Phys. Rev. A **86**, 033402 (2012).

[164] J. C. Diels and W. Rudolph, *Ultrashort laser pulse phenomena: fundamentals, techniques, and applications on a femtosecond time scale* (Academic Press, 2006).

[165] A. Corney, *Atomic And Laser Spectroscopy* (Oxford University Press, 2006).

[166] J. H. Eberly, C. V. Kunasz, and K. Wódkiewicz, "Time-dependent spectrum of resonance fluorescence," J. Phys. B **13**, 217 (1980).

[167] L. Young, D. A. Arms, E. M. Dufresne, R. W. Dunford, D. L. Ederer, C. Höhr, E. P. Kanter, B. Krässig, E. C. Landahl, E. R. Peterson, J. Rudati, R. Santra, and S. H. Southworth, "X-ray microprobe of orbital alignment in strong-field ionized atoms," Phys. Rev. Lett. **97**, 083601 (2006).

[168] M. Lax, "Formal theory of quantum fluctuations from a driven state," Phys. Rev. **129**, 2342–2348 (1963).

[169] J. D. Cresser, "Theory of the spectrum of the quantised light field," Physics Reports **94**, 47 – 110 (1983).

[170] D. W. Lindle, P. L. Cowan, R. E. LaVilla, T. Jach, R. D. Deslattes, B. Karlin, J. A. Sheehy, T. J. Gil, and P. W. Langhoff, "Polarization of molecular x-ray fluorescence," Phys. Rev. Lett. **60**, 1010–1013 (1988).

[171] S. H. Southworth, D. W. Lindle, R. Mayer, and P. L. Cowan, "Anisotropy of polarized x-ray emission from molecules," Phys. Rev. Lett. **67**, 1098–1101 (1991).

[172] S. H. Southworth, D. W. Lindle, R. Mayer, and P. L. Cowan, "Anisotropy of polarized x-ray emission from atoms and molecules," Nucl. Instrum. Methods Phys. Res., Sect. B **56-57, Part 1**, 304 – 308 (1991).

[173] R. D. Deslattes, R. E. LaVilla, P. L. Cowan, and A. Henins, "Threshold studies of a multivacancy process in the $K\beta$ region of argon," Phys. Rev. A **27**, 923–933 (1983).

[174] V. Schmidt, *Electron Spectrometry of Atoms Using Synchrotron Radiation* (Cambridge University Press, Cambridge, 1997).

[175] D. R. Hartree, "The wave mechanics of an atom with a non-Coulomb central field. Part I. Theory and methods," Math. Proc. Cambridge Phil. Soc. **24**, 89–110 (1928).

[176] V. Fock, "Näherungsmethode zur Lösung des quantenmechanischen Mehrkörperproblems," Z. Physik **61**, 126–148 (1930).

[177] J. C. Slater, "A simplification of the Hartree-Fock method," Phys. Rev. **81**, 385–390 (1951).

[178] F. Herman and S. Skillman, *Atomic Structure Calculations* (Prentice-Hall, Englewood Cliffs, NJ, 1963).

[179] C. Buth and R. Santra, "FELLA (Free Electron Laser Atomic, Molecular, and Optical Physics Program Package), Version 1.3.0." (2008). With contributions by M. Baertschy, K. Christ, C. H. Greene, H.-D. Meyer, and T. Sommerfeld.

[180] "Los Alamos National Laboratory Atomic Physics Codes, `http://aphysics2.lanl.gov/tempweb`," .

[181] R. D. Cowan, *Theory of Atomic Spectra* (University of California Press, Berkeley, 1981).

[182] C. P. Bhalla, N. O. Folland, and M. A. Hein, "Theoretical K-Shell Auger Rates, Transition Energies, and Fluorescence Yields for Multiply Ionized Neon," Phys. Rev. A **8**, 649–657 (1973).

[183] J. Nordgren, G. Bray, S. Cramm, R. Nyholm, J. Rubensson, and N. Wassdahl, "Soft x-ray emission spectroscopy using monochromatized synchrotron radiation (invited)," Rev. Sci. Instrum. **60**, 1690–1696 (1989).

[184] T. Pfeifer, Y. Jiang, S. Düsterer, R. Moshammer, and J. Ullrich, "Partial-coherence method to model experimental free-electron laser pulse statistics," Opt. Lett. **35**, 3441–3443 (2010).

[185] Y. H. Jiang, T. Pfeifer, A. Rudenko, O. Herrwerth, L. Foucar, M. Kurka, K. U. Kühnel, M. Lezius, M. F. Kling, X. Liu, K. Ueda, S. Düsterer, R. Treusch, C. D. Schröter, R. Moshammer, and J. Ullrich, "Temporal coherence effects in multiple ionization of N_2 via XUV pump-probe autocorrelation," Phys. Rev. A **82**, 041403(R) (2010).

[186] S. M. Cavaletto, Z. Harman, C. Buth, and C. H. Keitel, "X-ray frequency combs from optically controlled resonance fluorescence," arXiv:1302.3141 (2013). Submitted.

[187] C. Buth, F. He, J. Ullrich, C. H. Keitel, and K. Z. Hatsagortsyan, "Attosecond pulses at kiloelectronvolt photon energies from high-order-harmonic generation with core electrons," Phys. Rev. A **88**, 033848 (2013).

[188] M. Natori, M. Matsuzawa, and T. Watanabe, "Dynamic polarizabilities and other dipole properties of helium-like ions," Journal of the Physical Society of Japan **30**, 518–521 (1971).

[189] G. S. Agarwal, "Exact solution for the influence of laser temporal fluctuations on resonance fluorescence," Phys. Rev. Lett. **37**, 1383–1386 (1976).

[190] I. Barth and C. Lasser, "Trigonometric pulse envelopes for laser-induced quantum dynamics," J. Phys. B **42**, 235101 (2009).

[191] V. A. Yerokhin and K. Pachucki, "Theoretical energies of low-lying states of light helium-like ions," Phys. Rev. A **81**, 022507 (2010).

[192] V. S. Popov, "Tunnel and multiphoton ionization of atoms and ions in a strong laser field (keldysh theory)," Physics-Uspekhi **47**, 855 (2004).

[193] A. M. Perelomov, V. S. Popov, and M. V. Terent'ev, "Ionization of atoms in an alternating electric field," Sov. Phys. JETP **23**, 924 (1966).

[194] A. M. Perelomov and V. S. Popov, "Ionization of atoms in an alternating electrical field. iii," Sov. Phys. JETP **25**, 336 (1967).

[195] J. H. Eberly and M. V. Fedorov, "Spectrum of light scattered coherently or incoherently by a collection of atoms," Phys. Rev. A **45**, 4706–4712 (1992).

[196] G. Arfken, H. Weber, and F. Harris, *Mathematical Methods for Physicists: A Comprehensive Guide* (Academic Press, Waltham, Oxford, 2011).

[197] F. I. Gauthey, C. H. Keitel, P. L. Knight, and A. Maquet, "Role of initial coherence in the generation of harmonics and sidebands from a strongly driven two-level atom," Phys. Rev. A **52**, 525–540 (1995).

[198] M. Kiffner, J. Evers, and C. H. Keitel, "Quantum interference enforced by time-energy complementarity," Phys. Rev. Lett. **96**, 100403 (2006).

[199] M. Kiffner, J. Evers, and C. H. Keitel, "Interference in the resonance fluorescence of two incoherently coupled transitions," Phys. Rev. A **73**, 063814 (2006).

[200] I. P. Grant, *Relativistic quantum theory of atoms and molecules*, Springer Series on Atomic, Optical, and Plasma Physics (Springer, New York, Berlin, Heidelberg, 2007).

[201] P. Jönsson, X. He, C. Froese Fischer, and I. P. Grant, "The `grasp2K` relativistic atomic structure package," Comput. Phys. Commun. **177**, 597–622 (2007).

[202] P. Jönsson, G. Gaigalas, J. Bieroń, C. Froese Fischer, and I. P. Grant, "New version: Grasp2K relativistic atomic structure package," Comput. Phys. Commun. **184**, 2197–2203 (2013).

[203] V. Mäckel, R. Klawitter, G. Brenner, J. R. Crespo López-Urrutia, and J. Ullrich, "Laser spectroscopy on forbidden transitions in trapped highly charged Ar^{13+} ions," Phys. Rev. Lett. **107**, 143002 (2011).

[204] N. Rohringer, D. Ryan, R. A. London, M. Purvis, F. Albert, J. Dunn, J. D. Bozek, C. Bostedt, A. Graf, R. Hill, S. P. Hau-Riege, and J. J. Rocca, "Atomic inner-shell x-ray laser at 1.46 nanometres pumped by an x-ray free-electron laser," Nature **481**, 488–491 (2012).

[205] I. Hartl, T. R. Schibli, A. Marcinkevičius, D. C. Yost, D. D. Hudson, M. E. Fermann, and J. Ye, "Cavity-enhanced similariton Yb-fiber laser frequency comb: $3 \times 10^{14}\,\mathrm{W/cm^2}$ peak intensity at 136 MHz," Opt. Lett. **32**, 2870–2872 (2007).

[206] T. R. Schibli, I. Hartl, D. C. Yost, M. J. Martin, A. Marcinkevičius, M. E. Fermann, and J. Ye, "Optical frequency comb with submillihertz linewidth and more than 10 W average power," Nature Photonics **2**, 355–359 (2008).

[207] T. Eidam, S. Hanf, E. Seise, T. V. Andersen, T. Gabler, C. Wirth, T. Schreiber, J. Limpert, and A. Tünnermann, "Femtosecond fiber CPA system emitting 830 W average output power," Opt. Lett. **35**, 94–96 (2010).

[208] A. Ruehl, A. Marcinkevičius, M. E. Fermann, and I. Hartl, "80 W, 120 fs Yb-fiber frequency comb," Opt. Lett. **35**, 3015–3017 (2010).

[209] M. Y. Sander, S. Frolov, J. Shmulovich, E. P. Ippen, and F. X. Kärtner, "10 GHz femtosecond pulse interleaver in planar waveguide technology," Opt. Express **20**, 4102–4113 (2012).

[210] G. Darvasi, C. H. Keitel, and C. Buth. submitted, (2013).

[211] C. Buth, M. C. Kohler, J. Ullrich, and C. H. Keitel, "High-order harmonic generation enhanced by XUV light," Opt. Lett. **36**, 3530–3532 (2011).

[212] A. Derevianko and W. R. Johnson, "Two-photon decay of 2^1S_0 and 2^3S_1 states of heliumlike ions," Phys. Rev. A **56**, 1288–1294 (1997).

[213] S. Chen, M. Wu, M. B. Gaarde, and K. J. Schafer, "Quantum interference in attosecond transient absorption of laser-dressed helium atoms," Phys. Rev. A **87**, 033408 (2013).

[214] Z. Liu, C. Ott, S. M. Cavaletto, Z. Harman, C. H. Keitel, and T. Pfeifer, "Generation of high-frequency combs locked to atomic resonances by quantum phase modulation," arXiv:1309.6335 (2013). Submitted.

[215] S. M. Cavaletto, Z. Harman, C. Ott, C. Buth, T. Pfeifer, and C. H. Keitel, "Broadband high-resolution x-ray frequency combs," (2013). Submitted.

[216] A. Jeffrey and D. Zwillinger, *Table of Integrals, Series, and Products*, Table of Integrals, Series, and Products Series (Elsevier Science, 2007).

[217] "NIST Digital Library of Mathematical Functions," http://dlmf.nist.gov/, Release 1.0.6 of 2013-05-06. Online companion to [218].

[218] F. W. J. Olver, D. W. Lozier, R. F. Boisvert, and C. W. Clark, eds., *NIST Handbook of Mathematical Functions* (Cambridge University Press, New York, NY, 2010). Print companion to [217].

[219] J. H. Eberly and K. Wódkiewicz, "The time-dependent physical spectrum of light," J. Opt. Soc. Am. **67**, 1252–1261 (1977).

[220] X. Y. Huang, R. Tanaś, and J. H. Eberly, "Delayed spectrum of two-level resonance fluorescence," Phys. Rev. A **26**, 892–901 (1982).

[221] J. E. Golub and T. W. Mossberg, "Transient spectra of strong-field resonance fluorescence," Phys. Rev. Lett. **59**, 2149–2152 (1987).

[222] P. Rebernik Ribic and G. Margaritondo, "Status and prospects of x-ray free-electron lasers (X-FELs): a simple presentation," Journal of Physics D: Applied Physics **45**, 213001 (2012).

[223] T. Pfeifer and C. Ott. Private communication.

[224] T. J. Bürvenich, J. Evers, and C. H. Keitel, "Nuclear quantum optics with x-ray laser pulses," Phys. Rev. Lett. **96**, 142501 (2006).

[225] R. Röhlsberger, H.-C. Wille, K. Schlage, and B. Sahoo, "Electromagnetically induced transparency with resonant nuclei in a cavity," Nature **482**, 199–203 (2012).

[226] W.-T. Liao, A. Pálffy, and C. H. Keitel, "Coherent storage and phase modulation of single hard-x-ray photons using nuclear excitons," Phys. Rev. Lett. **109**, 197403 (2012).

[227] G. Geloni, E. Saldin, L. Samoylova, E. Schneidmiller, H. Sinn, T. Tschentscher, and M. Yurkov, "Coherence properties of the European XFEL," New Journal of Physics **12**, 035021 (2010).

[228] N. Rohringer and R. Santra, "X-ray nonlinear optical processes using a self-amplified spontaneous emission free-electron laser," Phys. Rev. A **76**, 033416 (2007).

Acknowledgements

Era già l'ora che volge il disio
ai navicanti e 'ntenerisce il core
lo dí c' han detto ai dolci amici addio;
e che lo novo peregrin d'amore
punge, se ode squilla di lontano
che paia il giorno pianger che si more.

Dante Alighieri, *Commedia, Purgatorio,* Canto VIII, 1–6

Zuerst möchte ich mich bei meinem Doktorvater, Prof. Christoph H. Keitel, dafür bedanken, in seiner Abteilung am Max-Planck-Institut für Kernphysik aufgenommen worden zu sein und von einem freundlichen und anregenden Arbeitsklima profitiert haben zu können. Seine Erfahrung, seine Unterstützung und insbesondere sein Vertrauen sind wertvolle Begleiter während der Jahre der Promotion gewesen.

Meinen Betreuern, Zoltán Harman und Christian Buth, gilt mein Dank dafür, dass sie mir mit ihrem Wissen zur Seite gestanden und mit Beachtung zugehört haben, um ein Projekt zu finden und zu entwickeln, das zu mir am besten passen würde. Ich freue mich darüber, auf zahlreiche Diskussionen und auf ihre gründliche Korrektur meiner Arbeiten und Publikationen gezählt haben zu können.

Ich danke Zoltán Harman insbesondere für seine Bereitschaft, mich jederzeit kurzfristig zu treffen, um meine ständig neuen Fragen zu besprechen, auf die uns meine Doktorarbeit hat stoßen lassen, und für seinen Optimismus, als ich stark daran zweifelte, dass ich je irgendeine Antwort würde finden können.

Christian Buth bin ich besonders dankbar für die Zusammenarbeit am Anfang meiner Promotion und vor allem dafür, dass er trotz der Distanz durch Skype und detaillierte E-Mails mit mir in Verbindung geblieben ist. Bei ihm bedanke ich mich auch dafür, mich zum Argonne-National-Laboratory eingeladen zu haben und sich während meiner Besuche darum gekümmert zu haben, dass ich meinen Aufenthalt genießen konnte.

Ich danke Sandro M. Wimberger für die Zustimmung, der zweite Gutachter dieser Doktorarbeit zu sein.

Für viele hilfreiche Diskussionen möchte ich mich bei Christian Ott und Thomas Pfeifer bedanken, die mir mit ihrem experimentellen Blickwinkel auf die Probleme, an denen wir zusammen gearbeitet haben, geholfen haben, hinter die formale Schönheit einer Formel zu schauen und mithilfe der Intuition das zu ergreifen, was sonst nur durchscheint.

Along with them, I wish to thank also Zuoye Liu for his collaboration in the project we have been working on.

I want to thank again Christian Buth and with him the whole Atomic, Molecular, and Optical Physics Group in the X-ray Science Division at Argonne National Laboratory for their hospitality during my very enjoyable stays in summer 2011 and 2012. In particular, I thank Elliot P. Kanter, Bertold M. Krässig, Antonio Picón, Stephen H. Southworth, and Linda Young for many helpful discussions.

Ein weiterer Experimentalphysiker, mit dem ich mich gefreut habe zu diskutieren und wissenschaftliche Themen zu besprechen, ist José R. Crespo López-Urrutia. Dafür ein großes Dankeschön.

Bei Prof. Carsten Müller möchte ich mich für seine Hilfsbereitschaft während der ersten Monate meiner Promotion bedanken.

Für ihre Zeit und Hilfe bei technischen und organisatorischen Problemen danke ich der Sekretärin unserer Abteilung, Sibel Babacan, und den vielen Systemadministratoren, Peter Brunner, Dominik Hertel und Carsten Pinnow, die während meiner Promotion aufeinander gefolgt sind.

Special thanks go to the proofreaders of my Thesis: Sven Augustin, K. Felix Mackenroth, Norman Neitz, and Matteo Tamburini.

For the nice atmosphere in our office, where the largest part of this thesis arose, I want to thank the many officemates with whom I had the pleasure to share my working days, in particular Nikolay Belov, Qurrat-ul-Ain Gulfam, Omri Har-Shemesh, Huayu Hu, Sebastian Lautz, Sarah J. Müller, Sebastian Meuren, Norman Neitz, Fernando Oster, Oleg D. Skoromnik, and Dominik Wörner.

Dafür, dass sich mein Aufenthalt in Deutschland gänzlich angenehm gestaltete, möchte ich Sven Augustin, K. Felix Mackenroth, Sarah J. Müller, Norman Neitz, Adriana Pálffy-Buß, Omri Har-Shemesh und Anton Wöllert danken. Darüber hinaus ein großes Dankeschön an Cosima Lawall, Juliane Thalheim, Dominic Eicher und Franka Voigt. Insbesondere bei Norman Neitz und Adriana Pálffy-Buß bedanke ich mich für die hoffentlich nicht zu belastende Mitwirkung an der Verbesserung meiner Ausdrucksfähigkeiten im Deutschen.

Tra i molti italiani conosciuti durante questa mia esperienza oltralpe desidero ringraziare in modo particolare Chiara Bertipaglia, Antonella Chiapparino, Massimo Petretich e Matteo Tamburini. Ringrazio inoltre Giorgia Guglielmi e l'ormai perfettamente integrato Alejandro Reyes per i molti momenti casalinghi che ho avuto il piacere di condividere con loro.

Infine, desidero ringraziare i miei genitori e mio fratello Carlo per il loro supporto continuo e incondizionato, senza il quale nulla di tutto ciò sarebbe stato possibile. A loro va in particolare la mia gratitudine perché so quanto costi loro la mia lontananza e so con che fatica tutto ciò venga celato.